

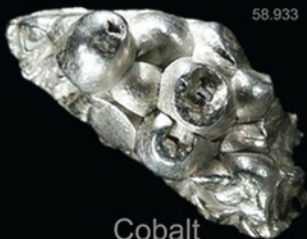






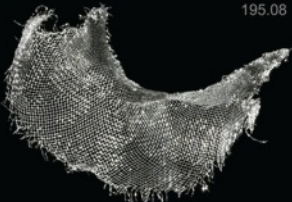

# Конденсированные среды и межфазные границы

РЕЦЕНЗИРУЕМЫЙ НАУЧНЫЙ ЖУРНАЛ

# Condensed Matter and Interphases

PEER-REVIEWED SCIENTIFIC JOURNAL

Том 26, № 2  
Vol. 26, No. 2  
2024

<p>Co 27 58.933</p>  <p>Cobalt</p>	<p>Ni 28 58.693</p>  <p>Nickel</p>	<p>Cu 29 63.546</p>  <p>Copper</p>
<p>Rh 45 102.91</p>  <p>Rhodium</p>	<p>Pd 46 106.42</p>  <p>Palladium</p>	<p>Ag 47 107.87</p>  <p>Silver</p>
<p>Ir 77 192.22</p>  <p>Iridium</p>	<p>Pt 78 195.08</p>  <p>Platinum</p>	<p>Au 79 196.97</p>  <p>Gold</p>



# Condensed Matter and Interphases

## Kondensirovannye sredy i mezhfaznye granitsy

Peer-reviewed scientific journal

Published since January 1999

Periodicity: Quarterly

Volume 26, No. 2, 2024

Full-text version is available in the Russian language on the website: <https://journals.vsu.ru/kcmf>

**Condensed Matter and Interphases** (Kondensirovannye Sredy i Mezhfaznye Granitsy) publishes articles in Russian and English dedicated to key issues of condensed matter and physicochemical processes at interfaces and in volumes.

**The mission of the journal** is to provide open access to the results of original research (theoretical and experimental) at the intersection of contemporary condensed matter physics and chemistry, material science and nanoindustry, solid state chemistry, inorganic chemistry, and physical chemistry, and to share scientific data in the **following sections**: atomic, electron, and cluster structure of solids, liquids, and interphase boundaries; phase equilibria and defect formation processes; structure and physical and chemical properties of interphases; laser thermochemistry and photostimulated processes on solid surfaces; physics and chemistry of surface, thin films and heterostructures; kinetics and mechanism of formation of film structures; electrophysical processes in interphase boundaries; chemistry of surface phenomena in sorbents; devices and new research methods.

**The journal accepts for publication**: reviews, original articles, short communications by leading Russian scientists, foreign researchers, lecturers, postgraduate and undergraduate students.

### FOUNDER AND PUBLISHER:

Voronezh State University

The journal is registered by the Russian Federal Service for Supervision of Communications, Information Technology and Mass Media, Certificate of Registration ПИ № ФС77-78771 date 20.07.2020

The journal is included in the List of peer reviewed scientific journals published by the Higher Attestation Commission in which major research results from the dissertations of Candidates of Sciences (PhD) and Doctor of Science (DSc) degrees are to be published. Scientific specialties of dissertations and their respective branches of science are as follows: 1.4.1. – Inorganic Chemistry (Chemical sciences); 1.4.4. – Physical Chemistry (Chemical sciences); 1.4.6. – Electrochemistry (Chemical sciences); 1.4.15. – Solid State Chemistry (Chemical sciences); 1.3.8. – Condensed Matter Physics (Physical sciences).

The journal is indexed and archived in: Russian Scientific Index Citations, Scopus, Chemical Abstract, EBSCO, DOAJ, CrossRef

Editorial Board and Publisher Office:  
1 Universitetskaya pl., Voronezh 394018  
Phone: +7 (432) 2208445  
<https://journals.vsu.ru/kcmf>  
E-mail: [kcmf@main.vsu.ru](mailto:kcmf@main.vsu.ru)

When reprinting the materials, a reference to the Condensed Matter and Interphases must be cited

The journal's materials are available under the Creative Commons "Attribution" 4.0 Global License



© Voronezh State University, 2024

### EDITOR-IN-CHIEF:

**Victor N. Semenov**, Dr. Sci. (Chem.), Full Professor, Voronezh State University, (Voronezh, Russian Federation)

### VICE EDITORS-IN-CHIEF:

**Evelina P. Domashevskaya**, Dr. Sci. (Phys.–Math.), Full Professor, Voronezh State University, (Voronezh, Russian Federation)

**Polina M. Volovitch**, Ph.D. (Chem.), Associate Professor, Institut de Recherche de Chimie (Paris, France)

### EDITORIAL BOARD:

**Nikolay N. Afonin**, Dr. Sci. (Chem.), Voronezh State Pedagogical University (Voronezh, Russian Federation)

**Vera I. Vasil'eva**, Dr. Sci. (Chem.), Full Professor, Voronezh State University, (Voronezh, Russian Federation)

**Aleksandr V. Vvedenskii**, Dr. Sci. (Chem.), Full Professor, Voronezh State University, (Voronezh, Russian Federation)

**Victor V. Gusarov**, Dr. Sci. (Chem.), Associate Member of the RAS, Ioffe Physical-Technical Institute RAS (St. Petersburg, Russian Federation)

**Vladimir E. Guterman**, Dr. Sci. (Chem.), Full Professor, Southern Federal University (Rostov-on-Don, Russian Federation)

**Boris M. Darinskii**, Dr. Sci. (Phys.–Math.), Full Professor, Voronezh State University, (Voronezh, Russian Federation)

**Vladimir P. Zlomanov**, Dr. Sci. (Chem.), Full Professor, Moscow State University, (Moscow, Russian Federation)

**Valentin M. Levlev**, Dr. Sci. (Phys.–Math.), Full Member of the RAS, Moscow State University, (Moscow, Russian Federation)

**Oleg A. Kozaderov**, Dr. Sci. (Chem.), Associate Professor, Voronezh State University, (Voronezh, Russian Federation)

**Andrey I. Marshakov**, Dr. Sci. (Chem.), Full Professor, Frumkin Institute of Physical Chemistry and Electrochemistry RAS (Moscow, Russian Federation)

**Irina Ya. Mittova**, Dr. Sci. (Chem.), Full Professor, Voronezh State University, (Voronezh, Russian Federation)

**Victor V. Nikonenko**, Dr. Sci. (Chem.), Full Professor, Kuban State University (Krasnodar, Russian Federation)

**Oleg V. Ovchinnikov**, Dr. Sci. (Phys.–Math.), Full Professor, Voronezh State University, (Voronezh, Russian Federation)

**Sergey N. Saltykov**, Dr. Sci. (Chem.), Associate Professor, Novolipetsk Steel (Lipetsk, Russian Federation)

**Vladimir F. Selemenev**, Dr. Sci. (Chem.), Full Professor, Voronezh State University, (Voronezh, Russian Federation)

**Vladimir A. Terekhov**, Dr. Sci. (Phys.–Math.), Full Professor, Voronezh State University, (Voronezh, Russian Federation)

**Evgeny A. Tutov**, Dr. Sci. (Chem.), Associate Professor, Voronezh State Technical University (Voronezh, Russian Federation)

**Pavel P. Fedorov**, Dr. Sci. (Chem.), Full Professor, Prokhorov General Physics Institute RAS (Moscow, Russian Federation)

**Vitaly A. Khonik**, Dr. Sci. (Phys.–Math.), Full Professor, Voronezh State Pedagogical University (Voronezh, Russian Federation)

**Andrey B. Yaroslavtsev**, Dr. Sci. (Chem.), Full Member of the RAS, Kurnakov Institute of General and Inorganic Chemistry RAS (Moscow, Russian Federation)

### INTERNATIONAL MEMBERS OF THE EDITORIAL BOARD:

**Mahammad Babanly**, Dr. Sci. (Chem.), Associate Member of the ANAS, Institute of Catalysis and Inorganic Chemistry ANAS (Baku, Azerbaijan)

**Tiziano Bellezze**, Dr. Sci. (Chem.), Marche Polytechnic University (Ancona, Italy)

**Mane Rahul Maruti**, Ph.D. (Chem.), Shivaji University (Kolhapur, India)

**Nguyen Anh Tien**, Ph.D. (Chem.), Associate Professor, University of Pedagogy (Ho Chi Minh City, Vietnam)

**Vladimir V. Pankov**, Dr. Sci. (Chem.), Full Professor, Belarusian State University (Minsk, Belarus)

**Fritz Scholz**, Dr. Sci., Professor, Institut für Biochemie Analytische Chemie und Umweltchemie (Greifswald, Germany)

**Mathias S. Wickleder**, Dr. Sci., Professor, University of Cologne (Cologne, Germany)

**Vladimir Sivakov**, Dr. rer. nat., Leibniz Institute of Photonic Technology (Jena, Germany)

### EXECUTIVE SECRETARY:

**Vera A. Logacheva**, Cand. Sci. (Chem.), Voronezh State University, (Voronezh, Russian Federation)

## CONTENTS

## Review

*Lavlinskaya M. S., Sorokin A. V., Holyavka M. G., Zuev Yu. F., Artyukhov V. G.*  
Stabilization of food emulsion by polysaccharides and protein-polysaccharide complexes: a short review

## Original articles

*Aliyev I. I., Mamedov E. I., Yusubov F. V., Masieva L.F., Gashimov Kh. M.*  
Physicochemical study of phase formation in the  $Sb_2S_3$ - $Cr_2Te_3$  system

*Artamonova O. V., Shvedova M. A.*  
Study of the processes of formation of the structure and strength gain of nanomodified cement systems during long-term hardening

*Belyanskaya I. A., Bocharnikova M. Yu., Murtazin M. M., Grushevskaya S. N., Kozaderov O. A., Vvedensky A. V.*  
Photoelectrochemical activity of oxide films on silver-palladium alloys in an alkaline solution

*Brezhnev N. Yu., Dorokhin M. V., Zavrazhnov A. Yu., Kolyshkin N. A., Nekrylov I. N., Trushin V. N.*  
High-temperature gallium sesquisulfides and a fragment of the  $T$ - $x$  diagram of the Ga – S system with these phases

*Gannova E. A., Grechkina M. V., Semenov V. N., Lukin A. N., Ivkov S. A., Samofalova T. V.*  
Deposition of lead sulfide films from “ $Pb(CH_3COO)_2 - N_2H_4CS$ ” aqueous solutions and their properties

*Ermakova Yu. A., Fedorov P. P., Voronov V. V., Batygov S. Kh., Kuznetsov S. V.*  
X-ray luminescence of  $Sr_{0.925-x}Ba_xEu_{0.075}F_{2.075}$  nanopowders

*Zartsyn I. D., Vvedensky A. V., Bobrinskaya E. V., Kozaderov O. A.*  
Coupling of anode reactions in the process of electrooxidation of glycine anion on gold

*Maskaeva L. N., Lysanova M. A., Lipina O. A., Voronin V. I., Kravtsov E. A., Pozdin A. V., Markov V. F.*  
Structural, optical, and photocatalytic properties of dispersions of CuS doped with  $Mn^{2+}$  and  $Ni^{2+}$

*Othman K. A., Azeez Y. H., Omer R. A., Kareem R. O.*  
Theoretical exploration of halogenated anthracene derivatives: unraveling electronic and molecular insights

187 *Petukhov I. V., Kichigin V. I., Kornilitsyn A. R., Yakimov A. S.*  
The influence of benzoic acid moisture on the proton exchange process in lithium niobate crystals

197 *Polkovnikov I. S., Panteleeva V. V., Shein A. B.*  
Anodic dissolution and passivation of manganese monosilicide in fluoride-containing sulfuric acid solutions

204 *Fedorov P. P., Volchek A. A., Voronov V. V., Alexandrov A. A., Kuznetsov S. V.*  
Stabilization of the  $Ba_4Y_3F_{17}$  phase in the NaF-BaF<sub>2</sub>-YF<sub>3</sub> system

213 *Khamaganova T. N.*  
Synthesis and characterization of lead and cadmium hexaborates doped with  $Cr^{3+}$

225 *Chetverikova A. G., Makarov V. N., Kanygina O. N., Seregin M. M., Yudin A. A.*  
The synergy of transformation of isomorphous phyllosilicate structures

238 *Chizhova E. A., Marozau M. V., Shevchenko S. V., Klyndyuk A. I., Zhuravleva Ya. Yu., Kononovich V. M.*  
Structure and electrical transport properties of cation-deficient derivatives of layered neodymium–barium ferrocuprocobaltite

247 *Shaposhnik A. V., Zvyagin A. A., Ryabtsev S. V., Dyakonova O. V., Vysotskaya E. A.*  
Synthesis and sensory properties of tungsten (VI) oxide-based nanomaterials

## Short communication

253 *Dobryden S. V., Akberova E. M., Mamonov D. R., Bepalova Ya. R., Vasil'eva V. I.*  
Influence of the particle size of sulfonated cation exchange resin on the physicochemical properties and surface morphology of MK-40 heterogeneous membranes

265 *Mashkina E. S.*  
 $1/f^2$  noise as a precursor of structural reconstructions near the melting point of crystalline materials with different types of chemical bonds



## Review

Review article

<https://doi.org/10.17308/kcmf.2024.26/11933>

## Stabilization of food emulsion by polysaccharides and protein-polysaccharide complexes: a short review

M. S. Lavlinskaya<sup>1</sup>, A. V. Sorokin<sup>1</sup>, M. G. Holyavka<sup>1,2,✉</sup>, Yu. F. Zuev<sup>3</sup>, V. G. Artyukhov<sup>1</sup><sup>1</sup>Voronezh State University,  
1 Universitetskaya pl., Voronezh 394018, Russian Federation<sup>2</sup>Sevastopol State University,  
33 Studencheskaya str., Sevastopol 299053, Russian Federation<sup>3</sup>Kazan Institute of Biochemistry and Biophysics, Federal Research Center  
“Kazan Research Center of Russian Academy of Science”  
2/31 Lobachevskiy str., Kazan 420111, Russian Federation**Abstract**

Emulsions are heterogeneous systems consisting of two immiscible liquids, widely used in the food industry as the basis for some products (mayonnaise, sauces, etc.) and components for the production of functional food products containing systems for targeted delivery of biologically active substances (vitamins, nutraceuticals, flavonoids, etc.). From a thermodynamic point of view, emulsions are unstable systems with excessive surface energy; therefore, they are characterized by rapid destruction through phase separation. For the solution to this problem, emulsifiers are used, amphiphilic molecules of various natures that reduce surface tension, i.e., possess surface activity. However, most of these stabilizers are synthetic and toxic products, which significantly limits their use in the food industry. Natural biopolymers, such as polysaccharides and proteins, as well as their complexes, are amphiphilic macromolecules that combine both polar and hydrophobic fragments, have surface-active properties, low toxicity and excellent biocompatibility, thus they can be considered as promising stabilizers for food emulsions. A special place among polysaccharides is occupied by chitosans and alginates, which, in addition to other advantages mentioned above, are accessible and cheap materials.

The purpose of this work was a brief overview of the prospects for using chitosan, sodium alginate and protein-polysaccharide complexes as stabilizers for emulsions and foams for food application. The article discusses the possibility of using chitosan, sodium alginate, propylene glycol alginate, as well as various protein-polysaccharide complexes as stabilizers for heterogeneous food systems, foams and emulsions, which are the basis of many food products. In addition, special attention is paid to the prospects for the introduction of polysaccharide-based emulsifiers into industrial production and the problems that must be solved for the successful development of emulsions stabilized by biopolymers, which are the basis for the creation of food products, are discussed.

**Keywords:** Chitosan, Sodium Alginate, Protein-Polysaccharide Complexes, Food Emulsion, Stabilization**Funding:** The work was funded by Russian Science Foundation, project No. 23-64-10020.**For citation:** Lavlinskaya M. S., Sorokin A. V., Holyavka M. G., Zuev Yu. F., Artyukhov V. G. Stabilization of food emulsion by polysaccharides and protein-polysaccharide complexes: a short review. *Condensed Matter and Interphases*. 2024;26(2): 187–196. <https://doi.org/10.17308/kcmf.2024.26/11933>**Для цитирования:** Лавлинская М. С., Сорокин А. В., Холявка М. Г., Зувев Ю. Ф., Артюхов В. Г. Стабилизация пищевых эмульсий полисахаридами и белок-полисахаридными комплексами: краткий обзор. *Конденсированные среды и межфазные границы*. 2024;26(2): 187–196. <https://doi.org/10.17308/kcmf.2024.26/11933>✉ Marina G. Holyavka, e-mail: [holyavka@rambler.ru](mailto:holyavka@rambler.ru)

© Lavlinskaya M. S., Sorokin A. V., Holyavka M. G., Zuev Yu. F., Artyukhov V. G., 2024



The content is available under Creative Commons Attribution 4.0 License.

## 1. Introduction

Emulsions, which are heterogeneous disperse systems, usually consist of two immiscible liquids, where one of them, the dispersed phase, is distributed in the form of droplets in the other, the continuous phase [1]. The use of emulsion systems is widespread in the food industry, for example, to improve the flavor characteristics of products, protect and deliver biologically active substances, and they are also the basis of some food products, such as mayonnaise, sauces, and creams [2].

The main problem that arises in the preparation and practical use of emulsions is their thermodynamic instability, expressed as destabilization and phase separation [3]. The addition of emulsifiers with surfactant and/or thickening properties ensures the formation of a stable emulsion. Now, synthetic surfactants are widely used to stabilize emulsions; however, their use can have a negative effect on the organism of consumers [4]. Thus, the possible binding of anionic surfactants to proteins, enzymes, and phospholipid membranes can lead to changes in the structure of human proteins and the dysfunction of enzymes and phospholipid membranes [5]. According to cytotoxicity tests, nonionic surfactants have fewer toxic effects than cationic, anionic and amphoteric surfactants, while the toxicity of cationic surfactants is the highest [6]. Therefore, replacing synthetic surfactants with biocompatible amphiphilic compounds is a key point in expanding the scope of application of emulsions in the creation of functional foods.

The use of natural polymers such as proteins, polysaccharides, or their complexes as emulsifiers and/or stabilizers of food emulsions appears to be a promising approach to obtain highly digestible products [3]. The most common emulsifiers currently used in the food industry are a mixture of a low molecular weight surfactant, a natural amphiphilic polymer and an auxiliary co-emulsifier [7]. Polysaccharides such as pectin, various gums, and galactomannans are used as amphiphilic polymers. [8, 9]. The choice of polysaccharide as a natural component is due to the fact that, compared to protein, the stabilizer of most emulsions of natural origin, polysaccharides form a more voluminous

hydration layer, leading to the increased stability of emulsions due to the structural factor [10]. In addition, the low digestibility of polysaccharides in the gastrointestinal tract slows down the rate of release of biologically active substances [11].

Thus, emulsions currently used in the food industry based on polysaccharides are multicomponent mixtures containing various synthetic low-molecular compounds. Therefore, the search for new alternative surfactants is an urgent task for the modern food industry, aimed at creating functional food products that combine not only energy value, but also biologically active additives. Promising polymers are chitosans and alginates, polysaccharides of marine origin, solutions of which have sufficient viscosity to stabilize two-component emulsion systems. At the same time, the use of protein-polysaccharide complexes allows combining the properties of both components of the system, regulating both the rheological and surface-active properties of the system and the affinity for biologically active substances, expanding the range of functional components (vitamins, antioxidants, flavonoids, etc.), implemented into the final product.

The purpose of this work was a brief overview of the prospects for using chitosan, sodium alginate, and protein-polysaccharide complexes as stabilizers for emulsions and foams for food use.

## 2. Use of chitosan, alginates and protein-polysaccharide complexes as emulsifiers

### 2.1. Chitosan and its use as a stabilizer for food emulsions

Chitosan is a randomized copolymer of D-glucosamine and N-acetyl-D-glucosamine, interconnected by 1,4- $\beta$ -glycosidic bonds, is a product of deacetylation of the natural polymer chitin - poly-N-acetyl-D-glucosamine, one of the most common natural polysaccharide, found in the shells of crustaceans and the fungus cell walls [12]. Significant scientific and practical interest in chitin and chitosan is due to their unique properties such as biocompatibility, low toxicity, biodegradability, and high sorption capacity for heavy metals and radionuclides [13].

The properties of chitosan are significantly influenced by its molecular weight (MW), which for unmodified polymers obtained from natural



chitin is in the range of 2–1000 kDa. Another equally important parameter that determines the ability of chitosan to dissolve in acidic media is the degree of deacetylation (DD). For a polysaccharide with a DD higher than 55 %, the dissolution in a 1% acetic acid solution is typical. Solubility is due to the protonation of the primary amino group at the C-2 position of the D-glucosamine unit; thus, in an acidic medium, chitosan is converted into a polycation, which is a rare phenomenon for natural polysaccharides [13].

The polymer is limitedly soluble in water; this is determined by the degree of deacetylation and the molecular weight. According to literature data, chitosan with an MW of less than 50 kDa and a DD of more than 80% is soluble at acidic and neutral pH values, and with a DD of more than 55% it is soluble at a pH below 6.5 ( $pK_a$  for chitosan) regardless of the molecular weight [13].

The diverse biological activity of chitosan, along with its safety for humans, determines the widespread use of this polysaccharide in the food industry. The antioxidant and antimicrobial activity of chitosan, as well as its ability to interact with various compounds [14–16], allow it to be used for the development of “smart packaging” that increases the shelf life of food products; its high emulsifying ability allows to replace synthetic surfactants in food technologies. The earliest mention of the use of chitosan in the food industry in patent data dates back to 1956: in a patent, chitosan hydrochloride was used as a modifying agent in the preparation and creation of chewing gum [13].

Chitosan is an effective emulsifier for stabilizing heterogeneous oil-in-water systems. The polysaccharide increases the viscosity of the dispersed phase, complicating the diffusion of dispersed particles and reducing the rate of droplet aggregation. In addition, the positively charged amino groups make chitosan an amphiphilic surfactant polymer. Chitosan can be used as the only emulsifier; however, the resulting emulsions are reversible due to sensitivity to pH. In an acidic media with  $pH < pK_a$  protonated chitosan forms polyelectrolyte complexes (PEC), interacting with the carbonyl groups of triglycerides, and in the case of increasing pH to values above  $pK_a$  PEC destruction and loss of emulsifying ability occurs. With increasing pH, the solubility of chitosan

decreases, and the emulsion remains stable due to the oil phase droplets adsorbed on the chitosan particles. With a reverse increase in the acidity of the medium, chitosan transforms into a soluble form, desorbing dispersed oil droplets, and the emulsion reversibly stratifies [17]. The emulsifying ability of chitosan largely depends on the degree of deacetylation and molecular weight: it increases for low-molecular chitosans at DD of less than 60% and more than 86%, while at DD values from 65 to 77% these properties significantly depend on the concentration of the polysaccharide [18]. In a majority of experimental studies on the use of chitosan as an emulsifier, it was considered as a component of complex compositions containing other surfactants. The presence of both chitosan and protein emulsifiers makes the heterogeneous system more stable. Using a mixture of chitosan with soy protein isolate can improve the digestibility and stability of emulsified carotenoids [19]. A complex containing chitosan modified with  $\beta$ -lactoglobulin fibers stabilizes fish oil emulsion in water [20]. It has also been shown that stable Pickering emulsions, emulsions in which solid particles containing corn oil act as a stabilizer, are formed when the polyelectrolyte complex of chitosan and gelatin is used as an emulsifier [21]. The ability of chitosan to form polyelectrolyte complexes in aqueous solutions can be used to increase the stability of easily degradable compounds, such as carotenoids [22] and anthocyanins [23].

## 2.2. Alginates and their use for stabilization of food emulsions

Sodium alginate, the sodium salt of alginic acid, is a recognized food ingredient widely used in the production of functional foods. As a food ingredient, the use of alginate is based on three main properties: the ability to form thick solutions, gelation, and film formation. The considered polysaccharide is widely used for the production of many new functional food products, such as food jelly, restructured meat, packaging and protective materials for packaged, sliced, or prepared fruits, vegetables, etc. In addition, new applications of sodium alginate may arise after its chemical, physical and biological modifications, leading to the production of derivatives with the required functional properties.

Sodium alginate is a polysaccharide isolated from brown algae, where it occurs as a component of the cell wall, performing structural functions similar to carrageenans and agar [24]

Being a polymeric acid, alginate consists of 1,4-linked  $\alpha$ -L-guluronic acid (G-units) and  $\beta$ -D-mannuronic acid (M-units) residues. These two acidic residues differ greatly in stereochemistry at the C-5 atom. Alginates obtained from different algae species differ in the content of G- and M-units, present in the polymer chain in the form of GG, MM and MG/GM blocks in different ratios, which leads to differences in the physical properties of alginate gels [25] and the characteristics of alginate-based products [24].

The wide practical use of alginate is based on its three main properties. Firstly, it is the ability to increase the viscosity of aqueous solutions. The second is the ability to turn into a gel when salts of divalent cations of various metals are added [25, 26] to an aqueous solution of sodium alginate. Unlike carrageenan or agar gels, temperature changes are not required for the formation of a heat-stable alginate gel, which saves not only energy, but also protects biologically active substances from thermal destruction. The third practically significant property of sodium alginate is the ability to form films and fibers. In addition, the unique structure of this polymer is biocompatible [27].

As a natural water-soluble polymer, alginate forms viscous aqueous solutions. The thickening properties of alginate are commonly used in the production of jams, marmalades and fruit sauces since the interactions between alginate and pectin are reversible upon heating and provide a higher viscosity than either component alone. Alginates are also used to thicken desserts and sauces such as mayonnaise. The use of alginate alone or in combination with other thickeners improves the organoleptic characteristics of a number of low-fat foods. The hydrophilic nature of alginate helps to retain water and improves the texture of food, resulting in improved food acceptance by consumers [28].

As a gelling agent, alginate forms stable gels over a wide temperature range and at low pH values, which can be used in the food industry. The introduction of alginates into the formulation of culinary creams provides

resistance to freezing/thawing and reduces the separation of solid and liquid components. In ice cream, alginate is often used in combination with other hydrocolloids for thickening and stabilization, which allows controlling the viscosity of the product, increasing resistance to heat shock, and reducing shrinkage and ice crystal formation. In addition, alginate is widely used in the creation of artificial products, for example, an analogue of fish caviar [28].

As an emulsifier in industry, it is currently not being proposed to use alginic acid or its salt, but a chemical modification product, propylene glycol alginate (PGA) (Fig. 1). This compound is an esterified alginate derivative, widely used in the food and beverage industry. PGA was first obtained by Kelco in 1949 [29].

Since in this compound the carboxyl group of alginic acid is substituted by propylene glycol ether, PGA dissolves in an acidic medium up to pH 3-4, under conditions under which sodium alginate precipitates as alginic acid. Resistance to acidic conditions and to the ionic strength of solution makes propylene glycol alginate a valuable component in foods and beverages with high acidity or divalent metal ion content. In addition, PGA also has high lipophilicity and emulsifying ability due to the propylene glycol moiety contained in its molecules.

The addition of 0.1% propylene glycol alginate increases the colloidal stability of fruit and vegetable juices without compromising their taste

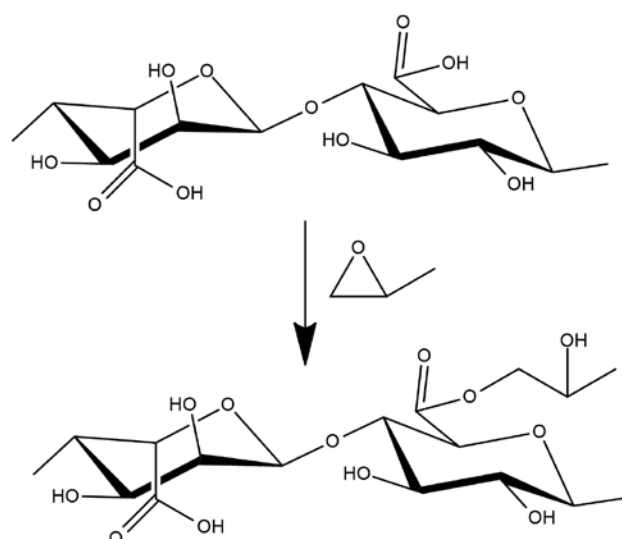


**Fig. 1.** Scheme of the propylene glycol alginate synthesis

and composition. Due to the high emulsifying characteristics of propylene glycol alginate, it is possible to obtain concentrates and juices enriched with dry substances (pulp, etc.), both hydrophilic and lipophilic, which has a beneficial effect on the consumer characteristics of the final product [28].

In the literature there is also information about the use of propylene glycol alginate in a mixture with some other polysaccharides (carboxymethyl cellulose, gums, etc.) as a stabilizer for protein drinks, beer foam, and soy milk [28]. It is noted that the required amount of stabilizer does not exceed 0.5%, out of which more than 60% is propylene glycol alginate, which does not affect the taste and consistency of the final product.

In addition, propylene glycol alginate has proven itself as a stabilizer for yoghurt with fruit fillings. Due to the acidic pH, the choice of stabilizers is quite limited, but in addition to maintaining high system uniformity and resistance to separation, the emulsifier provides a marketable appearance to the product [28].

The presence of hydrophobic fragments in the macromolecules of propylene glycol alginate, the latter acts as an effective stabilizer for salad dressings, improves the external and organoleptic characteristics of bread and the texture of pasta, reducing the pasta fragility [28, 30].

### **2.3. Stabilization of food emulsions and foams with protein-polysaccharide complexes**

Protein-polysaccharide complexes combine the physicochemical and functional properties of their constituent macromolecules and, accordingly, hydrophobic and hydrophilic properties. Consequently, they can be successfully used as agents stabilizing the air/water or oil/water interfaces in complex food systems [31].

Schmitt et al. [32] studied the surfactant properties at the air/water interface of  $\beta$ -lactoglobulin/acacia gum complexes prepared at pH 4.2 and a component ratio of 2:1 and compared them with the behavior of  $\beta$ -lactoglobulin. The surface activity of the complexes was similar for the value corresponding to the protein; however, the complexes formed stronger viscoelastic films with a thickness of about 250 Å at the interface. As a result, the gas permeability of films obtained

from associates was lower compared to films from native  $\beta$ -lactoglobulin. In addition, by reducing the rate of aggregation of air bubbles, the complexes stabilized water-air foams. The results obtained were used to formulate complex food products, such as fruit ices and sorbets, for which the stability of air bubbles in the foam correlates with improved organoleptic parameters of the product. Complexes of whey protein isolate and acacia gum exhibit similar properties, which allows to use them for the replacement of animal gelatin when creating vegetarian foods [33].

Complexes based on  $\beta$ -lactoglobulin and pectins are also used to stabilize the air/water interface [34]. In this case, the charge density of pectin, i.e. the degree of its methylation and the ratio of components determine the size of the resulting complexes and, consequently, their surface activity. The viscoelastic properties of the air/water interface are determined either by the adsorption of the complex or by the sequential adsorption of the components. In the latter case, the formation of viscoelastic films was observed. A study of the structure of the resulting films showed that both obtained samples contain a dense layer near the air/water interface, which probably consists of  $\beta$ -lactoglobulin. However, the thickness of the film obtained with sequentially adsorbed components is higher than for adsorbed complexes. It should be noted that associates based on ovalbumin and pectin or  $\beta$ -lactoglobulin and carboxylated pullulan also exhibit surface-active properties at the water-air interface and can be used to stabilize foam. It has been shown that napin, a protein isolated from rapeseed flour, forms complexes with pectins, which also stabilize aqueous foams and have a higher surface activity compared to the native protein [35].

Emulsions, widely used in the food industry, can also be stabilized with protein-polysaccharide complexes. If the complex is formed during the emulsification step, a mixed emulsion is produced [31]. There is also a layer-by-layer emulsion stabilization technique: in this case, the primary emulsion is stabilized by protein, and then a polysaccharide dispersion is added, inducing interfacial complexation, leading to the formation of so-called bilayer emulsions [36]. This approach is most commonly used on an industrial scale because it produces stable emulsions for a wide



range of compounds. A study of the rheological behavior of the sodium caseinate-dextran sulphate complex showed that the resulting interfacial layers at the interface are much more viscoelastic in the case of mixed emulsions [37]. Interestingly, the resulting emulsions showed different pH stability, especially in an acidic medium: mixed emulsions turned out to be much more resistant to flocculation compared to double-layer emulsions. These results have practical implications for the *in vivo* control of lipolysis. Ducel et al [38] reported high surface activity in an oil/water system for complexes of pea globulin or  $\alpha$ -gliadin with acacia gum. The resulting films were characterized by a long relaxation time and high elasticity. In addition, complexes obtained at a lower pH stabilize emulsions more effectively due to having a higher spreadability on the surface of oil droplets.

Cho and McClements [39] emphasized the importance of controlling the ratio of protein to polysaccharide and the concentration of the latter to ensure the colloidal stability of a bilayer emulsion obtained in the presence of a  $\beta$ -lactoglobulin-pectin complex at pH 3.5. Too low (<0.02%) or high (>0.1%) pectin content led to the formation of an unstable emulsion due to flocculation. Another study showed that the presence of 100 mM NaCl and  $\beta$ -lactoglobulin/citrus pectin complex produced more stable emulsions at pH 3–4 compared to emulsions stabilized by  $\beta$ -lactoglobulin alone. This is explained by the fact that in the presence of an electrolyte, shielding of the interfacial charge is achieved [40]. Some other protein-polysaccharide complexes ( $\beta$ -lactoglobulin with alginate,  $\iota$ -carrageenan or acacia gum) have been used to obtain acid-resistant bilayer emulsions and for industrial beverage production [41, 42].

The use of polycationic chitosan allows obtaining stable emulsions based on whey protein isolate at pH 6.0 [43]. As with other described systems, the ratio of protein and polysaccharide in the complex used plays an important role in stabilization. Interestingly, such systems form at a much lower pH (around 3.0) and can reduce surface tension as well as pure proteins. Stable concentrated emulsions containing up to 40% rapeseed oil can be obtained using a wide range of biopolymer concentrations ranging from 3.8

to 11.2%, which allows additional control of the volumetric viscosity of the resulting product. The stability of an emulsion containing 15% sunflower oil, stabilized with whey protein isolate, increases when using a complex of chitosan and acacia gum at pH 3.0. The use of the complex leads to the formation of monodisperse droplets, gel-like emulsions or clusters of oil droplets, depending on the ratio of chitosan to acacia gum [44].

A study of the emulsifying properties of a complex of whey protein isolate and carboxymethyl cellulose revealed a dependence on the protein/polysaccharide ratio for heterogeneous systems containing 10 and 20% oil fraction. It should be noted that the use of these complexes allows obtaining heat-stable emulsions, which is not observed for the stabilization with pure protein [45].

Complexes of soy protein isolate and hydrophobically modified pectin stabilize emulsions at pH 5.5. It has also been shown that protein-polysaccharide complexes are capable of stabilizing the outer interface of W/M/W emulsions obtained at pH  $\leq$  6.0 [45].

### 3. Problems and prospects for using polysaccharides for the stabilization of food emulsions

The complex compositions of food systems determine the high demands placed on emulsifiers, among which health and the environment safety, as well as the ability to maintain emulsifying properties during food processing, are especially important. Researchers proposing polysaccharides for the stabilization of emulsions are faced with problems of their interaction with other components of systems (electrostatic interactions with salts and proteins, the formation of hydrogen bonds with other macromolecules, hydrophobic interaction with polyphenols, etc.), and they are also subject to thermal destruction as a result of processing food products. Despite the fact that the principles of the influence of external factors on the emulsifying properties of polysaccharides seem to have already been finally established, the significantly different molecular structure of polysaccharides leads to significant variations in their emulsifying properties. Therefore, in the case of using a new, previously undescribed polysaccharide

as a food emulsifier, a full investigation of its colloidal chemical characteristics is required. In addition, there is virtually no information in the literature on changes in the emulsifying properties of polysaccharides during food processing (thermal or non-thermal), as well as on the molecular mechanisms of these changes. Thus, the introduction of natural polysaccharides as food emulsifiers is undoubtedly a labor-intensive task.

Currently, emulsion systems obtained using polysaccharides as emulsifiers are used mainly to create functional foods capable of targeted delivery and the stabilization of active substances, as well as to study the mechanisms of their action, release, digestion, absorption, and transportation. Therefore, the development of a functional product should also include many stages of research, such as determining the structural characteristics and interfacial behavior of the polysaccharide, emulsion characteristics (stability, droplet size, etc.), as well as studying the kinetics of metabolism and the bioavailability of released biologically active substances. The result of solving these problems can be used to create emulsion systems that could specifically deliver the optimal amount of biologically active substances, protecting them from destruction during movement through the gastrointestinal tract [31].

#### 4. Conclusion

Thus, polysaccharides, in particular chitosan and alginic acid derivatives, as well as protein-polysaccharide complexes, are promising for the development of multifunctional emulsion systems capable of not only maintaining the stability of a heterogeneous system for a long time, but also giving them functional properties, for example, as nano- and microcontainers for biologically active substances. The introduction of polysaccharide-based stabilizers into the production of food is difficult due to the labor-intensive processes for creating such systems. However, the fact that sodium alginate and chitosan are already successfully used in food technology as thickeners and components for “smart” and environmentally friendly food packaging increases the potential for these polysaccharides to find early use in other sectors of the food industry.

#### Contribution of the authors

The authors contributed equally to this article.

#### Conflict of interests

The authors declare that they have no known competing financial interests or personal relationships that could have influenced the work reported in this paper.

#### References

1. Koroleva M. Y., Yurtov E. V. Pickering emulsions: structure, properties and the use as colloidosomes and stimuli-sensitive emulsions. *Russian Chemical Reviews*. 2022;91(5): RCR5024. <https://doi.org/10.1070/RCR5024>
2. Bagale U., Kalinina I. V., Naumenko N. V., Kadi Ya. A. M., Malinin A. V., Tsaturov A. V. The possibilities of using double emulsions in the food industry. Part 2: formation of food systems of a new format. *Bulletin of South Ural State University, Series “Food and Biotechnology”*. 2023;11(1): 27–34. (in Russ.). <https://doi.org/10.14529/food230103>
3. Stuzhuk A. N., Gritskova I. A., Gorbato P. S., Shkol'nikov A. V., Kuznetsov A. A. Influence of dispersion conditions and nature of the emulsifier on the dispersity and stability of artificial polymer suspensions based on polyetherimide. *Russian Chemical Bulletin*. 2022;71(2): 382–388. <https://doi.org/10.1007/s11172-022-3423-4>
4. Nushtaeva A., Vilkova N. G. Hydrophobization of silica particles with various cationic surfactants. *Izvestiya Vysshikh Uchebnykh Zavedenii. Seriya Khimiya i Khimicheskaya Tekhnologiya (ChemChemTech)*. 2021;64(3): 41–45. <https://doi.org/10.6060/ivkkt.20216403.6321>
5. Paciello S., Russo T., De Marchi L., ... Freitas R. Sub-lethal effects induced in *Mytilus galloprovincialis* after short-term exposure to sodium lauryl sulfate: Comparison of the biological responses given by mussels under two temperature scenarios. *Comparative Biochemistry and Physiology Part C: Toxicology & Pharmacology*. 2023;70: 109644. <https://doi.org/10.1016/j.cbpc.2023.109644>
6. Han W., Long W., Peng L., Zhang W., Shi B. Effect of nonionic and anionic surfactant on ecotoxicity and micellization behaviors of dodecyl trimethyl ammonium bromide (DTAB). *Colloids and Surfaces A: Physicochemical and Engineering Aspects*. 2023;671: 131588. <https://doi.org/10.1016/j.colsurfa.2023.131588>
7. Amiri-Rigi A., Kesavan Pillai S., Naushad Emmambux M. Development of hemp seed oil nanoemulsions loaded with ascorbyl palmitate: Effect of operational parameters, emulsifiers, and wall materials. *Food Chemistry*. 2023;400: 134052. <https://doi.org/10.1016/j.foodchem.2022.134052>



8. Feng S., Guo Y., Liu F., ... Zhang Y. The impacts of complexation and glycosylated conjugation on the performance of soy protein isolate gum Arabic composites at the O/W interface for emulsion based delivery systems. *Food Hydrocolloids*. 2023;135: 108168. <https://doi.org/10.1016/j.foodhyd.2022.108168>
9. Niu H., Hou K., Chen H., Fu X. A review of sugar beet pectin stabilized emulsion: Extraction, structure, interfacial self assembly and emulsion stability. *Critical Reviews in Food Science and Nutrition*. 2022;64(3): 852–872. <https://doi.org/10.1080/10408398.2022.2109586>
10. Lin J., Guo X., Ai C., Zhang T., Yu S. Genipin crosslinked sugar beet pectin whey protein isolate/bovine serum albumin conjugates with enhanced emulsifying properties. *Food Hydrocolloids*. 2020;105: 105802. <https://doi.org/10.1016/j.foodhyd.2020.105802>
11. Anal A. K., Shrestha S., Sadiq, M. B. Biopolymeric based emulsions and their effects during processing, digestibility and bioaccessibility of bioactive compounds in food systems. *Food Hydrocolloids*. 2019;87: 691–702. <https://doi.org/10.1016/j.foodhyd.2018.09.008>
12. Sorokin A. V., Khol'yavka M. G., Lavlinskaya M. S. Synthesis of chitosan and *N*-vinylimidazole graft-copolymers and the properties of their aqueous solutions. *Condensed Matter and Interphases*. 2021;23(4), 570–577. <https://doi.org/10.17308/kcmf.2021.23/3676>
13. Kabanov V. L., Novinyuk L. V. Chitosan application in food technology: a review of recent advances. *Food Systems*. 2020;3(1):10–15. <https://doi.org/10.21323/2618-9771-2020-3-1-10-15>
14. Olshannikova S. S., Redko Y. A., Lavlinskaya M. S., Sorokin A. V., Holyavka M. G., Yudin N. E., Artyukhov V. G. Study of the proteolytic activity of ficin associates with chitosan nanoparticles. *Condensed Matter and Interphases*. 2022;24(4): 523–528. <https://doi.org/10.17308/kcmf.2022.24/10556>
15. Goncharova S. S., Redko Y. A., Lavlinskaya M. S., Sorokin A. V., Holyavka M. G., Kondratyev M. S., Artyukhov, V. G. Biocatalysts based on papain associates with chitosan nanoparticles. *Condensed Matter and Interphases*. 2023;25(2): 173–181. <https://doi.org/10.17308/kcmf.2023.25/11098>
16. Malykhina N. V., Olshannikova S. S., Holyavka M. G., Sorokin A. V., Lavlinskaya M. S., Artyukhov V. G., Faizullin D. A., Zuev Yu. F. Preparation of ficin complexes with carboxymethylchitosan and *N*-(2-hydroxy)propyl-3-trimethyl ammonium chitosan and the study of their structural features. *Russian Journal of Bioorganic Chemistry*. 2022; 48(Suppl 1): S50–S60 (2022). <https://doi.org/10.1134/S1068162022060176>
17. Liu H., Wang C., Zou S., Wei Z., Tong Z. Simple, reversible emulsion system switched by pH on the basis of chitosan without any hydrophobic modification. *Langmuir*. 2012;28(30): 11017–11024. <https://doi.org/10.1021/la3021113>
18. Rodríguez M. S., Albertengo L. A., Agulló E. Emulsification capacity of chitosan. *Carbohydrate Polymers*. 2002;48(3): 271–276. [https://doi.org/10.1016/s0144-8617\(01\)00258-2](https://doi.org/10.1016/s0144-8617(01)00258-2)
19. Zhang C., Xu W., Jin W., Shah B. R., Li Y., Li B. Influence of anionic alginate and cationic chitosan on physicochemical stability and carotenoids bioaccessibility of soy protein isolate-stabilized emulsions. *Food Research International*. 2015;77: 419–425. <https://doi.org/10.1016/j.foodres.2015.09.020>
20. Chang H. W., Tan T. B., Tan P. Y., Nehdi I. A., Sbihi H. M., Tan C. P. Microencapsulation of fish oil-in-water emulsion using thiol-modified  $\beta$ -lactoglobulin fibrils-chitosan complex. *Journal of Food Engineering*. 2020;264: 109680. <https://doi.org/10.1016/j.jfoodeng.2019.07.027>
21. Ji C., Luo Y. Plant protein-based high internal phase Pickering emulsions: Functional properties and potential food applications. *Journal of Agriculture and Food Research*. 2023;12: 100604. <https://doi.org/10.1016/j.jafr.2023.100604>
22. Roll Zimmer T. B., Barboza Mendonça C. R., Zambiasi R. C. Methods of protection and application of carotenoids in foods — A bibliographic review. *Food Bioscience*. 2022;48: 101829. <https://doi.org/10.1016/j.fbio.2022.101829>
23. He B., Ge J., Yue P., ... Ga X. Loading of anthocyanins on chitosan nanoparticles influences anthocyanin degradation in gastrointestinal fluids and stability in a beverage. *Food Chemistry*. 2017;221: 1671–1677. <https://doi.org/10.1016/j.foodchem.2016.10.120>
24. Antipova A. P., Sorokin A. V., Lavlinskaya M. S. Development of an obtaining method for a graft copolymer based on sodium alginate for potential biomedical applications. *Proceedings of Voronezh State University. Series: Chemistry. Biology. Pharmacy*. 2022; 4: 5–11. (In Russ.). Available at: <https://elibrary.ru/item.asp?id=49963545>
25. Makarova A. O., Derkach S. R., Khair T., Kazantseva M. A., Zuev Yu. F., Zueva O. S. Ion-induced polysaccharide gelation: peculiarities of alginate egg-box association with different divalent cations. *Polymers*. 2023;15: 1243. <https://doi.org/10.3390/polym15051243>
26. Zueva O. S., Khair T., Derkach S. R., Kazantseva M. A., Zuev Yu. F. Strontium-induced gelation of sodium alginate in the presence of carbon nanotubes: elemental analysis and gel structure.

*Journal of Composites Science*. 2023;7: 286. <https://doi.org/10.3390/jcs7070286>

27. Len'shina N. A., Konev A. N., Baten'kin A. A., ... Zagainov V. E. Alginate functionalization for the microencapsulation of insulin producing cells. *Polymer Science, Series B*. 2021;63(6): 640–656. <https://doi.org/10.1134/S1560090421060129>

28. Qin Y., Zhang G., Chen H. The applications of alginate in functional food products. *Journal of Nutrition and Food Science*. 2020;3(1): 13. Available at: <https://www.henrypublishinggroups.com/wp-content/uploads/2020/05/the-applications-of-alginate-in-functional-food-products.pdf>

29. Steiner A. B. *Manufacture of glycol alginates*. US Patent No. 2426215A. Publ. 26.08.1947.

30. Nogaeva U. V., Naumova A. A., Novinkov A. G., ... Abrosimova O. N. Comparative study of rheological properties of gels and creams on different carrier bases. *Drug development & registration*. 2022;11(3): 121–129. (In Russ.). <https://doi.org/10.33380/2305-2066-2022-11-3-121-129>

31. Ai C. Recent advances on the emulsifying properties of dietary polysaccharides. *eFood*. 2023;4(4): e106. <https://doi.org/10.1002/efd2.106>

32. Schmitt C., Kolodziejczyk E., Leser M. E. Interfacial and foam stabilization properties of  $\beta$ -lactoglobulin-acacia gum electrostatic complexes. In: *Food colloids: interactions, microstructure and processing*. E. Dickson (ed.). Royal Society of Chemistry; 2005. p. 284–300. <https://doi.org/10.1039/9781847552389-00284>

33. Schmitt C., Kolodziejczyk E. Protein-polysaccharide complexes: from basics to food applications. In: *Gums and stabilisers for the food industry*, 15. Williams P. A., Phillips G. O. (eds.). Royal Society of Chemistry; 2010. p. 211–222. <https://doi.org/10.1039/9781849730747-00211>

34. Ganzevles R. A., Cohen Stuart M. A., van Vliet T., de Jongh H. H. J. Use of polysaccharides to control protein adsorption to the air–water interface. *Food Hydrocolloids*. 2006;20: 872–878. <https://doi.org/10.1016/j.foodhyd.2005.08.009>

35. Schmidt I., Novales B., Boué F., Axelos M. A. V. Foaming properties of protein/pectin electrostatic complexes and foam structure at nanoscale. *Journal of Colloid and Interface Science*. 2010;345:316–324. <https://doi.org/10.1016/j.jcis.2010.01.016>

36. McClements D. J. Non-covalent interactions between proteins and polysaccharides. *Biotechnology Advances*. 2006;24: 621–625. <https://doi.org/10.1016/j.biotechadv.2006.07.003>

37. Jourdain L. S., Schmitt C., Leser M. E., Murray B. S., Dickinson E. Mixed layers of sodium caseinate + dextran sulfate: influence of order of addition to oil-water interface. *Langmuir*. 2009;25: 10026–10037. <https://doi.org/10.1021/la900919w>

38. Ducel V., Richard J., Popineau Y., Boury F. Rheological interfacial properties of plant protein Arabic gum coacervates at the oil–water interface. *Biomacromolecules*. 2005;6:790–796. <https://doi.org/10.1021/bm0494601>

39. Cho Y. H., McClements D. J. Theoretical stability maps for guiding preparation of emulsions stabilized by protein–polysaccharide interfacial complexes. *Langmuir*. 2009;25: 6649–6657. <https://doi.org/10.1021/la8006684>

40. Guzey D., Kim H. J., McClements D. J. Factors influencing the production of o/w emulsions stabilized by  $\beta$ -lactoglobulin–pectin membranes. *Food Hydrocolloids*. 2004;18: 967–975. <https://doi.org/10.1016/j.foodhyd.2004.04.001>

41. Harnsilawat T., Pongsawatmanit R., McClements D. J. Stabilization of model beverage cloud emulsions using protein-polysaccharide electrostatic complexes formed at the oil-water interface. *Journal of Agricultural and Food Chemistry*. 2006;54: 5540–5547. <https://doi.org/10.1021/jf052860a>

42. Guzey D., McClements D. J. Formation, stability and properties of multilayer emulsions for application in the food industry. *Advances in Colloid and Interface Science*. 2006;128–130: 227–248. <https://doi.org/10.1016/j.cis.2006.11.021>

43. Laplante S., Turgeon S. L., Paquin P. Effect of pH, ionic strength, and composition on emulsion stabilising properties of chitosan in a model system containing whey protein isolate. *Food Hydrocolloids*. 2005;19: 721–729. <https://doi.org/10.1016/j.foodhyd.2004.08.001>

44. Moschakis T., Murray B. S., Biliaderis C. Modifications in stability and structure of whey protein-coated o/w emulsions by interacting chitosan and gum arabic mixed dispersions. *Food hydrocolloids*. 2010;24: 8–17. <https://doi.org/10.1016/j.foodhyd.2009.07.001>

45. Schmitt C., Turgeon S. L. Protein/polysaccharide complexes and coacervates in food systems. *Advances in Colloid and Interface Science*. 2011;167(1–2): 63–70. <https://doi.org/10.1016/j.cis.2010.10.001>

## Information about the authors

*Maria S. Lavlinskaya.*, Cand. Sci. (Chem.), Senior Researcher, Department of Biophysics and Biotechnology, Voronezh State University (Voronezh Russian Federation).

<https://orcid.org/0000-0001-9058-027X>  
maria.lavlinskaya@gmail.com

*Andrey V. Sorokin*, Cand. Sci. (Biol.), Senior Researcher, Department of Biophysics and Biotechnology, Voronezh State University (Voronezh, Russian Federation).

<https://orcid.org/0000-0001-5268-9557>  
andrew.v.sorokin@gmail.com



*Marina G. Holyavka*, Dr. Sci. (Biol.), Professor, Department of Biophysics and Biotechnology, Voronezh State University; Professor at the Physics Department, Sevastopol State University (Voronezh, Sevastopol, Russian Federation).

<https://orcid.org/0000-0002-1390-4119>

[holyavka@rambler.ru](mailto:holyavka@rambler.ru)

*Yuriy F. Zuev*, Dr. Sci. (Chem.), Professor, Head of the Laboratory of Biophysical Chemistry of Nanosystems, Kazan Institute of Biochemistry and Biophysics, Kazan Scientific Center of Russian Academy of Science” (Kazan, Russian Federation).

<https://orcid.org/0000-0002-6715-2530>

[yufzuev@mail.ru](mailto:yufzuev@mail.ru)

*Valery G. Artyukhov*, Dr. Sci. (Biol.), Professor, Head of the Biophysics and Biotechnology Department, Voronezh State University (Voronezh Russian Federation).

<https://orcid.org/0000-0002-5872-8382>

[artyukhov@bio.vsu.ru](mailto:artyukhov@bio.vsu.ru)

*Received 13.09.2023; approved after reviewing 06.11.2023; accepted for publication 15.11.2023; published online 25.06.2024.*

*Translated by Valentina Mittova*



# Condensed Matter and Interphases

Kondensirovannye Sredy i Mezhfaznye Granitsy  
<https://journals.vsu.ru/kcmf/>

## Original articles

Research article

<https://doi.org/10.17308/kcmf.2024.26/11934>

## Physicochemical study of phase formation in the $\text{Sb}_2\text{S}_3\text{-Cr}_2\text{Te}_3$ system

I. I. Aliyev<sup>1</sup>✉, E. I. Mamedov<sup>2</sup>, F. V. Yusubov<sup>2</sup>, L.F. Masieva<sup>2</sup>, Kh. M. Gashimov<sup>3</sup>

<sup>1</sup>*Institute of Catalysis and Inorganic Chemistry n. a. M. Nagiyev  
113 H. Javid av., Baku Az 1143, Azerbaijan*

<sup>2</sup>*Azerbaijan Technical University  
116 H. Javid av., Baku Az 1146, Azerbaijan*

<sup>3</sup>*Azerbaijan State University of Economics  
6 Istiglaliyat str., Baku Az 1001, Azerbaijan*

### Abstract

Chromium chalcogenides and systems based on them have not been sufficiently studied. Chromium chalcogenide compounds  $\text{Cr}_2\text{X}_3$  (X = S, Se, Te), new phases and solid solutions based on them are widely used in semiconductor technology, since these are materials with thermoelectric and magnetic properties. The purpose of this study was the investigation of chemical interactions in the  $\text{Sb}_2\text{S}_3\text{-Cr}_2\text{Te}_3$  system, the construction of a phase diagram, and the search for new phases and solid solutions.

Using the methods of physicochemical analysis (differential thermal, X-ray phase, microstructural analysis, as well as density and microhardness measurements), the chemical interaction in the  $\text{Sb}_2\text{S}_3\text{-Cr}_2\text{Te}_3$  system was studied and its phase diagram was constructed. The phase diagram of the system is quasi-binary and is characterized by the formation of a quaternary compound  $\text{Cr}_2\text{Sb}_2\text{S}_3\text{Te}_3$ .

Compound  $\text{Cr}_2\text{Sb}_2\text{S}_3\text{Te}_3$  incongruently melted at 610 °C. Microstructural analysis showed that at room temperature solid solutions based on  $\text{Sb}_2\text{S}_3$  were formed in the system, which reached up to 5 mol. %  $\text{Cr}_2\text{Te}_3$ , and based on  $\text{Cr}_2\text{Te}_3$  up to – 8 mol. %  $\text{Sb}_2\text{S}_3$ . The  $\text{Sb}_2\text{S}_3\text{-Cr}_2\text{Te}_3$  eutectic formed in the Sb system contains 20 mol. %  $\text{Cr}_2\text{Te}_3$  and has a melting point of 430 °C. The  $\text{Cr}_2\text{Sb}_2\text{S}_3\text{Te}_3$  compound crystallizes in a tetragonal system with the unit cell parameters:  $a = 10.03$ ;  $c = 16.67$  Å,  $z = 7$ ,  $\rho_{\text{расч.}} = 5.72$  g/cm<sup>3</sup>,  $\rho_{\text{X-ray}} = 5.765$  g/cm<sup>3</sup>.

**Keywords:** System, Phase, Solid solution, Eutectic, Syngony

**For citation:** Aliyev I. I., Mamedov E. I., Yusubov F. V., Masieva L. F., Gashimov Kh. M. Physicochemical study of phase formation in the  $\text{Sb}_2\text{S}_3\text{-Cr}_2\text{Te}_3$  system. *Condensed Matter and Interphases*. 2024;26(2): 197–203. <https://doi.org/10.17308/kcmf.2024.26/11934>

**Для цитирования:** Алиев И. И., Мамедов Э. И., Юсубов Ф. В., Масиева Л. Ф., Гашимов Х. М. Физико-химическое исследование фазообразование в системе  $\text{Sb}_2\text{S}_3\text{-Cr}_2\text{Te}_3$ . *Конденсированные среды и межфазные границы*. 2024;26(2): 197–203. <https://doi.org/10.17308/kcmf.2024.26/11934>

✉ Imir I. Aliyev, e-mail: [aliyevimir@rambler.ru](mailto:aliyevimir@rambler.ru)

© Aliyev I. I., Mamedov E. I., Yusubov F. V., Masieva L. F., Gashimov Kh. M., 2024



The content is available under Creative Commons Attribution 4.0 License.



## 1. Introduction

The search for functional materials that can meet the ever-increasing needs of the electronics industry is always in the spotlight. Materials that meet these requirements include antimony chalcogenide compounds and alloys based on them. Antimony sulfides and selenides are used in optical systems as photosensitive materials [1–7]. Antimony tellurides are materials with thermoelectric properties, used as energy converters [8–15].

It is known that the element chromium and chalcogenide compounds are used, not only for the manufacture of magnetic materials, but also for the production of ferrimagnets of complex composition with other chalcogenides. Ternary and more complex compounds based on chromium chalcogenides have high ferromagnetic properties [16–19]. Therefore, the production of photosensitive and magneto-optical materials that retain the properties of the original compounds via the chemical interaction of photosensitive antimony chalcogenides with magnetic chromium chalcogenides is of both scientific and practical importance.

The  $\text{Sb}_2\text{S}_3$  compound melts congruently at 559.5 °C and crystallizes in the orthorhombic system with lattice parameters:  $a = 11.229$ ;  $b = 11.310$ ;  $c = 3.83$  Å, space gr.  $Pbnm-D_{2h}^{16}$ , density 4.63 g/cm<sup>3</sup>, microhardness 1400 MPa [20]. The  $\text{Cr}_2\text{Te}_3$  compound melts congruently at 1280 °C and crystallizes in a hexagonal system with lattice parameters:  $a = 6.811$ ;  $c = 12.062$  Å, space gr.  $hP20 - P31c$  [21]. Phase transition  $\alpha$ - $\text{Cr}_2\text{Te}_3$  has a temperature of 480 °C.

## 2. Experimental

Alloys of  $\text{Sb}_2\text{S}_3$ – $\text{Cr}_2\text{Te}_3$  were synthesized from  $\text{Sb}_2\text{S}_3$  and  $\text{Cr}_2\text{Te}_3$  components in an evacuated quartz ampoule at a pressure of 0.133 Pa in the temperature range 600–1100 °C. The samples were heat treated at 500 °C for 240 h to ensure equilibrium.

Equilibrium alloys were studied by differential thermal analysis (DTA), X-ray diffraction (XRD), microstructural analysis (MSA), as well as by microhardness and density measurements.

DTA analysis of the samples was carried out using a frequency pyrometer NTR-73, the error was  $\pm 5$  °C. The reordering of heating and cooling

curves were carried using an N. S. Kurnakov NTR-73 pyrometer. The studied substance was placed in a quartz ampoule with the length of 0.10–0.11 m and diameter  $8\text{--}10 \cdot 10^{-3}$  m, which was pumped out to 0.1333 Pa and sealed. A thermocouple passed through a hole of the ceramic block with corresponding diameter was placed below the sample. The tubular furnace, inside which a steel block was placed was used for heating. NaCl, KCl,  $\text{Na}_2\text{SO}_4$ ,  $\text{K}_2\text{SO}_4$  were used as reference compounds. Heating and cooling curves of these compounds were recorded under similar conditions with a heating rate of 10 °C/min. Based on the data obtained for the reference substances, a calibration curve was constructed and checked after 15 days. The study mainly analyzed the thermal effects detected in the heating curves. Chromel–alumel was used as a thermocouple.

XRD was carried out using D2 PHASER X-ray device in  $\text{CuK}_\alpha$  radiation with a Ni filter.

Microstructure analysis (MSA) was performed by microscopic study using MIM-8 microscope. The solution 1 N  $\text{HNO}_3$ :  $\text{H}_2\text{O}_2 = 1: 1$  was used as a clarifier to determine phase boundaries. Microhardness was measured using a PMT-3 metallographic microscope. The density of the samples was determined by the pycnometric method; toluene was used as a filler.

## 3. Results and discussion

$\text{Sb}_2\text{S}_3$ -rich samples easily melted, forming a compact mass. After synthesis,  $\text{Cr}_2\text{Te}_3$  compound was formed in the form of heterogeneous ingots. Therefore, the heterogeneous ingot was crushed into powder, pressed under a pressure of 200 atm and obtained in the form of tablets. In tablet form, the sample was placed in a quartz ampoule and sealed by sucking out the air and melting it in a gas lamp. Then solid-phase synthesis was carried out by heating the sample at a temperature of 800 °C for 100 h. After verification of the formation of  $\text{Cr}_2\text{Te}_3$  compound, alloys of the  $\text{Sb}_2\text{S}_3$ – $\text{Cr}_2\text{Te}_3$  system were synthesized.

The alloys of the  $\text{Sb}_2\text{S}_3$ – $\text{Cr}_2\text{Te}_3$  system were studied using physicochemical analysis methods. According to DTA data, it was established that two and three endothermic effects were obtained in the thermograms of the alloys.

After a phase analysis of the alloys of the system, it was found that the alloys in proximity to the initial components and containing 50 mol. %  $Cr_2Te_3$  are single-phase. At a content above 5 mol. %  $Cr_2Te_3$  the second phase was formed, i.e., two-phase regions appeared (Fig. 1b). The microstructures of alloys containing 5, 10, and 50 mol. %  $Cr_2Te_3$  Sb of  $Sb_2S_3-Cr_2Te_3$  systems are shown in Fig. 1. As can be seen, 2 mol. %  $Cr_2Te_3$  and the sample with 50 mol. %  $Cr_2Te_3$  were single-phase

solid solutions (Fig. 1a, c). The sample containing 10 mol. %  $Cr_2Te_3$  has two-phases (Fig. 1b).

For the conformation of DTA and MSA results, X-ray phase analysis of alloys of 30, 50 and 92 mol. %  $Cr_2Te_3$  of the  $Sb_2S_3-Cr_2Te_3$  systems was performed (Fig. 2). As can be seen from Fig. 2, diffraction lines of the sample 92 mol. %  $Cr_2Te_3$  did not differ from the X-ray diffraction pattern of the  $Cr_2Te_3$  compound, and a slight shift is observed. This sample is a solid solution based

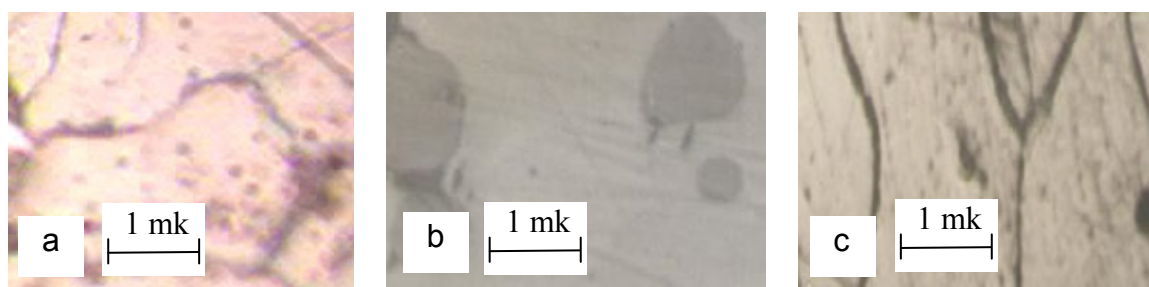


**Fig. 1.** Microstructures of alloys of  $Sb_2S_3-Cr_2Te_3$  system ( $\times 340$ ): a) – 5 mol %; b) – 10 mol %; c) – 50 ( $Cr_2Sb_2S_3Te_3$ ) mol %  $Cr_2Te_3$

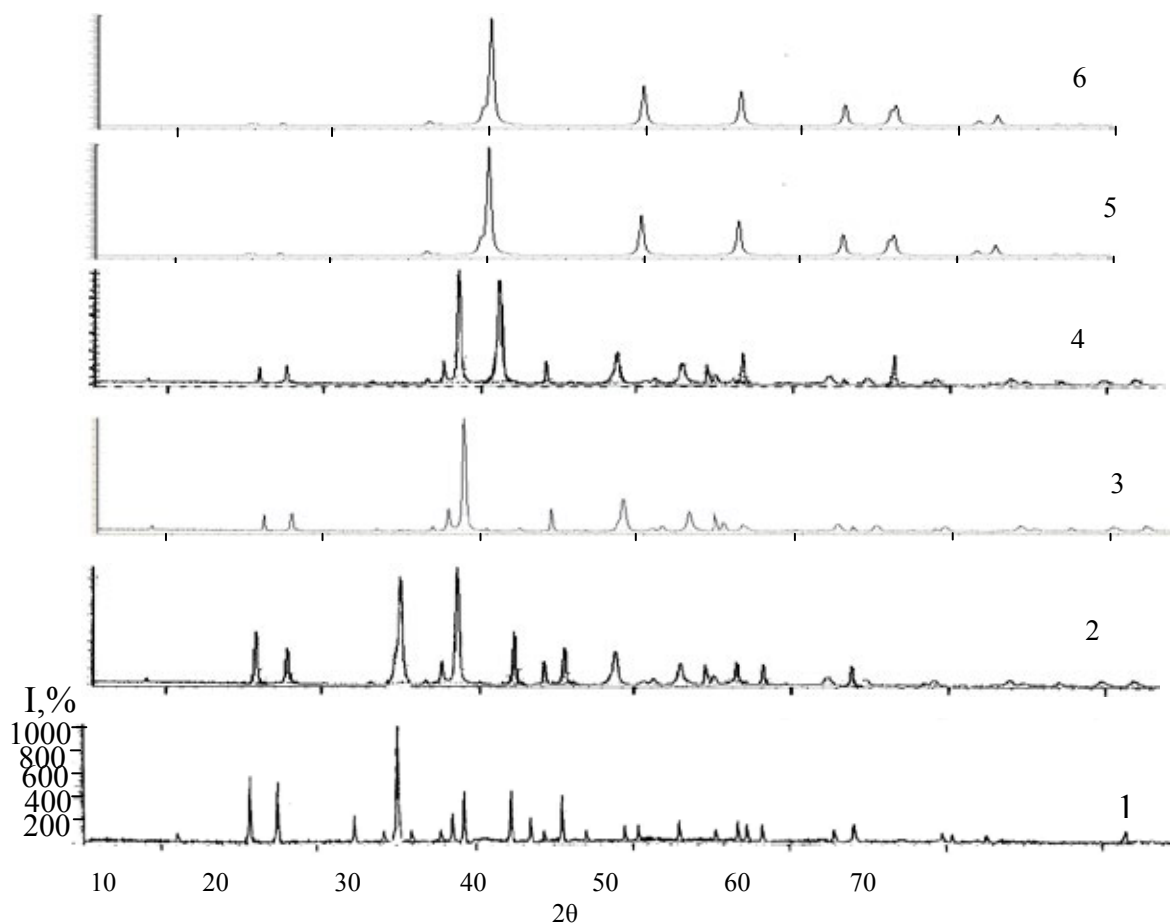


**Fig. 2.** Diffraction patterns of system alloys of  $Sb_2S_3-Cr_2Te_3$  system: 1 –  $Sb_2S_3$ ; 2 – 30; 3 – 50 ( $Cr_2Sb_2S_3Te_3$ ); 4 – 70; 5 – 92; 6 – 100 mol. %  $Cr_2Te_3$

on  $\text{Cr}_2\text{Te}_3$ . In the diffraction patterns of samples with 30 and 70 mol. %  $\text{Cr}_2\text{Te}_3$  diffraction lines of the original components were present, i.e. the samples were two-phase.

Diffraction peaks in the diffraction pattern of a sample containing 50 mol. %  $\text{Cr}_2\text{Te}_3$ , differed from the diffraction lines in the diffraction patterns of the original components by interplanar distances and intensity. As a result, a new quaternary compound containing  $\text{Cr}_2\text{Sb}_2\text{S}_3\text{Te}_3$  was obtained (Fig. 2). The  $\text{Cr}_2\text{Sb}_2\text{S}_3\text{Te}_3$  compound can be considered as a derivative of  $\text{CrSbTe}_3$ , obtained by anionic substitution of  $\text{Cr}_2\text{Sb}_2\text{S}_3\text{Te}_3$  (abbreviated as  $\text{CrSbS}_{1.5}\text{Te}_{1.5}$ ).

As a result of physicochemical analysis, a quasi-binary phase diagram of the  $\text{Sb}_2\text{S}_3$ - $\text{Cr}_2\text{Te}_3$  system was constructed (Fig. 3). The  $\text{Cr}_2\text{Sb}_2\text{S}_3\text{Te}_3$  compound was formed as a result of a peritectic reaction:  $\text{L} + \text{Cr}_2\text{Te}_3 \leftrightarrow \text{Cr}_2\text{Sb}_2\text{S}_3\text{Te}_3$  at  $610^\circ\text{C}$ .

Liquidus of  $\text{Sb}_2\text{S}_3$ - $\text{Cr}_2\text{Te}_3$  system consisted of monovariant equilibrium curves for an  $\alpha$ -solid solution based on the  $\text{Sb}_2\text{S}_3$  compound, a new compound  $\text{Cr}_2\text{Sb}_2\text{S}_3\text{Te}_3$  and  $\beta$ -solid solution based on  $\text{Cr}_2\text{Te}_3$  compound. The binary eutectic formed in the system has a  $\text{Cr}_2\text{Te}_3$  content of 20 mol. % and melting point  $430^\circ\text{C}$ .

Crystallization of the  $\alpha$ -solid solution was completed in the system in the concentration range of 0–20 mol. %  $\text{Cr}_2\text{Te}_3$ . In the range of 0–20 mol. %  $\text{Cr}_2\text{Te}_3$  two-phase alloys ( $\text{L} + \delta$ ) were below the liquidus curve (Fig. 3). Two-phase alloys consisting of ( $\delta + \text{Cr}_2\text{Sb}_2\text{S}_3\text{Te}_3$ ), below the solidus line crystallized in the region of 5–50 mol. %  $\text{Cr}_2\text{Te}_3$ . In the concentration range of 50–92 mol. %  $\text{Cr}_2\text{Te}_3$ , two-phase alloys ( $\text{Cr}_2\text{Sb}_2\text{S}_3\text{Te}_3 + \alpha$ ) were below the solidus line. Some physicochemical properties of the alloys are shown in Table 1.

As a result of microhardness measurements, three different values were obtained. The microhardness value (1400–1470) MPa corresponded to the microhardness of an  $\alpha$ -solid solution based on  $\text{Sb}_2\text{S}_3$ . The microhardness value (1750–1880) MPa corresponded to the microhardness of the  $\text{Cr}_2\text{Sb}_2\text{S}_3\text{Te}_3$  compound, and the value (2070–2150) MPa corresponded to the microhardness of the  $\beta$ -solid solution based on  $\text{Cr}_2\text{Te}_3$ . The dependence of the density of the alloys of the system on the composition showed that no sharp change was observed.

Based on the results of X-ray phase analysis, it was established that the  $\text{Cr}_2\text{Sb}_2\text{S}_3\text{Te}_3$

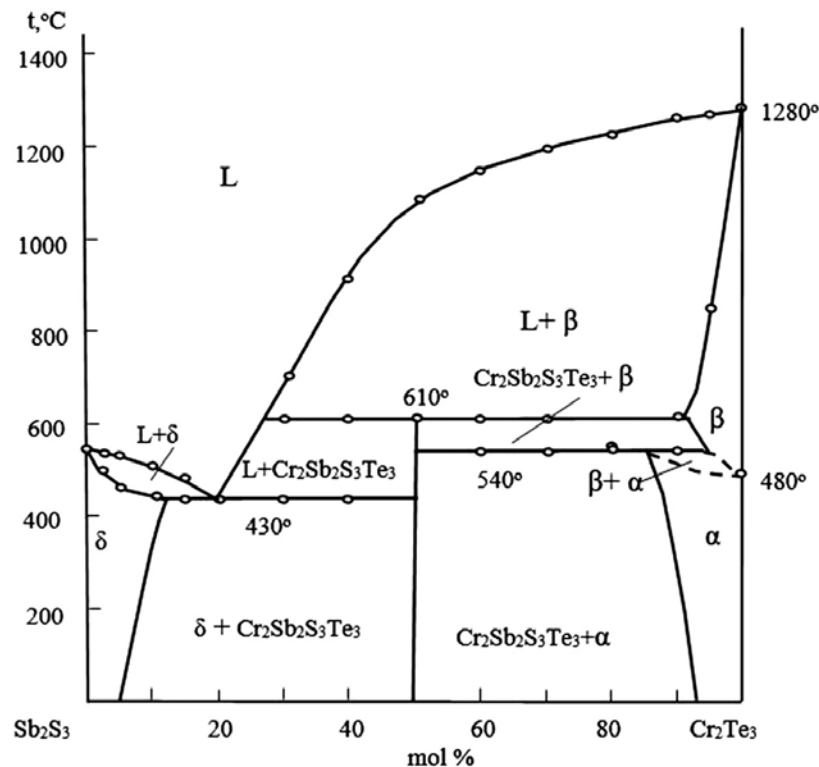


Fig. 3. Phase diagram of the  $\text{Sb}_2\text{S}_3$ - $\text{Cr}_2\text{Te}_3$  system



**Table 1.** Composition of alloys of the  $Sb_2S_3-Cr_2Te_3$  system, DTA results, determination of microhardness and density

Composition, mol. %		Thermal effects, °C	Density, $10^3 \text{ kg/m}^3$	Microhardness, MPa		
$Sb_2S_3$	$Cr_2Te_3$			$\alpha$	$Sb_2Cr_2S_3Te_3$	$\beta$
				$P = 0.1 \text{ H}$		$P = 0.2 \text{ H}$
100	0.0	560	4.63	1400	–	–
97	3.0	500, 555	4.70	1450	–	–
95	5.0	470, 530	4.78	1470	–	–
90	10	440, 515	4.86	1470	–	–
85	15	430, 480	4.97	–	–	–
80	20	430	5.06	eutectic	eutectic	–
70	30	430, 610, 700	5.29	–	–	–
60	40	430, 610, 920	5.51	–	1750	–
50	50	610, 1090	5.72	–	1750	3280
40	60	540, 610, 1150	5.94	–	1800	3280
30	70	540, 610, 1195	6.16	–	1850	3280
20	80	540, 610, 1230	6.39	–	1880	3280
10	90	540, 610, 1260	6.65	–	–	3280
5.0	95	850, 1270	6.83	–	–	3280
0.0	100	480, 1280	6.82	–	–	3250

**Table 2.** Interplanar distances ( $d$ ), intensity ( $I$ ) of lines and lattice indices (hkl) in the diffraction pattern of the  $Cr_2Sb_2S_3Te_3$  compound

No	$I, \%$	$d_{\text{exp.}}, \text{Å}$	$d_{\text{cal.}}, \text{Å}$	$1/d_{\text{exp.}}^2, \text{Å}^{-2}$	$1/d_{\text{cal.}}^2, \text{Å}^{-2}$	hkl
1	5.9	10.0289	10.0289	0.0099	0.0099	100
2	15.8	5.5561	5.5561	0.0324	0.0324	003
3	17.4	5.0252	5.0125	0.0396	0.0398	200
4	4.1	3.8528	3.8490	0.0674	0.0675	104
5	6.1	3.3509	3.3445	0.0891	0.0894	300
6	22.5	3.2277	3.2042	0.0960	0.0974	204
7	100	3.1236	3.1159	0.1025	0.1030	311
8	4.4	2.7857	2.7810	0.1288	0.1293	320
9	26	2.6254	2.6380	0.1451	0.1437	322
10	30.	2.3265	2.3344	0.1848	0.1835	331
11	19	2.1097	2.1035	0.2247	0.2260	217
12	23	2.0357	2.0404	0.2413	0.2402	108
13	8.3	1.9602	1.9672	0.2602	0.2584	510
14	8.6	1.7506	1.7453	0.3265	0.3283	426
15	7.2	1.6772	1.6718	0.3555	0.3578	600
16	4.9	1.5776	1.5788	0.4018	0.4012	601
17	6.2	1.5639	1.5665	0.4089	0.4075	540
18	7.1	1.4570	1.4580	0.4711	0.4704	339
19	6.0	1.3475	1.3492	0.5507	0.5493	722
20	6.8	1.3142	1.3170	0.5790	0.5765	730

compound crystallizes in a tetragonal system with lattice parameters:  $a = 10.03$ ;  $c = 16.67 \text{ Å}$ ,  $z = 7$ ,  $\rho_{\text{pycn.}} = 5.72 \text{ g/cm}^3$ ,  $\rho_{\text{x-ray}} = 5.75 \text{ g/cm}^3$ . Crystallographic data of  $Cr_2Sb_2S_3Te_3$  compound are shown in Table 2.

#### 4. Conclusions

Thus, the  $Sb_2S_3-Cr_2Te_3$  system was studied using physicochemical analysis methods and its phase diagram was constructed. It was established that the  $Sb_2S_3-Cr_2Te_3$  section is a quasi-binary

section of eutectic type. A quaternary compound  $\text{Cr}_2\text{Sb}_2\text{S}_3\text{Te}_3$  is formed in the system with an anion exchange of components in the ratio of 1:1. The  $\text{Cr}_2\text{Sb}_2\text{S}_3\text{Te}_3$  compound is formed by the peritectic reaction  $\text{M} + \text{Cr}_2\text{Te}_3 \leftrightarrow \text{Cr}_2\text{Sb}_2\text{S}_3\text{Te}_3$  at 610 °C. The eutectic with a composition of 20 mol. %  $\text{Cr}_2\text{Te}_3$  is formed in the system between the  $\alpha$  phase and  $\text{Cr}_2\text{Sb}_2\text{S}_3\text{Te}_3$  at a temperature of 430 °C. In the  $\text{Sb}_2\text{S}_3$  based system solid solutions reached up to 5 mol. %  $\text{Cr}_2\text{Te}_3$ , and in the system based on  $\text{Cr}_2\text{Te}_3$  it was up to 8 mol. %  $\text{Sb}_2\text{S}_3$ . Based on the results of X-ray phase analysis, it was established that the  $\text{Cr}_2\text{Sb}_2\text{S}_3\text{Te}_3$  compound crystallizes in a tetragonal system with lattice parameters:  $A = 10.03$ ;  $c = 16.67 \text{ \AA}$ ,  $z = 7$ , density  $\rho_{\text{печн.}} = 5.72 \text{ g/cm}^3$ ,  $\rho_{\text{X-ray}} = 5.5 \text{ g/cm}^3$ .

### Author contributions

Aliyev I. I. – writing the article and scientific supervision of research; Mamedov E. I. – idea for scientific work and writing the article; Yusubov F. V. – scientific editing of the text, final conclusions; Masieva L. F. – conducting research; Gashimov Kh. M – conducting research.

### Conflict of interests

The authors declare that they have no known competing financial interests or personal relationships that could have influenced the work reported in this paper.

### References

- Zhou Y., Wang L., Chen S., ... Tang J. Thin-film  $\text{Sb}_2\text{Se}_3$  photovoltaics with oriented one-dimensional ribbons and benign grain boundaries. *Nature Photonics*. 2015;9: 409–415. <https://doi.org/10.1038/nphoton.2015.78>
- Fernandez A., Merino M. Preparation and characterization of  $\text{Sb}_2\text{Se}_3$  thin films prepared by electrodeposition for photovoltaic applications. *Thin Solid Films*. 2000;366: 202–206. [https://doi.org/10.1016/s0040-6090\(00\)00716-1](https://doi.org/10.1016/s0040-6090(00)00716-1)
- Chen, C., Bobela D. C., Yang Y., ... Tang J. Characterization of basic physical properties of  $\text{Sb}_2\text{Se}_3$  and its relevance for photovoltaics. *Frontiers of Optoelectronics*. 2017;10: 18–30. <https://doi.org/10.1007/s12200-017-0702-z>
- Magomedov A. Z., Aliyev A. O., Aslanov M. A., Musaeva S. M., Javadova S. D. Features of the temperature dependence of the spectral distribution of photosensitivity of ferroelectric semiconductors  $\text{Sb}_2\text{S}_3\text{-Sb}_2\text{Se}_3$ . *Bulletin of Baku University. Series of physical and mathematical sciences*. 2004;4: 163–169. 169 (In Azerbaijani).
- Ju T., Koo B., Jo J. W., Ko M. J. Enhanced photovoltaic performance of solution-processed  $\text{Sb}_2\text{Se}_3$  thin film solar cells by optimizing device structure. *Current Applied Physics*. 2020;20(2): 282–287. <https://doi.org/10.1016/j.cap.2019.11.018>
- Kumar P., Sathiaraj T. S., Thangaraj R. Optical properties of amorphous  $\text{Sb}_2\text{Se}_3\text{:Sn}$  films. *Philosophical Magazine Letters*. 2010;90(3): 183–192 <https://doi.org/10.1080/09500830903520704>
- Rajpure K. Y., Bhosale C. H. Effect of Se source on properties of spray deposited  $\text{Sb}_2\text{Se}_3$  thin films. *Materials Chemistry and Physics*. 2000;62: 169–174. [https://doi.org/10.1016/s0254-0584\(99\)00173-x](https://doi.org/10.1016/s0254-0584(99)00173-x)
- Vieira E. M. F., Figueira J., Pires A. L., ... Goncalves L. M. Enhanced thermoelectric properties of  $\text{Sb}_2\text{Te}_3$  and  $\text{Bi}_2\text{Te}_3$  films for flexible thermal sensors. *Journal of Alloys and Compounds*. 2019;774(5): 1102–1116. <https://doi.org/10.1016/j.jallcom.2018.09.324>
- Zhang H., Liu C.-X., Qi X.-L., Dai X., Fang Z., Zhang, S.-C. Topological insulators in  $\text{Bi}_2\text{Se}_3$ ,  $\text{Bi}_2\text{Te}_3$  and  $\text{Sb}_2\text{Te}_3$  with a single Dirac cone on the surface. *Nature Physics*. 2009;5(6): 438–442. <https://doi.org/10.1038/nphys1270>
- Wang G., Cagin T. Electronic structure of the thermoelectric materials  $\text{Bi}_2\text{Te}_3$  and  $\text{Sb}_2\text{Te}_3$  from first-principles calculations. *Physical Review B*. 2007;76: 075201-8. <https://doi.org/10.1103/physrevb.76.075201>
- Xu B., Zhang J., Yu G., Ma S., Wang Y., Wang Y. Thermoelectric properties of monolayer  $\text{Sb}_2\text{Te}_3$ . *Journal of Applied Physics*. 2018;124(16): 165104. <https://doi.org/10.1063/1.5051470>
- Kulbachinskii V. A., Kytin V. G., Zinoviev D. A., ... Banerjee A. Thermoelectric properties of  $\text{Sb}_2\text{Te}_3$ -based nanocomposites with graphite. *Semiconductors*. 2019;53: 638–640 <https://doi.org/10.1134/s1063782619050129>
- Liu X., Chen J., Luo M., ... Tang J. Thermal evaporation and characterization of  $\text{Sb}_2\text{Se}_3$  thin film for substrate  $\text{Sb}_2\text{Se}_3\text{/CdS}$  solar cells. *ACS Applied Materials & Interfaces*. 2014;6: 10687–10695. <https://doi.org/10.1021/am502427s>
- Kutasov V. A. Shifting the maximum figure-of-merit of  $(\text{Bi, Sb})_2(\text{Te, Se})_3$  thermoelectrics to lower temperatures. In: *Thermoelectrics Handbook*. Boca Raton, FL, USA: CRC Press; 2005. 37-18–37-31. <https://doi.org/10.1201/9781420038903.ch37>
- Zargarova M. I., Mamedov A. N., Azhdarova D. S., Akhmedova (Veliev) J. A., Abilov C. I. *Inorganic substances synthesized and studied in Azerbaijan. Handbook*. Baku: Elm. Publ.; 2004. 462 p.
- Yamashita O., Yamauchi H., Yamaguchi Y. et al. Magnetic properties of the system  $\text{CuCr}_2\text{Se}_4\cdot x\text{Yx}$  ( $\text{Y} = \text{Cl, Br}$ ). *Journal of the Physical Society of Japan*. 1979;47(2): 450–454. <https://doi.org/10.1143/jpsj.47.450>

17. Koroleva L. I., Lukina L. N., Busheva E. V., Shabunina G. G., Aminov T. G.  $CuCr_2Se_{4-x}Sb_x$ : a new magnetic semiconductor. *Inorganic Materials*. 1999;35(12): 1217–1220. Available at: <https://elibrary.ru/item.asp?id=13328594>

18. Aminov T. G., Arbuzova T. I., Busheva E. V., Shabunina G. G.  $CuCr_{2-x}SSb_xSe_4$  and  $Cu_{1-y}Sb_yCr_2Se_4$  solid solution. *Inorganic Materials*. 2000;36(2): 114–118. <https://doi.org/10.1007/BF02758008>

19. Nakatani I., Nose H., Masumoto K. Magnetic properties of  $CuCr_2Se_4$  single crystals. *Journal of Physics and Chemistry of Solids*. 1978;39(7): 743–749. [https://doi.org/10.1016/0022-3697\(78\)90008-2](https://doi.org/10.1016/0022-3697(78)90008-2)

20. *Physico-chemical properties of semiconductor substances\**. Handbook. Moscow: Nauka Publ.; 1979. 339 p. (In Russ.)

21. Phase diagrams of binary metal systems\*. Handbook. 3 vol. / N. P. Lyakishev (ed.). Moscow: Mashinostroenie Publ.; 1997. 1023 p. (In Russ.)

\* Translated by author of the article

### Information about the authors

*Imir I. Aliyev*, Dr. Sci. (Chem.), Professor, Head of laboratory, Institute of Catalysis and Inorganic Chemistry n. a. M. Nagiyev National Academy of Sciences of Azerbaijan (Baku, Azerbaijan).

<https://orcid.org/0000-0002-7694-1400>

[aliyevimir@rambler.ru](mailto:aliyevimir@rambler.ru)

*Elman I. Mammadov*, Dr. Sci. (Chem.), Professor, Azerbaijan Technical University (Baku, Azerbaijan).

<https://orcid.org/0009-0000-8948-7019>

[kimya@aztu.edu.az](mailto:kimya@aztu.edu.az)

*Faxraddin V. Yusubov*, Dr. Sci. (Chem.), Professor, Head of Department, Azerbaijan Technical University (Baku, Azerbaijan).

<https://orcid.org/0000-0002-3496-8947>

[yusubov@asoiu.edu.az](mailto:yusubov@asoiu.edu.az)

*Laman F. Masieva*, postgraduate student, Azerbaijan Technical University (Baku, Azerbaijan).

<https://orcid.org/0000-0002-9908-7294>

[leman\\_mesiyeva@mail.ru](mailto:leman_mesiyeva@mail.ru)

*Khalig M. Gashimov*, PhD in Chemistry, Associate Professor, Azerbaijan State University of Economics (Baku, Azerbaijan).

<https://orcid.org/0000-0002-2208-2655>

[xaliq1949@mail.ru](mailto:xaliq1949@mail.ru)

Received 28.09.2023; approved after reviewing 10.11.2023; accepted for publication 15.11.2023; published online 25.06.2024.

Translated by Valentina Mittova





## Original articles

Research article

<https://doi.org/10.17308/kcmf.2024.26/11935>

## Study of the processes of formation of the structure and strength gain of nanomodified cement systems during long-term hardening

O. V. Artamonova, M. A. Shvedova✉

Voronezh State Technical University,  
20 letiya Oktyabrya str., 84, Voronezh 394006, Russian Federation

### Abstract

The study investigated the influence of nanoscale admixtures on the structure formation and strength characteristics of cement systems during their hardening with a duration of up to ten years. The study of the processes of structure formation of modified cement systems showed that there is a significant acceleration of the process of cement hydration during the early period of hardening, despite the decrease in water content. It was established that phase transformations and changes in phase composition in all systems were observed throughout the entire studied hardening period. At the same time, in the later stages of hardening, the appearance of stable hydrate new formations (xonotlite, afwillite, ettringite), capable of creating a lower-dimensional, dense and homogeneous structure of nanomodified cement stone was observed. This provides nanomodified cement systems with high compressive strength values ( $R_{\text{com}}$ ) both during the early and long stages of hardening. At the same time, the highest strength indicators throughout the entire study period ( $R_{\text{com}} = 85$  MPa, with a hardening duration of 28 days and  $R_{\text{com}} = 157$  MPa, with a hardening duration of 10 years) was characteristic for the cement system modified with a complex nanoscale admixture based on  $\text{SiO}_2$  particles.

**Keywords:** Cement systems,  $\text{SiO}_2$  nanoparticles, Carbon nanotubes, Structure formation, Long-term hardening, Compressive strength

**Acknowledgements:** The experimental studies were carried out using the facilities of the Professor Borisov Centre for Collective Use, Voronezh State Technical University which is partly supported by the Ministry of Science and Education of the Russian Federation, Project No. 075 – 15 – 2021 – 662.

**For citation:** Artamonova O. V., Shvedova M. A. Study of the processes of formation of the structure and strength gain of nanomodified cement systems during long-term hardening. *Condensed Matter and Interphases*. 2024;26(2): 204–212. <https://doi.org/10.17308/kcmf.2024.26/11935>

**Для цитирования:** Артамонова О. В., Шведова М. А. Исследование процессов структурообразования и набора прочности наномодифицированных цементных систем при продолжительном твердении. *Конденсированные среды и межфазные границы*. 2024;26(2): 204–212. <https://doi.org/10.17308/kcmf.2024.26/11935>

✉ Maria A. Shvedova, e-mail: [marishwedowa@mail.ru](mailto:marishwedowa@mail.ru)

© Artamonova O. V., Shvedova M. A., 2024



The content is available under Creative Commons Attribution 4.0 License.

## The designations accepted in the article

C – cement;

W – water;

W/C – water-cement ratio;

CNA - complex nano-additive based on SiO<sub>2</sub> particles;

CNT – carbon nanotubes

## 1. Introduction

Increasing and regulating the long-term strength of cement composites is an urgent problem for domestic and foreign researchers due to the wide practical significance of these materials. Now, this is especially important due to the production and use of new generation cement composites that have high strength and uniformity, and low porosity. Such performance indicators are achieved by nano- and micromodification of the structure of cement composites with various chemical admixtures, which at the same time represent both a component of the cement matrix and a technological method for achieving the required properties. Moreover, the role of chemical admixtures in the technology of modern cement composites increases in accordance with the increase in their influence on the hydration processes and formation of the structure of cement stone. In [1], the authors suggest that the increase in the strength of cement systems over time can be described by a sawtooth curve, which is due to the process of hydrolysis along the Si–O–Si bonds (providing 50–60% of the strength [2]), as a result of which physico-chemical changes in the structure of cement stone changes will occur.

Previously, in the studies of domestic [3–6] and foreign scientists [7–10], it was established that the use of chemical admixtures with a plasticizing effect in the technology of cement composites for structural purposes is the most reasonable way to regulate their phase composition, microstructure, and strength properties. For example, in studies [3, 4] the influence of the method of administration and dosage of the superplasticizer C-3 (based on sulfonated naphthalene formaldehyde polycondensates) on the formation of long-term strength of cement stone for up to 18 years was investigated. It was established that the strength characteristics of the studied cement systems depend on the concentration

of the superplasticizer and, in comparison with the reference unmodified system, can be both higher and lower. This is due to the fact that in a hardening cement paste, the simultaneous crystallization of new hydrate formations of various quantities and compositions from the (CaO)<sub>x</sub>–(SiO<sub>2</sub>)<sub>y</sub>–(H<sub>2</sub>O)<sub>z</sub> solid solution of implementation, formed in the early stages of cement hydration, occurs.

It should be noted that now modifying admixtures for cement composites are complex, i.e. they contain not only a superplasticizer, but also various micro- and nanoadmixture of inorganic nature [10–16]. At the same time, establishing the relationship between the parameters of the structural strength of cement composites with the technological dosing procedure and the optimal dosage of the admixture is the main task in the problem of modifying cement systems with modern complex admixtures.

In particular, our experimental studies [17–19], as well as the results obtained by other scientists [5–9], allowed to establish that complex admixtures based on nano-sized SiO<sub>2</sub>, as well as nanosized carbon and chrysotile tubes have a positive effect on the structure formation and strength characteristics of cement composites during the initial period of their hardening (up to 28 days).

Studies examining the influence of nanosized particles on the formation of the structure and strength characteristics of cement systems under long-term hardening are practically absent. However, this problem is relevant since it is assumed that at the later stages of hardening, chemically active nano-sized particles in the composition of cement composites can contribute to the occurrence of two differently directed processes - the evolution and self-organization of the structure of composites with a corresponding increase in their strength characteristics, or degradation of the structure, which may be associated with an increase in stresses and deformations over time, ultimately leading to the destruction of the material [20].

The purpose of this study was investigation of the processes of structure formation and strength gain of nanomodified hardened cement paste during its hardening duration of up to 10 years.

## 2. Experimental

The following ingredients were used as initial components for the creation of cement systems: ordinary Portland cement (C) CEM I 42.5 produced by JSC EUROCEMENT GROUP (Russian National State Standard 31108–2016); tap water (B) (Russian National State Standard 23732–2011); carbon nanotubes (CNT) of the fulleroid type *Nanocyl-7000* ( $l = 700\text{--}3000$  nm,  $d = 5\text{--}35$  nm) obtained by chemical vapor deposition; complex nano-sized admixture (CNA), consisting of  $\text{SiO}_2$  particles with medium diameter  $d_{av} \sim 10$  nm and superplasticizer grade *Sika® ViscoCrete® 20 HE* produced by LLC “Zika”. The synthesis of CNA was carried out by the sol-gel method, described in detail in [17].

The mixtures were prepared by mixing Portland cement with a liquid mixer containing nano-sized admixtures. The water-cement ratio (W/C) for each system was selected based on the normal density of the cement paste. Three systems were obtained: reference C – W (W/C = 0.45), C – CNA (W/C = 0.27), C – CNT (W/C = 0.27). The mass fraction of nanosized particles of CNA and CNT required for modifying cement systems was determined earlier [18, 19] and amounted to 0.01% by weight of cement. The molded samples were placed in a normal hardening chamber ( $T = 21$  °C,  $W = 100\%$ ), where they were kept for the required time (28 days, 1 year, 5 years, and 10 years).

A study of the degree of hydration ( $D_h$ ) and phase composition of cement systems was carried out using a diffractometer *ARL X'TRA* ( $\text{CuK}_\alpha$  radiation,  $\lambda = 1.541788$  Å) by powder X-ray diffractometry. Primary results were processed using the software package *PDWin 4.0* [21].

Calculation of  $D_h$  values of cement systems were carried out according to ratio (1). For this, the content of the alite phase ( $3\text{CaO}\cdot\text{SiO}_2$  ( $C_3S$ )) in a sample of pure cement clinker and in the studied cement systems [22] were determined:

$$C_h(C_3S) = \left(1 - \frac{I_{\text{mod}}}{I_0}\right) \cdot 100\%, \quad (1)$$

where  $I_{\text{mod}}$  – intensity of the maximum phase peak  $C_3S$  ( $d = 2.75$  Å) in cement stone samples of different composition and hardening age;  $I_0$  – intensity of the maximum peak of  $C_3S$  phase in the original cement ( $d = 2.75$  Å).

Features of the microstructure of cement systems were determined by scanning electron microscopy (SEM) using *Phenom XL* microscope,  $v_{\text{acc}} = 15$  kV,  $P = 0.10$  Pa) with a backscattered electron detector. A cement stone chip was used as a sample.

The study of the strength characteristics of cement systems was carried out using *INSTRON Sates 1500HDS* testing machine. For this, we destroyed a series (9–12 samples) of cube samples with the size of  $5\times 5\times 5$  cm. As a result of tests, it was established that the coefficient of variability within one series of samples was 7–10%.

## 3. Results and discussion

### 3.1. Processes of hydration and structure formation of cement systems

It was established that the intensity of cement hydration processes with the introduction of CNA and CNT increased significantly during the initial period of hardening (Figs. 1, 2). Already at the 28 days in nanomodified cement systems (C – CNA and C – CNT) the  $D_h$  index amounted to ~90%. In the reference system without modifiers, such value was recorded only after 10 years.

The phase composition of all studied systems (Fig. 1, Table 1) after 28 days of hardening was predominantly represented by phases of tobermorite-like ( $x\text{CaO}\cdot\text{SiO}_2\cdot z\text{H}_2\text{O}$ ), primary ( $\text{CaO}\cdot\text{SiO}_2\cdot\text{H}_2\text{O}$  – *CSH*) and secondary ( $2\text{CaO}\cdot\text{SiO}_2\cdot\text{H}_2\text{O}$  –  $C_2SH$ ) calcium silicate hydrates.

At this stage of hardening, in addition to the indicated phases in the C-CNA system, an additional formation of a phase of highly basic calcium silicate hydrate ( $3\text{CaO}\cdot\text{SiO}_2\cdot 2\text{H}_2\text{O}$ ) occurred, and in the reference system C – W the presence of a portlandite phase ( $\text{Ca}(\text{OH})_2$ ) was revealed.

It can be assumed, that the heterogeneous process of formation of silicate hydrate phases in the reference and modified cement systems proceeds differently. During the initial hardening period of up to 28 days, congruent dissolution and hydration of the main clinker minerals occurs [18]. In this case, a  $x\text{CaO}\cdot y\text{SiO}_2\cdot z\text{H}_2\text{O}$  solid solution of implementation of variable composition is formed, which subsequently undergoes decomposition into several phases. In the reference system C – W, the solid solution of implementation decomposes mainly into



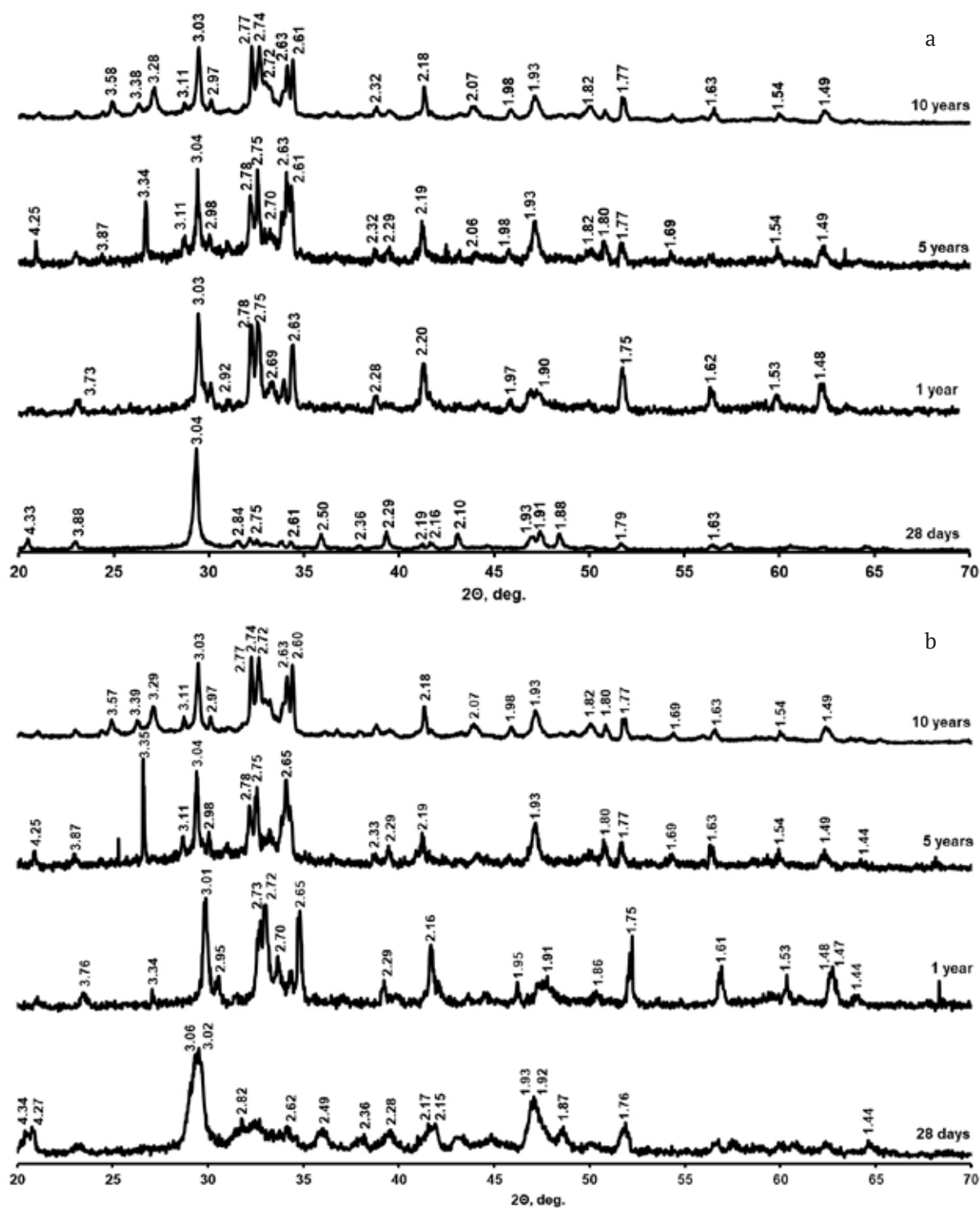


**Fig. 1.** X-Ray diffraction patterns of the nanomodified cement systems. Designated: a) C – CNA; b) C – CNT  $(\text{CaO})_x \cdot \text{SiO}_2 \cdot z\text{H}_2\text{O}$  ( $d = 3.34; 3.05; 2.93; 2.80; 2.31; 1.83$ );  $\text{CaO} \cdot \text{SiO}_2 \cdot \text{H}_2\text{O}$  ( $d = 4.24; 3.01; 2.78; 2.50; 2.23; 1.77$ );  $2\text{CaO} \cdot \text{SiO}_2 \cdot \text{H}_2\text{O}$  ( $d = 3.34; 3.01; 2.92; 2.25; 1.96; 1.81$ );  $3\text{CaO} \cdot \text{SiO}_2 \cdot 2\text{H}_2\text{O}$  ( $d = 3.33; 3.04; 2.92; 2.84; 1.88; 1.77$ );  $3(2\text{CaO} \cdot \text{SiO}_2) \cdot \text{H}_2\text{O}$  ( $d = 3.07; 2.97; 2.72; 2.62; 2.22; 1.74$ );  $2\text{CaO} \cdot 3\text{SiO}_2 \cdot \text{H}_2\text{O}$  ( $d = 4.24; 3.84; 3.36; 3.15; 2.85; 2.25$ );  $3\text{CaO} \cdot 2\text{SiO}_2 \cdot 3\text{H}_2\text{O}$  ( $d = 3.05; 2.74; 2.31; 2.21; 1.92; 1.68$ );  $2\text{CaO} \cdot \text{SiO}_2 \cdot 0.5\text{H}_2\text{O}$  ( $d = 2.99; 2.77; 2.67; 2.25; 1.80; 1.61$ );  $6\text{CaO} \cdot 6\text{SiO}_2 \cdot 2\text{H}_2\text{O}$  ( $d = 3.65; 3.23; 3.07; 2.83; 2.04; 1.95$ );  $\text{CaO} \cdot \text{Al}_2\text{O}_3 \cdot 8.5\text{H}_2\text{O}$  ( $d = 3.57; 3.13; 2.75; 2.58; 2.34; 1.79$ );  $4\text{CaO} \cdot \text{Al}_2\text{O}_3 \cdot 19\text{H}_2\text{O}$  ( $d = 2.88; 2.78; 2.67; 2.35; 1.93; 1.82$ );  $3\text{CaO} \cdot \text{Al}_2\text{O}_3 \cdot \text{SiO}_2 \cdot 4\text{H}_2\text{O}$  ( $d = 3.07; 2.74; 2.24; 1.99; 1.70; 1.64$ );  $\text{CaO} \cdot \text{Al}_2\text{O}_3 \cdot 2\text{SiO}_2 \cdot 4\text{H}_2\text{O}$  ( $d = 3.34; 3.19; 2.74; 2.70; 2.66; 1.81$ );  $3\text{CaO} \cdot \text{Fe}_2\text{O}_3 \cdot \text{CaSO}_4 \cdot 16\text{H}_2\text{O}$  ( $d = 3.40; 2.93; 2.55$ );  $3\text{CaO} \cdot \text{Al}_2\text{O}_3 \cdot 3\text{CaSO}_4 \cdot 32\text{H}_2\text{O}$  ( $d = 4.90; 3.02; 2.79; 1.62; 1.54; 1.50$ );  $\text{Ca}(\text{OH})_2$  ( $d = 3.11; 2.63; 1.93; 1.79; 1.69; 1.49$ ) [19]

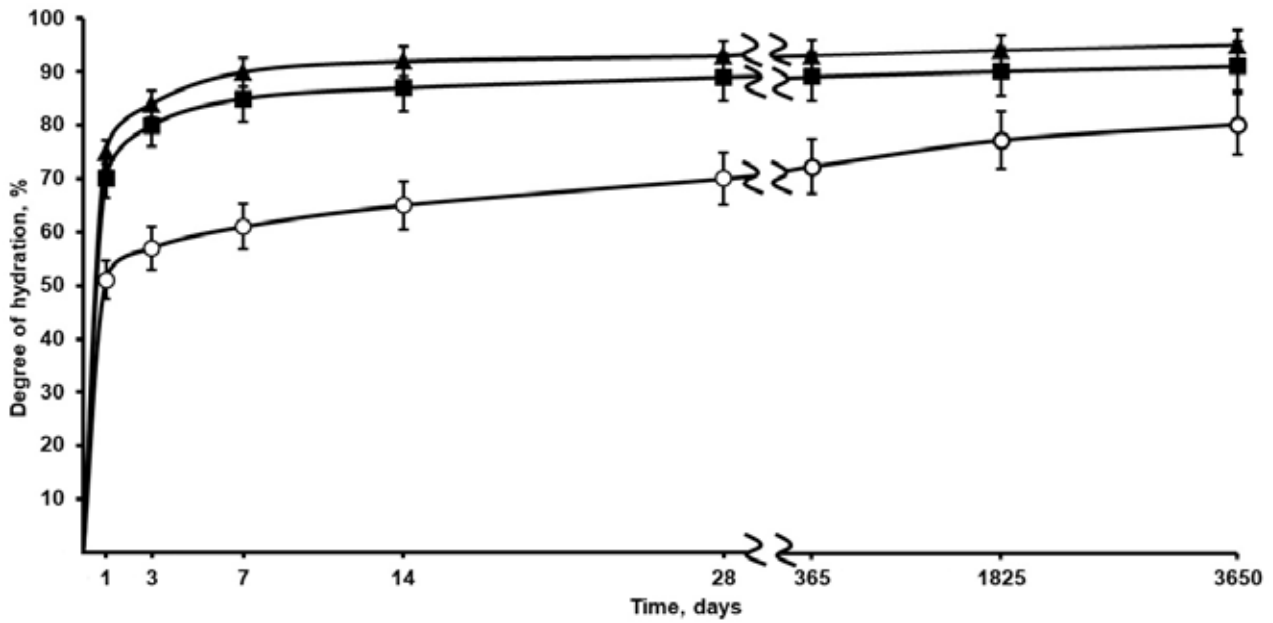


Fig. 2. Kinetics of hydration of cement systems with a duration of their hardening of up to 10 years. Designated: o – C – W; ▲ – C – CNA; ■ – C – CNT

Table 1. Phase composition and morphology of cement systems with a hardening duration of up to 10 years

System	Phase composition of system / morphology of crystals			
	28 days	1 year	5 years	10 years
C – W (W/C = 0.45)	xCaO·SiO <sub>2</sub> ·zH <sub>2</sub> O / Plate 2CaO·SiO <sub>2</sub> ·H <sub>2</sub> O / Plate CaO·SiO <sub>2</sub> ·H <sub>2</sub> O / Needle Ca(OH) <sub>2</sub> / Plate-prismatic	CaO·SiO <sub>2</sub> ·H <sub>2</sub> O / Needle xCaO·SiO <sub>2</sub> ·zH <sub>2</sub> O / Plate 2CaO·SiO <sub>2</sub> ·H <sub>2</sub> O / Plate Ca(OH) <sub>2</sub> / Plate-prismatic	2CaO·SiO <sub>2</sub> ·H <sub>2</sub> O / Plate (CaO) <sub>x</sub> ·SiO <sub>2</sub> ·zH <sub>2</sub> O / Plate CaO·Al <sub>2</sub> O <sub>3</sub> ·8.5H <sub>2</sub> O / Hexagonal plate Ca(OH) <sub>2</sub> / Plate-prismatic	2CaO·SiO <sub>2</sub> ·0.5H <sub>2</sub> O / Plate 3CaO·Al <sub>2</sub> O <sub>3</sub> ·SiO <sub>2</sub> ·4H <sub>2</sub> O / Hexagonal plate 3CaO·Fe <sub>2</sub> O <sub>3</sub> ·CaSO <sub>4</sub> ·16H <sub>2</sub> O / Hexagonal plate Ca(OH) <sub>2</sub> / Plate-prismatic
C – CNA (W/C = 0.27)	xCaO·SiO <sub>2</sub> ·zH <sub>2</sub> O / Plate 3CaO·SiO <sub>2</sub> ·2H <sub>2</sub> O / Hexagonal plate CaO·SiO <sub>2</sub> ·H <sub>2</sub> O / Needle	CaO·SiO <sub>2</sub> ·H <sub>2</sub> O / Needle 4CaO·Al <sub>2</sub> O <sub>3</sub> ·19H <sub>2</sub> O / Hexagonal plate 3(2CaO·SiO <sub>2</sub> )·2H <sub>2</sub> O / Hexagonal plate	CaO·SiO <sub>2</sub> ·H <sub>2</sub> O / Needle CaO·Al <sub>2</sub> O <sub>3</sub> ·2SiO <sub>2</sub> ·4H <sub>2</sub> O / Hexagonal plate 2CaO·3SiO <sub>2</sub> ·H <sub>2</sub> O / Hexagonal plate	6CaO·6SiO <sub>2</sub> ·H <sub>2</sub> O / Fibrous and Needle 3CaO·2SiO <sub>2</sub> ·3H <sub>2</sub> O / Fibrous and Needle 2CaO·SiO <sub>2</sub> ·H <sub>2</sub> O / Plate
C – CNT (W/C = 0.27)	xCaO·SiO <sub>2</sub> ·zH <sub>2</sub> O / Plate 2CaO·SiO <sub>2</sub> ·H <sub>2</sub> O / Plate CaO·SiO <sub>2</sub> ·H <sub>2</sub> O / Needle	CaO·SiO <sub>2</sub> ·H <sub>2</sub> O / Needle 3CaO·Al <sub>2</sub> O <sub>3</sub> ·SiO <sub>2</sub> ·4H <sub>2</sub> O / Hexagonal plate 3(2CaO·SiO <sub>2</sub> )·2H <sub>2</sub> O / Hexagonal plate	CaO·SiO <sub>2</sub> ·H <sub>2</sub> O / Needle 4CaO·Al <sub>2</sub> O <sub>3</sub> ·19H <sub>2</sub> O / Hexagonal plate 3CaO·2SiO <sub>2</sub> ·3H <sub>2</sub> O / Fibrous and Needle	6CaO·6SiO <sub>2</sub> ·H <sub>2</sub> O / Fibrous and Needle 3CaO·Al <sub>2</sub> O <sub>3</sub> ·3CaSO <sub>4</sub> ·32H <sub>2</sub> O / Fibrous and Needle 2CaO·SiO <sub>2</sub> ·0.5H <sub>2</sub> O / Plate

tobermorite and the  $C_2SH$  phase, while in modified systems, under the influence of active nano-sized particles, the formation of  $CSH$  calcium silicate hydrate phases with  $x = 0.8–1.5$  predominantly occurs.

It should be noted that over 10 years, phase transformations and changes in phase composition have been observed in all systems.

After 1 year of hardening the phase composition of the reference unmodified system practically did not change, but in nanomodified systems it changed significantly: the tobermorite-like phase transformed into highly basic calcium silicate hydrate ( $3(2CaO \cdot SiO_2) \cdot 2H_2O$ ); at the same time, a phase of highly basic hydrated calcium aluminate ( $4CaO \cdot Al_2O_3 \cdot 19H_2O$ ) is formed in the system with the addition of CNA, and the phase of calcium aluminosilicate hydrate ( $3CaO \cdot Al_2O_3 \cdot SiO_2 \cdot 4H_2O$ ) is formed in the system with the addition of CNT.

After 5 years of hardening in the reference system, low-basic hydrated calcium aluminate ( $CaO \cdot Al_2O_3 \cdot 8.5H_2O$ ) starts to form, which was typical for 1 year of hardening in nanomodified systems. An increased content of low-basic calcium aluminosilicate hydrates ( $CaO \cdot Al_2O_3 \cdot 2SiO_2 \cdot 4H_2O$ ) and calcium silicate hydrates ( $2CaO \cdot 3SiO_2 \cdot H_2O$ ) was observed in the modified C – CNA system. This may be due to the introduction of nanosized  $SiO_2$  particles into the system, which are related in their crystal chemical structure to the minerals of cement stone, and are capable of chemical interaction with clinker minerals of cement, which leads to a decrease in the basicity of the resulting silicate hydrate phases.

For the C – CNT system, on the contrary, the formation of stable highly basic hydrated calcium aluminate ( $4CaO \cdot Al_2O_3 \cdot 19H_2O$ ) and calcium silicate hydrate ( $3CaO \cdot 2SiO_2 \cdot 3H_2O$ ) was observed.

After 10 years of hardening in the reference system, highly basic silicate hydrates and calcium aluminosilicate hydrates start to form, as well as the low-sulphate form of calcium hydrosulfate ( $3CaO \cdot Fe_2O_3 \cdot CaSO_4 \cdot 16H_2O$ ).

It is worth noting that in the reference system C – W, the presence of the portlandite phase was recorded throughout the entire hardening process, in contrast to modified systems in which this phase was absent.

Thus, the phase composition of nanomodified systems during prolonged hardening was characterized by the formation of stable xonotlite minerals ( $6CaO \cdot 6SiO_2 \cdot H_2O$ ), while in the C – CNA system, afwillite was additionally formed ( $3CaO \cdot 2SiO_2 \cdot 3H_2O$ ), and in the system C – CNT, ettringite ( $3CaO \cdot Al_2O_3 \cdot 3CaSO_4 \cdot 32H_2O$ ) was formed. The data obtained are consistent with the results presented in [3].

The X-ray phase analysis data correlate well with the SEM results (Fig. 3). It was established that the morphology of particles of unmodified and nanomodified hardened cement paste differs throughout the entire studied hardening period. In the reference system C – W, with a hardening duration of 28 days (Fig. 3a), a heterogeneous structure of cement stone was formed, consisting mainly of an amorphous-crystalline silicate hydrate gel and large lamellar crystals of portlandite.

In nanomodified systems, during a similar period of hardening (Fig. 3d, g), the formation of nanosized crystallites with a small grain size occurs, forming a more uniform structure. At the same time, in the studied systems, the presence of a weakly crystallized gel, characteristic of primary low-basic calcium silicate hydrates, as well as fiber and needle-like new formations, probably formed by secondary high-basic calcium silicate hydrates was observed. It should be noted that crystallites form a large number of adjacent and intergrowth contacts with each other, which allows nanomodified systems to achieve high-performance  $R_{com}$  already in the early stages of hardening.

With a hardening duration of 5 years, the reference system (Fig. 3b) was characterized by a heterogeneous morphology of the cement stone, with predominantly lamellar crystals of different sizes; in the modified systems C – CNA and C – CNT (Fig. 3e, h), a predominantly fiber-plate and fiber-needle morphology of the resulting crystals was observed, respectively. After 10 years (Fig. 3f, i), the structure of the nanomodified cement stone can be characterized as dense, formed by crystallites of a predominantly fiber and lamellar structure, forming adjacent and intergrowth contacts with each other and other hydrate new formations.



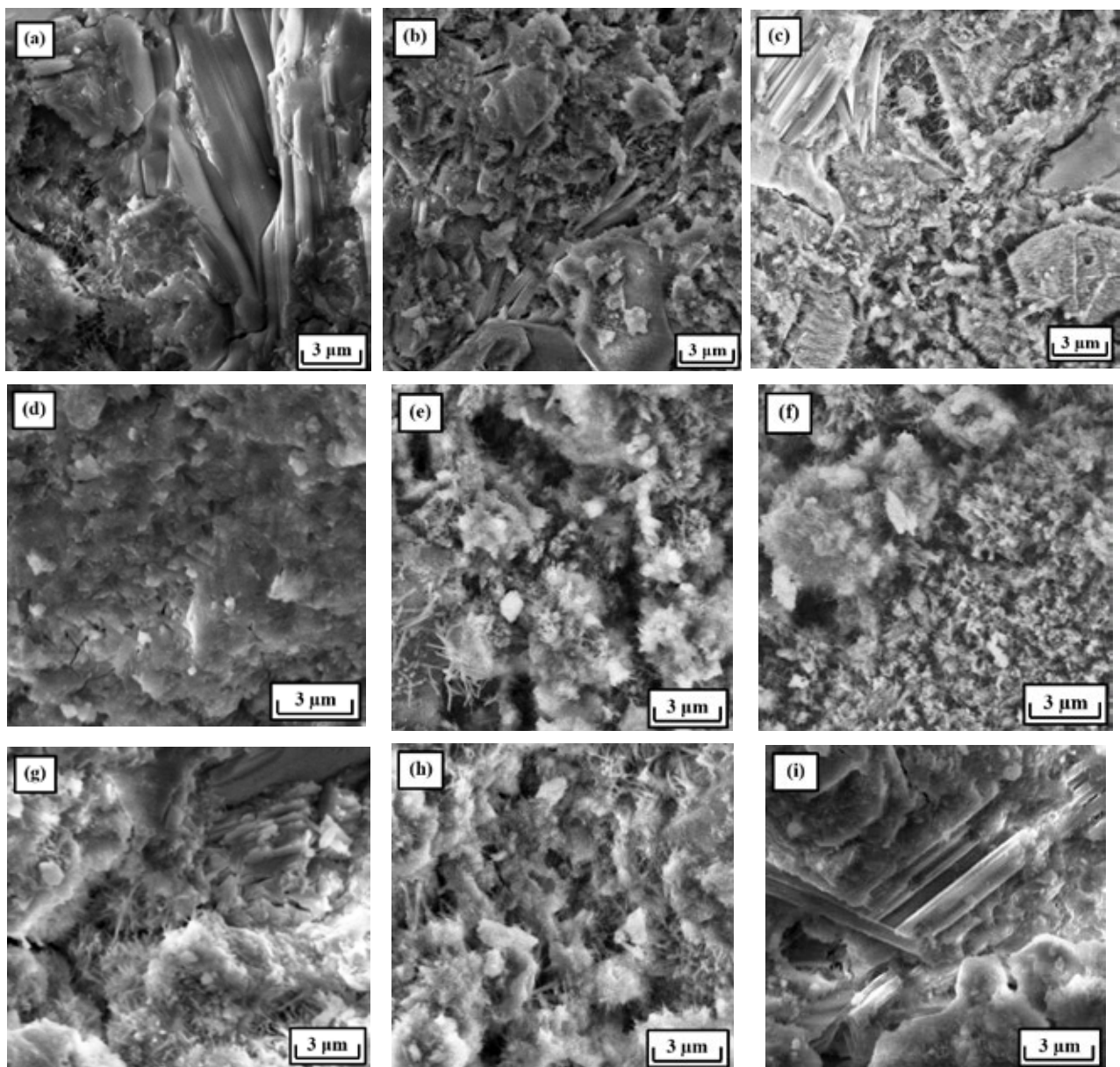


**Fig. 3.** Micrographs of the studied cement hardening systems: C – W (a, b, c); C – CNA (d, e, f); C – CNT (g, h, i) at different curing times (28 days – a, d, g; 5 years – b, e, h ; 10 years – c, f, i)

### 3.2. Strength characteristics of cement systems

The results of determining the compressive strength of the studied cement systems are presented in Table 2. It was found that after 28 days the  $R_{com}$  in the C – CNA system reached 85 MPa, and in the C – CNT system it was 78 MPa. A similar value (80 MPa) in the reference system without admixtures was achieved only after 10 years of hardening. Subsequently, during the entire hardening period for cement systems, a gradual increase in strength characteristics

was observed. Maximum value of the  $R_{com}$  was achieved after 10 years in the C – CNA system and composed 157 MPa.

The values of age-strength relation over time ( $\beta_t$ ), which was calculated as the ratio of the actual compressive strength ( $R_t$ ) of cement stone at a given age  $t$  to compressive strength ( $R_{28}$ ) at 28 days are shown in Table 2. It should be noted that higher  $\beta_t$  values were obtained for cement systems with CNA and CNT admixtures compared to the reference system throughout the entire studied hardening period.

**Table 2.** Kinetics of strength of cement systems with a duration of their hardening up to 10 years

System	W/C	Compressive strength ( $R_{com}$ ), MPa / Coefficient of strength increase ( $\beta_t$ ), rel. units.			
		28 days	1 year	5 years	10 years
C – W	0.45	53 / 1	68 / 1.28	74 / 1.39	80 / 1.51
C – CNA	0.27	85 / 1	111 / 1.31	132 / 1.55	157 / 1.85
C – CNT	0.27	78 / 1	103 / 1.32	112 / 1.44	121 / 1.55

#### 4. Conclusions

The positive effect of nanoscale admixtures on the processes of hydration and structure formation of cement systems with a hardening duration of up to 10 years has been established. Research results show that in nanomodified cement systems high degrees of hydration are achieved both during the early and long-term stages of hardening. In this case, the formation of stable hydrate new growths of various compositions, crystallizing mainly in the form of fibers and plates, characterized by a large number of adjacent and intergrowth contacts between themselves and other hydrate new growths occurs.

It was established that, in comparison with the reference system, cement systems with admixtures of nanosized particles were characterized by high values of compressive strength throughout the entire studied hardening time. The highest  $R_{com}$  both for 28th day of hardening (85 MPa) and with a hardening duration of 10 years (157 MPa) was characteristic for the cement system modified by CNA based on  $SiO_2$  particles.

#### Author contributions

Artamonova O. V. – scientific leadership, research concept, methodology development, text writing, final conclusions.

Shvedova M. A. – conducting research, review writing and editing.

#### Conflict of interests

The authors declare that they have no known competing financial interests or personal relationships that could have influenced the work reported in this paper.

#### References

1. Mchedlov-Petrosyan O. P., Chernyavsky V. L., Olginsky A. G. Late stages of cement hydration\*. *Cement*. 1982;9: 15–17. (In Russ.)

2. Sychev M. M. Some questions of chemistry of concrete and cement stone\*. *Russian Journal of Applied Chemistry*. 1981;LIV(9): 2036–2043. (In Russ.)

3. Makridin N. I., Maksimova I. N., Ovsyukova Yu. V. Long-term strength of the modified cement stone structure\*. Part 1. *Stroitel'nye Materialy (Construction Materials)*. 2010;10: 74–77. (In Russ.). Available at: <https://www.elibrary.ru/item.asp?id=15506100>

4. Maksimova I. N., Erofeev V. T., Makridin N. I., Poluboyarova Yu. V. Analysis of superplastizers phase composition and parameters of structural fracture mechanics of cement stone of different ages. *News of Higher Educational Institutions. Construction*. 2016;5(689): 29–38. (In Russ., abstract in Eng.). Available at: <https://www.elibrary.ru/item.asp?edn=wirxqn>

5. Potapov V. V., Tumanov A. V., Zakurazhnov M. S., Cerdan A. A., Kashutin A. N., Shalaev K. S. Enhancement of concrete durability by introducing  $SiO_2$  nanoparticles. *Glass Physics and Chemistry*. 2013;39(4): 425–430. <https://doi.org/10.1134/S1087659613040160>

6. Urkhanova L. A., Lkhasaranov S. A., Buyantuev S. L., Kuznetsova A. Yu. About the influence of carbon nanomaterials on the properties of cement and concrete. *Nanotechnologies in Construction: A Scientific Internet-Journal*. 2016;8(5): 16–41. <https://doi.org/10.15828/2075-8545-2016-8-5-16-41>

7. Reches Y. Nanoparticles as concrete additives: Review and perspectives. *Construction and Building Materials*. 2018;175: 483–495. <https://doi.org/10.1016/j.conbuildmat.2018.04.214>

8. Paul S. C., van Rooyen A. S., van Zijl G. P. A. G., Petrik L. F. Properties of cement-based composites using nanoparticles: A comprehensive review. *Construction and Building Materials*. 2018;189: 1019–1034. <https://doi.org/10.1016/j.conbuildmat.2018.09.062>

9. Tolchikov Yu. N., Mikhaleva Z. A., Tkachev A. G., Artamonova O. V., Kashirin M. A., Auad M. S. The effect of a carbon nanotubes-based modifier on the formation of the cement stone structure. *Advanced materials and technologies*. 2018;3: 49–56. <https://doi.org/10.17277/amt.2018.03.pp.049-056>

10. Najafi Kani E., Rafiean A. H., Alishah A., Hojjati Astani S., Ghaffar S. H.. The effects of nano- $Fe_2O_3$  on the mechanical, physical and microstructure of

- cementitious composites. *Construction and Building Materials*. 2021;266: 121137. <https://doi.org/10.1016/j.conbuildmat.2020.121137>
11. Singh M., Srivastava A., Bhunia D. Long term strength and durability parameters of hardened concrete on partially replacing cement by dried waste marble powder slurry. *Construction and Building Materials*. 2019;198: 553–569. <https://doi.org/10.1016/j.conbuildmat.2018.12.005>
12. Nili M., Afroughsabet V. The long-term compressive strength and durability properties of silica fume fiber-reinforced concrete. *Materials Science and Engineering A*. 2012;531: 107–111. <https://doi.org/10.1016/j.msea.2011.10.042>
13. Persson B. Seven-year study on the effect of silica fume in concrete. *Advanced Cement Based Materials*. 1998;7(3-4): 139–155. [https://doi.org/10.1016/S1065-7355\(98\)00003-0](https://doi.org/10.1016/S1065-7355(98)00003-0)
14. Ho L.S., Huynh T.-P. Long-term mechanical properties and durability of high-strength concrete containing high-volume local fly ash as a partial cement substitution. *Results in Engineering*. 2023;18: 101113. <https://doi.org/10.1016/j.rineng.2023.101113>
15. Huang Q., Xiong G., Fang Z., ... Zhu X. Long-term performance and microstructural characteristics of cement mortars containing nano-SiO<sub>2</sub> exposed to sodium sulfate attack. *Construction and Building Materials*. 2023;364: 130011. <https://doi.org/10.1016/j.conbuildmat.2022.130011>
16. Kaprielov S. S., Sheinfeld A. V., Dondukov V. G. Cements and additives for producing high-strength concrete. *Stroitel'nye Materialy (Construction Materials)*. 2017;11: 4–10. (In Russ., abstract in Eng.). Available at: <https://www.elibrary.ru/item.asp?id=30744332>
17. *Synthesis of nanomodifying additives for the technology of building composites. Monograph\**. O. V. Artamonova (Ed.). Voronezh: Voronezh GASU Publ.; 2016. 100 p. (in Russ.)
18. Artamonova O. V., Slavcheva G. S., Chernyshov E. M. Effectiveness of combined nanoadditives for cement systems. *Inorganic Materials*. 2017;53(10): 1080–1085. <https://doi.org/10.1134/S0020168517100028>
19. Artamonova O. V., Slavcheva G. S., Shvedova M. A. Effectiveness of nanotubular additives in the modification of cement systems. *Inorganic Materials*. 2020;56(1): 105–110. <https://doi.org/10.1134/S0020168520010021>
20. Artamonova O. V., Shvedova M. A. Effect of nanosized additives on structure formation and strength characteristics of cement stone with long hardening. *Technique and Technology of Silicates*. 2021;28(4): 159–164. (In Russ., abstract in Eng.). Available at: <https://www.elibrary.ru/item.asp?id=48238746>
21. JCPDS – International Centre for Diffraction Data. © 1987 – 1995. JCPDS – ICDD. Newtown Square, PA. 19073. USA. Available at: <https://www.icdd.com/>
22. Bullard J. W., Jennings H. M., Livingston R. A., ... Thomas J. J. Mechanisms of cement hydration. *Cement and Concrete Research*. 2011;41: 1208–1223. <https://doi.org/10.1016/j.cemconres.2010.09.011>

\* Translated by author of the article

#### Information about the authors

Olga V. Artamonova, Dr. Sci. (Tech.), Associate Professor, Professor at the Department of Chemistry and Chemical Technology of Materials, Voronezh State Technical University (Voronezh, Russian Federation). <https://orcid.org/0000-0001-9157-527X>  
ol\_artam@rambler.ru

Maria A. Shvedova, Cand. Sci. (Tech.), Research Fellow at the Higher School of Building Materials Science (Academy of Building Complex Development), Voronezh State Technical University (Voronezh, Russian Federation). <https://orcid.org/0000-0002-6484-8719>  
marishwedowa@mail.ru

Received 05.09.2023; approved after reviewing 09.10.2023; accepted for publication 15.11.2023; published online 25.06.2024.

Translated by Valentina Mittova





## Original articles

Research article

<https://doi.org/10.17308/kcmf.2024.26/12082>**Photoelectrochemical activity of oxide films on silver-palladium alloys in an alkaline solution**I. A. Belyanskaya, M. Yu. Bocharnikova, M. M. Murtazin, S. N. Grushevskaya , O. A. Kozaderov, A. V. VvedenskyVoronezh State University,  
1 Universitetskaya pl., Voronezh 394018, Russian Federation**Abstract**

The continuously increasing energy needs of humanity are causing a number of serious environmental problems. One of the methods for the solution of such problems is the photocatalytic or photoelectrochemical production of a fairly environmentally friendly fuel - hydrogen gas. The studies in this field are mainly associated with the search for semiconductor material that is most suitable for photocatalysis. Oxides of some metals, including silver, can be used as such a material. The photocatalytic or photoelectrochemical activity of the oxide is determined by the features of its electronic structure and can increase significantly when combined with another oxide. Therefore, anodic oxidation of binary alloys is considered as an accessible and, most importantly, controlled method for combining oxides of various metals. The aim of this study was to reveal the role of alloying of silver with palladium in the photoelectrochemical activity of oxide films anodically formed in deaerated 0.1 M KOH.

The anodic formation of oxide films was carried out by the potentiodynamic method in an alkaline medium on silver and its alloys with palladium, the concentration of which ranged from 5 to 30 at. %. Photoelectrochemical activity was assessed by the magnitude of the photocurrent generated in the oxide film directly during its formation and subsequent reduction. The photocurrent was measured in a pulsed lighting mode of the electrode surface with a quasimonochromatic LED with a wavelength of 470 nm.

A positive photocurrent was recorded on all studied samples, which indicates the predominance of donor structural defects in the forming oxide film. With an increase in the concentration of palladium in the alloy, the range of potentials of photoelectrochemical activity of formed anodically oxide films expanded. The maximum photocurrent achieved during the anodic potentiodynamic formation of the oxide film was higher, the lower the palladium concentration was. During the cathodic potentiodynamic reduction of the formed oxide films, it was possible to record even higher values of photocurrents than during their anodic formation. The highest photoelectrochemical activity, characterized by a photocurrent density of 2.89  $\mu\text{A}/\text{cm}^2$  and incidental proton-to-electron conversion efficiency of 7.6%, was observed in the oxide film anodically formed on silver by the time the potential reached 0.6 V. Comparable values of the photocurrent and quantum efficiency (2.12  $\mu\text{A}/\text{cm}^2$  and 5.6%) were recorded in the oxide film on the alloy with a palladium concentration of 10 at. % during its potentiodynamic reduction.

**Keywords:** Silver-palladium alloys, Anodic oxide formation, Photoelectrochemical activity, Photocurrent, Cyclic voltammetry

**Funding:** The study was supported by the Ministry of Science and Higher Education of the Russian Federation within the framework of state order to higher education institutions in the sphere of scientific research for 2022–2024, project No. FZGU-2022-0003.

**Acknowledgements:** The authors are grateful to the Centre for collective use of scientific equipment of Voronezh State University – Agapov B. L. for performing energy-dispersive microanalysis and Kannykin S. V. for performing X-ray diffractometry.

**For citation:** Belyanskaya I. A., Bocharnikova M. Y., Murtazin M. M., Grushevskaya S. N., Kozaderov O. A., Vvedenskii A. V. Photoelectrochemical activity of oxide films on silver-palladium alloys in alkaline solution. *Condensed Matter and Interphases*. 2024;26(2): 213–224. <https://doi.org/10.17308/kcmf.2024.26/12082>

✉ Svetlana N. Grushevskaya, e-mail: [sg@chem.vsu.ru](mailto:sg@chem.vsu.ru)

© Belyanskaya I. A., Bocharnikova M. Y., Murtazin M. M., Grushevskaya S. N., Kozaderov O. A., Vvedenskii A. V., 2024



The content is available under Creative Commons Attribution 4.0 License.

**Для цитирования:** Белянская И. А., Бочарникова М. Ю., Муртазин М. М., Грушевская С. Н., Козадеров О. А., Введенский А. В. Фотоэлектрохимическая активность оксидных пленок на серебряно-палладиевых сплавах в щелочном растворе. *Конденсированные среды и межфазные границы*. 2024;26(2): 213–224. <https://doi.org/10.17308/kcmf.2024.26/12082>

## 1. Introduction

Semiconductors based on metal oxides are used in modern technologies of opto- and microelectronics (including complementary metal-oxide-semiconductor structures), electrocatalysis, the manufacture of sensor and current-generating devices, as well as photocatalytic and photoelectrochemical hydrogen production [1–3]. Such technologies for production of hydrogen have been particularly intensively developed in recent decades, as they allow solving problems with continuously increasing energy needs by humanity in a fairly environmentally friendly way.

In both photocatalytic and photoelectrochemical processes the first stage is the illumination of the semiconductor material and the generation of electron-hole pairs [4–7]. At the next stage the charge carriers are separated in space, migrate to the interfaces and pass into the electrolyte. In the case of photocatalysis, photoinduced electrons and holes participate in reduction and oxidation processes occurring at the semiconductor/electrolyte interfaces [6]. In the case of photoelectrocatalysis, the reduction or oxidation process occurs at the semiconductor photoelectrode/electrolyte interface, and charge carriers move from one electrode to the second via the external circuit [7]. Due to the presence of similar steps, there is usually a correlation between the rate of the photocatalytic reaction and the photocurrent density [8, 9]. Thus, photocatalytic activity of semiconductor materials can be assessed based on the values of the photocurrent generated under illumination [9].

The efficiency of the processes of photocatalysis and photoelectrolysis is determined by the characteristics of the electronic structure of the semiconductor material and depends on the method of its preparation. The anodic oxidation of metals and alloys is one of the methods of the production of oxide films with controlled properties. The oxidation of alloys allow to synthesize oxide structures with complex chemical composition [2, 3], which can lead to an

increase in their photoelectrochemical activity [10].

Silver-based alloys, during anodic oxidation of which silver oxides are predominantly formed were considered as a model system in this study. Oxide Ag(I) is a narrow-bandgap semiconductor, used in electronics industry for the production of electrical, optical and magneto-optical data storage devices [11–13], for the manufacture of solar cells and photovoltaic devices [14]. In addition, Ag<sub>2</sub>O nanoparticles are used as catalysts [15], and high photocatalytic activity of the Ag<sub>2</sub>O/AgO redox pair in relation to the oxygen evolution reaction was demonstrated [16]. Catalysts based on silver and its oxides are promising materials for photocatalytic and photoelectrocatalytic decomposition of water [17, 18]. The effect of alloy formation on the properties of anodically formed silver oxides has not been studied properly.

In [19–21], this effect was studied using the alloys of silver with gold containing 1, 4 and 15 at. %. The objects of study were obtained by smelting. During potentiostatic anodic oxidation in a deaerated 0.1 M KOH solution, silver (I) oxide was formed on their surface, while gold remained thermodynamically stable. The photoelectrochemical properties of the formed oxide were studied by measuring the photocurrent as the deviation of the dark current during pulsed lighting mode of the electrode surface with a LED with a wavelength of 470 nm and an irradiation power of  $3.6 \cdot 10^{15}$  photon/cm<sup>2</sup>s. This method allows the characterization of the oxide directly during its formation. It has been established that the photocurrent density, and hence the photoelectrochemical activity in Ag<sub>2</sub>O silver oxides of n-type formed anodically on silver-gold alloys decreased sharply with increase in gold concentration. The maximum photoelectrochemical activity was recorded in Ag(I) oxide potentiostatically formed on silver. Silver oxides Ag<sub>2</sub>O and AgO, anodically formed on silver-zinc alloys, were investigated using the same methods in [22, 23]. The presence of up to 30 at. % of zinc in the alloy allows the presence

of a small amount of zinc oxide in the oxide film. However, an increase in the photocurrent due to the combination of these oxides was not observed. On the contrary, the photoelectrochemical activity of formed anodically oxide films slightly decreased with increased zinc concentration in the alloy.

In this study, palladium, with widely known catalytic and photocatalytic properties [24, 25], is considered as the second component of silver-based alloys. In alkaline solutions, palladium can oxidize and as the result its surface is being covered with an oxide film. Palladium oxide PdO is a p-type semiconductor [26] with a wide range of technological applications, including sensor production [26–28], catalysis [29, 30], photocatalysis and photoelectrolysis [31–33]. It was reported [29, 33] that doping with PdO oxide increases the photoelectrochemical activity of various oxides of other metals. Thin films  $\text{Ag}_{1-x}\text{Pd}_x$  ( $0 \leq x \leq 1$ ) with a thickness of  $\sim 70$  nm were synthesized using the vapor deposition method in [34]. Using cyclic voltammetry in an alkaline solution, it was shown that the catalytic activity for the oxygen evolution reaction increases up to 5 times compared to pure palladium. In [35], homogeneous nanoparticles of Ag–Pd alloys with a size of about 5 nm were obtained by the thermolysis of precursors. According to cyclic voltammetry and measurements of the amount of removed CO, it was shown that the activity of the alloys in relation to the oxygen evolution reaction was higher than the activity of pure components. Moreover, the experimentally measured activity was higher than that calculated based on the assumption about linear combination of the properties of the individual components. The activity of  $\text{AgPd}_2$  alloy was by 60% higher than that of pure palladium, and for  $\text{Ag}_4\text{Pd}$  alloy activity was 3.2 times higher than calculated by the linear combination method. Similar trends are observed for other alloys with a high silver content: it was higher for  $\text{Ag}_9\text{Pd}$  by 2.7 times and for  $\text{Ag}_2\text{Pd}$  by 2.3 times. The synergistic effect was associated with the special arrangement of the atoms of the individual components [35] – single palladium atoms were surrounded by silver atoms.

Taking into account the high catalytic activity of silver alloys with palladium described

in the literature, it can be assumed that the photoelectrochemical activity of oxides formed anodically on such alloys will increase in comparison with Ag(I) oxide formed on silver. The aim of this study was to reveal the role of formation of silver and palladium alloys in the photoelectrochemical activity of oxide films formed anodically in deaerated 0.1 M KOH. In contrast to the potentiostatic conditions of anodic oxidation considered in [19–23], stepwise polarization mode of electrodes for the detection of the potential region of the highest photocurrent values, and therefore the photoelectrochemical activity of the forming anodic films was used in this study.

## 2. Experimental

### 2.1. Materials and methods

Oxide films formed during the electrochemical oxidation of silver and silver alloys with palladium in a deaerated solution of 0.1 M KOH were used as objects of the study.

The alloys were obtained from silver and palladium with a purity of 99.99 mass. % by heating for two hours in evacuated ampoules at a temperature above the liquidus line. Slow cooling to room temperature was carried out in a closed oven. Calculated palladium concentration in samples  $X_{\text{Pd}}$  was 5, 10, 15, 20, and 30 at. %. These values will be used further in the text. The elemental composition of the resulting alloys was determined using energy dispersive X-ray analysis carried out using a JSM-6380LV JEOL scanning electron microscope with an INCA 250 microanalysis system\*. Phase composition of alloys was studied using ARL X'TRA X-ray diffractometer\*.

One cylindrical sample was made from each alloy. All samples are equipped with a current lead and reinforced with polymerized epoxy resin in such a way that the end surface remained open for access to the solution. The average geometric surface area was  $0.59 \pm 0.02$  cm<sup>2</sup>.

A working solution of 0.1 M KOH was prepared from a chemically pure reagent and bidistilled water, deaerated with chemically pure argon.

\* The results of the research were obtained using the Centre for the Collective Use of Scientific Equipment of Voronezh State University. URL: <https://ckp.vsu.ru>



## 2.2. Photoelectrochemical studies

Photoelectrochemical studies were carried out in a plexiglass cell with undivided anode and cathode spaces. The cell was protected from electromagnetic interference by a metal shield. The bottom of the cell was equipped with a quartz window for illumination of the horizontally oriented surface of the working electrode. The auxiliary electrode was a platinum wire, the reference electrode was silver oxide, prepared by the electrochemical oxidation of a silver plate at a current of 5 mA for 20 min in aerated 0.1 M KOH. The potential of such an electrode was 0.428 V relative to a standard hydrogen electrode. The potentials in the study are presented relative to the standard hydrogen electrode.

Before each measurement, the surface of the working electrode, made of silver or a silver-palladium alloy, was subjected to striping on sanding paper with decreasing grain size (P800, P1500 and P2500), and then polishing on chamois. The polished surface was degreased with isopropyl alcohol. This preparation was followed by a 5-minute cathodic standardization of the surface in a working solution at a potential of  $E_c = -0.3$  V. This potential value was below the equilibrium potentials of formation/reduction of both silver (0.41 V) and palladium (0.07 V) oxides. At the same time, it was noticeably higher than the equilibrium potential of the hydrogen electrode in 0.1 M KOH with pH 12.89 ( $-0.76$  V), which excluded the possibility of hydrogen incorporation into the electrode material.

The potential region for the formation of oxide films was determined by cyclic voltammetry. The potential was scanned with rate of 5 mV/s from  $E_c$  in the anodic direction until appearance of maximum current, presumably associated with the formation of Ag(I) oxide. After this, scanning was carried out at the same rate until the value  $E_c$ .

The photoelectrochemical activity of formed anodically oxides was assessed based on the photocurrent value, determined as the difference between the current under illumination and the current in the absence of illumination.

Illumination was carried out in pulsed mode with a quasimonochromatic emitting LED (Table 1).

The incidental proton-to-electron conversion efficiency (IPCE) was calculated using the equation [36]:

$$\text{IPCE (\%)} = 100\% \cdot 1240 \cdot i_{\text{ph}} / (\lambda \cdot P),$$

Where  $i_{\text{ph}}$  – photocurrent density ( $\text{mA}/\text{cm}^2$ ),  $\lambda$  – wavelength (nm),  $P$  – lighting power ( $\text{mW}/\text{cm}^2$ ).

To determine the potential range and level of photoelectrochemical activity of silver oxide, a stepwise polarization mode of the electrodes was carried out (Fig. 1). After cathodic preparation of the electrode surface at  $E_c$  the potential was switched to the initial value  $E_i = 0.48$  V. In preliminary experiments we established that below this value the photocurrent does not occur. From  $E_i$  value the potential increased every 5 min by 20 mV with continuous recording of the polarization current and photocurrent in a pulsed lighting mode of the electrode surface. After the maximum current in the voltammogram associated with the formation of silver oxide, the potential decreased with the same step until full disappearance of the photocurrent. The polarization current and photocurrent densities were calculated per the geometric surface area of the working electrodes.

Electrochemical and photoelectrochemical studies were carried out using a Compact-2015

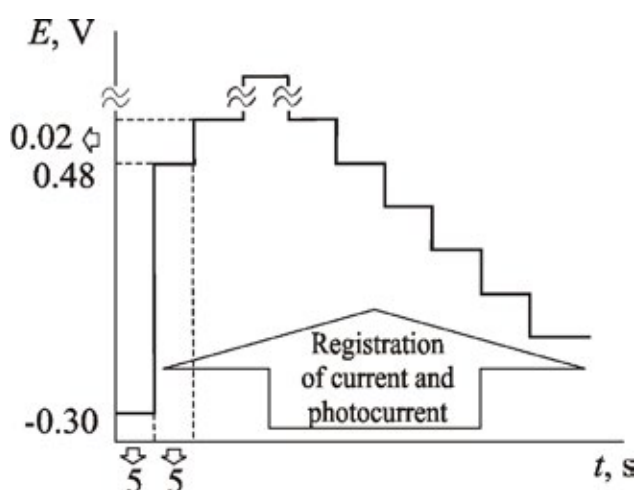


Fig. 1. Scheme of the potential step change in photoelectrochemical measurements

Table 1. The regime of pulse irradiation of oxide films on Ag–Pd alloys

LED wavelength	Irradiation power	Photon flux density	Pulse duration	Pulse frequency
470 nm	0.1 mW/cm <sup>2</sup>	$1.18 \cdot 10^{14}$ photon/(s·cm <sup>2</sup> )	1000 ms	5 Hz

PhotoEdition potentiostat, manufactured in the laboratory of renewable energy sources of manufactured at the Laboratory of Renewable Energy Sources of Saint Petersburg National research Academic University of the Russian Academy of Sciences.

### 3. Results and discussion

#### 3.1. Determination of the elemental and phase composition of alloys of the Ag-Pd system

According to the results of energy dispersive X-ray analysis of the obtained alloys, the palladium concentration was consistent with the calculated until it did not exceed 20 at. % (Table 2). On an alloy with a calculated palladium concentration of 30 at. % much lower  $X_{Pd}$  values have been experimentally determined. Probably such significant differences were due to the phase inhomogeneity of this sample.

According to X-ray diffractometry data, alloys with a palladium concentration of up to 20 at. % are characterized by the presence of only the alpha phase of the Ag(Pd) solid solution [37]. Similar results were obtained in [34, 35]. On the alloy with a calculated palladium concentration of 30 at. % in addition to the alpha phase Ag(Pd),

a palladium phase was detected (Fig. 2). It can be assumed that an accumulation of the palladium phase occurs in the surface zone of the obtained alloys. A similar segregation of palladium as an electropositive component of the alloy was revealed in [38, 39]. Despite the deviation from homogeneity, this alloy was considered in the study of the photoelectrochemical activity of the anodic oxide films formed on it.

#### 3.2. Cyclic voltammetry of alloys of the Ag-Pd system

The voltammograms obtained in a deaerated 0.1 M KOH solution for all the studied alloys had similar shape (Fig. 3). On the anodic branch of the voltammogram, the current remained practically zero until the potential exceeded 0.42-0.52 V. A further increase in the potential led to an increase in the current.

On alloys with a palladium concentration of  $X_{Pd} = 5-15$  at. % the maximum current A1 was recorded, the potential of which  $E_{A1}$  increased with increase in  $X_{Pd}$  (Table 3). On pure silver, the potential of A1 maximum was 0.56 V [21]. On alloys with  $X_{Pd} = 20$  and 30 at. % a clear A1 maximum was not recorded, therefore the range of potentials for obtaining the anodic branch of

**Table 2.** Calculated and experimental composition, parameters of cycle voltammetry of Ag-Pd alloys, current efficiency of oxide formation processes and oxides thickness

$\frac{X_{Pd}, \text{ at. \%}}{X_{Ag}, \text{ at. \%}}$ (calculated)	$\frac{5}{95}$	$\frac{10}{90}$	$\frac{15}{85}$	$\frac{20}{80}$	$\frac{30}{70}$
$\frac{X_{Pd}, \text{ at. \%}}{X_{Ag}, \text{ at. \%}}$ (experimental)	$\frac{5.01 \pm 0.01}{94.99 \pm 1.59}$	$\frac{9.81 \pm 0.03}{90.19 \pm 1.52}$	$\frac{15.67 \pm 0.05}{84.33 \pm 1.23}$	$\frac{20.51 \pm 0.08}{79.50 \pm 1.02}$	$\frac{23.05 \pm 0.71}{76.95 \pm 2.30}$
$E_{A1}, \text{ V}$	0.60	0.65	0.68	0.72	0.76
$q_a, \text{ mC/cm}^2$	59.5	53.2	58.6	77.0	45.8
$q_{C1}, \text{ mC/cm}^2$	49.2	34.0	37.4	33.9	14.5
$q_{C2}, \text{ mC/cm}^2$	–	–	–	16.4	10.3
$q_{C3}, \text{ mC/cm}^2$	8.0	13.4	16.4	23.4	13.1
$\eta(\text{Ag}_2\text{O}), \%$	83	64	64	44	32
$\eta(\text{AgO}), \%$	–	–	–	21	22
$\eta(\text{PdO}), \%$	13	25	28	30	29
$L(\text{Ag}_2\text{O}), \text{ nm}$	83	57	63	57	24
$L(\text{AgO}), \text{ nm}$	–	–	–	14	17
$L(\text{PdO}), \text{ nm}$	6	10	13	18	10

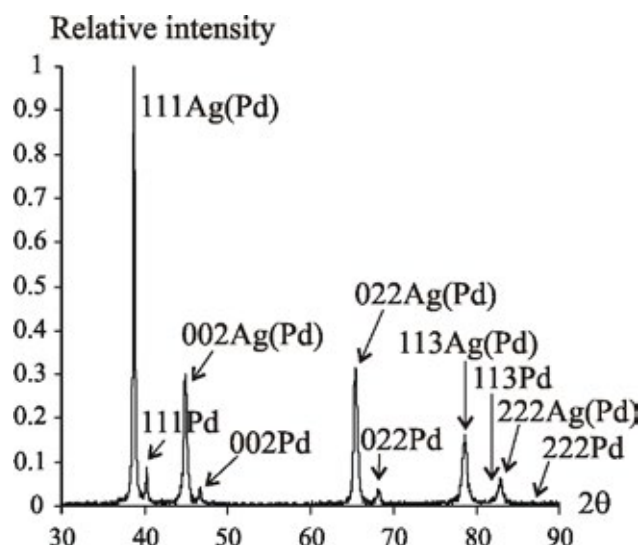


Fig. 2. X-ray diffraction patterns of the alloy with calculated palladium concentration of 30 at. %

voltammograms was expanded. As a result, it was possible to observe a small step instead of the A1 peak, followed by a current A2 maximum, the potential of which was 0.9 V and did not depend on the palladium concentration in the alloy. The current density at the A1 and A2 maxima decreased with increasing palladium concentration, respectively, with decreasing silver concentration in the alloy.

Several maxima were recorded on the cathodic branch of the cyclic voltammogram depending on the palladium concentration and the direction of potential scan. Thus, on alloys with a palladium concentration from 5 to 15 at. % two maxima of the cathode current were registered, and on alloys with a palladium concentration of 20 and 30 at. % – three maxima were revealed (Fig. 3). The potentials of the C1 and C2 maxima are almost do not depend on the concentration of palladium in the alloy, and the current densities in them decrease with increasing  $X_{Pd}$ . The maximum cathode current C3 was recorded only on alloys, while it is absent on pure silver. Its potential decreased from approximately –0.05 to –0.14 V with increasing  $X_{Pd}$  from 5 up to 30 at. %, and the amplitude generally increased.

Thermodynamic analysis and literature data can be used for the determination of the nature of the peaks. Thermodynamic analysis showed that both components of the investigated alloys were prone to oxide formation in the studied potential

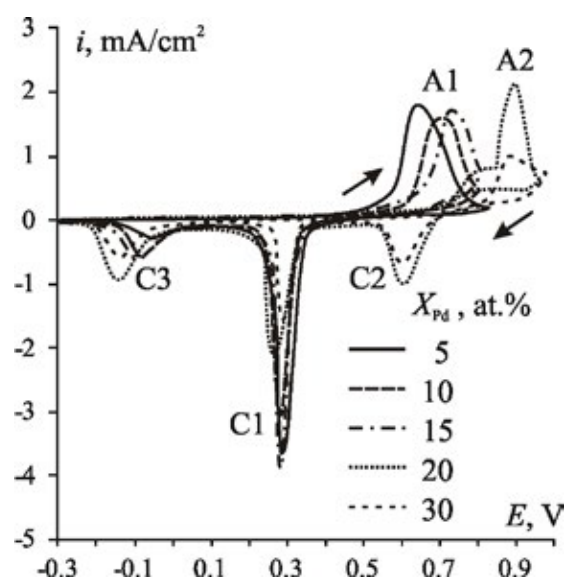
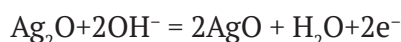
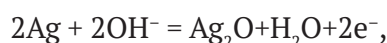


Fig. 3. Cycle voltammograms of Ag–Pd alloys in 0.1 M KOH at the potential scan rate of 5 mV/s

range. For the processes of formation of Ag(I) and Ag(II) oxides:



the equilibrium potentials in a 0.1 M KOH solution were  $E_{\text{Ag}_2\text{O}/\text{Ag}}^{\text{eq}} = 0.410$  V and  $E_{\text{AgO}/\text{Ag}_2\text{O}}^{\text{eq}} = 0.672$  V. In addition to the composition of the solution, the equilibrium potential depends on the composition of the electrode, namely, on the activity of silver. The less silver in the alloy, the higher the equilibrium potential for the formation of Ag(I) oxide.

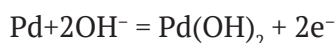
Literature data [35, 40] and the experimentally observed increase of the potentials of peak A1 with increasing palladium concentration indicated that this peak corresponds to the formation of Ag(I) oxide. The AgO oxide was formed on a sublayer of Ag(I) oxide, and therefore the equilibrium potential of its formation did not depend on the composition of the alloy, which was observed experimentally for the A2 peak.

Subsequent cathodic reduction confirmed these assumptions. Thus, if on alloys with a relatively low concentration of palladium (5–15 at. %) only one A1 maximum was observed on the anode branch, then two current maxima were recorded on the cathode branch (C1 and C3). For alloys with higher palladium concentrations (20 and 30 at. %) three current maxima were



recorded on the cathode branch (C1, C2, and C3). Since the maximum of the cathodic current C3 was not recorded on pure silver, probably it was associated with the reduction of oxidized forms of palladium formed in the anodic period of obtaining voltammograms on the alloys. A similar interpretation of this current maximum was given in [35].

For processes of formation of Pd(II) oxide or hydroxide:



difference between equilibrium potentials in 0.1 M KOH solution was small:  $E_{\text{Pd}(\text{OH})_2/\text{Pd}}^{\text{eq}} = 0.136 \text{ V}$  and  $E_{\text{PdO}/\text{Pd}}^{\text{eq}} = 0.089 \text{ V}$ . Thus, the equilibrium potentials for the formation of palladium oxide or hydroxide were lower than the equilibrium potential for the formation of silver oxide. However, the maximum current associated with the formation of palladium oxide or hydroxide was not recorded in the voltammograms (Fig. 3). This situation is typical for the anodic formation of palladium oxide on alloys with a relatively low palladium content [41]. Thus, it is impossible to determine the formation of palladium oxide from the shape of the anodic voltammogram. At the same time, the maximum current C3 was clearly visible on the cathode branch at potentials lower than the potential of the maximum current characterizing the reduction of silver oxides C1 and C2 (Fig. 3). The fact that the amplitude of the C3 peak increased with increasing palladium concentration confirmed its nature associated with the reduction of palladium oxide or hydroxide. For definiteness, we will assume that the oxidized form of palladium is the oxide. The area under the C1 peak of the reduction of silver (I) oxide was much larger than the area under the reduction peak of palladium oxide (Fig. 3). Consequently, the main oxidation product of the studied alloys was Ag(I) oxide.

Density of cathode charges  $q_{\text{C1}}$ ,  $q_{\text{C2}}$ , and  $q_{\text{C3}}$  was calculated as the area under C1, C2 and C3 peaks, characterizing the reduction of  $\text{Ag}_2\text{O}$ , AgO, and PdO oxides (Fig. 3). The charge  $q_{\text{C1}}$ , characterizing the reduction of Ag(I) oxide, decreased from 49.2 to 14.5 mC/cm<sup>2</sup> when  $X_{\text{Pd}}$  increased from 5 to 30 at. % (Table 2). The charge  $q_{\text{C3}}$ , characterizing the reduction of palladium oxide, increased

from 8.0 to 23.4 mC/cm<sup>2</sup> when  $X_{\text{Pd}}$  increased from 5 to 20 at.%, but decreased again during the transition to  $X_{\text{Pd}} = 30 \text{ at. \%}$ . On the cathode branch of voltammograms of alloys with  $X_{\text{Pd}} = 20$  and 30 at. %, C2 maximum, corresponding to the reduction of AgO oxide also appeared. Calculation of the area under this maximum led to  $q_{\text{C2}}$  values equal to 6.4 and 10.3 mC/cm<sup>2</sup> for alloys with a palladium concentration of 20 and 30 at. % respectively.

The current efficiency  $\eta(\text{Ag}_2\text{O})$ ,  $\eta(\text{AgO})$  and  $\eta(\text{PdO})$  was defined as the ratio of cathodic charges  $q_{\text{C1}}$ ,  $q_{\text{C2}}$  and  $q_{\text{C3}}$  to the total anode charge  $q_{\text{a}}$ , accumulated during the anodic period of voltammetry of alloys. For each of the oxides, the current efficiency values were less than 100%. When the palladium concentration in the alloy increased from 5 to 30 at. % for Ag(I) oxide, the current efficiency decreased from 83 to 32% (Table 2). For palladium oxide, on the contrary, the current efficiency increased from 13 to 29%. For the AgO oxide, formed on alloys with palladium concentrations of 20 and 30 at.%, the current efficiency was 21 and 22%, respectively. The current efficiency of oxide formation  $\eta(\text{Ag}_2\text{O}) + \eta(\text{AgO}) + \eta(\text{PdO})$  also was less than 100%, which indicated a possible contribution from the processes of anodic formation of soluble silver oxidation products. A similar pattern was observed for pure silver [19–21].

Based on the magnitude of the cathode charges, the thickness of the oxides formed during the anodic period of obtaining voltammograms was calculated using Faraday's law. It should be noted that this calculation represents approximate estimation. It was performed under the assumption of uniform distribution of one of the formed oxides over the electrode area. For Ag(I) oxide, the estimated thickness  $L(\text{Ag}_2\text{O})$  decreased from 83 nm on an alloy with  $X_{\text{Pd}} = 5 \text{ at. \%}$  up to 24 nm on alloy with  $X_{\text{Pd}} = 30 \text{ at. \%}$ . The estimated thickness of palladium oxide  $L(\text{Ag}_2\text{O})$  increased from 6 nm on an alloy with  $X_{\text{Pd}} = 5 \text{ at. \%}$  up to 18 nm on an alloy with  $X_{\text{Pd}} = 20 \text{ at. \%}$ . A decrease in thickness was observed on the alloy with  $X_{\text{Pd}} = 30 \text{ at. \%}$ , the decrease could be due to the impairment of the homogeneity of the structure of this alloy. The thickness of AgO oxide  $L(\text{Ag}_2\text{O})$ , formed on alloys with  $X_{\text{Pd}} = 20$  and 30 at. %, was 14 and 17 nm, respectively (Table 2).

The visualization of the structure of the oxide film formed in the potentiodynamic polarization regime is quite difficult. It can be assumed that as the potential increased, the first was formed palladium oxide with an island structure. A further increase in potential led to the formation of Ag(I) oxide in areas free of palladium oxide. Due to the growth and fusion of nuclei, the Ag(I) oxide layer can cover the palladium oxide. The formation of a mixed oxide phase cannot be ruled out.

### 3.3. Photoelectrochemical activity of silver oxide

In preliminary experiments, with a stepwise increase in potential from  $E_c$  with a step of 20 mV and a duration of each step of 5 min, it was revealed that the photocurrent was not recorded on the alloys until the potential reached 0.48 V. This finding indicates that during this time photosensitive oxide film did not form in an amount sufficient to exhibit photoelectrochemical activity. According to estimated calculations using the obtained current output (Table 2) the thickness of the Ag(I) oxide formed at the moment the potential reached 0.48 V did not exceed 4 nm. It should be noted that the equilibrium values for the formation of palladium oxide were already significantly exceeded. The thickness of the palladium oxide formed at this point cannot be estimated. However, it was obvious, that even if some palladium oxide was formed, its photoelectrochemical activity had not yet manifested itself.

At potentials of 0.48 V and higher, an anodic photocurrent started to be recorded on silver and alloys (Fig. 4), indicating the n-type conductivity of the formed oxide film. The lower the concentration of silver in the alloy, the higher the potential at which photocurrent starts to be

generated. With increasing potential in the anodic direction to values exceeding the potential of A1 maximum, photocurrent increased, reaching maximum values  $i_{ph}^{max}(A)$  at potentials  $E_{ph}^{max}(A)$  (Table 3). Values of  $E_{ph}^{max}(A)$  were higher than  $E_{A1}$  on voltammograms.

After changing the direction of potential scan to the cathode, the photocurrent continued to increase. This can be explained by the continuation of the formation process and thickening of the oxide film, since the polarization currents remained anodic. The exception was silver and an alloy with an atomic fraction of palladium of 5 at. %, where after changing the direction of potential scan, the photocurrent immediately started to decrease. On alloys with higher palladium content, the photocurrent started to decrease at lower potentials.

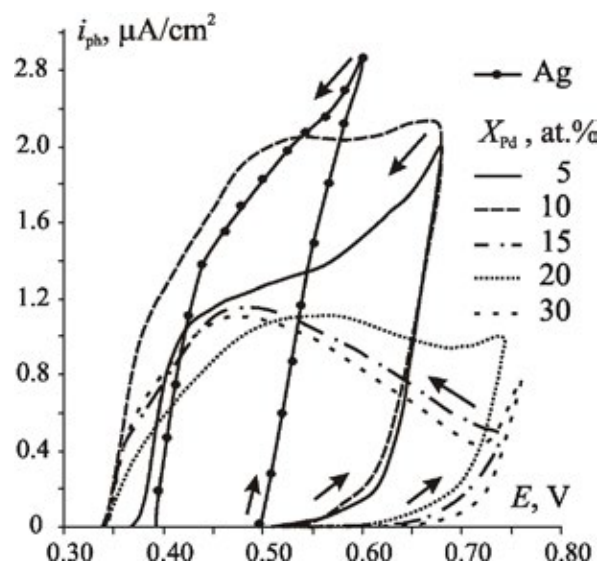


Fig. 4. Photocurrent during the anodic and cathodic direction of the potential change of silver and Ag-Pd alloys in 0.1 KOH

Table 3. Parameters of photoelectrochemical activity

$X_{Pd}$ , at. %	0	5	10	15	20	30
Anodic direction of potential scanning						
$E_{ph}^{max}(A)$ , V	0.60	0.68	0.68	0.74	0.74	0.76
$i_{ph}^{max}(A)$ , $\mu A/cm^2$	2.89	1.99	1.94	0.90	0.47	0.78
IPCE <sup>max</sup> (A), %	7.62	5.25	5.12	2.37	1.24	2.06
Cathodic direction of potential scanning						
$E_{ph}^{max}(C)$ , V	0.60	0.68	0.66	0.56	0.48	0.46
$i_{ph}^{max}(C)$ , $\mu A/cm^2$	2.89	1.99	2.12	1.11	1.16	1.10
IPCE <sup>max</sup> (C), %	7.62	5.25	5.59	2.93	3.06	2.90

The photoelectrochemical activity of the oxide on silver disappeared at 0.38 V, and on alloys, at approximately the same potential values, about 0.3 V, most probably corresponding to the complete reduction of silver oxide. Indeed, the C1 maximum, corresponding to the reduction of Ag(I) oxide, was observed in cyclic voltammograms at potentials of about 0.3 V. The C1 maximum on silver and the alloy with  $X_{\text{Pd}} = 5$  at. % was slightly higher than on other alloys. Since the reduction potentials of palladium oxide have not yet been achieved, its existence on the surface of alloys cannot be ruled out. However, photocurrent was no longer generated, e.g. palladium oxide was not a photoelectrochemically active material under experimental conditions. Nevertheless, the presence of palladium in the alloy made a certain contribution to the photoelectrochemical activity of anodically formed oxide films.

Thus, with increasing palladium, concentration potential  $E_{\text{ph}}^{\text{max}}(\text{A})$ , at which the maximum photocurrent was recorded in the anodic direction, also increased, and the maximum photocurrent density  $i_{\text{ph}}^{\text{max}}(\text{A})$  decreased (Table 3). The potential  $E_{\text{ph}}^{\text{max}}(\text{C})$ , at which the maximum photocurrent was recorded  $i_{\text{ph}}^{\text{max}}(\text{C})$ , decreased with increasing palladium concentration after changing the direction of potential scan from anodic to cathodic. The alloy with an atomic fraction of palladium of 10 at. % was characterized by the highest photoelectrochemical activity. On this alloy, as the potential swept to the cathode, the highest photocurrent density  $i_{\text{ph}}^{\text{max}}(\text{C})$  was recorded at  $E_{\text{ph}}^{\text{max}}(\text{C}) = 0.66$  V. This value was close to the anodic peak potential  $E_{\text{A1}}$  on the voltammogram (Table 2). In the oxide film on silver, it was possible to register higher photocurrent values of  $2.89 \mu\text{A}/\text{cm}^2$ , with incidental proton-to-electron conversion efficiency of 7.62%.

The maximum incidental proton-to-electron conversion efficiency, calculated based on the maximum values of photocurrent density, did not exceed 6% for all alloys. Changes of  $\text{IPCE}^{\text{max}}$  depending on the palladium concentration in the alloy, correlated with changes in the maximum photocurrent. When the potential swept to the anode, photoelectrocatalytic activity decreased with increasing palladium concentration in the alloy. When the potential swept to the cathode, the maximum photoelectrocatalytic activity was

recorded in an oxide film formed anodically on an alloy with an atomic fraction of palladium of 10 at. %.

#### 4. Conclusions

During the anodic oxidation of silver and alloys of the Ag–Pd system in an alkaline deaerated solution of 0.1 M KOH in the potential range up to 0.76 V (SHE), silver oxide (I) was predominantly formed. The current efficiency of its formation decreased from 83 to 32% with an increase in the calculated palladium concentration from 5 to 30 at. %. The formation of palladium oxide with a current efficiency of 6–18%, depending on the composition of the alloy, is also possible. The potential range of photoelectrochemical activity of formed anodically oxide films averaged from 0.35 to 0.76 V (st.h.e.). In the indicated potential range on silver and all alloys, under pulsed illumination, a positive photocurrent was generated, which indicated the predominance of donor structural defects in the forming oxide film. An increase in palladium concentration led to an expansion of the potential regions of photoelectrochemical activity of oxide films formed anodically on alloys of the Ag–Pd system. During the anodic potentiodynamic formation of an oxide film on alloys, the potential at which the maximum photocurrent was recorded increased with increasing palladium concentration, while the maximum photocurrent and the incidental proton-to-electron conversion efficiency generally decreased. During the cathodic potentiodynamic reduction of the formed oxide films, it was possible to record even higher photocurrents than during their anodic formation. The highest photoelectrochemical activity, characterized by the photocurrent density of  $2.89 \mu\text{A}/\text{cm}^2$  and the incidental proton-to-electron conversion efficiency of 7.62%, was observed in an oxide film formed anodically on silver. Comparable values ( $2.12 \mu\text{A}/\text{cm}^2$  and 5.59%) were registered in an oxide film of an alloy with an atomic fraction of palladium of 10 at. %, during its potentiodynamic reduction.

#### Contribution of the authors

The authors contributed equally to this article.

#### Conflict of interests

The authors declare that they have no known competing financial interests or personal



relationships that could have influenced the work reported in this paper.

## References

1. Septina W., Ikeda Sh., Khan M. A., ... Peter L. M. Potentiostatic electrodeposition of cuprous oxide thin films for photovoltaic applications. *Electrochimica Acta*. 2011;56(13): 4882–4888. <https://doi.org/10.1016/j.electacta.2011.02.075>
2. Strehblow H. H., Milosev I. Electrochemical behavior of Cu-xZn alloys in borate buffer solution at pH 9.2. *Journal of the Electrochemical Society*. 2003;150(11): B517–B524. <https://doi.org/10.1149/1.1615997>
3. Singh N., Choudhary S., Upadhyay S., Satsangi V. R., Dass S., Shrivastav R. Nanocrystalline Zn<sub>1-x</sub>Ag<sub>x</sub>O<sub>y</sub> thin films evolved through electrodeposition for photoelectrochemical splitting of water. *Journal of Solid State Electrochemistry*. 2014;18(2): 523–533. <https://doi.org/10.1007/s10008-013-2285-y>
4. Zhu S., Wang D. Photocatalysis: basic principles, diverse forms of implementations and emerging scientific opportunities. *Advanced Energy Materials*. 2017;7(23): 1700841. <https://doi.org/10.1002/aenm.201700841>
5. Navarro R. M., Álvarez Galván M. C., del Valle F., Villoria de la Mano J. A., Fierro J. L. G. Water splitting on semiconductor catalysts under visible-light irradiation. *ChemSusChem*. 2009;2(6): 471–485. <https://doi.org/10.1002/cssc.200900018>
6. Kozlova E. A., Parmon V. N. Heterogeneous semiconductor photocatalysts for hydrogen production from aqueous solutions of electron donors. *Russian Chemical Reviews*. 2017;86(9): 870. <https://doi.org/10.1070/rcr4739>
7. Ge J., Zhang Y., Heo Y.-J., Park S.-J. Advanced design and synthesis of composite photocatalysts for the remediation of wastewater: A review. *Catalysts*. 2019;9(2): 122. <https://doi.org/10.3390/catal9020122>
8. Sadovnikov S. I., Kozlova E. A., Gerasimov E. Yu., Rempel A. A., Gusev A. I. Enhanced photocatalytic hydrogen evolution from aqueous solutions on Ag<sub>2</sub>S/Ag heteronanostructure. *International Journal of Hydrogen Energy*. 2017;42(40): 25258–25266. <https://doi.org/10.1016/j.ijhydene.2017.08.145>
9. Markovskaya D. V., Gribov E. N., Kozlova E. A., Kozlov D. V., Parmon V. N. Modification of sulfide-based photocatalyst with zinc- and nickel-containing compounds: Correlation between photocatalytic activity and photoelectrochemical parameters. *Renewable Energy*. 2020;151: 286–294. <https://doi.org/10.1016/j.renene.2019.11.030>
10. He H., Liao A., Guo W., Luo W., Zhou Y., Zou Z. State-of-the-art progress in the use of ternary metal oxides as photoelectrode materials for water splitting and organic synthesis. *Nano Today*. 2019;28: 100763. <https://doi.org/10.1016/j.nantod.2019.100763>
11. Mehdi H. E., Hantehzadeh M. R., Valedbagi Sh. Physical properties of silver oxide thin film prepared by DC magnetron sputtering: effect of oxygen partial pressure during growth. *Journal of Fusion Energy*. 2013;32(1): 28–33. <https://doi.org/10.1007/s10894-012-9509-5>
12. Gao X.-Y., Wang S.-Y., Li J., ... Chen L.-Y. Study of structure and optical properties of silver oxide films by ellipsometry, XRD and XPS methods. *Thin Solid Films*. 2004;455–456: 438–442. <https://doi.org/10.1016/j.tsf.2003.11.242>
13. Barik U. K., Srinivasan S., Nagendra C. L., Subrahmanyam A. Electrical and optical properties of reactive DC magnetron sputtered silver oxide thin films: role of oxygen. *Thin Solid Films*. 2003;429(1-2): 129–134. [https://doi.org/10.1016/S0040-6090\(03\)00064-6](https://doi.org/10.1016/S0040-6090(03)00064-6)
14. Ida Y., Watase S., Shinagawa T., ... Izaki M. Direct electrodeposition of 1.46 eV band gap silver (I) oxide semiconductor films by electrogenerated acid. *Chemistry of Materials*. 2008;20(4): 1254–1256. <https://doi.org/10.1021/cm702865r>
15. Ferretti A. M., Ponti A., Molteni G. Silver(I) oxide nanoparticles as a catalyst in the azide-alkyne cycloaddition. *Tetrahedron Letters*. 2015;56(42): 5727–5730. <https://doi.org/10.1016/j.tetlet.2015.08.083>
16. Wei J., Lei Y., Jia H., Cheng J., Hou H., Zheng Z. Controlled in situ fabrication of Ag<sub>2</sub>O/AgO thin films by a dry chemical route at room temperature for hybrid solar cells. *Dalton Transactions*. 2014;43(29): 11333–11338. <https://doi.org/10.1039/c4dt00827h>
17. Wang W., Zhao Q., Dong J., Li J. A novel silver oxides oxygen evolving catalyst for water splitting. *International Journal of Hydrogen Energy*. 2011;36(13): 7374–7380. <https://doi.org/10.1016/j.ijhydene.2011.03.096>
18. Yin Z., Liangxu X., Cao S., Xiao Y. Ag/Ag<sub>2</sub>O confined visible-light driven catalyst for highly efficient selective hydrogenation of nitroarenes in pure water medium at room temperature. *Chemical Engineering Journal*. 2020;394: 125036. <https://doi.org/10.1016/j.cej.2020.125036>
19. Vvedenskii A. V., Grushevskaya S. N., Kudryashov D. A., Ganzha S. V. *Thin oxide films on metals and alloys: kinetics of anodic formation and photoelectrochemical properties*. Voronezh: Publishing and printing center «Nauchnaya kniga»; 2016. 296 p. (In Russ.)
20. Vvedenskii A., Grushevskaya S., Kudryashov D., Kuznetsova T. Kinetic peculiarities of anodic dissolution of silver and Ag-Au alloys under the conditions of oxide formation. *Corrosion Science*.

2007;49(12): 4523–4541. <https://doi.org/10.1016/j.corsci.2007.03.046>

21. Vvedenskii A., Grushevskaya S., Kudryashov D., Ganzha S. The influence of the conditions of the anodic formation and the thickness of Ag (I) oxide nanofilm on its semiconductor properties. *Journal of Solid State Electrochemical*. 2010;14(8): 1401–1413. <https://doi.org/10.1007/s10008-009-0952-9>

22. Belyanskaya I. A., Taran A. I., Grushevskaya S. N., Vvedenskii A. V. Anodic formation and characteristics of silver oxides on alloys of Ag-Zn system. *Proceedings of Voronezh State University. Series: Chemistry. Biology. Pharmacy*. 2020;(3): 5–13. (In Russ., abstract in Eng.). Available at: [https://elibrary.ru/title\\_about\\_new.asp?id=9907](https://elibrary.ru/title_about_new.asp?id=9907)

23. Bocharnikova M. Yu., Murtazin M. M., Grushevskaya S. N., Kozaderov O. A., Vvedensky A. V. Anodic formation and properties of nanoscale oxide layers on silver-zinc alloys with different concentrations of nonequilibrium vacancies. *Journal of Solid State Electrochemistry*. 2022;26(8): 1637–1644. <https://doi.org/10.1007/s10008-022-05204-z>

24. McCarthy S., Braddock D. C., Wilton-Ely J. D. E. T. Strategies for sustainable palladium catalysis. *Coordination Chemistry Reviews*. 2021;442: 213925. <https://doi.org/10.1016/j.ccr.2021.213925>

25. Li Z., Meng X. Recent development on palladium enhanced photocatalytic activity: A review. *Journal of Alloys and Compounds*. 2020;830: 154669. <https://doi.org/10.1016/j.jallcom.2020.154669>

26. Ryabtsev S. V., Ievlev V. M., Samoylov A. M., Kushev S. B., Soldatenko S. A. Microstructure and electrical properties of palladium oxide thin films for oxidizing gases detection. *Thin Solid Films*. 2017;636: 751–759. <https://doi.org/10.1016/j.tsf.2017.04.009>

27. Chiang Y.-J., Pan F.-M. PdO nanoflake thin films for CO gas sensing at low temperatures. *The Journal of Physical Chemistry C*. 2013;117: 15593–15601. <https://doi.org/10.1021/jp402074w>

28. Arora K., Srivastava S., Solanki P. R., Puri N. K. Electrochemical hydrogen gas sensing employing palladium oxide/reduced graphene oxide (PdO-rGO) nanocomposites. *IEEE Sensors Journal*. 2019;19(18): 8262–8271. <https://doi.org/10.1109/JSEN.2019.2918360>

29. Wang J., Fan X., Liu B., Li C., Bai J. Eu<sub>x</sub>O<sub>y</sub>-PdO catalyst concerted efficiently catalyzes Suzuki-Miyaura coupling reaction. *Materials Chemistry and Physics*. 2020;252: 123227. <https://doi.org/10.1016/j.matchemphys.2020.123227>

30. Mahara Y., Murata K., Ueda K., Ohyama J., Kato K., Satsuma A. Time resolved in situ DXAFS revealing highly active species of PdO nanoparticle catalyst for CH<sub>4</sub> oxidation. *ChemCatChem*. 2018;10: 3384–3387. <https://doi.org/10.1002/cctc.201800573>

31. Rao F., Zhu G., Wang M., ... Hojamberdiev M. Constructing the Pd/PdO/β-Bi<sub>2</sub>O<sub>3</sub> microspheres with enhanced photocatalytic activity for Bisphenol A degradation and NO removal. *Journal of Chemical Technology & Biotechnology*. 2020;95(3): 862–874. <https://doi.org/10.1002/jctb.6276>

32. Nguyen T. D., Cao V. D., Nong L. X., ... Vo D.-V. N. High photocatalytic performance of Pd/PdO-supported BiVO<sub>4</sub> nanoparticles for Rhodamine B degradation under visible LED light irradiation. *ChemistrySelect*. 2019;4(20): 6048–6054. <https://doi.org/10.1002/slct.201901295>

33. Zahra T., Ahmad K. S., Thomas A. G., ... Sohail M. Phyto-inspired and scalable approach for the synthesis of PdO-2Mn<sub>2</sub>O<sub>3</sub>: A nano-material for application in water splitting electro-catalysis. *RSC Advances*. 2020;10(50): 29961–29974. <https://doi.org/10.1039/D0RA04571C>

34. Zeledón Z. J. A., Stevens M. B., Gunasooriya G. T. K. K., ... Jaramillo T. F. Tuning the electronic structure of Ag-Pd alloys to enhance performance for alkaline oxygen reduction. *Nat Commun*. 2021;12: 620. <https://doi.org/10.1038/s41467-021-20923-z>

35. Slanac D. A., Hardin W. G., Johnston K. P., Stevenson K. J. Atomic ensemble and electronic effects in Ag-Rich AgPd nanoalloy catalysts for oxygen reduction in alkaline media. *Journal of the American Chemical Society*. 2012;134(23): 9812–9819. <https://doi.org/10.1021/ja303580b>

36. Grinberg V. A., Emec V. V., Majorova N. A., ... Codikov M. V. Photoelectrochemical activity of nanosized titania, doped with bismuth and lead, in visible light region. *Protection of Metals and Physical Chemistry of Surfaces*. 2019;55(1): 55–64. <https://doi.org/10.1134/S0044185619010121>

37. Belyanskaya I. A., Bocharnikova M. Yu., Grushevskaya S. N., Kozaderov O. A., Vvedenskii A. V., Kannykin S. V. Anodic formation and photoelectrochemical characteristics of Ag(I) oxide on the Ag-Pd-system alloys. *Russian Journal of Electrochemistry*. 2024;60(6): 468–477, in press.

38. Wouda P. T., Schmid M., Nieuwenhuys B. E., Varga P. STM study of the (111) and (100) surfaces of PdAg. *Surface Science*. 1998;417(2-3): 292–300. [https://doi.org/10.1016/S0039-6028\(98\)00673-6](https://doi.org/10.1016/S0039-6028(98)00673-6)

39. Zhao M., Brouwer J. C., Sloof W. G., Bottger A. J. Surface segregation of Pd-Cu alloy in various gas atmospheres. *International Journal of*

*Hydrogen Energy*. 2020;45: 21567e21572. <https://doi.org/10.1016/j.ijhydene.2020.05.268>

40. Hecht D., Borthen P., Strehblow H. -H. In situ examination of anodic silver oxide films by EXAFS in the reflection mode. *Journal of Electroanalytical Chemistry*. 1995;381: 113–121. [https://doi.org/10.1016/0022-0728\(94\)03611-6](https://doi.org/10.1016/0022-0728(94)03611-6)

41. Bolzan A. E. Phenomenological aspects related to the electrochemical behaviour of smooth palladium electrodes in alkaline solutions. *Journal of Electroanalytical Chemistry*. 1995;380: 127–138. [https://doi.org/10.1016/0022-0728\(94\)03627-F](https://doi.org/10.1016/0022-0728(94)03627-F)

*\*Translated by author of the article*

### Information about the authors

*Irina A. Belyanskaya*, postgraduate student, Voronezh State University (Voronezh, Russian Federation).

[belyanskaya\\_98@mail.ru](mailto:belyanskaya_98@mail.ru)

*Maria Y. Bocharnikova*, Engineer at the Department of Physical Chemistry, Voronezh State University (Voronezh, Russian Federation).

<https://orcid.org/0009-0003-5420-6848>

[nesterovamarija18@gmail.com](mailto:nesterovamarija18@gmail.com)

*Maksim M. Murtazin*, Cand. Sci. (Chem.), Junior Researcher at LLC “NPO Membranes” (Voronezh, Russian Federation).

<https://orcid.org/0009-0005-9574-4057>

[murtazin@chem.vsu.ru](mailto:murtazin@chem.vsu.ru)

*Svetlana N. Grushevskaya*, Cand. Sci. (Chem.), Associate Professor at the Department of Physical Chemistry, Voronezh State University (Voronezh, Russian Federation).

<https://orcid.org/0000-0002-7083-1438>

[sg@chem.vsu.ru](mailto:sg@chem.vsu.ru)

*Oleg A. Kozaderov*, Dr. Sci. (Chem.), Senior Researcher, Laboratory of Organic Additives for the Processes of Chemical and Electrochemical Deposition of Metals and Alloys Used in the Electronics Industry, Voronezh State University (Voronezh, Russian Federation).

<https://orcid.org/0000-0002-0249-9517>

[ok@chem.vsu.ru](mailto:ok@chem.vsu.ru)

*Alexander V. Vvedenskii*, Dr. Sci. (Chem.), Professor at the Department of Physical Chemistry, Voronezh State University (Voronezh, Russian Federation).

<https://orcid.org/0000-0003-2210-5543>

[alvved@chem.vsu.ru](mailto:alvved@chem.vsu.ru)

*Received 11.09.2023; approved after reviewing 02.10.2023; accepted for publication 15.11.2023; published online 25.06.2024.*

*Translated by Valentina Mittova*





# Condensed Matter and Interphases

Kondensirovannye Sredy i Mezhfaznye Granitsy  
<https://journals.vsu.ru/kcmf/>

## Original articles

Research article

<https://doi.org/10.17308/kcmf.2024.26/11936>

## High-temperature gallium sesquisulfides and a fragment of the $T$ - $x$ diagram of the Ga – S system with these phases

N. Yu. Brezhnev<sup>1</sup>, M. V. Dorokhin<sup>2</sup>, A. Yu. Zavrazhnov<sup>1✉</sup>, N. A. Kolyshkin<sup>3</sup>, I. N. Nekrylov<sup>1</sup>, V. N. Trushin<sup>2</sup>

<sup>1</sup>Voronezh State University,  
1 Universitetskaya pl., Voronezh 394018, Russian Federation

<sup>2</sup>Physical-Technical Research Institute of UNN (PTRI),  
23 Gagarin avenue, BLDG, Nizhny Novgorod 603950, Russian Federation

<sup>3</sup>National Research Center “Kurchatov Institute”,  
1 Acad. Kurchatov pl., Moscow 123098, Russian Federation

### Abstract

It is known that phases with disordered stoichiometric vacancies are promising candidates for new materials with outstanding thermoelectric, radiation-resistant, catalytic, and other properties, which can be explained by a large concentration of the so-called stoichiometric vacancies, caused by the fact that their stoichiometry does not correspond to the structural type. It is interesting to search for such compounds in A<sup>III</sup> – B<sup>VI</sup> semiconductor systems, whose sesquichalcogenides (Me<sub>2</sub>Ch<sub>3</sub>, Me = Ga, In; Ch = S, Se, Te) are known to have both sphalerite and wurtzite structures and the share of stoichiometric vacancies in the cationic sublattice of about 1/3. The purpose of our study was to determine or confirm the high-temperature structures of gallium sesquisulfides and determine the stability regions corresponding to the phases with these structures on refined  $T$ - $x$  diagrams in the high temperature region ( $T = 878$  °C).

Various methods of structure and thermal analysis allowed us to prove that at temperatures above 878 °C, close to the stoichiometry of Ga<sub>2</sub>S<sub>3</sub>, gallium sesquisulfide has four modifications similar in terms of structure, which are connected with each other and other phases of the Ga – S system by enantiotropic transitions. The study confirmed that  $\gamma$ -Ga<sub>2+8</sub>S<sub>3</sub> with a sphalerite-like cubic structure is formed over a narrow temperature range (878 – 922 °C). The composition of the phase was specified (59.3 mol %). The study demonstrated that at temperatures above 912 °C and a slight excess of gallium (up to ~1 mol %) as compared to the stoichiometry of Ga<sub>2</sub>S<sub>3</sub> two modifications are formed: a defected wurtzite-like structure ( $\beta$ -Ga<sub>2</sub>S<sub>3</sub>,  $P6_3mc$ ) and its derivative phase, whose structure has a lower symmetry ( $\alpha$ -Ga<sub>2</sub>S<sub>3</sub>,  $P6_1$ ) and reaches the stage of congruent melting ( $1109 \pm 2$  °C). The study also accounts for the existence of a distectoid transformation  $\alpha$ -Ga<sub>2</sub>S<sub>3</sub>  $\leftrightarrow$   $\beta$ -Ga<sub>2</sub>S<sub>3</sub> (~1040 °C). The fourth modification with a monoclinic structure ( $\alpha'$ -Ga<sub>2</sub>S<sub>3</sub>,  $Cc$ ) is stable over a temperature range from room temperature to ~1006 °C. Its composition satisfies the formula of Ga<sub>2</sub>S<sub>3</sub>. The article presents a corresponding  $T$ - $x$  diagram of the Ga – S system with the areas of existence of the said phases.

**Keywords:** Ga – S system, Phase diagram, Structure, Stoichiometric vacancies, Vacancy ordering, Synchrotron radiation for the structure analysis

**Acknowledgements:** *In situ* X-ray powder diffraction studies were performed using the equipment of the National Research Centre “Kurchatov Institute”. The authors are also grateful to A.V. Naumov, Associate Professor at the Department of General and Inorganic Chemistry of VSU, for his participation in discussions.

**For citation:** Brezhnev N. Y., Dorokhin M. V., Zavrazhnov A. Y., Kolyshkin N. A., Nekrylov I. N., Trushyn V. N. High-temperature gallium sesquisulfides and a fragment of the  $T$ - $x$  diagram of the Ga – S system with these phases. *Condensed Matter and Interphases*. 2024;26(2): 225–237. <https://doi.org/10.17308/kcmf.2024.26/11936>

**Для цитирования:** Брежнев Н. Ю., Дорохин М. В., Завражнов А. Ю., Колышкин Н. А., Некрылов И. Н., Трушин В. Н. Высокотемпературные сесквисульфиды галлия и фрагмент  $T$ - $x$ -диаграммы системы Ga – S с участием этих фаз. *Конденсированные среды и межфазные границы*. 2024;26(2): 225–237. <https://doi.org/10.17308/kcmf.2024.26/11936>

✉ Alexander Y. Zavrazhnov, e-mail: [alzavr08@rambler.ru](mailto:alzavr08@rambler.ru)

© Brezhnev N. Y., Dorokhin M. V., Zavrazhnov A. Y., Kolyshkin N. A., Nekrylov I. N., Trushyn V. N., 2024



The content is available under Creative Commons Attribution 4.0 License.

## 1. Introduction

It is known that when obtaining semiconductor materials, in order to control their properties a lot of attention is paid to the regulation of the concentration of point defects, including *vacancies*. However, structures of some of the promising semiconductors demonstrate disorder in one or several sublattices due to the fact that the stoichiometry of the materials does not correspond to the structural type. As a result, the occupancy of certain sites in one or several sublattices is significantly lower than 100%. In a number of compounds, such unoccupied vacancies, called *stoichiometric vacancies*, can have great concentrations, up to tens of mol % [1]. Since *stoichiometric vacancies* are essential structural elements, they cannot be strictly classified as point defects. However, several terms can be found in the literature on the problem, including defect structures and defect sphalerite (wurtzite, spinel) structures.

Structures with stoichiometric vacancies result in unique properties, which are not observed in compounds with classical vacancies\*. These properties include good thermoelectric properties, high radiation resistance, a wide variety of lattice parameters in films, etc. [1–6].

In our study, we focused on the samples of such substances in the Ga – S system, which is one of the least studied among the  $A(III) - B(VI)$  systems. It is known that gallium sulfides with stoichiometry close to  $Ga_2S_3$  crystallize in sphalerite- and wurtzite-like structures with stoichiometric vacancies in the cationic sublattice ( $\sim 1/3$  of the number of nodes) [7]. Detailed in the literature are a large variety of phases formed as a result of the ordered and disordered arrangement of these vacancies. However, little is known about the conditions for obtaining gallium sesquisulfides with a particular structure. Recent studies [8–10] demonstrated that besides the  $\alpha'$ - $Ga_2S_3$  phase (one of the derivatives of the defect wurtzite with ordered vacancies), which is stable over a wide temperature range, there is another compound –  $\gamma$ - $Ga_{2+\delta}S_3$ , which has a sphalerite-like cubic structure with disordered vacancies. This

modification is stable over a narrow temperature range as compared to other phases (from 878 to 922 °C) and is shifted towards a significant excess of gallium (0.5 mol %). At the same time, [9, 10] as earlier [11, 12] reported the presence of other gallium sesquisulfides on the phase diagram, whose regions of existence correspond to even higher temperatures than those of  $\gamma$ - $Ga_{2+\delta}S_3$ .

The purpose of our study was to determine or confirm the structures of gallium sesquisulfides and determine the stability regions corresponding to the phases with these structures on refined  $Tx$  diagrams in the high temperature region ( $T \geq 878$  °C).

## 2. Experimental

The study was divided into several stages. During the preliminary stage, we obtained gallium sulfide alloys with various concentrations of components using the method of direct two-temperature synthesis described in [8]. The compositions of the alloys (1–2 g) used in structural studies corresponded to the concentration range of 58.0–60.2 mol % with the concentration of sulfur in the samples changing at an interval of 0.1–0.2 mol %. Ampoules with the obtained ingots were annealed for 24 hours at temperatures from 900 to 1080 °C, after which they were quenched in iced water. The samples were then taken out of the ampoules and ground to powder.

During the first stage of the experiment, we conducted powder diffraction of the obtained alloys. Some of the samples were studied *in situ* under equilibrium conditions at high temperatures using synchrotron radiation. However, most of the powder diffraction patterns were obtained for quenched samples at room temperature.

During the second stage, we performed a differential thermal analysis of each of the samples and an analysis of the alloys with a wider concentration range: from 50.0 to 60.7 mol %. In our experiments, we used the methodology presented in [8, 13]. During the final stage, we compared the results obtained by means of different methods.

*The synchrotron radiation experiments were conducted at the National Research Centre “Kurchatov Institute” on the Structural Materials*

\* Classical vacancies can be explained by deviations of the composition of the solid phase from the ideal stoichiometry and disordering of the crystal structure at higher temperatures.

Science station of Kurchatov Synchrotron Radiation Source, channel K1.3b. The powder of the studied compound was put into a quartz-glass capillary with a diameter of 0.3–0.7 mm and a length of 25–30 mm. The vacuumed and sealed capillary was then put into a resistance heating furnace with a narrow X-Ray entrance slit. A chromel-alumel thermocouple was placed in 1–3 mm from the capillary. A *Dectris Pilatus 300K-W* detector was placed about 20 cm behind the sample (the distance was determined based on the diffraction data for the studied sample obtained at room temperature). The furnace heated to high temperatures (860 °C) in about 5 hours. The criterion used to estimate the time required to reach the equilibrium was the complete identity of the diffraction patterns obtained while increasing and decreasing the temperature step by step. The time required to obtain each diffraction pattern was ~ 0.5 hour.

The method was chosen due to the fact that a noticeable pressure of chemically aggressive vapors ( $\text{Ga}_2\text{S}$ ,  $\text{S}_2$ ) over gallium sulfides prevented us from using the equipment traditionally used in *HT-XRD* experiments. The walls of the capillary with a thickness of ~10  $\mu\text{m}$  are almost transparent for synchrotron radiation with a photon energy of 18055 eV (at a wavelength of 0.6867 Å). They absorb less than 2% of the energy. Together with the high energies of synchrotron radiation this allowed us to register the diffraction pattern of the powder in the capillary. The upper temperature limit was 1015 °C, which was only due to the characteristics of the heating element.

The X-ray crystallography of the annealed and quenched samples was performed at room temperature using an *Empyrean B.V.* diffractometer ( $\text{CuK}_{\alpha 1}$ -radiation in the  $2\theta$  range from 10° to 95°, step 0.02°, the exposure time at each point at least 0.2 s).

To analyze the data, we modelled calculated diffraction patterns of the powder based on the literature data using the *PowderCell 2.4* software package [14]. The experimental diffraction patterns obtained on the Kurchatov Synchrotron Radiation Source were integrated in the *Fit2D* software [15], which was also used to calibrate the distance between the sample and the detector. The results were presented in terms of the

$\text{CuK}_{\alpha 1}$ -radiation (1.54060 Å). The *Unitcell* software was used for the refinement of cell parameters [16]. The reflections observed on the diffraction patterns were identified by means of comparison with the literature data [10].

The differential thermal analysis (DTA) was conducted on a unit consisting of TPM-101 and TPM-200 sensor units and temperature sensors in the form of chromel-alumel and nichrosil-nisil thermocouples. The averaged signal being transmitted to the computer every second. The quantitative data was obtained using heating mode only with heating rates from 0.9 to 4.0 K/min. Relatively low heating rates were used to differentiate between phase transformations occurring at similar temperatures and to prevent the emergence of metastable states. Inaccuracies in the temperatures of phase transformations on the horizontal lines of the  $T$ - $x$  diagram were determined based on the statistical processing of all temperatures obtained for a particular horizontal for different compounds. The smallest possible inaccuracy was assumed to be  $\pm 2$  °C, which is a standard inaccuracy for chromel-alumel and nichrosil-nisil thermocouples. If the value obtained after statistical processing was lower, the final accuracy was still  $\pm 2$  °C.

The analysis of the DTA data allowed us to determine the inaccuracy in the composition of the samples. Alloys with compositions differing by 0.1 mol % demonstrated reproducibly different effects. For instance, the horizontal line at 910 °C – eutectic melting of  $\text{GaS} + \gamma\text{-Ga}_{2+8}\text{S}_5 \rightarrow \text{L}$  – was observed in samples with a concentration of sulfur of up to 59.2 mol %. However, it was not observed for the alloy with  $x_s = 59.3$  mol %. Therefore, we assumed that the concentration inaccuracy in the samples was close to  $\pm 0.1$  mol %.

The compositions of phases participating in non-variant equilibria were refined when comparing the peak areas on the DTA thermograms. It is obvious, that these areas are proportional to the molar heat of phase transformations. Then, when studying the disproportionation of the condensed phase  $\Phi_2$  into two other condensed phases (which occurs, for instance, during incongruent melting):





or the comproportionation of  $\Phi_1$  and  $\Phi_3$  into  $\Phi_2$  (a reaction is reverse to (1): for instance, eutectic melting) the absorption of heat by the sample is maximum, if the bulk composition of the studied compound coincides with the composition of the  $\Phi_2$  phase. This composition corresponds to the maximum peak area on the DTA thermogram\*.

Since it is extremely difficult to conduct thermographic experiments with identical amounts of substances, it is practical to analyze normalized areas ( $S^*$ ) rather than absolute areas ( $S$ ), where in formula (2)  $n$  is the amount of substance in a Stepanov ampoule:

$$S^* = \frac{S}{n}. \quad (2)$$

We should note that dependences  $S^* = f(x_s)$  are constructed according to the Tamman's method and consequently look similar to the Tamman's triangle [17].

### 3. Results

*Monoclinic  $\alpha'$ -Ga<sub>2</sub>S<sub>3</sub> and cubic sphalerite-like  $\gamma$ -Ga<sub>2+ $\delta$</sub> S<sub>3</sub> modifications.* The results of the powder diffraction analysis of the alloys of various compositions annealed at different temperatures (and quenched at these temperatures) are given in Figs. 1 and 2 and table 1. Fig. 1 demonstrates typical diffraction patterns, which vary depending on the annealing temperature and the composition of the alloy. The diffraction patterns close to curve 1 with a large number of diffraction maxima were observed for all the annealed samples in the studied concentration range (58.0–60.2 mol %), if the annealing temperatures were below 870 °C. The same diffraction patterns were observed for all the alloys which, instead of quenching, were slowly cooled to room temperature in the switched-off furnace. A full-profile analysis of the diffraction patterns demonstrated that the main phase in such samples was the monoclinic modification of  $\alpha'$ -Ga<sub>2</sub>S<sub>3</sub>. When the concentration of sulfur was from 59.8 to 60.2 mol %, this modification was the only one. At lower concentrations of chalcogen (58.0–59.6 mol %) an impurity phase appeared –

gallium monosulfide (a hexagonal modification of GaS-2H,  $P6_3mmc$ ).

At higher annealing temperatures (905 and 910 °C) alloys with an excess of gallium in relation to the stoichiometry of Ga<sub>2</sub>S<sub>3</sub> (the concentration of sulfur from 58.0 to 59.8 mol %) demonstrated rare wide maxima of a specific form, (curve 2, Fig. 1). Taking into account the data of transmission electron microscopy [10], these maxima indicated the presence of a sphalerite-like cubic structure  $\gamma$ -Ga<sub>2+ $\delta$</sub> S<sub>3</sub> with disordered stoichiometric vacancies. However, this did not happen in the alloys with the maximum concentration of sulfur (from 59.8 to 60.2 mol %), and monoclinic modification of  $\alpha'$ -Ga<sub>2</sub>S<sub>3</sub> remained at least up to 1000 °C.

The results of the high-temperature X-ray phase analysis of the alloy with the concentration of sulfur of 58.0 mol % conducted using synchrotron radiation (curve 2, Fig. 1) were thoroughly analyzed. They demonstrated that the cubic modification of  $\gamma$ -Ga<sub>2+ $\delta$</sub> S<sub>3</sub> can be stable as compared to other phases under equilibrium (it does not occur as a result of quenching and decomposition of other structures). For this composition, at temperatures 883, 893, and 903 °C  $\gamma$ -Ga<sub>2+ $\delta$</sub> S<sub>3</sub> coexisted with gallium monosulfide GaS. When the sample was kept at 918 °C, the diffraction maxima of GaS disappeared and the diffraction pattern demonstrated a wide halo together with rare peaks of the  $\gamma$ -phase. This indicates the formation of a sulfide melt as the second (impurity) phase. It should be noted that [10] describes the results of a similar study of this alloy. However, it only focused on the equilibrium at a single temperature (918 °C).

*Hexagonal high-temperature phases: wurtzite-like  $\beta$ -Ga<sub>2</sub>S<sub>3</sub> ( $P6_3mc$ ) and its derivative  $\alpha$ -Ga<sub>2</sub>S<sub>3</sub> ( $P6_1$ ).* [10] proved that at temperatures above 922 °C the sphalerite-like  $\gamma$ -Ga<sub>2+ $\delta$</sub> S<sub>3</sub> undergoes peritectic decomposition into a melt and another high-temperature phase  $\sim$ Ga<sub>2</sub>S<sub>3</sub>. However, the analysis of the structure of the substance obtained after quenching at  $T \geq 945$  °C always demonstrated a mixture of hexagonal phases ( $\alpha$ -Ga<sub>2</sub>S<sub>3</sub>,  $\beta$ -Ga<sub>2</sub>S<sub>3</sub>, and – for some samples – GaS).

In our study, we maintained the annealing temperature (from 940 to 1080 °C) of vacuumed quartz ampoules with ground alloys of various compositions close to Ga<sub>2</sub>S<sub>3</sub> for a long time

\* This is true, if we compare the results of DTA conducted using identical number of compounds with the same thermal conductivity and heat loss values. At the same time, changes in the quantity of the vapour phase equilibrium with  $\Phi_1$ ,  $\Phi_2$ , and  $\Phi_3$  should be negligibly small.



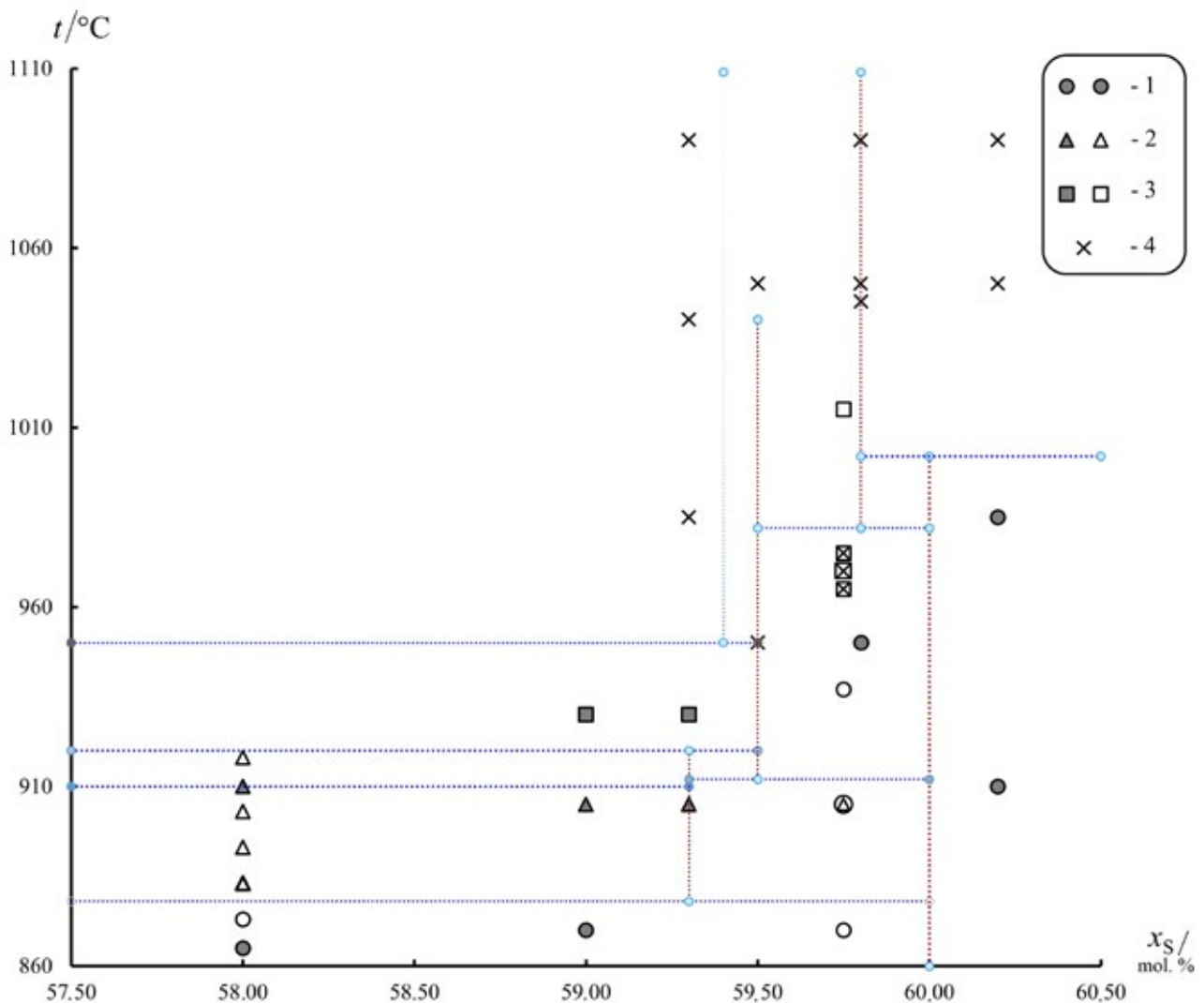


**Fig. 2.** Compositions of samples of the Ga – S system identified during X-ray powder analysis versus the  $T$ - $x$ -coordinates of the phase diagram. **Notation.** Annealed and quenched alloys are designated as dark, gray-filled figures – circles, triangles, squares, crosses; the samples, which studied *in situ* at high temperatures in a “synchrotron” experiment are designated as light figures without shading. Digital designations: 1 –  $\alpha'$ - $\text{Ga}_2\text{S}_3$  (+ traces of GaS for samples with  $x_S < 60.0$  mol %), 2 –  $\gamma$ - $\text{Ga}_{2+\delta}\text{S}_3$  (+ traces of GaS for temperatures less than 910 °C), 3 –  $\beta$ - $\text{Ga}_2\text{S}_3$ , 4 –  $\alpha$ - $\text{Ga}_2\text{S}_3$ . The dotted lines indicate the horizontals obtained from the DTA results; the compositions of the probable phases are marked as vertical dotted lines

in quenched samples over all the studied concentration range, up to the sample with the concentration of sulfur of 60.2 mol %. In all the experiments, phase  $\alpha$ - $\text{Ga}_2\text{S}_3$  was identified as the only one (curve 4, Fig. 1). The monoclinic modification  $\alpha'$ - $\text{Ga}_2\text{S}_3$ , which is the most stable at room temperature, was not registered even as an impurity phase and even in the samples with the highest concentration of sulfur (60.2 mol %).

The differential thermal analysis (DTA) allowed us to obtain an approximate  $T$ - $x$  diagram

of the Ga – S system. However, before we present the diagram, we should point out several characteristic features registered on differential heating curves for the alloys of Ga – S of various compositions.

*56.0–59.0 mol % region.* For the samples corresponding to this concentration interval, thermograms were registered, which, besides the minimum associated with the liquidus line, demonstrated deep endoeffects at temperatures of 878, 910, and 922 °C (Fig. 4a).



**Table 1.** Thermal stability of the condensed phases for the Ga – S system and the structures of these phases

Фаза	Lower temperature limit of the phase stability and the correspondent phase equilibrium	Upper temperature limit of the phase stability and the correspondent phase equilibrium	Structure, cell parameters and the presence of ordered (+) or disordered (-) vacancies	Состав твердой фазы, мол. % S
$\gamma$ -Ga <sub>2+δ</sub> S <sub>3</sub>	878 ± 2 °C, GaS + α'-Ga <sub>2</sub> S <sub>3</sub> = γ-Ga <sub>2+δ</sub> S <sub>3</sub> <b>(I)</b> , eutectoid	922 ± 4 °C, γ-Ga <sub>2+δ</sub> S <sub>3</sub> = β-Ga <sub>2</sub> S <sub>3</sub> + L, <b>(II)</b> peritectic	cubic, sphalerite-like, S.G. $F\bar{4}3m$ , $a = 5.17 - 5.21 \text{ \AA}$ , (-)	59.3
L расплав	910 ± 3 °C GaS + γ-Ga <sub>2</sub> S <sub>3</sub> = L, <b>(III)</b> eutectic	–	melt of gallium sulfides	–
β-Ga <sub>2</sub> S <sub>3</sub>	912 ± 3 °C, γ-Ga <sub>2+δ</sub> S <sub>3</sub> + α'-Ga <sub>2</sub> S <sub>3</sub> = β-Ga <sub>2</sub> S <sub>3</sub> , <b>(IV)</b> eutectoid	~1040 °C, β-Ga <sub>2</sub> S <sub>3</sub> = α-Ga <sub>2</sub> S <sub>3</sub> , <b>(V)</b> distectoid	Hexagonal, wurzite-like, S.G. $P6_3mc$ , $a = 3.682, b = 6.031 \text{ \AA}$ , (-)	59.8
α-Ga <sub>2</sub> S <sub>3</sub>	~950 °C (from the Ga-side), L + β-Ga <sub>2</sub> S <sub>3</sub> = α-Ga <sub>2</sub> S <sub>3</sub> , <b>(VI)</b> cathatectic ~982 °C (from the S-side), β-Ga <sub>2</sub> S <sub>3</sub> + α'-Ga <sub>2</sub> S <sub>3</sub> = α-Ga <sub>2</sub> S <sub>3</sub> , <b>(VII)</b> eutectoid	1109 ± 2 °C, α-Ga <sub>2</sub> S <sub>3</sub> = L, <b>(VIII)</b> Congruent melting	hexagonal, S.G. $P6_1$ , $a = 6.3883, b = 18.081 \text{ \AA}$ , (+)	59.0–60.2
α'-Ga <sub>2</sub> S <sub>3</sub>	Stable at RT	1002 ± 2 °C, α'-Ga <sub>2</sub> S <sub>3</sub> = L + α-Ga <sub>2</sub> S <sub>3</sub> , <b>(IX)</b> peritectic melting	моноклинная, ПГ $Cc$ , $a = 11.14, b = 6.41,$ $c = 7.04 \text{ \AA}, b = 121.2^\circ,$ (+)	60.0
GaS-(2H)	Stable at RT	967 ± 2 °C [10], GaS = L, <b>(XI)</b> congruent melting	Layered hexagonal, S.G. $P6_3mmc$ , $a = 3.59, b = 15.43 \text{ \AA}$ [10]	50.0

The results of the detailed\* differential thermal analysis (DTA) confirm the results of the structure analysis, which indicated the stability of the  $\gamma$ -Ga<sub>2+δ</sub>S<sub>3</sub> phase over a small range of temperatures and compositions. Furthermore, the results of the DTA allowed us to specify this range. Taking into account the results of the structure analysis, the first effect demonstrates that the lower limit of the temperature range is the eutectoid decomposition into GaS and monoclinic α'-Ga<sub>2</sub>S<sub>3</sub> (878±2 °C; equation **(I)**, Table 1). The latter effect indicates the upper limit of the  $\gamma$  phase. It is associated with incongruent melting, which, besides the melt, results in the formation of another high-temperature modification Ga<sub>2</sub>S<sub>3</sub> (922±2 °C; equation **(II)**, Table 1). Finally, the intermediate effect (910 °C) is associated with eutectic melting (equation **(III)**, Table 1).

\* The study included 75 samples. Each sample was analysed at three heating rates: 0.9, 1.9, and 3.8 K/min.

The analysis of the dependences of normalized areas of endoeffects on thermograms allowed us to specify the composition of the  $\gamma$ -Ga<sub>2+δ</sub>S<sub>3</sub> phase at the lower and the upper limits of existence of the phase on the  $T$ - $x$  diagram. According to Fig. 3, the lower limit corresponds to the concentration of sulfur of 59.3±0.1 mol %. A similar value was obtained for the upper limit of existence of this modification, which is 0.2 % less than stated in [10].

59.0–59.5 mol % region. In this concentration range, all the above mentioned peaks, except for the last one (910 °C), were also quite prominent, which indicated that the compositions were close to the region of existence of  $\gamma$ -Ga<sub>2</sub>S<sub>3</sub>.

59.5–59.8 mol % region. In this region, there was a decrease in the temperature of the effect (which was previously registered at 922 °C) to 916–917 °C. This indicated a change in the nature of the effect. Taking into account the X-ray data, the corresponding transformation

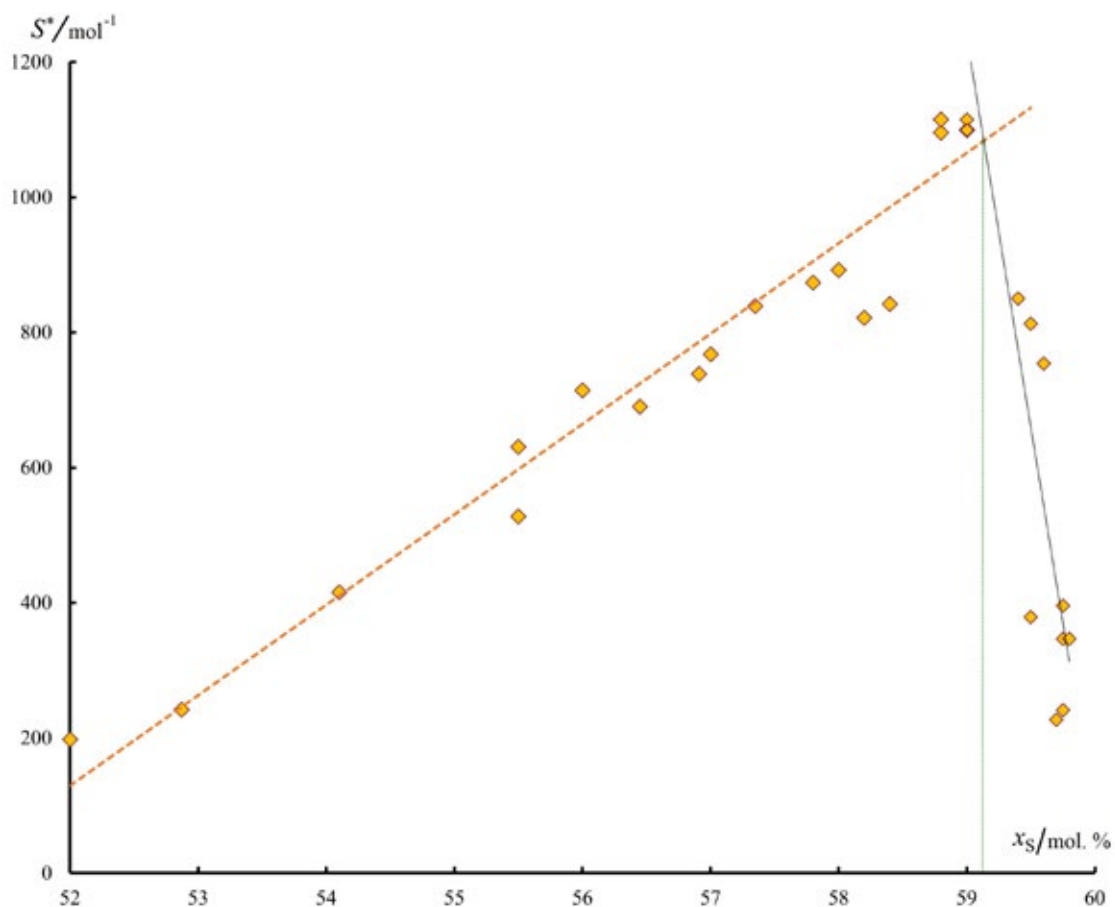


**Fig. 3.** The dependence of the reduced peak area on the alloy compositions for the DTA heating patterns, focused on the endo-effect observed at a temperature of  $\sim 878$  °C

is associated with the formation of a new phase  $\beta$ - $\text{Ga}_2\text{S}_3$  from  $\gamma$ - $\text{Ga}_{2+\delta}\text{S}_3$  and  $\alpha'$ - $\text{Ga}_2\text{S}_3$  according to the reaction reverse to eutectoid transformation – see equation (IV), Table 1.

The 59.8 mol % composition demonstrated a slight effect at 1040 °C (Fig. 4b), which can indicate the decomposition of the phase and which we classified as a distectoid transformation – equation (V), Table 1. Furthermore, at a temperature of 955–960 °C an additional endoeffect appeared (Fig. 4b), whose area increased at higher concentrations of sulfur in the studied samples. Taking into account the results of powder diffraction, we associated this effect with the formation of the  $\alpha$ - $\text{Ga}_2\text{S}_3$  phase from the melt and  $\beta$ - $\text{Ga}_2\text{S}_3$  according to the catatectic reaction (see equation (VI), Table 1).

**59.9 mol % composition.** This composition is interesting because all the above mentioned effects (878, 917, and 950 °C) disappear from the thermogram, while a new one appears and is reproduced at a temperature of  $\sim 982$  °C. We

interpreted this effect as satisfying equation (VII), Table 1.

**60.0–60.7 mol %s region.** All the thermal experiments conducted in this region demonstrated the presence of a strong effect at  $1002 \pm 2$  °C, which is most probably associated with the peritectic decomposition of the  $\alpha'$ - $\text{Ga}_2\text{S}_3$  phase (equation (IX), Table 1).

For the alloy with the concentration of sulfur of 60.0 mol %, the maximum liquidus temperature is reached and the form of the effect becomes typical for the phase transformation of the I kind. This indicates congruent melting of the  $\alpha$ - $\text{Ga}_2\text{S}_3$  phase ( $1109 \pm 2$  °C).

The results of the DTA (Table 1) together with the results of powder diffraction (Fig. 2) allowed us to obtain a fragment of the  $T$ - $x$  diagram of the Ga – S system refined for the concentration range from 50.0 to 60.7 mol %. The diagram is presented in Fig. 5.

**Metastable states in the Ga – S system.** As we have previously mentioned, three out

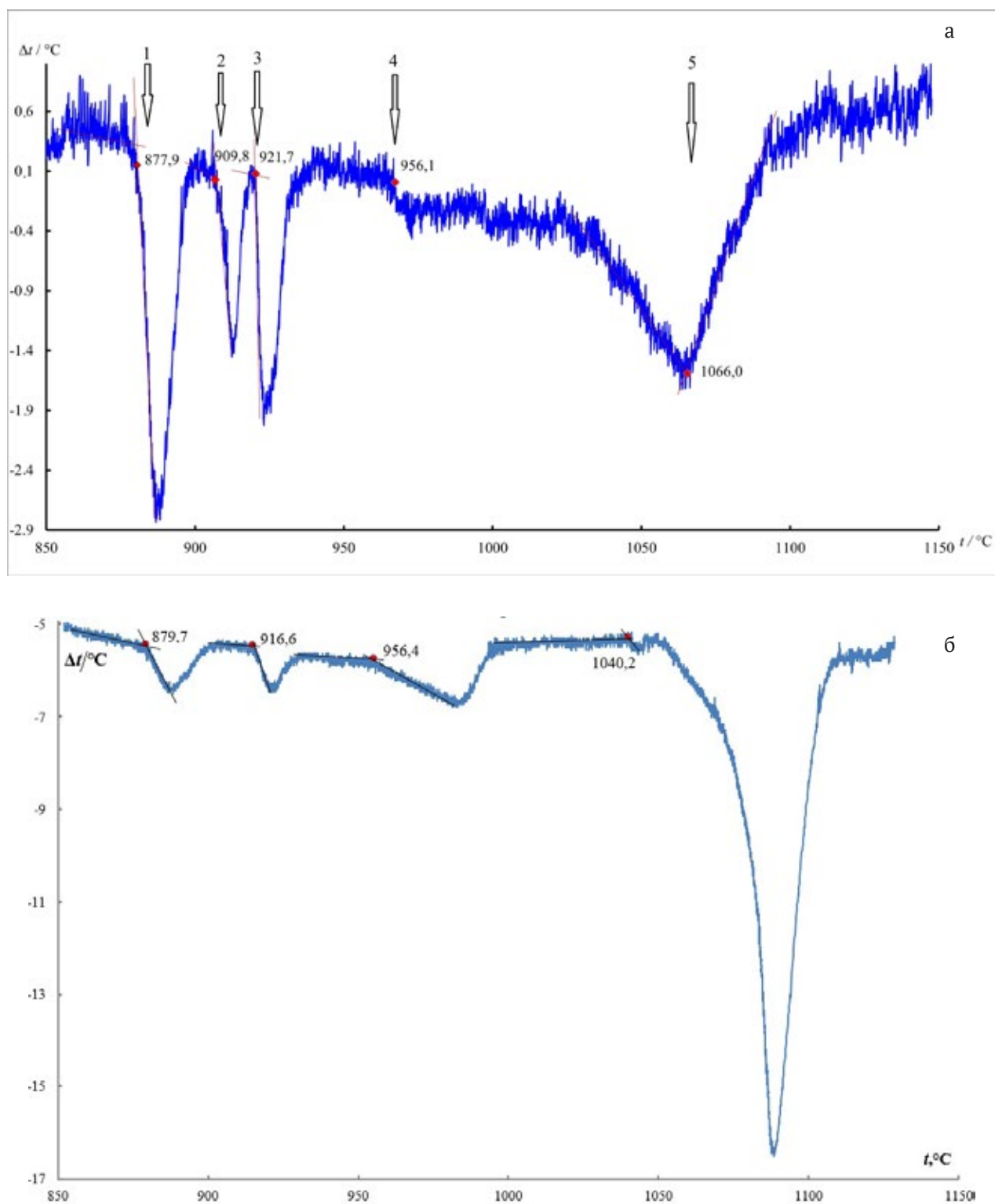


**Fig. 4.** DTA heating patterns of the Ga – S alloys with a sulfur content of 58.8 (a) and 59.8 (b) mol % S at rates of 2 and 4 K/min, respectively



of four phases of the  $\text{Ga}_2\text{S}_3$  family ( $\alpha$ ,  $\beta$ , and  $\gamma$ - $\text{Ga}_{2+\delta}\text{S}_3$ ) are metastable at room temperature and can be obtained only through quenching at high temperatures at which they are stable as compared to other phases. In order to determine the conditions under which these phases transform into their stable modifications at noticeable rates, samples of phases  $\alpha$ -,  $\beta$ -, and  $\gamma$  (with the concentration of sulfur of 59.8 mol % for the first two phases and 59.3 mol % for the third phase) were studied in DTA experiments, where they were heated starting with room temperature at a heating rate of  $\sim 2$  K/min. Thermograms of all the samples demonstrated noticeable exoeffects:  $\beta$ - $\text{Ga}_2\text{S}_3$  sulfide ( $460 \pm 10$  °C) was the most susceptible to decomposition; modifications  $\gamma$ - $\text{Ga}_{2+\delta}\text{S}_3$  and  $\alpha$ - $\text{Ga}_{2+\delta}\text{S}_3$  also demonstrated exoeffects close to 700 and 650 °C respectively. In all the cases, the result of the transformation was a monoclinic modification  $\alpha'$ - $\text{Ga}_2\text{S}_3$  (with an impurity of GaS). In order to determine the heat of the phase transition



a sample of the  $\beta$  modification was analyzed using a *Hitachi DSC 7020* differential scanning calorim-

eter over a temperature range from 25 to 600 °C in a highly pure (99.999 %) nitrogen atmosphere. The heat of the phase transformation calculated based on the peak area was 15.9 J/g, which corresponds to 3.75 kJ/mol in relation to the idealized stoichiometry of  $\text{Ga}_2\text{S}_3$ . Unfortunately, it was impossible to estimate the thermal effects of the relaxation of two other high-temperature phases in the  $\alpha'$  phase due to the temperature limitations ( $\sim 600$  °C) of the equipment.

During the DTA of the studied phase transformations observed during slow (2–4 K/min) cooling of the samples at temperatures outside the stability regions of high-temperature phases, the cooling curves demonstrated the same main effects as the heating curves. However, these effects correspond to significantly lower temperatures. Thus, the most high-temperature modification  $\alpha$ - $\text{Ga}_2\text{S}_3$ , which was in contact with melt L, (compositions from 58.0 to 59.5 mol %) is supercooled to a temperature of  $\sim 890$  °C, below which it transforms into  $\gamma$ - $\text{Ga}_{2+\delta}\text{S}_3$ . In turn,  $\gamma$ - $\text{Ga}_{2+\delta}\text{S}_3$  when slowly cooled decomposes into GaS and  $\alpha'$ - $\text{Ga}_2\text{S}_3$  only at 830–840 °C, i.e. It endures long-term supercooling up to almost 50 °C as compared to the lowest temperature of its

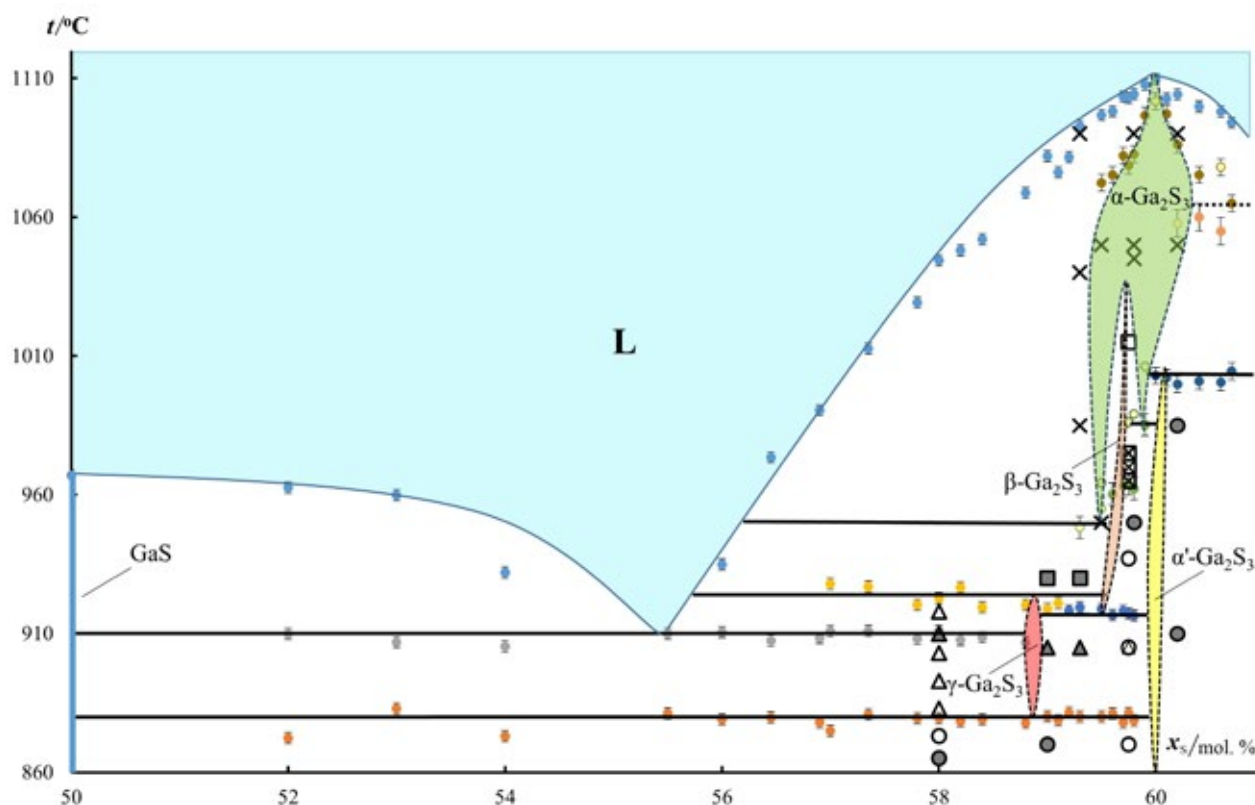


Fig. 5. Fragment of the *T*-*x*-diagram for the Ga – S system according to the data of this work

stability region. Other horizontal lines also shift noticeably towards lower temperatures. Thus, the eutectic horizontal satisfying the reaction reverse to (III) (Table 1) shifts by  $\sim 15$  °C from its position on the  $T$ - $x$  diagram, and the temperature of peritectic crystallization of  $\alpha'$ - $\text{Ga}_2\text{S}_3$  (reaction opposite to (IX), Table 1) shifts by  $\sim 25$  °C. Other peculiarities are that in cooling modes *a*) there were no transformations indicating the formation of the  $\beta$ - $\text{Ga}_2\text{S}_3$  phase and *b*) congruent crystallization of gallium sesquisulfide ( $\alpha$ - $\text{Ga}_2\text{S}_3$ ) proceeded almost without supercooling.

#### 4. Discussion

*A shift of the regions of existence of defect phases towards the excess of the cation former (Ga, In).* Let's consider the fact that the regions of existence of all sesquisulfides from the  $\text{Ga}_2\text{S}_3$  family are shifted towards an excess of the cation former (Ga). The only exception is the  $\alpha'$ - $\text{Ga}_2\text{S}_3$  phase whose composition corresponds to the ideal stoichiometry (60.0 mol %) within an inaccuracy of 0.1 mol %.

Here we can use the concept of *valence electron concentration* [18, 19], according to which structures with bonding networks close to the structure of diamond can be formed at a valence electron concentration (*VEC*) from 4.00 to 4.80 (in certain cases up to 4.92). *VEC* is defined as the number of valence electrons per formula unit. Despite being rather formal, this approach can be effective when predicting the stoichiometry of some solid-phase compounds. In particular, it explains a noticeable shift of the composition of the cubic  $\gamma$  phase  $\text{Ga}_{2+\delta}\text{S}_3$  towards an excess of gallium as compared to the ideal stoichiometry of  $\text{Ga}_2\text{S}_3$ . Thus, with the concentration of sulfur in the phase being 59.3 mol %, we obtain  $\delta = 0.06$  and *VEC*:

$$VEC = \frac{2.06 \cdot 3 + 3 \cdot 6}{(2.06 + 3)} = 4.77. \quad (5.1)$$

The actual *VEC* can be even smaller (by several hundredths) than the calculated value 4.77, because the electrons of the gallium atoms that partially occupy the vacancies in the cationic sublattice of the cubic  $\text{Ga}_{2+\delta}\text{S}_3$  phase may have little impact on the formation of the chemical bond. We should note that a small shift of the composition of the  $\gamma$  phase towards gallium as

compared to the ideal composition of  $\text{Ga}_2\text{S}_3$ , for which *VEC* would be almost 4.80, is in good agreement with the fact that the valence electron concentration in the structure tends to decrease. However, even after this shift *VEC*  $\approx 4.7$  is still close to the upper stability limit, which makes the  $\text{Ga}_{2+\delta}\text{S}_3$  phase metastable outside the narrow region of temperatures and compositions.

Taking into account the closeness of the bonding networks in wurtzite- and sphalerite-like structures, it is also logical that the homogeneity ranges of both wurtzite-like  $\beta$ - $\text{Ga}_2\text{S}_3$  and its modification  $\alpha$ - $\text{Ga}_2\text{S}_3$  shift towards gallium. It also explains the fact that these phases are only stable over a limited temperature range.

*Thermal stability.* Wurtzite-like modifications can exist at higher temperatures than sphalerite-like structures, which is common for many binary phases, for instance, ZnS [20]. It is logical that the homogeneity ranges of the phases based on a "defect" wurtzite  $\beta$ - and  $\alpha$ - $\text{Ga}_2\text{S}_3$  are generally located on the  $T$ - $x$  diagram of the Ga – S system above the region of existence of the *sphalerite-like* modification  $\gamma$ - $\text{Ga}_{2+\delta}\text{S}_3$ .

*Characteristics that require further analysis.* As quite unexpected came the fact that a more ordered phase  $\beta$ - $\text{Ga}_2\text{S}_3$  has a narrow homogeneity range, while its superstructural modification  $\alpha$ - $\text{Ga}_2\text{S}_3$  with ordered vacancies has a wider homogeneity range and can be formed at higher temperatures than the  $\beta$  phase. This fact requires further analysis. At the same time, the vacancies of the  $\alpha$ - $\text{Ga}_2\text{S}_3$  phase are only relatively ordered. This structure demonstrates crystallographically different positions of gallium in the cationic sublattice, which changes the symmetry and induces the transition  $P6_3mc \rightarrow P6_1$ . Different cationic positions in the  $\alpha$ - $\text{Ga}_2\text{S}_3$  structure are partially occupied to different degrees. However, they remain disordered, because partial occupation is stochastic. On the contrary, stoichiometric vacancies of another modification of the wurtzite-like structure of the  $\beta$  phase, a monoclinic  $\alpha'$ - $\text{Ga}_2\text{S}_3$ , are almost completely ordered. As a result, this phase is significantly different in terms of stability from the disordered and partially ordered modifications:  $\alpha'$ - $\text{Ga}_2\text{S}_3$  is almost completely stoichiometric and stable over a wide range of temperatures, starting from room temperature.

Although some of the results of the study require further research, we can conclude that the results are relevant, because they were obtained using various methods and are in good agreement with each other.

## 5. Conclusions

Using several independent methods of structure analysis (X-ray powder diffraction and high-temperature diffraction by means of synchrotron radiation), we confirmed that the high-temperature phase found during electron-diffraction studies (TEM, DAED) and formed at temperatures from 878 to 922 °C has a cubic sphalerite-like structure  $F\bar{4}3m$  with disordered stoichiometric vacancies. The composition of the phase further referred to as  $\gamma\text{-Ga}_{2+\delta}\text{S}_3$  was specified ( $\delta \approx 0.06$  or  $x_s = 59.3$  mol %). The study demonstrated that at temperatures above 912 °C and a slight excess of gallium (up to ~1 mol %) as compared to the stoichiometry of  $\text{Ga}_2\text{S}_3$  two modifications are formed: a defected wurtzite-like structure ( $\beta\text{-Ga}_2\text{S}_3$ ,  $P6_3mc$ ) and its derivative phase, the structure of which has lower symmetry ( $\alpha\text{-Ga}_2\text{S}_3$ ,  $P6_1$ ). For the first time the wurtzite-like ( $\beta\text{-Ga}_2\text{S}_3$ ,  $P6_3mc$ ) and sphalerite-like ( $\gamma\text{-Ga}_{2+\delta}\text{S}_3$ ) defect structures (with disordered vacancies) were obtained under equilibrium and studied *in situ* by means of synchrotron radiation.

For the first time a phase diagram of the Ga – S system was obtained and the regions of existence of the three above listed high-temperature gallium sesquisulfides and a modification of gallium sesquisulfide ( $\alpha'\text{-Ga}_2\text{S}_3$ ,  $Cc$ ), stable at room temperature, were determined.

## Contribution of the authors

At the end of the Conclusions the authors should include notes that explain the actual contribution of each co-author to the work.

## Conflict of interests

The authors declare that they have no known competing financial interests or personal relationships that could have influenced the work reported in this paper.

## References

1. Dingqi T., Haiyun L., Yuan D., Zhengliang D., Jiaolin C. Engineered cation vacancy plane responsible for the reduction in lattice thermal conductivity and

improvement in thermoelectric property of  $\text{Ga}_2\text{Te}_3$  based semiconductors. *RSC Advances*. 2014;4: 34104–34109. <https://doi.org/10.1039/c4ra04463k>

2. Fedorov P. P., Yarotskaya E. G. Zirconium dioxide. Review. *Condensed Matter and Interphases*. 2021;23(2): 169–187. <https://doi.org/10.17308/kcmf.2021.23/3427>

3. Budanov A. V., Tatokhin E. A., Strygin V. D., Rudnev E. V. High-symmetry in  $\text{In}_2\text{Se}_3$  and  $\text{Ga}_2\text{Se}_3$  cubic modifications obtained during interaction of InAs and GaAs substrates and selenium. *Condensed Matter and Interphases*. 2012;14(4): 412–417. (In Russ., abstract in Eng.). Available at: <https://www.elibrary.ru/item.asp?id=18485334>

4. Bezryadin N. N., Kotov G. I., Kuzuhov S. V. ... Ryazanov A. N. Surface phase  $\text{Ga}_2\text{Se}_3$  на GaP (111). *Condensed Matter and Interphases*. 2013;15(4): 382–386. (In Russ., abstract in Eng.). Available at: <https://www.elibrary.ru/item.asp?id=20931229>

5. Mikhailyuk E. A., Prokopova T. V., Bezryadin N. N. Modeling of processes of current flow films  $\text{A}^{\text{III}}_2\text{B}^{\text{VI}}_3$  in heterostructures on the basis of indium arsenide. *Condensed Matter and Interphases*. 2015; 17(2): 181–191. (In Russ., abstract in Eng.). Available at: <https://www.elibrary.ru/item.asp?id=23816619>

6. Plirdpring T., Kurosaki K., Kosuga A., ... Yamanaka S. Effect of the amount of vacancies on the thermoelectric properties of CuGaTe ternary compounds. *Materials Transactions (Special Issue on Thermoelectric Conversion Materials VII)*. 2012;53(7): 1212–1215. <https://doi.org/10.2320/matertrans.e-m2012810>

7. Olmstead M. A., Ohuchi F. S. Group III selenides: Controlling dimensionality, structure, and properties through defects and heteroepitaxial growth. *Journal of Vacuum Science & Technology A: Vacuum, Surfaces, and Films*. 2021;39(2): 020801. <https://doi.org/10.1116/6.0000598>

8. Zavrazhnov A., Berezin S., Kosykov A., Naumov A., Berezina M., Brezhnev N. The phase diagram of the Ga–S system in the concentration range of 48.0–60.7 mol% S. *Journal of Thermal Analysis and Calorimetry*. 2018;134: 483–492. <https://doi.org/10.1007/s10973-018-7124-z>

9. Volkov V. V., Sidey V. I., Naumov A. V., ... Zavrazhnov A. Y. The cubic high-temperature modification of gallium sulphide ( $x_s = 59$  mol %) and the *T, x*-diagram of the Ga – S system. *Condensed Matter and Interphases*. 2019;21(1): 37–50. (In Russ., abstract in Eng.). <https://doi.org/10.17308/kcmf.2019.21/715>

10. Volkov V. V., Sidey V. I., Naumov A. V., ... Zavrazhnov A. Yu. Structural identification and stabilization of the new high-temperature phases in A(III) – B(VI) systems (A = Ga, In, B = S, Se). Part 1: High-temperature phases in the Ga – S system. *Journal*



of *Alloys and Compounds*. 2022;899: 163264. <https://doi.org/10.1016/j.jallcom.2021.163264>

11. Pardo M., Tomas A., Guittard M. Polymorphisme de Ga<sub>2</sub>S<sub>3</sub> et diagramme de phase Ga – S. *Materials Research Bulletin*. 1987;22(12): 1677–1684. [https://doi.org/10.1016/0025-5408\(87\)90011-0](https://doi.org/10.1016/0025-5408(87)90011-0)

12. Pardo M., Guittard M., Chlouet A., Tomas A. Diagramme de phases gallium-soufre et études structurales des phases solides. *Journal of Solid State Chemistry*. 1993;102: 423–433. <https://doi.org/10.1006/jssc.1993.1054>

13. Sushkova T. P., Semenova G. V., Proskurina E. Y. Phase relations in the Si–Sn–As system. *Condensed Matter and Interphases*. 2023;25(2), 237–248. <https://doi.org/10.17308/kcmf.2023.25/11110>

14. Kraus W., Nolze G. PowderCell 2.0 for Windows. *Powder Diffraction*. 1998;13(4): 256–259. Available at: [https://www.researchgate.net/publication/257022604\\_PowderCell\\_20\\_for\\_Windows](https://www.researchgate.net/publication/257022604_PowderCell_20_for_Windows)

15. Hammersley A. P., Svensson S. O., Hanfland M., Fitch A. N., Hausermann D. Two-dimensional detector software: From real detector to idealised image or two-theta scan. *High Pressure Research*. 1996;14(4–6): 235–248. <https://doi.org/10.1080/08957959608201408>

16. Holland T. J. B., Redfern S. A. T. UNITCELL: a nonlinear least-squares program for cell-parameter refinement and implementing regression and deletion diagnostics. *Journal of Applied Crystallography*. 1997;30(1): 84. <https://doi.org/10.1107/s0021889896011673>

17. Fedorov P. I., Fedorov P. P., Drobot D. V., Samartsev A. M. *Errors in constructing state diagrams of binary systems: a textbook\**. Moscow: MITHT named after M. V. Lomonosova Publ.; 2005. 181 p. (In Russ.)

18. Parthé E. *Elements of inorganic structural chemistry*. CH-1213: Petit-Lancy, Switzerland; 1996. 230 p.

19. Sangiovanni D. G., Kaufmann K., Vecchio K. Valence electron concentration as key parameter to control the fracture resistance of refractory high-entropy carbides. *Science Advances*. 2023;9(37): 1–11. <https://doi.org/10.1126/sciadv.adi2960>

20. Gilbert B., Frazer B. H., Zhang H., ... De Stasio G. X-ray absorption spectroscopy of the cubic and hexagonal polytypes of zinc sulfide. *Physical Review B*. 2002;66: 245205. <https://doi.org/10.1103/physrevb.66.245205>

## Information about the authors

*Nikolay Y. Brezhnev*, Junior Researcher at the Department of General and Inorganic Chemistry, Voronezh State University (Voronezh, Russian Federation).

<https://orcid.org/0000-0002-3287-8614>  
brezhnevnick@gmail.com

*Michael V. Dorokhin*, Dr. Sci (Phys.-Math.), Leading Researcher at the Physical-Technical Research Institute of UNN (PTRI) (Nizhny Novgorod, Russian Federation).

<https://orcid.org/0000-0001-5238-0090>  
dorokhin@nifti.unn.ru

*Alexander Y. Zavrazhnov*, Dr. Sci. (Chem.), Full Professor, Department of General and Inorganic Chemistry, Voronezh State University (Voronezh, Russian Federation).

<https://orcid.org/0000-0003-0241-834X>  
alexander.zavrazhnov@gmail.com

*Nikolay A. Kolyshkin*, Research Engineer at the National Research Center “Kurchatov Institute” (Moscow, Russian Federation).

<https://orcid.org/0000-0003-3437-6391>  
nickelprog@mail.ru

*Ivan N. Nekrylov*, post-graduate student at the Department of General and Inorganic Chemistry, Voronezh State University (Voronezh, Russian Federation).

<https://orcid.org/0000-0003-4491-4739>  
Icq492164858@gmail.com

*Vladimir N. Trushin*, Dr. Sci (Phys.-Math.), Leading Researcher at the Physical-Technical Research Institute of UNN (PTRI) (Nizhny Novgorod, Russian Federation).

<https://orcid.org/0000-0001-5104-6592>  
trushin@phys.unn.ru

Received 08.09.2023; approved after reviewing 02.10.2023; accepted for publication 15.11.2023; published online 25.06.2024.

Translated by Yulia Dymant



## Original articles

Research article

<https://doi.org/10.17308/kcmf.2024.26/12070>**Deposition of lead sulfide films from “ $\text{Pb}(\text{CH}_3\text{COO})_2 - \text{N}_2\text{H}_4\text{CS}$ ” aqueous solutions and their properties**E. A. Gannova, M. V. Grechkina, V. N. Semenov, A. N. Lukin, S. A. Ivkov, T. V. Samofalova Voronezh State University,  
1 Universitetskaya pl., Voronezh 394018, Russian Federation**Abstract**

The article presents the results of the study of lead sulfide films obtained by the aerosol pyrolysis of solutions of complex compounds of lead acetate and thiourea at temperatures of 300 and 400 °C. The concentration areas of existence of lead (II) hydroxo complexes were determined. We determined the domination regions of  $[\text{Pb}(\text{N}_2\text{H}_4\text{CS})_4]^{2+}$  complexes, which are precursors during the deposition of lead sulfide films.

The crystal structure, phase composition, and surface morphology of the synthesized films were studied by X-ray phase analysis and atomic force microscopy. It was found that under these deposition conditions, the crystallized PbS films have a cubic structure and are textured in the (200) crystallographic direction. When the concentration of thiourea in the initial solution increases, there is an increase in the values of the average and root-mean-square roughness, as well as the relief height difference of the synthesized samples.

PbS films obtained at a temperature of 400 °C are characterized by a denser packing of grains and a perfect surface microstructure. By optical spectrophotometry, we determined the band gap of synthesized PbS, which is from 0.41 to 0.45 eV for direct allowed transitions.

**Keywords:** PbS films, Aerosol pyrolysis method, Atomic force microscopy, Thiourea complex compounds, X-ray phase analysis, Transmission spectra

**Acknowledgements:** The crystal structure and surface morphology of the samples were studied by X-ray diffraction and atomic force microscopy using the equipment of the Centre for Collective Use of Scientific Equipment of Voronezh State University. URL: <https://ckp.vsu.ru>

**For citation:** Gannova E. A., Grechkina M. V., Semenov V. N., Lukin A. N., Ivkov S. A., Samofalova T. V. Deposition of lead sulfide films from “ $\text{Pb}(\text{CH}_3\text{COO})_2 - \text{N}_2\text{H}_4\text{CS}$ ” aqueous solutions and their properties. *Condensed Matter and Interphases*. 2024;26(2): 238–246. <https://doi.org/10.17308/kcmf.2024.26/12070>

**Для цитирования:** Ганнова Е. А., Гречкина М. В., Семенов В. Н., Лукин А. Н., Ивков С. А., Самофалова Т. В. Осаждение пленок сульфида свинца из водных растворов « $\text{Pb}(\text{CH}_3\text{COO})_2 - \text{N}_2\text{H}_4\text{CS}$ » и их свойства. *Конденсированные среды и межфазные границы*. 2024;26(2): 238–246. <https://doi.org/10.17308/kcmf.2024.26/12070>

✉ Samofalova T. V., e-mail: [TSamofalova@bk.ru](mailto:TSamofalova@bk.ru)

© Gannova E. A., Grechkina M. V., Semenov V. N., Lukin A. N., Ivkov S. A., Samofalova T. V., 2024



The content is available under Creative Commons Attribution 4.0 License.

## 1. Introduction

Films of lead sulfide, which is a narrow-bandgap semiconductor, are widely used as for creating efficient photovoltaic converters, photodetectors, and photoresistors, temperature-sensitive sensors, IR detectors in the infrared region of the spectrum [1–5]. An urgent task is to synthesize PbS films with a given crystal structure and variable properties. The main methods for obtaining lead sulfide layers are chemical synthesis methods, such as chemical deposition and aerosol pyrolysis from solutions of sulfur-containing precursors [6–10]. Varying the crystal structure, optical and electrophysical properties of sulfide films provides an economical and technically accessible method for the aerosol pyrolysis of solutions of thiourea complex compounds (TCCs). The main idea of the method is the thermal destruction of complex compounds with the formation of a solid phase of metal sulfide [11, 12]. The aim of this work was to study the process of deposition of lead sulfide thin films by the aerosol pyrolysis of aqueous solutions of “Pb(CH<sub>3</sub>COO)<sub>2</sub> – N<sub>2</sub>H<sub>4</sub>CS”, as well as to analyze the surface morphology, phase composition, and optical properties of the synthesized layers.

## 2. Experimental

To produce complex compounds and to deposit PbS films, we used chemically pure Pb(CH<sub>3</sub>COO)<sub>2</sub>·3H<sub>2</sub>O and extra pure N<sub>2</sub>H<sub>4</sub>CS (thiourea). The concentration of the metal salt in the sprayed solution was 0.1 mol/l, the concentration of thiourea was between 0.4 and 1 mol/l. PbS films were obtained by the aerosol pyrolysis of aqueous solutions of “Pb(CH<sub>3</sub>COO)<sub>2</sub> – N<sub>2</sub>H<sub>4</sub>CS” on a heated substrate at temperatures of 300 and 400 °C. The substrates were silica plates, which were prewashed in nitric acid and chromic mixture, then washed repeatedly in distilled water. Each sample was sprayed for 1 minute.

X-ray phase analysis was carried out on a DRON 4-07 X-ray diffractometer with CuK $\alpha$ -radiation at the X-ray tube accelerating voltage of 29 kV and an anode current of 26 mA. The phase composition of the films was determined by comparing the experimental values of interplanar distances  $d_{hkl}$  obtained from diffraction patterns with reference data [13].

We studied the surface morphology of the samples using a SOLVER P47 atomic force microscope, analyzing the following parameters: arithmetic mean deviation of the surface profile  $R_a$ , RMS roughness, relief height difference  $\Delta$ , and height of the largest number of grains  $h$ . In this study, we used Etalon series HA\_FM composite polysilicon cantilevers by TipsNano with a curvature radius of 10 nm and gold reflective coating.

The transmission spectra of PbS films were measured using a Vertex 70 Fourier spectrometer on a quartz substrate in the range of wavenumbers from 7000 to 2500 cm<sup>-1</sup>. To determine the optical band gap  $E_g$ , we used the Tauc formula for direct allowed transitions [14, 15]:

$$(\alpha d)_n = \frac{A(h\nu - E_g)^{\frac{1}{2}}}{h\nu}, \quad (1)$$

where  $h\nu$  is the photon energy,  $d$  is the sample thickness, and  $\alpha$  is the absorption coefficient. Considering the non-uniformity of the thickness of the studied films within the analyzed dimensions, we normalized the transmission spectra [16]:

$$(\alpha d)_n = \frac{(\alpha d)_{hv} - (\alpha d)_{\min}}{(\alpha d)_{\max} - (\alpha d)_{\min}} \quad (2)$$

The band gap was determined by extrapolation of the linear parts of the dependences  $((\alpha d)_n h\nu)^2 = f(h\nu)$  to zero. The experimental data were processed using Origin Pro 8.5.

## 3. Results and discussion

During the deposition of metal sulfide films by the aerosol pyrolysis of solutions of thiourea complex compounds, the processes leading to the formation of sulfide on a heated substrate begin already in the initial solution. They start with the formation of a covalent bond between the lead cation and the sulfur atom (NH<sub>2</sub>)<sub>2</sub>CS [10, 17]. Therefore, in order to understand the deposition mechanism of PbS layers, we studied ionic equilibria in the “Pb(CH<sub>3</sub>COO)<sub>2</sub> – N<sub>2</sub>H<sub>4</sub>CS” solution taking into account the stability constants of different complexes. We determined the optimal concentration areas of thiourea complexes ( $C_{TU} = 5 \cdot 10^{-1}$  mol/l,  $C_{pb}^{2+} = 5 \cdot 10^{-4}$  mol/l), which are sulfide precursors.



Comparing the stability constants of lead complexes (II) in aqueous solutions [18], it can be noted that the highest values are for hydroxo complexes. Therefore, when analyzing the “lead salt – thiourea” solution, we first considered the hydrolysis process as complexation, in which hydroxyl ions are incoming ligands.

We calculated the fractions of hydroxo complexes in the “lead salt – thiourea” system at the initial concentration of  $C_{Pb^{2+}} = 1 \cdot 10^{-2}$  mol/l (in this case, the Pb(OH)<sub>2</sub> precipitation does not occur) using the formulas in [11]. As can be seen from the calculated distribution diagram (Fig. 1), the pH at the beginning of the formation of Pb<sup>2+</sup> hydroxo complexes is 4.5 (their fraction in the solution is 0.03 %). The concentration of hydroxo complexes increases sharply with increasing pH. In this case, it is possible to suppress hydrolysis in the solution by an excess of thiourea. Thus, the hydroxo groups are replaced with thiourea molecules in the inner sphere of the complex compound.

To model the initial solution taking into account the formation of thiourea complexes, we calculated and built three-dimensional diagrams and cross section lines of equal fractions. The methodology for their construction is provided in [19]. For the calculation, we used the experimental stability constants of homoligand complexes [18], the constants for mixed-ligand complexes were calculated using the formula [11]

$$\lg K_{ij} = \frac{i \lg K_{im} + j \lg K_{jm}}{i+j} + \lg \frac{m!}{i!j!}.$$

Here  $K_{ij}$  is the stability constant of the mixed [PbTU<sub>i</sub>(CH<sub>3</sub>COO)<sub>j</sub>] complex ( $i + j = m$ ),  $K_{im}$  and  $K_{jm}$  are the stability constants of the homogeneous complexes [Pb(TU)<sub>m</sub><sup>2+</sup>] and [Pb(CH<sub>3</sub>COO)<sub>m</sub><sup>2-m</sup>], respectively, and  $\frac{m!}{i!j!}$  are the comproportionation constants.

Thus, we determined the domination areas of thiourea complex compounds, which are precursors during the deposition of lead sulfide films. Fig. 2 shows the three-dimensional diagram and the cross section lines of equal fractions for

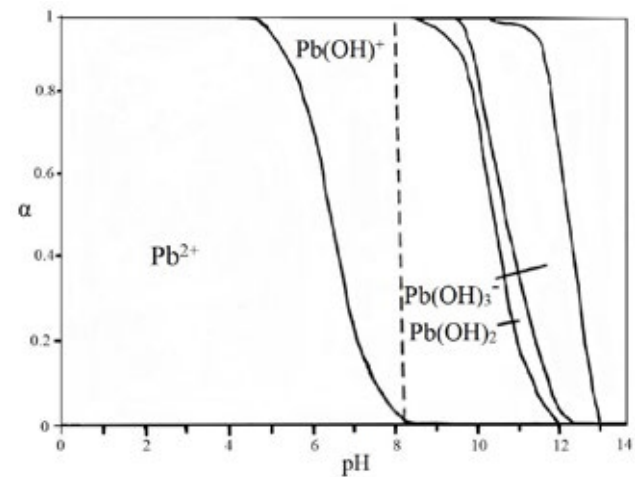


Fig. 1. Distribution diagram of lead (II) hydroxo complexes

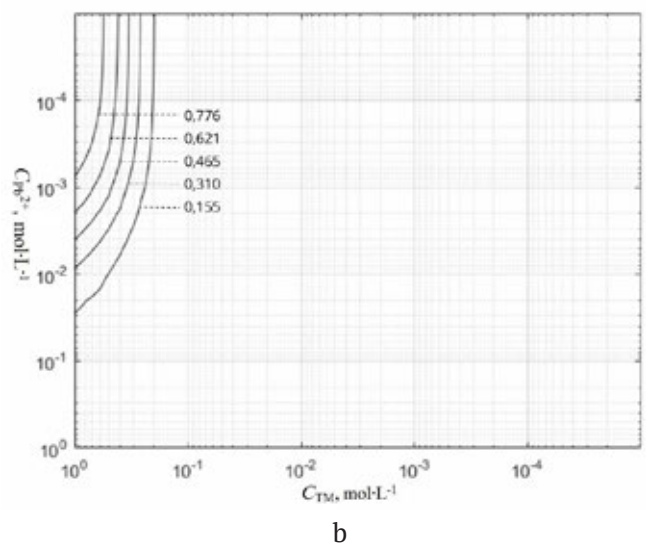
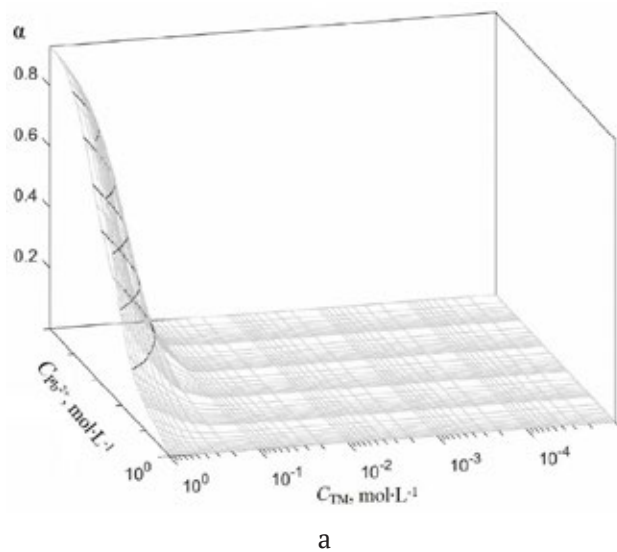


Fig. 2. Three-dimensional distribution diagrams (a) and cross section lines of equal fractions (b) for the [Pb(N<sub>2</sub>H<sub>4</sub>CS)<sub>4</sub>]<sup>2+</sup> complexes in the “Pb(CH<sub>3</sub>COO)<sub>2</sub> – N<sub>2</sub>H<sub>4</sub>CS” system

“ $\text{Pb}(\text{CH}_3\text{COO})_2 - \text{N}_2\text{H}_4\text{CS}$ ” aqueous solutions of the  $[\text{Pb}(\text{N}_2\text{H}_4\text{CS})_4]^{2+}$  complex.

In the “ $\text{Pb}(\text{CH}_3\text{COO})_2 - \text{N}_2\text{H}_4\text{CS}$ ” aqueous solution, a complex compound is formed, in which thiourea enters the inner sphere, and it binds to the metal cation by a donor sulfur atom already in the initial solution [9]. This is how the fragments of the sulfide structure are formed in the inner sphere of the complex compound obtained in the sprayed solution by the interaction of the lead salt and  $\text{N}_2\text{H}_4\text{CS}$ . When the thiourea complex compound decomposes on a heated substrate, the most thermally stable product, PbS, is released.

When determining the structure of PbS films, we obtained diffraction patterns in the form of dependence of the diffracted radiation intensity on spatial coordinates for samples synthesized at different concentration ratios of lead acetate and thiourea. The obtained diffraction patterns are shown in Fig. 3. The halo, which appears on the diffraction patterns of each film in the range of angles from 15 to 25°, refers to the amorphous

structure of the cuvette on which the samples were placed during imaging.

The X-ray phase analysis data (Table 1) suggest that the deposited PbS films crystallize in a cubic structure of the *B1* type (space group). The values of interplanar distances of experimentally obtained lead sulfide films are close to the values of the reference polycrystalline lead sulfide. We obtained its diffraction pattern using the same diffractometer with the same imaging parameters. Table 2 shows that the deviations of the values of interplanar distances of the etalon and lead sulfide thin films are much smaller than the error limit of the device. This indicates the high quality of the synthesized lead sulfide layers.

For all studied PbS films, the interplanar distances for each crystallographic plane *hkl* practically coincide with each other, and the intensities of the same diffraction maxima are different (Table 1, Fig. 3). All the diffraction patterns show the highest intensity at the reflection (200), and the half-width of this peak

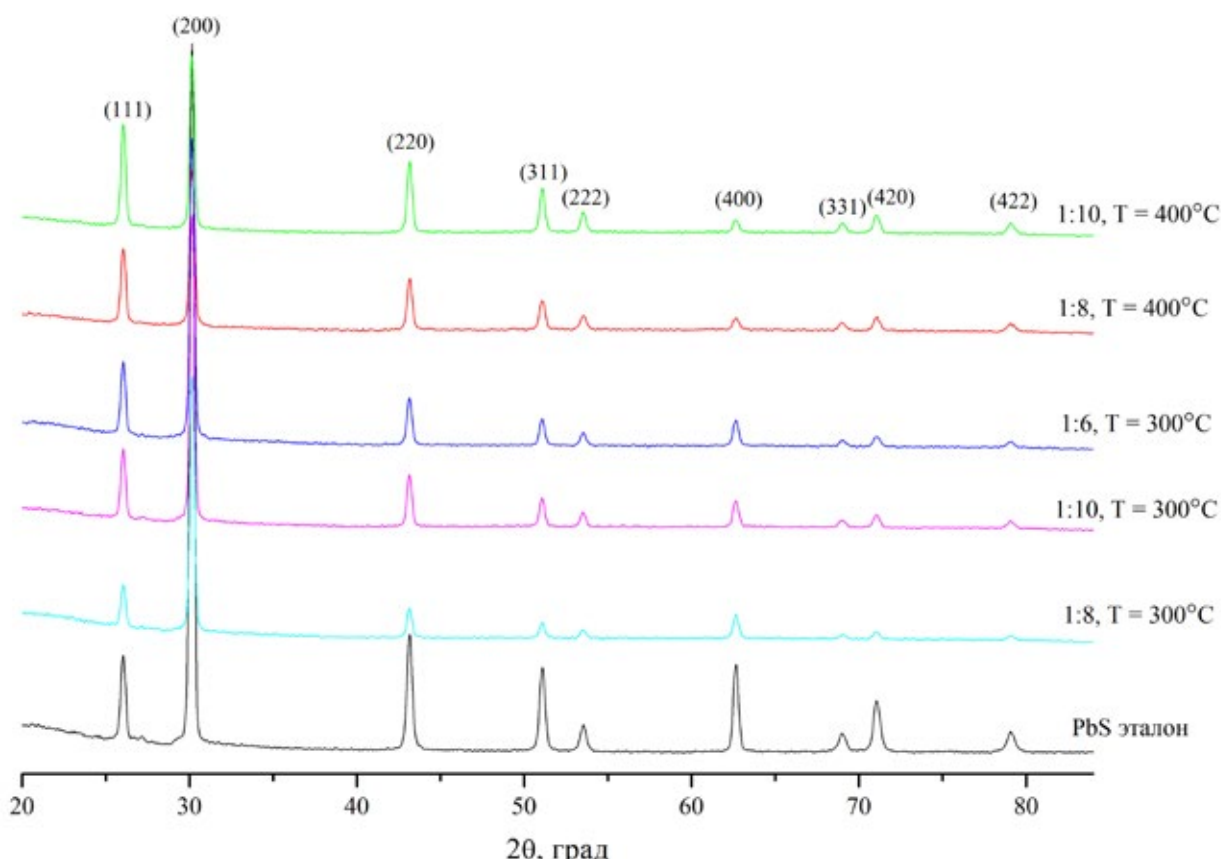


**Fig. 3.** Diffraction patterns of PbS films obtained at different temperatures and component ratios of  $\text{C}(\text{Pb}(\text{CH}_3\text{COO})_2):\text{C}(\text{N}_2\text{H}_4\text{CS})$

**Table 1.** Characteristics of the interplanar distances of the deposited PbS films compared with

Interplane distance <i>d</i> , Å	Deposition temperature and molar ratios of components in the system «Pb(CH <sub>3</sub> COO) <sub>2</sub> – N <sub>2</sub> H <sub>4</sub> CS»					Database [13]	
	300 °C			400 °C		<i>d</i> , Å	h k l
	1:6	1:8	1:10	1:8	1:10		
3.4205	3.4205	3.4205	3.4205	3.4205	3.4205	3.4260	1 1 1
2.9640	2.9640	2.9592	2.9592	2.9640	2.9640	2.9670	2 0 0
2.0964	2.0964	2,0964	2.0964	2.0964	2.0964	2.0980	2 2 0
1.7874	1.7874	1.7890	1.7890	1.7874	1.7874	1.7890	3 1 1
1.7112	1.7127	1.7127	1.7127	1.7127	1.7127	1.7130	2 2 2
1.4828	1.4828	1,4828	1.4817	1.4828	1.4828	1.4830	4 0 0
1.3602	1.3610	1.3602	1.3602	1.3602	1.3602	1.3610	3 3 1
1.3259	1.3267	1.3267	1.3259	1.3267	1.3267	1.3270	4 2 0
1.2100	1.2100	1.2119	1.2113	1.2113	1.2113	1.2110	4 2 2

**Table 2.** Comparison of the interplanar distances of experimental samples with the lead sulfide standard

Peak number	Standard PbS [13]	Deposition temperature 300°C						Deposition temperature 400°C			
		PbS 1:6		PbS 1:8		PbS 1:10		PbS 1:8		PbS 1:10	
		<i>d</i> , Å	<i>d</i> , Å	Δ <i>d</i> , Å	<i>d</i> , Å	Δ <i>d</i> , Å	<i>d</i> , Å	Δ <i>d</i> , Å	<i>d</i> , Å	Δ <i>d</i> , Å	<i>d</i> , Å
1	3.4205	3.4205	0	3.4205	0	3.4205	0	3.4205	0	3.4205	0
2	2.9640	2.9640	0	2.9640	0	2.9592	0.0048	2.9640	0	2.9592	0.0048
3	2.0964	2.0964	0	2.0964	0	2.0964	0	2.0964	0	2.0964	0
4	1.7874	1.7874	0	1.7874	0	1.7890	0.0016	1.7874	0	1.7890	0.0016
5	1.7112	1.7112	0	1.7127	0.0015	1.7127	0.0015	1.7127	0.0015	1.7127	0.0015
6	1.4828	1.4828	0	1.4828	0	1.4828	0	1.4828	0	1.4817	0.0011
7	1.3610	1.3602	0.0008	1.3610	0	1.3602	0.0008	1.3602	0.0008	1.3610	0
8	1.3267	1.3259	0.0008	1.3267	0	1.3267	0	1.3267	0	1.3259	0.0008
9	1.2113	1.2100	0.0013	1.2100	0.0013	1.2119	0.0006	1.2113	0	1.2113	0
10	1.1416	1.1421	0.0005	1.1421	0.0005	1.1416	0	1.1421	0.0005	1.1421	0.0005
11	0.9895	0.9892	0.0003	0.9892	0.0003	0.9895	0	0.9902	0.0007	0.9888	0.0007

was the same for all samples. In general, this may indicate the preferential orientation of crystallites in this direction. Changing the molar ratio of components in the “Pb(CH<sub>3</sub>COO)<sub>2</sub> – N<sub>2</sub>H<sub>4</sub>CS” system did not change the phase composition and crystal structure of the formed lead sulfide films. In the case of hydrochemical deposition, PbS layers with a cubic structure were also formed [20–22].

Previous studies [23–25] have showed that PbS films can crystallize in a cubic structure close to the *DO*<sub>3</sub> type, with a partially disordered (statistical) distribution of sulfur atoms over octahedral and tetrahedral positions. Since in the lead sulfide lattice the octahedral positions of the *B1* structural type are predominantly occupied, a highly defective *B1* structure with a

high concentration of sulfur vacancies in regular octahedral positions and interstitial sulfur atoms in tetrahedral positions is formed [23, 24].

We studied the surface morphology of PbS films and obtained surface scans of the samples in the semi-contact mode of atomic force microscopy (AFM). Fig. 4 shows AFM images of the surface microrelief of lead sulfide films within the scanned area (scan area of 5x5 μm<sup>2</sup>) synthesized at different molar ratios of the initial solution components.

According to AFM data, the surface of the obtained samples is composed of a set of rounded grains with pronounced boundaries, which form complex aggregates (Fig. 4). The average sizes of grains and their aggregates are 205–240 nm and 330–365 nm, respectively (Table 3).



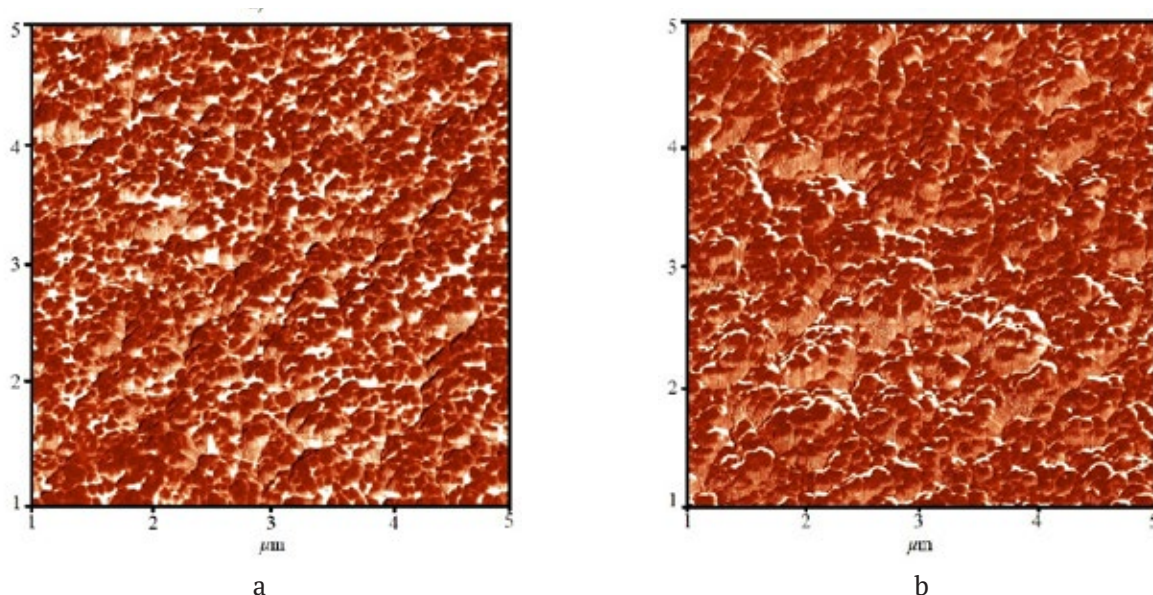


**Fig. 4.** AFM images of the surface of the PbS films synthesized at 400°C and C(PbCH<sub>3</sub>(COO)<sub>2</sub>):C(N<sub>2</sub>H<sub>4</sub>CS) ratios of 1:8 (a) and 1:10 (b)

With increasing thiourea concentration in the initial solution, the average ( $R_a$ ) and RMS ( $R_q$ ) roughness, as well as relief height difference ( $\Delta$ ) increase, indicating the formation of films with more prominent surface relief. PbS samples obtained at the same ratios of C(Pb(CH<sub>3</sub>COO)<sub>2</sub>):C(N<sub>2</sub>H<sub>4</sub>CS), at 400 °C, have smoother surfaces compared to films synthesized at 300 °C. Thus, an increase in the deposition temperature leads to the formation of PbS films with a more perfect structure and denser packing of grains. Similar results concerning the effect of temperature on the microstructure of pyrolytic films of lead sulfide were obtained in [26].

When studying the optical properties of PbS films, we used the power-law dependences

of the absorption coefficient on the photon energy (Fig. 5) to determine the optical band gap (Table 4). The samples obtained at temperatures of 300–400 °C and varying molar ratios of components are characterized by the band gap  $E_g$  from 0.41 to 0.45 eV. The obtained results are in good agreement with literature data [9, 15]. The component ratio in the sprayed solution practically does not affect the optical band gap.

#### 4. Conclusions

Lead sulfide films were synthesized by aerosol pyrolysis of aqueous solutions of “Pb(CH<sub>3</sub>COO)<sub>2</sub> – N<sub>2</sub>H<sub>4</sub>CS” at temperatures of 300 and 400 °C. It was shown that the pH at the beginning of formation

**Table 3.** Morphological properties of PbS films

T, °C	C(Pb(CH <sub>3</sub> COO) <sub>2</sub> ):C(N <sub>2</sub> H <sub>4</sub> CS)	Δ, nm	R <sub>a</sub> , nm	R <sub>q</sub> , nm	h, nm	Grain size/ aggregate size, nm
300	1:6	569	47	62	370	225 / 340
	1:8	669	78	97	375	215 / 330
	1:10	717	87	85	375	240 / 365
400	1:8	623	64	81	380	205 / 330
	1:10	673	70	90	375	215 / 350

**Table 4.** Optical band gap (eV) of lead sulfide films

Synthesis temperature, °C	The ratio of components in the system “Pb(CH <sub>3</sub> COO) <sub>2</sub> – N <sub>2</sub> H <sub>4</sub> CS”			
	1:4	1:6	1:8	1:10
300	0.43	0.45	0.45	0.45
400	0.43	0.44	0.41	0.42

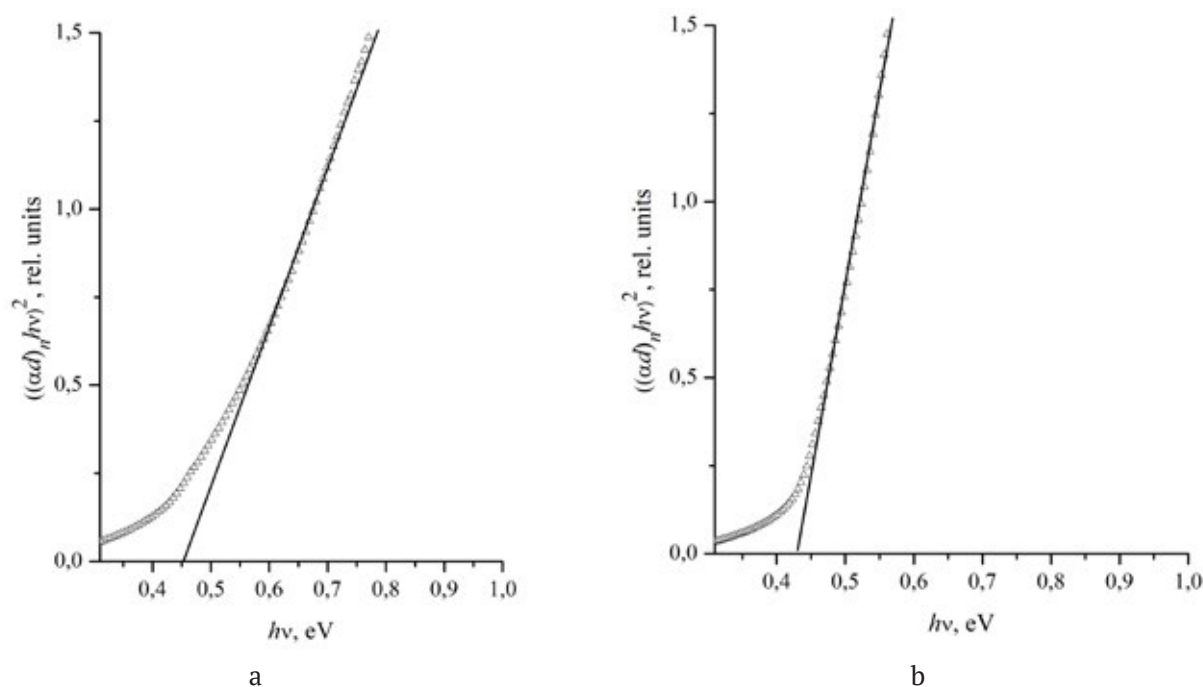


**Fig. 5.** Power-law dependences of the absorption coefficient on the photon energy for PbS films deposited from the “Pb(CH<sub>3</sub>COO)<sub>2</sub> – N<sub>2</sub>H<sub>4</sub>CS” solutions: a – at 300 °C, component ratio of 1:6; б – at 400 °C, component ratio of 1:10

of lead (II) hydroxo complexes in the solution was 4.5 and their fraction in the solution was 0.03 %. In this case, it is possible to suppress hydrolysis by an excess of thiourea, i.e., by replacing the hydroxo group with N<sub>2</sub>H<sub>4</sub>CS molecules. In order to model the initial solution taking into account the formation of thiourea complexes, we calculated and built three-dimensional diagrams and cross section lines of equal fractions for the [Pb(N<sub>2</sub>H<sub>4</sub>CS)<sub>4</sub>]<sup>2+</sup> complex. Thus, we chose the initial concentrations of the components: C<sub>TU</sub> = 5·10<sup>-1</sup> mol/l, C<sub>Pb<sup>2+</sup></sub> = 5·10<sup>-4</sup> mol/l.

X-ray phase analysis showed that PbS films with cubic structure and preferential orientation (200) were formed from solutions of thiourea complexes of lead. The surface of lead sulfide films was formed by a set of rounded grains with average sizes between 205 and 240 nm, which formed complex aggregates (330–365 nm). We determined that sulfide layers with less dense packing of grains and more prominent surface relief were formed with an increase in the thiourea concentration in the sprayed solution. PbS films deposited at 400 °C had a smoother surface.

Using the data of transmission spectra, we obtained the band gap of PbS for direct transitions

(0.41–0.45 eV). The ratios of the initial solution components have little effect on the optical properties of the deposited layers.

### Contribution of the authors

The authors contributed equally to this article.

### Conflict of interests

The authors declare that they have no known competing financial interests or personal relationships that could have influenced the work reported in this paper.

### References

1. Varlashov I. B., Mitasov P. V., Miroshnikova I. N., Miroshnikov B. N., Mohammed H. S. H. Examination of photosensitive structures based on PbS by auger electron spectroscopy. *Vestnik Moskovskogo Energeticheskogo Instituta*. 2015;2: 103–107. (In Russ., abstract in Eng.). Available at: [https://www.elibrary.ru/download/elibrary\\_23378338\\_69530465.pdf](https://www.elibrary.ru/download/elibrary_23378338_69530465.pdf)
2. Akhmedov O. R., Guseinaliyev M. G., Abdullaev N. A., Abdullaev N. M., Babaev S. S., Kasumov N. A. Optical properties of PbS thin films. *Semiconductors*. 2016;50(1): 50–53. <https://doi.org/10.1134/S1063782616010036>
3. Gite A. B. Synthesis and electrical, optical, electrochemical properties of chemically deposited PbS thin films. *Oriental Journal of Physical Sciences*.

2018;3(1): 10–16. <https://doi.org/10.13005/OJPS03.01.03>

4. Uhuegbu C. C. Growth and characterization of lead sulphide thin film for solar cell fabrication. *Canadian Journal on Scientific and Industrial Research*. 2011; 2(6): 230–241. Available at: [https://www.researchgate.net/publication/310147417\\_Growth\\_and\\_Characterization\\_of\\_Lead\\_Sulphide\\_Thin\\_Film\\_for\\_Solar\\_Cell\\_Fabrication](https://www.researchgate.net/publication/310147417_Growth_and_Characterization_of_Lead_Sulphide_Thin_Film_for_Solar_Cell_Fabrication)

5. Kouissa S., Djemel A., Aida M. S., Djouadi M. A. PbS infrared detectors: experiment and simulation. *Sensors & Transducers Journal*. 2015;193(10): 106–113. Режим доступа: [https://www.sensorsportal.com/HTML/DIGEST/october\\_2015/Vol\\_193/P\\_2743.pdf](https://www.sensorsportal.com/HTML/DIGEST/october_2015/Vol_193/P_2743.pdf)

6. Markov V. F., Maskaeva L. N., Ivanov P. N. *Hydrochemical deposition of metal sulfide films: modeling and experiment\**. Ekaterinburg: UrO RAN Publ.; 2006, 217 p. (in Russ.)

7. Maskaeva L. N., Mostovshchikova E. V., Markov V. F., ... Mikhailova A. I. Cobalt-doped chemically deposited lead-sulfide. *Semiconductors*. 2022;56: 91–100. <https://doi.org/10.1134/S1063782622010122>

8. Grevtseva I. G., Smirnov M. S., Chirkov K. S., Latyshev A. N., Ovchinnikov O. V. Synthesis and luminescent properties of PbS/SiO<sub>2</sub> core-shell quantum dots. *Condensed Matter and Interphases*. 2024;26(1): 45–54. <https://doi.org/10.17308/kcmf.2024.26/11808>

9. Semenov V. N., Ovechkina N. M., Krysin M. Yu., Volkov V. V., Samofalova T. V. Deposition of PbS films by pyrolysis of atomized solutions of lead Thiourea complexes. *Russian Journal of Applied Chemistry*. 2022;95. 264–269. <https://doi.org/10.1134/S1070427222020057>

10. Egorov N. B., Usov V. F., Eremin L. P., Lariov A. M. Thermolysis of lead thiosulfate thiourea complexes. *Inorganic Materials*. 2010;46(11): 1248–1253. <https://doi.org/10.1134/S0020168510110166>

11. Semenov V. N. *The processes of formation of thin layers of semiconductor sulfides from thiourea complex compounds\**. Doc. chem. sci. diss. Abstr. Voronezh: 2002. 355 p. (In Russ.)

12. Krunks M., Mellikov E. Metal sulfide thin films by chemical spray pyrolysis. *Proceedings of SPIE*. 2001;4415: 60–65. <https://doi.org/10.1117/12.425472>

13. The International Centre for Diffraction Data. *Powder Diffraction File*. 2012. № 01-077-0244.

14. Ukhanov Yu. I. *Optical properties of semiconductors\**. M.: Nauka Publ.; 1977. 468 p. (In Russ.)

15. Sadovnikov S. I., Kozhevnikova N. S., Gusev A. I. Optical properties of nanostructured lead sulfide films with a DO<sub>3</sub> cubic structure. *Semiconductors*. 2011;45(12): 1559–1570. <https://doi.org/10.1134/S1063782611120116>

16. Logacheva V. A., Lukin A. N., Afonin N. N., Serbin O. V. Synthesis and optical properties of cobalt-

modified titanium oxide films. *Optics of Surfaces and Interfaces*. 2019;126(6): 674–680. <https://doi.org/10.1134/S0030400X19060158>

17. Kozhevnikova N. S., Markov V. F., Maskaeva L. N. Chemical deposition of metal sulfides from aqueous solutions: from thin films to colloidal particles. *Russian Journal of Physical Chemistry A*. 2020;94(12): 2399–2412. <https://doi.org/10.1134/S0036024420120134>

18. *New reference book for chemist and technologist. Chemical equilibrium. Properties of solutions\**. Vol. 3. St. Petersburg: «Professional» Publ.; 2004. P. 118. (in Russ)

19. Semenov V. N., Volkov V. V., Pereslyckih N. V. Complexation processes in «PbCl<sub>2</sub> – N<sub>2</sub>H<sub>4</sub>CS» aqueous solutions during deposition of lead sulphide films. *Condensed Matter and Interphases*. 2021;23(4): 543–547. <https://doi.org/10.17308/kcmf.2021.23/3673>

20. Zaman S., Mansoor M., Abubakar A., Asim M. M. AFM investigation and optical band gap study of chemically deposited PbS thin films. *Materials Science and Engineering*. 2016;146: 1–7. <https://doi.org/10.1088/1757-899X/146/1/012034>

21. Ezekoye B. A., Emeakaroha T. M., Ezekoye V. A., Ighodalo K. O., Offor P. O. Optical and structural properties of lead sulphide (PbS) thin films synthesized by chemical method. *International Journal of the Physical Science*. 2015;10(13): 386–390. <https://doi.org/10.5897/IJPS2015.4354>

22. Tohidi T., Jamshidi-Ghaleh K., Namdar A., Abdi-Ghaleh R. Comparative studies on the structural, morphological, optical, and electrical properties of nanocrystalline PbS thin films grown by chemical bath deposition using two different bath compositions. *Materials Science in Semiconductor Processing*. 2014;25: 197–206. <http://dx.doi.org/10.1016/j.mssp.2013.11.028>

23. Sadovnikov S. I., Gusev A. I., Rempel A. A. Nanostructured lead sulfide: synthesis, structure and properties. *Russian Chemical Reviews*. 2016;85(7): 731–758. <https://doi.org/10.1070/RCR4594>

24. Sadovnikov S. I., Gusev A. I. Structure and properties of PbS films. *Journal of Alloys and Compounds*. 2013;573. 65–75. <https://doi.org/10.1016/J.JALLCOM.2013.03.290>

25. Sadovnikov S. I., Kozhevnikova N. S. Microstructure and crystal structure of nanocrystalline powders and films of PbS. *Physics of the Solid State*. 2012;54(8): 1554–1561. <https://doi.org/10.1134/S1063783412080276>

26. Samofalova T. V., Ovechkina N. M., Kharin A. N., Semenov V. N. Surface microstructure of pyrolytic lead sulphide films. *Condensed matter and interphases*. 2013;15(3): 332–336. (In Russ., abstract in Eng.). Available at: <https://www.elibrary.ru/item.asp?id=20296110>

\* Translated by author of the article

**Information about the authors**

*Elena A. Gannova*, Master of the Department of General and Inorganic Chemistry, Voronezh State University (Voronezh, Russian Federation).

[gannova00@mail.ru](mailto:gannova00@mail.ru)

*Margarita V. Grechkina*, Leading Engineer-Physicist of the Center for Collective Use of Scientific Equipment, Voronezh State University (Voronezh, Russian Federation).

<https://orcid.org/0000-0002-7873-8625>

[grechkina\\_m@mail.ru](mailto:grechkina_m@mail.ru)

*Victor N. Semenov*, Dr. Sci. (Chem.), Professor, Chair of Department of General and Inorganic Chemistry, Voronezh State University (Voronezh, Russian Federation).

<https://orcid.org/0000-0002-4247-5667>

[office@chem.vsu.ru](mailto:office@chem.vsu.ru)

*Anatoly N. Lukin*, Cand. Sci. (Phys.-Math.), Leading Engineer-Physicist of the Center for Collective Use of Scientific Equipment, Voronezh State University (Voronezh, Russian Federation).

<https://orcid.org/0000-0001-6521-8009>

[ckp\\_49@mail.ru](mailto:ckp_49@mail.ru)

*Sergey A. Ivkov*, Cand. Sci. (Phys.-Math.), Lead Electronics Engineer of the Department of Solid State Physics and Nanostructures, Voronezh State University (Voronezh, Russia).

<https://orcid.org/0000-0003-1658-5579>

[ivkov@phys.vsu.ru](mailto:ivkov@phys.vsu.ru)

*Tatyana V. Samofalova*, Cand. Sci. (Chem.), Associate Professor of the Department of General and Inorganic Chemistry, Voronezh State University (Voronezh, Russian Federation).

<https://orcid.org/0000-0002-4277-4536>

[TSamofalova@bk.ru](mailto:TSamofalova@bk.ru)

*Received 26.10.2023; approved after reviewing 06.11.2023; accepted for publication 15.11.2023; published online 25.06.2024.*

*Translated by Anastasiia Ananeva*





# Condensed Matter and Interphases

Kondensirovannye Sredy i Mezhfaznye Granitsy  
<https://journals.vsu.ru/kcmf/>

## Original articles

Research article

<https://doi.org/10.17308/kcmf.2024.26/11937>

## X-ray luminescence of $\text{Sr}_{0.925-x}\text{Ba}_x\text{Eu}_{0.075}\text{F}_{2.075}$ nanopowders

Yu. A. Ermakova, P. P. Fedorov, V. V. Voronov, S. Kh. Batygov, S. V. Kuznetsov✉

Prokhorov General Physics Institute of the Russian Academy of Sciences,  
38, Vavilova str., Moscow 119991, Russian Federation

### Abstract

We synthesized powders of single-phase solid solutions  $\text{Sr}_{0.925-x}\text{Ba}_x\text{Eu}_{0.075}\text{F}_{2.075}$  ( $x = 0.00, 0.20, 0.25, 0.30, 0.35$  and  $0.40$ ) by a precipitation technique from nitrate aqueous solutions. The lattice parameters increase linearly as the barium content increases. We recorded a significant increase in the X-ray luminescence intensity of europium at increasing barium content. Upon increasing barium content, the intensity of the luminescence of strong  ${}^5\text{D}_0 \rightarrow {}^7\text{F}_1$  band increases exponentially, and we observed blue and red shifts in the position of the europium luminescence bands for  ${}^5\text{D}_0 \rightarrow {}^7\text{F}_1$  and  ${}^5\text{D}_0 \rightarrow {}^7\text{F}_4$ , respectively.

**Keywords:** Strontium fluoride, Barium fluoride, Europium, X-ray luminescence

**Funding:** The study was supported by Russian Science Foundation grant No. 22-13-00401, <https://rscf.ru/en/project/22-13-00401/>.

**For citation:** Ermakova Yu. A., Fedorov P. P., Voronov V. V., Batygov S. Kh., Kuznetsov S. V. X-ray luminescence of  $\text{Sr}_{0.925-x}\text{Ba}_x\text{Eu}_{0.075}\text{F}_{2.075}$  nanopowders. *Condensed Matter and Interphases*. 2024;26(2): 247–252. <https://doi.org/10.17308/kcmf.2024.26/11937>

**Для цитирования:** Ермакова Ю. А., Федоров П. П., Воронов В. В., Батыгов С. Х., Кузнецов С. В. Рентгенолюминесценция нанопорошков  $\text{Sr}_{0.925-x}\text{Ba}_x\text{Eu}_{0.075}\text{F}_{2.075}$ . *Конденсированные среды и межфазные границы*. 2024;26(2): 247–252. <https://doi.org/10.17308/kcmf.2024.26/11937>

✉ Sergey V. Kuznetsov e-mail: [kouznetsovsv@gmail.com](mailto:kouznetsovsv@gmail.com)

© Ermakova Yu. A., Fedorov P. P., Voronov V. V., Batygov S. Kh., Kuznetsov S. V., 2024



The content is available under Creative Commons Attribution 4.0 License.

## 1. Introduction

A new direction in diamond photonics is the incorporation of rare-earth elements into the diamond crystal lattice in such a way as to form a luminescent center with luminescence bands of the incorporated ion. To date, there are two main technological approaches. The first one is the use of precursors (both inorganic and organic) obtained by chemical vapor deposition (CVD) or high pressure-high temperature (HPHT) methods [1–5]. The second method is the incorporation of nanoparticles of the target composition and their physical encapsulation inside the diamond using the CVD method [6]. The second approach shows the most intense luminescence. This is due to the fact that the incorporated target substances have rigorously selected functional compositions. Europium is used as a luminescent ion in most of the studies, since it is a probe element that allows both to detect the local environment and control its change, and to detect the reduction processes due to the possibility of the  $\text{Eu}^{3+} \rightarrow \text{Eu}^{2+}$  transition. So far,  $\text{Eu}_2\text{O}_3$  [2],  $\text{CeF}_3$  [7],  $\text{HoF}_3$  [8],  $\text{EuF}_3$  [9], and  $\beta\text{-NaGdF}_4\text{:Eu}$  [10] have been successfully incorporated to diamond. To interpret the luminescence response reliably, it is necessary to achieve the highest luminescence intensity from the designed composite material. For this purpose, it is necessary to select a luminophore composition that does not exhibit concentration quenching or polymorphic transformations at the high temperatures of the nanoparticle incorporation process. Fluorides of alkaline-earth elements [11, 12] are effective thermally stable luminescent matrices with a wide range of doping with rare earth elements. They do not exhibit polymorphic transformations up to the melting point. To prepare fluoride powders, various synthesis methods are used, such as mechanochemistry, combustion, fluoroacetate decomposition, solvothermal and hydrothermal techniques, as well as co-precipitation from aqueous solutions, which allows obtaining large batches of powders [13–17]. In the series of  $\text{CaF}_2 \rightarrow \text{SrF}_2 \rightarrow \text{BaF}_2$  difluorides having the same structural type, the energy of matrix phonons decreases [18]. This may lead to an increase in the luminescence light output by preventing multiphonon relaxation. Solid solutions based

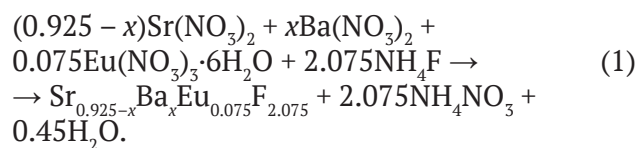
on barium fluoride and rare earth elements are not synthesized by solution-based techniques. This is why the main attention is focused on the strontium fluoride matrix. In the literature, there is a large amount of data on the photoluminescent characteristics of europium [19–24]. Drobysheva et al. [25] determined that the optimal concentrations for  $\text{SrF}_2\text{:Eu}$  solid solutions are 7.5 and 15.0 mol. % Eu when excited by X-ray tubes with tungsten and silver anodes, respectively. An increase in the luminescence intensity can be achieved by reducing the phonon energy of the matrix through replacing the matrix cation with a heavier one. In the case of the strontium fluoride matrix, it is barium fluoride.

The aim of the study was to test the approach of increasing the luminescence intensity of europium by making the matrix heavier in the concentration series of  $\text{Sr}_{1-x}\text{Ba}_x\text{F}_2\text{:Eu}$  (7.5 mol. %) at a variable barium content.

## 2. Experimental

*Initial reagents.* The initial substances were:  $\text{Sr}(\text{NO}_3)_2$  (99.99 %, Lanhit),  $\text{Ba}(\text{NO}_3)_2$  (99.99 %, Vekton),  $\text{Eu}(\text{NO}_3)_3 \cdot 6\text{H}_2\text{O}$  (99.99 %, Lanhit),  $\text{NH}_4\text{F}$  (chemically pure, Lanhit), and bidistilled water of our own production. We did not further purify the reagents.

*Synthesis methodology.* By precipitation from aqueous solutions, we synthesized a concentration series of  $\text{Sr}_{0.925-x}\text{Ba}_x\text{Eu}_{0.075}\text{F}_{2.075}$  solid solution powders ( $x = 0.00, 0.20, 0.25, 0.30, 0.35$  and  $0.40$ ) by equation (1).



The powders were synthesized by the dropwise addition of nitrate solution ( $C = 0.08$  M) into a polypropylene reactor with ammonium fluoride solution (0.16 M, 7% excess). The resulting suspension was stirred using a magnetic mixer for 2 hours. After sedimentation of the precipitate, the mother solution was decanted, and the precipitate was washed with a 0.5 % ammonium fluoride solution. The efficiency of nitrate ion washing out was controlled by qualitative reaction with diphenylamine. The washed precipitate was air-

dried at 45 °C. High-temperature treatment was carried out in platinum crucibles at 600 °C for 1 hour at a heating rate of 10 °/min.

X-ray diffraction (XRD) was performed on a Bruker D8 Advance diffractometer with  $\text{CuK}\alpha$  radiation ( $\lambda = 1.5406 \text{ \AA}$ ). The lattice parameters ( $a$ ) and coherent scattering regions ( $D$ ) were calculated in TOPAS ( $R_{wp} < 7$ ).

The X-ray luminescence spectra of single-phase powders were recorded at room temperature on an FSD-10 minispectrometer (JSC *Optofiber*) in the range of 200–1100 nm with a resolution of 1 nm under excitation by an X-ray tube with a chromium anode operating at 30 kV and 30 mA.

### 3. Results of synthesis

#### of $\text{Sr}_{0.925-x}\text{Ba}_x\text{Eu}_{0.075}\text{F}_{2.075}$ solid solutions

The X-ray diffraction patterns of the  $\text{Sr}_{0.925-x}\text{Ba}_x\text{Eu}_{0.075}\text{F}_{2.075}$  solid solution samples with the molar fraction of barium of 0.00, 0.20, 0.25, 0.30, 0.35, and 0.40, air-dried at 45 °C and heat-treated at 600 °C are shown in Fig. 1a. Annealing at 600 °C is necessary to dehydrate the powders and increase the luminescence intensity by removing the hydroxyl ion that quenches the luminescence.

The X-ray diffraction analysis showed that the synthesis of the solid solutions resulted in the formation of single-phase powders of fluorite structure (JCPDS# 06-0262,  $a = 5.800 \text{ \AA}$  for  $\text{SrF}_2$ ), but with a shifted position of X-ray reflections. This indicates a change in lattice parameters proportional to the amount of  $\text{BaF}_2$  doping component. The process is followed by the incorporation of additional fluorine ions for electrostatic compensation and the formation of clusters such as  $\text{REE}_6\text{F}_{36}$  (REE are rare-earth elements). The results of calculating the lattice parameters are summarized in Table 1 and presented in Fig. 2. The X-ray reflections are highly broadened, indicating the synthesis of nanoscale substances (Table 1). The size of the coherent scattering regions  $D$  was about 16–18 nm. The synthesized powders were heat-treated at 600 °C in order to dehydrate them. The process temperature was chosen based on literature review. The X-ray diffraction patterns of the heat-treated samples are provided in Fig. 1b. Comparing the X-ray diffraction patterns of the samples, we revealed a narrowing of the X-ray reflections. This indicates an increase in the coherent scattering region by several times and an increase in the

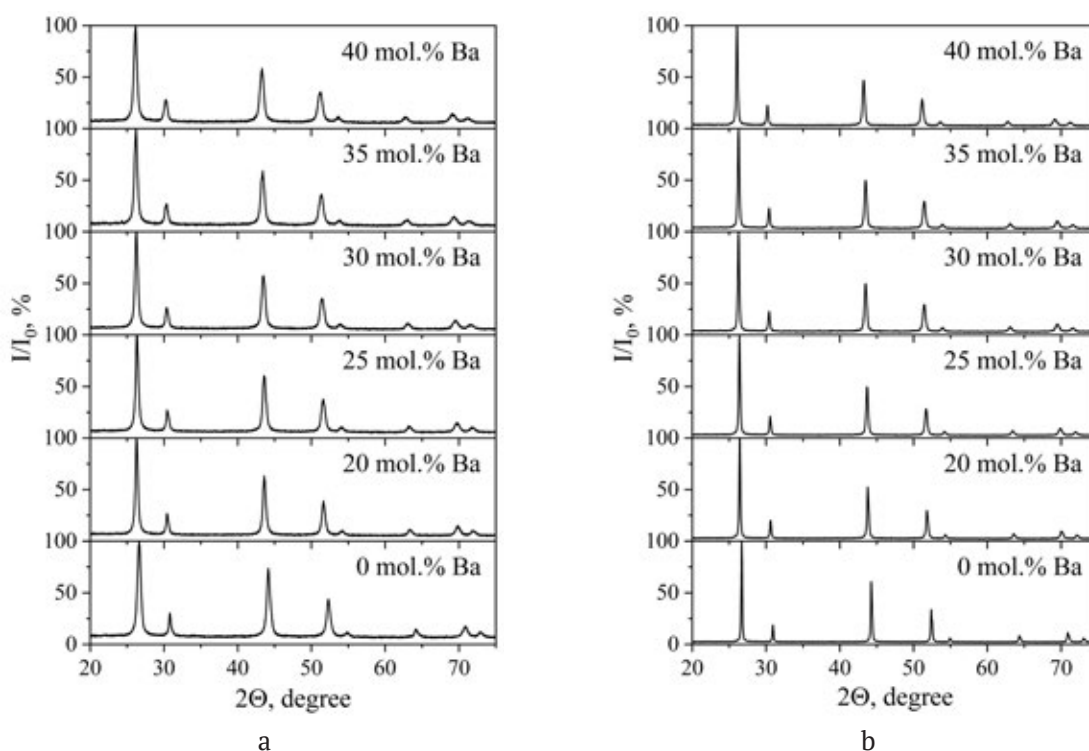


**Fig. 1.** X-ray diffraction patterns of  $\text{Sr}_{0.925-x}\text{Ba}_x\text{Eu}_{0.075}\text{F}_{2.075}$  solid solutions: a – after drying in air at temperature of 45 °C, b – after heat treatment at temperature of 600 °C

**Table 1.** Lattice parameters of  $\text{Sr}_{0.925-x}\text{Ba}_x\text{Eu}_{0.075}\text{F}_{2.075}$  solid solutions

Sample composition	Heat treatment			
	45 °C		600 °C	
	$a, \text{Å}$	$D, \text{nm}$	$a, \text{Å}$	$D, \text{nm}$
$\text{Sr}_{0.925}\text{Eu}_{0.075}\text{F}_{2.075}$	5.800(1)	14(1)	5.793(1)	77(1)
$\text{Sr}_{0.725}\text{Ba}_{0.200}\text{Eu}_{0.075}\text{F}_{2.075}$	5.869(1)	18(1)	5.859(1)	103(4)
$\text{Sr}_{0.675}\text{Ba}_{0.250}\text{Eu}_{0.075}\text{F}_{2.075}$	5.885(3)	15(1)	5.875(1)	65(5)
$\text{Sr}_{0.625}\text{Ba}_{0.300}\text{Eu}_{0.075}\text{F}_{2.075}$	5.901(1)	17(1)	5.889(1)	89(5)
$\text{Sr}_{0.575}\text{Ba}_{0.350}\text{Eu}_{0.075}\text{F}_{2.075}$	5.915(1)	16(1)	5.905(1)	70(8)
$\text{Sr}_{0.525}\text{Ba}_{0.400}\text{Eu}_{0.075}\text{F}_{2.075}$	5.930(1)	16(1)	5.921(1)	100(6)

particle size, which is confirmed by the calculation (Table 1). The calculated lattice parameters are described by the linear equation  $a = 5.794 + 0.003x$  ( $x = \text{mol.}\% \text{BaF}_2$ ) ( $R^2 = 0.999$ ) (Fig. 2). They are slightly lower, which confirms the dehydration process during heat treatment (Table 1).

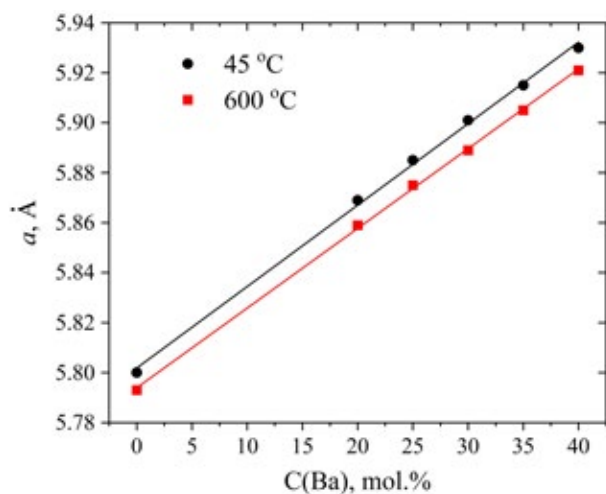
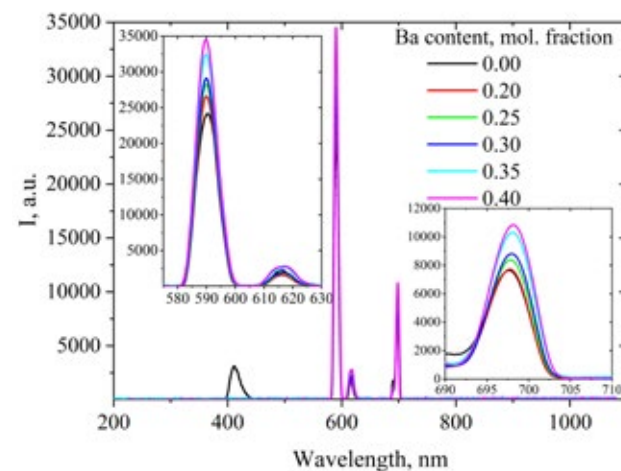
The X-ray luminescence spectra of single-phase solid solution samples of  $\text{Sr}_{0.925-x}\text{Ba}_x\text{Eu}_{0.075}\text{F}_{2.075}$  after heat treatment at 600 °C are shown in Fig. 3. The luminescence spectra show trivalent europium luminescence bands with maxima at 590 nm, 617 nm, and 698 nm, corresponding to the  $^5\text{D}_0 \rightarrow ^7\text{F}_i$  transitions ( $i = 1, 2, 4$ ). The barium-free composition has a band of divalent europium.

Analysis of the X-ray luminescence spectra revealed that the intensity of the europium luminescence bands increases with increasing barium content ( $^5\text{D}_0 \rightarrow ^7\text{F}_1$  with a maximum around 590 nm and  $^5\text{D}_0 \rightarrow ^7\text{F}_4$  with a maximum around 698 nm). The increase in the intensity of the  $^5\text{D}_0 \rightarrow ^7\text{F}_2$  band is less significant. This band

is complex and consists of several components, whose intensity varies as the barium content increases. When the barium content increases, the  $^5\text{D}_0 \rightarrow ^7\text{F}_1$  luminescence band undergoes a blue shift, and  $^5\text{D}_0 \rightarrow ^7\text{F}_4$  undergoes a red shift of the maximum. The intensity of the  $^5\text{D}_0 \rightarrow ^7\text{F}_1$  luminescence band increases with increasing barium content (Fig. 4) according to the exponential function  $I = 24445 + 230e^{(10x)}$  with approximation reliability criterion ( $R^2 = 0.99227$ ).

#### 4. Conclusions

Powders of single-phase solid solutions of  $\text{Sr}_{0.925-x}\text{Ba}_x\text{Eu}_{0.075}\text{F}_{2.075}$  ( $x = 0.00, 0.20, 0.25, 0.30, 0.35, \text{ and } 0.40$ ) were synthesized by precipitation from nitrate aqueous solutions using ammonium fluoride as a fluorinating agent. The lattice parameters of the samples after heat treatment at 45 °C and 600 °C increased linearly with increasing barium content. After heat treatment at 600 °C, the coherent scattering region increased from 16–

**Fig. 2.** Dependence of the lattice parameters of the  $\text{Sr}_{0.925-x}\text{Ba}_x\text{Eu}_{0.075}\text{F}_{2.075}$  solid solution on the Ba content**Fig. 3.** Luminescence spectra of  $\text{Sr}_{0.925-x}\text{Ba}_x\text{Eu}_{0.075}\text{F}_{2.075}$  solid solutions



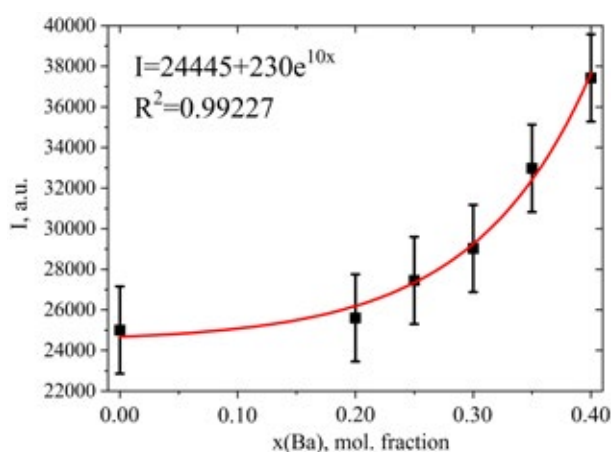


**Fig. 4.** Dependence of luminescence intensity of band  ${}^5\text{D}_0 \rightarrow {}^7\text{F}_1$  on the barium content in the  $\text{Sr}_{0.925-x}\text{Ba}_x\text{Eu}_{0.075}\text{F}_{2.075}$  solid solution

18 nm to 70–103 nm. We recorded a significant increase in the X-ray luminescence intensity of europium for  ${}^5\text{D}_0 \rightarrow {}^7\text{F}_1$  with a maximum around 590 nm and  ${}^5\text{D}_0 \rightarrow {}^7\text{F}_4$  with a maximum around 698 nm at constant europium concentration and increasing barium content. The intensity of the  ${}^5\text{D}_0 \rightarrow {}^7\text{F}_1$  luminescence band increased with increasing barium content according to the exponential function  $I = 24445 + 230e^{10x}$ . Upon the increase in barium content, we observed blue and red shifts in the position of the europium luminescence bands for  ${}^5\text{D}_0 \rightarrow {}^7\text{F}_1$  and  ${}^5\text{D}_0 \rightarrow {}^7\text{F}_4$ , respectively.

### Contribution of the authors

The authors contributed equally to this article.

### Conflict of interests

The authors declare that they have no known competing financial interests or personal relationships that could have influenced the work reported in this paper.

### References

- Lebedev V. T., Shakhov F. M., Vul A. Y., ... Fomin E. V. X-ray excited optical luminescence of Eu in diamond crystals synthesized at high pressure high temperature. *Materials*. 2023;16: 830. <https://doi.org/10.3390/ma16020830>
- Magyar A., Hu W., Shanley T., Flatté M. E., Hu E., Aharonovich I. I. Synthesis of luminescent europium defects in diamond. *Nature Communications*. 2014;5(1): 3523. <https://doi.org/10.1038/ncomms4523>
- Yudina E. B., Aleksenskii A. E., Bogdanov S. A., ... Vul' A. Y. CVD nanocrystalline diamond film doped with Eu. *Materials*. 2022;15: 5788. <https://doi.org/10.3390/ma15165788>
- Borz dov Y. M., Khokhryakov A. F., Kupriyanov I. N., Nechaev D. V., Palyanov Y. N. Crystallization of diamond from melts of europium salts. *Crystals*. 2020;10: 376. <https://doi.org/10.3390/cryst10050376>
- Palyanov Y. N., Borz dov Y. M., Khokhryakov A. F., Kupriyanov I. N. High-pressure synthesis and characterization of diamond from europium containing systems. *Carbon*. 2021;182: 815–824. <https://doi.org/10.1016/j.carbon.2021.06.081>
- Sedov V., Kuznetsov S., Martyanov A., Ralchenko V. Luminescent diamond composites. *Functional Diamond*. 2022;2: 53–63. <https://doi.org/10.1080/26941112.2022.2071112>
- Chen H.-J., Wang X.-P., Wang L.-J., ... Liu L.-H. Bright blue electroluminescence of diamond/ $\text{CeF}_3$  composite films. *Carbon*. 2016;109: 192–195. <https://doi.org/10.1016/j.carbon.2016.07.061>
- Chen J.-X., Wang X.-P., Wang L.-J., Yang X.-W., Yang Y. White electroluminescence of diamond/ $\text{HoF}_3$ /diamond composite film. *Journal of Luminescence*. 2020;224: 117310. <https://doi.org/10.1016/j.jlum.2020.117310>
- Sedov V. S., Kuznetsov S. V., Ralchenko V. G., ... Konov V. I. Diamond- $\text{EuF}_3$  nanocomposites with bright orange photoluminescence. *Diamond and Related Materials*. 2017;72: 47–52. <https://doi.org/10.1016/j.diamond.2016.12.022>
- Sedov V., Kouznetsov S., Martyanov A., ... Fedorov P. Diamond–rare earth composites with embedded  $\text{NaGdF}_4:\text{Eu}$  nanoparticles as robust photo- and X-ray-luminescent materials for radiation monitoring screens. *ACS Applied Nano Materials*. 2020;3: 1324–1331. <https://doi.org/10.1021/acsnm.9b02175>
- Sobolev B. P. *The rare earth trifluorides: the high temperature chemistry of the rare earth trifluorides. P.1. The High Temperature Chemistry of the Rare Earth Trifluorides*. Institut d'Estudis Catalans; 2000. 540 p
- Sobolev B. P. *The rare earth trifluorides. P. 2. Introduction to materials science of multicomponent metal fluoride crystals*. Institut d'Estudis Catalans, Barcelona, 2001. 520 p.
- Heise M., Scholz G., Krahl T., Kemnitz E. Luminescent properties of  $\text{Eu}^{3+}$  doped  $\text{CaF}_2$ ,  $\text{SrF}_2$ ,  $\text{BaF}_2$  and  $\text{PbF}_2$  powders prepared by high-energy ball milling. *Solid State Sciences*. 2019;91: 113–118. <https://doi.org/10.1016/j.solidstatesciences.2019.03.014>
- Peng J., Hou S., Liu X., ... Su Z. Hydrothermal synthesis and luminescence properties of hierarchical  $\text{SrF}_2$  and  $\text{SrF}_2:\text{Ln}^{3+}$  ( $\text{Ln}=\text{Er}, \text{Nd}, \text{Yb}, \text{Eu}, \text{Tb}$ ) micro/nanocomposite architectures. *Materials Research Bulletin*. 2012;47: 328–332. <https://doi.org/10.1016/j.materresbull.2011.11.030>
- Krahl T., Beer F., Relling A., Gawlitza K., Rurack K., Kemnitz E. Toward luminescent composites

by phase transfer of  $\text{SrF}_2:\text{Eu}^{3+}$  nanoparticles capped with hydrophobic antenna ligands. *ChemNanoMat*. 2020;6: 1086–1095. <https://doi.org/10.1002/cnma.202000058>

16. Ermakova Y. A., Pominova D. V., Voronov V. V., ... Kuznetsov S. V. Synthesis of  $\text{SrF}_2:\text{Yb}:\text{Er}$  ceramic precursor powder by co-precipitation from aqueous solution with different fluorinating media:  $\text{NaF}$ ,  $\text{KF}$  and  $\text{NH}_4\text{F}$ . *Dalton Transactions*. 2022;51: 5448–5456. <https://doi.org/10.1039/D2DT00304J>

17. Kuznetsov S., Ermakova Y., Voronov V., ... Turshatov A. Up-conversion quantum yields of  $\text{SrF}_2:\text{Yb}^{3+},\text{Er}^{3+}$  sub-micron particles prepared by precipitation from aqueous solution. *Journal of Materials Chemistry C*. 2018;6: 598–604. <https://doi.org/10.1039/C7TC04913G>

18. Ermakova Yu. A., Alexandrov A. A., Fedorov P. P., ... Kuznetsov S. V. Synthesis of single-phase  $\text{Sr}_{1-x}\text{Ba}_x\text{F}_2$  solid solutions by co-precipitation from aqueous solutions. *Solid State Sciences*. 2022;130: 106932. <https://doi.org/10.1016/j.solidstatesciences.2022.106932>

19. Cortelletti P., Pedroni M., Boschi F., ... Speghini A. Luminescence of  $\text{Eu}^{3+}$  activated  $\text{CaF}_2$  and  $\text{SrF}_2$  nanoparticles: effect of the particle size and codoping with alkaline ions. *Crystal Growth & Design*. 2018;18: 686–694. <https://doi.org/10.1021/acs.cgd.7b01050>

20. Yagoub M. Y. A., Swart H. C., Noto L. L., O'Connell J. H., Lee M. E., Coetsee E. The effects of Eu-concentrations on the luminescent properties of  $\text{SrF}_2:\text{Eu}$  nanophosphor. *Journal of Luminescence*. 2014;156: 150–156. <https://doi.org/10.1016/j.jlumin.2014.08.014>

21. Yuzenko K. V., Kabelitz A., Schökel A., Guilherme Buzanich A. Local structure of europium-doped luminescent strontium fluoride nanoparticles: Comparative X-ray absorption spectroscopy and diffraction study. *ChemNanoMat*. 2021;7: 1221–1229. <https://doi.org/10.1002/cnma.202100281>

22. Pan Y., Wang W., Zhou L., ... Li L.  $\text{F}^-$ - $\text{Eu}^{3+}$  charge transfer energy and local crystal environment in  $\text{Eu}^{3+}$  doped calcium fluoride. *Ceramics International*. 2017;43: 13089–13093. <https://doi.org/10.1016/j.ceramint.2017.06.197>

23. Trojan-Piegza J., Wang Z., Kinzhybalov V., Zhou G., Wang S., Zych E. Spectroscopic reflects of structural disorder in  $\text{Eu}^{3+}/\text{Pr}^{3+}$ -doped  $\text{La}_{0.4}\text{Gd}_{1.6}\text{Zr}_2\text{O}_7$  transparent ceramics. *Journal of Alloys and Compounds*. 2018;769: 18–26. <https://doi.org/10.1016/j.jallcom.2018.07.233>

24. Binnemans K. Interpretation of europium(III) spectra. *Coordination Chemistry Reviews*. 2015;295: 1–45. <https://doi.org/10.1016/j.ccr.2015.02.015>

25. Drobysheva A. R., Ermakova Yu. A., Alexandrov A. A., ... Kuznetsov S. V. X-ray luminescence of  $\text{SrF}_2:\text{Eu}$  nanopowders. *Optics and Spectroscopy*. 2023;131: 633. <https://doi.org/10.61011/EOS.2023.05.56516.58-22>

26. Fedorov P., Sobolev B. P. Concentration dependence of unit-cell parameters of phases  $\text{M}_{1-x}\text{R}_x\text{F}_{2+x}$  with the fluorite structure. *Soviet Physics. Crystallography*. 1992;37: 651–656.

### Information about the authors

*Yulia A. Ermakova*, Junior Researcher at the Prokhorov General Physics Institute of the Russian Academy of Sciences (Moscow, Russian Federation).

<https://orcid.org/0000-0002-9567-079X>

[yulia.r89@mail.ru](mailto:yulia.r89@mail.ru)

*Pavel P. Fedorov*, Dr. Sci. (Chem.), Full Professor, Chief Researcher at the Prokhorov General Physics Institute of the Russian Academy of Sciences (Moscow, Russian Federation).

<https://orcid.org/0000-0002-2918-3926>

[ppfedorov@yandex.ru](mailto:ppfedorov@yandex.ru)

*Valery V. Voronov*, Cand. Sci. (Phys.–Math.), Leading Researcher at the Prokhorov General Physics Institute of the Russian Academy of Science (Moscow, Russian Federation).

<https://orcid.org/0000-0001-5029-8560>

[voronov@lst.gpi.ru](mailto:voronov@lst.gpi.ru)

*Sergey Kh. Batygov*, Cand. Sci. (Phys.–Math.), Leading Researcher at the Prokhorov General Physics Institute of the Russian Academy of Science (Moscow, Russian Federation).

<https://orcid.org/0000-0001-9862-0504>

[sbatygov@mail.ru](mailto:sbatygov@mail.ru)

*Sergey V. Kuznetsov*, Cand. Sci. (Chem.), Head of the Laboratory at the Prokhorov General Physics Institute of the Russian Academy of Science (Moscow, Russian Federation).

<https://orcid.org/0000-0002-7669-1106>

[kouznetzovsv@gmail.com](mailto:kouznetzovsv@gmail.com)

Received 18.10.2023; approved after reviewing 31.10.2023; accepted for publication 15.11.2023; published online 25.06.2024.

Translated by Anastasiia Ananeva



## Original articles

Research article

<https://doi.org/10.17308/kcmf.2024.26/11938>**Coupling of anode reactions in the process of electrooxidation of glycine anion on gold**

I. D. Zartsyn, A. V. Vvedensky, E. V. Bobrinskaya✉, O. A. Kozaderov

Voronezh State University,  
1 Universitetskaya pl., Voronezh 394018, Russian Federation**Abstract**

Electrochemical processes involving organic substances are complex multi-stage reactions. In our opinion, it is incorrect to describe their kinetics using the principle of independent partial processes (or their individual stages) since electrode reactions can be coupled due to competition for active surface sites, due to common intermediate stages, or through an electron. In this case, the theory of coupled reactions or the graph-kinetic method should be used to provide the kinetic description of the process. In general, graph theory makes it possible to identify the relationship between the “structure” and the kinetic behavior of complex systems by means of graphical analysis. In the case of electrochemical reactions, structural elements are substances adsorbed on the metal surface and (or) a set of substances interacting in the reactions. The relationship between their concentrations can be characterized quantitatively by a transformation law, for example, the law of effective masses. Thus, a graph is a set of reacting substances and a sequence of reactions represented graphically. Graphs allow setting a system of kinetic equations and analyzing them by associating a certain behavior of the system with the structure of the corresponding graph. Under the assumption that one intermediate particle is involved in each elementary stage, the kinetic expressions will be linear, which corresponds to the first-order reaction model.

Graph-kinetic analysis of the processes within the  $\text{Au|Gly}^-, \text{OH}^-, \text{H}_2\text{O}$  system confirmed that the partial multi-stage reactions of anode oxidation of glycine and hydroxyl anions are kinetically coupled. We obtained expressions for partial currents of electrooxidation of hydroxide ions and glycine anions during the anodic process occurring on gold in an alkaline glycine-containing solution. It was shown that with an increase in the anode potential, the nature of the limiting stage of the anodic process changes.

Formal constants of rates and equilibria of electrochemical reactions involving particles of background electrolyte and glycinate ion were calculated. It was found that the rates of partial oxidation reactions of adsorbed OH particles and  $\text{OH}^-$  are significantly higher than those of organic anions ( $\text{Gly}^-$  and  $\text{HCOO}^-$ ). This indicates that the kinetics of the electrooxidation processes of  $\text{Gly}^-$  in the  $\text{Au|Gly}^-, \text{OH}^-, \text{H}_2\text{O}$  system are determined by the kinetic features of the electrooxidation reactions of hydroxide ions.

**Keywords:** Graph-kinetic analysis, Coupled processes, Electrooxidation, Glycine, Voltammetry**Funding:** The study was supported by the Ministry of Science and Higher Education of the Russian Federation within the framework of state order to higher education institutions in the sphere of scientific research for 2022-2024, project № FZGU-2022-0003.**For citation:** Zartsyn I. D., Vvedenskii A. V., Bobrinskaya E. V., Kozaderov O. A. Coupling of anode reactions in the process of electrooxidation of glycine anion on gold. *Condensed Matter and Interphases*. 2024;26(2): 253–264. <https://doi.org/10.17308/kcmf.2024.26/11938>**Для цитирования:** Зарцын И. Д., Введенский А. В., Бобринская Е. В., Козадепов О. А. Сопряжение анодных реакций в процессе электроокисления аниона глицина на золоте. *Конденсированные среды и межфазные границы*. 2024;26(2): 253–264. <https://doi.org/10.17308/kcmf.2024.26/11938>✉ Bobrinskaya Elena Valerievna, e-mail: [elena173.68@mail.ru](mailto:elena173.68@mail.ru)

© Zartsyn I. D., Vvedenskii A. V., Bobrinskaya E. V., Kozaderov O. A., 2024



The content is available under Creative Commons Attribution 4.0 License.



## 1. Introduction

When several multi-stage processes occur on the surface of the electrode, they can be interconnected through intermediate particles (intermediates) and thus influence each other. In this case, the kinetics of the electrode reaction should be described using the graph method, which is often used to analyze enzymatic reactions in biochemistry [1–4]. In general, graph theory makes it possible to identify the relationship between the “structure” and the kinetic behavior of complex systems by means of graphical analysis. In this case, the “structure” is understood as the interaction and relationship between the elements of a given system, and its behavior is described by analyzing its response to an external disturbance. The partial and total  $i, E$ -dependencies are calculated by sequentially considering various kinetic situations that differ in the assumption about the nature of the limiting stage or take into account the presence of several slow stages with comparable rates. Comparing the total  $i, E$ -dependency with the experimental polarization  $i, E$ -curve allows drawing a conclusion about the preferred route of the process, which makes it possible to find a set of kinetic constants for individual stages.

It is particularly important to know the route of a complex multi-stage process when predicting the behavior of an electrochemical system in which multi-stage processes occur on metals and alloys in the presence of surface-active organic additives of various nature. Interconnection between individual electrode reactions through intermediates is another important factor influencing the kinetics of such processes. Based on their regularities, it is possible to identify the role of the organic compound in the formation of electrochemical transformation products (for example, electrooxidation or electrodeposition) with specified characteristics. This is especially important for modern microelectronics since understanding the kinetics of complex multi-stage processes in electrolytes with organic surface-active additives contributes to determining optimal conditions for the formation of interconnections between elements of integrated circuits by the void-free filling of holes in the dielectric with metal in the presence

of electrochemically active organic compounds with high adsorption capacity.

A typical example of a complex multi-step process is anodic oxidation of a monoaminoacetic acid (glycine) anion on an Au electrode in an aqueous alkaline solution. The areas of adsorption potentials and electrochemical activity of  $\text{Gly}^-$  and  $\text{OH}^-$  on gold overlap, which predetermines the potential for the mutual influence of partial reactions. In addition,  $\text{OH}^-$  anions [5–11] are directly involved in the heterogeneous electrooxidation reaction of the glycine anion. It is reasonable to assume that partial heterogeneous processes in the  $\text{Au}|\text{OH}^-, \text{H}_2\text{O}$  and  $\text{Au}|\text{Gly}^-, \text{OH}^-, \text{H}_2\text{O}$  systems will be kinetically coupled both due to the competition of  $\text{OH}^-$ ,  $\text{Gly}^-$ , intermediates and their electrooxidation products for active sites on the Au surface and due to the presence of common stages of the oxidation reactions of hydroxide and glycinate ions.

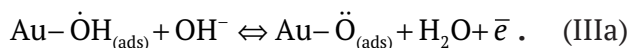
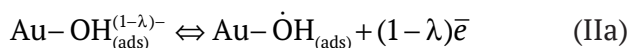
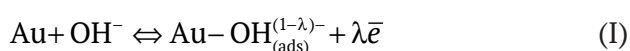
The purpose of this work was to use the method of graph-kinetic analysis to distinguish the partial oxidation currents of hydroxide ions and glycine anions during the general anodic process occurring on gold in an alkaline glycine-containing solution. It is possible that this will allow answering, at least qualitatively, the basic question: whether the kinetics of the anodic destruction of the glycine anion is its own or subordinate to the regularities of electrooxidation of hydroxide ions.

## 2. Calculation procedure

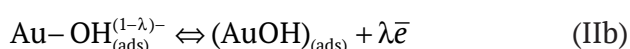
*Selecting the reaction scheme.* To use the graph-kinetic method successfully, it is necessary to construct a detailed kinetic reaction scheme.

The process of anodic oxidation of  $\text{OH}^-$  on gold in an aqueous medium has several stages. According to numerous researches [12–21], it proceeds via the chemisorption stage of the anion, most likely with partial charge transfer, and is accompanied by the sequential formation of mono- and biradical forms of adsorbed atomic oxygen. Earlier, we used the method of kinetic diagrams to analyze partial anodic processes in the  $\text{Au}|\text{OH}^-, \text{H}_2\text{O}$  system. The shape of the general stationary voltammogram was determined by calculation. A possible reaction scheme for the electroconversion of  $\text{OH}^-$  ion is:

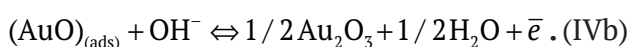




Here,  $\lambda$  is the degree of partial charge transfer from an adsorbed particle with a charge  $z = 1$  per metal; eventually  $z_{\text{ads}} = 1 - \lambda$  [21]. It is assumed [22–24] that the radical ion state is stabilized due to the overlap of  $6s$ - and  $sp^3$ -AO for Au and  $\text{OH}^-$ , respectively. However, the appearance of 2D Au(I) and Au(II) compounds on the surface is possible in such processes as:



The formation of the phase Au(III) oxide at sufficiently high potentials can be the result of a process involving  $\text{Au}-\ddot{\text{O}}_{(\text{ads})}$  or  $(\text{AuO})_{\text{ads}}$ :



When choosing between alternative routes for anodic formation of  $\text{Au}_2\text{O}_3$ : via (IIa), (IIIa), and (IVa) or (IIb), (IIIb), and (IVb) stages, we preferred the first scenario due to the results of quantum chemical modeling. Therefore, this scenario was used later on, during the stage of constructing graphs for the intermediates of heterogeneous

processes of  $\text{OH}^-$  oxidation in the aqueous medium  $\dot{\text{O}}\text{H}$  and  $\ddot{\text{O}}$ .

The potential range of anodic release of molecular oxygen, which further complicates oxide formation on gold in an alkaline medium, was not considered in the study.

The main current maxima on the voltammogram of glycine anion oxidation have more positive values than the adsorption current maxima in the  $\text{Au}|\text{OH}^-, \text{H}_2\text{O}$  system [6, 10, 30, 31], however, they have noticeably more negative values than the  $\text{Au}_2\text{O}_3$  peak (Fig. 1). According to [6], the six-electron, generally anodic, process goes through the stage of dissociative  $\text{Gly}^-$  chemisorption, the products of which,  $(-\text{NH}_2\dot{\text{C}}\text{H}_2$  and  $-\text{COO}^-)$ , are then anodically oxidized to  $\text{CN}^-$ ,  $\dot{\text{N}}\text{H}_2$ , and  $\text{CO}_2$ . According to the method of a rotating ring-disc electrode [28], at  $E > 0.35$  V, adsorbed methylamine can also be formed. However, the results of *in situ* FTIR reflection spectroscopy [5, 6] indicate that the main intermediates of anode destruction of Gly on polycrystalline gold are formate ions. What is more, this method did not detect the formation of methylamine. In addition, the absorption bands corresponding to  $\text{CN}^-$ ,  $\text{OCN}^-$ , and  $\text{CO}_2$ , as well as  $\text{Au}(\text{CN})_2^+$  were reliably recorded. Taking into account these data, the putative scheme of the glycine anion oxidation, which reflects the features of the anodic transformation of  $\text{OH}^-$  and the possibility of coupling of individual reactions, is as follows:

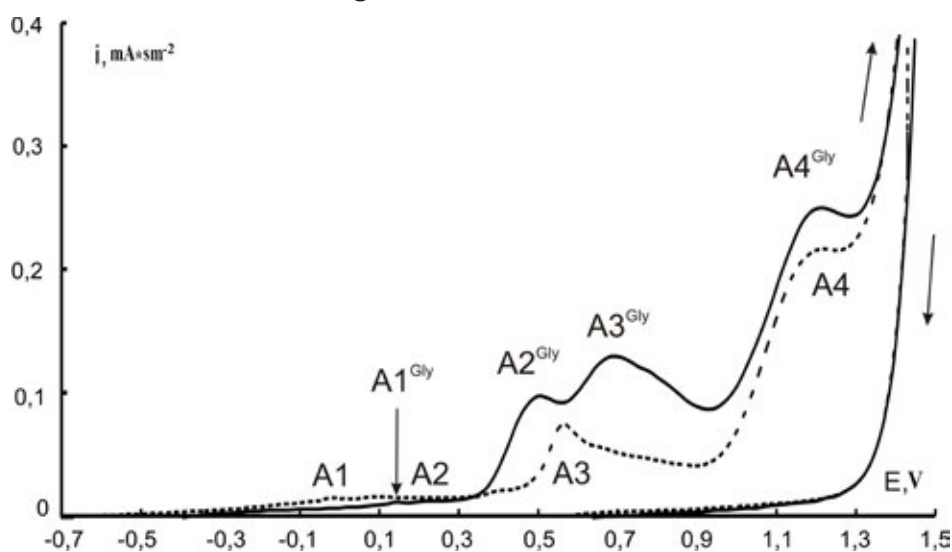
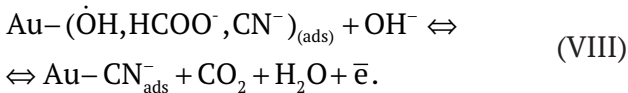
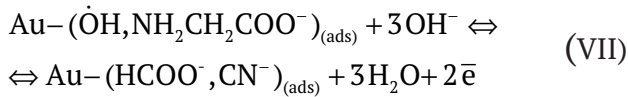
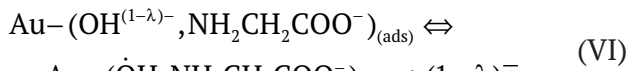
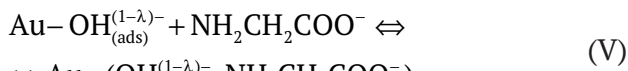
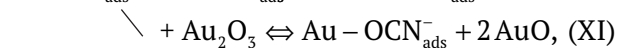
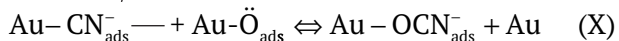
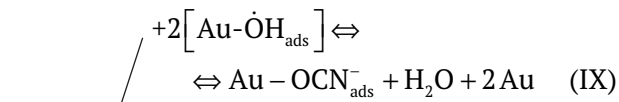


**Fig. 1.** Cyclic voltammograms obtained on a gold electrode in a background solution (dotted line) and with the addition of 0.03 M glycine;  $\nu = 0.10$  B/c [10]

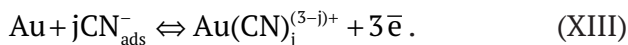
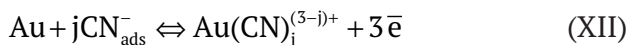


It is assumed that during stage (V) the glycine anion adsorption occurs on the gold surface partially occupied by adsorbed OH<sup>-</sup> anions, however, there is the possibility of their additional oxidation through (VI) resulting in the formation of  $\dot{\text{O}}\text{H}$ . Stages (VII) and (VIII) correspond to the destruction of the glycine anion and the intermediate.

In the general case, the heterogeneous chemical reactions of additional oxidation of the adsorbed cyanide ion should also be taken into account:



Also, it is necessary to take into account that at sufficiently high potentials gold can also dissolve, which leads to the formation of gold Au(III) cyanide and cyanate complexes as a result of the following reactions:



When equations were recorded, it was assumed that the surface activity of H<sub>2</sub>O, CO<sub>2</sub>, and gold complexes was significantly lower than that of other adsorbates. In addition, it was assumed that processes (IIIa), (IIIb), (IVa), (IVb), (VII), and (VIII) involve OH<sup>-</sup> ions directly from the electrode layer of the solution, rather than those adsorbed on gold since interpreting these reactions as purely surface reactions would significantly complicate the construction of the corresponding graphs.

*Initial kinetic ratios.* Let us assume that the surface initially contains only one type of active adsorption centers. The number of these centers is  $N$  (expressed in mol/cm<sup>2</sup>). It is not only constant, but also significantly less than the number of metal atoms. This makes it possible to use the Langmuir isotherm model in the analysis.

Let  $N_i$  and  $N_j$  be the number of active surface sites occupied by particles of the  $i$ -th and  $j$ -th types, respectively. The change in the state of the active site during  $i \leftrightarrow j$  process may be associated not only with the oxidation/reduction of particles, but also with their adsorption/desorption. Each of these processes is interpreted as a kinetically reversible first-order reaction, the rate of which is:

$$v_{ij} = k_{ij}N_i - k_{ji}N_j = N(k_{ij}\Theta_i - k_{ji}\Theta_j). \quad (1)$$

Here,  $k_{ij}$  and  $k_{ji}$  are the formal rate constants, while  $\Theta_i$  and  $\Theta_j$  are the proportion of surface adsorption centers occupied by reagents and products. It was assumed that there were no diffusion limitations for all types of particles; features of the structure of the electrical double layer were not explicitly taken into account.

The current covering of adsorption centers was assumed to be stationary. In this approximation

$$\sum_i k_{ij}\Theta_i = \sum_j k_{ji}\Theta_j \quad (2)$$

actually represents the so-called stationary kinetic adsorption isotherm, where

$$\sum_i \Theta_i + \sum_j \Theta_j = 1. \quad (3)$$

Since  $k_{ij} = k_{ij}^0 c_i^v$ , and  $k_{ji} = k_{ji}^0 c_j^v$ , the concentration equilibrium constant is  $K_{ij} = k_{ij}/k_{ji} = K_{ij}^0 (c_i^v/c_j^v)$ . Here,  $K_{ij}^0 = k_{ij}^0/k_{ji}^0$  is the standard equilibrium constant, and  $c^v$  is the volumetric molar concentration.

The rate constants of adsorption stages involving singly charged anions with due account of the possibility of partial charge transfer are as follows:

$$k_{ij} = k_{ji}^0(E^0)c_i^v \exp\left[\lambda\beta F(E - E^0)/RT\right] \quad (4a)$$

$$k_{ji} = k_{ji}^0(E^0)c_j^v \exp\left[-\lambda\alpha F(E - E^0)/RT\right], \quad (4b)$$

Whereas for electrochemical stages with their participation, they are:

$$k_{ij} = k_{ji}^0(E^0)c_i^v \exp\left[(1-\lambda)\beta F(E - E^0)/RT\right] \quad 5a$$

$$k_{ji} = k_{ji}^0(E^0)c_j^v \exp[-(1-\lambda)\alpha F(E - E^0)/RT]. \quad (5b)$$

Here,  $E$  and  $E^0$  are the current and standard electrode potentials for a given reaction;  $\alpha$  and  $\beta$  are cathodic and anodic charge transfer coefficients (hereinafter  $\alpha = \beta = 0.5$ ). If the adsorption of a charged particle is not accompanied by a redistribution of electron density, then the influence of  $E$  on the rate constants in equations (4a), (4b), (5a), and (5b) disappears, and formulas (5a) and (5b) take their usual form. It is obvious that in the general case the values of  $K_{ij}$ ,  $K_{ji}$  also depend on the potential, although to varying degrees.

### 3. Analysis of kinetic diagrams

*Au|OH, H<sub>2</sub>O system.* Let us assume that the anodic processes occurring in gold in an alkaline background electrolyte are stationary. Such an assumption is necessary at this stage, since it is extremely difficult to obtain a complete equation for the nonstationary anodic voltammogram, including the potential range of all current maxima even in the background electrolyte solution. The task is even more complicated if, along with the oxidation of hydroxide ions, the electrooxidation of the glycine anion occurs in the same potential range. According to the analysis technique proposed in [1-4], a kinetic diagram of the anodic process on the Au electrode in a background alkaline electrolyte can be constructed as follows (Fig. 2). Here, the initial state (1) is the free active site of the gold surface initially occupied by a water molecule; the vertices of the graph correspond to the successive transformation of the OH<sup>-</sup> ion: Au-OH<sub>ads</sub><sup>-</sup>, Au-ÖH<sub>ads</sub>, Au-Ö<sub>ads</sub> and Au<sub>2</sub>O<sub>3</sub>. The covering of the surface with each type of adsorption centers is, respectively,  $\Theta_1, \Theta_2, \Theta_3, \Theta_4$ ,

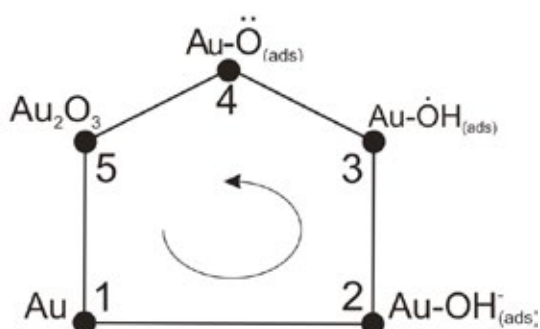
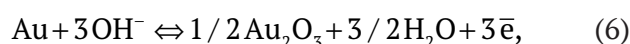


**Fig. 2.** Graph-kinetic diagram of adsorption and electrochemical processes occurring on an Au electrode in an alkaline medium in the region of potentials preceding the anodic release of molecular oxygen

and  $\Theta_5$ ; traversing the loop counterclockwise is positive. The overall reaction:



representing the sum of stages (I), (IIa), (IIIa), and (IVa), proceeds at the rate:

$$i_{15} = 3F(k_{15}\Theta_1 - k_{51}\Theta_5). \quad (7)$$

Each of these stages corresponds to the corresponding graph edge. To simplify the calculation procedure, the principle of the limiting stage was used, and kinetic situations with comparable speeds of two or more stages were not considered.

Let us assume that, for example, in the potential range of anodic peak A1 on the  $i, E$ -dependency (Fig. 1), the slowest is stage (I), while the rest of the stages are quasi-equilibrium. Since  $k_{12} \ll k_{ij}$  and  $k_{21} \ll k_{ij}$ , after a series of transformations, expression (7) can be represented in a fairly simple form:

$$i_{15} \approx i_{12} = 3F \left( \frac{k_{12}K_{23}K_{34}K_{45}K_{15}^{-1} - k_{21}}{1 + K_{23} + K_{23}K_{34} + K_{23}K_{34}K_{45} + K_{23}K_{34}K_{45}K_{15}^{-1}} \right). \quad (8)$$

In this case, the effect of kinetic coupling of individual stages is manifested through a change in values  $\Theta_1$  and  $\Theta_5$ , each of which is determined by a set of equilibrium constants from all stages of the process. It should be noted that under the procedure [2-4], expression (8) is written based on a fairly simple graphical algorithm, the structure of the graph is analyzed, and the system of equations (1)-(3) is not solved.

By subsequently assuming stages (IIa), (IIIa), and (IVa) as limiting, in a similar way we obtained expressions for the rate of the total oxidation reaction for gold in an alkaline medium in the potential range of peaks A2, A3, and A4:

$$i_{15} \approx i_{23} = 3F \left( \frac{k_{23} - k_{32}K_{54}K_{45}K_{21}K_{15}}{1 + K_{21} + K_{21}K_{15} + K_{21}K_{15}K_{54} + K_{21}K_{15}K_{54}K_{45}} \right) \quad (9)$$

$$i_{15} \approx i_{34} = 3F \left( \frac{k_{34}K_{23} - k_{43}K_{15}K_{21}K_{54}}{1 + K_{21} + K_{23} + K_{21}K_{15}K_{54} + K_{21}K_{15}} \right) \quad (10)$$

$$i_{15} \approx i_{45} = 3F \left( \frac{k_{45}K_{23}K_{34} - k_{54}K_{21}K_{15}}{1 + K_{21} + K_{23} + K_{23}K_{34} + K_{21}K_{15}} \right). \quad (11)$$

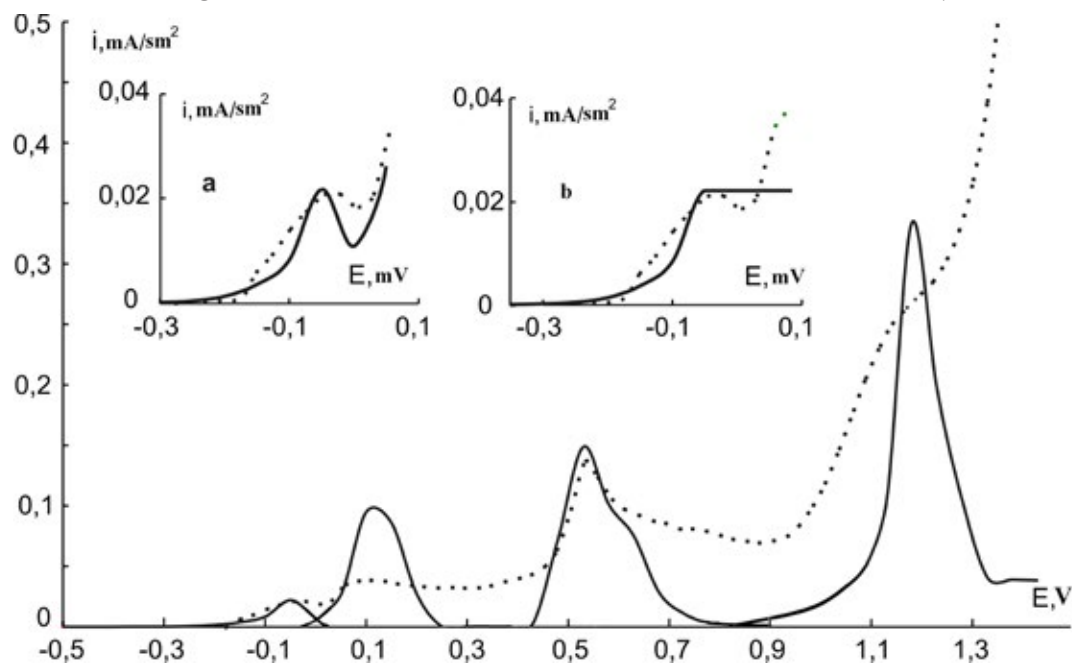
**Table 1.** Values of rate constants and equilibria constants of partial reactions occurring in the system Au|OH<sup>-</sup>,H<sub>2</sub>O

Constant	Edge of the graph				
	(1↔2)	(2↔3)	(3↔4)	(4↔5)	(5↔1)
$k_{ij}^0, \text{c}^{-1}$	$2.5 \cdot 10^{-7}$	$1.0 \cdot 10^{-9}$	$6.5 \cdot 10^{-1}$	$2.5 \cdot 10^{-4}$	–
$k_{ji}^0, \text{c}^{-1}$	$1.7 \cdot 10^{-13}$	$2.5 \cdot 10^{15}$	$4.3 \cdot 10^{21}$	$2.5 \cdot 10^{29}$	–
$K_{ij}^0$	$1.5 \cdot 10^6$	$4.0 \cdot 10^{-25}$	$1.5 \cdot 10^{-22}$	$1.0 \cdot 10^{-33}$	$9 \cdot 10^{-74}$

The sets of constants necessary for calculations were found by the brute force search based on the condition of best matching the position of each of the calculated and experimental anodic maxima. In addition, the values of the rate constants of direct and reverse reactions were determined (Table 1). It should be noted that the values of the equilibrium constants of individual stages by an order of magnitude coincided with the values of constants that could be calculated from known reference data [32]. The calculation showed that within the selected assumptions, the position of each of the four anodic current maxima on the calculated voltammogram correlated with the corresponding peak on the experimental  $i, E$ -dependence (Fig. 3). However, the A1 maximum on the calculated voltammogram could be obtained only by assuming  $\lambda \neq 0$ . Otherwise, in this potential range there is a horizontal

platform rather than a peak, which contradicts the experimental data (Fig. 3, inserts a and b).

Au|Gly<sup>-</sup>, OH<sup>-</sup>, H<sub>2</sub>O system. In the general case, the anodic processes in this system include the entire spectrum of reactions (I)–(XIII). Accordingly, the kinetic graph should consist of five interconnected cycles: anodic processes on Au in a background solution, the same, but with the addition of glycine, anodic reactions of additional oxidation of formate ions and cyanide ions, and dissolution of gold itself. However, the processes of OCN<sup>-</sup> and Au(CN)<sup>(5-)-</sup> formation occur at any noticeable rate only at high anodic potentials, that is why at this stage of the graph-kinetic analysis reactions (VIII) – (XIII) were not considered. The same applies to reactions (IVa) and (IVb) which correspond to the formation of gold oxide (III) at the potential of the A4 peak since its position and amplitude are practically insensitive to the


**Fig. 3.** The calculated voltammogram obtained in the Au|OH<sup>-</sup>,H<sub>2</sub>O system in comparison with the experimental one (dotted line). Inset: The maximum area A1, taking into account (a) and without taking into account the partial charge transfer (b) during the adsorption of the hydroxide ion



presence of glycine in the solution (Fig. 1). As a result, the kinetic analysis concerns only the potential range covering the anode peaks A1<sup>Gly</sup>, A2<sup>Gly</sup>, and A3<sup>Gly</sup>, i.e. it is limited to the study of coupled partial processes of adsorption and anodic oxidation of OH<sup>-</sup> and Gly anions and the additional oxidation of HCOO<sup>-</sup>. The graph corresponding to them contains three interconnected cycles: a, b, and c (Fig. 4A). However, it is also quite difficult to provide an analytical description of the processes within this graph, that is why further simplifications were made assuming that stages VI and VII proceed together. The resulting graph now contains only 2 cycles (Fig. 4B), in which the stage 1↔2 is common. Accordingly, the equilibrium constant  $K_{56}$  is multiplicative and is the product of the corresponding equilibrium constants of stages VI and VII. Therefore, it is impossible to separately determine the latter within the framework of this simplification.

It was assumed that in each cycle it was possible to distinguish a limiting stage in the

corresponding potential range, the kinetic regularities of which determine the shape of the partial anodic  $i, E$ -curve. It is reasonable to assume that, similar to the background electrolyte solution, with the growth of  $E$ , the nature of the limiting stage changes, so does the nature of the particles involved in the oxidation reactions in both cycles. The following most probable kinetic situations were considered:

*Kinetic route I.* In the potential range of the A1<sup>Gly</sup> – A2<sup>Gly</sup> maxima, the limiting stage in cycle **a** is (2↔3), and in cycle **b**, it is stage (5↔6). The total anodic current in this case should consist of partial currents of anodic oxidation of anions of hydroxyl  $i_{14}$  and glycine  $i_{17}$ \*

$$i_{14} = 2Fk_{25} \left( \frac{K_{12}(k_{52} + k_{67}k_{71})}{k_{52}k_{67}k_{71} \left( 1 + K_{21} + K_{14} + K_{71} + K_{14}K_{34} + K_{21}K_{52} + K_{67}K_{71} \right)} \right) \quad (12)$$

\* Although stage 1↔7 is an adsorption stage, the amount of adsorbate is determined by the rate of electrooxidation of glycine and additional oxidation of formate.

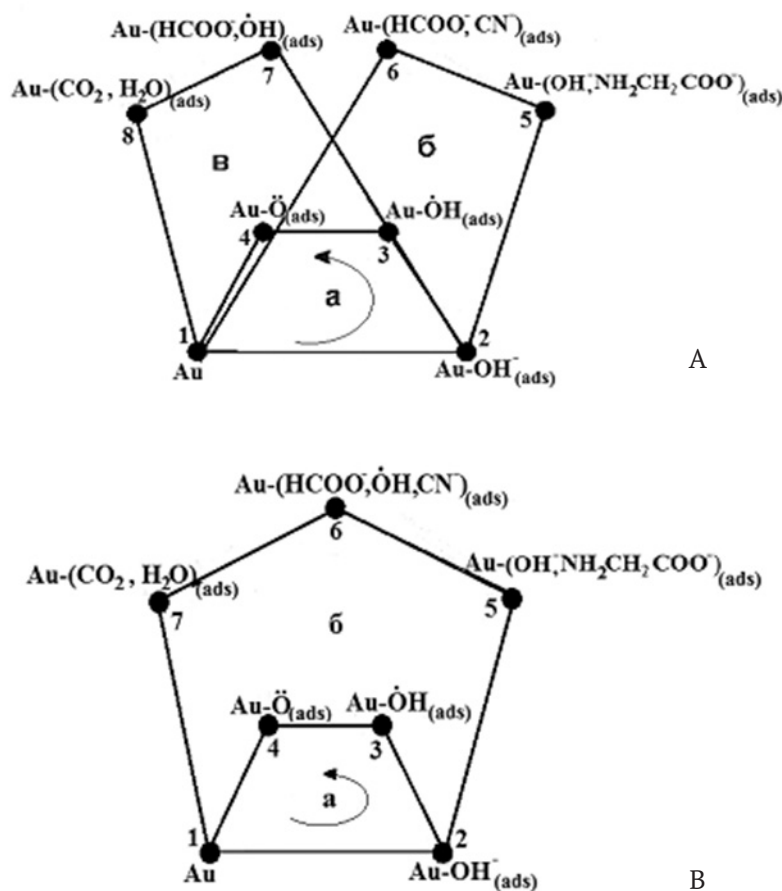


**Fig. 4.** General (A) and simplified (B) kinetic graphs of conjugated anode processes in the Au|Gly, OH<sup>-</sup>, H<sub>2</sub>O system in the region of anode maxima potentials A1<sup>Gly</sup> – A3<sup>Gly</sup>

$$i_{17} = 3Fk_{56} \left( \frac{K_{12}K_{25}}{1 + K_{21} + K_{14} + K_{71} + K_{14}K_{34} + K_{21}K_{52} + K_{67}K_{71}} \right). \quad (13)$$

*Kinetic Route II.* In the range of the A3<sup>Gly</sup> maximum, monoradicals are involved in the anodic process of cycle **a**  $\dot{O}H$ , while in cycle **b**, there is additional oxidation of formate ions. If in this case the limiting stages are (3 $\leftrightarrow$ 4) and (6 $\leftrightarrow$ 7), then:

$$i_{14} = 2Fk_{34} \left( \frac{K_{12}K_{23}}{k_{52}k_{65}k_{71} \left( 1 + K_{21} + K_{41} + K_{71} + K_{21}K_{32} + K_{21}K_{52} + K_{21}K_{52}K_{65} \right)} \right) \quad (14)$$

$$i_{17} = 3Fk_{67} \left( \frac{K_{12}K_{25}K_{56}(k_{41} + k_{32}k_{21})}{k_{52}k_{41} \left( 1 + K_{21} + K_{41} + K_{71} + K_{21}K_{32} + K_{21}K_{52} + K_{21}K_{52}K_{65} \right)} \right). \quad (15)$$

*Kinetic Route III.* Assuming that the nature of the limiting stage in cycle **b** does not change with the growth of the anode potential, i.e. the total current consists of the partial currents of the monoradical  $\dot{O}H$  and the glycine anion oxidation, processes (3 $\leftrightarrow$ 4) and (5 $\leftrightarrow$ 6) may be limiting. Wherein:

$$i_{14} = 2Fk_{34} \left[ \frac{K_{23}(k_{52} + k_{67}k_{71})}{k_{52}k_{67}k_{71}(1 + K_{21} + K_{23} + K_{25} + K_{21}K_{17} + K_{21}K_{14} + K_{21}K_{17}K_{76})} \right] \quad (16)$$

$$i_{17} = 3Fk_{56} \left[ \frac{K_{12}K_{25}(k_{41} + k_{32})}{k_{52}k_{41} \left( 1 + K_{21} + K_{23} + K_{25} + K_{21}K_{17} + K_{21}K_{14} + K_{21}K_{17}K_{76} \right)} \right]. \quad (17)$$

Since stages (2 $\leftrightarrow$ 5) and (1 $\leftrightarrow$ 7) are adsorption stages, they were not considered as limiting.

In all cases, the rate of the corresponding partial process is determined by the rate of its limiting stage, however, equations (12)–(17) have constants corresponding to the processes in both cycles, which actually reflects the effect of their mutual influence.

For the numerical calculation of partial currents, it is necessary to know the sets of the corresponding constants, the values of which were determined, as before, by brute force search. The starting point in determining the values of  $k_{ij}^o$ ,  $k_{ji}^o$ , and  $K_{ij}^o$  for partial background processes were the values of the constants given in Table 1. The brute force search procedure was completed when reaching the values of the sets of constants

that allowed matching the potentials' maxima of the calculated and experimental voltammograms.

The calculated partial voltammograms obtained under the assumption that there was any of the three possible kinetic situations are presented in Fig. 5 (a–d).

In the potential range of the A1 maximum, the introduction of the glycine anion led to an increase in the potential of the first maximum on the partial  $i, E$ -dependence corresponding to  $OH^-$  adsorption with partial charge transfer (as compared to the background solution), however, the rate of electrooxidation of  $Gly^-$  in the same potential range was negligibly small (Fig. 5a).

The A2 maximum on the partial curve in the  $Au|Gly^-, OH^-, H_2O$  system associated with the formation of  $\dot{O}H$  increased much more significantly as compared to the same maximum in the background solution (Fig. 5b). In this range, there was a process of glycine electrooxidation, the rate of which was maximum at  $E \approx 0.45$  V.

The anodic A3 maximum on the partial  $i, E$ -dependence corresponding to the electrooxidation of  $\dot{O}H$  and the formation of  $Au-\dot{O}$  also increased in the presence of glycine, however, to a much smaller degree (Fig. 5c). Along with the electrooxidation of glycine, the process of formate ion additional oxidation was also possible. This process reached the maximum rate at  $E \approx 0.60$  V.

Finally, if we assume that the nature of the limiting stage for processes involving oxygen changes and for cycle **b** in any potential range the glycine electrooxidation reaction (5 $\leftrightarrow$ 6) is limiting, then the kinetic situation *III* is observed. The corresponding calculated partial  $i, E$ -dependencies are shown in Fig. 5d.

It is characteristic that the position of the maximum on the partial voltammogram corresponding to the process  $\dot{O}H \rightarrow \dot{O}$ , remained practically unchanged (Fig. 5c and d). Whereas the maximum on the partial  $i, E$ -curve of glycine oxidation shifted considerably to the anodic region (Fig. 5b and d) and fell into the potential range of the anodic release of oxygen. The latter, however, contradicts the experimental data [10]. Therefore, we can come to the conclusion that in the  $Au|Gly^-, OH^-, H_2O$  system, with an increase in the anode potential, the kinetic situations *I* and *II* are consistently observed, which means that the nature of the limiting stages really changes.

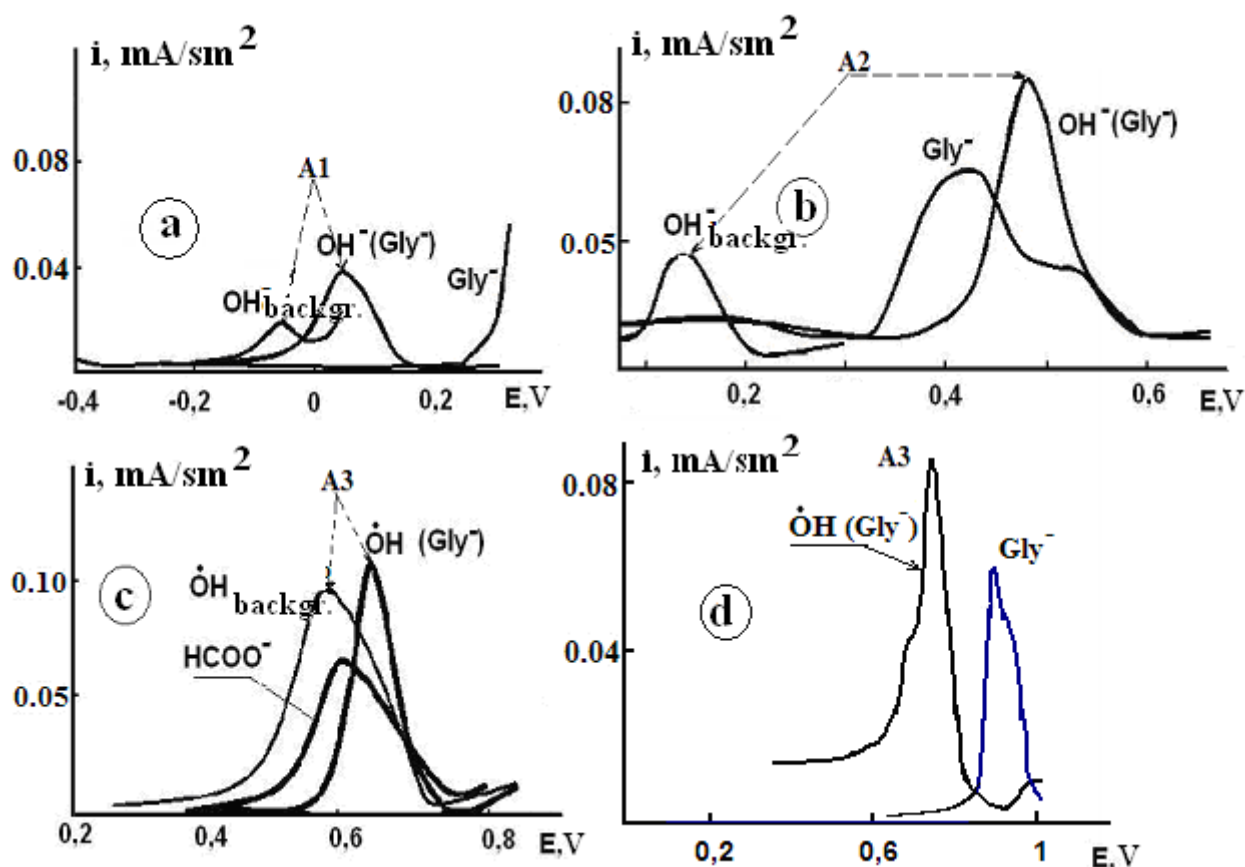


Fig. 5. Partial voltammograms calculated under the assumption that I (a-b); II (c) or III variant of the kinetic scheme (d) is realized

It is important that in any of the considered potential ranges, the rate of partial oxidation reactions for adsorbed OH and OH particles were significantly higher than that of electroactive organic particles. In the framework of formal kinetics of “parallel” reactions, this means that in the Au|Gly<sup>-</sup>,OH<sup>-</sup>,H<sub>2</sub>O system, the kinetics of the glycine anion electroconversion was mainly determined by the kinetic features of the process of hydroxide ions electrooxidation.

The total voltammogram obtained by adding the partial  $i,E$ -characteristics of the processes involving OH<sup>-</sup> and Gly<sup>-</sup> is shown in Fig. 6. The insert to the figure shows a fragment for the potential range of the A3<sup>Gly</sup> peak found under the assumption that kinetic situation III was observed. The discrepancy between the calculated and experimental  $i,E$ -dependence, both in terms of the maximum position and shape, once again confirms that this kinetic variant of Gly oxidation does not occur in practice.

With regards to variants I and II of the kinetic scheme, the position of the maxima on the

calculated and experimental voltamperograms practically coincided with each other. It is clear that in the potential range of the A1<sup>Gly</sup> maximum, the overall rate of the process was determined only by the regularities of the electroconversion of oxygen on gold. In the range of the A2<sup>Gly</sup> maximum, both the electro-oxidation reaction of OH<sup>-</sup> ions and glycine anions contributed to the total current of the anodic process. Finally, the total anodic process at the A3<sup>Gly</sup> potential consisted of three partial processes: the formation of an oxygen biradical, the electrooxidation of the formate ion, and the electrooxidation of glycine, which was oxidized in this region at a low but non-zero rate.

The rate and equilibrium constants of the processes occurring in cycles a and b calculated from the values of the sets of constants for partial reactions are presented in Table 2.

The analysis of these data showed that the values of the formal rate and equilibrium constants of electrochemical stages  $2 \leftrightarrow 3$  and  $3 \leftrightarrow 4$  for reactions with joint participation of ON<sup>-</sup> and Gly<sup>-</sup>

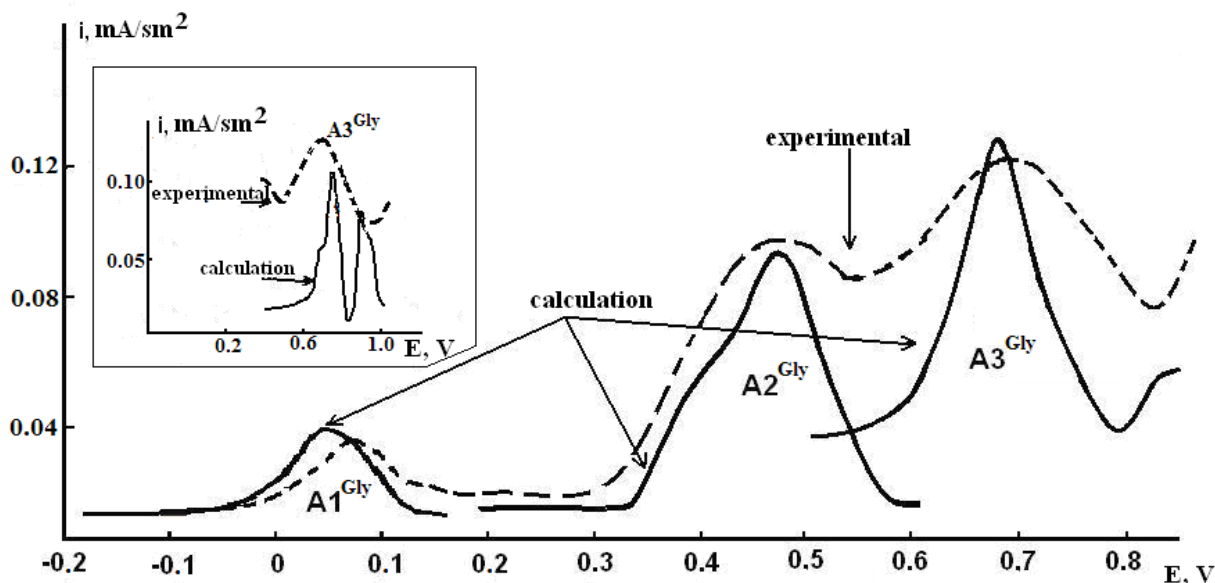


**Fig. 6.** Calculated total voltammogram obtained by graph-kinetic analysis under the assumption of the implementation of the I and II variants of the kinetic scheme; experimental  $i, E$ -dependence (dotted line). The inset is a fragment of the total  $i, E$ -dependence in the region of  $A3^{Gly}$  maximum potentials under the assumption of the implementation of the III variant of the kinetic scheme of the anodic oxidation process of the  $Gly^-$  anion

**Table 2.** Values of rate constants and equilibrium constants of partial reactions occurring in the  $Au|Gly^-, OH^-, H_2O$  system

Constant	Edge of the graph							
	1 $\leftrightarrow$ 2	2 $\leftrightarrow$ 3	3 $\leftrightarrow$ 4	4 $\leftrightarrow$ 1	2 $\leftrightarrow$ 5	5 $\leftrightarrow$ 6	6 $\leftrightarrow$ 7	7 $\leftrightarrow$ 1
$k_{ij}^0, c^{-1}$	$2.5 \cdot 10^{-2}$	$1.1 \cdot 10^{-9}$	$6.5 \cdot 10^{-1}$	$4.6 \cdot 10^{-22}$	$1.6 \cdot 10^4$	$6.0 \cdot 10^{-9}$	$6.0 \cdot 10^{-9}$	$9.0 \cdot 10^{-5}$
$k_{ji}^0, c^{-1}$	$4.2 \cdot 10^{-6}$	$9.7 \cdot 10^9$	$4.4 \cdot 10^{21}$	$2.1 \cdot 10^{-4}$	$1.0 \cdot 10^{-2}$	$7.2 \cdot 10^{-4}$	$7.0 \cdot 10^{-4}$	$1.3 \cdot 10^4$
$K_{ij}^0$	$5.8 \cdot 10^5$	$1.1 \cdot 10^{-19}$	$1.5 \cdot 10^{-22}$	$2.2 \cdot 10^{-18}$	$1.6 \cdot 10^6$	$8.3 \cdot 10^{-6}$	$8.5 \cdot 10^{-4}$	$6.9 \cdot 10^{-7}$

differ little from those obtained for the  $Au|OH^-, H_2O$  system, while the constants characterizing the process of hydroxide ion adsorption change significantly in the presence of glycine anion, which, in our opinion, once again indicates that the processes of electrooxidation of organic particles are governed by the kinetic regularities of anodic processes involving  $OH^-$  ions.

#### 4. Conclusions

1. The method of kinetic diagrams was used to analyze anodic processes in the  $Au|Gly^-, OH^-, H_2O$  system with a limited number of active sites on the gold surface. It was confirmed that partial multi-stage reactions of anodic oxidation of glycine and hydroxyl anions are kinetically coupled.

2. It was shown that with an increase in the anode potential, the nature of the limiting

stages of processes, both with the participation of background and organic particles, changes. Otherwise, the calculated  $i, E$  dependencies differ significantly from the experimental data.

3. Formal rate and equilibria constants of electrochemical reactions involving particles of background electrolyte and the position of the anodic maximum associated with the formation of an oxygen biradical are not very sensitive to the presence of  $Gly^-$  in the solution. However, the rates of partial oxidation reactions of adsorbed  $OH$  and  $\dot{O}H$  particles are significantly higher than those of organic anions ( $Gly^-$  and  $HCOO^-$ ). This indicates that the kinetics of the electrooxidation processes of  $Gly^{is}$  in the  $Au|Gly^-, OH^-, H_2O$  system are determined by the kinetic features of the electrooxidation reactions of hydroxide ions.



## Contribution of the authors

The authors contributed equally to this article.

## Conflict of interests

The authors declare that they have no known competing financial interests or personal relationships that could have influenced the work reported in this paper.

## References

1. Goldshtein B. N., Volkenshtein M. V. Investigation of nonstationary complex monomolecular reactions by the graph method\*. *Doklady of the USSR Academy of Sciences*. 1968;78: 386–388. (In Russ.)
2. Goldshtein B. N., Magarshak D. B., Volkenshtein M. V. Analysis of monosubstrate enzyme reactions by graph method\*. *Doklady of the USSR Academy of Sciences*. 1970;191: 1172–1174. (In Russ.)
3. Goldshtein B. N., Volkenshtein M. V. Simple kinetic models explaining critical phenomena in enzymatic reactions with enzyme and substrate isomerization\*. *Doklady of the USSR Academy of Sciences*. 1988;22: 1381–1392. (In Russ.)
4. Goldshtein B. N., Shevelev E. A., Volkenshtein M. V. Stability analysis of enzyme systems with feedbacks by the graph method\*. *Doklady of the USSR Academy of Sciences*. 1983;273: 486–488. (In Russ.)
5. Zhen C.-H., Sun S.-G., Fan C.-J., Chen S.-P., Mao B.-W., Fan Y.-J. In situ FTIRS and EQCM studies of glycine adsorption and oxidation on Au (111) electrode in alkaline solutions. *Electrochimica Acta*. 2004;49(8): 1249–1255. <https://doi.org/10.1016/j.electacta.2003.09.048>
6. Zhen Ch.-H. Adsorption and oxidation of glycine on Au film electrodes in alkaline solutions. *Acta Physico-Chimica Sinica*. 2003;19: 60–64. <https://doi.org/10.3866/pku.whxb20030114>
7. Beltowska-Brzezinka M., Uczak T., Holze R. Electrocatalytic oxidation of mono- and polyhydric alcohols on gold and platinum. *Journal of Applied Electrochemistry*. 1997;27: 999–1011. <https://doi.org/10.1023/a:1018422206817>
8. Štrbac S., Hamelin A., Adžić R. R. Electrochemical indication of surface reconstruction of (100), (311) and (111) gold faces in alkaline solutions. *Journal of Electroanalytical Chemistry*. 1993;362: 47–53. [https://doi.org/10.1016/0022-0728\(93\)80005-3](https://doi.org/10.1016/0022-0728(93)80005-3)
9. Chang S. C., Ho Y., Weaver M. J. Applications of real-time FTIR spectroscopy to the elucidation of complex electroorganic pathways: electrooxidation of ethylene glycol on gold, platinum, and nickel in alkaline solution. *Journal of the American Chemical Society*. 1991;113(25): 9506–9513. <https://doi.org/10.1021/ja00025a014>
10. Kraschenko T. G., Bobrinskaya E. V., Vvedenskii A. V., Kuleshova N. E. Kinetics of electrochemical oxidation of anion glycine on gold. *Condensed Matter and Interphases*. 2014;16(1): 42–49. (In Russ., abstract in Eng.). Available at: <https://www.elibrary.ru/item.asp?id=21490889>
11. Beltramo G. L., Shubina T. E., Koper M. T. M. Oxidation of formic acid and carbon monoxide on gold electrodes studied by surface-enhanced Raman spectroscopy and DFT. *ChemPhysChem*. 2005;6: 2597–2606. <https://doi.org/10.1002/cphc.200500198>
12. Martins M. E., Córdova O. R., Arvia A. J. The potentiodynamic electroformation and electroreduction of the O-containing layer on gold in alkaline solutions. *Electrochimica Acta*. 1981;26: 1547–1554. [https://doi.org/10.1016/0013-4686\(81\)85127-4](https://doi.org/10.1016/0013-4686(81)85127-4)
13. Bruckenstein S., Shay M. An in situ weighing study of the mechanism for the formation of the adsorbed oxygen monolayer at gold electrode *Journal of Electroanalytical Chemistry and Interfacial Electrochemistry*. 1985;188: 131–136. [https://doi.org/10.1016/s0022-0728\(85\)80057-7](https://doi.org/10.1016/s0022-0728(85)80057-7)
14. Burke L. D., Cunnane V. J., Lee B. H. Unusual postmonolayer oxide behavior of gold electrodes in base. *Journal of The Electrochemical Society*. 1992;139: 399–406. <https://doi.org/10.1149/1.2069230>
15. Vitus C. M., Davenport A. J. In situ scanning tunneling microscopy studies of the formation and reduction of a gold oxide monolayer on Au(111). *Journal of The Electrochemical Society*. 1994;141(5): 1291–1298. <https://doi.org/10.1149/1.2054912>
16. Goldshtein B. N., Zalkind Ts. I., Veselovskii V. I. Electrochemical adsorption of oxygen on a gold electrode in solutions of chloric and sulfuric acids\*. *Soviet Electrochemistry*. 1973;9(5): 699–702. (In Russ.)
17. Chen A., Lipkowski J. Electrochemical and spectroscopic studies of hydroxide adsorption at the Au(111) electrode. *The Journal of Physical Chemistry B*. 1999;103: 682–691. <https://doi.org/10.1021/jp9836372>
18. Vetter K. J. *Elektrochemische kinetik*. Springer Berlin, Heidelberg; 1961. <https://doi.org/10.1007/978-3-642-86547-3>
19. Tremiliosi-Filho G., Gonzalez E. R., Motheo A. J., Belgsir E. M., Léger J.-M., Lamy C. *Journal of Electroanalytical Chemistry*, 1998;444: 31–39. [https://doi.org/10.1016/S0022-0728\(97\)00536-6](https://doi.org/10.1016/S0022-0728(97)00536-6)
20. Nechaev I. V., Vvedenskii A. V. Quantum chemical modeling of hydroxide ion adsorption on group IB metals from aqueous solutions. *Protection of Metals and Physical Chemistry of Surfaces*. 2009;45(4): 391–397. <https://doi.org/10.1134/s2070205109040029>
21. Patritio E. M., Olivera P. P., Sellers H. The nature of chemisorbed hydroxyl radicals. *Surface Science*. 1994;306: 447–458. [https://doi.org/10.1016/0039-6028\(94\)90085-x](https://doi.org/10.1016/0039-6028(94)90085-x)

22. Alonso C., Gonzalez-Velasco J. Study of the electrooxidation of 1,3-propanediol on a gold electrode in basic medium. *Journal of Applied Electrochemistry*. 1988;18: 538–545. <https://doi.org/10.1007/bf01022248>
23. Safronov A. U., Kristensen P. A. IR spectroscopic characteristics of the surface of the gold electrode in solutions with different pH\*. *Soviet Electrochemistry*. 1990;26(7): 869–873. (In Russ.)
24. Kirk D. W., Foulkes F. R., Graydon W. F. The electrochemical formation of Au(I) hydroxide on gold in aqueous potassium hydroxide. *Journal of The Electrochemical Society*. 1980;127(10): 1069–1076. <https://doi.org/10.1149/1.2129819>
25. Icenhower D. E., Urbach H. B., Harrison J. H. Use of the potential-step method to measure surface oxides. *Journal of The Electrochemical Society*. 1970;117(12): 1500–1506. <https://doi.org/10.1149/1.2407359>
26. Štrbac S., Adžić R. R. The influence of OH- chemisorption on the catalytic properties of gold single crystal surfaces for oxygen reduction in alkaline solutions. *Journal of Electroanalytical Chemistry*. 1996;403: 169–181. [https://doi.org/10.1016/0022-0728\(95\)04389-6](https://doi.org/10.1016/0022-0728(95)04389-6)
27. Burke L. D. Scope for new applications for gold arising from the electrocatalytic behaviour of its metastable surface states. *Gold Bulletin*. 2004;37(1-2): 125–135. <https://doi.org/10.1007/bf03215520>
28. Dobberpuhl D. A., Johnson D. C. Pulsed electrochemical detection at ring of a ring-disk electrode applied to a study of amine adsorption at gold electrodes. *Analytical Chemistry*. 1995;67: 1254–1258. <https://doi.org/10.1021/ac00103a017>
29. Xiao Sun S.-G., Yao J.-L., Wu Q.-H., Tian Z.-Q. Surface-enhanced Raman spectroscopic studies of dissociative adsorption of amino acids on platinum and gold electrodes in alkaline solutions. *Langmuir*. 2002;18: 6274–6279. <https://doi.org/10.1021/la025817f>
30. Burke L. D., Nugent P. F. The electrochemistry of gold: II the electrocatalytic behaviour of the metal in aqueous media. *Gold Bull.* 1998;31: 39–49. <https://doi.org/10.1007/bf03214760>
31. Brown D. H., Smith W. E., Fox P., Sturrock R. D. The reactions of gold (0) with amino acids and the significance of these reactions in the biochemistry of gold. *Inorganica Chimica Acta*. 1982;(67): 27–30. [https://doi.org/10.1016/s0020-1693\(00\)85035-5](https://doi.org/10.1016/s0020-1693(00)85035-5)
32. Suhotin A. M. *Handbook of electrochemistry\**. Moscow: Khimiya Publ.; 1981. 487 p. (In Russ.)
- \* Translated by author of the article

### Information about the authors

Ilya D. Zartsyn, Dr. Sci. (Chem.), Professor of the Department of Physical Chemistry of the Voronezh State University (Voronezh, Russian Federation).  
zar-vrn@mail.ru

Alexander V. Vvedenskii, Dr. Sci. (Chem.), Full Professor of the Department of Physical Chemistry of the Voronezh State University (Voronezh, Russian Federation).  
<https://orcid.org/0000-003-2210-5543>  
alvved@chem.vsu.ru

Elena V. Bobrinskaya, Cand Sci. (Chem.), Associate Professor of the Department of Physical Chemistry of the Voronezh State University (Voronezh, Russian Federation).  
<https://orcid.org/0000-0001-7123-4224>  
elena173.68@mail.ru

Oleg A. Kozaderov, Dr. Sci. (Chem.), Docent, Head of the Department of Physical Chemistry, Voronezh State University (Voronezh, Russian Federation).  
<https://orcid.org/0000-0002-0249-9517>  
ok@chem.vsu.ru

Received 10.04.2023; approved after reviewing 19.04.2023; accepted for publication 15.06.2023; published online 25.06.2024.

Translated by Irina Charychanskaya



# Condensed Matter and Interphases

Kondensirovannye Sredy i Mezhfaznye Granitsy  
<https://journals.vsu.ru/kcmf/>

## Original articles

Research article

<https://doi.org/10.17308/kcmf.2024.26/11939>

## Structural, optical, and photocatalytic properties of dispersions of CuS doped with Mn<sup>2+</sup> and Ni<sup>2+</sup>

L. N. Maskaeva<sup>1,2✉</sup>, M. A. Lysanova<sup>1</sup>, O. A. Lipina<sup>3</sup>, V. I. Voronin<sup>4</sup>, E. A. Kravtsov<sup>4</sup>,  
A. V. Pozdin<sup>1</sup>, V. F. Markov<sup>1,2</sup>

<sup>1</sup>Ural Federal University named after the first President of Russia B.N. Yeltsin,  
19 Mira str., Ekaterinburg 620002, Russian Federation

<sup>2</sup>Ural Institute of State Fire Service of EMERCOM of Russia  
22 Mira str., Ekaterinburg 620022, Russian Federation

<sup>3</sup>Institute of Solid State Chemistry of the Ural Branch of the Russian Academy of Sciences,  
91 Pervomaiskaya str., Ekaterinburg 620041, Russian Federation

<sup>4</sup>M. N. Mikheev Institute of Metal Physics of Ural Branch of Russian Academy of Sciences  
18 S. Kovalevskaya str., Ekaterinburg 620108, Russian Federation

### Abstract

By calculating the ionic equilibria in the system  $\text{CuCl}_2 (\text{Mn}^{2+}, \text{Ni}^{2+}) - \text{NaCH}_3\text{COO} - \text{N}_2\text{H}_4\text{CS}$ , we determined the concentration regions of the formation of copper sulfide (CuS), both undoped and doped with transition metals (Mn, Ni). Using chemical deposition on frosted glass substrates, we obtained powders and thin films of CuS(Mn) and CuS(Ni) doped with manganese or nickel with a thickness of 170–200 nm. The X-ray diffraction demonstrated that CuS based dispersions have the hexagonal covelline structure (space group  $P6_3mmc$ ). The band gap  $E_g$  of CuS films (2.08 eV) grows to 2.37 and 2.49 eV after doping with nickel and manganese, respectively. The study demonstrated that CuS(Ni) powders have optimal photocatalytic properties in the visible spectral region. The degree of photodegradation of a methylene blue organic dye increases in alkaline environments.

**Keywords:** Chemical bath deposition, Copper sulfide, Thin films, Powders, Doping, Manganese, Nickel, Methylene blue, Photocatalytic degradation

**Funding:** The research was carried out with the financial support of the Ministry of Science and Higher Education of the Russian Federation (agreement No. 075-15-2022-1118 of June 29, 2022). The optical properties were studied at the Institute of Solid State Chemistry of the Ural Branch of the Russian Academy of Sciences (Grant No. 124020600024-5), and the X-ray crystallography was conducted at M. N. Mikheev Institute of Metal Physics of the Ural Branch of the Russian Academy of Sciences.

**For citation:** Maskaeva L. N., Lysanova M. A., Lipina O. A., Voronin V. I., Kravtsov E. A., Pozdin A. V., Markov V. F. Structural, optical, and photocatalytic properties of dispersions of CuS doped with Mn<sup>2+</sup> and Ni<sup>2+</sup>. *Condensed Matter and Interphases*. 2024;26(2): 265–279. <https://doi.org/10.17308/kcmf.2024.26/11939>

**Для цитирования:** Маскаева Л. Н., Лысанова М. А., Липина О. А., Воронин В. И., Кравцов Е. А., Поздин А. В., Марков В. Ф. Структурные, оптические и фотокаталитические свойства дисперсий CuS, легированных Mn<sup>2+</sup> и Ni<sup>2+</sup>. *Конденсированные среды и межфазные границы*. 2024;26(2): 265–279. <https://doi.org/10.17308/kcmf.2024.26/11939>

✉ Larisa N. Maskaeva, e-mail: [larisamaskaeva@yandex.ru](mailto:larisamaskaeva@yandex.ru)

© Maskaeva L. N., Lysanova M. A., Lipina O. A., Voronin V. I., Kravtsov E. A., Pozdin A. V., Markov V. F., 2024



The content is available under Creative Commons Attribution 4.0 License.

## 1. Introduction

Water treatment is currently of a great importance due to the increasing negative impact of oil refineries, chemical plants specializing in fabric dyeing and the manufacturing of leather, as well as plants manufacturing synthetic resins, pesticides, agricultural chemicals, medicine, etc. Toxic organic compounds formed as a result of the production processes are accumulated in wastewater and have negative carcinogenic, teratogenic, and mutagenic effects on the human body [1].

The most efficient and cost-effective methods of decomposition of organic compounds into harmless final products (H<sub>2</sub>O, CO<sub>2</sub>) are photocatalysis and photoelectrocatalysis, which occur under ultraviolet or visible light in the presence of catalysts. Ref. [2] presents a review and analysis of studies focusing on the use of inorganic semiconductors (metal oxides and chalcogenides) as catalysts which facilitate the decomposition of a large number of organic compounds. As a result of the analysis of the advantages and drawbacks of various photocatalytic materials the authors determined the main requirements to heterogeneous photocatalysts, including a relatively high-efficiency visible light adsorption, which facilitates the formation of electron-hole pairs and prevents volume recombination, as well as chemical stability and a low production cost.

Titanium dioxide TiO<sub>2</sub> ( $E_g = 3.2$  eV) is a metal oxide semiconductor photocatalyst that has been most thoroughly studied over several decades now. This material demonstrates a high photocatalytic activity, chemical stability, and durability, and is relatively inexpensive to produce [3]. However, the photocatalytic activity of the oxide is usually observed under ultraviolet radiation, whose share in the solar spectrum is ~8%. According to previous studies, it is currently important to create effective photocatalysts with a band gap less than 3.2 eV and active in the visible spectral region. Therefore, an increased attention is paid to materials based on transition metal chalcogenides and some other inorganic semiconductors which have unique optical, electric, photoelectric, and catalytic properties. In order to assess photocatalytic properties,

controlled photolysis of common organic dyes is analyzed, including methylene blue (MB) [4], rhodamine B [5], and methyl orange (MO) [6].

The most promising compound based on a metal chalcogenide is non-toxic copper monosulfide (CuS), a *p*-type semiconductor with a band gap of 1.2–2.4 eV [7,8]. Effective separation of photoexcited charge carriers in copper(II) sulfide is accounted for by its structural properties, namely by the presence of vacancy defects [9]. At the same time, the characteristic location of electron bands with corresponding redox potentials facilitates the generation of photoactive centers ( $\cdot\text{OH}$  and  $\cdot\text{O}^{2-}$  radicals) and thus ensures the degradation of toxic organic compounds under visible light [10].

The search for new photocatalysts that would ensure the effective decomposition of organic compounds under visible light motivated researchers to synthesize nanostate CuS in the form of hierarchical hollow nanospheres [11], caved superstructures [12], nanoparticles [13], nanowires [14], nanorods [15], nanoribbons [16], nanoplates [17, 18], nanoflowers [19], and hierarchical structures [20]. Of particular interest is a study of a controlled synthesis of CuS caved superstructures and their application in the catalysis of organic dyes degradation in the absence of light. The synthesis was performed by means of oxidation of hydroxide radicals produced from H<sub>2</sub>O<sub>2</sub> in the catalytic reaction [12]. According to the previously published data, the use of the nanodispersed state CuS for the photocatalytic removal of organic compounds from aqueous media is a promising method. However, effective photocatalysis under visible light requires modification of the copper sulfide surface.

It is known that the introduction of foreign impurity ions alters the coordination environment of the host metal ions in the metal sulfide lattice and modifies the electronic structure of the compound as a result of the formation of localized electron energy levels in the band gap. For this reason, although it is possible to effectively use undoped copper sulfide for photodegradation, it is often doped with ions of transition metals including Zn<sup>2+</sup>, Ni<sup>2+</sup>, Co<sup>2+</sup>, and Mn<sup>2+</sup> [21,22]. Thus, Sreelekha et al. [23] obtained nanoparticles of copper sulfide doped



with cobalt. The effectiveness of photocatalytic processes in their presence was 1.3 times higher than that of undoped copper sulfide nanoparticles under the same conditions. According to the authors, the increased effectiveness of CuS(Co) is explained by the changes in the electronic structure of the compound, which result in a slower recombination of photogenerated charge carriers. The authors also synthesized copper sulfide nanoparticles doped with iron [24] and nickel [25]. The most effective were structures containing 3 at.% of Fe and 3 at.% of Ni. The effectiveness of photodegradation of rhodamine under visible light in the presence of these structures was 98.53 and 98.46%, respectively. The effectiveness of the catalysts for both systems increased dramatically as compared to undoped copper sulfide. The authors believe that the improvement of photocatalytic properties of doped copper sulfide is explained by both the changes in the electronic structure and a larger number of catalytically active centers on the surface of the semiconductor.

To obtain nanostructures based on copper sulfide, a large number of methods are used, including chemical deposition from aqueous solutions of sodium sulfide Na<sub>2</sub>S or hydrogen sulfide H<sub>2</sub>S [26], the SILAR method [27], hydrothermal synthesis [28], solid-phase synthesis [29], and sonoelectrochemical synthesis [30].

The synthesis method largely determines the morphological features and the crystal structure of photocatalysts, which in turn determine the capacity of physical and chemical photodegradation. A method that deserves special attention is the chemical bath deposition (CBD) method. It is fairly simple and the most energy-effective, and can be conducted at relatively low temperatures. The process is easy to control, which makes it possible to vary the composition and functional properties of metal sulfides in the form of both thin films and powders [31]. An important advantage of this method is that it allows forecasting the conditions of the synthesis of both binary and ternary compounds using the calculation methodology described in [31].

In our study, we focused on the conditions for hydrochemical synthesis of CuS(Ni) and CuS(Mn)

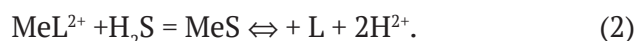
films and powders in reaction systems of various compositions. We analyzed their composition, structure, optical, and photocatalytic properties using methylene blue (MB).

## 2. Thermodynamic conditions for the formation of solid phases of sulfides and hydroxides of copper(II), manganese, and nickel

Hydrochemical deposition of the solid phase of metal sulfides involves a set of complex intermolecular interactions in the system's volume including hydrolytic decomposition of thiourea with the formation of hydrosulfuric acid H<sub>2</sub>S and cyanamide H<sub>2</sub>CN<sub>2</sub>:



followed by the formation of the metal sulfide



An analysis of ionic equilibria aimed at determining the conditions for the formation of sulfides and hydroxides of copper, manganese, and nickel was conducted in reaction systems CuCl<sub>2</sub> – CH<sub>3</sub>COONa – CH<sub>3</sub>COOH – N<sub>2</sub>H<sub>4</sub>CS, CuCl<sub>2</sub> – MnCl<sub>2</sub> – CH<sub>3</sub>COONa – N<sub>2</sub>H<sub>4</sub>CS, and CuCl<sub>2</sub> – NiSO<sub>4</sub> – CH<sub>3</sub>COONa – N<sub>2</sub>H<sub>4</sub>CS at 298 K. The preliminary criterion of the formation of metal sulfides MeS in diluted solutions was the following equation:

$$\text{IP}_{\text{MeS}} = \text{SP}_{\text{MeS}} \quad (3)$$

where IP<sub>MeS</sub> is the ionic product of the metal sulfide and SP<sub>MeS</sub> is the solubility product of the solid phase of MeS.

The portion of uncomplexed active ions of Me<sup>n+</sup> capable of entering into a chemical reaction with S<sup>2-</sup> was determined based on the expression:

$$\alpha_{\text{Me}^{2+}} = \frac{[\text{Me}^{2+}]}{C_{\text{Me}^{2+}}} = \frac{1}{1 + \frac{[L_1]}{k_1} + \frac{[L_{1,2}]^2}{k_{1,2}} + \dots + \frac{[L_{1,2,\dots,n}]^n}{k_{1,2,\dots,n}}}, \quad (4)$$

where C<sub>Me<sup>2+</sup></sub> is the total analytical concentration of the metal salt in the solution; L<sub>1</sub>, L<sub>1,2</sub>, L<sub>1,2,...,n</sub> is the concentration of the ligand; and k<sub>1</sub>, k<sub>1,2</sub>, k<sub>1,2,...,n</sub> are the instability constants of various complex forms of the metal.

Using the reference values of thermodynamic stability constants of complexed ions Cu<sup>2+</sup>, Mn<sup>2+</sup>, and Ni<sup>2+</sup>, we analyzed ionic equilibria in all the

above listed systems. Fig. 1 presents dependence diagrams of fractions of complexed ions of copper (a), manganese (b), and nickel (c) on the pH. The dotted line indicates the pH of chemical deposition of the analyzed metal sulfides.

To determine the minimum concentration of the metal salt  $C_H$  required for the formation of the solid phase of MeS taking into account critical nuclei in the analyzed systems, we used the following expression [31]:

$$pC_H = pSP_{MeS} - p\alpha_{Me^{2+}} - \left( \frac{pk_{H_2S} - 2pH + 0.5pK_C + 0.5p[N_2H_4CS]_H + 0.5p\frac{\beta_c}{\beta_s}}{RTr_{cr}} \right) \cdot \frac{0.86\sigma V_M}{RTr_{cr}}, \quad (5)$$

where  $p$  – is the negative logarithm;  $pSP_{MeS}$  is the value of the solubility product ( $pSP_{CuS} = 35.2$ ,  $pSP_{MnS} = 12.6$ ,  $pSP_{NiS} = 20.45$ ) [32];  $\alpha_{Me^{2+}}$  is the fraction of free metal ions;  $k_{H_2S}$ ,  $k_{H_2CN_2}$  are ionization constants of H<sub>2</sub>S (19.88) [32] and H<sub>2</sub>CN<sub>2</sub> (21.52) [32];  $K_C$  – is the constant of hydrolytic decomposition of thiourea,  $pK_C = 22.48$ , [31];  $[N_2H_4CS]_H$  is the initial concentration of thiourea;  $\beta_c$  and  $\beta_s$  were determined based on expressions  $\beta_s = [H_3O^+]^2 + k_{HS^-}[H_3O^+] + k_{H_2S}$ ,  $\beta_c = [H_3O^+]^2 + k_{HCN_2^-}[H_3O^+] + k_{H_2CN_2}$  [31];  $\sigma$  is the specific surface energy of the metal sulfide (surface tension) assumed to be 1.0 J/m<sup>2</sup> [31];  $V_M$  is the molar volume of the metal sulfide ( $V_{M(CuS)} = 3.19 \cdot 10^{-5}$  m<sup>3</sup>/mol,  $V_{M(MnS)} = 2.18 \cdot 10^{-5}$  m<sup>3</sup>/mol,  $V_{M(NiS)} = 1.68 \cdot 10^{-5}$  m<sup>3</sup>/mol);  $r_{cr}$  is the radius of the critical nucleus assumed to be  $3.5 \cdot 10^{-9}$  m [31];  $R$  is the universal gas constant; and  $T$  is temperature.

Besides the formation of MeS, chemical deposition in an alkaline medium is accompanied by other reactions, in particular the formation of metal hydroxides. The conditions for their formation were calculated based on the equation [31]:

$$pC_H = pSP_{Me(OH)_2} - p\alpha_{Me^{2+}} - 2pK_W + 2pH, \quad (6)$$

where  $C_H$  is the minimum concentration of the salt required for the formation of the solid phase of metal hydroxides (Cu(OH)<sub>2</sub>, Mn(OH)<sub>2</sub>, Ni(OH)<sub>2</sub>), whose solubility products are  $pSP_{Cu(OH)_2} = 19.66$ ,  $pSP_{Mn(OH)_2} = 12.72$ , and  $pSP_{Ni(OH)_2} = 17.19$  respectively;  $K_W$  is the ionic product of water [32].

Calculations of the formation regions of sulfides and hydroxides of copper, manganese, and nickel are presented in Fig. 2 as dependence diagrams in the coordinates “initial concentration of metal salt  $pC_H$  – pH of the solution – concentration of thiourea  $[N_2H_4CS]$ ”. The concentration planes correspond to the start of the formation of CuS (lilac), MnS (red), NiS (blue), Cu(OH)<sub>2</sub> (orange), Mn(OH)<sub>2</sub> (yellow), and Ni(OH)<sub>2</sub> (green).

Fig. 2 demonstrates that for all the systems the deposition starts with the formation of the solid phase of copper sulfide. The solid phase of copper sulfide without copper hydroxide is formed between the concentration planes corresponding to CuS and Cu(OH)<sub>2</sub> over the whole pH range (a). It is possible that in the pH region limited by the concentration planes of CuS, Cu(OH)<sub>2</sub>, and Mn(OH)<sub>2</sub> (b) or CuS, Cu(OH)<sub>2</sub>, and Ni(OH)<sub>2</sub> (c) only copper sulfide is formed. Codeposition of CuS and MnS (b) or CuS and NiS (c) with a large number of impurity phases

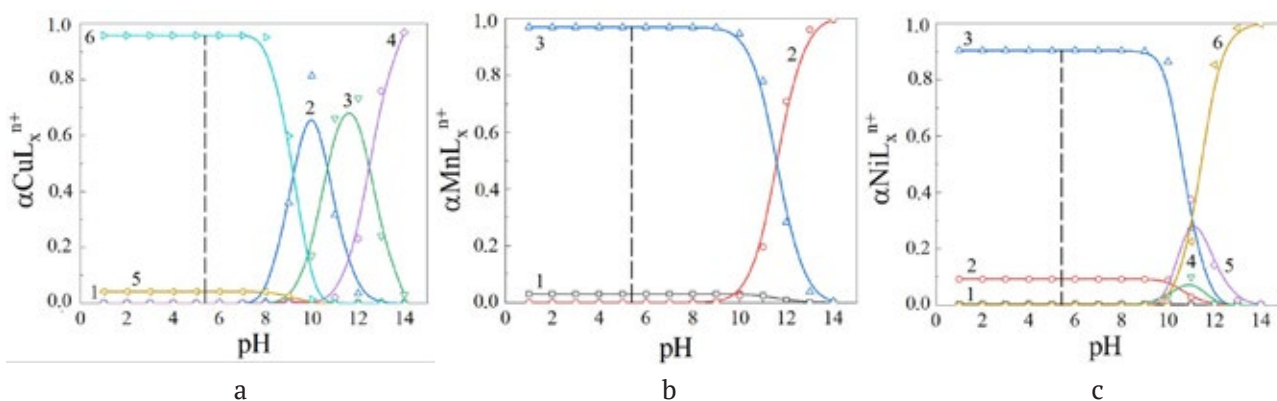


**Fig. 1.** Diagrams of ionic equilibria in the systems (a)  $CuCl_2 - CH_3COONa - N_2H_4CS$ :  $CuOH^+(1)$ ,  $Cu(OH)_2(2)$ ,  $Cu(OH)_3^-(3)$ ,  $Cu(OH)_4^{2-}(4)$ ,  $CuCH_3COO^+(5)$ ,  $Cu(CH_3COO)_2(6)$ ; (b)  $MnCl_2 - CH_3COONa - N_2H_4CS$ :  $Mn^{2+}(1)$ ,  $MnOH^+(2)$ ,  $MnCH_3COO^+(3)$ ; (c) « $NiSO_4 - CH_3COONa - N_2H_4CS$ :  $Ni^{2+}(1)$ ,  $NiCH_3COO^+(2)$ ,  $Ni(CH_3COO)_2(3)$ ,  $NiOH^+(4)$ ,  $Ni(OH)_2(5)$ ,  $Ni(OH)_3^-(6)$

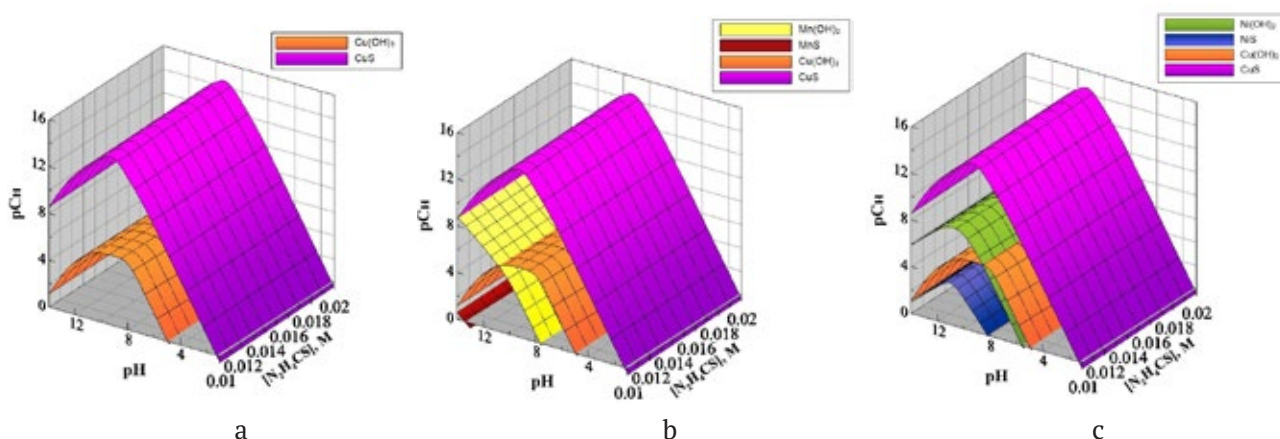


**Fig. 2.** Boundary conditions for the formation of poorly soluble phases CuS, MnS, NiS, Cu(OH)<sub>2</sub>, Mn(OH)<sub>2</sub>, Ni(OH)<sub>2</sub> in the systems CuCl<sub>2</sub> – CH<sub>3</sub>COONa – N<sub>2</sub>H<sub>4</sub>CS (a), CuCl<sub>2</sub> – MnCl<sub>2</sub> – CH<sub>3</sub>COONa – N<sub>2</sub>H<sub>4</sub>CS (b), and CuCl<sub>2</sub> – NiSO<sub>4</sub> – CH<sub>3</sub>COONa – N<sub>2</sub>H<sub>4</sub>CS (c) depending on the pH of the environment and the concentration of chalcogenide. The calculations were conducted for [NaAc] = 2 M and T = 298 K

of hydroxides of these metals is possible in the pH range 13.5–14.0 and 8.0–14.0 respectively. It should be taken into account that the thermodynamic conditions were determined at room temperature (298 K). Therefore, we can assume that an increase in the deposition temperature might affect the deposition regions of the analyzed compounds. For this reason, we conducted preliminary experiments to determine the temperature of the synthesis and the initial concentration of all the reactants and confirmed that the most promising region of formation of copper sulfide films doped with manganese or nickel is the weak acidic region (pH = 5–6).

### 3. Experimental

The hydrochemical deposition of CuS films on substrates and powders in the reactor volume was performed from a reaction mixture containing 0.03 M of CuCl<sub>2</sub>, 0.012 M of thiourea N<sub>2</sub>H<sub>4</sub>CS, and 2.0 M of NaCH<sub>3</sub>COO providing for the ligand environment. In order to obtain doped CuS(Mn) and CuS(Ni) dispersions, 0.005 M of MnCl<sub>2</sub> and NiSO<sub>4</sub> was introduced into the reactor. The films were deposited on frosted quartz substrates degreased with ethyl alcohol for 120 minutes at 353 K in a TS–TB–10 thermostat. The accuracy of the maintained operating temperature was ±0.1°.

To study the morphology and elemental composition of the films, a Tescan Vega 4 LMS Scanning Electron Microscope was used together with an Oxford Xplore EDS – AZtecOne energy

dispersive spectroscopy (EDS) system. The size of the film and powder particles was determined using the Measure software and Grapher and Origin graphic editors.

The thickness of the films was measured using an MII-4M microinterferometer with a measurement error within 10%.

Phase and structure analyzes of the synthesized thin films and powders were conducted by means of X-ray diffraction using two diffractometers: a Rigaku MiniFlex600 (Rigaku, Japan) with a copper anode CuK<sub>α</sub> (powders) and an Empyrean Series 2 (PANalytical) with a cobalt anode CoK<sub>α</sub> (films). To determine the crystal structure of the thin films we used X-ray reflectometry at an angle of 5°. The experimental X-ray diffraction patterns were described by means of a full-profile analysis (Rietveld method) [33] using the FullProf Suite software [34].

The transmittance spectra of the CuS, CuS(Mn), and CuS(Ni) films deposited on frosted glass substrates were registered using a UV-3600 spectrophotometer (Shimadzu, Japan). The device has a double beam optical scheme, a halogen lamp (visible and near IR spectral region) and a deuterium lamp (UV region). The recording was performed using a standard procedure in the UV, visible, and IR spectral regions at 1 nm intervals.

The adsorption and photocatalytic activity of the synthesized films and powders were studied using a PE-5300VI spectrophotometer. To register the optical density of the studied solutions, we plotted an experimental dependence of the optical



density of aqueous solutions on the concentration of methylene blue in the concentration range from 10<sup>-7</sup> to 10<sup>-4</sup> M.

To determine the photocatalytic properties, a 3.0×2.4 cm<sup>2</sup> thin film or a 0.012 g weighed portion of powder of the analyzed metal sulfides were put into 10 ml of a methylene blue solution with a concentration of 10<sup>-5</sup> M and exposed to visible light for 4 hours or 15 minutes respectively with constant stirring. The optical density was measured at certain periods (1 hour for the film and 5 minutes for the powder). The source of radiation was a 60 W incandescent lamp.

It is known that the pH of a solution plays an important role in the photodegradation of dyes, because it affects the formation of hydroxyl radicals [35]. Therefore, in our study, we analyzed the effect of the pH of a MB solution on the ratio of the contribution of the adsorption and photocatalytic components during the decolorization of the solution with the pH ranging from 6.0 to 9.5. The study was conducted as follows. 0.012 g weighed portions of powder were kept in an alkali solution with a known pH for 30 minutes with constant stirring. After this they were put into 20 ml of a MB solution with a concentration of 10<sup>-4</sup> M and kept for 30 minutes either in complete darkness or under radiation with constant stirring. The degree of decolorization of the dye in the experiments conducted in the dark was considered to be only the result of adsorption of the dye on the surface of the powder. The degree of photocatalytic decomposition of the molecules of methylene blue was considered equal to the difference between the degree of decolorization of the dye under radiation and the degree of decolorization of the dye in the dark. The degree of decolorization of the dye was calculated using the formula:

$$D = \frac{C_0 - C}{C_0} \cdot 100\%, \quad (7)$$

where  $C_0$  is the initial concentration of the dye, M; and  $C$  is the concentration of the dye after applying the catalyst.

## 4. Results and discussion

### 4.1. Morphology and elemental composition

In our study we analyzed 170–200 nm thin films with good adhesion to the substrate

and powders of copper sulfide and CuS doped with manganese and nickel, i.e. CuS(Mn) and CuS(Ni). Their electron microscopic images and particle size distribution histograms are shown in Figs. 3 and 4. Clear unimodal size distribution of particles was observed in both films and powders. The thin film layer of CuS consists of globular grains and has the most homogeneous microstructure. When doped with manganese and nickel salts, crescent-shaped grains are formed with the size ranging from 40 to 200 nm. However, the number of nanosized particles forming CuS, CuS(Mn), and CuS(Ni) films grows from 27 to 50 and to 56% respectively.

The analysis of the microstructure of powders of copper sulfide and CuS(Mn) and CuS(Ni) doped with transition metals demonstrated that they consist of spherical grains with ~ 30, 46, and 61% of nanoparticles. The latter are agglomerates of smaller nanoparticles.

The elemental analyzes demonstrated that the chemical composition of the films and powders includes copper (46.30–47.99 at.%) and sulfur (43.80–53.35 at.%). The ratio of the metal and chalcogen in the studied compounds allows us to conclude that bivalent copper sulfide is formed. The content of manganese and nickel was 0.13 and 0.15 at.%, respectively.

### 4.2. X-ray diffraction analysis

To obtain accurate information about the crystal structure and the degree of defectiveness of the synthesized films, we conducted a comprehensive analyzes of experimental X-ray diffraction patterns by means of the Rietveld method using the FullProf software. Experimental X-ray diffraction patterns of fine powders and thin films of undoped CuS, as well as of CuS(Mn) and CuS(Ni) doped with transition metals, are given in Fig. 5a and Fig. 6a.

A comparison of the experimental X-ray diffraction patterns of the powders and thin films of CuS, CuS(Mn), and CuS(Ni) to the X-ray diffraction pattern of a reference coarse-grained powder of copper sulfide with a covellite structure (Fig. 5a and Fig. 6a) allowed us to assume that the diffraction reflections of the studied samples correspond to the hexagonal phase of covellite with a space group  $P6_3/mmc$ . Their fine-grained nature can be observed in Fig. 5b and 6b,



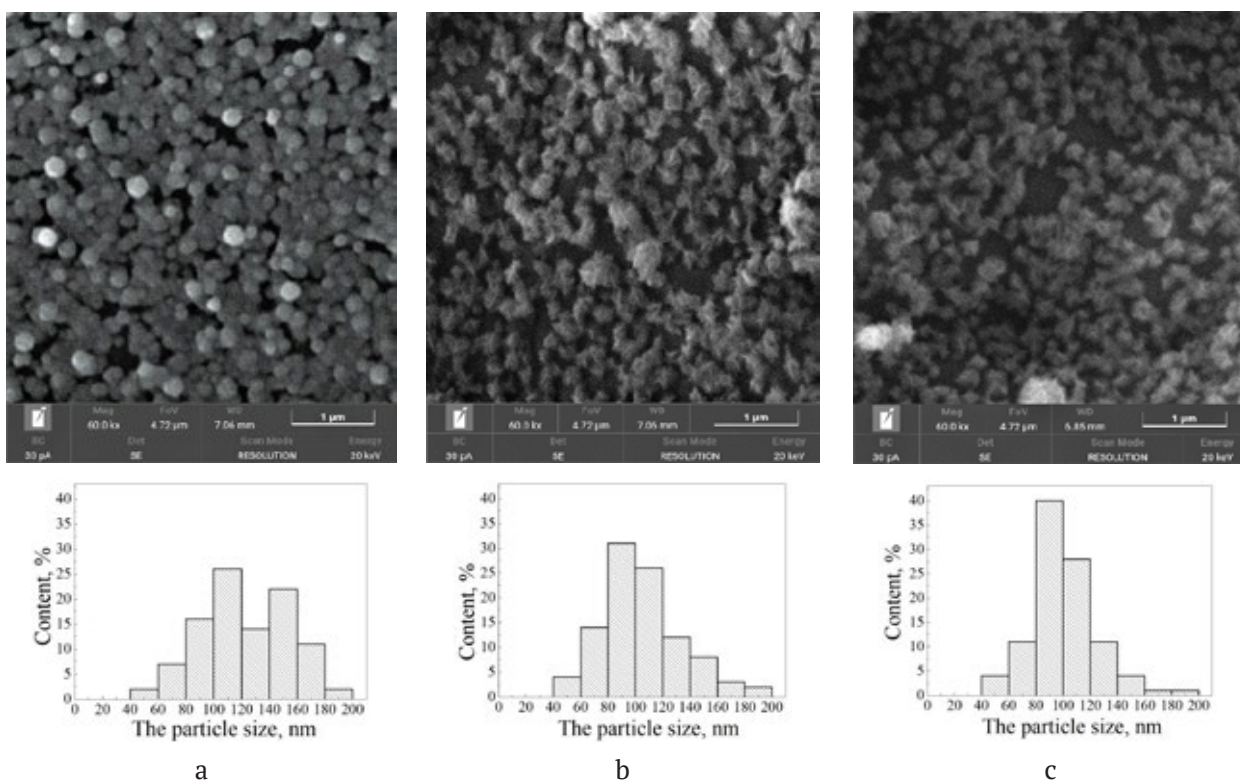


**Fig. 3.** Electron microscopic images of the films of undoped copper sulfide (a), and CuS doped with manganese (b) and nickel (c) together with particle size distribution histograms

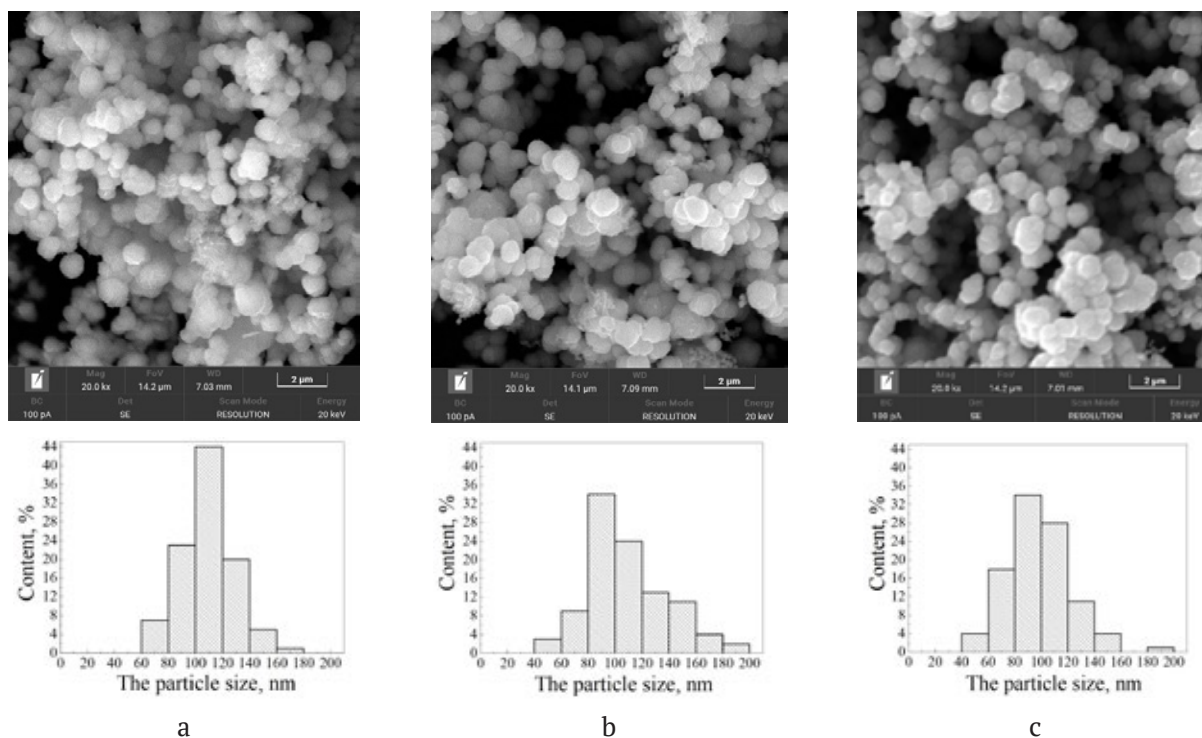


**Fig. 4.** Electron microscopic images of the powders of undoped copper sulfide (a), and CuS doped with manganese (b) and nickel (c) together with particle size distribution histograms

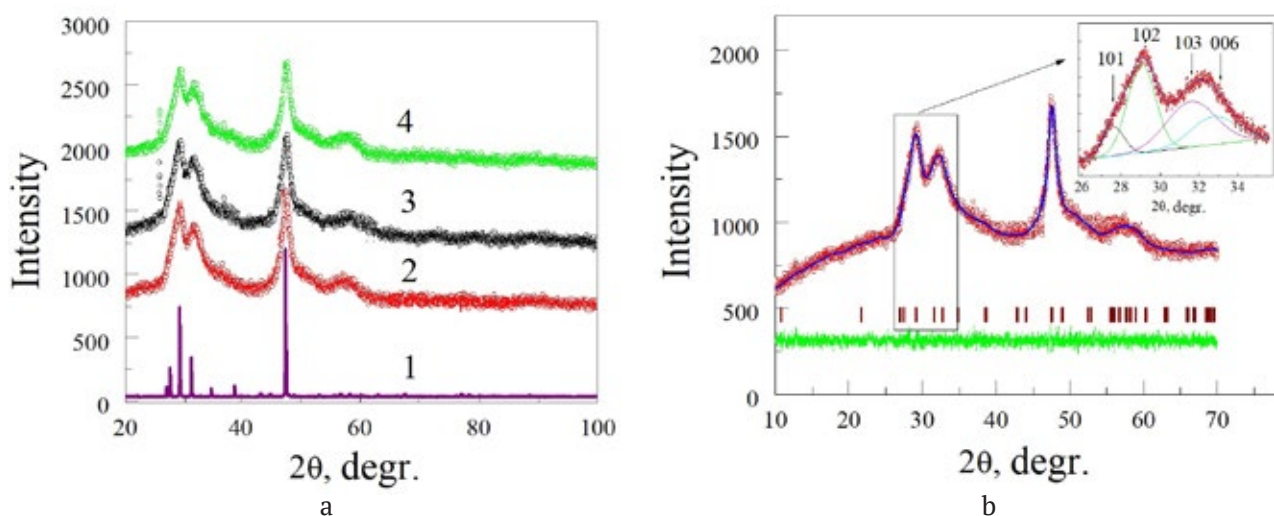


**Fig. 5.** Experimental X-ray diffraction patterns of CuS (2), CuS(Mn) (3), and CuS(Ni) (4) powders are shifted along the Y-axis for clarity. The calculated X-ray diffraction pattern of the reference CuS (1) with the hexagonal covelline structure (space group  $P6_3/mmc$ ) (a). Experimental X-ray diffraction pattern (red circles) and the calculated (blue line) and differential (green line) curves for CuS. The angular positions of the Bragg reflections are indicated with dashes (b). The insert shows the decomposition of the profile into separate peaks

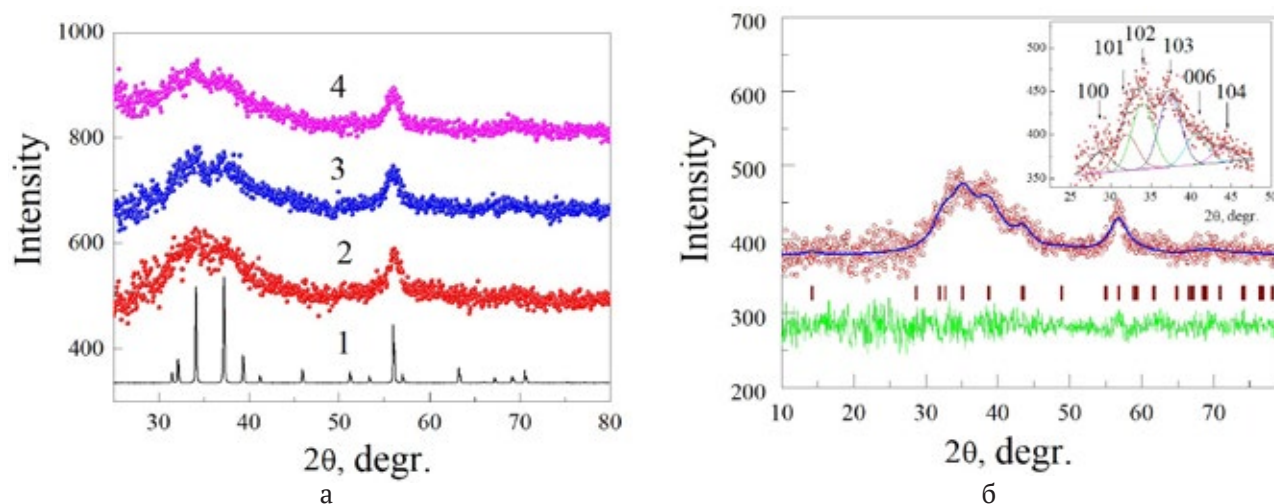


**Fig. 6.** Experimental X-ray diffraction patterns of CuS (2), CuS(Mn) (3), and CuS(Ni) (4) films are shifted along the Y-axis for clarity. The calculated X-ray diffraction pattern of the reference CuS (1) with the hexagonal covelline structure (space group  $P6_3/mmc$ ) (a). Experimental X-ray diffraction pattern (red circles) and the calculated (blue line) and differential (green line) curves for CuS(Mn). The angular positions of the Bragg reflections are indicated with dashes (b). The insert shows the decomposition of the profile into separate peaks

which describe the profile of a fragment of the experimental X-ray diffraction patterns by means of decomposition of the broad reflections of the covelline phase characteristic for the scattering from small particles. Therefore, the analyzes of the experimental X-ray diffraction patterns was performed based on a model of the covelline fine crystal structure. To achieve a good agreement between the experimental profile of the X-ray diffraction patterns and the calculated one, we varied the lattice parameters and the particle

size assuming the anisotropy of their shape and taking into account a slight texture forming in the synthesized compounds. This is connected with the fact that during the synthesis of powder samples with a covelline crystal structure a texture can develop along the selected axis (in our study, axis “c” was 4 times larger than axes “a” and “b”) as well as the deviation of the particle shape from the isotropic one. This calculation algorithm taking into account the anisotropy of the grain size was also applied to the analyzes

of the X-ray diffraction patterns of the studied CuS, CuS(Mn), and CuS(Ni) films formed from microfine particles. Fig. 5b and 6b present a comparative analyzes of the experimental X-ray diffraction pattern of the CuS powder and the CuS(Mn) thin film to their theoretical profiles calculated using the model of the hexagonal covelline structure (space group  $P6_3/mmc$ ). The figures demonstrate a good agreement between the experimental and the calculated profiles assuming that a covelline phase is implemented in the volume of the powder and the film with a particle size of several nanometers. The refined structural parameters of the crystal lattice of the studied dispersions given in table 1 are in agreement with JCPDS 06-0464.

Table 1 shows that the doping of the powders with transition metals resulted in an increase in the crystal lattice volume from 0.2080(4) to 0.2091(5) nm<sup>3</sup>, while the doping of the films resulted in a decrease in the crystal lattice volume from 0.2060(8) to 0.1897(9) nm<sup>3</sup>. This can be caused by the fact that impurity ions might penetrate into the crystal lattice of copper sulfide in powders, while in the films copper ions are partially replaced by manganese or nickel ions.

The diffraction reflections observed on the X-ray diffraction patterns of all the films are broadened due to a decrease in the coherent scattering regions. The results of the analyzes demonstrated that an averaged particle size ( $\langle D \rangle$ ) of CuS, CuS(Mn), and CuS(Ni) films and powders is nanoscale, i.e. it is smaller than the grain diameter determined by means of the scanning electron microscopy (Fig. 4). This is

explained by the fact that nanoparticles form larger agglomerates. A similar effect was observed by Pal M. et al. [36] during chemical deposition of CuS powders.

### 4.3. Optical properties

The optical properties of the CuS and CuS(Me) films were studied in the range of 200–1800 nm. The transmittance spectra in Fig. 7a demonstrate that the films absorb most of the radiation. The maximum light transmission of the film (8.2%) is observed for CuS(Ni). The spectra of all the films demonstrate a decline at 400–700 nm (1.77–3.1 eV) characteristic of the CuS phase.

The band gap  $E_g$  was calculated for direct allowed transitions. For this, we build function  $(\alpha hv)^2 = f(hv)$  demonstrated in Fig. 7b. Of the greatest interest was the region of 1.77–3.1 eV, where, as mentioned before, the optical characteristics change noticeably. Graphical methods demonstrated that  $E_g$  of the undoped CuS film was 2.08 eV, while the band gaps of CuS(Ni) and CuS(Mn) films were 2.37 and 2.49 eV, respectively.

A slight difference between the experimental band gaps indicates the similarity of the electronic structure of the samples, which, in turn, indicates a similarity in the morphological properties and the absence of the factors (quantum confinement effects, defects, etc.) affecting the  $E_g$ . The obtained results are in agreement with the previously published values for CuS and CuS(Me) films [38–40].

Therefore, the doping of copper sulfide with transition metals resulted in an increase in the

**Table 1.** Crystal lattice parameters ( $a$ ,  $c$ ), volume ( $V$ ), particle size along the crystallographic directions ( $L(h00/0k0)$ ,  $L(00l)$ ) and average size ( $\langle D \rangle$ ) of powders and films of CuS, CuS(Mn), CuS(Ni)

Parameters	Powders			Films		
	CuS	CuS(Mn)	CuS(Ni)	CuS	CuS(Mn)	CuS(Ni)
$a$ , $b$ , nm	0.38228(8)	0.38192(6)	0.38214(6)	0.3807(2)	0.3811(8)	0.3811(2)
$c$ , nm	1.6438(7)	1.6480(9)	1.6532(9)	1.641(4)	1.595(9)	1.509(9)
$V$ , nm <sup>3</sup>	0.20804(6)	0.20818(6)	0.20909(5)	0.2060(8)	0.2006(9)	0.1897(9)
$L(h00/0k0)$	2.0	2.6	2.7	2.3	2.2	2.2
$L(00l)$	5.0	5.5	5.7	3.4	4.3	4.5
$\langle D \rangle$ , nm	2.5	3.3	3.5	1.7	2.6	2.5
$L(h00/0k0)$	2.0	2.6	2.7	2.3	2.2	2.2
$L(00l)$	5.0	5.5	5.7	3.4	4.3	4.5
$\langle D \rangle$ , nm	2.5	3.3	3.5	1.7	2.6	2.5
$L(00l)/L(h00)$	2.5	2.12	2.11	–	–	–



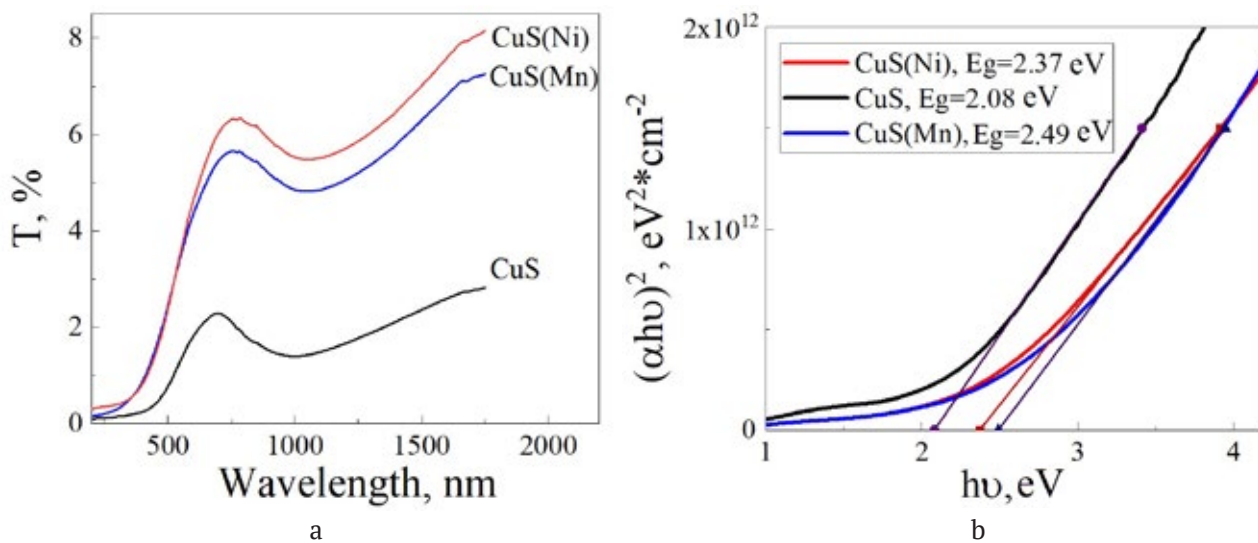


**Fig. 7.** The transmittance spectra of the CuS, CuS(Ni), and CuS(Mn) films (a); results of the graphical estimation of the band gap (b)

band gap. This can be explained by the formation of substitutional solid solutions of  $Mn_xCu_{1-x}S$ , because according to the existing literature [41, 42] the band gap of MnS is 3.1–3.8 eV. As for the doping of copper sulfide with nickel, the obtained band gap of 0.15–1.0 eV [37, 43] cannot be explained in the same way as the above described increase in  $E_g$ . A thermodynamic estimate of the synthesis conditions demonstrated the possibility of formation of nickel hydroxide  $Ni(OH)_2$  in the analyzed reaction mixture, which is an indirect semiconductor with a band gap of 3.95 eV [44]. Based on the composition of the reaction mixture we can assume that an oxide NiO phase is formed in the films with a band gap of 3.2–3.5 eV, which can also result in an increase in the band gaps of CuS(Ni) films [45].

#### 4.4. Photocatalytic and adsorption activity

We know that during chemical deposition in a reactor, CuS, CuS(Mn), and CuS(Ni) solid phases are formed both on the substrate (in the form of films) and in the volume of the reaction mixture (in the form of powder). Therefore, in our study we performed a comparative analyzes of the adsorption and photocatalysis of methylene blue (MB). Fig. 8 demonstrates the dependence of the decolorization of the MB dye on the duration of exposure to visible light in the presence of CuS(Mn) (a) and CuS(Ni) (b) catalyst films obtained from reaction mixtures containing 0 (1), 0.001 (2), 0.005 (3), and 0.01 (4) M of  $MnCl_2$

( $NiSO_4$ ) respectively, and in the presence of CuS(Ni) (1) and CuS(Mn) (2) catalyst powders obtained from reaction mixtures containing 0.005 M of nickel (manganese) salt. The kinetic curves of the decolorization of MB demonstrate that the degree of decolorization of the dye solution under visible light in the presence of CuS, CuS(Mn), and CuS(Ni) catalyst powders reaches 90–97% over 15 minutes, while in the presence of catalyst thin films the degree of decolorization reaches only 18–35% (CuS(Mn)) and 34–38% (CuS(Ni)) over four hours.

The effectiveness of the studied catalysts is demonstrated in Fig. 9. Both CuS(Ni) films and powders were more active catalysts for the decolorization of MB. Based on their effectiveness, the powders can be ordered as follows  $CuS \rightarrow CuS(Mn) \rightarrow CuS(Ni)$ . This agrees well with their specific surface area, which increases from 11.6 to 15.7 and 17.4  $m^2/g$  respectively. Therefore the surface area of CuS(Mn) and CuS(Ni) powders is 1.4–1.5 times larger than the surface area of the CuS powder. Powders are also known to have a “looser” microstructure due to a larger number of surface atoms and the difference in the size and shape of the particles. The presence of voids and pores in the catalyst powders is proved by the deviation of the particles from the isotropic shape demonstrated by the X-ray diffraction and an increase in the volume of the crystal lattice in the series  $CuS (0.20804(6) nm^3) \rightarrow CuS(Mn) (0.20818(6) nm^3) \rightarrow CuS(Ni) (0.20909(5) nm^3)$ .



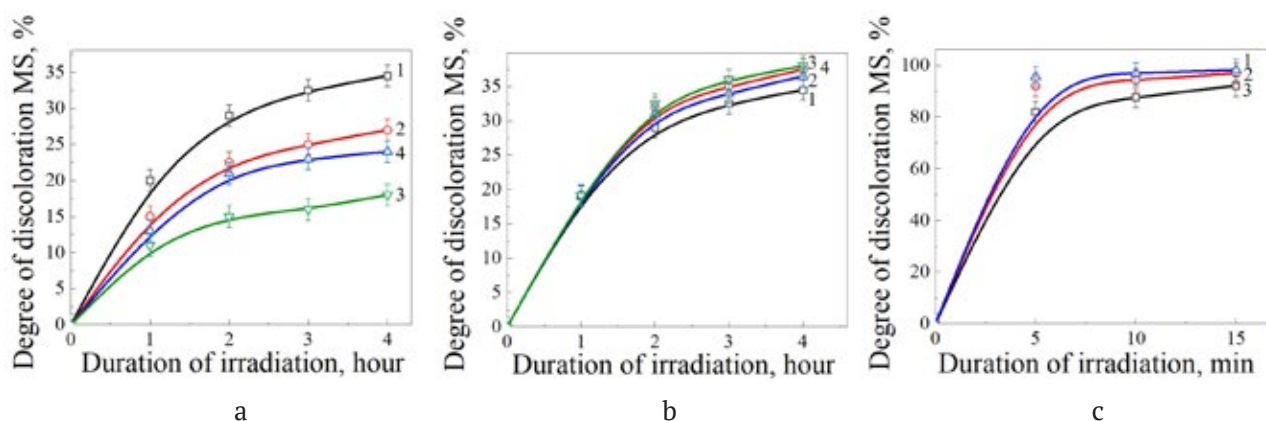


**Fig. 8.** Dependence of the degree of decolorization of the MB dye on the duration of exposure to visible light in the presence of CuS(Mn) (a) and CuS(Ni) (b) catalyst films obtained from reaction mixtures containing 0 (1), 0.001 (2), 0.005 (3), and 0.01 (4) M of MnCl<sub>2</sub> (NiSO<sub>4</sub>) respectively, and in the presence of CuS(Ni) (1) and CuS(Mn) (2) catalyst powders obtained from reaction mixtures containing 0.005 M of nickel (manganese) salt and undoped CuS (3) (c).

The resulting decolorization of the solution is determined based on the cumulative effect of the adsorption of the MB dye on the surface of the photocatalyst and photocatalytic decomposition of the dye molecules. Therefore, the main factors that impact the effectiveness of the decolorization of the solution caused by the above mentioned processes, is the specific surface area of the solid solution introduced in the system and its modification, as well as the degree of defectiveness of its crystal structure.

It is known [21] that the pH of a solution affects the surface charge of the particles of photocatalysts and the catalytic reactions potential, and therefore the degree of adsorption and photodegradation of dyes. An effective way to modify the surface of copper sulfide is to increase the alkalinity of the environment. This is explained by an increased contribution of the electrostatic attraction facilitating the transfer of electrons between the dye molecules and the surface of the dispersed phase adsorbing OH<sup>-</sup> ions from the solution, as well as by the formation in the alkaline medium of a small number of organic compounds of active radicals ·OH and ·O<sup>2-</sup> which facilitate photodegradation.

To separate the processes of adsorption and photocatalysis in the pH range from 6 to 9.5 we conducted comparative experiments with and without optical radiation in the visible spectral region. 0.012 g weighed portions of powder were kept in an alkali solution with a known pH for 30 minutes with constant stirring. After this they

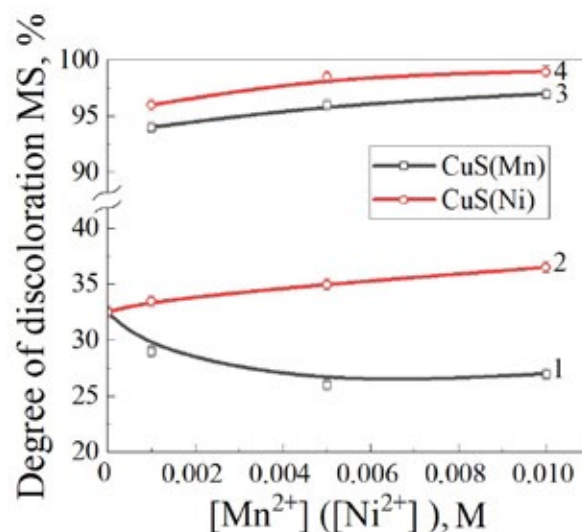


**Fig. 9.** Dependence of the degree of decolorization of the MB dye in the presence of films (1, 2) and powders (3, 4) CuS(Mn) (1, 3) and CuS(Ni) (2, 4) on the concentration of manganese (nickel) salts in the reaction mixture

were put into a dye solution with a concentration of 10<sup>-4</sup> M. The decolorization of the dye in the experiments conducted in the dark was considered to be only the result of adsorption of the dye on the surface of the powder. The degree of photocatalytic decomposition of the molecules of methylene blue was considered equal to the difference between the degree of decolorization of the dye under radiation and the degree of decolorization of the dye in the dark. The obtained dependences of the adsorption capacity and the photocatalytic activity of photocatalyst powders CuS, CuS(Mn), and CuS(Ni) on the pH of the MB solution are

given in Fig. 10. In an acidic environment, the decolorization of the dye occurs mostly due to its adsorption on the surface of the powder. At higher pH the degree of photocatalytic decomposition of MB in the presence of photocatalyst powders CuS(Mn) and CuS(Ni) increases.

The maximum photocatalytic activity was demonstrated by copper sulfide doped with nickel. With pH = 9.5 the degree of decomposition of MB was 12.9%. Its photocatalytic activity was 1.2 times higher than that of CuS(Mn) and 1.5 times higher than that of CuS. The results of the experiments demonstrated an increase in both the sorption and photocatalytic activity in the series CuS → CuS(Mn) → CuS(Ni).

We should note that the presented results are of a great interest both in terms of the use of dispersions for photocatalysis of a relatively low optical radiation in the visible region and in terms of quite active kinetics of the process of photodegradation of MB, taking into account the short (5–15 min) time of contact between the solution and the introduced catalyst.

## 5. Conclusions

Using chemical deposition of fixed concentrations of copper chloride, sodium acetate, and thiourea with the concentration of manganese or nickel salts varying from 0.001 to 0.01 M we obtained powders and thin films of CuS and its modifications CuS(Mn) and CuS(Ni) with a thickness of 180–200 nm. The introduction

of manganese or nickel salts into the reaction mixture during the chemical deposition to 0.005 M results in insignificant changes in the shape and size of the grains of the formed copper sulfide. The average particle size of doped copper sulfide is 20% smaller than the average particle size of undoped copper sulfide. The X-ray diffraction analysis demonstrated that a finely dispersed solid phase is formed in both films and powders based on the hexagonal covelline structure CuS (space group  $P6_3/mmc$ ). The transmittance spectra of the CuS and CuS(Mn, Ni) films were studied in the wavelength range from 200 to 1800 nm. The study demonstrated that doping with the studied transition metals results in an increase in the band gap from 2.08 eV (CuS) to 2.49 eV (CuS(Mn)) and 2.37 eV (CuS(Ni)).

The results of the comparative study of the adsorption and photocatalytic characteristics of the synthesized dispersions (in our study used with methylene blue) demonstrated a higher degree of decolorization of solutions over a shorter time interval under visible light and in the presence of catalyst powders. The results of the experiments demonstrated an increase in both the sorption and photocatalytic activity in the series CuS → CuS(Mn) → CuS(Ni). The maximum photocatalytic activity was demonstrated by copper sulfide doped with nickel. With the pH = 9.5 the degree of decomposition of MB was 12.9% over the first 15 minutes.

## Contribution of the authors

The authors contributed equally to this article.

## Conflict of interests

The authors declare that they have no known competing financial interests or personal relationships that could have influenced the work reported in this paper.

## References

1. Lin Q. D., Zhao L. H., Xing B. Synthesis and characterization of cubic mesoporous bridged for removing organic pollutants from water. *Chemosphere*. 2014;103: 188–196. <https://doi.org/10.1016/j.chemosphere.2013.11.062>
2. Lysanova M. A., Maskaeva L. N., Markov V. F. Application of metal oxides and sulfides as photocatalysts. *Butlerov Communications*. 2023;73(1): 1–19. (In Russ., abstract in Eng.). <https://doi.org/10.37952/ROI-jbc-01/23-73-1-1>

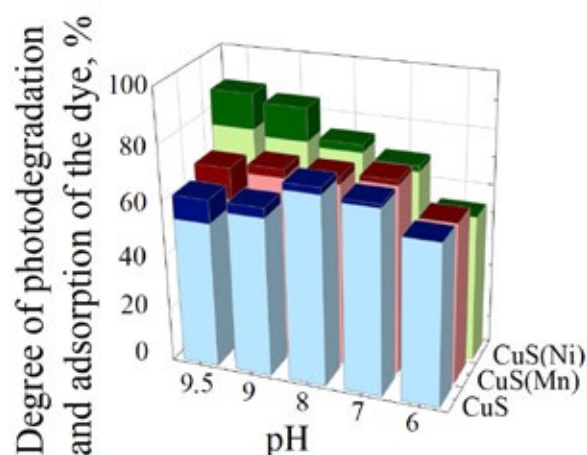


**Fig. 10.** Dependence of the adsorption capacity (lower part) and the photocatalytic activity (upper part) of photocatalyst CuS(Mn) and CuS(Ni) powders on the pH of the MB solution

3. Fujishima A., Honda K. Electrochemical photolysis of water at a semiconductor electrode. *Nature*. 1972;238(5358): 37–38. <https://doi.org/10.1038/238037a0>
4. Shu Q. W., Lan J., Gao M. X., Wang J., Huang C. Z. Controlled synthesis of CuS caved superstructures and their application to the catalysis of organic dye degradation in the absence of light. *CrystEngComm*. 2015;17(6): 1374–1380. <https://doi.org/10.1039/c4ce02120g>
5. Sreelekha N., Subramanyam K., Amaranatha R. D. Structural, optical, magnetic and photocatalytic properties of Co doped CuS diluted magnetic semiconductor nanoparticles. *Applied Surface Science*. 2016;378: 330–340. <https://doi.org/10.1016/j.apsusc.2016.04.003>
6. Chen J., Liu W., Gao W. Tuning photocatalytic activity of In<sub>2</sub>S<sub>3</sub> broadband spectrum photocatalyst based on morphology. *Applied Surface Science*. 2016;368: 288–297. <https://doi.org/10.1016/j.apsusc.2016.02.008>
7. Tanveer M., Cao C., Aslam I., ... Mahmood A. Facile synthesis of CuS nanostructures: structural, optical and photocatalytic properties. *Science of Advanced Materials*. 2014;6(12): 2694–2701. <https://doi.org/10.1166/sam.2014.1988>
8. Bagul S. V., Chavhan S. D., Sharma R. Growth and characterization of Cu<sub>x</sub>S (x = 1.0, 1.76, and 2.0) thin films grown by solution growth technique (SGT). *Journal of Physics and Chemistry of Solids*. 2007;68(9): 1623–1629. <https://doi.org/10.1016/j.jpcs.2007.03.053>
9. Tanveer M., Cao C., Aslam I., ... Mahmood A. Synthesis of CuS flowers exhibiting versatile photocatalyst response. *New Journal of Chemistry*. 2015;39(2): 1459–1468. <https://doi.org/10.1039/c4nj01834f>
10. Chaki S. H., Deshpande M. P., Tailor J. P. Characterization of CuS nanocrystalline thin films synthesized by chemical bath deposition and dip coating techniques. *Thin Solid Films*. 2014;550: 291–297. <https://doi.org/10.1016/j.tsf.2013.11.037>
11. Meng X., Tian G., Chen Y., ... Fu H. Hierarchical CuS hollow nanospheres and their structure-enhanced visible light photocatalytic properties. *CrystEngComm*. 2013;15(25): 5144. <https://doi.org/10.1039/c3ce40195b>
12. Shu Q. W., Lan J., Gao M. X., Wang J., Huang C. Z. Controlled synthesis of CuS caved superstructures and their application to the catalysis of organic dye degradation in the absence of light. *CrystEngComm*. 2015;17(6): 1374–1380. <https://doi.org/10.1039/c4ce02120g>
13. Dutta A., Dolui S. K. Preparation of colloidal dispersion of CuS nanoparticles stabilized by SDS. *Materials Chemistry and Physics*. 2008;112(2): 448–452. <https://doi.org/10.1016/j.matchemphys.2008.05.072>
14. Feng C., Zhang L., Wang Z. Synthesis of copper sulfide nanowire bundles in a mixed solvent as a cathode material for lithium-ion batteries. *Journal of Power Sources*. 2014;269: 550–555. <https://doi.org/10.1016/j.jpowsour.2014.07.006>
15. Kalyanikutty K. P., Nikhila M., Maitra U., Rao C. N. R. Hydrogel-assisted synthesis of nanotubes and nanorods of CdS, ZnS and CuS, showing some evidence for oriented attachment. *Chemical Physics Letters*. 2006;432(1–3): 190–194. <https://doi.org/10.1016/j.cplett.2006.10.032>
16. Tan C., Lu R., Xue P., Bao C., Zhao Y. Synthesis of CuS nanoribbons templated by hydrogel. *Materials Chemistry and Physics*. 2008;112(2): 500–503. <https://doi.org/10.1016/j.matchemphys.2008.06.015>
17. Liu Y., Qin D., Wang L., Cao Y. A facile solution route to CuS hexagonal nanoplatelets. *Materials Chemistry and Physics*. 2007;102(2–3): 201–206. <https://doi.org/10.1016/j.matchemphys.2006.12.004>
18. Savariraj A. D., Viswanathan K. K., Prabakar K. CuS nano flakes and nano platelets as counter electrode for quantum dots sensitized solar cells. *Electrochimica Acta*. 2014;149: 364–369. <https://doi.org/10.1016/j.electacta.2014.10.141>
19. Yang Y. J., Zi J., Li W. Enzyme-free sensing of hydrogen peroxide and glucose at a CuS nanoflowers modified glassy carbon electrode. *Electrochimica Acta*. 2014;115: 126–130. <https://doi.org/10.1016/j.electacta.2013.10.168>
20. Li F., Wu J., Qin Q., Li Z., Huang X. Controllable synthesis, optical and photocatalytic properties of CuS nanomaterials with hierarchical structures. *Powder Technology*. 2010;198(2): 267–274. <https://doi.org/10.1016/j.powtec.2009.11.018>
21. Kovaleva D. S., Gorokhovskiy A. V., Tretyachenko E. V., Kosarev A. V. The effect of the hydrogen index on the photodegradation of methylene blue under the action of sunlight with the participation of modified potassium polytitanates. *Fundamental Research*. 2015;7(2): 1401–1406. (In Russ.). Available at: <https://fundamental-research.ru/ru/article/view?id=37162>
22. Carp O., Huisman C. L., Reller A. Photoinduced reactivity of titanium dioxide. *Progress in Solid State Chemistry*. 2004;32(1–2): 33–177. <https://doi.org/10.1016/j.progsolidstchem.2004.08.001>
23. Sreelekha N., Subramanyam K., Amaranatha Reddy D. Structural, optical, magnetic and photocatalytic properties of Co doped CuS diluted magnetic semiconductor nanoparticles. *Applied Surface Science*. 2016;378: 330–340. <https://doi.org/10.1016/j.apsusc.2016.04.003>
24. Sreelekha N., Subramanyam K., Amaranatha Reddy D., ... Vijayalakshmi R. P. Efficient photocatalytic degradation of rhodamine-B by Fe doped CuS diluted magnetic semiconductor nanoparticles under the simulated sunlight irradiation. *Solid State Sciences*.



- 2016;62: 71–81. <https://doi.org/10.1016/j.solidstatesciences.2016.11.001>
25. Subramanyam K., Sreelekha N., Amaranatha Reddy D., Murali G., Rahul Varma K., Vijayalakshmi R. P. Chemical synthesis, structural, optical, magnetic characteristics and enhanced visible light active photocatalysis of Ni doped CuS nanoparticles. *Solid State Sciences*. 2017;65: 68–78. <https://doi.org/10.1016/j.solidstatesciences.2017.01.008>
26. Lewis A. E. Review of metal sulphide precipitation. *Hydrometallurgy*. 2010;104(2): 222–234. <https://doi.org/10.1016/j.hydromet.2010.06.010>
27. Shu Q. W., Lan J., Gao M. X., Wang J., Huang C. Z. Controlled synthesis of CuS caved superstructures and their application to the catalysis of organic dye degradation in the absence of light. *CrystEngComm*. 2015;17(6): 1374–1380. <https://doi.org/10.1039/c4ce02120g>
28. Raghavendra K. V. G., Rao K. M., Kumar N. T. U. Hydrothermal synthesis of CuS/CoS nano composite as an efficient electrode for the supercapattery applications. *Journal of Energy Storage*. 2021;40: 102749. <https://doi.org/10.1016/j.est.2021.102749>
29. Wang W., Ao L. Synthesis and characterization of crystalline CuS nanorods prepared via a room temperature one-step, solid-state route. *Materials Chemistry and Physics*. 2008;109(1): 77–81. <https://doi.org/10.1016/j.matchemphys.2007.10.035>
30. Zhao Y., Pan H., Lou Y., Qiu X., Zhu J., Burda C. Plasmonic Cu<sub>2-x</sub>S nanocrystals: Optical and structural properties of copper-deficient copper(I) sulfides. *Journal American Chemical Society*. 2009;131(12): 4253–4261. <https://doi.org/10.1021/ja805655b>
31. Markov V. F., Maskaeva L. N., Ivanov P. N. *Hydrochemical deposition of metal sulfide films: modeling and experiment\**. Ekaterinburg: UrO RAS Publ.; 2006. 217 p. (In Russ.)
32. Lurie Yu. Yu. *Handbook of analytical chemistry\**. Moscow: Khimiya Publ. 1971. 456 p. (In Russ.)
33. Rietveld H. M. A profile refinement method for nuclear and magnetic structures. *Journal of Applied Crystallography*. 1969;2(2): 65–71. <https://doi.org/10.1107/S0021889869006558>
34. Rodrigues-Carvajal J. Recent advances in magnetic structure determination by neutron powder diffraction. *Physica B: Condensed Matter*. 1993;192: 55. [https://doi.org/10.1016/0921-4526\(93\)90108-I](https://doi.org/10.1016/0921-4526(93)90108-I)
35. Odo J., Matsumoto K., Shinmoto E., Hatae Y., Shiozaki A. Spectrofluorometric determination of hydrogen peroxide based on oxidative catalytic reactions of p-hydroxyphenyl derivatives with metal complexes of thiacalix[4]arenetetrasulfonate on a modified anion-exchanger. *Analytical Sciences*. 2004;20(4): 707–710. <https://doi.org/10.2116/analsci.20.707>
36. Pal M., Mathews N. R., Sanchez-Mora E., Pal U., Paraguay-Delgado F., Mathew X. Synthesis of CuS nanoparticles by a wet chemical route and their photocatalytic activity. *Journal of Nanoparticle Research*. 2015;17(7): 1–12. <https://doi.org/10.1007/s11051-015-3103-5>
37. Okamura H., Naitoh J., Nanba N., Matoba M., Nishioka M., Anzai S. Optical study of the metal-nonmetal transition in NiS. *Solid State Communications*. 1998;112(2): 91–95. [https://doi.org/10.1016/s0038-1098\(99\)00277-x](https://doi.org/10.1016/s0038-1098(99)00277-x)
38. Subramanyam K., Sreelekha N., Reddy D. A., ... Vijayalakshmi R. P. Influence of Mn doping on structural, photoluminescence and magnetic characteristics of covellite-phase CuS nanoparticles. *Journal of Superconductivity and Novel Magnetism*. 2017;31(4): 1161–1165. <https://doi.org/10.1007/s10948-017-4296-x>
39. Subramanyam K., Sreelekha N., Amaranatha Reddy D., Murali G., Rahul Varma K., Vijayalakshmi R. P. Chemical synthesis, structural, optical, magnetic characteristics and enhanced visible light active photocatalysis of Ni doped CuS nanoparticles. *Solid State Sciences*. 2017;65: 68–78. <https://doi.org/10.1016/j.solidstatesciences.2017.01.008>
40. Sharma L. K., Kar M., Choubey R. K., Mukherjee S. Low field magnetic interactions in the transition metals doped CuS quantum dots. *Chemical Physics Letters*. 2021;780: 138902. <https://doi.org/10.1016/j.cplett.2021.138902>
41. Hosseini-Hajivar M. M., Jamali-Sheini F., Yousefi R. Microwave-assisted solvothermal synthesis and physical properties of Zn-doped MnS nanoparticles. *Solid State Sciences*. 2019;93: 31–36. <https://doi.org/10.1016/j.solidstatesciences.2018.10.010>
42. Gümüç C., Ulutaş C., Esen R., Özkendir O. M., Ufuktepe Y. Preparation and characterization of crystalline MnS thin films by chemical bath deposition. *Thin Solid Films*. 2005;492(1–2): 1–5. <https://doi.org/10.1016/j.tsf.2005.06.016>
43. Zhang P., Wu L. J., Pan W. G., Bai S. C., Guo R. T. Efficient photocatalytic H<sub>2</sub> evolution over NiS-PCN Z-scheme composites via dual charge transfer pathways. *Applied Catalysis B: Environmental*. 2021;289: 120040. <https://doi.org/10.1016/j.apcatb.2021.120040>
44. Tang Z. K., Liu W. W., Zhang D. Y., Lau W. M., Liu L. M. Tunable band gap and magnetism of the two-dimensional nickel hydroxide. *RSC Advances*. 2015;5(94): 77154–77158. <https://doi.org/10.1039/c5ra10380k>
45. Ukoba K. O., Eloka-Eboka A. C., Inambao F. L. Review of nanostructured NiO thin film deposition using the spray pyrolysis technique. *Renewable and Sustainable Energy Reviews*. 2018;82: 2900–2915. <https://doi.org/10.1016/j.rser.2017.10.041>

\* Translated by author of the article



### Information about the authors

*Larisa N. Maskaeva*, Dr. Sci. (Chem.), Professor at the Department of Physical and Colloidal Chemistry, Ural Federal University named after the first President of Russia B. N. Yeltsin; Professor at the Department of Chemistry and Gorenje Processes, Ural Institute of State Fire Service of EMERCOM of Russia (Ekaterinburg, Russian Federation).

<https://orcid.org/0000-0002-1065-832X>  
l.n.maskaeva@urfu.ru

*Maria A. Lysanova*, Engineer at the Department of Physical and Colloidal Chemistry, Ural Federal University named after the first President of Russia B. N. Yeltsin (Ekaterinburg, Russian Federation).

<https://orcid.org/0009-0004-5702-8706>  
maria.lysanova@bk.ru

*Olga A. Lipina*, Senior Research, Institute of Solid State Chemistry of the Ural Branch of the Russian Academy of Sciences (Ekaterinburg, Russian Federation).

<https://orcid.org/0000-0003-3685-5337>  
LipinaOlgaA@yandex.ru

*Vladimir I. Voronin*, Senior Researcher, M. N. Mikheev Institute of Metal Physics of the Ural Branch of the Russian Academy of Sciences (Ekaterinburg, Russian Federation).

<https://orcid.org/0000-0002-3901-9812>  
voronin@imp.uran.ru

*Evgeny A. Kravtsov*, Head of Laboratory for Neutron-Synchrotron Research of Nanostructures, M.N. Mikheev Institute of Metal Physics of the Ural Branch of the Russian Academy of Sciences (Ekaterinburg, Russian Federation).

<https://orcid.org/0000-0002-5663-5692>  
kravtsov@imp.uran.ru

*Andrei V. Pozdin*, Assistant at the Department of Physical and Colloidal Chemistry, Ural Federal University named after the first President of Russia B. N. Yeltsin (Ekaterinburg, Russian Federation).

<https://orcid.org/0000-0002-6465-2476>  
andrei.pozdin@urfu.ru

*Markov Vyacheslav Filippovich*, Dr. Sci. (Chem.), Head of the Department of Physical and Colloidal Chemistry, Ural Federal University Named After the First President of Russia B. N. Yeltsin; Chief Researcher at the Department of Chemistry and Gorenje Processes, Ural Institute of State Fire Service of EMERCOM of Russia (Ekaterinburg, Russian Federation).

<https://orcid.org/0000-0003-0758-2958>  
v.f.markov@urfu.ru

*Received 02.11.2023; approved after reviewing 14.11.2023; accepted for publication 15.11.2023; published online 25.06.2024.*

*Translated by Yulia Dymant*

**Original articles**

Research article

<https://doi.org/10.17308/kcmf.2024.26/12043>**Theoretical exploration of halogenated anthracene derivatives: unraveling electronic and molecular insights****K. A. Othman<sup>1</sup>✉, Y. H. Azeez<sup>2</sup>, R. A. Omer<sup>1,3</sup>, R. O. Kareem<sup>2</sup>**<sup>1</sup>*Koya University, Faculty of Science & Health, Department of Chemistry, Koya KOY45, Kurdistan Region – F.R., Iraq*<sup>2</sup>*University of Halabja, College of Science, Department of Physics, Halabja 46018, Iraq*<sup>3</sup>*Department of Pharmacy, College of Pharmacy, Knowledge University, Erbil 44001, Iraq***Abstract**

This research article delves into the profound ramifications of halogenation on anthracene within the captivating domain of polycyclic aromatic hydrocarbons (PAHs). By employing Density Functional Theory (DFT) calculations, the study comprehensively explores the intricate interplay between halogen atoms and the molecular framework of anthracene. The entwining of halogens such as fluorine, chlorine, and bromine with aromatic rings orchestrates a symphony of changes, reshaping electronic structures, reactivity, and optical behaviors. This investigation traverses diverse analytical landscapes, encompassing molecular orbitals and Density of States analysis, UV-visibility spectra, infrared spectroscopy, nuclear magnetic resonance (NMR), and natural bond orbital (NBO) analysis, unveiling the intricate tapestry of molecular modifications. The electronic transitions, vibrational signatures, and NMR shifts of halogenated derivatives illuminate the dynamic effects of halogenation. Moreover, the study contemplates their potential across medicinal, environmental, and optoelectronic landscapes. Ultimately, this exploration presents a comprehensive narrative that harmonizes theoretical insights with practical applications.

**Keywords:** PAHs, Halogenation, Electronic Properties, DFT, Energy States, Frequency Analysis**Acknowledgments:** We would like to thank the heads of the chemistry departments at Koya University for their support.**For citation:** Othman K. A., Azeez Y. H., Omer R. A., Kareem R. O. Theoretical exploration of halogenated anthracene derivatives: unraveling electronic and molecular insights. *Condensed Matter and Interphases*. 2024;26(2): 280–294. <https://doi.org/10.17308/kcmf.2024.26/12043>**Для цитирования:** Осман Х. А., Азиз Ю. Х., Омер Р. А., Карим Р. О. Теоретическое исследование галогенированных производных антрацена: электронный и молекулярный аспект. *Конденсированные среды и межфазные границы*. 2024;26(2): 280–294. <https://doi.org/10.17308/kcmf.2024.26/12043>✉ Khdir A. Othman, [khdirehmed@koyauniversity.org](mailto:khdirehmed@koyauniversity.org)

© Othman K. A., Azeez Y. H., Omer R. A., Kareem R. O., 2024



The content is available under Creative Commons Attribution 4.0 License.

## 1. Introduction

Anthracene, a fundamental polycyclic aromatic hydrocarbon (PAH), embodies the intricate interplay among fused aromatic rings [1, 2]. Recent scientific attention has pivoted towards understanding the transformative impact of halogenation on these molecules, with halogens like fluorine, chlorine, and bromine intricately engaging with anthracene and reshaping its potential [3]. Halogenation is a precision tool that crafts a fresh narrative for PAHs, meticulously refining electronic structure and reactivity, altering energy levels, influencing absorption spectra, and sculpting fluorescence behavior [4–6]. The derivatives of halogenated anthracene beckon across diverse scientific horizons. In the realm of medicine, these derivatives hold promise as antibacterial and antifungal agents, candidates for innovative therapies against cancer and infectious diseases, and as components of advanced drug delivery systems [7–11]. Environmental considerations arise as halogenated PAHs traverse the realms of air, water, and soil, shaping their destiny and toxicity profiles, underscoring the importance of ecological understanding [12–14].

In this research endeavor, we embark on a computational journey, dissecting the effects of halogenation on anthracene and its derivatives. Employing analytical methods spanning molecular orbitals, UV-visibility, IR spectroscopy, NMR, Potential Energy Maps (PES), and more, we unravel the intricate tapestry of these molecules. From unraveling drug likeness to unveiling electronic intricacies, this study contributes to comprehending halogenated anthracene derivatives and their applications.

## 2. Computational procedure

In this study, Density Functional Theory (DFT) calculations were conducted using the Gaussian 09 computational package. The B3LYP functional was employed for molecular optimization, employing the 6-311G basis set [15–18].

## 3. Results and discussion

Anthracene and its derivatives doped with fluorine, chlorine, and bromine underwent design via GaussView. Subsequently, a DFT model was employed to optimize their structures,

utilizing the B3LYP/6-311G basis set known for its appropriateness in capturing low-energy configurations (i.e., basis set with the lowest energy [19–21]).

### 3.1. Molecular orbitals (MOs) and density of states (DOS) analysis

MOs and DOS analysis are pivotal for comprehending a material's electronic structure [22–24]. MOs define electron distribution within molecules, while DOS analysis illustrates energy level distribution (Figs. 1, 2). The energy gap, exemplified by the difference between the Highest Occupied Molecular Orbital (HOMO) and Lowest Unoccupied Molecular Orbital (LUMO) energies, significantly influences reactivity and optical attributes [25, 26]. For instance, in the context of halogen-doped anthracene, the undoped molecule displays a HOMO-LUMO gap of 3.5785 eV. Upon fluorine, chlorine, or bromine substitution, this gap decreases by 0.0069, 0.0224, and 0.0301 eV respectively, due to changes in electron distribution. This interplay between MOs, DOS analysis, and energy gap values offers a comprehensive understanding of electronic transitions, reactivity, and optical behavior in the realm of molecules and materials [27, 28]. Fig. 2 shows that the halogen-doped structures have higher DOS than anthracene, which means they have more available electron states at a given energy level. This could affect their electrical and optical properties.

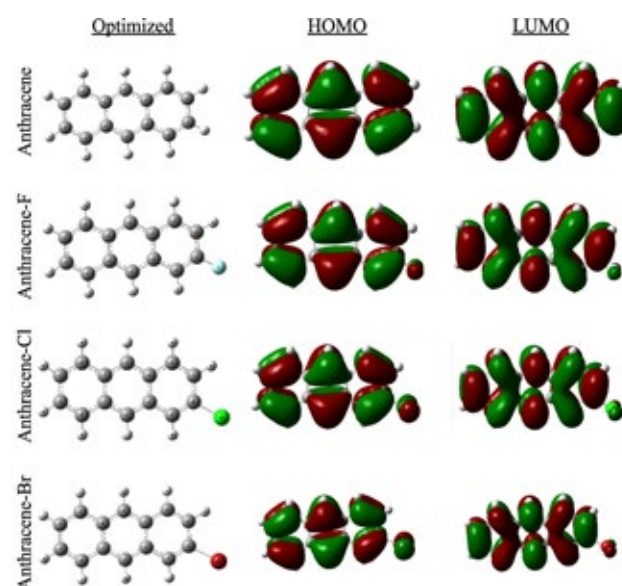
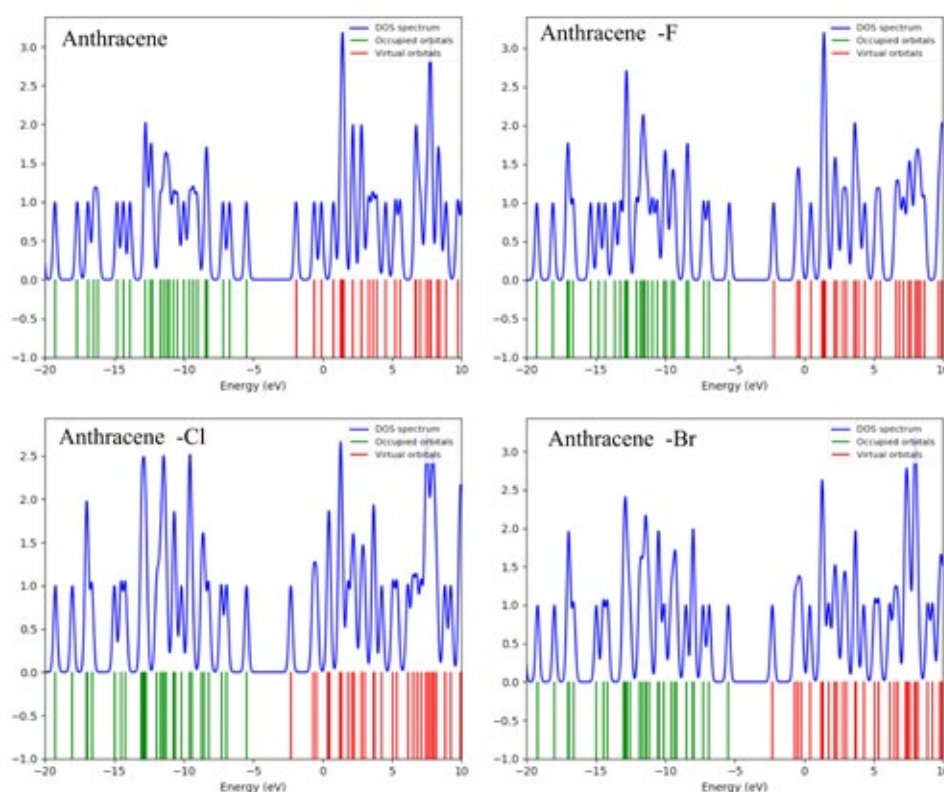


Fig. 1. Optimized structures and MOs of anthracene and its structures doped with halogens



**Fig. 2.** DOS analysis for anthracene and its halogen-doped structures

The quantum chemical parameters of anthracene and its halogen-substituted derivatives vary systematically with the size of the halogen atom (Table 1). For example, the total energy of the compounds decreases as the halogen atom becomes larger [29], from  $-14684.7709$  eV for anthracene to  $-84714.4531$  eV for anthracene-Br. This is because the halogen atoms have more electrons, Doping anthracene with halogens leads to a decrease in  $E_{\text{HOMO}}$  and  $E_{\text{LUMO}}$ . This effect is due to the higher electronegativity of halogen atoms, causing electron repulsion from the aromatic ring. Consequently, the  $\Delta E$  (HOMO-LUMO gap) of the compounds decreases in the order anthracene > anthracene-F > anthracene-Cl > anthracene-Br, indicating increased polarizability with larger halogen atoms [30–32].

The ionization potential ( $I$ ) and electron affinity ( $A$ ) of anthracene and its halogen derivatives increase with the size of the halogen atom, from 5.4899 eV and 1.9114 eV for anthracene to 5.6988 eV and 2.1504 eV for anthracene-Br, respectively. This is due to the lower HOMO and LUMO energies, which affect the ease of electron removal and addition [33]. The chemical hardness ( $\eta$ ) and softness ( $S$ ) of anthracene and

its halogen derivatives are inversely related to the size of the halogen atom [34]. The  $\eta$  values decrease from 1.7892 eV for anthracene to 1.7742 eV for anthracene-Br, due to the smaller HOMO-LUMO gap and higher polarizability. The  $S$  values increase from  $0.5589$  eV $^{-1}$  for anthracene to  $0.5636$  eV $^{-1}$  for anthracene-Br, due to the smaller HOMO-LUMO gap and higher reactivity. The electrophilicity ( $\omega$ ) and nucleophilicity ( $Nu$ ) of anthracene and its derivatives vary with the halogen doping. The  $\omega$  values exhibit an ascending trend from 3.8269 eV for anthracene to 4.3407 eV for anthracene-Br, due to the enhanced electrophilic nature of the halogens. The  $Nu$  values display a descending trend accordingly [35, 36]. The different halogen substituents (F, Cl, Br) have an impact on the electronic properties of the compounds, influencing parameters like  $\Delta E$  backdonation and the transfer electron fraction  $\Delta N$  (Fe). The specific effects are influenced by the nature of the halogen atom and its electronic interactions within the molecular structure

### 3.2. Ultraviolet-visible (UV-Vis) analysis

Gaussian software facilitated energy calculations, optimizing the structure with the



6-311G(d,p) basis set. The TD-SCF method was applied for electronic transition and absorption spectrum analysis [37–39]. Fig. 3 illustrates absorption coefficient variation with incident light wavelength, highlighting greater coefficients representing enhanced light absorption.

Anthracene possesses a series of conjugated double bonds, which impart it with various intriguing properties, notably its capability to absorb UV light [40–42].

Anthracene doping with the first three halogens increases electron density in the HOMO and LUMO orbitals. This reduces the energy gap between the HOMO and LUMO orbitals and affects the optical properties of the anthracene molecule. Consequently, the electrons at the HOMO of the doped molecules require energy with a lower frequency and higher wavelength to transition from HOMO to LUMO [43]. This phenomenon enhances the likelihood of the doped molecules absorbing light in the visible spectrum (Fig. 3). As a result, the doped molecules exhibit more pronounced coloration compared to the undoped molecules (i.e.,  $\lambda = 382.8, 384.3, 387,$  and  $430.2$  nm for Anthracene,

anthracene-F, anthracene-Br, and anthracene-Cl respectively).

### 3.3. Infrared (IR) analysis

Gaussian software was utilized to perform energy calculations, resulting in the optimized structure obtained through the 6-311G(d,p) basis set [40, 44].

The identification of conjugated rings within the anthracene structure is facilitated by its distinctive aromatic C–H stretching. Notably, the C–H stretching vibrations of PAHs are commonly observed around  $3100\text{ cm}^{-1}$  [45–49]. This study calculates the theoretically estimated aromatic C–H stretching vibrational modes within the range of  $3154\text{--}3188\text{ cm}^{-1}$  (Fig. 4).

The study's exploration of halogen doping's impact on the infrared (IR) spectra of anthracene uncovers noteworthy transformations. Initially, the introduction of halogen atoms induces shifts in absorption peak positions, signifying changes in molecular vibrations and bond strengths (e.g., C=C-H in undoped anthracene at  $3154\text{--}3188\text{ cm}^{-1}$ , shifting to  $3295\text{--}3321\text{ cm}^{-1}$  for fluorine-doped anthracene). Moreover, novel absorption bands

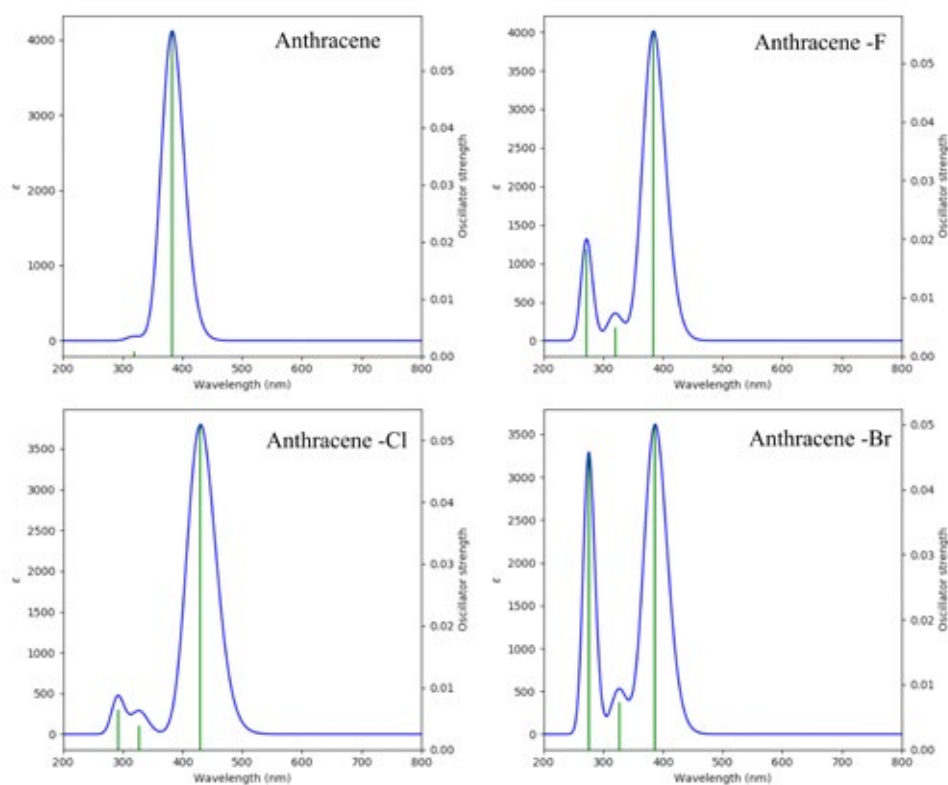


Fig. 3. UV-Vis. absorption spectra of anthracene and its halogen-doped derivatives

emerge, indicating the formation of fresh vibrational modes and functional groups. The study also detects alterations in intensity and band width for specific absorption peaks, indicative of variations in molecular flexibility and rigidity. Notably, the presence of halogen atoms introduces distinct IR absorption peaks linked to the halogen groups themselves. Collectively, this investigation offers valuable insights into the modifications induced by halogen doping, shedding light on their intricate influence on the IR spectra of these molecules.

### 3.4. Nuclear magnetic resonance (NMR)

Fig. 5 illustrates the theoretically computed H-NMR and C-NMR structures for both pristine anthracene and its derivatives doped with the first three halogen group members. The NMR calculations were performed using Gaussian 09 software. The shielding range for normal anthracene spans from  $-50$  to  $100$  ppm [24]. Notably, introducing fluorine caused a ppm shift ranging from  $-100$  to  $300$  ppm. This ppm shifts persisted when chlorine replaced fluorine, spanning from  $-200$  to  $700$  ppm. With

the introduction of bromine, the ppm shift intensified, ranging from  $-500$  to  $2000$  ppm. This trend indicated an expanded shielding range corresponding to the increasing electronegativity of the halogen family. Fig. 5 portrays the original NMR peaks of undoped anthracene, with more carbon resonances at the upfield and fewer at the downfield. The introduction of fluorine led to a notable transformation in molecule orientation. A distinct medium peak for fluorine emerged at  $290.128$  ppm, while carbon and hydrogen atoms underwent chemical environment changes due to inductive and neighboring effects. The same pattern held when chlorine and later bromine replaced fluorine, manifesting peaks at  $704.749$  and  $1968.174$  ppm, respectively. This observation underscores the linear relationship between NMR peaks generated by halogen family members in anthracene and their electronegativity.

### 3.5. Potential energy map (PEM) and charge distribution

The PES and charge distribution significantly impact the molecular orientation and influence the optical and electrical properties of the

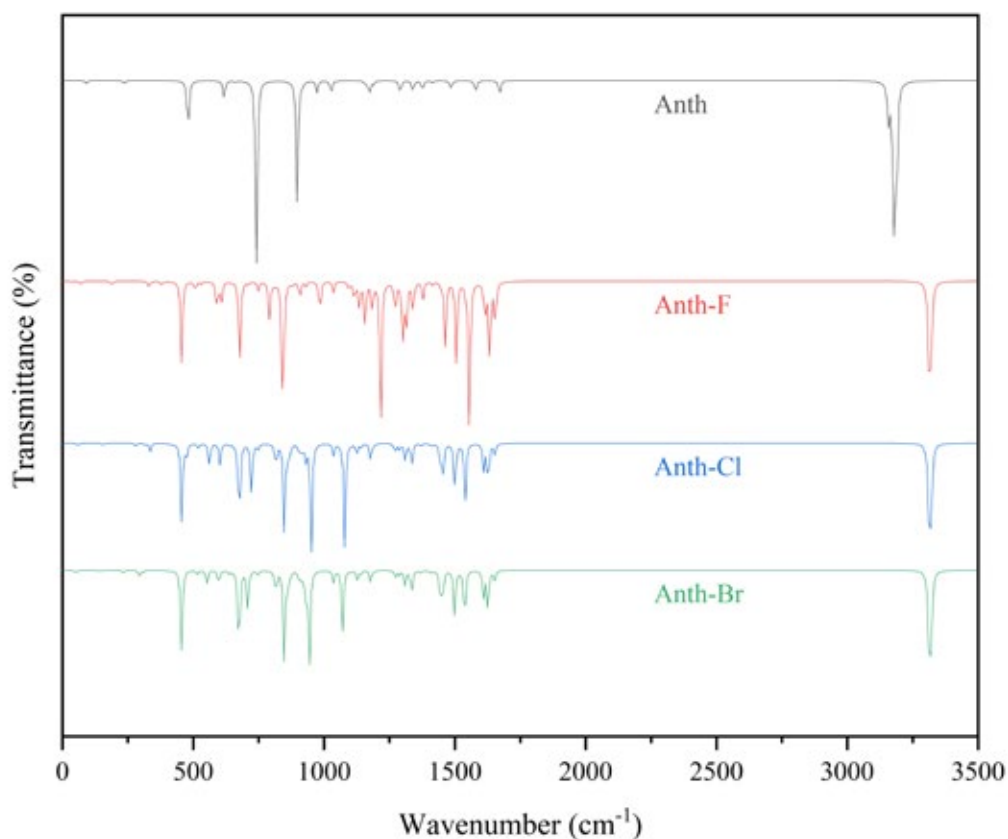


Fig. 4. IR spectrum for anthracene and its halogenation with F, Cl and Br

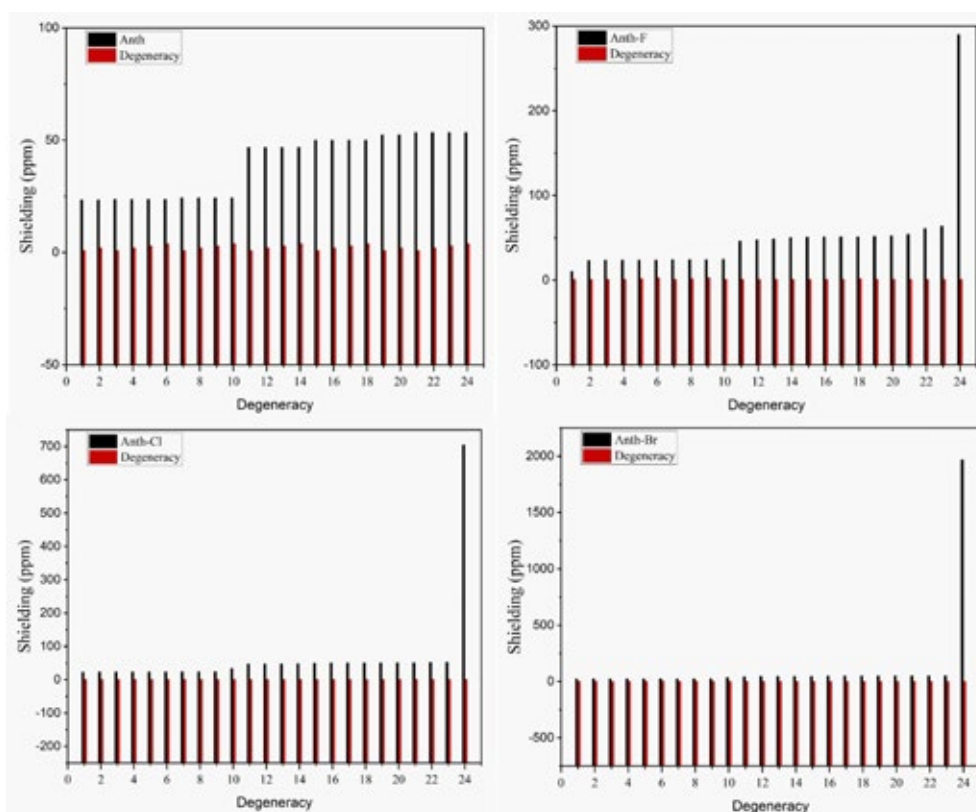


Fig. 5. NMR of anthracene and its halogen-doped derivatives

molecules [50–52]. Fig. 6 shows the PESs of anthracene and its halogen-doped derivatives. These maps illustrate how the charge distribution of a molecule varies in three dimensions, using different colors to indicate high and low charge density regions. The charge distribution is calculated as the net charge on each atom or group of atoms in a molecule. The arrows in Figure 6 represent the direction and magnitude of the dipole moments of each molecule. The dipole moment is a vector quantity that measures the molecular polarity, or the degree of separation

of positive and negative charges in a molecule. A higher dipole moment indicates a more polar molecule.

Anthracene has a symmetrical charge distribution and no net dipole moment, as shown in Fig. 6 and Table 1. This means that it is a non-polar molecule with no net charge. However, when anthracene is doped with halogens, such as fluorine, chlorine, or bromine, its charge distribution and polarity change dramatically. Halogens are more electronegative than carbon and hydrogen [53], which means that they pull

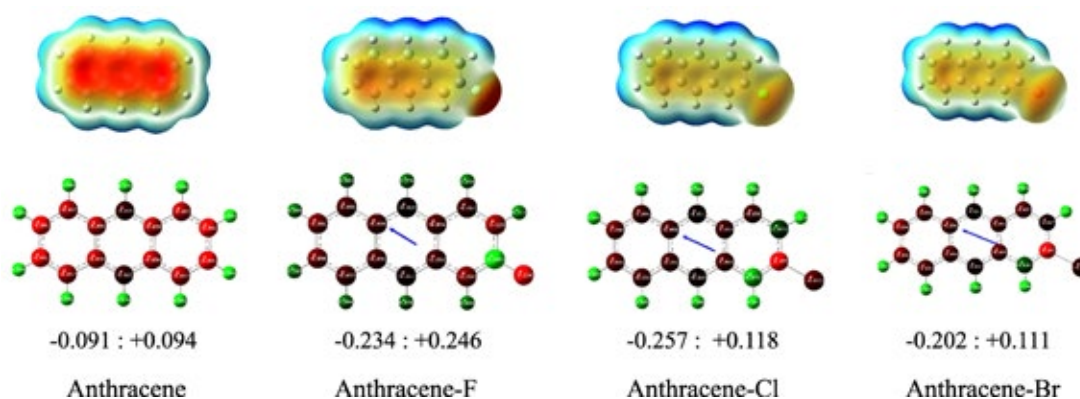


Fig. 6. PEM and charge distributions for anthracene and its halogen-doped structures

**Table 1.** Quantum chemical parameter's values of study compounds

Quantum chemical parameters	Anthanthrene	Anthanthrene-F	Anthanthrene-Cl	Anthanthrene-Br
Total Energy (eV)	-14684.7709	-17385.8899	-27191,7283	-84714.4531
$E_{\text{HOMO}}$ (eV)	-5.4899	-5.6231	-5.7072	-5.6988
$E_{\text{LUMO}}$ (eV)	-1.9114	-2.0515	-2.1511	-2.1504
$\Delta E$ (eV)	3.5785	3.5716	3.5561	3.5484
Ionization potential $I$ (eV)	5.4899	5.6231	5.7072	5.6988
Electron affinity $A$ (eV)	1.9114	2.0515	2.1511	2.1504
Chemical hardness « $\eta$ » (eV)	1.7892	1.7858	1.7780	1.7742
Chemical softness $S$ (eV <sup>-1</sup> )	0.5589	0.5600	0.5624	0.5636
Electronegativity $\chi$ (eV)	3.7006	3.8373	3.9292	3.9246
Chemical potential $\mu$ (eV)	-3.7006	-3.8373	-3.9292	-3.9246
Electrophilicity $\omega$ (eV)	3.8269	4.1228	4.3414	4.3407
Nucleophilicity $Nu$ (eV <sup>-1</sup> )	0.2613	0.2426	0.2303	0.2304
$\Delta E$ backdonation	-0.4473	-0.4464	-0.4445	-0.4436
Transfer electron fraction $\Delta N$	2.9517	2.8239	2.7300	2.7282
Dipole-moment (Debye), « $\mu D$ »	0.0000	1.7247	2.3449	2.2182

more electrons towards themselves. This causes a shift of electron density from the carbon rings to the halogen atom, creating an asymmetrical charge distribution and a net dipole moment in the molecule. Table 1 show that chlorine-doped anthracene has the largest dipole moment (2.3449), followed by bromine-doped (2.2182), and fluorine-doped anthracene (1.7247). This implies that chlorine-doped anthracene is the most polar and reactive molecule among the four shown in Fig. 6.

### 3.6. Reduced density gradient (RDG) and noncovalent interactions (NCI)

The innovative utilization of reduced density gradient (RDG) and noncovalent interactions (NCI) has revolutionized the exploration of weak intermolecular forces. Through the RDG methodology, the NCI index serves as a compelling tool to substantiate non-covalent interactions. RDG is a dimensionless parameter that synergizes density and its derivative. Employing Multiwfn for RDG in eq. (1) scatter plots and VMD for 3D isosurfaces, the visualization of these intricate interactions is enriched:

$$RDG(r) = \frac{1|\nabla\rho(r)|}{2(3\pi r^2)^{\frac{1}{3}}\rho^{\frac{4}{3}}(r)}. \quad (1)$$

The investigative NCI pursuits are founded on an isosurface threshold of 0.5, within the

RDG isosurface scope of -0.035 to 0.02 atomic units, as elegantly showcased in Fig. 7. This analysis is further elevated through graphical representation, which correlates the function  $\rho(r)$  with the sign of  $\lambda_2$ , offering profound insights into molecular interactions. The polarity of  $\text{sign}(\lambda_2)\rho$  yields invaluable predictions: a negative value signifies attractive, bound interactions, while a positive value signifies repulsive, non-bonded interactions. The scatter graphs in Fig. 7 transcends visual complexity. By stratifying spikes based on  $\text{sign}(\lambda_2)\rho$ , distinct color-coded zones emerge—red for robust repulsion, green for delicate attraction (van der Waals), and blue for potent intermolecular interactions, particularly robust hydrogen bonding. These advancements underscore the pivotal role of RDG and NCI methodologies in decoding intricate intermolecular dynamics [54–58].

When compared to other compounds, those containing fluorine display a heightened concentration of points on the graph. This finding indicates that weak hydrogen bonds and van der Waals interactions within fluorine-containing compounds are more robust. This insight is underscored by the red patches in Fig. 7, which are localized within aromatic rings and signify significant repulsive interactions. Furthermore, in the same Fig. 7, a green isosurface linked to the anthracene compound emerges, highlighting van der Waals interactions. This specific isosurface's



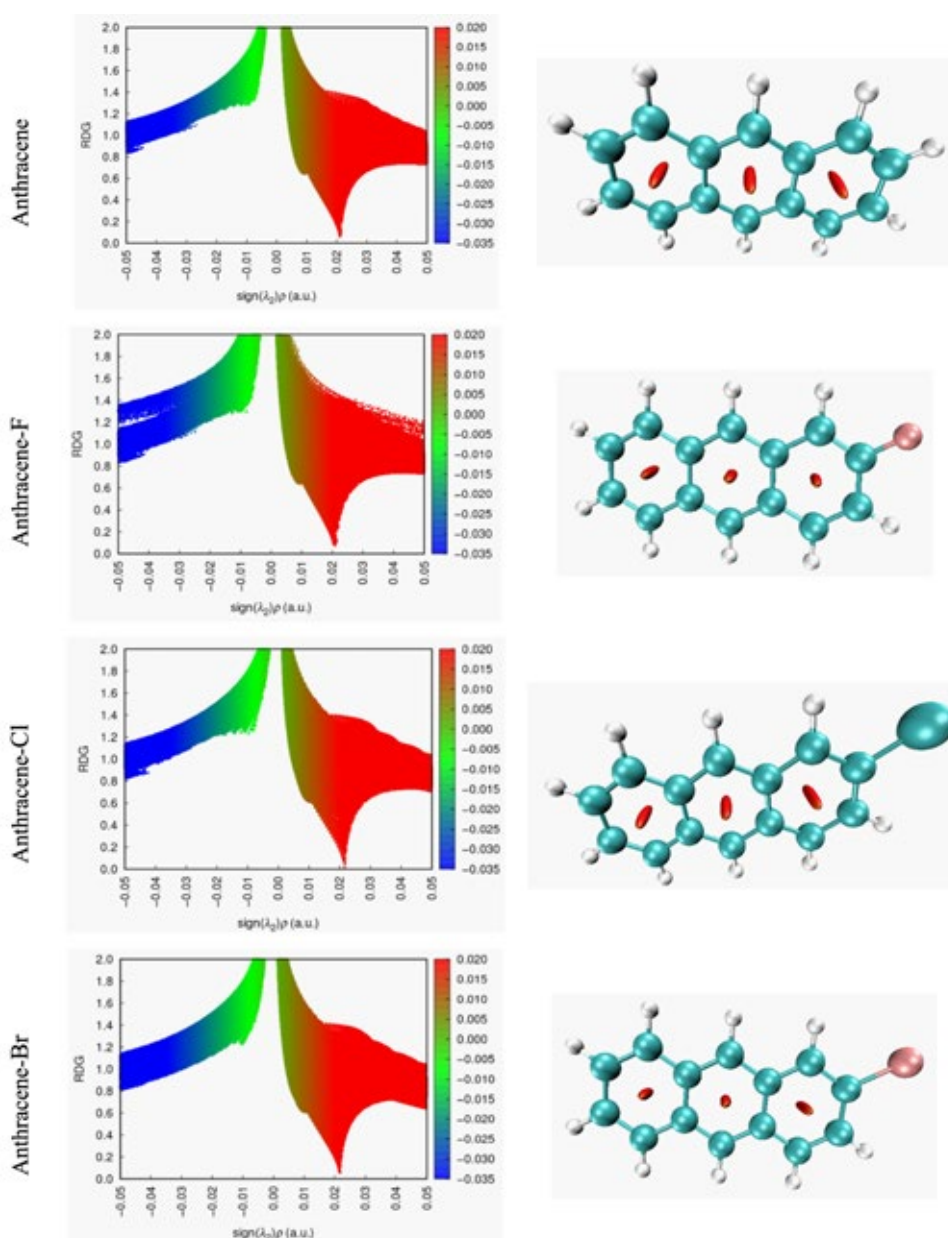


**Fig. 7.** RDG Analysis of Studied Compounds – Weak and Strong Interactions

positioning corroborates the presence of these interactions. Simultaneously, it provides evidence for weak hydrogen bonding and additional hydrogen-hydrogen contacts (H–H).

Evaluating a compound's potential as a drug involves essential steps, often employing Molinspiration property values in alignment with Lipinski's rule of five. This widely recognized guideline suggests that successful drugs typically adhere to specific criteria: fewer than five hydrogen bond donors, less than ten hydrogen bond acceptors, a molar refractivity within 40 to 160, a polar surface area below  $140 \text{ \AA}^2$ , a molecular

weight under 500, and containing fewer than ten rotatable bonds [59, 60].

Table 2 shows how the molecular properties of anthracene and its halogenated derivatives vary depending on the type of halogen attached. The molecular weight of anthracene increases with the size and polarizability of the halogen, making it less volatile and dense. The HBA of anthracene increases by one when fluorine is added, enhancing its hydrogen bonding and solubility. The PSA of anthracene and its derivatives remains zero, indicating a low polarity and a high permeability. These properties

**Table 2.** Molinspiration property values for the studied compounds

Descriptors	Anthracene				Expected range
	Neutral	+Cl	+Br	+F	
Hydrogen bond donor (HBD)	0	0	0	0	5
Hydrogen bond acceptors (HBA)	0	0	0	1	10
Molar Refractivity	61.45	66.46	69.15	61.41	40–160
Polar surface area (PSA) Å <sup>2</sup>	0.00	0.00	0	0	140
Molecular weight	178.23	212.67	257.13	196.22	500
Number of rotatable bonds	0	0	0	0	10

are important for the chemical and biological behavior of these molecules.

### 3.7. Natural bond orbital (NBO) analysis

Utilizing B3LYP/6–31G(d, p) theoretical methods, this study extensively investigated the NBO configuration of the compound in question. The main focus was on elucidating interactions between Lewis and non-Lewis orbitals, shedding light on intramolecular and intermolecular hydrogen bonding, as well as  $\pi$  electron dispersion. Stabilization energy, a measure of delocalization interactions, was evaluated using second-order energy for individual donor NBOs ( $i$ ) and acceptor NBOs ( $j$ ) in eq. (2), leading to  $E^{(2)}$  values capturing electron delocalization. This concept is mathematically expressed by the equation [61–65]:

$$E^{(2)}q = \Delta E_{ij} = q_i \frac{F(i, j)^2}{\epsilon_j - \epsilon_i} \quad (2)$$

Here, “ $q_i$ ” denotes donor orbital occupancy, “ $\epsilon_j$ ” and “ $\epsilon_i$ ” represent diagonal elements, and “ $F(i, j)$ ” signifies NBO Fock matrix elements. Table 3 provides an in-depth exploration through Second Order Perturbation Theory Analysis of the Fock Matrix in NBO for a range of compounds, specifically Anthracene and its derivatives: Anthracene (neutral), Anthracene (+Cl), Anthracene (+Br), and Anthracene (+F). The table unveils a rich tapestry of insights into the interactions between donor and acceptor NBOs, revealing  $E^{(2)}$  values that correspond to significant stabilization energies. Moreover, it showcases the differences in energy ( $E(j) - E(i)$ ) in atomic units and the associated  $F(i, j)$  values in atomic units, further underlining the complex interplay of

forces within these molecules. Drawing attention to specific examples, Anthracene (+Br) stands out with a remarkable transition, as the LP (3) Br 24 orbital donates to the  $\pi^*$  C 17 – C 20 acceptor, resulting in a substantial stabilization energy of 78.61 kcal/mol. This transition underscores the magnitude of intermolecular interactions, indicative of a strong binding affinity between the Br atom and the phenyl ring. Comparing across the various derivatives, Anthracene (+F) demonstrates noteworthy interactions as well. Here,  $\pi$  C 1 – C 6 engages with  $\pi^*$  C 4 – C 5, leading to a stabilization energy of 17.39 kcal/mol. This interaction, while energetically favorable, highlights the relatively weaker influence of fluorine compared to other substituents like chlorine and bromine.

### 3.8. Nonlinear optical (NLO) properties

NLO materials are of paramount importance in the realm of nonlinear optics, playing a pivotal role in fields such as information technology and various industrial applications. The optimization of geometry was carried out through the B3LYP/6–31G+(d,p) method, followed by an initial static analysis. The computation of the three-dimensional tensor, denoted as ( $\beta_0$ ) representing the initial static hyperpolarizability, involved equations for its x, y, and z components (eq. (3)). These components contribute to determining the overall static dipole moment ( $\mu_t$ ), the mean polarizability ( $\alpha_0$ ), and the initial static hyperpolarizability ( $\beta_0$ ) [61, 66]:

$$\mu_t = \left[ \mu_x^2 + \mu_y^2 + \mu_z^2 \right]^{\frac{1}{2}},$$

$$\alpha_t = \frac{(\alpha_{xx} + \alpha_{yy} + \alpha_{zz})}{3},$$

**Table 3.** Second order perturbation theory analysis of Fock Matrix in NBO for Studied Compounds

Anthracene (neutral)				
Donor NBO ( <i>i</i> )	Acceptor NBO ( <i>j</i> )	<i>E</i> (2) kcal/mol	<i>E</i> ( <i>j</i> )– <i>E</i> ( <i>i</i> ) a.u.	<i>F</i> ( <i>i,j</i> ) a.u.
$\pi$ C 1 – C 2	$\pi^*$ C 3 – C 4	17.63	0.28	0.063
$\pi$ C 1 – C 2	$\pi^*$ C 9 – C 10	18.4	0.29	0.068
$\sigma$ C 1 – H 7	$\sigma^*$ C 5 – C 6	4.96	1.04	0.064
$\pi$ C 9 – C 10	$\pi^*$ C 1 – C 2	17.17	0.3	0.066
$\pi$ C 9 – C 10	$\pi^*$ C 11 – C 12	16.43	0.3	0.063
$\sigma$ C 9 – H 13	$\sigma$ C 2 – C 3	4.59	1.04	0.062
$\pi$ C 18 – C 19	LP (1) C 5	35.32	0.16	0.085
LP (1) C 5	$\pi^*$ C 3 – C 4	69.28	0.14	0.106
LP (1) C 5	$\pi^*$ C 18 – C 19	52.46	0.14	0.099
LP*(1) C 6	$\pi^*$ C 1 – C 2	69.27	0.14	0.106
Anthracene (+Cl)				
$\pi$ C 1 – C 2	$\pi^*$ C 9 – C 10	21.32	0.28	0.071
$\sigma$ C 1 – H 7	$\sigma^*$ C 5 – C 6	4.65	1.1	0.064
$\sigma$ C 2 – C 9	$\sigma^*$ C 2 – C 3	4.76	1.26	0.069
$\sigma$ C 6 – C 17	$\sigma^*$ C 20 – Cl 24	5.09	0.83	0.058
$\pi$ C 11 – C 12	$\pi^*$ C 9 – C 10	19.14	0.28	0.066
$\pi$ C 18 – C 19	$\pi^*$ C 4 – C 5	18.92	0.29	0.069
LP*(1) C 3	$\pi^*$ C 1 – C 2	72.87	0.14	0.107
LP (1) C 6	$\pi^*$ C 1 – C 2	67.29	0.14	0.104
LP (1) C 6	$\pi^*$ C 17 – C 20	78.61	0.12	0.106
$\pi^*$ C 17 – C 20	$\pi^*$ C 18 – C 19	191.31	0.01	0.077
Anthracene (+Br)				
$\sigma$ C 1 – C 6	$\sigma^*$ C 5 – C 6	4.85	1.26	0.07
$\sigma$ C 6 – C 17	$\sigma^*$ C 20 – Br 24	5.23	0.78	0.057
$\pi$ C 9 – C 10	$\pi^*$ C 1 – C 2	19.86	0.29	0.07
$\pi$ C 11 – C 12	$\pi^*$ C 9 – C 10	19.13	0.28	0.066
$\sigma$ C 12 – H 16	$\sigma^*$ C 2 – C 3	4.85	1.1	0.066
$\sigma$ C 18 – C 19	$\sigma^*$ C 20 – Br 24	5.32	0.79	0.058
LP*(1) C 3	$\pi^*$ C 1 – C 2	72.77	0.14	0.107
LP (1) C 6	$\pi^*$ C 17 – C 20	78.4	0.12	0.106
LP (3) Br 24	$\pi^*$ C 17 – C 20	10.54	0.31	0.054
$\pi^*$ C 17 – C 20	$\pi^*$ C 18 – C 19	196.36	0.01	0.077
Anthracene (+F)				
$\pi$ C 1 – C 6	$\pi^*$ C 4 – C 5	17.39	0.28	0.063
$\pi$ C 1 – C 6	$\pi^*$ C 17 – C 20	18.45	0.28	0.066
$\sigma$ C 1 – H 7	$\sigma^*$ C 2 – C 3	4.97	1.04	0.064
$\sigma$ C 4 – H 8	$\sigma^*$ C 5 – C 6	5.01	1.04	0.065
$\pi$ C 17 – C 20	$\pi^*$ C 18 – C 19	15.31	0.31	0.062
$\pi$ C 18 – C 19	$\pi^*$ C 4 – C 5	15.86	0.3	0.065
LP*(1) C 2	$\pi^*$ C 1 – C 6	69.7	0.14	0.105
LP*(1) C 2	$\pi^*$ C 9 – C 10	51.66	0.14	0.098
LP (1) C 3	$\pi^*$ C 11 – C 12	52.31	0.14	0.099
LP (3) F 24	$\pi^*$ C 17 – C 20	19.73	0.44	0.087

$$\beta_t = (\beta_x^2 + \beta_y^2 + \beta_z^2)^{\frac{1}{2}} \beta_x = \beta_{xxx} + \beta_{xyz} + \beta_{xzz} \beta_y = \beta_{yy} + (3) \\ + \beta_{xy} + \beta_{yz} \beta_z = \beta_{zzz} + \beta_{xxz} + \beta_{yzz}.$$

Notably, significant magnitudes of specific polarizability and hyperpolarizability components indicate a pronounced dispersion of charge in particular orientations [67, 68] Table 4 presents the computed values for compounds with different substitutions (+Cl, +Br, +F), revealing their molecular dipole moments ( $\mu$ ), mean polarizabilities ( $\alpha_0$ ), and initial hyperpolarizabilities ( $\beta_0$ ). These values, initially provided in atomic units (a.u.), have been conveniently converted into electrostatic units (e.s.u.) for better comparability. Remarkably, the dipole moments of the compounds (+Cl, +Br, +F) surpass that of the well-known molecule Urea ( $\mu = 1.3732$  D), often employed as a benchmark in NLO investigations.

Turning to polarizabilities, the results highlight that anthracene exhibits heightened polarizability when subjected to a positive inductive effect (+F), whereas Anthracene displays reduced polarizability under a positive inductive effect (+Br). In the context of NLO systems, the magnitude of ( $\beta_0$ ) holds substantial significance. Notably, the computed  $\beta_0$  values for the examined compounds are comparatively lower than the benchmark value of urea ( $343.272 \cdot 10^{-33}$  esu), suggesting that these compounds might have limited potential for practical NLO applications.

#### 4. Conclusions

In this comprehensive research article, the profound impact of halogenation on anthracene has been intricately unveiled. Through DFT calculations, we navigated the intricacies of electronic structure, reactivity, and optical behavior as they respond to the presence of halogen atoms. The resulting insights underscore the delicate symphony of changes introduced by halogens like fluorine, chlorine, and bromine, reshaping the properties and potential of these PAHs. Analytical explorations, spanning MOs, UV-visibility spectra, vibrational signatures, NMR shifts, and NBO analysis, collectively illustrate the multifaceted impact of halogenation. This research extends beyond theoretical boundaries to embrace practical realms, offering glimpses

**Table 4.** Nonlinear optical properties of the title compounds

Parameters	Anthracene			
	Neutral	+Cl	+Br	+F
$\mu_x$	0.00	1.00	-0.91	0.16
$\mu_y$	0.00	2.11	1.96	1.72
$\mu_z$	0.00	0.00	0.00	0.00
$\mu_t$	0.00	2.33	2.16	1.73
$\alpha_{xx}$	-88.00	-82.73	-87.81	-73.86
$\alpha_{yy}$	-70.76	-92.01	-93.64	-85.13
$\alpha_{zz}$	-71.35	-99.63	-105.33	-91.38
$\alpha_0$	-76.70	-91.46	-95.59	-83.46
$\alpha(esu) * 10^{-24}$	-11.37	-13.55	-14.17	-12.37
$\beta_{xxx}$	0.00	3.00	26.22	-13.72
$\beta_{xyy}$	0.00	16.86	3.93	17.15
$\beta_{xzz}$	0.00	-3.38	16.47	-6.69
$\beta_x$	0.00	16.48	46.62	-3.26
$\beta_{yyy}$	0.00	53.18	-64.00	-34.45
$\beta_{xyx}$	0.00	3.46	-30.20	4.96
$\beta_{yzz}$	0.00	-11.73	-53.29	16.86
$\beta_y$	0.00	44.91	-147.50	-12.63
$\beta_{zzz}$	0.00	0.00	0.00	0.00
$\beta_{xxz}$	0.00	0.00	0.00	0.00
$\beta_{yyz}$	0.00	0.00	0.00	0.00
$\beta_z$	0.00	0.00	0.00	0.00
$\beta_0(esu) * 10^{-33}$	0.00	47.84	154.69	13.4

into advancements in medicine, considerations for the environment, and the potential of organic electronics. As we draw the curtains on this symphony of insights, we find that halogenation, with its transformative effects, holds the promise of enhancing anthracene's properties across a spectrum of scientific domains, seamlessly blending theoretical understanding with real-world applications.

#### Contribution of the authors

The authors contributed equally to this article.



## Conflict of interests

The authors declare that they have no known competing financial interests or personal relationships that could have influenced the work reported in this paper.

## References

1. Rebaz O. Rashid R., Othman K. Exploring The Synthesis of 1,2,4-Triazole Derivatives: A Comprehensive Review. *Journal of Physical Chemistry and Functional Materials*. 2023;6(1): 43–56, <https://doi.org/10.54565/jphcfum.1263834>
2. Omar R. Koparir P., Koparir M. Synthesis of 1,3-thiazole derivatives. *Indian Drugs*. 2021;58(1): 7–19. <https://doi.org/10.53879/id.58.01.12427>
3. Tang M., Yu Q., Wang Z., ... Zhang F. L. Synthesis of polycyclic aromatic hydrocarbons (PAHs) via a transient directing group. *Organic Letters*. 2018;20(23): 7620–7623. <https://doi.org/10.1021/acs.orglett.8b03359>
4. Lawal A. T. and Fantke P. Polycyclic aromatic hydrocarbons. A review. *Cogent Environmental Science*. 2017;3(1): 1339841. <https://doi.org/10.1080/23311843.2017.1339841>
5. Ding Z. B. Tommasini M., Maestri M. A topological model for predicting adsorption energies of polycyclic aromatic hydrocarbons on late-transition metal surfaces. *Reaction Chemistry & Engineering*. 2019;4(2): 410–417. <https://doi.org/10.1039/c8re00229k>
6. Rebaz O. Ahmed L. Koparir P., Jwameer H. Impact of solvent polarity on the molecular properties of dimetridazole. *El-Cezeri Fen ve Mühendislik Dergisi*. 2022;9(2): 740–747. <https://doi.org/10.31202/ecjse.1000757>
7. Mccoull K. D. Rindgen D. Blair I. A. and Penning T. M. Synthesis and characterization of polycyclic aromatic hydrocarbon o-quinone depurinating N7-guanine adducts. *Chemical Research in Toxicology*. 1999;12(3): 237–246, <https://doi.org/10.1021/tx980182z>
8. Sahoo B. M. Ravi Kumar B. V. V., Banik B. K., Borah P. Polyaromatic hydrocarbons (PAHs): structures, synthesis and their biological profile. *Current Organic Synthesis*. 2020;17(8): 625–640. <https://doi.org/10.2174/1570179417666200713182441>
9. Barbosa F., Jr. Rocha B. A., Souza M. C. O., ... Campiglia A. D. Polycyclic aromatic hydrocarbons (PAHs): Updated aspects of their determination, kinetics in the human body, and toxicity. *Journal of Toxicology and Environmental Health, Part B*. 2023;26(1): 28–65. <https://doi.org/10.1080/10937404.2022.2164390>
10. Palmer A. J. Ghani R. A. Kaur N. Phanstiel O., Wallace H. M. A putrescine–anthracene conjugate: a paradigm for selective drug delivery. *Biochemical Journal*. 2009;424(3): 431–438. <https://doi.org/10.1042/BJ20090815>
11. Koparir P., Parlak A. E., Karatepe A., Omar R. A. Elucidation of potential anticancer, antioxidant and antimicrobial properties of some new triazole compounds bearing pyridine-4-yl moiety and cyclobutane ring. *Arabian Journal of Chemistry*. 2022;15(7): 103957. <https://doi.org/10.1016/j.arabj.2022.103957>
12. Haritash A. K., Kaushik C. P. Biodegradation aspects of Polycyclic Aromatic Hydrocarbons (PAHs): A review. *Journal of Hazardous Materials*. 2009;169(1–3): 1–15. <https://doi.org/10.1016/j.jhazmat.2009.03.137>
13. Abdel-Shafy H. I., Mansour M. S. M. A review on polycyclic aromatic hydrocarbons: Source, environmental impact, effect on human health and remediation. *Egyptian Journal of Petroleum*. 2016;25(1): 107–123. <https://doi.org/10.1016/j.ejpe.2015.03.011>
14. Li W., Wu S. Challenges of halogenated polycyclic aromatic hydrocarbons in foods: Occurrence, risk, and formation. *Trends in Food Science & Technology*. 2023;131: 1–13. <https://doi.org/10.1016/j.tifs.2022.11.015>
15. Montgomery Jr. J. A., Frisch M. J., Ochterski J. W., Petersson G. A. A complete basis set model chemistry. VI. Use of density functional geometries and frequencies. *The Journal of Chemical Physics*. 1999;110(6): 2822–2827. <https://doi.org/10.1063/1.477924>
16. Rasul H. H., Mamad D. M., Azeez Y. H., Omer R. A., Omer K. A. Theoretical investigation on corrosion inhibition efficiency of some amino acid compounds. *Computational and Theoretical Chemistry*. 2023;1225: 114177. <https://doi.org/10.1016/j.comptc.2023.114177>
17. Omer R. A. Koparir P., Ahmed L. Theoretical determination of corrosion inhibitor activities of 4-allyl-5-(pyridin-4-yl)-4H-1,2,4-triazole-3-thiothione tautomerism. *Indian Journal of Chemical Technology*. 2022;29(1): 75–81. <https://doi.org/10.56042/ijct.v29i1.51231>
18. Omer R., Koparir P., Koparir M., Rashid R., Ahmed L., Hama J. Synthesis, Characterization and DFT Study of 1-(3-Mesityl-3-methylcyclobutyl)-2-((4-phenyl-5-(thiophen-2-yl)-4H-1,2,4-triazol-3-yl)thio)ethan-1-one. *Protection of Metals and Physical Chemistry of Surfaces*. 2022;58(5): 1077–1089. <https://doi.org/10.1134/S2070205122050185>
19. Costa A. C., Jr. Ondar G. F., Versiane O., ... Tellez Soto C. A. DFT: B3LYP/6-311G (d, p) vibrational analysis of bis-(diethyldithiocarbamate)zinc (II) and natural bond orbitals. *Spectrochimica Acta Part A: Molecular and Biomolecular Spectroscopy*. 2013;105: 251–258. <https://doi.org/10.1016/j.saa.2012.11.097>

20. Tirado-Rives J., Jorgensen W. L. Performance of B3LYP density functional methods for a large set of organic molecules. *Journal of Chemical Theory and Computation*. 2008;4(2): 297–306. <https://doi.org/10.1021/ct700248k>
21. Nasidi I. I., Kaygili O., Majid A., Bulut N., Alkhedher M., ElDin S. M. Halogen doping to control the band gap of ascorbic acid: A theoretical study. *ACS Omega*. 2022; 7(48): 44390–44397. <https://doi.org/10.1021/acsomega.2c06075>
22. Dittmer D. C., Chang P. L., Davis F. A., Iwanami M., Stamos I., Takahashi K. Derivatives of thiacyclobutene (thiete). VI. Synthesis and properties of some thietes. *The Journal of Organic Chemistry*. 1972;37(8): 1111–1115. <https://doi.org/10.1021/jo00973a008>
23. Becke A. D. Density-functional thermochemistry. III. The role of exact exchange. *The Journal of Chemical Physics*. 1993;98(7): 5648–5652. <https://doi.org/10.1063/1.464913>
24. Wilbur D., Manning W. B., Hilton B. D., Muschik G. M. Carbon-13 NMR of polycyclic aromatic compounds. 1-Methoxybenz[a]anthracene-7, 12-diones. *Organic Magnetic Resonance*. 1982;18(2): 63–67. <https://doi.org/10.1002/mrc.1270180202>
25. Aihara J. Reduced HOMO–LUMO gap as an index of kinetic stability for polycyclic aromatic hydrocarbons. *The Journal of Physical Chemistry A*. 1999;103(37): 7487–7495. <https://doi.org/10.1021/jp990092i>
26. Sun Z., Wu J. Open-shell polycyclic aromatic hydrocarbons. *Journal of Materials Chemistry*. 2012;22(10): 4151–4160. <https://doi.org/10.1039/C1JM14786B>
27. Aziz S. B., Abdullah O. G., Hussein A. M., ... Mohammed A. R. Optical properties of pure and doped PVA:PEO based solid polymer blend electrolytes: two methods for band gap study. *Journal of Materials Science: Materials in Electronics*. 2017;28: 7473–7479. <https://doi.org/10.1007/s10854-017-6437-1>
28. Sarmah A., Hobza P. Directly linked metalloporphyrins: a quest for bio-inspired materials. *Materials Advances*. 2020;1(6): 1895–1908. <https://doi.org/10.1039/d0ma00461h>
29. Lazarou Y. G., Prosmittis A. V., Papadimitriou V. C., Papagiannakopoulos P. Theoretical calculation of bond dissociation energies and enthalpies of formation for halogenated molecules. *The Journal of Physical Chemistry A*. 2001;105(27): 6729–6742. <https://doi.org/10.1021/jp010309k>
30. Tang M. L., Bao Z. Halogenated materials as organic semiconductors. *Chemistry of Materials*. 2011;23(3): 446–455. <https://doi.org/10.1021/cm102182x>
31. Akbas E., Othman K. A., Çelikezen F. Ç., ... Mardinoglu A. Synthesis and biological evaluation of novel benzylidene thiazolo pyrimidin-3(5H)-one derivatives. *Polycyclic Aromatic Compounds*. 2023: 1–18. <https://doi.org/10.1080/10406638.2023.2228961>
32. Wang D., Chen L., Shi C., ... Chen Y. Quantum spin Hall insulator in halogenated arsenene films with sizable energy gaps. *Scientific Reports*. 2016;6(1): 28487. <https://doi.org/10.1038/srep28487>
33. Janietz S., Bradley D., Grell M., Giebeler C., Inbasekaran M., Woo E. Electrochemical determination of the ionization potential and electron affinity of poly(9,9-dioctylfluorene). *Applied Physics Letters*. 1998;73(17): 2453–2455. <https://doi.org/10.1063/1.122479>
34. Pearson R. G. Chemical hardness and density functional theory. *Journal of Chemical Sciences*. 2005;117: 369–377. <https://doi.org/10.1007/BF02708340>
35. Chattaraj P. K., Roy D. R. Update 1 of: electrophilicity index. *Chemical Reviews*. 2007;107(9): PR46–PR74. <https://doi.org/10.1021/cr078014b>
36. Mayr H., Patz M. Scales of nucleophilicity and electrophilicity: a system for ordering polar organic and organometallic reactions. *Angewandte Chemie International Edition in English*. 1994;33(9): 938–957. <https://doi.org/10.1002/anie.199409381>
37. Ceylan Ü., Tarı G. Ö., Gökce H., Açar E. Spectroscopic (FT–IR and UV–Vis) and theoretical (HF and DFT) investigation of 2-Ethyl-N-[(5-nitrothiophene-2-yl)methylidene]aniline. *Journal of Molecular Structure*. 2016;1110: 1–10. <https://doi.org/10.1016/j.molstruc.2016.01.019>
38. Esme A. Experimental (FT-IR, FT-Raman, and UV-Vis) and quantum chemical calculations on monomer and dimer structures of 1-hydroxy-2-naphthoic acid using the DFT and TD-DFT methods. *Indian Journal of Pure & Applied Physics (IJPAP)*. 2019;57(11): 822–835. Режим доступа: <http://op.niscpr.res.in/index.php/IJPAP/article/view/21985>
39. Jagdale B. S., Ashok Adole V., Bhavsing Pawar T., Desale B. S. Molecular structure, frontier molecular orbitals, MESP and UV–visible spectroscopy studies of ethyl 4-(3,4-dimethoxyphenyl)-6-methyl-2-oxo-1,2,3,4-tetrahydropyrimidine-5-carboxylate: a theoretical and experimental appraisal. *Material Science Research India*. 2020;17(Special issue 1): 13–26. <https://doi.org/10.13005/msri.17.special-issue1.04>
40. Li A., Draine B. Do the infrared emission features need ultraviolet excitation? The polycyclic aromatic hydrocarbon model in UV-poor reflection nebulae. *The Astrophysical Journal*. 2002;572(1): 232–237. <https://doi.org/10.1086/340285>
41. Arfsten D. P., Schaeffer D. J., Mulveny D. C. The effects of near ultraviolet radiation on the toxic effects of polycyclic aromatic hydrocarbons in animals and plants: a review. *Ecotoxicology and Environmental Safety*. 1996;33(1): 1–24. <https://doi.org/10.1006/eesa.1996.0001>

42. Jones R. N. The ultraviolet absorption spectra of anthracene derivatives. *Chemical Reviews*. 1947;41(2): 353–371. <https://doi.org/10.1021/cr60129a013>
43. Makula P., Pacia M., Macyk W. How to correctly determine the band gap energy of modified semiconductor photocatalysts based on UV-vis spectra. *The Journal of Physical Chemistry Letters*. 2018;9(23): 6814–6817. <https://doi.org/10.1021/acs.jpcllett.8b02892>
44. Wodrich M. D., Corminboeuf C., Schreiner P. R., Fokin A. A., Schleyer P. v. R. How accurate are DFT treatments of organic energies? *Organic Letters*. 2007;9(10): 1851–1854. <https://doi.org/10.1021/ol070354w>
45. Swofford R. L., Long M. E., Albrecht A. C. C–H vibrational states of benzene, naphthalene, and anthracene in the visible region by thermal lensing spectroscopy and the local mode model. *The Journal of Chemical Physics*. 1976;65(1): 179–190. <https://doi.org/10.1063/1.432815>
46. Ricks A. M., Douberly G. E., Duncan M. A. The infrared spectrum of protonated naphthalene and its relevance for the unidentified infrared bands. *The Astrophysical Journal*. 2009;702(1): 301–306. <https://doi.org/10.1088/0004-637X/702/1/301>
47. Szczepanski J., Vala M., Talbi D., Parisel O., Ellinger Y. Electronic and vibrational spectra of matrix isolated anthracene radical cations: Experimental and theoretical aspects. *The Journal of Chemical Physics*. 1993;98(6): 4494–4511. <https://doi.org/10.1063/1.465009>
48. McClellan A. L., Pimentel G. C. Vibrational assignment and thermodynamic properties of naphthalene. *The Journal of Chemical Physics*. 1955;23(2): 245–248. <https://doi.org/10.1063/1.1741948>
49. Srivastava A., Singh V. B. Theoretical and experimental studies of vibrational spectra of naphthalene and its cation. *Indian Journal of Pure & Applied Physics*. 2007;45: 714–720.
50. Haenen H. T. M. Potential probe measurement analysis and charge distribution determination. *Journal of Electrostatics*. 1977;2: 203–222. [https://doi.org/10.1016/0304-3886\(77\)90054-7](https://doi.org/10.1016/0304-3886(77)90054-7)
51. Solano E. A., Mayer P. M. A complete map of the ion chemistry of the naphthalene radical cation? DFT and RRKM modeling of a complex potential energy surface. *The Journal of Chemical Physics*. 2015;143(10). <https://doi.org/10.1063/1.4930000>
52. Pi X., Sun F., Gao J., ... Liu H. A new insight into the SO<sub>2</sub> adsorption behavior of oxidized carbon materials using model adsorbents and DFT calculations. *Physical Chemistry Chemical Physics*. 2019;21(18): 9181–9188. <https://doi.org/10.1039/c8cp07782g>
53. Modelli A., Mussoni L., Fabbri D. Electron affinities of polycyclic aromatic hydrocarbons by means of B3LYP/6-31+G\* calculations. *The Journal of Physical Chemistry A*. 2006;110(20): 6482–6486. <https://doi.org/10.1021/jp0605911>
54. Domingo L. R., Aurell M. J., Pérez P., Contreras R. Quantitative characterization of the global electrophilicity power of common diene/dienophile pairs in Diels–Alder reactions. *Tetrahedron*. 2002;58(22): 4417–4423. [https://doi.org/10.1016/s0040-4020\(02\)00410-6](https://doi.org/10.1016/s0040-4020(02)00410-6)
55. Boukabcha N., Benmohammed A., Belhachemi M. H. M., ... Djafri A. Spectral investigation, TD-DFT study, Hirshfeld surface analysis, NCI-RDG, HOMO-LUMO, chemical reactivity and NLO properties of 1-(4-fluorobenzyl)-5-bromolindolin-2,3-dione. *Journal of Molecular Structure*. 2023;1285: 135492. <https://doi.org/10.1016/j.molstruc.2023.135492>
56. Lu T., Chen F. Multiwfn: A multifunctional wavefunction analyzer. *Journal of Computational Chemistry*. 2012;33(5): 580–592. <https://doi.org/10.1002/jcc.22885>
57. Humphrey W., Dalke A., Schulten K. VMD: Visual molecular dynamics. *Journal of Molecular Graphics*. 1996;14(1): 33–38. [https://doi.org/10.1016/0263-7855\(96\)00018-5](https://doi.org/10.1016/0263-7855(96)00018-5)
58. Saidj M., Djafri A., Rahmani R., ... Chouaih A. Molecular structure, experimental and theoretical vibrational spectroscopy, (HOMO-LUMO, NBO) investigation, (RDG, AIM) analysis, (MEP, NLO) study and molecular docking of ethyl-2-[[4-ethyl-5-(quinolin-8-yloxymethyl)-4H-1,2,4-triazol-3-yl] sulfanyl] acetate. *Polycyclic Aromatic Compounds*. 2023;43(3): 2152–2176. <https://doi.org/10.1080/10406638.2022.2039238>
59. Walters W. P., Murcko M. A. Prediction of ‘drug-likeness’. *Advanced Drug Delivery Reviews*. 2002;54(3): 255–271. [https://doi.org/10.1016/s0169-409x\(02\)00003-0](https://doi.org/10.1016/s0169-409x(02)00003-0)
60. Ursu O., Rayan A., Goldblum A., Oprea T. I. Understanding drug-likeness. *WIREs Computational Molecular Science*. 2011;1(5): 760–781. <https://doi.org/10.1002/wcms.52>
61. Ranjith P., Ignatious A., Panicker C. Y., ... Anto P. Synthesis, spectroscopic characterization, DFT, molecular docking and in vitro antibacterial potential of novel quinoline derivatives. *Journal of Molecular Structure*. 2022;1264: 133315. <https://doi.org/10.1016/j.molstruc.2021.131217>
62. Sumathi D., Thanikachalam V., Bharanidharan S., Saleem H., Babu N. R. Vibrational Characterization and Molecular Electronic Investigations of 2-acetyl-5-methylfuran using FT-IR, FT-Raman, UV-VIS, NMR, and DFT Methods. *Journal of Fluorescence*. 2022;32: 1005–1017. <https://doi.org/10.1007/s10895-022-02903-8>



63. Abbas T., Bendjeddou A., Villemin D. Structure, electronic properties, NBO, NLO and chemical reactivity of bis (1, 4-dithiafulvalene) derivatives: functional density theory study. *International Journal of Advanced Chemistry*. 2017;6(1): 18–25. <https://doi.org/10.14419/ijac.v6i1.8668>
64. Villemin D., Abbas T., Bendjeddou A. Molecular structure, HOMO, LUMO, MEP, natural bond orbital analysis of benzo and anthraquinodimethane derivatives. *Pharmaceutical and Biological Evaluations*. 2018;5(2): 27. <https://doi.org/10.26510/2394-0859.pbe.2018.04>
65. Abbas T., Bendjeddou A., Villemin D. Molecular structure, NBO analysis, first hyper polarizability, and homo-lumo studies of  $\pi$ -extended tetrathiafulvalene (EXTTF) derivatives connected to  $\pi$ -nitro phenyl by density functional method. *International Journal of Advanced Chemistry*. 2018;6(1): 114. <https://doi.org/10.14419/ijac.v6i1.11126>
66. Obot I., Macdonald D., Gasem Z. Density functional theory (DFT) as a powerful tool for designing new organic corrosion inhibitors. Part 1: An overview. *Corrosion Science*. 2015;99: 1–30. <https://doi.org/10.1016/j.corsci.2015.01.037>
67. Khan M. U., Khalid M., Asim S., ... Imran M. Exploration of nonlinear optical properties of triphenylamine-dicyanovinylene coexisting donor- $\pi$ -acceptor architecture by the modification of  $\pi$ -conjugated linker. *Frontiers in Materials*. 2021;8: 719971. <https://doi.org/10.3389/fmats.2021.719971>
68. Al-Shamiri H. A. S., Sakr M. E. M., Abdel-Latif S. A., ... Elwahy A. H. M. Experimental and theoretical studies of linear and non-linear optical properties of novel fused-triazine derivatives for advanced technological applications. *Scientific Reports*. 2022;12(1): 19937. <https://doi.org/10.1038/s41598-022-22311-z>

### Information about the authors

*Yousif Hussein Azeez*, MSc in Advanced Materials Science, Lecturer at the Department of physics, Halabja University (Iraq).

<https://orcid.org/0000-0001-5357-7856>  
yousif.husain@uoh.edu.iq

*Khdir Ahmed Othman*, MSc In Organic Chemistry, Lecturer at the Department of Chemistry, Faculty of Science and Health, Koya University, (Kurdistan Region – F.R., Iraq).

<https://orcid.org/0000-0002-7763-2976>  
khdir.ahmed@koyauniversity.org

*Rebaz Anwar Omer*, PhD in Organic Chemistry, Head of Chemistry Department, Faculty of Science and Health, Koya University (Kurdistan Region – F.R., Iraq).

<https://orcid.org/0000-0002-3774-6071>  
rebaz.anwar@koyauniversity.org

*Rebaz Obaid Kareem*, MSc in General Physics, Lecturer at the Department of Physics, Faculty of Science/ Physics Department, Halabja University (Kurdistan Region – Iraq).

<https://orcid.org/0000-0001-6273-1309>  
rebaz.kareem@uoh.edu.iq

Received 16.12.2023; approved after reviewing 14.03.2024; accepted for publication 15.03.2024; published online 25.06.2024.





## Original articles

Research article

<https://doi.org/10.17308/kcmf.2024.26/11940>

## The influence of benzoic acid moisture on the proton exchange process in lithium niobate crystals

I. V. Petukhov<sup>✉</sup>, V. I. Kichigin, A. R. Kornilitsyn, A. S. Yakimov

Perm State University,  
15 ul. Bukireva, Perm 614990, Russian Federation

### Abstract

The purpose of this study was the investigation of the influence of water impurities in benzoic acid, used as a source of protons during proton exchange on lithium niobate crystals, on the process of formation of proton exchange waveguides, their structure and phase composition.

To carry out the research, prism coupling method, X-ray diffraction analysis, IR absorption spectroscopy, and optical microscopy in polarized light were used. It was established that an increase in the moisture content in benzoic acid affected the optical characteristics of the waveguides and slightly increased the stress (strain) of the proton exchange layers. Subsequent annealing significantly equalized the characteristics of the waveguides.

When performing proton exchange, the moisture content of benzoic acid must be taken into account to obtain reproducible and stable performance of integrated optical devices with proton exchange waveguides.

**Keywords:** Lithium niobate, Proton exchange, Waveguide, Structure, Phase composition, Benzoic acid, Melt, Moisture

**Funding:** The study was funded by the Russian Foundation for Basic Research and the Perm Krai within the framework of scientific project No. 20-42-596001.

**For citation:** Petukhov I. V., Kichigin V. I., Kornilitsyn A. R., Yakimov A. S. The influence of benzoic acid moisture on the proton exchange process in lithium niobate crystals. *Condensed Matter and Interphases*. 2024;26(2): 295–303. <https://doi.org/10.17308/kcmf.2024.26/11940>

**Для цитирования:** Петухов И. В., Кичигин В. И., Корнилицын А. Р., Якимов А. С. Влияние влажности бензойной кислоты на процесс протонного обмена в кристаллах ниобата лития. *Конденсированные среды и межфазные границы*. 2024;25(2): 295–303. <https://doi.org/10.17308/kcmf.2024.26/11940>

✉ Igor V. Petukhov, e-mail: [petukhov-309@yandex.ru](mailto:petukhov-309@yandex.ru)

© Petukhov I. V., Kichigin V. I., Kornilitsyn A. R., Yakimov A. S., 2024



The content is available under Creative Commons Attribution 4.0 License.

## 1. Introduction

Proton exchange (PE) is one of the main modern technologies for producing optical waveguides in lithium niobate (LN) crystals for the manufacture of various integrated optical devices [1, 2]. The most widely used source of protons in PE is benzoic acid (BA) [3–5]. When LN is immersed into the molten BA part of the lithium ions in the surface layer of the  $\text{LiNbO}_3$  crystal is substituted by hydrogen ions, and an  $\text{H}_x\text{Li}_{1-x}\text{NbO}_3$  solid solution is formed. Proton penetration depth into  $\text{LiNbO}_3$  depends on conditions, it ranges from fractions of a micron to several microns. As a result, the refractive index  $n_e$  of the surface (proton exchange) layer of the crystal increases [3, 6–9], which is a prerequisite for the appearance of the waveguide properties of this layer.

Immediately after proton exchange and subsequent annealing, depending on the value of normalized concentration  $x$  of protons, seven different  $\text{H}_x\text{Li}_{1-x}\text{NbO}_3$  phases can form [3, 8]. The formation of  $\alpha$ -phases ( $x < 0.12$ ) during post-exchange annealing ensures the stable optical characteristics of waveguides and restoration of the electro-optical coefficient.

Despite the fact that PE is a widely used technological process, its individual aspects continue to be actively researched [10–12].

To obtain reproducible characteristics of waveguides, it is not enough to strictly control the duration of processing and annealing, as well as the temperature regime. The process of formation of optical waveguides is influenced by the chemical composition of lithium niobate [13]. In congruent lithium niobate, commonly used for integrated optical devices, the ratio  $\text{Li}_2\text{O}:\text{Nb}_2\text{O}_5$  may vary among different manufacturers [13, 14], therefore the characteristics of the formed waveguides will also differ.

The proton exchange process is also affected by the presence of impurities in benzoic acid, including water impurities. The moisture content in BA varies among different manufacturers; the moisture content of BA is also affected by the conditions and duration of storage of benzoic acid. The influence of moisture impurities in BA on the PE process was noted in a number of studies [15–18].

It was previously shown that benzoic acid in melts is present predominantly in an

undissociated state in the form of dimers [19]. Moisture impurities increase the electrical conductivity of benzoic acid melts, promote its dissociation and somewhat accelerate proton exchange [20].

This study is a continuation of a previously conducted research into the electrical conductivity of benzoic acid melts with a controlled content of moisture impurities [20]. The goal of the study was to establish the influence of controlled moisture content in BA on the process of proton exchange, the phase composition of proton exchange layers and the optical characteristics of PE waveguides.

## 2. Experimental

To evaluate the effect of moisture impurities on the PE process, several samples of benzoic acid were used: 1) benzoic acid, analytical grade as-received (hereinafter this sample is called unprocessed BA (NBA)); 2) BA after drying in a desiccator over anhydrous calcium chloride for 7 days (DBA); 3) BA after exposure to conditions of relative humidity of air of 100% for 5–7 days (WBA). When dried over anhydrous  $\text{CaCl}_2$  the BA weight decreased by approximately 0.02%; when exposed to conditions of 100% moisture, the BA weight increased by ~0.02%.

For the study, samples of congruent lithium niobate (X-cut) produced by CQT (PRC) with the size of 15x10x1 mm were used. Proton exchange was carried out in a melt of benzoic acid at a temperature of 175 °C for 6 h, which led to the formation of a multi-mode waveguide. After PE, the reactor with the samples was removed from the furnace to cool to room temperature. Post-exchange annealing was carried out in an air atmosphere at 370 °C.

For the obtained planar waveguides, the depth profiles of the extraordinary refractive index  $n_e(x)$  were determined by the prism coupling method using the inverse Wentzel–Kramers–Brillouin method [21] and  $\Delta n_e(0)$  values at the surface of the waveguide at wavelength  $\lambda = 0.633 \mu\text{m}$  were determined.

For the detection of changes on the surface of the proton-exchanged layer of the LN crystal caused by phase transformations, the optical microscopy in polarized light (Olympus BX 51) was used.

X-ray diffraction studies of lithium niobate samples were carried out using DRON-UM1 double crystal diffractometer in Co-anode radiation (wavelength  $\lambda_{\beta} = 1.62073 \text{ \AA}$ ). The  $\theta/2\theta$ -curves were registered and used for the determination of  $\varepsilon_{33}$  strain in the direction of the normal to the surface according to Bragg equation:

$$\varepsilon_{33} = \Delta d/d = -\Delta\theta \operatorname{ctg} \theta,$$

where  $\Delta d$  is change in interplanar spacing  $d$ ,  $\Delta\theta$  is the angular distance between the diffraction reflection maxima from the lithium niobate substrate and from the corresponding PE phase,  $\theta$  – Bragg reflection angle.

Lithium niobate samples after PE were also studied using IR absorption spectroscopy on a Hewlett Packard Spectrum Two spectrophotometer in the range  $400\text{--}6000 \text{ cm}^{-1}$ .

### 3. Results and discussion

The refractive index profile of the waveguides after PE has a stepwise character (Fig. 1). In all three cases, the  $\Delta n_e(0)$  had similar values, which probably indicated a qualitatively identical phase composition of the uppermost layer of the proton-exchanged region. The depth of the waveguide layer obtained in the WBA was noticeably higher than for the other two BA samples. This indicated a more intense PE in the presence of water impurities.

In the IR spectra of the samples after proton exchange (Fig. 2), the following pattern can be noted: a wide peak at  $3200\text{--}3400 \text{ cm}^{-1}$ , corresponding to interstitial protons (presumably the  $\beta_2$ -phase), was the most intense for the proton exchange layers obtained in the WBA, and in the DBA the peak intensity was the lowest. The same is true for the narrow peak corresponding to absorption at  $3500 \text{ cm}^{-1}$ . Measurements of IR spectra indicated a natural increase in the concentration of protons in the PE layer on lithium niobate with an increase in the moisture content in benzoic acid used for PE.

After PE, regardless of the amount of impurity water in the BA, two peaks were recorded on the  $\theta/2\theta$ -curves (Fig. 3). It should be noted that after PE in the melt of dried benzoic acid, the intensity of these peaks was maximum. Decomposition of the obtained curves allowed to identify a larger number of peaks corresponding to different proton-exchange phases (Table 1).

The lithium niobate peak had a shoulder on the right, due to the presence of the  $\alpha$ -phase, formed at the PE-layer/ $\text{LiNbO}_3$  interface and characterized by the lowest proton concentration [3]. There were three phases in the proton exchange layers (the  $\beta_1$ -,  $\beta_2$ -phases and probably the  $\kappa_2$ -phase). With the increasing ordinal number of the  $\beta$ -phase, the concentration of protons increased [3]. The phase with a higher proton concentration was located closer to the

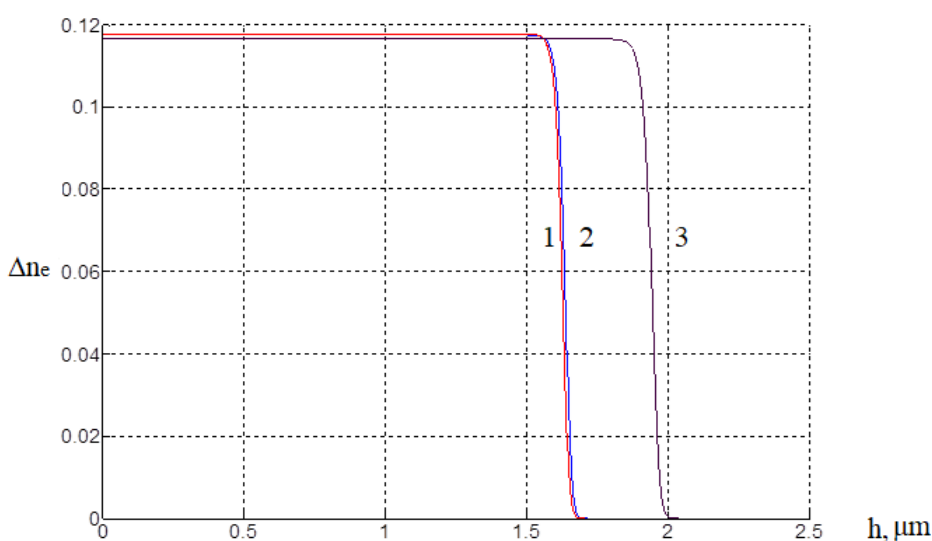


**Fig. 1.** Refractive index profiles in proton-exchanged waveguides, PE  $175 \text{ }^\circ\text{C}$ , 6 h in different samples of benzoic acid: 1 – DBA, 2 – NBA, 3 – WBA

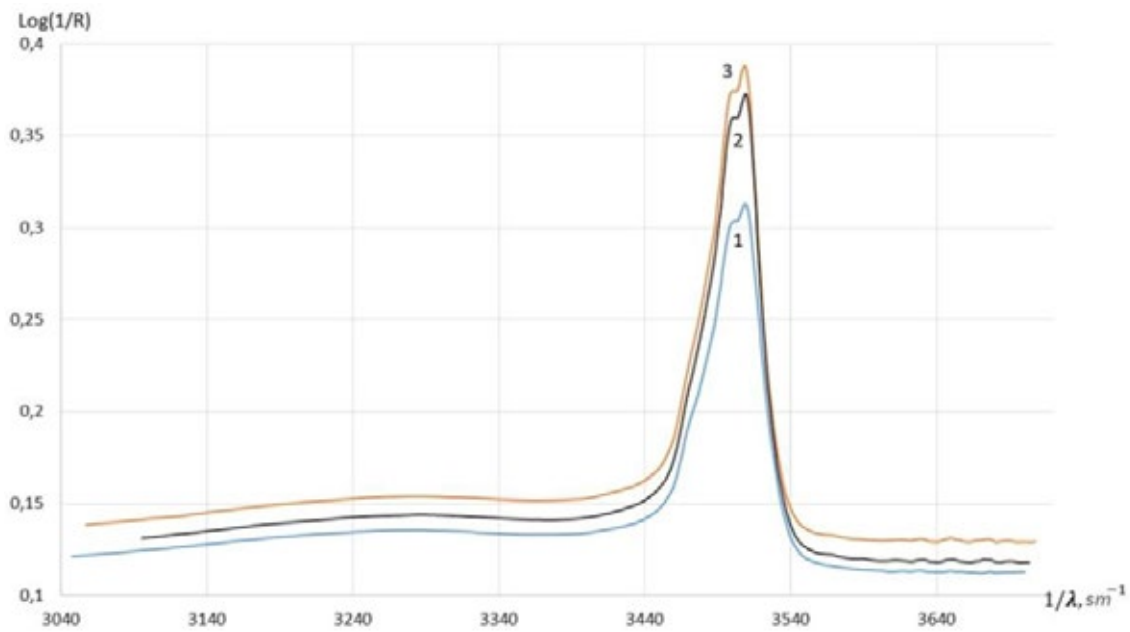


Fig. 2. IR absorption spectra of lithium niobate after PE 175 °C, 6 h: 1 – DBA, 2 – NBA, 3 – WBA

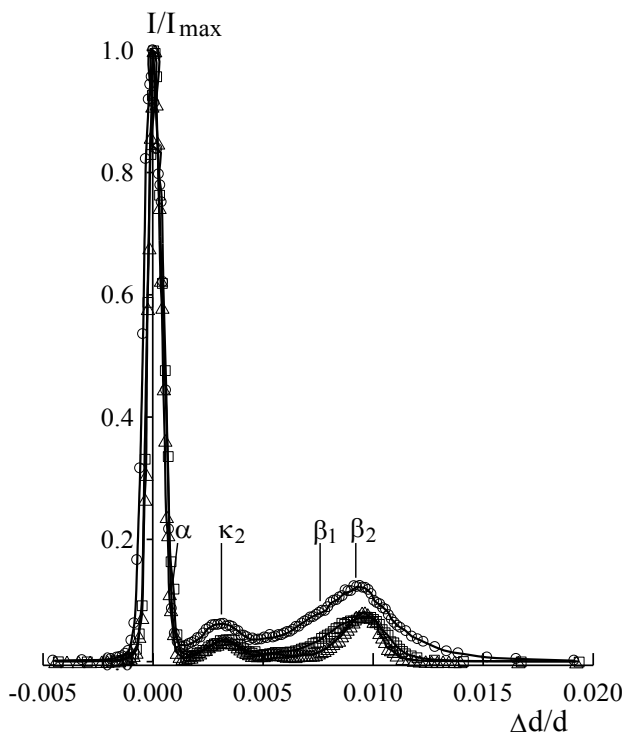


Fig. 3.  $\theta/2\theta$  curves for proton-exchanged layers on lithium niobate after PE 175 °C, 6 h. (○) in DBA, (Δ) in NBA, (□) in WBA. Reflection from (110) planes

crystal surface [3, 22]. Although, according to the authors of [3], the formation of the  $\kappa_2$ -phase is possible only as a result of annealing, according to the results of [23], the  $\kappa_2$ -phase, probably, can form immediately after PE (in the 175 °C, 6 h mode).

As the moisture content in BA increased, the proportion of the  $\beta_1$ -phase also increased, and increase in the strains of the most stressed  $\beta_2$ -phase was observed. In [3, 8] it was stated that the  $\beta_1$ -phase is the most stressed on the X-cut of  $\text{LiNbO}_3$  (under PE conditions at 240 °C). However, the results of a study [23], in which a gradual etching of the PE layer obtained at 175 °C was performed, indicated that the etching off a  $\beta_2$ -phase located on the surface decreased the intensity of the peak with the highest strain values.

The decrease in the intensity of the peaks corresponding to proton-exchange phases with increasing moisture content in the BA was possibly due to higher stresses and higher structure imperfection of these phases. A similar ratio of intensities of proton-exchange phases occurred when comparing the  $\theta/2\theta$ -curves of lithium niobate without treatment and with pre-treatment of the crystal surface with Ar plasma before proton exchange [24]. Plasma treatment significantly increased the structure imperfection of a thin surface layer of lithium niobate, led to an increase in strain in proton-exchange phases and a decrease in the intensity of the corresponding peaks on the  $\theta/2\theta$ -curves. The results obtained may indicate an intensification of proton exchange as the content of water impurities in benzoic acid increases.



**Table 1.** Decomposition of the peaks in  $\theta/2\theta$  curves for proton-exchanged layers obtained in different samples of benzoic acid

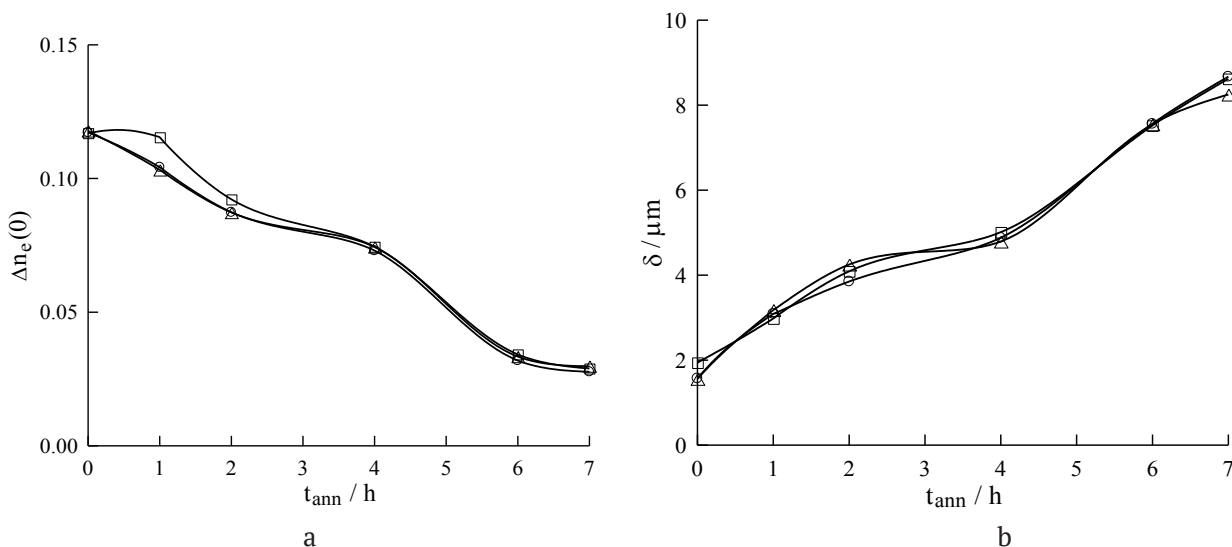
Benzoic acid	Peak (phase)	Relative peak intensity	$\epsilon_{33} \cdot 10^3$	Full width at half maximum $\cdot 10^5$	Relative peak area, %
DBA	1(LN)	0.95	0	0.74	42.7
	2( $\alpha$ )	0.48	0.42	0.51	14.8
	3( $\kappa_2$ )	0.058	3.10	3.06	10.7
	4( $\beta_1$ )	0.022	6.05	2.00	2.7
	5( $\beta_2$ )	0.12	9.21	4.09	29.1
HBK	1(LN)	0.82	0	0.51	43.6
	2( $\alpha$ )	0.45	0.33	0.57	26.5
	3( $\kappa_2$ )	0.022	3.20	1.34	3.0
	4( $\beta_1$ )	0.012	4.10	9.96	12.8
	5( $\beta_2$ )	0.073	9.49	1.86	14.1
WB	1(LN)	0.91	0	0.61	49.8
	2( $\alpha$ )	0.37	0.47	0.64	21.4
	3( $\kappa_2$ )	0.033	3.18	2.32	6.9
	4( $\beta_1$ )	0.029	7.98	3.93	10.3
	5( $\beta_2$ )	0.058	9.86	2.24	11.7

An increase in the benzoic acid moisture led to an increase in the concentration of protons in the PE layer. This can explain the slower decrease in the refractive index (Fig. 4) for samples obtained in the WBA during annealing at the initial stage. The observed changes correspond to the literature data [15, 16].

Annealing for 2 h changed the phase composition of the PE layers (Fig. 5, Table 2). The results of decomposition of  $\theta/2\theta$ -curves obtained

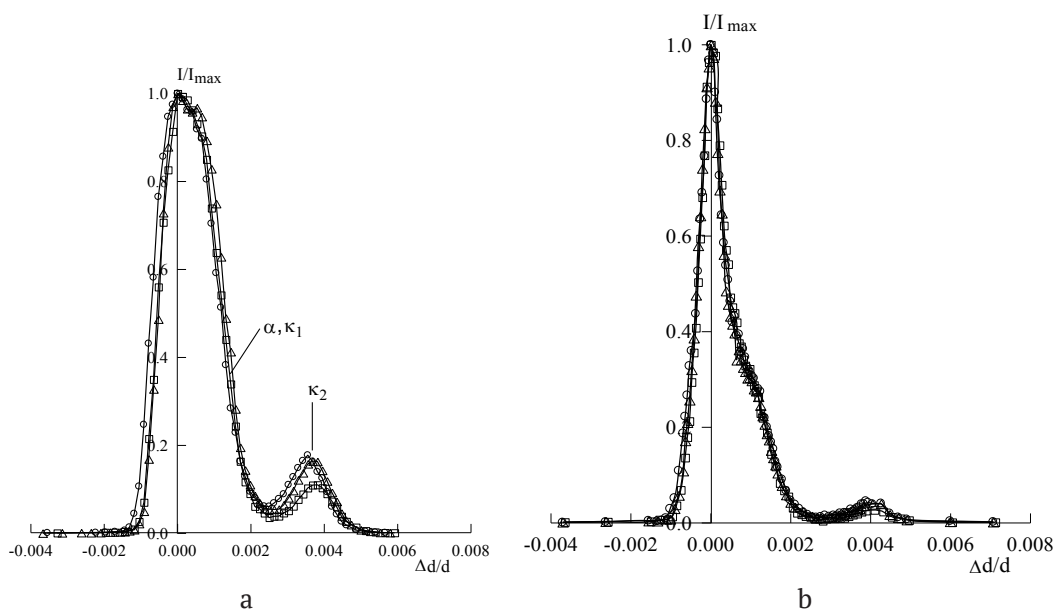
for two orders of reflection are shown in Table 2. The presence of the  $\kappa_1$ -phase was more clearly visible on the  $\theta/2\theta$ -curves of the second order of reflection (Fig. 5b).

During annealing the  $\beta$ -phases located at the surface of the PE layer turned into the  $\kappa_2$ - and  $\kappa_1$ -phases; the presence of the  $\kappa_1$ -phase was confirmed by micrographs of the surface of protonated layers (Fig. 6). The resulting modulated structures represented the formations


**Fig. 4.**  $\Delta n_e(0)$  (a) and waveguide depth (b) as functions of annealing duration. (○) PE in DBA, (△) PE in NBA, (□) PE in WBA

**Table 2.** Decomposition of the peaks in  $\theta/2\theta$  curves for proton-exchanged layers obtained in different samples of benzoic acid, after annealing 370 °C, 2 h

Benzoic acid	Peak (phase)	Relative peak intensity	$\epsilon_{33} \cdot 10^3$	Full width at half maximum $\cdot 10^5$	Relative peak area, %
Reflection from (110) planes					
DBA	1 (LN)	0.93	0	0.58	52.1
	2 ( $\alpha$ )	0.48	0.83	0.44	20.1
	3 ( $\kappa_1$ )	0.31	1.32	0.59	17.8
	4 ( $\kappa_2$ )	0.17	3.53	0.60	10.0
NBA	1 (LN)	0.87	0	0.42	37.4
	2 ( $\alpha$ )	0.54	0.44	0.43	23.8
	3 ( $\kappa_1$ )	0.48	0.93	0.60	28.7
	4 ( $\kappa_2$ )	0.16	3.67	0.62	10.1
WBA	1 (LN)	0.83	0	0.47	42.4
	2 ( $\alpha$ )	0.55	0.74	0.48	28.0
	3 ( $\kappa_1$ )	0.31	1.21	0.66	22.0
	4 ( $\kappa_2$ )	0.11	3.85	0.63	7.5
Reflection from (220) planes					
DBA	1 (LN)	0.97	0	0.33	60.0
	2 ( $\alpha$ )	0.24	0.67	0.30	13.7
	3 ( $\kappa_1$ )	0.23	1.20	0.50	21.7
	4 ( $\kappa_2$ )	0.04	3.97	0.61	4.7
NBA	1 (LN)	0.96	0	0.36	65.9
	2 ( $\alpha$ )	0.16	0.69	0.23	7.0
	3 ( $\kappa_1$ )	0.26	1.13	0.46	22.6
	4 ( $\kappa_2$ )	0.04	3.95	0.65	4.5
WBA	1 (LN)	0.99	0	0.36	67.4
	2 ( $\alpha$ )	0.19	0.67	0.23	8.2
	3 ( $\kappa_1$ )	0.25	1.13	0.45	21.4
	4 ( $\kappa_2$ )	0.03	4.03	0.58	2.9


**Fig. 5.**  $\theta/2\theta$  curves for proton-exchanged layers on lithium niobate after PE 175 °C, 6 h and annealing 370°C, 2 h. (○) PE in DBA, (△) PE in NBA, (□) PE in WBA. Reflection from the planes: a – (110), b – (220)



**Fig. 6.** Micrograph of lithium niobate sample after proton exchange (175 °C, 6 h) and annealing (370 °C, 2 h)

of  $\kappa_1$ -phase as a result of relaxation of high internal stresses in proton-exchange layers [25]. Phase  $\kappa_2$ , which was formed during PE under the  $\beta$ -phases, upon annealing was transformed into the  $\kappa_1$  and  $\alpha$  phases.

An analysis of the results shown in Table 2 indicated an increase in  $\epsilon_{33}$  values, corresponding to the  $\kappa_2$ -phase, with increasing content of moisture impurities in benzoic acid. It also follows from the decomposition of reflections from (110) planes that an increase in moisture content increased the total intensity of proton-exchange phases ( $\kappa_2$ -,  $\kappa_1$ - and  $\alpha$ -phases). In the case of reflection from the (220) planes, which contain information about the structure of deeper layers, an increase in the moisture of the BA led to an increase in the intensity of reflections from lithium niobate, while the total intensity from the  $\kappa_2$ - and  $\kappa_1$ -phases changed slightly.

As the annealing duration increased, the differences in the characteristics of the waveguides obtained in the DBA, NBA, and WBA decreased (Fig. 4). The  $\Delta n_e$  value is determined by the phase composition and concentration of protons in the PE layer. For each phase the dependence of  $\Delta n_e$  from normalized  $x$  concentration in  $H_xLi_{1-x}NbO_3$  is different. The strongest dependence of  $\Delta n_e(0)$  on  $x$  was observed at average  $x$  values (about 0.4), and at high  $x$  and especially at low  $x$  the dependence was weak [4]. Upon annealing  $> 4$  h, the transition to the  $\alpha$ -phase (low  $x$ ) begins, and the dependence of  $\Delta n_e(0)$  on  $x$  significantly weakened. The maximum difference  $\Delta n_e(0)$  for

DBA and WBA was observed at an annealing time of 1–2 h (Fig. 4a), when the main phases were  $\kappa_2$ - and  $\kappa_1$ -phases ( $x = 0.12$ – $0.44$  [26]), for which  $d\Delta n_e(0)/dx$  had the highest values. The reduction of differences in the depth  $\delta$  of waveguides with an annealing time of more than 4 h (Fig. 4b) can be explained by the fact that the effective proton diffusion coefficient  $D_H$  in the PE layer on lithium niobate depends on  $x$ . In the  $\alpha$ -phase region this dependence was quite strong, and with increase in  $x$  the  $D_H$  magnitude in X-cut crystals decreased [27]. Since the hydrogen concentration in the PE layer obtained in the WBA was higher, the diffusion coefficient in it was lower and weakened the possible increase of  $\delta$  due to the higher  $x$  in the layer adjacent to the surface of the crystal.

Thus, the presence of small amounts of water in BA accelerates proton exchange. This may be due to the fact that water impurities in the benzoic acid melt promote both the transition of BA dimers into monomers and the dissociation of benzoic acid. This indicates an increase in the electrical conductivity of benzoic acid melts with increasing impurity water content [20]. The relatively small effects were due to the low concentration of water, even in the acid with the highest moisture content there was one molecule of water per about 300 molecules of benzoic acid. However, to obtain reproducible optical characteristics of integrated optical devices that use proton exchange, the moisture content of the benzoic acid used for proton exchange must be controlled.

#### 4. Conclusions

The presence of moisture in benzoic acid used for proton exchange on lithium niobate crystals, affects the optical characteristics of waveguides and slightly increases the stress (strain) of the proton exchange layers. Subsequent annealing significantly equalizes the characteristics of the waveguides.

When performing proton exchange, the moisture content of benzoic acid must be taken into account to obtain reproducible and stable performance of integrated optical devices with proton exchange waveguides.

#### Contribution of the authors

The authors contributed equally to this article.

## Conflict of interests

The authors declare that they have no known competing financial interests or personal relationships that could have influenced the work reported in this paper.

## References

- Korkishko Yu. N., Fedorov V. A., Kostritskii S. M., ... Laurell F. Proton exchanged LiNbO<sub>3</sub> and LiTaO<sub>3</sub> optical waveguides and integrated optic devices. *Microelectronic Engineering*. 2003;69: 228–236. [https://doi.org/10.1016/S0167-9317\(03\)00302-2](https://doi.org/10.1016/S0167-9317(03)00302-2)
- Kuneva M. Optical waveguides obtained via proton exchange technology in LiNbO<sub>3</sub> and LiTaO<sub>3</sub> – a short review. *International Journal of Scientific Research in Science and Technology*. 2016;2(6): 40–50.
- Korkishko Yu. N., Fedorov V. A. Structural phase diagram of proton-exchange H<sub>x</sub>Li<sub>1-x</sub>NbO<sub>3</sub> waveguides in lithium niobate crystals. *Crystallography Reports*. 1999;44(2): 237–246. Available at: <https://elibrary.ru/item.asp?id=13324513>
- de Almeida J. M. M. Design methodology of annealed H<sup>+</sup> waveguides in ferroelectric LiNbO<sub>3</sub>. *Optical Engineering*. 2007;46(6): 064601. <https://doi.org/10.1117/1.2744364>
- Cai L., Wang Y., Hu H. Low-loss waveguides in a single-crystal lithium niobate thin film. *Optics Letters*. 2015;40(13): 3013–3016. <https://doi.org/10.1364/OL.40.003013>
- Suchoski P. G., Findakly T. K., Leonberger F. J. Stable low-loss proton-exchanged LiNbO<sub>3</sub> waveguide devices with no electro-optic degradation. *Optics Letters*. 1988;13(11): 1050–1052. <https://doi.org/10.1364/OL.13.001050>
- Korkishko Y. N., Fedorov V. A., Feoktistova O. Y. LiNbO<sub>3</sub> optical waveguide fabrication by high-temperature proton exchange. *Journal of Lightwave Technology*. 2000;18(4): 562–568. <https://doi.org/10.1109/50.838131>
- Korkishko Yu. N., Fedorov V. A. Structural phase diagram of H<sub>x</sub>Li<sub>1-x</sub>NbO<sub>3</sub> waveguides: the correlation between optical and structural properties. *IEEE Journal of Selected Topics in Quantum Electronics*. 1996;2(2): 187–196. <https://doi.org/10.1109/2944.577359>
- Bazzan M., Sada C. Optial waveguides in lithium niobate: Recent developments and applications. *Applied Physics Reviews*. 2015;2(4): 040603. <https://doi.org/10.1063/1.4931601>
- Dörrer L., Tüchel P., Hüger E., Heller R., Schmidt H. Hydrogen diffusion in proton-exchanged lithium niobate single crystals. *Journal of Applied Physics*. 2021;129: 135105. <https://doi.org/10.1063/5.0047606>
- Dörrer L., Tüchel P., Uxa D., Schmidt H. Lithium tracer diffusion in proton-exchanged lithium niobate. *Solid State Ionics*. 2021;365: 115657. <https://doi.org/10.1016/j.ssi.2021.115657>
- Demin V. A., Petukhov M. I., Ponomarev R. S., Kuneva M. Dynamics of the proton exchange process in benzoic acid interacting with lithium niobate crystals. *Langmuir*. 2023;39(31): 10855–10862. <https://doi.org/10.1021/acs.langmuir.3c00957>
- Kostritskii S. M., Korkishko Y. N., Fedorov V. A., ... Aillerie M. Phase composition of channel proton-exchanged waveguides in different near-congruent LiNbO<sub>3</sub>. *Ferroelectrics Letters Section*. 2020;47(1–3): 9–15. <https://doi.org/10.1080/07315171.2020.1799627>
- Volk T., Wöhlecke M. *Lithium niobate: defects, photorefraction and ferroelectric switching*. Berlin: Springer, 2008. 249 p. <https://doi.org/10.1007/978-3-540-70766-0>
- Petukhov I. V., Kichigin V. I., Mushinskii S. S., Minkin A. M., Shevtsov D. I. Effect of water contained in benzoic acid on the proton exchange process, the structure and the properties of proton-exchange waveguides in lithium niobate single crystals. *Condensed Matter and Interphases*. 2012;14(1): 119–123. (In Russ., abstract in Eng.). Available at: <https://elibrary.ru/item.asp?id=17711946>
- Mushinsky S. S., Minkin A. M., Kichigin V. I., ... Shur V. Ya. Water effect on proton exchange of X-cut lithium niobate in the melt of benzoic acid. *Ferroelectrics*. 2015;476(1): 84–93. <https://doi.org/10.1080/00150193.2015.998530>
- Rambu A. P., Apetrei A. M., Doutre F., Tronche H., De Micheli M. P., Tascu S. Analysis of high-index contrast lithium niobate waveguides fabricated by high vacuum proton exchange. *Journal of Lightwave Technology*. 2018;36(13): 2675–2684. <https://doi.org/10.1109/JLT.2018.2822317>
- Rambu A. P., Apetrei A. M., Tascu S. Role of the high vacuum in the precise control of index contrasts and index profiles of LiNbO<sub>3</sub> waveguides fabricated by high vacuum proton exchange. *Optics and Laser Technology*. 2019;118: 109–114. <https://doi.org/10.1109/JLT.2018.2822317>
- Kichigin V. I., Petukhov I. V., Mushinskii S. S., Karmanov V. I., Shevtsov D. I. Electrical conductivity and IR spectra of molten benzoic acid. *Russian Journal of Applied Chemistry*. 2011;84(12): 2060–2064. <https://doi.org/10.1134/S1070427211120081>
- Kichigin V. I., Petukhov I. V., Kornilitsyn A. R., Mushinsky S. S. Influence of humidity of benzoic acid on the electrical conductivity of its melts. *Condensed Matter and Interphases*. 2022;24(3): 315–320. <https://doi.org/10.17308/kcmf.2022.24/9853>
- Kolosovskii E. A., Petrov D. V., Tsarev A. V. Numerical method for the reconstruction of the refractive index profile of diffused waveguides. *Soviet Journal of Quantum Electronics*. 1981;11(12):



1560–1566. <https://doi.org/10.1070/QE1981v-011n12ABEH008650>

22. Kuneva M. Surface phase detection of proton-exchanged layers in  $\text{LiNbO}_3$  and  $\text{LiTaO}_3$  by IR reflection spectroscopy. *Bulgarian Chemical Communications*. 2013;45(4): 474–478.

23. Azanova I. S., Shevtsov D. I., Zhundrikov A. V., Kichigin V. I., Petukhov I. V., Volyntsev A. B. Chemical etching technique for investigations of a structure of annealed and un-annealed proton exchange channel  $\text{LiNbO}_3$  waveguides. *Ferroelectrics*. 2008;374(1): 110–121. <https://doi.org/10.1080/00150190802427234>

24. Mushinsky S. S., Petukhov I. V., Kichigin V. I., Sidorov D. I., Semenova O. R., Ponomarev R. S. Influence of the pretreatment of lithium niobate surface with plasma and ultraviolet radiation on the proton exchange in benzoic acid melts. *IEEE 22nd International Conference of Young Professionals in Electron Devices and Materials (EDM)*. 2021;283–286. <https://doi.org/10.1109/EDM52169.2021.9507647>

25. Mushinsky S. S., Kichigin V. I., Petukhov I. V., Permyakova M. A., Shevtsov D. I. Structural phase transformations of proton-exchanged layers of lithium niobate during annealing. *Ferroelectrics*. 2017;508(1): 40–48. <https://doi.org/10.1080/00150193.2017.1286702>

26. Korkishko Yu. N., Fedorov V. A. Composition of different crystal phases in proton exchanged waveguides in  $\text{LiNbO}_3$ . In: Wong K. K. (Ed.), *Properties of Lithium Niobate*. Chapter 3.2. London: INSPEC, The Institution of Electrical Engineers; 2002. p. 50–54.

27. Ito K., Kawamoto K. The dependence of the diffusion coefficient on the proton concentration in the proton exchange of  $\text{LiNbO}_3$ . *Japanese Journal of Applied Physics*. 1997;36(11): 6775–6780. <https://doi.org/10.1143/JJAP.36.6775>

### Information about the authors

*Igor V. Petukhov*, Cand. Sci. (Chem.), Associate Professor at the Department of Physical Chemistry, Perm State University, (Perm, Russian Federation).

<https://orcid.org/0000-0002-3110-668x>  
petukhov-309@yandex.ru

*Vladimir I. Kichigin*, Cand. Sci. (Chem.), Research Fellow, Research Fellow at the Department of Physical Chemistry, Perm State University (Perm, Russian Federation).

<https://orcid.org/0000-0002-4668-0756>  
kichigin@psu.ru

*Andrey R. Kornilitsyn*, Engineer, Photonics Laboratory, Perm State University (Perm, Russian Federation).

<https://orcid.org/0000-0002-8267-0168>

*Aleksandr S. Yakimov*, Student, Faculty of Chemistry, Perm State University (Perm, Russian Federation).

fantom.500@mail.ru

*Received 10.08.2023; approved after reviewing 07.09.2023; accepted for publication 16.10.2023; published online 25.06.2024.*

*Translated by Valentina Mittova*



## Original articles

Research article

<https://doi.org/10.17308/kcmf.2024.26/11941>**Anodic dissolution and passivation of manganese monosilicide in fluoride-containing sulfuric acid solutions**I. S. Polkovnikov<sup>1</sup>✉, V. V. Panteleeva<sup>1</sup>, A. B. Shein<sup>1</sup><sup>1</sup>Perm State University

15 ul. Bukireva, Perm 614990, Russian Federation

**Abstract**

The purpose of this study was to investigate the anode resistance of manganese monosilicide MnSi in fluoride-containing sulfuric acid solutions and the concentration effect of sodium fluoride on the anodic dissolution and passivation of the silicide.

The study was carried out on a single-crystal MnSi sample in 0.5 M H<sub>2</sub>SO<sub>4</sub> + (0.0025–0.05) M NaF solutions. The study presents micrographs and elemental composition of the electrode surface after anodic polarization from *E* corrosion to *E* = 3.2 V in 0.5 M H<sub>2</sub>SO<sub>4</sub> and 0.5 M H<sub>2</sub>SO<sub>4</sub> + 0.05 M NaF solutions. A stronger etching of the electrode surface was observed in the presence of fluoride ions; elemental analysis showed an increase in the oxygen content in certain areas of the silicide surface associated with the formation of manganese and silicon oxides and their partial removal at high polarization values.

The kinetic regularities of the MnSi-electrode anodic dissolution were studied by the methods of polarization, capacitance, and impedance measurements. It was established that the addition of fluoride ions leads to weaker barrier properties of the silicon dioxide surface film, which determines the high silicide resistance in a fluoride-free medium. The order of the reaction was calculated for the MnSi anodic dissolution for NaF depending on the potential. In the region of low anodic potentials (from *E*<sub>cor</sub> to *E* ≈ –0.2 V), the reaction order ranged from 1.8 to 1.1, which was due to the high influence of silicon in the composition of the silicide and its oxidation products. With an increase in the polarization value (up to *E* = 0.9 V), the reaction order decreased to 0.5. An increase in the contribution of manganese ionization and oxidation reactions to the kinetics of the anodic dissolution of the silicide was observed. The silicide passivation in a fluoride-containing electrolyte was characterized by higher values of the dissolution current density (10<sup>–4</sup>–10<sup>–3</sup> A/cm<sup>2</sup>) as compared to a fluoride-free electrolyte (10<sup>–6</sup> A/cm<sup>2</sup>), the reaction order in region of the passive state was ~1.0. Passivation was due to the formation of MnO<sub>2</sub> and SiO<sub>2</sub> oxides on the surface. In the transpassivation region (*E* ≥ 2.0 V), there was a weak dependence of the current density on the concentration of fluoride ions. Oxygen release was observed on the surface of the electrode, and the formation of MnO<sub>4</sub><sup>–</sup> ions was recorded in the near-electrode layer. The article discusses mechanisms and kinetic regularities of anodic processes on an MnSi-electrode in sulfuric acid solution in the presence of fluoride ions.

**Keywords:** Manganese monosilicide, Sulfuric acid electrolyte, Sodium fluoride, Anodic dissolution, Impedance

**Для цитирования:** Полковников И. С., Пантелеева В. В., Шеин А.Б. Анодное растворение и пассивация моносилицида марганца в сернокислых фторидсодержащих средах. *Конденсированные среды и межфазные границы*. 2024;26(2): 304–313. <https://doi.org/10.17308/kcmf.2024.26/11941>

**For citation:** Polkovnikov I. S., Panteleeva V. V., Shein A. B. Anodic dissolution and passivation of manganese monosilicide in fluoride-containing sulfuric acid solutions. *Condensed Matter and Interphases*. 2024;26(2): 304–313. <https://doi.org/10.17308/kcmf.2024.26/11941>

✉ Igor S. Polkovnikov, e-mail: [igorpolkovnikov@mail.ru](mailto:igorpolkovnikov@mail.ru)

© Polkovnikov I. S., Panteleeva V. V., Shein A.B., 2024



The content is available under Creative Commons Attribution 4.0 License.

## 1. Introduction

Many branches of science and technology face difficulties when using fluoride-containing solutions [1–10]. This mainly concerns enterprises involved in the production of metals from ores [3–6]. Due to the technological process, fluorides can accumulate in the water system and the fume-collecting chimney at the enterprise. The main danger of fluorides is associated with their concentration and the formation of hydrogen fluoride, which destroys metal structures and causes various types of corrosion [5, 6].

One way to protect steels from corrosion damage is to use alloying additives, which can affect the rate of steel dissolution in corrosive media. Metallurgy uses transition metal silicides as alloying additives, which are introduced into steel in the form of finished alloys or so-called ferroalloys (ferrosilicon, ferrosilicomanganese, ferromanganese, etc.). The introduction of ferrosilicomanganese into manganese silicide-based steel increases the wear and shock resistance of steel. It improves its corrosion characteristics due to the formation of surface barrier films and decreases the melting point of the alloy, which significantly reduces the cost of steel production [11–13]. A high content of silicon in steel favorably affects its elastic properties, resistance to corrosion and oxidation at high temperatures [11, 12, 14]. Manganese and iron form a solid solution, which increases steel hardness and strength. Manganese is used for desulfurization, which prevents the appearance of iron-sulfur bonds [13, 15].

The electrochemical behavior of manganese silicides ( $\text{MnSi}$  and  $\text{Mn}_5\text{Si}_3$ ) in a fluoride-free acidic medium has been previously studied [16, 17]. These studies revealed high anode resistance of silicides due to the formation of a  $\text{SiO}_2$ -based barrier film on their surface. Since silicon dioxide is unstable in fluoride-containing media [18], it is expected that the anodic behavior of silicides will largely depend on the concentration of fluorides in the solution. This paper presents the results of the study of the anode resistance of manganese monosilicide  $\text{MnSi}$  in 0.5 M  $\text{H}_2\text{SO}_4$  + (0.0025–0.05) M NaF solutions. This study revealed the concentration effect of sodium fluoride on the anodic dissolution and passivation of manganese monosilicide.

## 2. Experimental

Manganese monosilicide  $\text{MnSi}$  was obtained by the Czochralski method in the industrial single crystal growing furnace OKB-8093 (“Redmet-8”). The sample was pulled out using an alumina rod at a speed of 0.4 mm/min. To provide a better mixing of the melt and to create a more uniform temperature field, the crucible with melt and the seed were rotated in opposite directions with frequencies within the ranges of 0–15 and 0–60 rpm, respectively. The finished sample was placed in a fluoroplastic holder and filled with epoxy resin, which was then polymerized. The working area of the electrode surface was 0.1 cm<sup>2</sup>.

Electrochemical measurements were carried out at a temperature of 25 °C under natural aeration conditions in unstirred 0.5 M  $\text{H}_2\text{SO}_4$  + (0.0025–0.05) M NaF solutions. The solutions were prepared with chemically pure  $\text{H}_2\text{SO}_4$ , NaF reagents, and deionized water (water resistivity, 18.2 M $\Omega$ ·cm, organic carbon content, 4  $\mu\text{g/l}$ ). Sodium fluoride was introduced into the solution immediately before the experiment.

Polarization and impedance measurements were taken using a Solartron 1255/1287 unit (Solartron Analytical) in an YASE-2 (pyrex glass) electrochemical cell with separated cathode and anode sections. A saturated silver chloride electrode was used as the reference electrode and a platinum electrode was used as the auxiliary electrode. The potentials in the work were given relative to the standard hydrogen electrode, the current densities  $i$  were given per unit of the geometric area of the electrode.

Cyclic current-voltage curves in a 0.5 M  $\text{H}_2\text{SO}_4$  + 0.05 M NaF solution were recorded within the range from  $E$  corrosion to the anodic region at a potential sweep rate of  $v = 10$  mV/s. Before the measurement of the impedance spectra, the current was stabilized at each potential. After that, the impedance was measured at this value of  $E$  and higher potentials, and the potential was changed with a fixed step. Anodic potentiostatic curves for a given value of  $E$  were plotted based on the obtained  $i$  values. The range of frequencies  $f(\omega/2\pi)$  used for impedance measurements was from 20 kHz to 0.02 Hz, while the amplitude of the alternating signal was 5–10 mV.

The morphology and surface composition of the samples before and after electrochemical

tests were investigated using a Hitachi S-3400N scanning electron microscope (Japan) with a Bruker Quantax 200 attachment for energy-dispersive analysis (Germany). The images were obtained in high vacuum at an acceleration voltage of 10 kV in the mode of secondary electron scattering.

The polarization and impedance data were measured and processed using the programs CorrWare2, ZPlot2, and ZView2 (Scribner Associates, Inc.).

### 3. Results and discussion

The anodic potentiostatic curves of the MnSi-electrode recorded in the potential range from  $E_{\text{cor}}$  to  $E = 3.2$  B in solutions of  $\text{H}_2\text{SO}_4$  with the addition of NaF are shown in Fig. 1. The introduction of fluoride ions into the solution resulted in significant changes in the shape of the silicide polarization curve. With an increase in the concentration of fluoride ions the anode peaks became noticeably more pronounced. The dissolution rate of MnSi in the 0.5 M  $\text{H}_2\text{SO}_4$  solution containing a minimum concentration of NaF (at  $E \approx 0.5$  V) was two orders of magnitude higher than that for a fluoride-free sulfuric acid solution. In the presence of fluoride ions, the transition to the transpassivation region occurred at higher anodic potentials.

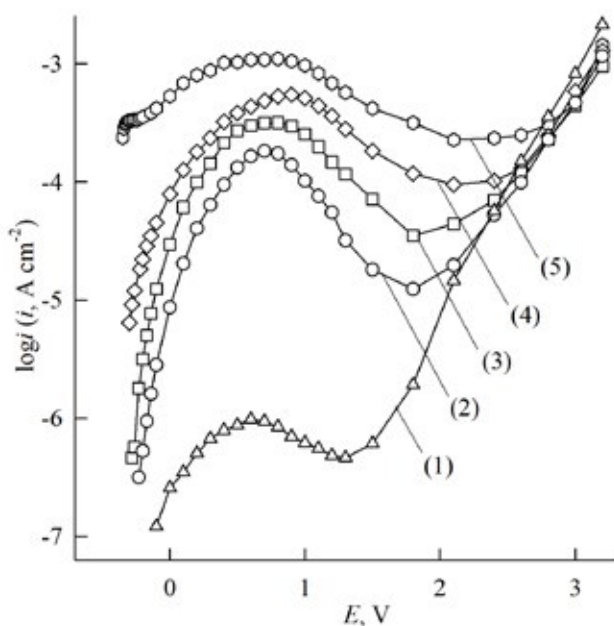
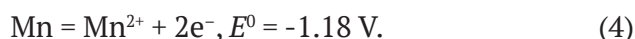
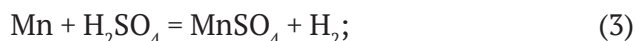
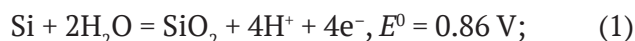


**Fig. 1.** Anodic potentiostatic curves of MnSi-electrode in 0.5 M  $\text{H}_2\text{SO}_4$  (1) и 0.5 M  $\text{H}_2\text{SO}_4 + (x)$  M NaF, where  $x = 0.0025$  (2); 0.005 (3); 0.01 (4), 0.05 (5)

Anodic polarization curves for manganese monosilicide in 0.5 M  $\text{H}_2\text{SO}_4 + (0.0025\text{--}0.05$  M NaF) solutions can be divided into several characteristic sections. Section I (from  $E_{\text{cor}}$  to  $E \approx -0.2$  V) corresponds to the region of active dissolution characterized by a rapid increase in current density with an increase in potential. In a solution with a concentration of 0.05 M NaF, a slight change in current was recorded. In this region, a weak gas emission was observed on the electrode surface. The intensity of gas formation decreased with an increase in the potential and a decrease in the concentration of NaF. According to [19], silicon in acidic media is oxidized to form silicon dioxide, which can dissolve in the presence of HF. According to [20, 21], during the oxidation of silicon in fluoride-containing media in the region of low anodic polarizations hydrogen can form on its surface. Manganese in acidic media is unstable, it can spontaneously dissolve with the release of hydrogen [22, 23]. Along with chemical dissolution, there is electrochemical oxidation of manganese with the formation of  $\text{Mn}^{2+}$  ions. The transformations of silicon and manganese in this section of the polarization curve can be described by the following equations:



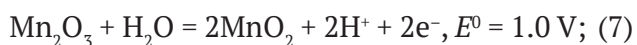
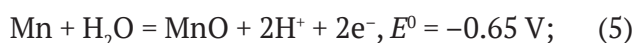
On the surface of MnSi in a 0.5  $\text{H}_2\text{SO}_4$  solution without the addition of NaF at low anodic potentials there was no gas release. Manganese in the composition of the silicide in a fluoride-free electrolyte was more stable due to the formation of a silicon dioxide surface film [16, 17]. The addition of sodium fluoride weakened the passivation action of silicon dioxide and thus led to the activation of the processes of manganese and silicon dissolution in the composition of the silicide, which, apparently, was accompanied by the release of hydrogen.

Section II (from  $-0.2$  V to 0.9 V) is characterized by a further increase in the density of the silicide dissolution current, however, the rate of  $i$  increase fell with an increase in  $E$  (the slope of the polarization curve changed). With an increase in the concentration of NaF, the range



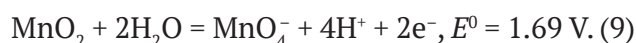
of the recorded anode peak markedly expanded. Section III (from 0.9 V to 2.0 V) is characterized by a gradual decrease in current density which ends with a narrow passivation region. Section IV (from 2.0 to 3.2 V) characterizes the passivation region. At this section of the polarization curves at  $E > 2.6$  V small gas (oxygen) bubbles formed on the surface of the electrode and the space near the electrode was colored crimson. As compared to the fluoride-free solution, oxygen release was observed at higher values of potential (in a fluoride-free medium at  $E \geq 2.2$  V).

The kinks on the MnSi-electrode polarization curves in the fluoride-containing electrolyte are probably related to the formation of manganese oxides:



The solubility of manganese (II) oxide in acidic media is quite high, and it cannot cause deep passivation of the electrode [24]. According to [22], the passivation of manganese is possibly due to the formation of  $\text{Mn}_2\text{O}_3$  and  $\text{MnO}_2$  oxides on its surface. However, manganese (III) oxide in an

acidic medium is unstable and disproportionate to the formation of manganese (II) and (IV) compounds. Manganese dioxide is more stable in acids and its formation can cause passivation of the electrode. Oxidation of manganese dioxide with the formation of permanganate ions leads to its removal from the surface of the electrode [23]:



The results of microscopic examination of the surface of manganese monosilicide before and after electrochemical tests are shown in Fig. 2. Anodic polarization of the MnSi-electrode in a 0.5 M  $\text{H}_2\text{SO}_4$  solution caused partial etching of the electrode surface (Fig. 2b). The addition of fluoride ions to the solution (Fig. 2c) led to the formation of a more developed surface relief, there were pronounced convex regions.

Elemental analysis of the silicide surface (Table 1) showed that in the fluoride-free solution the surface layer of the electrode was depleted of manganese and there was an increase in the oxygen content (as compared to the original sample). The latter was probably due to the selective dissolution of manganese from the silicide surface layer at low anodic polarizations and due to the oxidation of silicon to low-soluble silicon in the acidic media of silicon dioxide. In

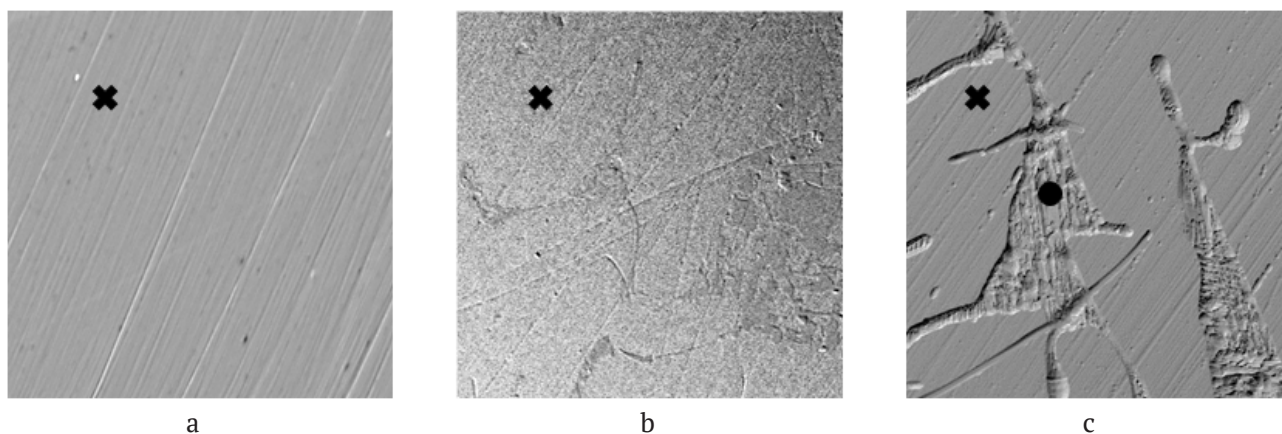


**Fig. 2.** Microphotographs of MnSi surface ( $\times 400$ ) before (a) and after etching in 0.5 M  $\text{H}_2\text{SO}_4$  (b) and 0.5 M  $\text{H}_2\text{SO}_4 + 0.05$  M NaF (c) at  $E = 3.2$  V

**Table 1.** Elemental analysis of the MnSi electrode surface at the point (Fig. 2)

Elements		Mn, at.%	Si, at.%	O, at.%
Initial sample		46.5 $\pm$ 2.3	49.6 $\pm$ 2.5	3.9 $\pm$ 0.2
Sample after polarization from $E_{\text{cor}}$ to $E = 3.2$ V at $v = 0.1$ mV/s	in 0.5 M $\text{H}_2\text{SO}_4$	21.2 $\pm$ 0.6	58.4 $\pm$ 2.9	20.6 $\pm$ 0.6
	in 0.5 M $\text{H}_2\text{SO}_4 + 0.05$ M NaF ( $\times$ )	45.9 $\pm$ 2.3	49.3 $\pm$ 2.5	4.8 $\pm$ 0.2
	in 0.5 M $\text{H}_2\text{SO}_4 + 0.05$ M NaF ( $\bullet$ )	28.5 $\pm$ 1.4	31.3 $\pm$ 1.6	40.2 $\pm$ 2.0

the fluoride-containing electrolyte, an increased oxygen content was recorded in the region of the convex areas; the ratio of the amount of manganese and silicon corresponded to the ratio of the elements in the  $\text{MnO}_2$  and  $\text{SiO}_2$  oxides. Outside the convex region, the composition of the silicide surface differed slightly from that of the original sample.

Similar dependencies indicate the formation of oxides on the MnSi surface with its anodic polarization up to 3.2 V. In a fluorine-free medium, a film consisting mainly of silicon dioxide was formed; in the presence of sodium fluoride, manganese and silicon oxides (probably  $\text{MnO}_2$  and  $\text{SiO}_2$ ) were formed, which partially dissolved in the solution when interacting with the components of the electrolyte.

The degree of fluoride ion concentration influencing the rate of anodic processes on the silicide is shown in Fig. 3. It can be seen that the dependence of the reaction order  $n_{\text{NaF}} = \partial \lg i / \partial \lg C_{\text{NaF}}$  of the manganese monosilicide anodic dissolution for  $\text{F}^-$  ions is a mirror reflection of the anodic curve with the lowest of the studied sodium fluoride concentrations equal to 0.0025 M. At low concentrations of fluoride

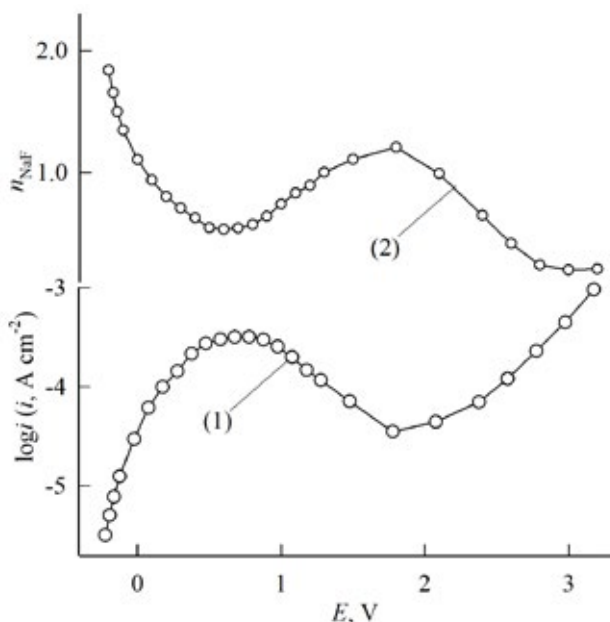
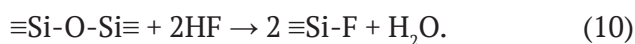


**Fig. 3.** Graphs of the dependences of electrochemical quantities on the potential of the MnSi-electrode: (1) Anodic potentiostatic curve in 0.5 M  $\text{H}_2\text{SO}_4$  + 0.0025 M NaF; (2) The dependence of  $n_{\text{NaF}}$  on the potential in 0.5 M  $\text{H}_2\text{SO}_4$  + (0.0025–0.05) M NaF

ions, the content of silicon dioxide on the silicide surface was still high and the rate of the oxidation process seemed to be limited by the rate of dissolution of silicon dioxide interacting with HF (which formed when NaF was introduced into an acidic medium). The film thickness at each potential value was determined by the successive processes of electrochemical oxidation of silicon and chemical dissolution of silicon dioxide until it reached a steady state.

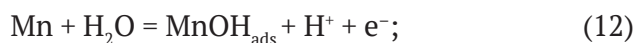
Previous research [18] distinguishes two ways of dissolving silicon dioxide depending on the amount of silicon in the samples. With a high silicon content in silicides, silicon atoms are not isolated from each other, which can lead to the formation of  $\equiv\text{Si-O-Si}\equiv$  siloxane groups, therefore, etching will proceed according to equation (10) and a second reaction order for HF should be expected:



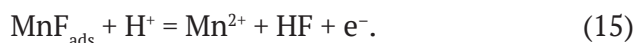
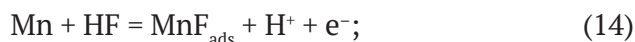
With a low silicon content, isolated Si-OH silanol groups can be formed, the limiting stage of their dissolution will be reaction 11, according to which the HF reaction order is equal to one:



As a result of the silicon dioxide dissolution, the processes associated with the ionization of manganese are activated. The electrochemical dissolution of manganese in acidic media can be represented by the following stages [25]:



When the solution contains hydrofluoric acid, HF molecules can take part in the process of manganese ionization, for example, according to the scheme:



Due to the fact that the dissolution of silicon dioxide is characterized by the first (reaction 11) or second (reaction 10) order for HF and the dissolution of manganese has the first order (reaction 14), it can be concluded that in the region of the first anodic section the process of the MnSi-electrode dissolution will be predominantly determined by the dissolution of silicon dioxide.

The values for the reaction order in this region gradually decreased from 1.8 to 1.1 (Fig. 3), which seems to indicate the mixed nature of the bonds on the silicide surface: both silanol and siloxane groups were present.

With increasing polarization, the values of the reaction order decreased to  $\sim 0.5$ ; according to Fig. 3, the minimum of the reaction order corresponded to the maximum on the anodic curves ( $E \approx 1.0$  V). The papers [22–24, 26] describe the abnormal dissolution of manganese in acidic fluoride-free media, while in the silicide composition manganese is more stable [16, 17]. The addition of sodium fluoride appears to activate the anodic dissolution of manganese from the silicide. As a result, the recorded current mainly corresponded to the processes of manganese oxidation and dissolution (reactions 3, 4, and 5), which were weakly dependent on the presence of HF in the composition of the electrolyte. The latter caused low  $n_{\text{NaF}}$  values.

At  $E > 0.9$  V, the reaction order began to gradually increase and reached a peak at the potentials of the passivation region on the polarization curves. Apparently, this was due to the accumulation of passivating products of manganese and silicon anodic oxidation ( $\text{Mn}_2\text{O}_3$ ,  $\text{MnO}_2$ , and  $\text{SiO}_2$  oxides) on the surface of the

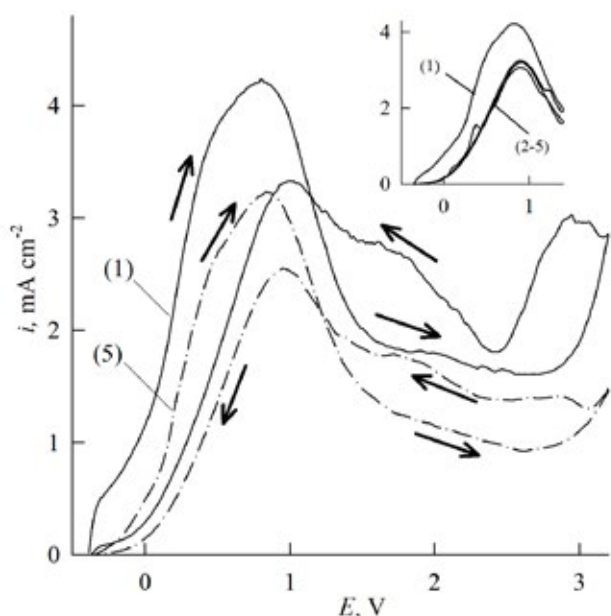
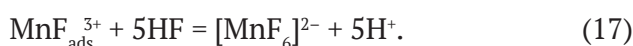
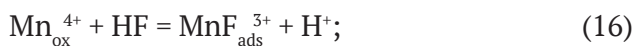


**Fig. 4.** Cyclic voltammograms of the MnSi-electrode in 0.5 M  $\text{H}_2\text{SO}_4$  + 0.05 M NaF. The number is the polarization cycle. In the upper right corner - 5 cycles of polarization at the reversal potential  $E_{\text{revers}} = 1.4$  V

electrode, which dissolved with the participation of HF molecules. The authors of [27, 28] proposed a scheme for the process of nickel (II) and iron (III) oxides dissolution in an acidic fluoride-containing electrolyte. According to [28], for manganese (IV) oxide it is:



In the transpassivation region, the reaction order approaches zero.

The shape of CVA curves indicates the occurrence of several MnSi-electrode oxidation and dissolution processes in a fluoride-containing electrolyte (Fig. 4). In the first polarization cycle, three anode peaks in both forward and reverse directions were recorded on the CVA curve in the potential range from  $E_{\text{cor}}$  to  $E = 3.2$  V. As the number of the polarization cycle increased, a slight decrease in the values of the dissolution current density were observed. With a gradual decrease in the reversal potential, first to 2.2 V (up to the passivation region), then to 1.4 V (up to the beginning of the passivation region), the shape of the CVA curves in the forward and reverse directions remained unchanged. A more noticeable decrease in the manganese silicide dissolution currents with an increase in the polarization cycle at a reversal potential of 3.2 V as compared to  $E$  reversal to 1.4 and 2.2 V indicates the accumulation of passivating products of anodic oxidation on the silicide surface which were not completely removed in the presence of fluoride and caused partial passivation of the electrode.

Fig. 5 shows the dependence of the differential capacitance of the MnSi-electrode on the potential in semi-logarithmic coordinates. The values of the differential capacitance were calculated from the ratio  $C = -1/(\omega Z''')$ , where  $\omega$  is the angular frequency of the alternating current,  $Z'''$  is the imaginary part of impedance at a frequency of 10 kHz. The maximum values of the differential capacitance were observed at potentials close to  $E_{\text{cor}}$  and were  $\sim 16.5$   $\mu\text{F}/\text{cm}^2$  in a solution containing 0.05 M NaF. With a gradual increase in the potential, the differential capacity decreased sharply. The drop was sharper with a higher concentration of fluoride ions in the solution. At potentials above 1.0 V, the values of



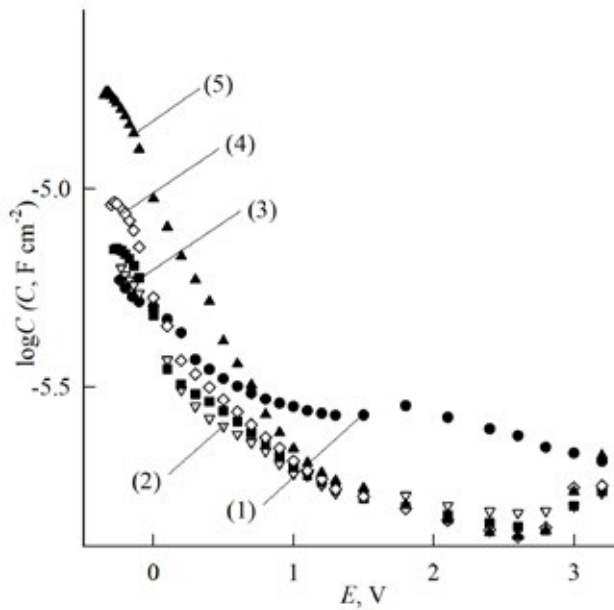


**Fig. 5.** Dependence of the logarithm of the differential capacitance on the potential of the MnSi-electrode in 0.5 M H<sub>2</sub>SO<sub>4</sub> (1) and 0.5 M H<sub>2</sub>SO<sub>4</sub> + (x) M NaF, where x = 0.0025 (2); 0.005 (3); 0.01 (4), 0.05 (5)

the differential capacitance did not depend on the concentration of fluoride ions. Similar to the polarization curves (Fig. 1),  $C, E$ -dependencies can be divided into four linear sections, the change in the slope of which indicates changes in the surface state. A gradual decrease in the values of the differential capacitance from 16.5 to 2  $\mu\text{F}/\text{cm}^2$  may indicate the formation of compounds on the silicide surface characterized by low conductivity (resistivity  $\rho(\text{SiO}_2) \approx (10^{12} - 10^{16}) \Omega\cdot\text{cm}$  [21];  $\rho(\text{Mn}_2\text{O}_3) \approx 10^5 \Omega\cdot\text{cm}$ ;  $\rho(\text{MnO}_2) \approx (10^{-1} - 10^2) \Omega\cdot\text{cm}$  [29]). According to reactions 10 and 11, a large number of Si-F bonds should be expected. According to authors [30, 31], the polarizability of Si-F bonds is less than that of Si-OH bonds.

The MnSi-electrode impedance spectra in sulfuric acid solutions with the addition of sodium fluoride are more complex than in a fluoride-free solution [16]. The form of the impedance spectra changed with the shape of the polarization curve and the variation in the concentration of fluoride ions (Fig. 6), which indicates the diversity of the silicide dissolution and passivation processes.

At the potentials of anodic section I, in solutions with a low concentration of NaF ( $\leq 0.01$  M), capacitive semicircles with the center in the region  $Z'' > 0$  were recorded on the complex

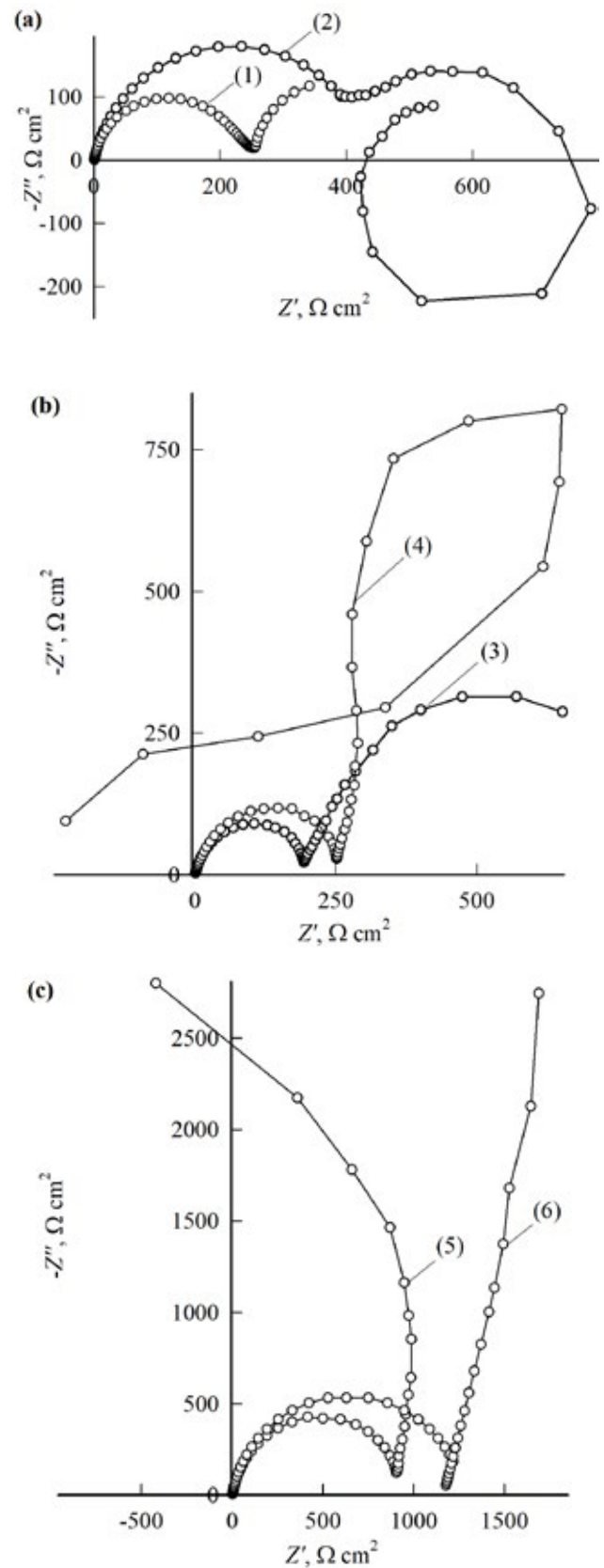


**Fig. 6.** Impedance spectra of MnSi electrode in 0.5 M H<sub>2</sub>SO<sub>4</sub> + 0.05 M NaF at E, V: -0.32 (1); 0 (2); 0.9 (3); 1.1 (4); 1.8 (5); 2.6 (6)



Z-plane. The system was characterized by high values of the impedance modulus  $|Z|$  ( $\sim 90 \text{ k}\Omega\cdot\text{cm}^2$ ).  $|Z|$  increased with an increase in polarization. Similar dependencies were also observed for MnSi in a fluoride-free sulfuric acid solution ( $|Z| \approx 250 \text{ k}\Omega\cdot\text{cm}^2$ ), in which the behavior of the silicide was determined by a silicon dioxide barrier film [16]. Apparently, with a low content of fluoride ions, the passivating effect of silicon dioxide persists, but the barrier properties of the oxide film weaken. With a concentration of NaF equal to 0.05 M, an additional capacitive semicircle appeared on the impedance spectra in the low frequency (LF) region (Fig. 6A). This indicates the staged nature of the oxidation processes of the components of manganese silicide, which are accompanied by adsorption of intermediates on the electrode surface (reactions 10–15). The form of the impedance spectra confirms the assumptions made on the basis of constant current measurements and calculations of the  $n_{\text{NaF}}$  reaction order.

The impedance spectra in the potential region of anodic section II (Fig. 6a,  $E = 0 \text{ B}$ ) contained several semicircles: at least two capacitive semicircles in the high-frequency (HF) region, one inductive semicircle, and one capacitive arc in the low-frequency region. With an increase in the potential, the diameter of the low-frequency semicircles decreased and at certain potentials several loops were recorded. More complex impedance graphs as compared to the graphs in section I indicates the presence on the silicide surface in this region of the potentials of several types of intermediates formed during the manganese and silicon ionization (reactions 10–12, 14). Intermediates formed during the dissolution of manganese (II) oxide in the presence of fluoride ions were probably also recorded.

When the anodic polarization curve approached its maximum (at  $E$  from 0.5 to 0.8 V), an increase in the diameter of the second capacitive semicircle was observed. Near the maximum  $E \approx 0.9 \text{ V}$ , this section of the impedance spectra had the form of an almost vertical straight line, in the low-frequency region a distorted capacitive semicircle was also recorded (Fig. 6b). At the end of anodic section III (at  $E = 1.8 \text{ V}$ ), the impedance spectra contained a high-frequency

capacitive semicircle and a low-frequency semicircle, which at  $\omega \rightarrow 0$  was recorded in the region of negative  $Z'$ . With a further increase in potential, the diameter of the LF semicircle increased markedly faster than the diameter of the HF semicircle (Fig. 6c). The form of impedance spectra indicates the occurrence of passivation processes (reactions 1, 5–8), which correlated with the region of negative slope  $di/dE$  on the anodic polarization curves at these  $E$  (Fig. 1).

In the region of oxygen release potentials, the impedance spectra of manganese silicide in a fluoride-containing electrolyte had the same form as in a fluoride-free solution, i.e. two well-divided capacitive semicircles. At maximum polarization ( $E = 3.2 \text{ V}$ ), an inductive low-frequency arc was also observed. The latter indicates the destruction of the oxide film on the surface of the MnSi-electrode in a fluoride-free solution and the removal of manganese and silicon oxides ( $\text{MnO}_2$  and  $\text{SiO}_2$ ) in the fluoride-containing electrolyte, which provides for a release of oxygen.

#### 4. Conclusions

The study of the anodic behavior of the MnSi-electrode in 0.5 M  $\text{H}_2\text{SO}_4$  + (0.0025 – 0.05) M NaF solutions indicates a strong influence of fluoride ions on the processes of anodic dissolution and passivation of silicide. The silicon dioxide surface film, which is stable in acid, dissolves when fluoride ions are added. As a result, the process of anodic dissolution of manganese monosilicide is activated. It was established that at low anodic polarizations (from  $E_{\text{cor}}$  to  $E \approx -0.2 \text{ V}$ ), the influence of silicon dioxide persists, the rate of its dissolution determines the anode resistance of the silicide. In the potential range (from  $-0.2 \text{ V}$  to  $0.9 \text{ V}$ ), manganese ionization and oxidation reactions (up to  $\text{Mn}^{2+}$ ,  $\text{MnO}$ ) make a significant contribution to the kinetics of anodic processes. Manganese monosilicide passivation is observed at potentials (from  $0.9 \text{ V}$  to  $2.0 \text{ V}$ ) and is associated with the formation of manganese and silicon oxides ( $\text{Mn}_2\text{O}_3$ ,  $\text{MnO}_2$ , and  $\text{SiO}_2$ ). In the region of transpassivation (from  $2.0$  to  $3.2 \text{ V}$ ), the processes of oxygen release and further manganese oxidation (up to  $\text{MnO}_4^-$ ) are recorded.

#### Contribution of the authors

The authors contributed equally to this article.

## Conflict of interests

The authors declare that they have no known competing financial interests or personal relationships that could have influenced the work reported in this paper.

## References

1. Aoun A., Darwiche F., Hayek S. A., Doumit J. The fluoride debate: the pros and cons of fluoridation. *Preventive Nutrition and Food Science*. 2018;23(3): 171–180. <https://doi.org/10.3746/pnf.2018.23.3.171>
2. Genuino H. C., Opembe N. N., Njagi E. C., McClain S., Suib S. L. A review of hydrofluoric acid and its use in the car wash industry. *Journal of Industrial and Engineering Chemistry*. 2012; 18(5): 1529–1539. <https://doi.org/10.1016/j.jiec.2012.03.001>
3. Bordzilowski J., Darowicki K. Anti-corrosion protection of chimneys and flue gas ducts. *Anti-Corrosion Methods and Materials*. 1998;45(6): 388–396. <https://doi.org/10.1108/00035599810236243>
4. Palazzo A. Fluoride corrosivity on mild steel in cooling systems. *Materials Performance*. 2017;56: 44–48. Available at: <https://www.materialsperformance.com/articles/material-selection-design/2017/07/fluoride-corrosivity-on-mild-steel-in-cooling-systems>
5. D'yachenko A. N., Kraydenko R. I., Kurchenko E. I. Corrosion resistance of steels and alloys in fluoride salts. *Bulletin of PNRPU. Mechanical Engineering, Materials Science*. 2017;19(4): 75–89. (In Russ., abstract in Eng.). <https://doi.org/10.15593/2224-9877/2017.4.05>
6. Dai H., Shi S., Yang L., Guo C., Chen X. Recent progress on the corrosion behavior of metallic materials in HF solution. *Corrosion Reviews*. 2021;39(4): 313–337. <https://doi.org/10.1515/corrrev-2020-0101>
7. Luo Z., Zuo J., Jiang H.,... Wei W. Inhibition effect of fluoride ion on corrosion of 304 stainless steel in occluded cell corrosion stage in the presence of chloride ion. *Metals*. 2021;11(350): 1–16. <https://doi.org/10.3390/met11020350>
8. Guo S., Zhang J., Wu W., Zhou W. Corrosion in the molten fluoride and chloride salts and materials development for nuclear applications. *Progress in Materials Science*. 2018;97: 448–487. <https://doi.org/10.1016/j.pmatsci.2018.05.003>
9. Nikitina E. V., Karfidov E. A., Zaikov Yu. P. Corrosion of advanced metal materials in fluoride melts for liquid salt reactors. *Melts*. 2021;1: 21–45. (In Russ., abstract in Eng.). <https://doi.org/10.31857/S0235010621010072>
10. Kerroum Y., Guenbour A., Bellaouchou A., Idrissi H., García-Antón J., Zarrouk A. Chemical and physical effects of fluoride on the corrosion of austenitic stainless steel in polluted phosphoric acid. *Journal of Bio- and Tribo-Corrosion*. 2019;5(3): 68. <https://doi.org/10.1007/s40735-019-0261-5>
11. Ulyanin E. A., Svistunova T. V., Levin F. L. *Highly alloyed corrosion-resistant alloys*. Moscow: Metallurgiya Publ.; 1987. 88 p. (in Russ.).
12. Tolmanov N. D., Chernova G. P. *Corrosion and corrosion-resistant alloys*. Moscow: Metallurgiya Publ.; 1973. 231 p. (In Russ.).
13. Mysik V. F., Zhdanov A. V., Pavlov V. A. *Metallurgy of ferroalloys: technological calculations: a textbook*. Ekaterinburg: Ural University Publishing House; 2018. 536 p. (In Russ.). Available at: <https://elar.urfu.ru/handle/10995/64931>
14. Maznichevsky A. N., Goikhenberg Yu. N., Sprikut R. V. Influence of silicon and microalloying elements on the corrosion resistance of austenitic steel. *Bulletin of the South Ural State University. Series "Metallurgy"*. 2019;19(2): 14–24. (In Russ., abstract in Eng.). <https://doi.org/10.14529/met190202>
15. Handayani D., Okhuysen V., Wagner N. Machinability of high Mn steel using tool life criteria. *International Journal of Metalcasting*. 2023;17(3): 1–8. <https://doi.org/10.1007/s40962-023-01044-3>
16. Russkikh M. A., Polkovnikov I. S., Panteleeva V. V., Shein A. B. Passivation on manganese monosilicide in sulfuric acid electrolytes. *Bulletin of Perm University. Chemistry*. 2020;10(2): 50–59. (In Russ., abstract in Eng.). <https://doi.org/10.17072/2223-1838-2020-2-221-232>
17. Polkovnikov I. S., Panteleeva V. V., Shein A. B. Anodic dissolution and passivation of Mn<sub>5</sub>Si<sub>3</sub> electrode in acidic and alkaline media. *Bulletin of Perm University. Chemistry*. 2019;9(3): 250–265. (In Russ., abstract in Eng.). <https://doi.org/10.17072/2223-1838-2019-3-250-265>
18. Knotter D. M. Etching mechanism of vitreous silicon dioxide in HF-based solutions. *Journal of the American Chemical Society*. 2000;122(18): 4345–4351. <https://doi.org/10.1021/ja993803z>
19. Lehmann V. *Electrochemistry of silicon: instrumentation, science. Materials and applications*. Weinheim: Wiley-VCH Verlag GmbH; 2002. 273 p. <https://doi.org/10.1002/3527600272>
20. Memming R., Schwandt G. Anodic dissolution of silicon in hydrofluoric acid solutions. *Surface Science*. 1966;4: 109–124. [https://doi.org/10.1016/0039-6028\(66\)90071-9](https://doi.org/10.1016/0039-6028(66)90071-9)
21. Zhang X. G. *Electrochemistry of silicon and its oxide*. New York: Kluwer Academic/ Plenum Publ.; 2001. 510 p.
22. Agladze R. I., *Manganese electrochemistry*. Tbilisi: Publishing House of the Academy of Sciences of the GSSR; 1957. 518 p. (In Russ.).
23. Kemmitt R. D. W., Peacock R. D. *The chemistry of manganese, technetium and rhenium*. Pergamon;

1973. 876 p. <https://doi.org/10.1016/B978-0-08-018870-6.50005-6>

24. Kolotyrtkin Y. M., Agladze T. R. Chemical dissolution of manganese\*. *Protection of Metals*. 1968;4(6): 721–724. (In Russ).

25. Burstein G. T., Wright G. A., The anodic dissolution of nickel. I. Perchlorate and fluoride electrolytes. *Electrochimica Acta*. 1975;20: 95–99. [https://doi.org/10.1016/0013-4686\(75\)85049-3](https://doi.org/10.1016/0013-4686(75)85049-3)

26. Toro N., Saldaña M., Gálvez E.,...Hernández P. C. Optimization of parameters for the dissolution of Mn from manganese nodules with the use of tailings in an acid medium. *Minerals*. 2019;9(7): 387–398. <https://doi.org/10.3390/min9070387>

27. Löchel B., Strehblow H.-H., Sakashita M. Breakdown of passivity of nickel by fluoride. *Journal of The Electrochemical Society*. 1984;131(3): 522–529. <https://doi.org/10.1149/1.2115620>

28. Löchel B., Strehblow H.-H. Breakdown of passivity of iron by fluoride. *Electrochimica Acta*. 1983;28(4): 565–571. [https://doi.org/10.1016/0013-4686\(83\)85043-9](https://doi.org/10.1016/0013-4686(83)85043-9)

29. Lazarev V. B., Krasov V. G., Shaplygin I. S. *Electrical conductivity of oxide systems and film structures\**. Moscow: Nauka Publ.; 1978. 168 p. (In Russ).

30. Baklanov M. Green M., Maex K. *Dielectric films for advanced microelectronics*. John Wiley & Sons; 2007. 512 p. <https://doi.org/10.1002/9780470017944>

31. Seshan K., Schepis D. *Handbook of thin film deposition*. Norwich, New York, U.S.A.: William Andrew Publ.; 2018. 470 p. <https://doi.org/10.1016/b978-0-12-812311-9.00030-x>

\*Translated by author of the article

### Information about the authors

Igor S. Polkovnikov, Postgraduate student at the Department of Physical Chemistry, Perm State University (Perm, Russian Federation).

<https://orcid.org/0000-0003-4381-6467>

[igorpokovnikov@mail.ru](mailto:igorpokovnikov@mail.ru)

Viktoria V. Panteleeva, Cand. Sci. (Chem.), Associate Professor, Department of Physical Chemistry, Perm State University (Perm, Russian Federation).

<https://orcid.org/0000-0002-1506-6665>

[vikpant@mail.ru](mailto:vikpant@mail.ru)

Anatoliy B. Shein, Dr. Sci. (Chem.), Professor at the Department of Physical Chemistry (Perm State University (Perm, Russian Federation).

<https://orcid.org/0000-0002-2102-0436>

[ashein@psu.ru](mailto:ashein@psu.ru)

Received 06.06.2023; approved after reviewing 24.11.2023; accepted for publication 15.12.2023; published online 25.06.2024.

Translated by Irina Charychanskaya



## Original articles

Research article

<https://doi.org/10.17308/kcmf.2024.26/11942>**Stabilization of the  $Ba_4Y_3F_{17}$  phase in the NaF-BaF<sub>2</sub>-YF<sub>3</sub> system****P. P. Fedorov<sup>✉</sup>, A. A. Volchek, V. V. Voronov, A. A. Alexandrov, S. V. Kuznetsov***Prokhorov General Physics Institute of the Russian Academy of Sciences,  
38, Vavilova str., Moscow 119991, Russian Federation***Abstract**

The paper describes the study of the phase formation in the NaF-BaF<sub>2</sub>-YF<sub>3</sub> system. It involved solid-phase sintering of the components in a fluorinating atmosphere at 750 °C for two weeks and quenching them in liquid nitrogen.

The prepared samples were placed in nickel capillaries, which, together with barium hydrofluoride, BaF<sub>2</sub>·HF, were placed in copper containers. The containers were sealed by argon arc welding. The fluorinating atmosphere was created by pyrolysis of barium hydrofluoride, BaF<sub>2</sub>·HF. X-ray powder diffraction was carried out using a Bruker D8 Advanced diffractometer (CuKα-radiation). TOPAS, DifWin, and Powder 2.0 software were used to process X-ray diffraction patterns.

Sodium fluoride is a good sintering additive, its introduction in the amount of 5 mol % NaF was enough to synthesize sintered mass with clear X-ray diffraction patterns. The experiment revealed the formation of a solid solution based on the Ba<sub>4</sub>Y<sub>3</sub>F<sub>17</sub> compound with a trigonally distorted fluorite structure (space group *R*-3) with a content of up to ~ 20 mol % of NaF. The parameters of the trigonal cell were related to the parameter *a*<sub>0</sub> of the fluorite subcell by the ratios  $a \sim \sqrt{7}/2a_0$  and  $c \sim 2\sqrt{3}a_0$ . The general formula for the resulting solid solution is Ba<sub>4-*x-y*</sub>Y<sub>3-*x*</sub>NaF<sub>2+*x-y*</sub>. The introduction of sodium fluoride reduced the parameters of the trigonal lattice and was accompanied by the formation of anion vacancies. Structure stabilization expressed in the expansion of the homogeneity region of the phase based on Ba<sub>4</sub>Y<sub>3</sub>F<sub>17</sub> seems to be associated with the disappearance of interstitial fluorine ions surrounded by anions in the Ba<sub>4</sub>Y<sub>3</sub>F<sub>17</sub> structure, both in the cuboctahedral cavity of the Y<sub>6</sub>F<sub>36</sub> clusters and in the centre of the F<sub>8</sub> cubes.

The corresponding solid solution can be used to create new photonics materials. The NaF-BaF<sub>2</sub>-YF<sub>3</sub> system is similar to the previously studied NaF-BaF<sub>2</sub>-GdF<sub>3</sub> system.

**Keywords:** Sodium fluoride, Barium fluoride, Yttrium fluoride, Solid solution

**Funding:** The study was supported by Russian Science Foundation grant No. 22-13-00167, <https://rscf.ru/en/project/22-13-00167/>

**Acknowledgements:** The study was conducted using the equipment of the Centre for Collective Use of the Prokhorov General Physics Institute of the Russian Academy of Sciences.

**For citation:** Fedorov P. P., Volchek A. A., Voronov V. V., Alexandrov A. A., Kuznetsov S. V. Stabilization of the Ba<sub>4</sub>Y<sub>3</sub>F<sub>17</sub> phase in the NaF-BaF<sub>2</sub>-YF<sub>3</sub> system. *Condensed Matter and Interphases*. 2024;26(2): 314–320. <https://doi.org/10.17308/kcmf.2024.26/11942>

**Для цитирования:** Федоров П. П., Волчек А. А., Воронов В. В., Александров А. А., Кузнецов С. В. Стабилизация фазы Ba<sub>4</sub>Y<sub>3</sub>F<sub>17</sub> в системе NaF-BaF<sub>2</sub>-YF<sub>3</sub>. *Конденсированные среды и межфазные границы*. 2024;26(2): 314–320. <https://doi.org/10.17308/kcmf.2024.26/11942>

✉ Pavel P. Fedorov, e-mail: [ppfedorov@yandex.ru](mailto:ppfedorov@yandex.ru)

Fedorov P. P., Volchek A. A., Voronov V. V., Alexandrov A. A., Kuznetsov S. V., 2024



The content is available under Creative Commons Attribution 4.0 License.



## 1. Introduction

When studying the phase diagrams of barium fluoride (BaF<sub>2</sub>) systems with rare earth fluorides (RF<sub>3</sub>) for R = Sm-Lu, Y, Tkachenko and Sobolev [1-3] discovered that along with solid solutions of Ba<sub>1-x</sub>R<sub>x</sub>F<sub>2+2x</sub> fluorite structure and BaR<sub>2</sub>F<sub>8</sub> (R = Ho-Lu, Y) compounds, ordered fluorite-related Ba<sub>4</sub>R<sub>3</sub>F<sub>17</sub> phases also formed. Earlier, single crystals of this phase were grown from a non-stoichiometric melt by Guggenheim and Johnson, however, they mistakenly described their composition as BaRF<sub>5</sub> [4]. Kieser and Greis [5-7] found that a slow cooling of solid solutions of Ba<sub>1-x</sub>R<sub>x</sub>F<sub>2+2x</sub> synthesized at 1000 °C leads to their ordering and the formation of trigonally distorted phases of Ba<sub>4</sub>R<sub>3</sub>F<sub>17</sub> for R = Ce-Lu. They correctly determined the space group symmetry as *R*-3. The interpretation of the crystal structure of Ba<sub>4</sub>R<sub>3</sub>F<sub>17</sub> (R = Yb, Y) [8] confirmed that these data were correct [5]. The repeated structural study [9] did not produce any new results. Isostructural compounds Pb<sub>4</sub>R<sub>3</sub>F<sub>17</sub> (R = Sm-Lu, Y) [10], Pb<sub>8</sub>Y<sub>6</sub>F<sub>32</sub>O [11], and Ba<sub>4</sub>Bi<sub>3</sub>F<sub>17</sub> [12] were also synthesized.

A feature of BaF<sub>2</sub>-RF<sub>3</sub> systems is that solid solutions of Ba<sub>1-x</sub>R<sub>x</sub>F<sub>2+2x</sub> based on barium fluoride do not form during low-temperature syntheses. Co-precipitation from aqueous solutions results in the formation of phases of the fluorite structure containing 40–50 mol % RF<sub>3</sub> without any signs of ordering [13–16]. This cubic phase was also synthesized for bismuth fluoride [17]. Following the mistake of Guggenheim and Johnson, the composition of such phases is often described as BaRF<sub>5</sub> [18–21]. The absence of any signs of trigonal distortion characteristic of Ba<sub>4</sub>R<sub>3</sub>F<sub>17</sub> phases in these samples can be interpreted as a manifestation of the Ostwald's step rule [22, 23]: metastable cubic phases of the corresponding composition are precursors of ordered phases stable at synthesis temperatures.

Phases synthesized in this way have low solubility in water unlike barium fluoride nanoparticles. These phases are matrices for photonics materials [4, 18–21, 24–31].

When the phase formation was studied at 350–500 °C using BaF<sub>2</sub>-RF<sub>3</sub> systems from the sodium nitrate melt and sodium fluoride as a fluorinating agent [32], it was found that for the REE of the yttrium subgroup, sodium fluoride introduced to the reaction products

[33, 34] (unlike the REE of the cerium subgroup [35, 36]).

The purpose of this work was to study the NaF-BaF<sub>2</sub>-YF<sub>3</sub> systems by the method of solid-phase synthesis in order to establish the composition of the formed phases.

## 2. Experimental

The following reagents were used in the experiment: NaF (Reagent grade, Chimmed), BaF<sub>2</sub> (99.99%, LANHIT), and YF<sub>3</sub> (99.99%, LANHIT). The initial powders were further purified from oxygen-containing impurities by melting under CF<sub>4</sub> fluorinating atmosphere in graphite crucibles. The resulting polycrystalline fluorides were ground and, following stoichiometric calculations, mixtures of polycrystalline fluoride powders were prepared. The mixtures were ground in an agate mortar for 15 minutes with ethyl alcohol to achieve uniform composition, then dried at 60 °C under an IR lamp for 10 minutes and ground again for 3 minutes. The prepared powders were stored in a desiccator to avoid hydration.

The prepared samples were placed in nickel capillaries, which, together with barium hydrofluoride, BaF<sub>2</sub>·HF, were placed in copper containers. The containers were sealed by argon arc welding. When heated, barium hydrofluoride decomposed and formed a fluorinating atmosphere.

The ground mixtures of NaF, BaF<sub>2</sub>, and YF<sub>3</sub> were sintered under the following conditions: exposure temperature 750 °C, heating time 2.5 h, and exposure time 336 h. After sintering, the containers were quenched in liquid nitrogen.

The used annealing and quenching method was similar to the method which was used to study phase equilibria in the MF<sub>2</sub>-RF<sub>3</sub>, M = Ca, Sr, Ba systems in [1, 37, 38]. Quenching in liquid nitrogen is less efficient than quenching in water due to the low heat of vaporization of liquid nitrogen and the low heat capacity of gaseous nitrogen, however, it prevents the possibility of pyrohydrolysis of samples when water enters the container due to catastrophic cracking of welds.

The synthesized samples were examined by X-ray phase analysis and partially by thermal analysis. X-ray powder diffraction (XRD) was carried out using a Bruker D8 Advance diffractometer (CuK $\alpha$ -radiation). TOPAS, DifWin,

and Powder 2.0 software were used to process X-ray diffraction patterns.

### 3. Results and discussion

Phase equilibria in the NaF-BaF<sub>2</sub>-YF<sub>3</sub> system are very complex. It should be noted that sintering in the binary BaF<sub>2</sub>-YF<sub>3</sub> system at 750 °C for two weeks did not result in equilibrium. X-ray diffraction patterns recorded a mixture of phases, including the reflections of the BaY<sub>2</sub>F<sub>8</sub> compound. It should be noted that the study of this system in [1,2] was limited to a temperature of 870 °C. The equilibrium time determined by the diffusion coefficients of cations became too long with a decrease in temperature [39], however, the addition of at least 5 mol % sodium fluoride allowed synthesis sample with clear X-ray diffraction patterns.

Fig. 1 shows a section of the phase diagram of NaF-BaF<sub>2</sub>-YF<sub>3</sub> built using the data of the X-ray phase analysis of the annealed samples. The homogeneity region of the solid solution based on Ba<sub>4</sub>Y<sub>3</sub>F<sub>17</sub> was distinctly contoured. The maximum content of sodium fluoride in this solid solution was about 20 mol % NaF. The lattice parameters of this solid solution (*R* phase) are given in Table 1. It can be observed (Fig. 2) that an increase in the amount of sodium in the solid solution led to

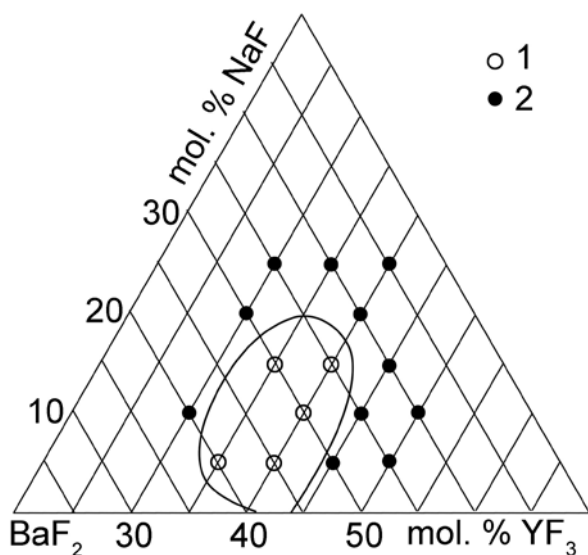


**Fig. 1.** Concentration region of the *R* phase in the NaF-BaF<sub>2</sub>-YF<sub>3</sub> system at 750 °C. (1) single-phase samples, (2) two- or three-phase samples

a decrease in the lattice parameters.

It should be noted that the binary BaF<sub>2</sub>-YF<sub>3</sub> system had a small homogeneity region of this phase. According to [5], it is 41–44 mol % YF<sub>3</sub>. As can be seen from Fig. 1, the introduction of sodium dramatically expanded the homogeneity region. Thus, it can be stated that the heterovalent isomorphism [40] stabilized the crystal lattice of the *R* phase. The same phenomenon was observed earlier in the NaF-BaF<sub>2</sub>-GdF<sub>3</sub> system [41].

Naturally, we can expect a partial cationic substitution of yttrium ions of similar sizes with sodium. Such substitution takes place, for example, in the fluorite phase formed in the NaF-YF<sub>3</sub> system [3]. The study of the structure of the fluorite-like phases formed in the NaF-BaF<sub>2</sub>-YF<sub>3</sub> system showed that sodium is also able to partially substitute barium in its crystallographic positions (BaNa<sub>0.25</sub>Y<sub>2.75</sub>F<sub>10.5</sub> phase) [34].

The studied *R* phase is a derivative of the structural type of fluorite. Its general formula can be written as follows: Ba<sub>1-x-y</sub>Y<sub>x</sub>NaF<sub>2+x-y</sub>. The parameters of the trigonal cell were related to the parameter *a*<sub>0</sub> of the fluorite subcell by the ratios  $a \sim \sqrt{7}/2a_0$  and  $c \sim 2\sqrt{3}a_0$  [5, 8]. The structure of Ba<sub>4</sub>Y<sub>3</sub>F<sub>17</sub> has Y<sub>6</sub>F<sub>37</sub> complexes of 6 yttrium ions with an internal cuboctahedral cavity formed by anions, which includes an additional fluorine ion located in a single-charge environment (F<sub>8</sub> positions in [8, 12]). In addition, there are

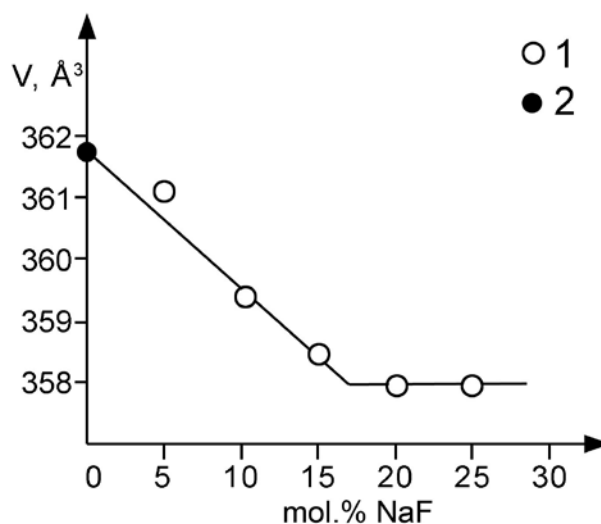


**Fig. 2.** Change in molar volume of the *R* phase at constant content of yttrium fluoride (40 mol % YF<sub>3</sub>). (1) our data, (2) data of Greis and Kieser [6], extrapolation to 40 mol % YF<sub>3</sub>

**Table 1.** X-ray characteristics of the solid solution (*R* phase). Trigonal crystal system, space group *R*-3, *Z* = 6 when calculated for the formula  $Ba_4R_3F_{17}$ 

Composition of the fluoride mixture, mol%	Lattice parameters <i>R</i> phase, Å	Unit cell volume, Å <sup>3</sup>	Mole volume, Å <sup>3</sup>
5% NaF – 60% BaF <sub>2</sub> – 35% YF <sub>3</sub> single-phase sample	<i>a</i> = 11.141 <i>c</i> = 20.57	2211.5	368.6
5% NaF – 55% BaF <sub>2</sub> – 40% YF <sub>3</sub> single-phase sample	<i>a</i> = 11.074 <i>c</i> = 20.41	2167.0	361.2
5% NaF – 50% BaF <sub>2</sub> – 45% YF <sub>3</sub>	<i>a</i> = 11.046 <i>c</i> = 20.36	2150.9	358.5
5% NaF – 45% BaF <sub>2</sub> – 50% YF <sub>3</sub>	<i>a</i> = 11.081 <i>c</i> = 20.35	2163.9	360.7
10% NaF – 60% BaF <sub>2</sub> – 30% YF <sub>3</sub>	<i>a</i> = 11.131 <i>c</i> = 20.63	2213.2	368.9
10% NaF – 50% BaF <sub>2</sub> – 40% YF <sub>3</sub> single-phase sample	<i>a</i> = 11.055 <i>c</i> = 20.37	2156.2	359.4
10% NaF – 45% BaF <sub>2</sub> – 45% YF <sub>3</sub>	<i>a</i> = 11.040 <i>c</i> = 20.36	2149.1	358.2
10% NaF – 40% BaF <sub>2</sub> – 50% YF <sub>3</sub>	<i>a</i> = 11.049 <i>c</i> = 20.35	2151.9	358.7
15% NaF – 50% BaF <sub>2</sub> – 35% YF <sub>3</sub> single-phase sample	<i>a</i> = 11.101 <i>c</i> = 20.47	2184.5	364.1
15% NaF – 45% BaF <sub>2</sub> – 40% YF <sub>3</sub> single-phase sample	<i>a</i> = 11.044 <i>c</i> = 20.36	2150.7	358.5
15% NaF – 40% BaF <sub>2</sub> – 45% YF <sub>3</sub>	<i>a</i> = 11.040 <i>c</i> = 20.36	2148.8	358.1
15% NaF – 35% BaF <sub>2</sub> – 50% YF <sub>3</sub>	<i>a</i> = 11.068 <i>c</i> = 20.41	2164.9	360.8
20% NaF – 50% BaF <sub>2</sub> – 30% YF <sub>3</sub>	<i>a</i> = 11.146 <i>c</i> = 20.60	2215.8	369.3
20% NaF – 40% BaF <sub>2</sub> – 40% YF <sub>3</sub>	<i>a</i> = 11.038 <i>c</i> = 20.36	2147.9	358.0
25% NaF – 40% BaF <sub>2</sub> – 35% YF <sub>3</sub>	<i>a</i> = 11.065 <i>c</i> = 20.39	2162.0	360.3
25% NaF – 35% BaF <sub>2</sub> – 40% YF <sub>3</sub>	<i>a</i> = 11.038 <i>c</i> = 20.36	2148.0	358.0
25% NaF – 30% BaF <sub>2</sub> – 45% YF <sub>3</sub>	<i>a</i> = 11.042 <i>c</i> = 20.36	2149.3	358.2
30% NaF – 30% BaF <sub>2</sub> – 40% YF <sub>3</sub>	<i>a</i> = 11.040 <i>c</i> = 20.36	2149.2	358.2

the same interstitial fluorine ions in the cubic environment (F7 positions according to [8, 12]). These interstitial fluorine ions should disappear with the appearance of anionic vacancies, which results in the crystal structure stabilization.

#### 4. Conclusions

Therefore, the study showed that in the ternary NaF-BaF<sub>2</sub>-YF<sub>3</sub> system, the introduction of sodium fluoride stabilizes the  $Ba_4Y_3F_{17}$  phase and expands its homogeneity region. The

corresponding solid solution can be used to create new photonics materials.

#### Contribution of the authors

The authors contributed equally to this article.

#### Conflict of interests

The authors declare that they have no known competing financial interests or personal relationships that could have influenced the work reported in this paper.

## References

1. Tkachenko N. L., Shvantner M., Sobolev B. P. Phase diagram of the  $BaF_2-YF_3$  system. *Neorganicheskie materialy [Inorganic Materials]*. 1977;13(5): 847–849. (In Russ).
2. Sobolev B. P., Tkachenko N. L. Phase diagrams of  $BaF_2-(Y, Ln)F_3$  systems. *Journal of the Less Common Metals*. 1982;85: 155–170. [https://doi.org/10.1016/0022-5088\(82\)90067-4](https://doi.org/10.1016/0022-5088(82)90067-4)
3. Sobolev B. P. *The rare earth trifluorides. Part 1. The high temperature chemistry of the rare earth trifluorides*. Barcelona: Institut d'Estudis Catalans; 2000. 520 c.
4. Guggenheim H. J., Johnson L. F. New fluoride compounds for efficient infrared-to-visible conversion. *Applied Physics Letters*. 1969;15(2): 51–52. <https://doi.org/10.1063/1.1652898>
5. Kieser M., Greis O. Darstellung und Eigenschaften der Fluoritüberstrukturhasen  $Ba_4SE_3F_{17}$  mit  $SE = Ce-Nd, Sm-Lu$  und  $Y$ . *Zeitschrift für anorganische und allgemeine Chemie*. 1980;469: 164–171. <https://doi.org/10.1002/zaac.19804690123>
6. Greis O., Kieser M. Electron diffraction from single crystals of  $Ba_4Pr_3F_{17}$ ,  $Ba_4Nd_3F_{17}$ ,  $Ba_4Gd_3F_{17}$  and  $Ba_4Dy_3F_{17}$ . *Journal of the Less Common Metals*. 1980;75(1): 119–123. [https://doi.org/10.1016/0022-5088\(80\)90376-8](https://doi.org/10.1016/0022-5088(80)90376-8)
7. Greis O., Haschke J. M. Rare earth fluorides. *Handbook on the physics and chemistry of rare earths*. K. A. Gschneidner & Le Roy Eyring (eds.). Amsterdam, N.Y., Oxford: 1982;5: 387–460. [https://doi.org/10.1016/S0168-1273\(82\)05008-9](https://doi.org/10.1016/S0168-1273(82)05008-9)
8. Maksimov B. A., Dudka A. P., Genkina E. A., ... Golubev A. M. The fluorite-matrix-based  $Ba_4R_3F_{17}$  ( $R = Y, Yb$ ) crystal structure. Ordering of cations and specific features of the anionic motif. *Crystallography Reports*. 1996;41(1): 50–57. Available at: <https://elibrary.ru/item.asp?id=13237398>
9. Tyagi F. K., Kohler J. Preparation and structural elucidation of new anion-excess fluorite variant  $Ba_4Er_3F_{17}$ . *Solid State Science*. 2001;3: 689–695. [https://doi.org/10.1016/S1293-2558\(01\)01167-0](https://doi.org/10.1016/S1293-2558(01)01167-0)
10. Greis O., Uwais B. M., Horne W. Preparation and characterization of superstructure phases  $Pb_4R_3F_{17}$  with  $R = Sm, Gd$  and  $Er$  to  $Lu$ . *Zeitschrift für anorganische und allgemeine Chemie*. 1989;186: 104–107.
11. Dib A., Aleonard S. J. Structure cristalline de  $Pb_8Y_6F_{32}$ . *Journal of Solid State Chemistry*. 1986;64(2): 148–161. [https://doi.org/10.1016/0022-4596\(86\)90134-9](https://doi.org/10.1016/0022-4596(86)90134-9)
12. Dombrovski E. N., Serov T. V., Abakumov A. M., Ardashnikova E. I., Dolgikh V. A., Van Tendeloo G. The structural investigation of  $Ba_4Bi_3F_{17}$ . *Journal of Solid State Chemistry*. 2004;177(1): 312–318. <https://doi.org/10.1016/j.jssc.2003.08.022>
13. Kuznetsov S. V., Yarotskaya I. V., Fedorov P. P., ... Osiko V. V. Preparation of nanopowdered  $M_{1-x}R_xF_{2+x}$  ( $M = Ca, Sr, Ba$ ;  $R = Ce, Nd, Er, Yb$ ) solid solutions. *Russian Journal of Inorganic Chemistry* 2007;52(3): 315–320. <https://doi.org/10.1134/s0036023607030035>
14. Kuznetsov S. V., Fedorov P. P., Voronov V. V., Samarina K. S., Ermakov R. P., Osiko V. V. Synthesis of  $Ba_4R_3F_{17}$  ( $R$  stands for rare-earth elements) powders and transparent compacts on their base. *Russian Journal of Inorganic Chemistry*. 2010;55(4): 484–493. <https://doi.org/10.1134/S0036023610040029>
15. Fedorov P. P., Mayakova M. N., Kuznetsov S. V., ... Osiko V. V. Co-Precipitation of Yttrium and Barium Fluorides from Aqueous Solutions. *Materials Research Bulletin*. 2012;47: 1794–1799. <https://doi.org/10.1016/j.materresbull.2012.03.027>
16. Mayakova M. N., Voronov V. V., Iskhakova L. D., Kuznetsov S. V., Fedorov P. P. Low-temperature phase formation in the  $BaF_2-CeF_3$  system. *Journal of Fluorine Chemistry*. 2016;187: 33–39. <https://doi.org/10.1016/j.jfluchem.2016.05.008>
17. Fedorov P. P., Mayakova M. N., Kuznetsov S. V., ... Iskhakova L. D. Coprecipitation of barium-bismuth fluorides from aqueous solutions: Nanochemical effects. *Nanotechnologies in Russia*. 2011;6(3-4): 203–210. <https://doi.org/10.1134/s1995078011020078>
18. Zhang C., Ma P., Li C., ... Lin J. Controllable and white upconversion luminescence in  $BaYF_5:Ln^{3+}$  ( $Ln = Yb, Er, Tm$ ) nanocrystals. *Journal of Materials Chemistry*. 2011;21: 717–723. <https://doi.org/10.1039/C0JM02948C>
19. Lei Y., Pang M., Fan W., ... Zhang H. Microwave-assisted synthesis of hydrophilic  $BaYF_5:Tb/Ce, Tb$  green fluorescent colloid nanocrystals. *Dalton Transactions*. 2011;40: 142–145. <https://doi.org/10.1039/C0DT00873G>
20. Lei L., Chen D., Huang F., Yu Y., Wang Y. Syntheses and optical properties of monodisperse  $BaLnF_5$  ( $Ln = La-Lu, Y$ ). *Journal of Alloys and Compounds*. 2012;540: 27–31. <https://doi.org/10.1016/j.jallcom.2012.06.078>
21. Karbowski M., Cichos J. Does  $BaYF_5$  exist? – The  $BaF_2-YF_3$  solid solution revisited using photoluminescence spectroscopy. *Journal of Alloys and Compounds*. 2016;673: 258–264. <https://doi.org/10.1016/j.jallcom.2016.02.255>
22. Ostwald W. Studien ueber die Bildung und Umwandlung fester Koerper. *Zeitschrift für Physikalische Chemie*. 1897;22: 289–330. <https://doi.org/10.1515/zpch-1897-2233>
23. Threifall T. Structural and thermodynamic explanations of Ostwald's rule. *Organic Process Research & Development*. 2003;7(6): 1017–1027. <https://doi.org/10.1021/op030026l>



24. Nizamutdinov A. S., Kuznetsov S. V., Madirov E. I., ... Fedorov P. P. Down-conversion luminescence of Yb<sup>3+</sup> in novel Ba<sub>4</sub>Y<sub>3</sub>F<sub>17</sub>:Yb:Ce solid solution by excitation of Ce<sup>3+</sup> in UV spectral range. *Optical Materials*. 2020;108: 110185. <https://doi.org/10.1016/j.optmat.2020.110185>
25. Tomkus M., Natansohn S. J. Anti-Stokes phosphors in BaF<sub>2</sub>-RF<sub>3</sub> systems. *Journal of The Electrochemical Society*. 1971;118(3): 70.
26. Johnsen L. F., Guggenheim H. J., Rich T. C., Ostermayer F. W. Infrared-to-visible conversions by rare-earth ions in crystals. *Journal of Applied Physics*. 1972;43(3): 1125–1137. <https://doi.org/10.1063/1.1661225>
27. Rich T. C., Pinnow D. A. Exploring the ultimate efficiency in infrared-to visible converting phosphors activated with Er and sensitized with Yb. *Journal of Applied Physics*. 1972;43(5): 2357–2365. <https://doi.org/10.1063/1.1661503>
28. Xincen L., Gang X., Powell R. C. Fluorescence and energy-transfer characteristics of rare earth ions in BaYF<sub>5</sub> crystals. *Journal of Solid State Chemistry*. 1986;62: 83–91. [https://doi.org/10.1016/0022-4596\(86\)90219-7](https://doi.org/10.1016/0022-4596(86)90219-7)
29. Liu F., Wang Y., Chen D., ... Huang P. Upconversion emission of a novel glass ceramic containing Er<sup>3+</sup>:BaYF<sub>5</sub> nano-crystals. *Materials Letters*. 2007;61(28): 5022–5025. <https://doi.org/10.1016/j.matlet.2007.03.089>
30. Vetrone F., Mahalingam V., Capobianco J. H. Near-infrared to blue upconversion in colloidal BaYF<sub>5</sub>:Tm<sup>3+</sup>,Yb<sup>3+</sup> nanocrystals. *Chemistry of Materials*. 2009;21: 1847–1851. <https://doi.org/10.1021/cm900313s>
31. Shan Z., Chen D., Yu Y., ... Wang Y. Upconversion luminescence of Ho<sup>3+</sup> sensitized by Yb<sup>3+</sup> in transparent glass ceramic embedding BaYF<sub>5</sub> nanocrystals. *Materials Research Bulletin*. 2010;45(8): 1017–1020. <https://doi.org/10.1016/j.materresbull.2010.04.004>
32. Fedorov P., Mayakova M., Alexandrov A., ... Ivanov V. The melt of sodium nitrate as a medium for the synthesis of fluorides. *Inorganics*. 2018;6(2):38. <https://doi.org/10.3390/inorganics6020038>
33. Alexandrov A. A., Petrova L. A., Pominova D. V., ... Fedorov P. P. Novel fluoride matrix for dual-range optical sensors and visualization. *Applied Sciences*. 2023;13(18): 9999. <https://doi.org/10.3390/app13189999>
34. Fedorov P. P., Volkov S. V., Vaitieva Yu. A., Alexandrov A. A., Kuznetsov S. V., Konushkin V. A. Fluorite-like phases based on barium fluorides and rare-earth elements. *Zhurnal strukturnoi khimii [Journal of Structural Chemistry]*. 2024;65(5): 126843. (In Russ). [https://doi.org/10.26902/JSC\\_id126843](https://doi.org/10.26902/JSC_id126843)
35. Fedorov P. P., Alexandrov A. A., Voronov V. V., Mayakova M. N., Baranchikov A. E., Ivanov V. K. Low-temperature phase formation in the SrF<sub>2</sub>-LaF<sub>3</sub> system. *Journal of the American Ceramic Society*. 2021;104(6): 2836–2848. <https://doi.org/10.1111/jace.17666>
36. Alexandrov A. A., Bragina A. G., Sorokin N. I., ... Fedorov P. P. Low-temperature phase formation in the BaF<sub>2</sub>-LaF<sub>3</sub> system. *Neorganicheskie materialy [Inorganic Materials]*. 2023;59(3): 306–316. (In Russ). <https://doi.org/10.31857/S0002337X23030016>
37. Sobolev B. P., Fedorov P. P. Phase diagrams of the CaF<sub>2</sub>-(Y,Ln)F<sub>3</sub> systems. I. Experimental. *Journal of the Less Common Metals*. 1978;60(1): 33–46. [https://doi.org/10.1016/0022-5088\(78\)90087-5](https://doi.org/10.1016/0022-5088(78)90087-5)
38. Sobolev B. P., Seiranian K. B. Phase diagrams of systems SrF<sub>2</sub>-(Y,Ln)F<sub>3</sub>. II. Fusibility of systems and thermal behavior of phases. *Journal of Solid State Chemistry*. 1981;39(2): 337–344. [https://doi.org/10.1016/0022-4596\(81\)90268-1](https://doi.org/10.1016/0022-4596(81)90268-1)
39. Fedorov P. P. Third law of thermodynamics as applied to phase diagrams. *Russian Journal of Inorganic Chemistry*. 2010;55(11): 1722–1739. <https://doi.org/10.1134/s0036023610110100>
40. Fedorov P. P. Heterovalent isomorphism and solid solutions with a variable number of ions in the unit cell. *Russian Journal of Inorganic Chemistry*. 2000;45(3):268–291. Available at: <https://www.elibrary.ru/item.asp?id=13360696>
41. Pavlova L. N., Fedorov P. P., Olkhovaya L. A., Ikrami D. D., Sobolev B. P. Ordering of the heterovalent solid solution of the fluorite structure in the NaF-BaF<sub>2</sub>-GdF<sub>3</sub> system. *Kristallografiya [Crystallography Reports]*. 1993;38(2): 164–169. (In Russ).

### Information about the authors

*Pavel P. Fedorov*, Dr. Sci. (Chem.), Full Professor, Chief Researcher at the Prokhorov General Physics Institute of the Russian Academy of Sciences (Moscow, Russian Federation).

<https://orcid.org/0000-0002-2918-3926>  
ppfedorov@yandex.ru

*Angelina A. Volchek*, Acting Junior Researcher at the Prokhorov General Physics Institute of the Russian Academy of Sciences (Moscow, Russian Federation).

<https://orcid.org/0000-0001-7743-1376>  
angelina.vol4ek@yandex.ru

*Valery V. Voronov*, Cand. Sci. (Phys.–Math.), Leading Researcher at the Prokhorov General Physics Institute of the Russian Academy of Sciences (Moscow, Russian Federation).

<https://orcid.org/0000-0001-5029-8560>  
voronov@lst.gpi.ru

*Alexander A. Alexandrov*, Junior Researcher at the Prokhorov General Physics Institute of the Russian Academy of Sciences (Moscow, Russian Federation).

<https://orcid.org/0000-0001-7874-7284>

[alexandrov1996@yandex.ru](mailto:alexandrov1996@yandex.ru)

*Sergey V. Kuznetsov*, Cand. Sci. (Chem.), Head of the Laboratory at the Prokhorov General Physics Institute of the Russian Academy of Science (Moscow, Russian Federation).

<https://orcid.org/0000-0002-7669-1106>

[kouznetzovsv@gmail.com](mailto:kouznetzovsv@gmail.com)

*Received 29.11.2023; approved after reviewing 11.12.2023; accepted for publication 15.12.2023; published online 25.06.2024.*

*Translated by Irina Charychanskaya*



## Original articles

Research article

<https://doi.org/10.17308/kcmf.2024.26/11943>Synthesis and characterization of lead and cadmium hexaborates doped with Cr<sup>3+</sup>T. N. Khamaganova *Baikal Institute of Nature Management Siberian Branch of the Russian Academy of Sciences,  
6 Sakhyanovoy str., Ulan-Ude 670047, Buryatia, Russian Federation*

## Abstract

Borates doped with transition metals (Mn, Cu, Cr) exhibit a significant and long-lasting luminescence at room temperature, high power, and other outstanding characteristics. Therefore, the purpose of the study was to establish the possibility of the formation of borate materials containing chromium and the determination of their structure and thermal properties.

New phases of variable composition were synthesized in the  $\text{PbCd}_{2-x}\text{B}_6\text{O}_{12} \cdot x\text{Cr}^{3+}$  system by heterovalent substitution of  $\text{Cd}^{2+}$  ions with  $\text{Cr}^{3+}$  ions using solid-phase reactions at 640 °C. The phases were isolated in the concentration range  $0 \leq x \leq 7.0$  mol % and characterized by X-ray phase analysis (XRD), differential scanning calorimetry (DSC) and IR spectroscopy. According to XRD and IR spectra, the resulting borates crystallize in a monoclinic cell and are assigned to one structural type (space group  $P2_1/n$ ,  $Z = 4$ ).

The crystallographic characteristics of the new phases have been determined. The crystal lattice parameters and their volumes decrease monotonically, indicating the formation of a continuous series of substitutional solid solutions in the studied concentration range. According to the DSC results, the sample  $\text{PbCd}_{2-x}\text{B}_6\text{O}_{12} \cdot 0.03\text{Cr}^{3+}$  melts incongruently at 729 °C.

**Keywords:** Polycrystals of lead and cadmium borates,  $\text{Cr}^{3+}$  ions, Solid-state reaction method, Solid solutions, X-ray phase analysis, DSC, IR spectroscopy

**Funding:** The study received financing within the framework of state order No. 0273-2021-0008 to the Baikal Institute of Nature Management, Siberian Branch of the Russian Academy of Sciences.

**Acknowledgements:** The research was carried out using the scientific equipment of the Laboratory of Oxide Systems of the Baikal Institute of Nature Management, Siberian Branch of the Russian Academy of Sciences and the Centre for Collective Use of Equipment of the Baikal Institute of Nature Management, Siberian Branch of the Russian Academy of Sciences. The author is grateful to O. Zh. Ayurova for recording the IR spectra of the synthesized borates.

**For citation:** Khamaganova T. N. Synthesis and characterization of lead and cadmium hexaborates doped with  $\text{Cr}^{3+}$ . *Condensed Matter and Interphases*. 2024;26(2): 321–326. <https://doi.org/10.17308/kcmf.2024.26/11943>

**Для цитирования:** Хамаганова Т. Н. Синтез и характеристика гексаборатов свинца и кадмия, легированных  $\text{Cr}^{3+}$ . *Конденсированные среды и межфазные границы*. 2024;26(2): 321–326. <https://doi.org/10.17308/kcmf.2024.26/11943>

 Tatyana N. Khamaganova, e-mail: [khama@binm.ru](mailto:khama@binm.ru)

© Khamaganova T. N., 2024



The content is available under Creative Commons Attribution 4.0 License.

## 1. Introduction

One of the effective ways to improve the functional properties of many classes of inorganic compounds is the substitution of cations in their crystal structures. By the substitution of cations within the structural type, it is possible to carry out not only the directed synthesis of the desired crystalline phase, but also to set and regulate the necessary physicochemical properties [1–5].

In the excitation spectrum at 300 nm near the absorption edge of PbCd<sub>2</sub>B<sub>6</sub>O<sub>12</sub> hexaborate two broad emission bands were detected at 510 nm and 617 nm [6]. According to the authors of [6], the emission bands are an integral property of the undoped compound and are consistent with the emission bands in CdB<sub>4</sub>O<sub>7</sub> and Cd<sub>2</sub>B<sub>6</sub>O<sub>11</sub>.

The obtained temperature dependences of the thermoluminescence intensity of the obtained new series of PbCd<sub>2-x</sub>B<sub>6</sub>O<sub>12</sub>:xM borates on the composition of active ions (M = Mn<sup>2+</sup>, Eu<sup>3+</sup>, Cu<sup>2+</sup>) were promising [7–9]. Thermal fluorescence curves for samples of solid solutions of the PbCd<sub>2</sub>B<sub>6</sub>O<sub>12</sub>:Cu<sup>2+</sup> ( $x = 0.01; 0.03; 0.05; 0.06; 0.08$ ) system upon excitation with ultraviolet light for 5 min are shown in Fig. 1. The results of thermoluminescent sensitivity measurements were normalized by the signal from the standard, which was LiF:Mg,Ti lithium fluoride (TLD-100). The thermoluminescence intensities of the studied series of borates were not inferior to the

intensity of the first maximum of the industrial phosphor (TLD-100) [9].

The data obtained allow us to consider materials based on lead and cadmium hexaborate as promising phosphors. Chromium ions Cr<sup>3+</sup> are among the well-known activators successfully used to create luminescent materials for modern lighting technology [10–14]. The investigation of the properties of the described above hexaborates with active chromium ions Cr<sup>3+</sup> for the assessment of the efficiency of thermoluminescent properties, which are expected to be studied in the future, is of interest.

The purpose of this study was to obtain polycrystalline samples of phases based on double lead and cadmium borate PbCd<sub>2</sub>B<sub>6</sub>O<sub>12</sub>, doped with chromium ions Cr<sup>3+</sup>, studying them using X-ray diffraction, IR spectroscopy and differential scanning calorimetry.

## 2. Experimental

Synthesis of powder preparations PbCd<sub>2-x</sub>B<sub>6</sub>O<sub>12</sub>:xCr<sup>3+</sup> was carried out using the method of solid-phase reactions, varying the activator content from 1 to 7 mol %.

The starting reagents were chemically pure boric acid H<sub>3</sub>BO<sub>3</sub> and metal oxides PbO, CdO, Cr<sub>2</sub>O<sub>3</sub> (OOO Krasny Khimik, Russia). Metal oxides were pre-calcined at 500 °C for 5–6 h. Stoichiometric amounts of the starting reagents were annealed in the range from 400 to 640 °C for 150 h with repeated intermediate homogenization. The synthesis temperature was successively increased by 50–100 °C. Before each increase in temperature, the samples were homogenized and their phase composition was determined using X-ray powder diffraction analysis (XRD). Identification of doped phases was carried out by comparison with the X-ray diffraction pattern of individual PbCd<sub>2</sub>B<sub>6</sub>O<sub>12</sub> borate, the structure of which was determined for a single crystal [6].

X-ray diffraction data of polycrystals of the synthesized borates were obtained using D8 ADVANCE Bruker AXS powder autodiffractometer with a Vantec-1 detector (CuK<sub>α</sub>-radiation). The imaging of the samples was performed at room temperature in the diffraction angle range of 10–60° with a scanning step of 0.02°. The experimental intensities were processed and the unit cell parameters of the obtained phases were

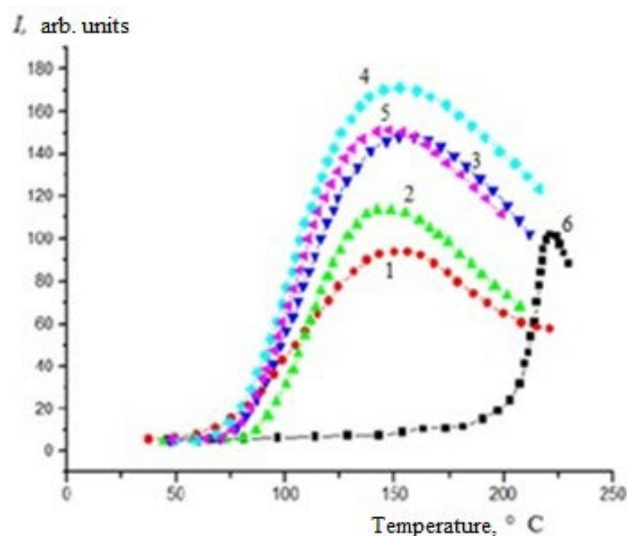


**Fig. 1.** Thermal luminescence curves of PbCd<sub>2-x</sub>B<sub>6</sub>O<sub>12</sub>:xCu<sup>2+</sup> samples with  $x = 0.03$  (1), 0.05 (2), 0.07 (3), 0.06 (4), 0.08 (5); LiF – (6) upon excitation with UV for 5 min



refined using the TOPAS 4.2 software package [15]. Diffraction patterns of doped samples and pure lead and cadmium hexaborate are shown in Fig. 2. Monophasicity of polycrystals of pure PbCd<sub>2</sub>B<sub>6</sub>O<sub>12</sub> and activated PbCd<sub>2-x</sub>B<sub>6</sub>O<sub>12</sub>: 0.03 Cr<sup>3+</sup> was confirmed by thermal analysis.

Thermoanalytical studies were carried out by differential scanning calorimetry (DSC) using a Netzsch STA 449c F1 JUPITER synchronous thermal analyzer. A sample weighing 19.7 mg was placed in a Pt crucible with a lid and heated in an argon atmosphere in the range of 25–800 °C. The sample heating rate was 10 °C/min.

Infrared absorption spectra of the synthesized compounds were recorded using ALPHA IR Fourier spectrometer (BRUKER) in tablets with KBr in the range of 400–4000 cm<sup>-1</sup>. Interpretation of the spectra and assignment of absorption bands were performed based on data from [16–20].

### 3. Results and discussion

The crystal structure of PbCd<sub>2</sub>B<sub>6</sub>O<sub>12</sub> is a three-dimensional framework formed by boron-oxygen layers [(B<sub>6</sub>O<sub>12</sub>)<sup>6-</sup>]<sub>n</sub>, extending parallel to the plane *ab* [6]. Between them are one-dimensional tunnels of 8-membered rings filled with Cd(2)O<sub>6</sub>-octahedra chains. Chains of Cd(2)O<sub>6</sub>-octahedra, connected by common edges, form new two-

dimensional [Cd<sub>2</sub>B<sub>6</sub>O<sub>12</sub>]<sup>4-</sup> layers also parallel to the *ab* plane. Two-dimensional [Cd<sub>2</sub>B<sub>6</sub>O<sub>12</sub>]<sup>4-</sup> layers, connecting by bridging dimers of edge-linked Cd(1)O<sub>7</sub>- polyhedra, form a three-dimensional [Cd<sub>2</sub>B<sub>6</sub>O<sub>12</sub>]<sup>2-</sup> anion network. Pb<sup>2+</sup> ions with CN = 7 are located in the voids of the three-dimensional frame. The boron atoms in the structure are coordinated by three and four oxygen atoms.

XRD of samples activated with chromium ions showed the absence of impurity phases. The X-ray diffraction patterns of the borates of the studied system were indexed using the method of structural analogy using single-crystal data of PbCd<sub>2</sub>B<sub>6</sub>O<sub>12</sub> [6]. Crystallographic characteristics based on the results of indexing X-ray diffraction patterns are given in Table 1. All doped borates crystallize in the monoclinic system, sp. gr. *P2<sub>1</sub>/n*.

In the structure of monoclinic PbCd<sub>2</sub>B<sub>6</sub>O<sub>12</sub> cadmium atoms exhibited double coordination with coordination number (CN) = 6 and 7. Radius of Cr<sup>3+</sup> ion for CN = 6 according to [21] was 0.615 Å, which was slightly less than the radius of the Cd<sup>2+</sup> ion, which for this coordination has a value of 0.65 Å, and for CN = 7 is 0.745 Å. The insignificant content of the dopant and their small size compared to the radius of the substituent ions did not lead to a restructuring of the structure, as evidenced by the lattice parameters of the solid solutions. It can be seen that the resulting phases crystallize

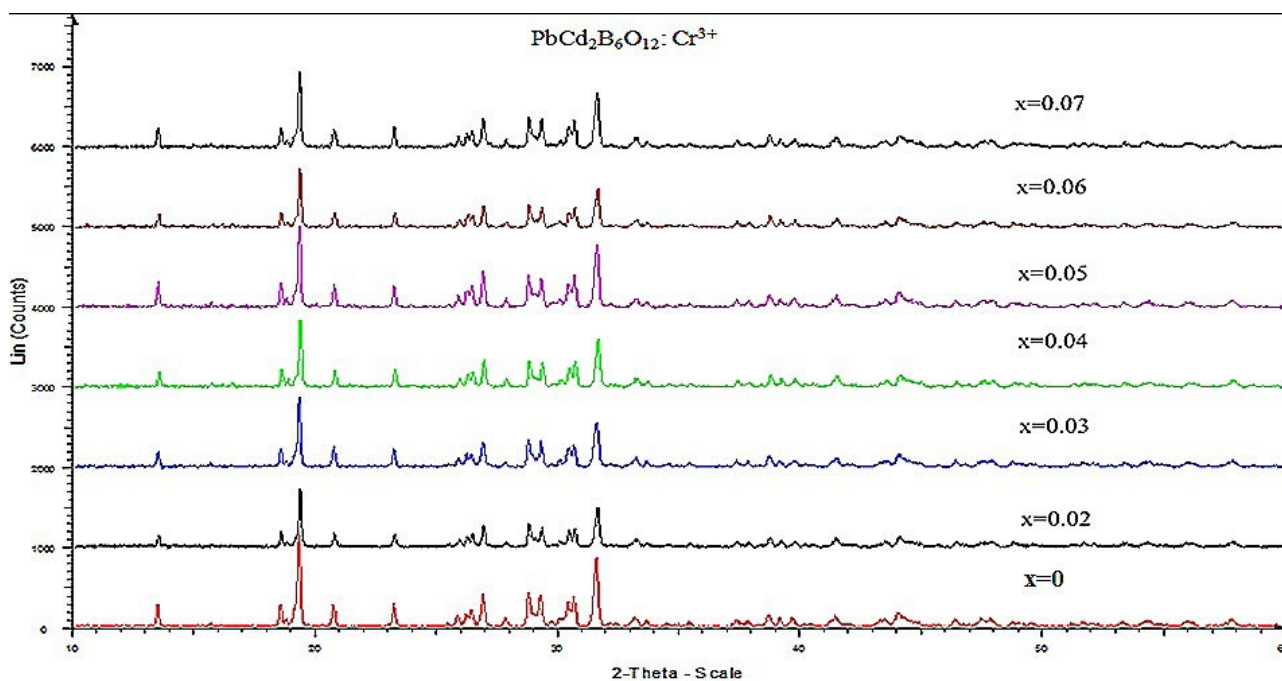


Fig. 2. X-ray diffraction patterns of the PbCd<sub>2-x</sub>B<sub>6</sub>O<sub>12</sub>:xCr<sup>3+</sup> system

**Table 1.** Crystallographic and thermal characteristics of phases PbCd<sub>2-x</sub>B<sub>6</sub>O<sub>12</sub>: xCr<sup>3+</sup> (sp. gr. P2<sub>1</sub>/n, Z = 4)

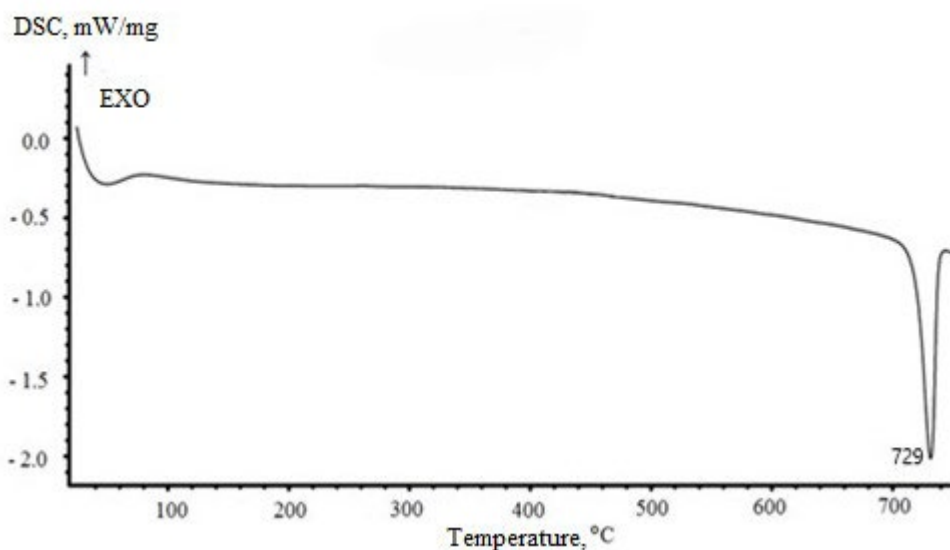
Phase	<i>a</i> , Å	<i>b</i> , Å	<i>c</i> , Å	β, deg.	<i>V</i> , Å <sup>3</sup>	<i>T</i> <sub>melt</sub> , °C
PbCd <sub>2</sub> B <sub>6</sub> O <sub>12</sub> [6]	6.5570(3)	6.9924(4)	19.2094(10)	90.285(4)	880.72(8)	731
PbCd <sub>2</sub> B <sub>6</sub> O <sub>12</sub>	6.5618(3)	6.9868(4)	19.2081(8)	90.250(3)	880.61(7)	734
PbCd <sub>2-x</sub> B <sub>6</sub> O <sub>12</sub> : 0.02 Cr <sup>3+</sup>	6.5605(5)	6.9885(9)	19.213(2)	90.253(6)	880.9(2)	
PbCd <sub>2-x</sub> B <sub>6</sub> O <sub>12</sub> : 0.03 Cr <sup>3+</sup>	6.5598(6)	6.9861(7)	19.219(1)	90.246(5)	880.8(1)	729
PbCd <sub>2-x</sub> B <sub>6</sub> O <sub>12</sub> : 0.04 Cr <sup>3+</sup>	6.5573(6)	6.9855(7)	19.204(2)	90.248(6)	879.7(1)	
PbCd <sub>2-x</sub> B <sub>6</sub> O <sub>12</sub> : 0.05 Cr <sup>3+</sup>	6.5567(7)	6.9852(6)	19.217(1)	90.244(6)	880.0(1)	
PbCd <sub>2-x</sub> B <sub>6</sub> O <sub>12</sub> : 0.06 Cr <sup>3+</sup>	6.5546(6)	6.9793(7)	19.215(6)	90.228(6)	878.9(1)	
PbCd <sub>2-x</sub> B <sub>6</sub> O <sub>12</sub> : 0.07 Cr <sup>3+</sup>	6.5508(5)	6.9801(8)	19.207(2)	90.224(5)	878.3(1)	

in the same structural type as the original matrix, forming a continuous series of PbCd<sub>2-x</sub>B<sub>6</sub>O<sub>12</sub>: xCr<sup>3+</sup> substitutional solid solutions in the considered concentration range 0 ≤ x ≤ 7.0 mol. %.

In Fig. 3 the heating curve of PbCd<sub>2-x</sub>B<sub>6</sub>O<sub>12</sub>: 0.03Cr<sup>3+</sup> sample, containing one endothermic effect at 729 °C, corresponding to the melting process of the sample is shown. As the temperature increased, the mass of borate remained constant until it melted. A similar thermal effect was discovered for pure hexaborate PbCd<sub>2</sub>B<sub>6</sub>O<sub>12</sub> [7].

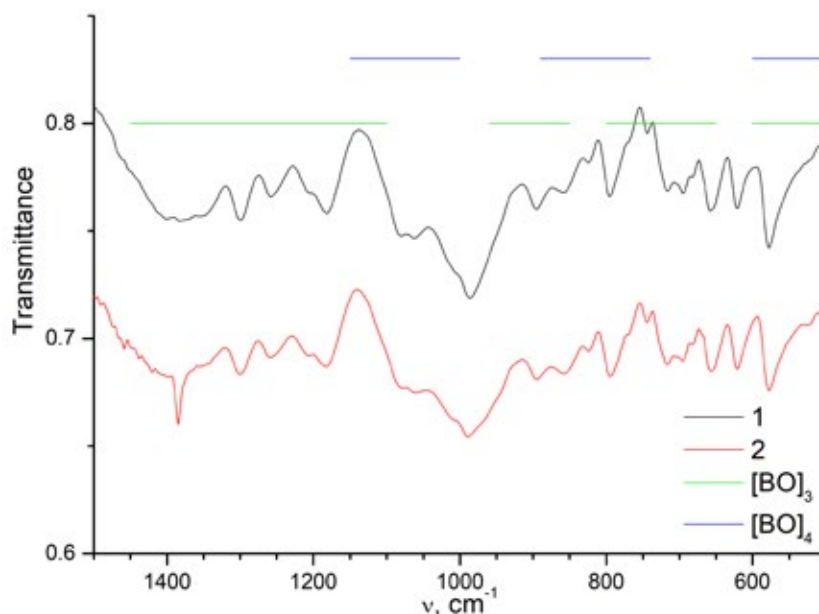
X-ray diffraction pattern of PbCd<sub>2-x</sub>B<sub>6</sub>O<sub>12</sub>: 0.03Cr<sup>3+</sup> powder melt contained the main reflections of phases identified as CdB<sub>4</sub>O<sub>7</sub>, PbO, pointing at incongruent melting pattern of borate. The XRD results were in agreement with our previously obtained data [7–9]. The melting temperatures of some activated lead and cadmium borates are shown in Table 2.

IR spectra of PbCd<sub>2</sub>B<sub>6</sub>O<sub>12</sub> (1) and PbCd<sub>2-x</sub>B<sub>6</sub>O<sub>12</sub>: 0.03 Cr<sup>3+</sup> (2) samples, presented in Fig. 4, contained a large number of bands in the region of 600–1400 cm<sup>-1</sup> and show significant similarities. The complex structure of the boron-oxygen framework of the studied borates did not allow a strict interpretation of the spectra. The similarity in the shape and location of the absorption bands indicated the same type of coordination of boron atoms in both phases and confirmed the XRD results on the similarity of their crystal structures. The bands in the absorption spectra were due to the presence of PbCd<sub>2</sub>B<sub>6</sub>O<sub>12</sub> BO<sub>3</sub>-triangles and BO<sub>4</sub>-tetrahedra in the structure, vibrations of which are usually observed in the spectral range 400–2000 cm<sup>-1</sup>. Spectrum (2) included intense bands at 1384, 1299, 1183, 989, 795 cm<sup>-1</sup>. Bands with lower intensity were observed at 1260, 1063, 895, 656,

**Fig. 3.** Heating curve of PbCd<sub>2-x</sub>B<sub>6</sub>O<sub>12</sub>:0.03Cr<sup>3+</sup> sample

**Таблица 2.** Термические характеристики фаз PbCd<sub>2-x</sub>B<sub>6</sub>O<sub>12</sub>: xCr<sup>3+</sup> (пр. гр. P2<sub>1</sub>/n, Z = 4)

Polycrystals	$T_{\text{melt}}, ^\circ\text{C}$	Melting pattern	Reference
PbCd <sub>2</sub> B <sub>6</sub> O <sub>12</sub>	731	incongruent	[6]
PbCd <sub>2</sub> B <sub>6</sub> O <sub>12</sub>	734	incongruent	[7]
Pb <sub>1-x</sub> Cd <sub>2</sub> B <sub>6</sub> O <sub>12</sub> : 0.03Eu <sup>3+</sup>	732	incongruent	[8]
PbCd <sub>2-x</sub> B <sub>6</sub> O <sub>12</sub> : 0.05Cu <sup>2+</sup>	728	incongruent	[9]
PbCd <sub>2-x</sub> B <sub>6</sub> O <sub>12</sub> : 0.03Cr <sup>3+</sup>	729	incongruent	present study

**Fig. 4.** IR spectra of samples PbCd<sub>2</sub>B<sub>6</sub>O<sub>12</sub> (1) and PbCd<sub>2-x</sub>B<sub>6</sub>O<sub>12</sub>:0.03Cr<sup>3+</sup> (2)

620, 577, 414 cm<sup>-1</sup>. Interatomic distances B–O in triangles varied within 1.334(9)–1.396(9) Å and were significantly shorter than in tetrahedrons (1.430(9)–1.538(8) Å [6]. Consequently, the high-frequency bands of the spectrum at 1384 cm<sup>-1</sup> and 1299 cm<sup>-1</sup> were caused by antisymmetric stretching vibrations ( $\nu_3$ ) BO<sub>3</sub> groups. Peaks in the lower frequency region (<1200 cm<sup>-1</sup>) were associated with symmetrical stretching vibrations of ( $\nu_1$ )BO<sub>3</sub> and ( $\nu_3$ )BO<sub>4</sub> groups. Absorption bands in the region of 577–795 cm<sup>-1</sup> were due to various deformation vibrations ( $\nu_2$ ) and ( $\nu_4$ ) of corrugated layer [(B<sub>6</sub>O<sub>12</sub>)<sup>6-</sup>]. Observed absorption peaks at 414 cm<sup>-1</sup> can be classified as deformation ( $\nu_2$ ) vibration of bonds in boron-oxygen tetrahedra.

#### 4. Conclusions

Phases of variable composition were obtained by heterovalent substitution of cadmium ions with chromium ions in the double borate PbCd<sub>2</sub>B<sub>6</sub>O<sub>12</sub> using solid-phase reactions. Substitutional

solid solutions of PbCd<sub>2-x</sub>B<sub>6</sub>O<sub>12</sub>: xCr<sup>3+</sup> system were revealed in the concentration range 0 ≤ x ≤ 7.0 mol %. According to the XRD results, the parameters and volumes of monoclinic cells monotonically decreased with increasing activator content. Changes in the cell parameters of the new phases were consistent with the ionic radii of the activator and the substituted matrix ions. The incongruent melting temperature of PbCd<sub>2</sub>B<sub>6</sub>O<sub>12</sub>: 0.03Cr<sup>3+</sup> was 729 °C.

#### Conflict of interests

The author declares that they has no known competing financial interests or personal relationships that could have influenced the work reported in this paper.

#### References

1. Trunov V. K., Efremov V. A., Velikodny Yu. A. *Crystal chemistry and properties of double molybdates and tungstates*. Leningrad: Science Publ.; 1986. 173 p. (In Russ.)

2. Urusov V. S. Solid solutions in the realm of minerals. *Soros Educational Journal*. 1996;11: 54–60. (In Russ., abstract in Eng.). Available at: [https://web.archive.org/web/20051028213236/http://journal.issep.rssi.ru/articles/pdf/9611\\_054.pdf](https://web.archive.org/web/20051028213236/http://journal.issep.rssi.ru/articles/pdf/9611_054.pdf)
3. Kozhevnikova N. M., Mokhosoev M. V. *Triple molybdates*. Ulan-Ude: Buryat State University Publ.; 2000. 298 p. (In Russ.)
4. Ivanov-Shits A. K., Murin I. V. *Solid state ionics*: Vol. 1. St. Petersburg: St. Petersburg State University Publ.; 2001. 616 p. (In Russ.)
5. Petkov V. I. Complex phosphates formed by metal cations in oxidation states I and IV\*. *Russian Chemical Reviews*. 2012;81(7): 606–637. (In Russ.). Available at: <https://elibrary.ru/item.asp?id=17788409>
6. Hao Y.-C., Xu X., Kong F., Song J.-L., Mao J.-G. PbCd<sub>2</sub>B<sub>6</sub>O<sub>12</sub> and EuZnB<sub>5</sub>O<sub>10</sub>: syntheses, crystal structures and characterizations of two new mixed metal borates. *CrystEngComm*. 2014;16: 7689–7695. <https://doi.org/10.1039/c4ce00777h>
7. Khamaganova T. mN. Synthesis and thermoluminescence properties of PbCd<sub>2-x</sub>Mn<sub>x</sub>B<sub>6</sub>O<sub>12</sub> solid solutions. *Inorganic Materials*. 2019;55(3): 290–294. <https://doi.org/10.1134/s0020168519030117>
8. Khamaganova T. N., Khumaeva T. G., Perevalov A. V. Synthesis and thermoluminescence of borates Pb<sub>1-x</sub>Eu<sub>x</sub>Cd<sub>2</sub>B<sub>6</sub>O<sub>12</sub>. *Russian Journal of Applied Chemistry*. 2020;93(9): 1387–1391. <https://doi.org/10.1134/s1070427220090116>
9. Khamaganova T. N. Synthesis and luminescence spectra of copper-containing monoclinic PbCd<sub>2</sub>B<sub>6</sub>O<sub>12</sub>-based materials. *Inorganic Materials*. 2023;59(4): 379–384. <https://doi.org/10.1134/s0020168523040039>
10. Shao Q. Y., Ding H., Yao L. bQ., Xu J. F., Liang C., Jiang J. Q. Photoluminescence properties of a ScBO<sub>3</sub>:Cr<sup>3+</sup> phosphor and its applications for broadband near-infrared LEDs. *RSC Advances*. 2018;8: 12035–12042. <https://doi.org/10.1039/c8ra01084f>
11. Fang M. H., Huang P.-Y., Bao Z., ... Liu R.-S. Penetrating biological tissue using light-emitting diodes with a highly efficient near-infrared ScBO<sub>3</sub>: Cr<sup>3+</sup> phosphor. *Chemistry of Materials*. 2020;32: 2166–2171. <https://doi.org/10.1021/acs.chemmater.0c00101>
12. Malysa B., Meijerink A., Jüstel T. Temperature dependent photoluminescence of Cr<sup>3+</sup> doped Sr<sub>8</sub>MgLa(PO<sub>4</sub>)<sub>7</sub>. *Optical Materials*. 2018;85: 341–348. <https://doi.org/10.1016/j.optmat.2018.09.001>
13. Du J. R., Poelman D. Identifying near-infrared persistent luminescence in Cr<sup>3+</sup>-doped magnesium gallogermanates featuring afterglow emission at extremely low temperature. *Advanced Optical Materials*. 2020;8: 1901848. <https://doi.org/10.1002/adom.201901848>
14. Jia Z. W., Yuan C. X., Liu Y. F., ... Jiang J. Strategies to approach high performance in Cr<sup>3+</sup>-doped phosphors for high-power NIR-LED light sources. *Light: Science & Applications*. 2020;9(1): 86. <https://doi.org/10.1038/s41377-020-0326-8>
15. Bruker AXS TOPAS V4: General profile and structure analysis software for powder diffraction data. *User's Manual*. Karlsruhe, Germany: Bruker AXS; 2008. 68 p. Available at: <http://algor.fis.uc.pt/jap/TOPAS%204-2%20Users%20Manual.pdf>
16. Weir C. E., Schroeder R. A. Infrared spectra of the crystalline inorganic borates. *Journal of Research of the National Bureau of Standards Section A: Physics and Chemistry*. 1964;68A (5): 465–487. <https://doi.org/10.6028/jres.068a.045>
17. Egorysheva A. V., Burkov V. I., Kargin Yu. F., Plotnichenko V. G., Koltashev V. V. Vibrational spectra of crystals of bismuth borates. *Crystallography Reports*. 2005;50(1): 127–136. <https://doi.org/10.1134/1.1857259>
18. Pir P. V., Shabanov E. V., Dotsenko V. P. Synthesis and IR spectroscopic study of strontium borates. *Vestnik Odesskogo natsional'nogo universiteta [Bulletin of Odessa National University]*. 2005;10(1): 21–27. (In Russ., abstract in Eng.). Available at: <https://elibrary.ru/item.asp?id=24355545>
19. Dobretsova E. A., Boldyrev K. N., Chernyshev V. A., Petrov V. P., Maltsev V. V., Leonyuk N. I. Infrared spectroscopy of europium borates EuM<sub>3</sub>(BO<sub>3</sub>)<sub>4</sub> (M = Al, Cr, Fe, Ga) with a huntite mineral type of structure. *Bulletin of the Russian Academy of Sciences: Physics*. 2017;81(5): 546–550. <https://doi.org/10.3103/s1062873817050094>
20. Shmurak S. Z., Kedrov V. V., Kiselev A. P., Fursova T. N., Zver'kova I. I. Structural and spectral characteristics of La<sub>0.99-x</sub>Y<sub>x</sub>Eu<sub>0.01</sub>BO<sub>3</sub> orthoborates. *Physics of the Solid State*. 2022;64(8): 961–972. <https://doi.org/10.21883/PSS.2022.08.54611.359>
21. Shannon R. D. Revised effective ionic radii and systematic studies of interatomic distances in halides and chalcogenides. *Acta Crystallographica Section A*. 1976;A32: 751–767. <https://doi.org/10.1107/s0567739476001551>

### Information about the authors

Khamaganova Tatyana Nikolaevna, Cand. Sci. (Chem.), Associate Professor, Senior Research Fellow, Laboratory of Oxide Systems, Baikal Institute of Nature Management, Siberian Branch of the Russian Academy of Sciences (Ulan-Ude, Russian Federation).

<https://orcid.org/0000-0002-8970-1481>  
khama@binm.ru

Received 23.08.2023; approved after reviewing 15.11.2023; accepted for publication 15.12.2023; published online 25.06.2024.

Translated by Valentina Mittova





# Condensed Matter and Interphases

Kondensirovannye Sredy i Mezhfaznye Granitsy  
<https://journals.vsu.ru/kcmf/>

## Original articles

Research article

<https://doi.org/10.17308/kcmf.2024.26/11944>

## The synergy of transformation of isomorphous phyllosilicate structures

A. G. Chetverikova<sup>1✉</sup>, V. N. Makarov<sup>1</sup>, O. N. Kanygina<sup>1</sup>, M. M. Seregin<sup>2</sup>, A. A. Yudin<sup>1</sup>

<sup>1</sup>Orenburg State University,  
13 Pobedy ave., Orenburg 460018, Russian Federation

<sup>2</sup>LLC «BO-ENERGO.ASTS»,  
19 Prospect Mira, building 1, Moscow 129090, Russian Federation

### Abstract

The article presents an analysis of the synergy of structural transformations of phyllosilicates subjected to high temperatures and microwave radiation in terms of the destruction and formation of crystal structures. Studying the synergy of transformations of crystal structures is essential for the development of new materials and technologies, because it helps to create materials with unique properties, which cannot be obtained when using the same factors separately.

The material used in the study was a polymineral complex, which contained quartz, montmorillonite, kaolinite, chlorite, paragonite, and iron oxides (listed from the largest to the smallest mass fraction). The methods used in the study allowed us to assess the structural transformations. Averaged structural formulas of the studied phyllosilicates were calculated using the oxygen method combined with a recalculation method based on the results of a microprobe analysis. Differential thermal analysis demonstrated a synergistic effect of high temperature and microwave fields registered as a decrease in the temperature gradient of the ceramics and initiation of the sintering process at lower temperatures and with greater intensity. All the treated samples contained the amorphous phase in significant concentrations: from 15 to 25 vol. %. Half of the three-layer phyllosilicates (chlorite and montmorillonite) were destroyed by the microwave field. Kaolinite and paragonite practically did not react to external factors. The synergistic effect was the most obvious in the structural transformations of silicon and iron oxides.

Our experiments demonstrated for the first time the mechanism of formation of magnetite and hematite crystals from X-ray amorphous iron-containing films covering the particles of clay minerals. The use of the MW field and the resulting dehydration led to the formation of crystals of nuclei of iron oxides. The following high-temperature processes activated an increase in aggregated iron (magnetite and hematite). The X-ray diffraction analysis determined the presence of a synergistic effect in the evolution of structures, which could not be identified by means of IR-spectroscopy. The EPR spectroscopy allowed us to register the states of rare irregular cells with foreign paramagnetic atoms. The shift of the foreign Fe<sup>3+</sup> from the geometric centers of octahedral crystal cells towards the minima of potential energy caused by the Jahn-Teller effect decreased the potential energy of the crystal lattice. At the same time, some chemical bonds forming the crystal cell became stronger, while others weakened.

**Keywords:** Crystal cell, Transformation, Montmorillonite, Kaolinite, Chlorite, Paragonite, Microwave field, Heat treatment

**Acknowledgments:** The authors are grateful to M. S. Syrtanov, a member of the laboratory of the National Research Tomsk Polytechnic University, for providing methodological assistance.

**For citation:** Chetverikova A. G., Makarov V. N., Kanygina O. N., Seregin M. M., Yudin A. A. The synergy of transformation of isomorphous phyllosilicate structures. *Condensed Matter and Interphases*. 2024;26(2): 327–338. <https://doi.org/10.17308/kcmf.2024.26/11944>

**Для цитирования:** Четверикова А. Г., Макаров В. Н., Каныгина О. Н., Серегин М. М., Юдин А. А. Синергизм трансформации изоморфных структур филлосиликатов. *Конденсированные среды и межфазные границы*. 2024;26(2): 327–338. <https://doi.org/10.17308/kcmf.2024.26/11944>

✉ Anna G. Chetverikova, e-mail: [kr-727@mail.ru](mailto:kr-727@mail.ru)

© Chetverikova A. G., Makarov V. N., Kanygina O. N., Seregin M. M., Yudin A. A., 2024



The content is available under Creative Commons Attribution 4.0 License.

## 1. Introduction

Within the modern paradigm, a structure has the following characteristics: morphometric (size, shape, surface of the structural elements, and their quantitative description), geometric (spatial composition of the structural elements), and energy characteristics (types of structural bonds and the total energy of the structure). However, this approach does not fully reflect the dynamics of structures that have spatial and temporal nature [1].

The synergy of transformation of a crystal structure is a combination of processes facilitating its evolution at various levels. Interactions can occur between physical parameters, for instance temperature and electromagnetic fields, and between chemical factors, including the concentration of foreign ions or phases and synthesis activators [2, 3].

Studying the synergy of transformations of crystal structures is essential for the development of new materials and technologies, because it helps to create materials with unique properties, which cannot be obtained when using the same factors separately. The synergistic effect results in the formation of new crystal phases, which have higher thermal conductivity and strength [4] or flame retardancy [5]. There are some studies focusing on the combined effect of the temperature field, the microwave field, and impurity ions on condensed matter [6]. However, there appear to be no publications concerning the synergistic effect of these factors during the transformation of crystal cells of phyllosilicates.

Earlier studies demonstrated that microwave field treatment of montmorillonite can result in structural transformations (restructuring of the crystal structure and amorphization) caused by heating [7]. It is known [8, 9] that high temperature treatment of phyllosilicates results in the structural degradation of clay minerals.

In order to develop functional materials with good sorption properties, it is important to analyze the effect of various fields on phyllosilicates. [10] considers the effect of a 10-minute exposure to microwave radiation on the morphology, phase composition, and sorption capacity of montmorillonite clay. The authors demonstrated that phyllosilicates can be modified, but did

not explain the transformations occurring at micro- and mesolevels. [11] determined that both resistance heating and microwave radiation have a positive effect on the sorption capacity of montmorillonite. The authors suggested a hypothesis that the changes in the sorption properties of phyllosilicate containing materials subjected to MW field and heat treatment are caused by the transformation of isomorphous structures.

It is therefore important to consider the synergistic effect of high temperature and microwave radiation on structural transformation of the particles of the montmorillonite polymineral complex (M-PMC).

The purpose of our study was to analyze the synergy of structural transformations of phyllosilicates subjected to high temperatures and microwave radiation in terms of destruction and formation of crystal structures.

## 2. Experimental

### 2.1. Materials

In our study, we analyzed samples of montmorillonite clay (M-PMC) mined in the Orenburg Region. The samples were ground using an iMold milling machine and subjected to sieve analysis with the mesh size of 26  $\mu\text{m}$ . The montmorillonite yield of the polymineral complex was over 30% and the total amount of clay minerals was – 50%. A large number of organic compounds determined by means of Raman spectroscopy were removed with a 30%  $\text{H}_2\text{O}_2$  solution.

The elemental composition of the obtained A sample, expressed in form of oxides, was determined by means of chemical analysis according to [12]. According to the X-ray powder diffraction performed in [13] clay is a polymineral complex, which contains quartz, montmorillonite, kaolinite, chlorite, paragonite, and iron oxides (listed from the largest to the smallest mass fraction). Table 1 presents the structural formulas and volume fractions of their crystalline phases in the A sample.

Powder samples (A) were subjected to microwave radiation for 10 minutes. The source of the MW field was a 750 W magnetron with a radiation frequency of 2.45 GHz [14]. A 10 mm layer of dispersed samples was put into a

cuvette on a rotating plate in order to average the heating conditions at a humidity of  $70\pm 5\%$  (sample **B**). The temperature of the samples in the MW field was up to  $220\text{--}250\text{ }^\circ\text{C}$ . The third sample **C** was heated to  $900\text{ }^\circ\text{C}$  at a heating rate of  $5\text{ }^\circ\text{C}/\text{min}$ . The fourth sample **BC** was obtained by sequential MW irradiation and heating up to  $900\text{ }^\circ\text{C}$ .

The understanding and modeling of structural transformations caused by the synergistic effect of the MW field and high temperatures requires a comprehensive experimental analysis at millimeter-, micro-, and nanosize levels. Accurate information can only be obtained when controlling the reproducibility of results. In our study, we used methods that allowed us to assess the dynamics of structural transformations caused by MW field and temperature in the presence of foreign elements. In particular, we focused on crystallochemical characteristics (2.1), physicochemical properties (2.2–2.5), and the fine structure (method 2.6).

## 2.2. Crystallochemical analysis

Structural formulas given in Table 1 do not show the distribution of the foreign elements between tetrahedral, octahedral, and interlayer positions in the crystal lattice. According to [15], these positions should be taken into account when analyzing the chemical structure of layered silicates. In order to calculate the crystal chemical formulas of the studied phyllosilicates, we used a classical oxygen method combined with a

recalculation method based on the results of a microprobe analysis [16].

## 2.3. Differential thermal analysis

Structural transformations in the samples were registered by means of differential thermal analysis (DTA). The thermograms were obtained using a Thermoscan-2 unit (OOO Analitpribor, Russia) with a heating rate of  $5\text{ }^\circ\text{C}/\text{min}$  from  $25$  to  $1000\text{ }^\circ\text{C}$ . The error for temperature measurement was  $\pm 1\text{ }^\circ\text{C}$ . Aluminum oxide powder ( $\text{Al}_2\text{O}_3$ ) with a weight of  $0.5\text{ g}$  and sealed in a quartz container was used as a reference. The weight of the studied sample put into a quartz crucible was  $0.50\pm 0.01\text{ g}$ .

## 2.4. Infrared spectroscopy

The IR spectra of the samples were obtained using an Infralyum FT-02 IR Fourier spectrometer (OOO Lumex, Russia). The spectrometer had an attachment for disturbed total internal reflection (DTIR) with a single reflection zinc selenide ( $\text{ZnSe}$ ) crystal. The measurements were performed over the range of  $550\div 4000\text{ cm}^{-1}$  with a resolution of  $2\text{ cm}^{-1}$ . The Bessel apodization was used for the Fourier transform. The spectra were recorded in the mode of accumulation of 60 scans with the correction of the base line.

## 2.5. X-ray phase analysis

The X-ray phase analysis of the powders was conducted using a Shimadzu XRD 7000S diffractometer (Shimadzu Corporation, Japan) with a OneSight matrix detector. Diffraction patterns were recorded under the following

**Table 1.** Phase composition of the sample

Mineral / Space group [12]	Structural formula / mineral classification [13]	Fraction, vol. %
$\beta$ -Quartz <i>P6<sub>2</sub>22</i>	$\text{SiO}_2$ Simple oxide	>40
Montmorillonite <i>B2/m</i>	$(\text{Na,Ca})_{0.33}(\text{Al}_{1.67}\text{Mg}_{0.33})(\text{Si}_4\text{O}_{10})(\text{OH})_2 \cdot n\text{H}_2\text{O}$ three-layer phyllosilicate (T-O-T): two tetrahedral silica-oxygen (T) and one octahedral alumina-oxygen (O) sheets	30
Kaolinite <i>P1</i>	$\text{Al}_2(\text{Si}_2\text{O}_5)(\text{OH})_4$ two-layer phyllosilicate: T-O structure	10
Chlorite <i>C2/m</i>	$(\text{Mg,Fe})_{6-x}(\text{Al,Fe})_{2x}\text{Si}_{4-x}\text{O}_{10}(\text{OH})_8$ three-layer phyllosilicate: T-O-T structure	10
Paragonite <i>B2/b</i>	$\text{NaAl}_2(\text{Si}_3\text{Al})\text{O}_{10}(\text{OH})_2$ two-layer phyllosilicate: T-O structure	5
Magnetite, hematite <i>Fd<math>\bar{3}m</math>, R<math>\bar{3}</math></i>	$\text{Fe}^{2+}\text{Fe}^{3+}_2\text{O}_4$ , $\text{Fe}_2\text{O}_3$ Simple oxide	<5



conditions: anode of the X-ray tube – Cu (copper), rotation of the sample, angles  $2\theta$ : from 5 to  $140^\circ$ , scanning rate of  $1^\circ/\text{min}$ , step of  $0.2^\circ$ .

## 2.6 EPR spectroscopy

The EPR spectra of the initial samples and the treated samples were registered using a CMS8400 compact automatic controlled spectrometer (Adani, Belarus) at room temperature. The spectra were registered under the following conditions: frequency of 9.86 GHz, magnetic field of 1–7 T, magnetic field modulation frequency of 200 kHz.

## 3. Results and discussion

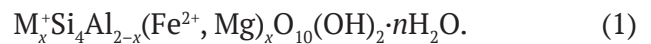
### 3.1. Structural formulas of phyllosilicates with isomorphous ions

Morphometric and monomineral analyses of the M-PMC samples were performed using a JCM-6000 scanning electron microscope (JEOL, Japan). Fig. 1a demonstrates the matrix structure of the dispersion system: the microstructure consists of solid structural elements (Fig. 1b), i.e. mineral particles, oxide grains, and their associations that determine the dispersion of the system. It is obvious that the structure consists of powdered quartz grains (1) and microaggregates of clay (2) and clay powder particles (3). The powdered grains were rounded and had the elemental composition of Si, O; their size varied from 1 to  $5\ \mu\text{m}$ . Some of the quartz grains were, as usual [17], covered with a thin film of iron oxides, and some were covered with clay coats. Microaggregates (2) consisted of clay particles

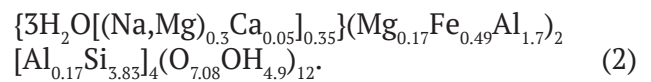
of kaolinite (O, Si, Al, Fe, Ti), mostly isometric or slightly elongated and with the size varying from fractions of a micron to several microns.

Isometric microaggregates (3) were looser and consisted of fine thin particles connected by clay bridges. Their size was  $10\text{--}20\ \mu\text{m}$ . Montmorillonite and chlorite microaggregates with similar crystal structures and microelemental composition (O, Si, Al, Fe, Na, Mg, Ca) usually have a thin leaf-like shape [18]. The boundaries between the primary particles were hardly identifiable because one microaggregate gradually transformed into another.

A general crystal chemical formula of montmorillonite taking into account the isomorphous ions is presented as follows [19]:



$x$  varies within quite a wide range (from 0.1 to 0.6), because it is often impossible to obtain a monomineral fraction of the clay mineral for chemical analysis. Metal cations (M) are represented by ions of alkali and alkaline earth elements (Na, Ca, Mg, etc.) located in the interlayers of the structure. They compensate for the negative charge of the octahedral layers. The calculated formula of the studied montmorillonite is presented as follows (2):



The averaged calculated structural formula of kaolinite also demonstrates a high degree of isomorphism:

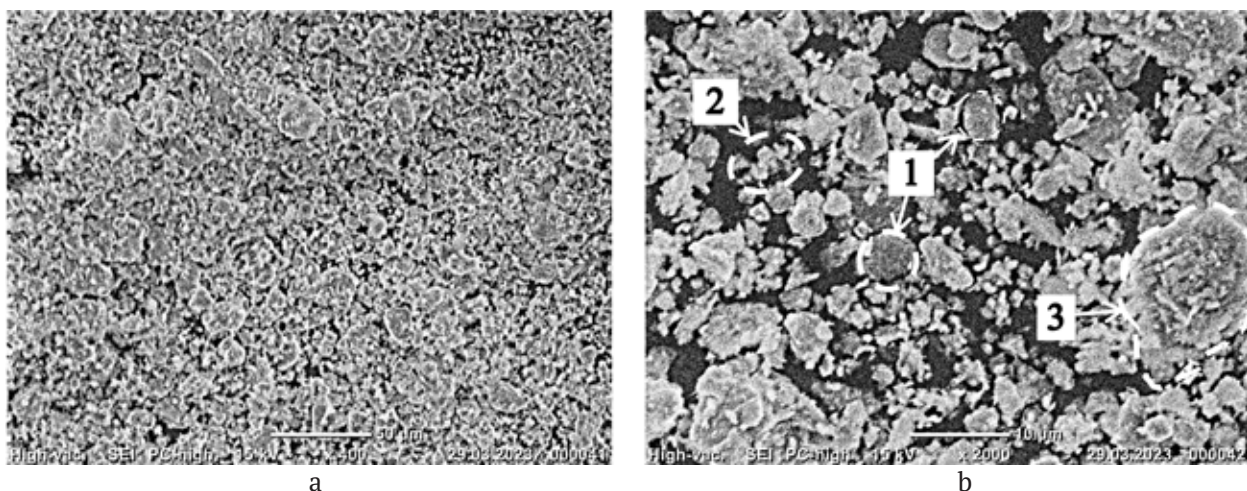
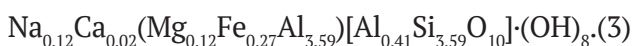
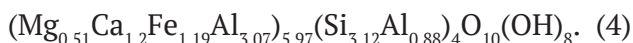


Fig. 1. Matrix microstructure: general view (a) and solid structural elements (b)





Chlorite should have a strictly specific structure without any deviations in the ratios of group coefficients. Therefore, the recalculated structural formula (4) is close to a typical chlorite formula:



The structural formula of paragonite cannot be specified due to its low concentration (because it is difficult to obtain a monomineralic fraction).

### 3.2. Interpretation of the differential thermal analysis (DTA)

Fig. 2 presents the thermograms of samples A and B. Analyzing the empirical dependences, we identified 5 main stages of structural transformation of the A and B samples. The obtained thermograms of A and B are in good agreement with the results obtained in [20].

During the first stage of heating (from 25 to 310 °C) of the A sample, an intense endothermic effect was observed, which is quite common for complexes containing clay minerals. During this stage, most of the water is removed from interparticle capillaries and the diffuse region of the electrical double layer [21]. The derivatogram of the B sample did not demonstrate any endothermic effects during this stage. Most of the physically bound water was removed as a result of the MW radiation.

During the second stage, the condition of the A and B samples stabilized, and all the energy was used for heating.

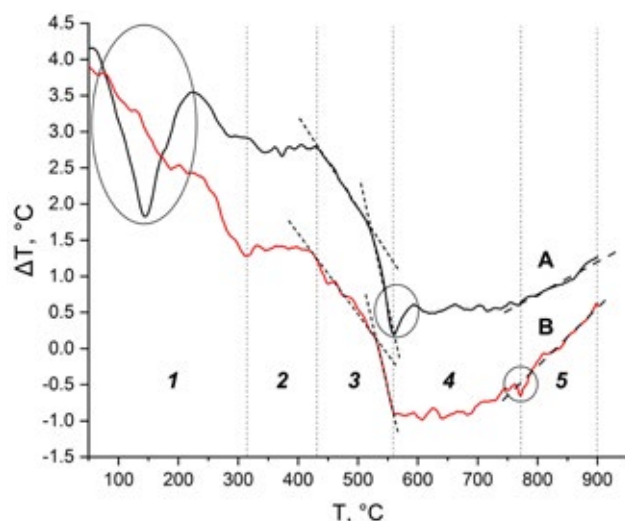


Fig. 2. Thermograms of samples A and B

During the third stage, within the temperature range from 430 to 540 °C, samples A and B demonstrated synchronized decomposition, which might be caused by the removal of chemically bound water from the structure of phyllosilicates [22, 23]. At the end of the third stage, another, less intense, endothermic effect was observed in the A sample. As a result, the dispersion system transformed into a more equilibrium state during the fourth stage. The effect is common for both metakaolinization of clay minerals within the set temperature range and the  $\beta \rightarrow \alpha$ -quartz transformation. There was not such an endothermic effect in the B sample.

During the fourth stage, at a temperature of about 700 °C the sintering process (agglomeration) was observed in the B sample. The process started 70 °C earlier and was more active than in the A sample. The sintering proceeded during the fifth stage. This is the synergistic effect of high temperature and the microwave field: their combined use resulted in a decrease in the temperature gradient of the B sample and facilitated the initiation of the sintering process at lower temperatures and with greater intensity.

### 3.3. Interpretation of the IR spectra (transformation of the chemical bonds)

The main task of the IR spectroscopy was to specify the nature of the chemical bonds in sample A and their transformations in samples B, C, and BC. The obtained IR spectra are presented

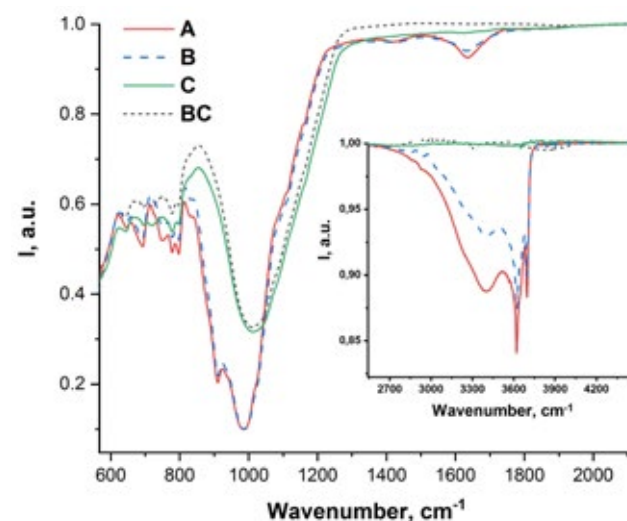


Fig. 3. IR spectra of the samples: A, B, C, BC

**Table 2.** Characteristic modes of interatomic bonds in M-PMC samples according to FTIR-spectroscopy results

Wavenumber, cm <sup>-1</sup>				Oscillation type	Mineral
A	B	C	BC		
645	645	645	645	O-Si(Al)-O [24–26]	Montmorillonite/Chlorite, Kaolinite
693	693	694	694	Si-O [27]	Quartz
750	750	750	750	Si-O-Al [25, 26]	Kaolinite
778	778	778	778	Si-O [27]	Quartz
797	797	796	796		
833	833	831	831	Al(Mg)-OH [24–26, 28]	Montmorillonite, Kaolinite
878	878	–	–	Al(Fe)-OH [28]	Montmorillonite
911	910	–	–	Al(Al)-OH [25, 26, 28]	Montmorillonite, Kaolinite
935	935	–	–		
985	988	1010	1010	O-Si-O [24–26, 28]	Montmorillonite/Chlorite, Kaolinite
1025, 1113, 1164	1025, 1113, 1164	1088, 1164	1088, 1164		
1636	1636	–	–	Constitutional water (OH-group) [24, 28]	Montmorillonite/Chlorite
3397	3397	–	–		
3620	–	–	–	Constitutional water (OH-group) [25–27]	Kaolinite
3649, 3670, 3696	3620, 3649, 3670, 3696	–	–	Constitutional water (OH-group) [24–26, 28]	Montmorillonite, Kaolinite

in Fig. 3. The results of the analysis of the IR spectra are given in Table 2. The base lines of the spectra were corrected and the absorption maxima were normalized so that the samples with close structure of the absorption bands were as similar as possible.

When comparing the absorption bands of the obtained spectra to the results of previous studies it is impossible to reliably differentiate between montmorillonite and chlorite, when both of them are present in the clay, due to the similarity of their spectra [24].

A broad absorption band at 990–1000 cm<sup>-1</sup> is explained by Si-O-Si vibrations in tetrahedral layers of montmorillonite or chlorite crystals [24, 28]. The presence of these minerals is confirmed by a profile near 3000–3700 cm<sup>-1</sup>, where the A

spectrum shows a weak absorption band with a maximum at 3620 cm<sup>-1</sup> caused by the vibrations of the O-H group in the three-layer structure of the mineral. Montmorillonite and chlorite have interlayer water molecules, which was demonstrated by an additional broad absorption band resulting from the O-H vibrations of the adsorbed water with the transmission minima at 3400 and 1636 cm<sup>-1</sup> [24, 28]. Two clear intense peaks of the O-H vibrations at 3620 and 3696 cm<sup>-1</sup> in the spectrum of the sample indicated the presence of kaolinite [25, 26]. Three absorption bands at – 1025, 1113, and 1164 cm<sup>-1</sup> corresponded to the O-Si-O bonds in the kaolinite structure similar to the lines at 935 and 909 cm<sup>-1</sup>, which appeared as a result of Al(Al)-OH vibrations.

The intensity of the peak at  $645\text{ cm}^{-1}$  corresponding to the bending vibrations of O-Si(Al)-O in chlorite was close to that of kaolinite bands [24].

For the main peak of the O-Si-O vibration, the montmorillonite lattice demonstrated adjacent lines corresponding to the bending vibrations of the O-H groups coordinated with Al(Al), Al(Mg), and Al(Fe). The presence of the absorption bands corresponding to the latter two substitutions indicated a significant level of isomorphism of the structures [24]. The studied M-PMC demonstrated intense Al(Mg)-OH absorption bands at  $830\text{ cm}^{-1}$  and Al-(Fe)-OH - absorption bands at  $878\text{ cm}^{-1}$ . Therefore, the A sample contained a large amount of magnesium and iron, which replaced aluminum in phyllosilicates crystals with the T-O-T structure.

A weak band at  $694\text{ cm}^{-1}$  and even weaker bands at  $777$  and  $796\text{ cm}^{-1}$  indicated the presence of quartz [27].

The spectra of the B samples demonstrated a decrease in the intensity of the absorption bands at  $3386$  and  $1636\text{ cm}^{-1}$ , associated with the release of water molecules from the interlayer space of montmorillonite and chlorite.

The spectra of the C sample did not demonstrate any absorption bands corresponding to the vibrations of the OH groups. Besides, there were no broad absorption bands at  $3380$  and  $1636\text{ cm}^{-1}$ , which indicated the absence of constitutional water in the structure. The identification of the obtained spectra was hindered by the possibility of formation of amorphous silicon oxide whose absorption bands overlapped with the absorption bands of anhydrous aluminosilicates.

The spectrum of the BC sample had the same absorption profile as the spectrum of the C sample. However, the relative intensities of both the main absorption band of the O-Si-O bond and the absorption bands at other wave numbers differed. We assume that this can be caused by the formation of various phases of the IR amorphous quartz and distorted structures of clay minerals.

We did not manage to determine the behavior of paragonite under various conditions by means of the IR spectroscopy, because the main absorption bands of this mineral overlapped with the absorption bands of the main phases of the M-PMC [29].

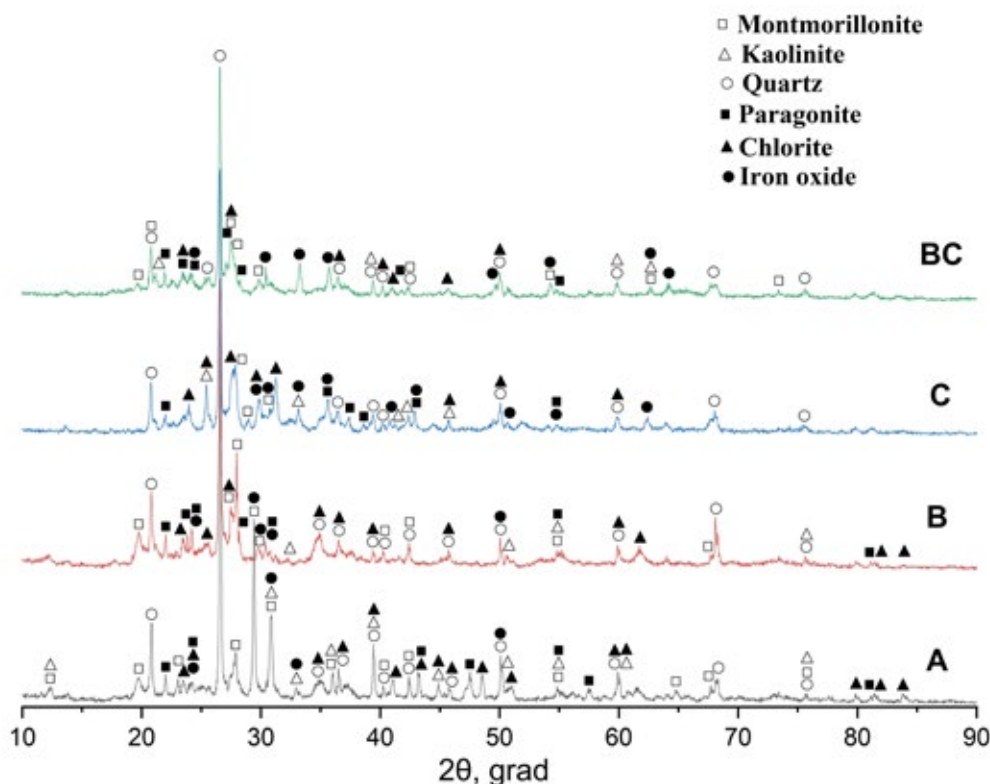


Fig. 4. Diffraction patterns of the samples: A, B, C, BC (bottom-up)

### 3.4. Evolution of phase compositions

Fig. 4 shows the diffraction patterns of samples **A**, **B**, **C**, and **BC** (in the bottom-up order). The greatest effect observed for all the treated samples (B, C, BC) was the formation of an amorphous phase in significant concentrations. The most intense amorphization was registered for samples **B** (22 vol. %) and **BC** (25 vol. %). As a result of resistance heating up to 900 °C, 15% of crystalline modifications transformed into the amorphous phase.

The second greatest effect was the decomposition of 23% of montmorillonite. The main cause of this process was high-temperature heating (samples **B** and **BC**). Half of the montmorillonite crystal lattices were destroyed by the MW field (15%). Earlier we demonstrated [30] that the degree of amorphization of montmorillonite depends on the mode of the MW treatment and can reach up to 50–70%.

The next phyllosilicates whose crystal lattice was destroyed by the MW field was a thermally stable three-layer chlorite. Its volume fraction remained intact after heating (sample **C**), but was twice as small in samples **B** and **BC**.

Kaolinite and paragonite practically do not react to external factors: the distorted kaolinite cells disappear and paragonite crystallizes [31].

The synergistic effect was the most obvious in the structural transformations of silicon and iron oxides. Silicon oxides demonstrated a decrease in the symmetry of the newly formed phases and an increase in their specific surface as well as inhomogeneity of size distribution [32]. The fraction of quartz in samples **B** and **C** decreased by 5–7%, while in the **BC** sample it decreased by 10–12%. Our experiments demonstrated for the first time the mechanism of formation of magnetite and hematite crystals from X-ray amorphous (Table 1) iron containing films covering the particles of clay minerals (Fig. 1b). The use of the MW field and the resulting dehydration led to the formation of crystalline nuclei of iron oxides (sample **B**). At high temperatures, the formation of aggregated iron crystals (magnetite and hematite) intensified reaching the maximum level (11%) in sample **BC**.

The X-ray diffraction analysis determined the presence of a synergistic effect in the evolution of structures, which could not be identified by means of IR-spectroscopy.

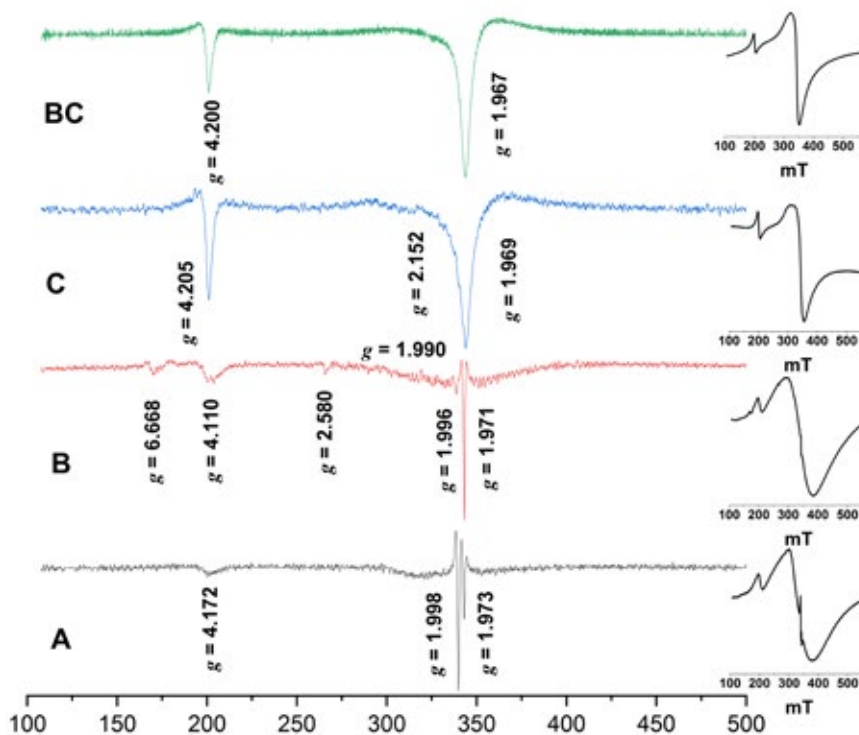


Fig. 5. EPR spectra of the samples: **A**, **B**, **C**, **BC** (bottom-up)



### 3.5. Paramagnetic centers in the structure

Electron paramagnetic resonance makes it significantly easier to identify structural transformations due to the presence of paramagnetic impurities in minerals. EPR spectroscopy has recently become an important method in the studies of clays. There are a lot of studies focusing on paramagnetic centers or radicals associated with clays. The interpretation of the experimental data obtained by means of EPR spectroscopy is only possible, when reliable identification methods are used (X-ray phase analysis, IR spectroscopy).

$\text{Fe}^{2+}$  ( $3d^6$ ) ions are not Kramer ions and are usually invisible for EPR spectroscopy [33], while the observed  $\text{Fe}^{3+}$  ( $3d^5$ ) ion is quite common in minerals. Fig. 5 demonstrates the second derivatives of the EPR spectra of the four samples with well identifiable signals. The frames on the right hand side show the general views of the spectra (the first derivatives).

The EPR spectrum of the initial sample (A) contained 4 peaks. A narrow peak ( $\Delta B \approx 16.2$  mT), located in a weak magnetic field with  $g = 4.172$  is common for phyllosilicates and corresponds to the  $\text{Fe}^{3+}$  ( $J = 5/2$ ) ion, which replaces  $\text{Al}^{3+}$  in octahedral positions with rhombic distortion [34]. A broad ( $\Delta B \approx 40$  mT) line with  $g = 2.111$  indicated the presence of thin films covering the iron oxides on clay particles. Furthermore, in the field near 340 mT (338.3 and 342.5) an asymmetrical double peak is observed comprised by two narrow ( $\Delta B \approx 3$  mT) lines with  $g = 1.998$  and  $g = 1.973$  respectively. The replacement of the native cation of the crystal lattice with a cation with a greater charge (or an anion with a smaller charge) stabilized the electron paramagnetic center in the structure, whose  $g$ -factor was usually [33] below 2. Such paramagnetic centers appeared, for instance, in the case of heterovalent isomorphism. The  $\text{O}^-$  oxygen form, common in minerals, was also observed in the EPR spectra [35].

After subjection to the MW field (sample B) two additional signals appeared in the spectrum. A line with  $g = 4.110$  corresponding to isolated  $\text{Fe}^{3+}$  ions with distorted octahedral and tetrahedral environments became complicated on the side of the weak field with a peak with  $g = 6.668$ . This indicated an increase in the crystallinity of

phyllosilicates. A signal with  $g = 2.580$  appeared, and the line with  $g = 1.990$  intensified. They are associated with [36] both the formation of a metastable iron-peroxide complex and the formation of clusters of  $\text{Fe}^{3+}$  ions in iron-containing phyllosilicates. The intensity of the signals from defects decreased by 5–6 times symbatically with their concentrations. A line with  $g \approx 2$  became two times broader due to an increase in the fraction of aggregative iron oxides. Such lines are usually observed in phyllosilicates, where the  $\text{Fe}^{3+}$  ion replaces the structural  $\text{Mg}^{2+}$  ion (for instance, in chlorite).

As a result of resistance heating (sample C), the amplitude increased by 3–4 times, and the width of the low field line decreased (by  $\Delta B \approx 5$  mT), because the positions of isomorphous iron ions in the lattice became equivalent. The signals associated with defects disappeared, and the fraction of aggregated iron in the paramagnetic ( $g = 1.969$ ) and ferromagnetic ( $g = 2.152$ ) states increased. Both lines of  $\text{Fe}^{3+}$  ions in the EPR spectrum of sample BC were the narrowest and the most symmetrical as compared to the other samples. Unlike the X-ray structural analysis, which studies the whole volume of the samples, the EPR spectroscopy allowed us to register the states of rare irregular cells with foreign paramagnetic atoms. The shift of the foreign  $\text{Fe}^{3+}$  ions from the geometric centers of octahedral crystal cells towards the minima of potential energy caused by the Jahn-Teller effect decreased the potential energy of the crystal lattice [37, 38]. At the same time, some chemical bonds forming the crystal cell became stronger, while others weakened.

## 4. Conclusions

The combined use of the high-temperature and MW fields results in the evolution of the structure: montmorillonite microaggregates and iron containing coatings covering them, as well as the crystal cells of three-layer clay minerals are destroyed. The octahedral layers of the particles are distorted. Foreign  $\text{Fe}^{3+}$  ions are introduced, which then participate in the crystallization of magnetite and hematite. The most obvious structural transformations include the formation of crystalline phases of iron oxides resulting from the synergistic effect of external factors.

## Author contributions

Chetverikova A. G. - research concept, analysis of the results, the EPR spectroscopy, text writing and editing. Makarov V. N. - analysis of the results, DTA analysis, graphs plotting, text writing and editing. Kanygina O. N. - analysis of the results, methodology development, X-ray diffractometry, text writing and editing. Seregin M. M. - analysis of the IR spectroscopy results. Yudin A. A. - chemical analysis.

## Conflict of interests

The authors declare that they have no known competing financial interests or personal relationships that could have influenced the work reported in this paper.

## References

1. Kolomenskiy E. N., Korolev V. A. Information entropy analysis of the structure formation in clay soils\*. *Inzhenernaya geologiya [Engineering Geology]*. 1982;(5): 34–45. (in Russ.)
2. Belachew N., Bekele G. Synergy of magnetite intercalated bentonite for enhanced adsorption of congo red dye. *Silicon*. 2020;12(3): 603–612. <https://doi.org/10.1007/s12633-019-00152-2>
3. Zdorenko N. M., Alyabyeva T. M., Kormosh T. M. About synergism effect of complex additive of kaolin and clay suspension. *Refractories and Industrial Ceramics*. 2012;(4-5): 64–66. (in Russ., abstract in Eng.). Available at: <https://elibrary.ru/pbcinp>
4. Tsotetsi T. A., Mochane M. J., Motaung T. E., ... Liganiso Z. L. Synergistic effect of EG and cloisite 15A on the thermomechanical properties and thermal conductivity of EVA/PCL blend. *Materials Research*. 2017;20(1): 109–118. <https://doi.org/10.1590/1980-5373-MR-2016-0277>
5. Isitman N. A., Gunduz H. O., Kaynak C. Nanoclay synergy in flame retarded/glass fibre reinforced polyamide 6. *Polymer Degradation and Stability*. 2009;94(12): 2241–2250. <https://doi.org/10.1016/j.polymdegradstab.2009.08.010>
6. Ayres C., Lawler D. F., Kirisits M. J., Saleh N. B. Synergy between microwave radiation and silver ions or nanoparticles for inactivating *Legionella pneumophila*. *Environmental Science and Technology Letters*. 2021;8(7): 581–588. <https://doi.org/10.1021/acs.estlett.1c00371>
7. Chetverikova A. G., Filyak M. M., Kanygina O. N. Influence of high-frequency microwave radiation on montmorillonite structure parameters. *Ceramica*. 2019;65(376): 635–640. <https://doi.org/10.1590/0366-69132019653762767>
8. Yang J. N., Li Z. Y., Xu Y. X., Nie S. B., Liu Y. Effect of nickel phyllosilicate on the morphological structure, thermal properties and wear resistance of epoxy nanocomposites. *Journal of Polymer Research*. 2020;27(9): 274. <https://doi.org/10.1007/s10965-020-02250-x>
9. Barry K., Lecomte-Nana G. L., Seynou M., ... Peyratout C. Comparative properties of porous phyllosilicate-based ceramics shaped by freeze-tape casting. *Ceramics*. 2022;5(1): 75–96. <https://doi.org/10.3390/ceramics5010007>
10. Prokhina A. V., Shapovalov N. A., Latypova M. M. Modification of the surface of clay minerals with high concentrations of montmorillonite in a high-frequency electromagnetic field\*. *Sovremennye naukoemkie tekhnologii [Modern high technology]*. 2011;(1): 135–136. (in Russ.). Available at: <https://elibrary.ru/nbfqnl>
11. Khodosova N. A., Belchinskaya L. I., Novikova L. A. Effect of different mechanisms of heating of layered aluminosilicate on sorption processes Communication 1. Effect of preliminary thermal and electromagnetic (microwave) heating of montmorillonite on sorption of water. *Sorbtsionnye i Khromatograficheskie Protssy*. 2017;17(5): 781–791. (in Russ.). <https://doi.org/10.17308/sorpchrom.2017.17/439>
12. Anisina I. N., Chetverikova A. G., Kanygina O. N. Effect of the batch mixture composition on the kinetics of sintering of montmorillonite containing clays\*. *Inorganic Materials: Applied Research*. 2012;(12): 48–52. (in Russ.). Available at: <https://elibrary.ru/item.asp?id=19096983>
13. Anisina I. N., Chetverikova A. G., Kanygina O. N. Activation aspects of siliceous ceramics synthesis from montmorillonite containing clay\*. *Vestnik of the Orenburg State University*. 2012;(4(140)): 170–174. (in Russ.). Available at: <https://elibrary.ru/item.asp?id=17921809>
14. Kanygina O. N., Filyak M. M., Chetverikova A. G. Microwave-induced phase transformations of natural clay in air and humid media. *Inorganic Materials*. 2018;54(9): 904–909. <https://doi.org/10.1134/s0020168518090042>
15. Borneman-Starynkevich I. D. *Calculating mineral formulas*. Moscow, Nauka Publ.; 1964. 218 p. (In Russ.)
16. Bulakh A. G., Zolotarev A. A., Krivovichev V. G. *Structure. Isomorphism, formulas, and classification of minerals*. Saint-Petersburg: St. Petersburg State University Publ., 2014. 132 p. (In Russ.)
17. Sokolov V. N., Chernov M. S., Shlykov V. G., ... Krupskaya V. V. Mineral nanoparticles in dispersive soils\*. *Journal of Surface Investigation: X-Ray, Synchrotron and Neutron Techniques*. 2008;(9): 88–92.

(In Russ.). Available at: <https://elibrary.ru/item.asp?id=11155131>

18. Beaufort D., Rigault C., Billon S., ... Patrier P. Chlorite and chloritization processes through mixed-layer mineral series in low-temperature geological systems – a review. *Clay Minerals*. 2015;50(4): 497–523. <https://doi.org/10.1180/claymin.2015.050.4.06>

19. Drits V. A., Kossovskaya A. G. *Clay minerals: smectites and mixed-layer formations*. Moscow, Nauka Publ.; 1990. 214 p. (In Russ.)

20. Makarov V. N. *An energy-based approach to the description of structural transformations in iron oxides and aluminosilicates comprising natural clay minerals\**. Cand. Phys.-Math. Sci. diss. of: 1.3.8. Tver: 2022. (in Russ.). Available at: <https://www.dissercat.com/content/opisanie-strukturnykh-prevrashchenii-v-oksidakh-zheleza-i-aluminosilikatakh-sostavlyayushchik>

21. Vanetsev A. S., Tretyakov Y. D. Microwave-assisted synthesis of individual and multicomponent oxides. *Russian Chemical Reviews*. 2007;76(5): 397–413. <https://doi.org/10.1070/rc2007v076n05abeh003650>

22. Escalera E., Antti M. L., Odén M. Thermal treatment and phase formation in kaolinite and illite based clays from tropical regions of Bolivia. *IOP Conference Series: Materials Science and Engineering*. IOP Publishing. 2012;31(1): 012028. <https://doi.org/10.1088/1757-899x/31/1/012017>

23. Makarov V. N., Kanygina O. N. Model of destruction of montmorillonite crystal structure in a microwave field. *Nanosystems: Physics, Chemistry, Mathematics*. 2020;11(2): 153–160. <https://doi.org/10.17586/2220-8054-2020-11-2-153-160>

24. Jovanovski G., Makreski P. Minerals from macedonia. XXX. Complementary use of vibrational spectroscopy and x-ray powder diffraction for spectrostructural study of some cyclo-, phyllo- and tectosilicate minerals. A review. *Macedonian Journal of Chemistry and Chemical Engineering*. 2016;35(2): 125–155. <https://doi.org/10.20450/mjce.2016.1047>

25. Tironi A., Trezza M. A., Irassar E. F., Scian A. N. Thermal treatment of kaolin: effect on the pozzolanic activity. *Procedia Materials Science*. 2012;(1): 343–350. <https://doi.org/10.1016/j.mspro.2012.06.046>

26. Khang V. C., Korovkin M. V., Ananyeva L. G. Identification of clay minerals in reservoir rocks by FTIR spectroscopy. *OP Conference Series: Earth and Environmental Science*. 2016;43(1): 012004. <https://doi.org/10.1088/1755-1315/43/1/012004>

27. Fricke H. H., Mattenklott M., Parlar H., Hartwig A. Method for the determination of quartz and cristobalite [Air Monitoring Methods, 2015]. *The MAK-Collection for Occupational Health and Safety*. 2002;1(1): 401–436. <https://doi.org/10.1002/3527600418.am0sio2fste2015>

28. Tyagi B., Chudasama C. D., Jasra R. V. Determination of structural modification in acid activated montmorillonite clay by FT-IR spectroscopy. *Spectrochimica Acta Part A: Molecular and Biomolecular Spectroscopy*. 2006;64(2): 273–278. <https://doi.org/10.1016/j.saa.2005.07.018>

29. Klopogge J. T., Frost R. L. Infrared emission spectroscopic study of some natural and synthetic paragonites. *Applied Spectroscopy*. 1999;53(9): 1071–1077. <https://doi.org/10.1366/0003702991948071>

30. Chetverikova A. G., Kanygina O. N., Filiak M. M., Ogerchuk S. A. Structural and morphological peculiarities of montmorillonite treated with microwave radiation. *Physics and Chemistry of Materials Treatment*. 2019;(3): 5–12. (In Russ., abstract in Eng.). <https://doi.org/10.30791/0015-3214-2019-3-5-12>

31. Comodi P., Zanazzi P. F. Structural thermal behavior of paragonite and its dehydroxylate: a high-temperature single-crystal study. *Physics and Chemistry of Minerals*. 2000;27: 377–385. <https://doi.org/10.1007/s002690000085>

32. Kanygina O. N., Filiak M. M., Chetverikova A. G. Structural transformations in aluminum and silicon oxides in microwave fields. *Materials Science*. 2020;5: 37–42. <https://doi.org/10.31044/1684-579x-2020-0-5-37-42>

33. Hall P. L. The application of electron spin resonance spectroscopy to studies of clay minerals. I. Isomorphous substitutions and external surface properties. *Clay Minerals*. 1980;15(4): 321–335. <https://doi.org/10.1180/claymin.1980.015.4.01>

34. Sorieul S., Allard T., Morin G., ... Calas G. Native and artificial radiation-induced defects in montmorillonite. An EPR study. *Physics and Chemistry of Minerals*. 2005;32: 1–7. <https://doi.org/10.1007/s00269-004-0427-6>

35. Gilinskaya L. G., Grigorieva T. N., Razvorotneva L. I., Trofimova L. B. Composition and physicochemical properties of natural blue clays\*. *Chemistry for Sustainable Development*. 2008;16(2): 147–157. (in Russ.). Available at: <https://elibrary.ru/item.asp?id=11532517>

36. Badmaeva S. V. *Synthesis of Al-, Al/Fe intercalated montmorillonites and analysis of their physicochemical properties\**. Cand. Chem. Sci. diss.: 02.00.04. Irkutsk: 2005. (in Russ.). Available at: <https://www.dissercat.com/content/sintez-al-feal-interkalirovannykh-montmorillonitov-i-issledovanie-ikh-fiziko-khimicheskikh-s>

37. Worasith N., Goodman B. A., Neampan J., ... Ferrage E. Characterization of modified kaolin from the Ranong deposit Thailand by XRD, XRF, SEM, FTIR and EPR techniques. *Clay Minerals*. 2011;46(4): 539–559. <https://doi.org/10.1180/claymin.2011.046.4.539>

38. Kuzakov A. S. *Electron paramagnetic resonance of degenerate orbitals in three-coordinate Ni(I)*

*complexes*\*. Cand. Phys.-Math. Sci. diss. Irkutsk: 2012. (In Russ.). <https://www.dissercat.com/content/elektronnyi-paramagnitnyi-rezonans-orbitalno-vyrozhdennykh-sostoyanii-v-trikoordinatsionnykh>

\* *Translated by author of the article*

### Information about the authors

*Anna G. Chetverikova*, Cand. Sci. (Phys.-Math.), Associate Professor, Dean of the Physics Faculty, Orenburg State University (Orenburg, Russian Federation).

<https://orcid.org/0000-0002-7045-3588>

[kr-727@mail.ru](mailto:kr-727@mail.ru)

*Valery N. Makarov*, Cand. Sci. (Phys.-Math.), Associate Professor, Department at Physics and Methods of Teaching Physics, Orenburg State University (Orenburg, Russian Federation).

<https://orcid.org/0000-0001-5749-1427>

[makarsvet13@gmail.com](mailto:makarsvet13@gmail.com)

*Olga N. Kanygina*, Dr. Sci. (Phys.-Math.), Professor, Professor at the Department of Chemistry, Orenburg State University (Orenburg, Russian Federation).

<https://orcid.org/0000-0001-6501-900X>

[onkan@mail.ru](mailto:onkan@mail.ru)

*Mikhail M. Seregin*, Analytical Chemist, BO-ENERGO.ASTS LLC, (Moscow, Russian Federation).

<https://orcid.org/0000-0002-2263-9679>

[Sereginmm@lumex.ru](mailto:Sereginmm@lumex.ru)

*Alexander A. Yudin*, Lector at the Department of Chemistry, Orenburg State University (Orenburg, Russian Federation).

<https://orcid.org/0000-0003-2424-0781>

[yudin-s97@yandex.ru](mailto:yudin-s97@yandex.ru)

*Received 15.08.2023; approved after reviewing 08.10.2023; accepted for publication 15.11.2023; published online 25.06.2024.*

*Translated by Yulia Dymant*





## Original articles

Research article

<https://doi.org/10.17308/kcmf.2024.26/11945>**Structure and electrical transport properties of cation-deficient derivatives of layered neodymium–barium ferrocuprocobaltite**

E. A. Chizhova, M. V. Marozau, S. V. Shevchenko, A. I. Klyndyuk✉, Ya. Yu. Zhuravleva, V. M. Kononovich

*Belarusian State Technological University,  
13<sup>a</sup> Sverdlova str., Minsk 220006, Republic of Belarus***Abstract**

Layered double perovskites (LDP) based on rare earth elements, barium, and 3d-metals with high electrical conductivity and electrocatalytic activity in the oxygen reduction reaction are promising cathode materials for medium-temperature solid oxide fuel cells based on proton- or oxygen-conducting solid electrolytes. For the improvement of the functional characteristics of LDP, various strategies are used: a) creating composites based on LDP, b) the partial substitution of cations, and c) the creation of a deficiency of cations in various positions in the LDP structure. The advantage of the latter strategy is that it does not require complicating the chemical and, as a rule, phase composition of the LDP. The purpose of this study was the investigation of the effect of neodymium and barium deficiency on the structural and electrical transport characteristics of  $\text{NdBaFeCo}_{0.5}\text{Cu}_{0.5}\text{O}_{6-\delta}$  LDP.

The samples were obtained by the ceramic method and characterized using X-ray phase analysis, IR absorption spectroscopy, iodometry, electron microscopy, thermal analysis, as well as electrical conductivity and thermo-EMF measurements methods. Creation of up to 10 mol. % of vacancies in neodymium or barium sublattices had little effect on the values of the oxygen nonstoichiometry index ( $\delta$ ) and unit cell parameters of  $\text{NdBaFeCo}_{0.5}\text{Cu}_{0.5}\text{O}_{6-\delta}$  derivatives. However, it led to an increase in the crystallite size (determined by the Scherrer, Williamson–Hall and size–strain methods) and the thermal stability of these phases. The values of electrical conductivity and the Seebeck coefficient of ceramics, in general, increased, and the activation energies of the electrical transfer process decreased when a deficiency of neodymium or barium was created in its structure. In the temperature range 300–700 K, the weighted mobility of charge carriers (“holes”) varied within 0.04–0.8  $\text{cm}^2/(\text{V}\cdot\text{s})$  and increased with increasing temperature, which is typical for the polaron conduction mechanism, and their concentration varied in the range  $(0.1–3)\cdot 10^{20} \text{ cm}^{-3}$ , increased exponentially with increasing temperature and, in general, when a deficiency of neodymium or barium in the  $\text{NdBaFeCo}_{0.5}\text{Cu}_{0.5}\text{O}_{6-\delta}$  structure was created.

**Keywords:** Layered double perovskites, Cation deficiency, Structure, Thermal stability, Electrical conductivity, Thermo-EMF, Weighted mobility, Concentration of charge carriers

**Acknowledgments:** studies using powder X-ray diffraction, IR absorption spectroscopy, electron microscopy and thermal analysis were carried out using the equipment of the Centre for Physico-Chemical Research Methods of the Belarusian State Technological University.

**For citation:** Chizhova E. A., Marozau M. V., Shevchenko S. V., Klyndyuk A. I., Zhuravleva Ya. Yu., Kononovich V. M. Structure and electrical transport properties of cation-deficient derivatives of layered neodymium–barium ferrocuprocobaltite. *Condensed Matter and Interphases*. 2024;26(2): 339–348. <https://doi.org/10.17308/kcmf.2024.26/11945>

**Для цитирования:** Чижова Е. А., Морозов М. В., Шевченко С. В., Клындюк А. И., Журавлева Я. Ю., Кононович В. М. Структура и электротранспортные свойства катиондефицитных производных слоистого феррокупрокобальтита неодима–бария. *Конденсированные среды и межфазные границы*. 2024;26(2): 339–348. <https://doi.org/10.17308/kcmf.2024.26/11945>

✉ Andrei I. Klyndyuk, e-mail: [klyndyuk@belstu.by](mailto:klyndyuk@belstu.by)

© Chizhova E. A., Marozau M. V., Shevchenko S. V., Klyndyuk A. I., Zhuravleva Ya. Yu., Kononovich V. M., 2024



## 1. Introduction

High values of electrical conductivity and the Seebeck coefficient of  $\text{LnBa}(M', M'', M''')_2\text{O}_{6-\delta}$  (Ln – Y, rare earth element (REE),  $M', M'', M'''$  – 3d-metal) compounds, related to oxygen-deficient layered double perovskites (LDP), as well as the presence in their structure of electrochemically active transition metal ions and weakly bound oxygen determines the interest in these complex oxides as functional materials for various purposes, including high-temperature thermoelectrics, cathode materials of solid oxide fuel cells (SOFC), working elements of chemical semiconducting gas sensors, membranes for oxygen separation, etc. [1–4]. LDP are semiconductors with a band gap of about 1.5 eV [5].

Functional characteristics of  $\text{LnBa}(M', M'', M''')_2\text{O}_{6-\delta}$  phases can be improved by introducing of nano- and microparticles of a different nature into them, the targeted substitution of cations, or creating their deficiency in various positions of the crystal structure of these compounds [3, 6–8], and the latter method of modification is interesting since it can be carried out without complication of the chemical composition of complex  $\text{LnBa}(M', M'', M''')_2\text{O}_{6-\delta}$  oxides [9].

The authors [10–12] found that cation-deficient  $\text{Ln}_{1-x}\text{BaCo}_2\text{O}_{6-\delta}$  (Ln – Pr, Nd, Sm) LDP were formed when the deficiency of cations in the REE sublattice of their structure up to 5 mol. % was created. A deficiency of REE in LDP promoted the formation of oxygen vacancies in their structure, which led to an increase in the parameters of the crystal structure and a slight decrease in electrical conductivity [10–12]. However, it significantly reduced their specific surface resistance and increased the output power of electrochemical cells in which they act as cathodes [11].

The creation of barium deficiency in the structure of layered cobaltites  $\text{LnBaCo}_2\text{O}_{6-\delta}$  (Ln – La, Pr, Nd, Sm) [10, 13–19], in general, similarly affected the oxygen nonstoichiometry, structural characteristics, electrical transport properties, and electrochemical performance of these phases, although several differences were observed. Thus, the width of the barium homogeneity region of the  $\text{LnBaCo}_2\text{O}_{6-\delta}$  phases was wider than for REE, and reaches 10 and 15 mol. % for Ln = Pr [15,

16] and Ln = La [13], respectively. Parameters of the unit cell of  $\text{LnBa}_{1-x}\text{Co}_2\text{O}_{6-\delta}$  (Ln – Pr, Nd) LDP decreases slightly, and the electrical conductivity of ceramics increases significantly when a barium deficiency is created in it [15–17], while the greatest increase in electrical conductivity was observed for  $\text{PrBa}_{0.92}\text{Co}_2\text{O}_{6-\delta}$  [14],  $\text{PrBa}_{0.96}\text{Co}_2\text{O}_{6-\delta}$  [15],  $\text{NdBa}_{0.95}\text{Co}_2\text{O}_{6-\delta}$  [17] samples.

It was established in [20] that the creation of cobalt deficiency in the structure of the complex oxide  $\text{PrBaCo}_2\text{O}_{6-\delta}$  led to an increase in unit cell parameters, oxygen nonstoichiometry index, and a decrease in electrical conductivity and specific surface resistance of  $\text{PrBaCo}_{2-x}\text{O}_{6-\delta}$  phases and an increase in the output power of cells in which they acted as cathodes, and a composition with  $x = 0.06$  was characterized by the highest electrochemical performance.

Layered  $\text{LnBaCo}_2\text{O}_{6-\delta}$  cobaltites had the highest electrochemical activity in the oxygen reduction reaction among LDP, however, their thermal expansion coefficients (TEC) significantly exceeded those for typical solid electrolytes (SE) [2–4, 7, 8]. In this regard, a low thermomechanical compatibility of SE and  $\text{LnBaCo}_2\text{O}_{6-\delta}$  was observed, which limited the practical use of REE–barium cobaltites in various SOFC. A decrease in the TEC of layered cobaltites can be caused by the partial substitution of cobalt in their structure with other 3d-metals, which in many cases also led to an improvement in the electrochemical performance of these phases [3]. Thus, the complex modification of layered  $\text{LnBaCo}_2\text{O}_{6-\delta}$  oxides by partial substitution of cobalt in them and the creation of a deficiency of rare earth elements and barium can be considered as a promising method for developing electrode materials for medium-temperature SOFC with improved functional characteristics [18].

Previously, we studied the effect of cation deficiency in various sublattices of the  $\text{LnBaCuFeO}_{6-\delta}$  (Ln – Y, La) structure on their oxygen stoichiometry ( $6-\delta$ ), crystal lattice parameters, thermal and electrical properties [21, 22], and it has also been shown that  $\text{NdBa}(\text{Fe}, \text{Co}, \text{Cu})\text{O}_{6-\delta}$  LDP are of interest as cathode materials for medium-temperature SOFC [23]. It was shown in [24] that the substitution of barium ions with strontium ions in  $\text{NdBaFeCo}_{0.5}\text{Cu}_{0.5}\text{O}_{6-\delta}$  led to a decrease in

TEC and an increase in the electrical conductivity of this complex oxide.

The purpose of this study was investigation of the effect of neodymium and barium deficiency on the thermal stability and the structural and electrical transport characteristics of  $\text{NdBaFeCo}_{0.5}\text{Cu}_{0.5}\text{O}_{6-\delta}$  LDP.

## 2. Experimental

LDP samples with the composition  $\text{Nd}_{0.90}\text{BaFeCo}_{0.5}\text{Cu}_{0.5}\text{O}_{6-\delta}$  (N090B),  $\text{Nd}_{0.95}\text{BaFeCo}_{0.5}\text{Cu}_{0.5}\text{O}_{6-\delta}$  (N095B),  $\text{NdBaFeCo}_{0.5}\text{Cu}_{0.5}\text{O}_{6-\delta}$  (NB),  $\text{NdBa}_{0.95}\text{FeCo}_{0.5}\text{Cu}_{0.5}\text{O}_{6-\delta}$  (NB095) and  $\text{NdBa}_{0.90}\text{FeCo}_{0.5}\text{Cu}_{0.5}\text{O}_{6-\delta}$  (NB090) were synthesized using a standard ceramic method from neodymium (NO-L), iron (III) (extra pure grade 2–4), cobalt (II, III) (pure grade), and copper (II) (pure grade) oxides and barium carbonate (pure grade), which were mixed in specified stoichiometric ratios and grounded using a Pulverizette 6.0 mill from Fritsch (crucible material and grinding balls was  $\text{ZrO}_2$ ). Then, the resulting powders were pressed into tablets with a diameter of 19 mm and a height of 2–3 mm, which were annealed in air for 40 h at 1173 K [23, 24]. Annealed samples were crushed in an agate mortar, re-grounded using a Pulverizette 6.0 mill (Fritsch) and pressed into bars with the size of  $5 \times 5 \times 30$  mm. The samples were sintered in air for 9 h at 1273 K. For the measurements of electrical conductivity, rectangular parallelepipeds with a size of  $4 \times 4 \times 2$  mm were cut from sintered ceramics.

The identification of samples and determination of their unit cell parameters were carried out using X-ray phase analysis (XRD) (X-ray diffractometer Bruker D8 XRD Advance,  $\text{CuK}_\alpha$ -radiation) and IR absorption spectroscopy (Nexus ThermoNicolet IR Fourier spectrometer) ( $\Delta\nu = \pm 2 \text{ cm}^{-1}$ ). The oxygen nonstoichiometry index of the samples ( $\delta$ ) were determined using iodometric titration according to the method [25] ( $\Delta\delta = \pm 0.01$ ), taking into account the presence of  $3d$ -metals in various oxidation states ( $\text{Fe}^{+3}, \text{Co}^{+4}, \text{Co}^{+3}, \text{Cu}^{+2}$ ), which were reduced into  $\text{Co}^{+2}, \text{Cu}^{+}$ , and  $\text{Fe}^{+2}$  during titration.

The average size of coherent scattering areas (CSA,  $D$ ), comparable to the crystallite sizes, were calculated based on the XRD results using the Scherrer equation (1) [26]:

$$D = \frac{K\lambda}{\beta \cos \Theta}, \quad (1)$$

where  $K = 0.9$ ;  $\lambda$  – wavelength of  $\text{CuK}_\alpha$ -radiation, nm;  $\beta$  – the width of the integral peak at half-maximum, rad;  $\Theta$  – Bragg angle, rad.

Additionally, the CSA and microstrain values were calculated using the Williamson–Hall method (2) and the size–strain method (3) [27]:

$$\beta \cos \Theta = \frac{K\lambda}{D} + 4\varepsilon \sin \Theta, \quad (2)$$

$$(d\beta \cos \Theta)^2 = \frac{K\lambda}{D} (d^2 \beta \cos \Theta) + \left(\frac{\varepsilon}{2}\right)^2, \quad (3)$$

where  $\varepsilon$  – microstrain value;  $d$  – interplanar distance, nm.

Apparent density ( $\rho_{\text{app}}$ ) ceramics were determined based on the geometric dimensions and the weight of the samples, the relative density ( $\rho_{\text{rel}}$ ) of ceramics and its total porosity ( $\Pi$ ) was calculated as:

$$\rho_{\text{rel}} = \frac{\rho_{\text{app}}}{\rho_{\text{XRD}}} \cdot 100\%, \quad (4)$$

$$\Pi = \left( \frac{\rho_{\text{XRD}} - \rho_{\text{app}}}{\rho_{\text{XRD}}} \right) \cdot 100\%, \quad (5)$$

where  $\rho_{\text{XRD}}$  – theoretical (X-ray) density of samples.

Open porosity ( $\Pi_o$ ) was determined based on the water absorption of the samples, and closed ( $\Pi_c$ ) porosity was determined as the difference between total and open porosity.

The microstructure of the samples was studied by scanning electron microscopy (SEM) using JSM-5610 LV scanning electron microscope, as well as using an ALTAMI MET 1D digital metallographic microscope (Altami, Russian Federation).

The thermal stability of LDP powders was studied in air in the temperature range 300–1100 K using a TGA/DSC-1/1600 HF thermoanalytical system. Electrical conductivity ( $\sigma$ ) and thermo-EMF ( $S$ ) of the resulting ceramic samples, after applying contacts to their ends by burning silver paste, were studied in air in the temperature range of 300–1100 K according to the methods of [21, 22] ( $\delta\sigma \leq 5\%$ ,  $\delta S \leq 10\%$ ). Conduction ( $E_\sigma$ ) and thermo-EMF activation energies of samples

( $E_s$ ) were calculated from the linear parts of the dependences  $\ln(\sigma \cdot T) = f(1/T)$  and  $S = f(1/T)$ , respectively. Weighted mobility of the main charge carriers ( $\mu$ ), as well as their concentration ( $p$ ) were calculated based on experimentally determined values of electrical conductivity ( $\sigma$ ) and Seebeck coefficient ( $S$ ) of cation-deficient ceramics using the method [28]. The activation energy of the main charge carriers ( $E_p$ ) was calculated based on the dependences  $\ln p = f(1/T)$ , using the equation:

$$p = p_0 \exp\left[-\frac{E_p}{kT}\right], \quad (6)$$

where  $p_0$  – constant,  $k$  – Boltzmann constant,  $T$  – temperature.

### 3. Results and discussion

After the final stage of synthesis, all samples, within the error of X-ray phase analysis, were single-phase (Fig. 1a) and had a double perovskite

structure ( $a = b \approx a_p$ ,  $c \approx 2a_p$ , sp. gr.  $P4/mmm$  [18, 23]). The crystal lattice parameters of the cation-deficient samples were close to those for the base phase (NB) (Table 1) and increased slightly when vacancies were created in the neodymium sublattice, which is consistent with the results of [10–12]. The axial ratio ( $c/2a$ ) of the samples, in general, increased with the formation of neodymium or barium vacancies in their structure, which indicates a decrease in the degree of tetragonal distortion of their perovskite structure.

The value of the oxygen nonstoichiometry index of the double perovskites obtained in this study varied within the range of 0.28–0.32 (Table 1), slightly increasing when a deficiency of cations in the structure of the  $\text{NdBaFeCo}_{0.5}\text{Cu}_{0.5}\text{O}_{6-\delta}$  phase was created.

In the IR absorption spectra of the studied LDP samples (Fig. 1b), four expressed absorption bands with extrema at  $357\text{--}374\text{ cm}^{-1}$  ( $\nu_1$ ),  $467\text{--}468\text{ cm}^{-1}$  ( $\nu_2$ ),  $577\text{--}580\text{ cm}^{-1}$  ( $\nu_3$ ) and  $650\text{--}661\text{ cm}^{-1}$

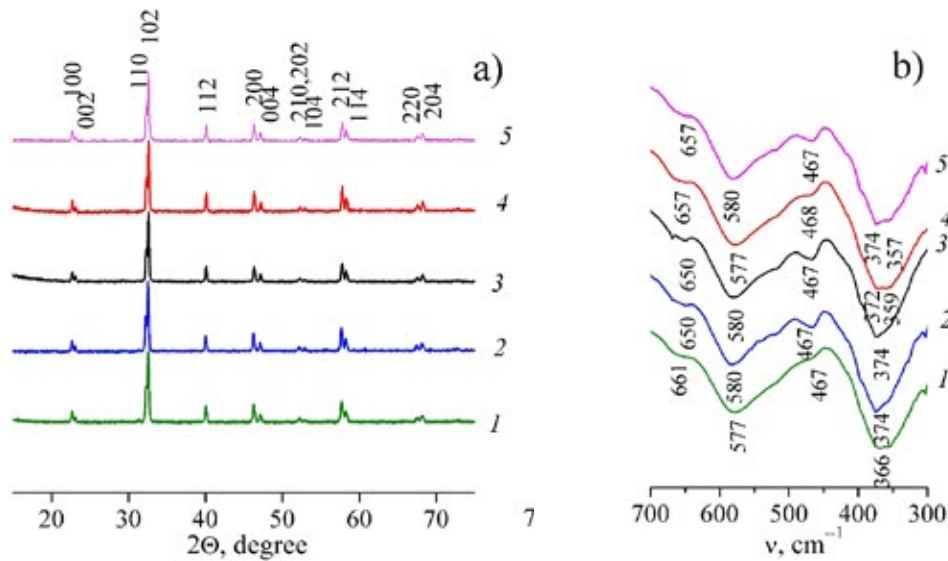


**Fig. 1.** X-ray powder diffractograms (a) and IR absorption spectra (b) of N090B (1), N095B (2), NB (3), NB095 (4), NB090 (5)

**Table 1.** Lattice constants ( $a$ ,  $c$ ,  $V$ ), tetragonal distortion degree ( $c/2a$ ) and oxygen nonstoichiometry index of cation-deficient  $\text{NdBaFeCo}_{0.5}\text{Cu}_{0.5}\text{O}_{6-\delta}$  perovskites

Sample	$a$ , nm	$c$ , nm	$V$ , nm <sup>3</sup>	$c/2a$	$\delta$
N090B	0.39274	0.77267	0.1192	0.9837	0.30
N095B	0.39261	0.77095	0.1188	0.9818	0.32
NB	0.39212	0.77072	0.1185	0.9828	0.28
NB095	0.39145	0.76965	0.1179	0.9831	0.30
NB090	0.39182	0.77128	0.1184	0.9842	0.31



( $\nu_4$ ) were observed, which according to [29] correspond to valence ( $\nu_2, \nu_3$ ) and deformation vibrations of bonds (Fe,Co,Cu)–O–(Fe,Co,Cu) in layers [(Fe,Co,Cu)O<sub>2</sub>]<sub>( $\nu_1-\nu_3$ )</sub> of crystal structure of these phases and in the direction perpendicular to these layers ( $\nu_4$ ), and for compositions NB095 and NB090, splitting of  $\nu_1$  band into two with extremes at 357–359 and 372–374 cm<sup>-1</sup> was noted. The position of the extrema in the IR absorption spectra of the samples practically did not change with changes in their cation composition, which was in good agreement with the results of X-ray diffraction and iodometry, according to which the creation of a deficiency of cations in the structure of NdBaFeCo<sub>0.5</sub>Cu<sub>0.5</sub>O<sub>6- $\delta$</sub>  LDP has little effect on the parameters of its crystal structure and oxygen stoichiometry.

The CSA values corresponding to the average crystallite sizes in the samples, determined by various methods, were somewhat different from each other (Table 2, Fig. 2), however, there was a pronounced tendency towards an increase in the

CSA with an increase in the cation deficiency in the LDP structure, explained by an increase in the diffusion mobility of the elements of their crystal structure with an increase in the degree of its defectness. The microstrain values of the samples determined using the Williamson–Hall and size–strain methods were close, with the exception of the N090B composition, characterized by significantly higher values  $\epsilon$ . According to the results of microscopy, the ceramic grains had a shape close to isometric, and their size was 3–5  $\mu\text{m}$  and practically did not change with changes in the cationic composition of the ceramic. Thus, the grains of the studied ceramics turned out to be polycrystalline and contained several tens crystallites each.

The apparent density of ceramics increased, and its porosity, accordingly, decreased with increasing deficiency of neodymium or barium cations in its composition (Table 3). This finding indicates that the sintering of ceramics based on the NdBaFeCo<sub>0.5</sub>Cu<sub>0.5</sub>O<sub>6- $\delta$</sub>  phase increased with

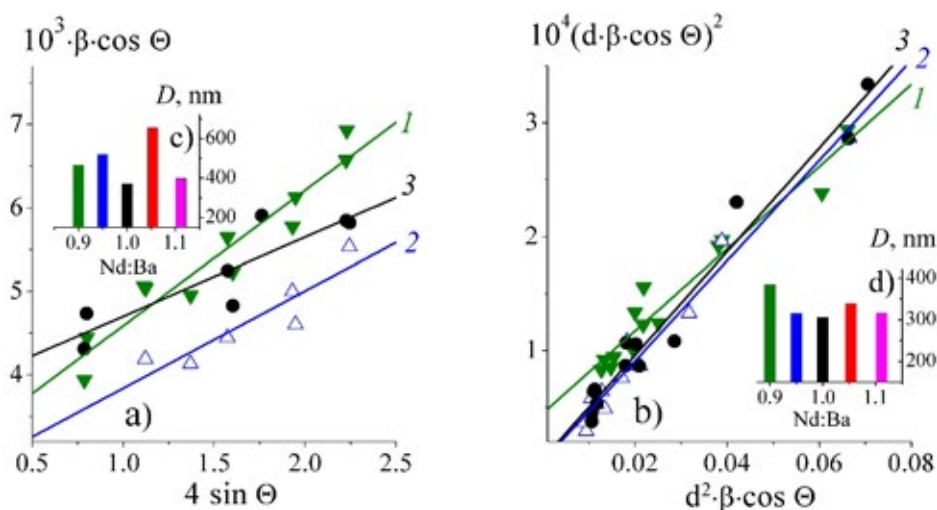


**Fig. 2.** Williamson–Hall (a) and size–strain plots (b) of N090B (1), N095B (2), NB (3), coherent scattering area values (c, d)

**Table 2.** Values of coherent scattering area ( $D$ ) and microstrains of NdBaFeCo<sub>0.5</sub>Cu<sub>0.5</sub>O<sub>6- $\delta$</sub>  ceramic samples, calculated using Sherrer, Williamson–Hall, and size–strain (S–S) methods

Sample	Sherrer	Williamson–Hall		S–S	
	$D$ , nm	$D$ , nm	$\epsilon$	$D$ , nm	$\epsilon$
N090B	252.9	467.4	0.0016	384.6	0.0134
N095B	303.8	519.9	0.0012	314.8	0.0033
NB	288.7	370.2	0.0009	305.1	0.0044
NB095	330.8	655.0	0.0010	339.4	0.0029
NB090	293.2	398.9	0.0008	316.2	0.0024

**Table 3.** X-ray ( $\rho_{\text{XRD}}$ ), apparent ( $\rho_{\text{app}}$ ), relative ( $\rho_{\text{rel}}$ ) density, full ( $\Pi$ ), open ( $\Pi_o$ ), and closed ( $\Pi_c$ ) porosity of  $\text{NdBaFeCo}_{0.5}\text{Cu}_{0.5}\text{O}_{6-\delta}$  ceramics

Образец	$\rho_{\text{XRD}}$ , g/cm <sup>3</sup>	$\rho_{\text{app}}$ , g/cm <sup>3</sup>	$\rho_{\text{rel}}$ , %	$\Pi$ , %	$\Pi_o$ , %	$\Pi_c$ , %
N090B	6.47	6.08	94.0	6.0	1.9	4.1
N095B	6.59	6.09	92.4	7.6	2.3	5.3
NB	6.71	6.06	90.3	9.7	5.7	4.0
NB095	6.65	6.39	96.1	3.9	1.7	2.2
NB090	6.52	6.17	94.6	5.4	1.8	3.6

the creation of cation vacancies in its structure, which, as mentioned above, is explained by an increase in the diffusion mobility of the cations included in their composition due to an increase in the defectiveness of the crystal structure of LDP. The highest value of apparent density (6.39 g/cm<sup>3</sup>) and the lowest porosity (3.9%) were recorded for composition NB095. It is interesting to note that the creation of cation vacancies predominantly reduced the open porosity of the ceramics, while the closed porosity of the cation-deficient samples varied within a fairly narrow range (3.6–5.3%) and was close to that for the base composition (NB) (4.0%), with the exception of the NB095 sample, characterized by the lowest closed porosity (2.2%) (Table 3).

Based on the results of thermal analysis (Fig. 3), we can conclude that the studied powders were thermally stable up to temperatures  $T^* = 685\text{--}745$  K, above which some ( $\approx 0.3\text{--}0.5\%$ )

weight loss caused by the release of mobile oxygen from samples (1– $\delta$ ) and an increase in the oxygen nonstoichiometry index (Fig. 3b) were observed [23–25]. In this case, the highest weight loss was observed for the composition N090B, and the lowest for samples N095B and NB090 (Fig. 3a). The  $T^*$  value was minimal for the basic  $\text{NdBaFeCo}_{0.5}\text{Cu}_{0.5}\text{O}_{6-\delta}$  LDP and increased when a deficiency of neodymium or barium was created in its structure (Fig. 3c). Thus, the creation of vacancies in the sublattices of neodymium or barium of the  $\text{NdBaFeCo}_{0.5}\text{Cu}_{0.5}\text{O}_{6-\delta}$  phase led to an increase in its thermal stability. It should be noted that the thermal stability and sintering ability of the studied samples, in general, change symbatically with changes in their cation composition, which is in good agreement with the results we obtained earlier when studying LDP in the  $\text{NdBaFeCo}_{0.5}\text{Cu}_{0.5}\text{O}_{6-\delta}\text{--NdSrFeCo}_{0.5}\text{Cu}_{0.5}\text{O}_{6-\delta}$  system [24].

The studied LDP are semiconductors ( $\partial\sigma/\partial T > 0$ ) of  $p$ -type ( $S > 0$ ) (Fig. 4a, b), the nature of the electrical conductivity of which changes to metallic ( $\partial\sigma/\partial T < 0$ ) near  $T_{\text{max}} = 992\text{--}1050$  K (Fig. 4d). In this case, a change in the nature of the temperature dependence of their Seebeck coefficient was observed (from  $\partial S/\partial T < 0$  at  $T < T_{\text{min}} = 900\text{--}1052$  K (Fig. 4f) to  $\partial S/\partial T > 0$  at  $T > T_{\text{min}}$ ), which was due to the release of mobile oxygen from the ceramic structure (1– $\delta$ ). The  $T_{\text{max}}$  and  $T_{\text{min}}$  values were significantly higher  $T^* = 685\text{--}745$  K (Fig. 3b), since the release of oxygen from the volume of sintered ceramics into the gas phase (air) occurs with greater diffusion difficulties than from powders. A comparison of the results of this study with the data we obtained earlier investigating the electrical transport properties of LDP [21–25] allowed us to conclude that the conductivity of ceramics is determined by the electrical conductivity of the

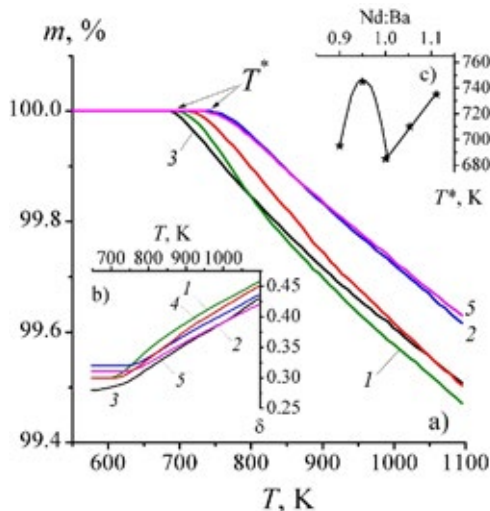


**Fig. 3.** Dependences of mass loss (a), and oxygen nonstoichiometry index (b) of N090B (1), N095B (2), NB (3), NB095 (4), NB090 (5) phases vs temperature, and dependence of temperature of beginning of mass loss (c) of these compounds vs their composition

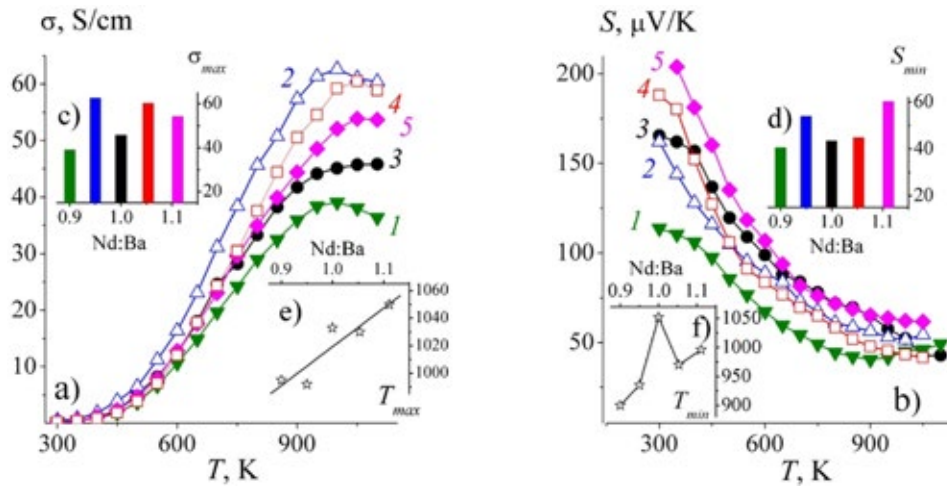


**Fig. 4.** Temperature (a, b) and concentration (c–f) dependences of electrical conductivity (a, c), Seebeck coefficient (b, d), and temperatures of extrema on the  $\sigma = f(T)$  (e) and  $S = f(T)$  (f) dependences of N090B (1), N095B (2), NB (3), NB095 (4), NB090 (5) ceramics

grains, the contributions of grain boundaries and contacts are insignificant, and the ohmicity of the contacts is confirmed by the linearity of their current-voltage characteristics. The values of the electrical conductivity and the Seebeck coefficient of ceramics, in general (with the exception of N090B composition), increase when a deficiency of cations is created in it (Fig. 4c, d, Table 4). The temperature  $T_{\max}$  value on dependencies  $\sigma = f(T)$  for the studied LDP, in general, increased with increasing Nd:Ba ratio in its structure, while the temperature  $T_{\min}$  on dependencies  $S = f(T)$  was maximal for the basic composition (NB) and decreased when neodymium or barium vacancies were created in its structure (Fig. 4e, f, Table 4).

The LDP investigated in this study were polaronic conductors [3, 10–17, 21–24], for which the dependence of electrical transport properties on temperature is described by the equations:

$$\sigma = \frac{A}{T} \exp\left[-\frac{E_{\sigma}}{kT}\right], \quad (7)$$

$$S = \frac{k}{e} \left(-\frac{E_S}{kT} + B\right), \quad (8)$$

where  $k$  – Boltzmann constant,  $T$  – temperature,  $A$  and  $B$  – constants,  $E_{\sigma} = E_S + E_m$  and  $E_S$  – activation energies of electrical conductivity and thermo-EMF,  $E_S$  – the excitation energy of polarons, and  $E_m$  – activation energy of their transfer [30]. As can be seen from the data in Table 4, the activation energies of the electrical transfer process ( $E_{\sigma}$ ,  $E_S$  and  $E_m$ ) in the studied ceramic samples, in general, decreased when a deficiency of neodymium or barium was created. For the studied LDP  $E_{\sigma} > E_S$  ( $E_m > 0$ ) (Table 4), from which it follows that the charge carriers in them are small radius polarons (SRP).

Weighted mobility of charge carriers ( $\mu$ ) in the studied samples in the temperature range

**Table 4.** Values of electrical conductivity at room temperature ( $\sigma_{300}$ ), maximal electrical conductivity ( $\sigma_{\max}$ ), minimal Seebeck coefficient ( $S_{\min}$ ), temperatures of extrema on the temperature dependences of electrical conductivity and Seebeck coefficient ( $T_{\max}$ ,  $T_{\min}$ ), and activation energies of electrical transport ( $E_{\sigma}$ ,  $E_S$ ,  $E_m$ ) in the  $\text{NdBaFeCo}_{0.5}\text{Cu}_{0.5}\text{O}_{6-8}$  ceramic samples

Sample	$\sigma_{300}$ , S/cm	$\sigma_{\max}$ , S/cm	$T_{\max}$ , K	$S_{\min}$ , $\mu\text{V/K}$	$T_{\min}$ , K	$E_{\sigma}$ , eV	$E_S$ , eV	$E_m$ , eV
N090B	0.230	39.1	995	40.6	900	0.281	0.051	0.230
N095B	0.461	62.6	992	53.9	935	0.267	0.049	0.218
NB	0.208	45.8	1033	43.5	1052	0.305	0.067	0.238
NB095	0.206	60.2	1030	44.8	970	0.308	0.069	0.239
NB090	0.250	54.2	1050	60.3	996	0.281	0.087	0.194

300–700 K varied within  $0.04\text{--}0.8\text{ cm}^2/(\text{V}\cdot\text{s})$  and increased with increasing temperature (Fig. 5a), which is characteristic for the polaron conduction mechanism. The values of  $\mu$  changed non-monotonically with changes in the cation composition and oxygen nonstoichiometry index ( $\delta$ ) of samples (Fig. 5c, d). The concentration of charge carriers “holes” in the same temperature range varied within the range  $(1\text{--}30)\cdot 10^{19}\text{ cm}^{-3}$  (Fig. 5b), in general, increased with the creation of a deficiency of neodymium or barium cations (Fig. 5e), as well as with increase in  $\delta$  (Fig. 5e), and increased exponentially with increasing temperature. The activation energy of charge carriers ( $E_p$ ), varied within  $0.150\text{--}0.174\text{ eV}$  and increased with increasing Nd:Ba ratio in the structure of the ceramics.

#### 4. Conclusions

Cation-deficient ceramics based on  $\text{NdBaFeCo}_{0.5}\text{Cu}_{0.5}\text{O}_{6-\delta}$  LDP was obtained using solid-phase reactions. The structure, oxygen stoichiometry, thermal stability, electrical conductivity, and thermo-EMF of the samples were studied. It was shown that the creation of up to 10 mol. % deficiency of neodymium or barium in the  $\text{NdBaFeCo}_{0.5}\text{Cu}_{0.5}\text{O}_{6-\delta}$  phase did not significantly affect the parameters of its crystal structure and oxygen nonstoichiometry index, but led to the growth of crystallites, improved the sintering of ceramics, increased its thermal stability, and improved the electrical transport properties. The activation energies of the processes of electrical transfer, weighted mobility

and concentration of the main charge carriers (“holes”) in the studied materials were calculated, the influence of the cationic composition and oxygen stoichiometry of ceramics on its structural, thermal and electrical transport characteristics were analyzed. The approach used in this study can be effectively applied to the development of electrode materials for medium-temperature solid oxide fuel cells based on oxygen-ion- or proton-conducting solid electrolytes.

#### Authors contributions

Chizhova E. A. – synthesis of materials, processing and interpreting the results, data visualization, writing the article. Marozau M. V. – conducting research, processing the results. Shevchenko S. V. – synthesis of materials, conducting research. Klyndyuk A. I. – scientific supervision, research concept, interpreting the results, final conclusions, writing the article. Zhuravleva Ya. Yu. – conducting research, processing and interpreting results. Kononovich V. M. - conducting research.

#### Conflict of interests

The authors declare that they have no known competing financial interests or personal relationships that could have influenced the work reported in this paper.

#### References

1. Jacobson A. J. Materials for solid oxide fuel cells. *Chemistry of Materials*. 2010;22(3): 660–670. <https://doi.org/10.1021/cm902640j>

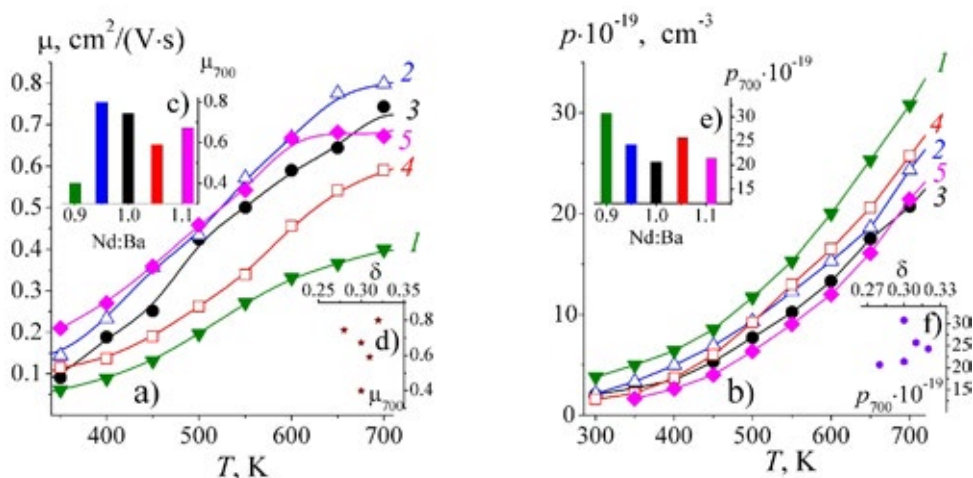


**Fig. 5.** Dependences of weighted mobility (a, c, e) and charge carriers concentration (b, d, f) in N090B (1), N095B (2), NB (3), NB095 (4), NB090 (5) ceramics vs temperature (a, b) and composition of the samples (c–f)



2. Afroze S., Karim A. H., Cheok Q., Eriksson S., Azad A. K. Latest development of double perovskite electrode materials for solid oxide fuel cells: a review. *Frontiers in Energy*. 2019;13: 770–797. <https://doi.org/10.1007/s11708-019-0651-x>
3. Klyndyuk A. I., Chizhova E. A., Kharytonau D. S., Medvedev D. A. Layered oxygen-deficient double perovskites as promising cathode materials for solid oxide fuel cells. *Materials*. 2022;15(1): 141. <https://doi.org/10.3390/ma15010141>
4. Kumar R. M., Khandale A. P. A review on recent progress and selection of cobalt-based cathode materials for low temperature solid oxide fuel cells. *Renewable and Sustainable Energy Reviews*. 2022;156: 111985. <https://doi.org/10.1016/j.rser.2021.111985>
5. Zeng C., Zhan B., Butt S., ... Nan C.-W. Electrical and thermal conduction behaviors in La-substituted GdBaCuFeO<sub>5+δ</sub> ceramics. *Journal of American Ceramic Society*. 2015;98(10): 3179–3184. <https://doi.org/10.1111/jace.13728>
6. Tsvetkov D. S., Ivanov I. L., Malyskin D. A., Sednev A. L., Sereda V. V., Zuev A. Yu. Double perovskites REBaCo<sub>2-x</sub>M<sub>x</sub>O<sub>6-δ</sub> (RE = La, Pr, Nd, Eu, Gd, Y; M = Fe, Mn) as energy-related materials: an overview. *Pure and Applied Chemistry*. 2019;19(6): 923–940. <https://doi.org/10.1515/pac-2018-1103>
7. Kaur P., Singh K. Review of perovskite-structure related cathode materials for solid oxide fuel cells. *Ceramics International*. 2020;46: 5521–5535. <https://doi.org/10.1016/j.ceramint.2019.11.066>
8. Istomin S. Ya., Lyskov N. V., Mazo G. N., Antipov E. V. Electrode materials based on complex d-metal oxides for symmetrical solid oxide fuel cells. *Russian Chemical Reviews*. 2021;90(6): 644–676. <https://doi.org/10.1070/RCR4979>
9. Su Ch., Wang W., Shao Z. Cation-deficient perovskites for clean energy conversion. *Account of Materials Research*. 2021;2: 477–488. <https://doi.org/10.1021/accounts.mr.1c00036>
10. Jiang X., Shi Y., Zhou W., ... Jiang L. Effects of Pr<sup>3+</sup>-deficiency on structure and properties of PrBaCo<sub>2</sub>O<sub>5+δ</sub> cathode material – A comparison with Ba<sup>2+</sup>-deficiency case. *Journal of Power Sources*. 2014;272: 371–377. <https://doi.org/10.1016/j.jpowsour.2014.08.091>
11. Yi K., Sun L., Li Q., ... Grenier J.-C. Effect of Nd-deficiency on electrochemical properties of NdBaCo<sub>2</sub>O<sub>6-δ</sub> cathode for intermediate-temperature solid oxide fuel cell. *International Journal of Hydrogen Energy*. 2016;41: 10228–10238. <https://doi.org/10.1016/j.ijhydene.2016.04.248>
12. Jiang X., Xu Q., Shi Y., ... Zhang Q. Synthesis and properties of Sm<sup>3+</sup>-deficient Sm<sub>1-x</sub>BaCo<sub>2</sub>O<sub>5+δ</sub> perovskite oxides as cathode materials. *International Journal of Hydrogen Energy*. 2014;39: 10817–10823. <http://dx.doi.org/10.1016/j.ijhydene.2014.04.203>
13. Pang S. L., Jiang X. N., Li X. N., ... Zhang Q. Y. Structure and properties of layered-perovskite LaBa<sub>1-x</sub>Co<sub>2</sub>O<sub>5+δ</sub> (x = 0–0.15) as intermediate-temperature cathode material. *Journal of Power Sources*. 2013;240: 54–59. <https://doi.org/10.1016/j.jpowsour.2013.04.005>
14. Pang S., Jiang X., Li X., Wang Q., Su Z. Characterization of Ba-deficient PrBa<sub>1-x</sub>Co<sub>2</sub>O<sub>5+δ</sub> as cathode material for intermediate temperature solid oxide fuel cells. *Journal of Power Sources*. 2012;204: 53–59. <https://doi.org/10.1016/j.jpowsour.2012.01.034>
15. Wang J., Meng F., Xia T., ... Grenier J.-C. Superior electrochemical performance and oxygen reduction kinetics of layered perovskite PrBa<sub>x</sub>Co<sub>2</sub>O<sub>5+δ</sub> (x = 0.90–1.00) oxides as cathode materials for intermediate-temperature solid oxide fuel cells. *International Journal of Hydrogen Energy*. 2014;39: 18392–18404. <http://dx.doi.org/10.1016/j.ijhydene.2014.09.041>
16. Pang S., Wang W., Chen T., ... Fan J. The effect of potassium on the properties of PrBa<sub>1-x</sub>Co<sub>2</sub>O<sub>5+δ</sub> (x = 0.00–0.10) cathodes for intermediate-temperature solid oxide fuel cells. *International Journal of Hydrogen Energy*. 2016;41: 13705–13714. <http://dx.doi.org/10.1016/j.ijhydene.2016.05.0460>
17. Donazzi A., Pelosato R., Cordaro G., Stucchi D., Cristiani C., Dotelli G., Sora N. Evaluation of Ba deficient NdBaCo<sub>2</sub>O<sub>5+δ</sub> oxide as cathode material for IT-SOFC. *Electrochimica Acta*. 2015;182: 573–587. <https://doi.org/10.1016/j.electacta.2015.09.117>
18. Cordaro G., Donazzi A., Pelosato R., ... Dotelli G. Structural and electrochemical characterization of NdBa<sub>1-x</sub>Co<sub>2-y</sub>Fe<sub>y</sub>O<sub>5+δ</sub> as cathode for intermediate temperature solid oxide fuel cells. *Journal of Electrochemical Society*. 2020;167: 024502. <https://doi.org/10.1149/1945-7111/ab628b>
19. Kim C. G., Woo S. H., Song K. E., ... Kim J. H. Enhanced electrochemical properties of non-stoichiometric layered perovskites, Sm<sub>1-x</sub>BaCo<sub>2</sub>O<sub>5+δ</sub>, for IT-SOFC cathodes. *Frontiers in Chemistry*. 2021;9: 633863. <https://doi.org/10.3389/fchem.2021.633863>
20. Zhang L., Li Sh., Sun L., Huo L., Zhao H. Co-deficient PrBaCo<sub>2-x</sub>O<sub>6-δ</sub> perovskites as cathode materials for intermediate-temperature solid oxide fuel cells: enhanced electrochemical performance and oxygen reduction kinetics. *International Journal of Hydrogen Energy*. 2018;43: 3761–3775. <https://doi.org/10.1016/j.ijhydene.2018.01.018>
21. Klyndyuk A. I., Chizhova E. A. Structure and electrical and transport properties of cation-deficient samples of perovskite ferrocuprates RBaCuFeO<sub>5+δ</sub> (R = Y, La). *Physics of the Solid State*. 2008;50(4): 603–608. <https://doi.org/10.1134/S1063783408040021>
22. Klyndyuk A. I., Chizhova E. A. Effect of cation deficiency on the structure and properties of layered lanthanum barium ferrocuprate. *Russian Journal of*

*Inorganic Chemistry*. 2008;53(4): 524–529. <https://doi.org/10.1134/S0036023608040074>

23. Klyndyuk A. I., Kharytonau D. S., Mosiałek M., ... Zimowska M. Double substituted NdBa(Fe,Co,Cu)<sub>2</sub>O<sub>5+δ</sub> layered perovskites as cathode materials for intermediate-temperature solid oxide fuel cells – correlation between structure and electrochemical properties *Electrochimica Acta*. 2022;411: 140062 <https://doi.org/10.1016/j.electacta.2022.140062>

24. Klyndyuk A. I., Zhuravleva Ya. Yu., Gundilovich N. N., Chizhova E. A. Structural, thermal, and electrical properties of solid solutions in the NdBaFeCo<sub>0.5</sub>Cu<sub>0.5</sub>O<sub>5+δ</sub>–NdSrFeCo<sub>0.5</sub>Cu<sub>0.5</sub>O<sub>5+δ</sub> system. *Inorganic Materials*. 2023;59(1): 86–92. <https://doi.org/10.1134/S0020168523010089>

25. Klyndyuk A. I., Zhuravleva Ya. Yu. Structure and physicochemical properties of NdBa<sub>1-x</sub>Ca<sub>x</sub>FeCo<sub>0.5</sub>Cu<sub>0.5</sub>O<sub>5+δ</sub> solid solutions (0.00 ≤ x ≤ 0.40). *Russian Journal of Inorganic Chemistry*. 2022;67(12):2084–2089. <https://doi.org/10.1134/S0036023622601404>

26. Goryachko A. I., Ivanin S. N., Buz'ko V. Yu. Synthesis, microstructural and electromagnetic characteristics of cobalt-zinc ferrite. *Condensed Matter and Interphases*. 2020;22(4): 446–452. <https://doi.org/10.17308/kcmf.2020.22/3115>

27. Nikam C. U., Kadam S. R., Shotole R. S., ... Kale G. H. Williamson–Hall and size strain plot based micro-structural analysis and evaluation of elastic properties of Dy<sup>3+</sup> substituted Co–Zn nano-spinels. *Journal of Physics: Conference Series*. 2023;2426: 012029. <https://doi.org/10.1088/1742-6596/2426/1/012029>

28. Snyder G. J., Snyder A. H., Wood M., Gurunathan R., Snyder B. H., Niu C. Wighted mobility. *Advanced Materials*. 2020;35: 2001537. <https://doi.org/10.1002/adma.202001537>

29. Atanassova Y. K., Popov V. N., Bogachev G. G., ... Pissas M. Raman- and infrared active phonons in YBaCuFeO<sub>5</sub>: experimental and lattice dynamics. *Physical Review B*. 1993;47: 15201–15207. <https://doi.org/10.1103/PhysRevB.47.15201>

30. Mott N., Davis E. *Electronic processes in non-crystalline materials*. 2<sup>nd</sup>ed. New York, USA, Oxford: Oxford University Press; 1979. 590 p.

## Information about the authors

*Ekaterina A. Chizhova*, Cand. Sci. (Chem.), Associate Professor, Associate Professor at the Department of Physical, Colloid and Analytical Chemistry, Belarusian State Technological University (Minsk, Republic of Belarus).

<https://orcid.org/0000-0002-2793-5071>  
chizhova@belstu.by

*Maksim V. Marozau*, Student, Belarusian State Technological University (Minsk, Republic of Belarus).

<https://orcid.org/0009-0000-0819-9681>  
wozmor@mail.ru

*Svetlana V. Shevchenko*, Cand. Sci. (Chem.), Associate Professor at the Department of Physical, Colloid and Analytical Chemistry, Belarusian State Technological University (Minsk, Republic of Belarus).

<https://orcid.org/0009-0007-6950-9939>  
shevchenko@belstu.by

*Andrei I. Klyndyuk*, Cand. Sci. (Chem.), Associate Professor, Associate Professor at the Department of Physical, Colloid and Analytical Chemistry, Belarusian State Technological University (Minsk, Republic of Belarus).

<https://orcid.org/0000-0003-0566-4386>  
klyndyuk@belstu.by

*Yana Yu. Zhuravleva*, postgraduate student at the Department of Physical, Colloid and Analytical Chemistry, Belarusian State Technological University (Minsk, Republic of Belarus).

<https://orcid.org/0009-0009-2162-0202>  
ya.yu.zhuravleva@mail.ru

*Vladimir M. Kononovich*, Researcher of Physical and Chemical Investigations Method Center of Belarusian State Technological University (Minsk, Republic of Belarus).

<https://orcid.org/0009-0003-9230-7025>  
rfarfa@mail.ru

Received 27.07.2023; approved after reviewing 29.09.2023; accepted for publication 16.10.2023; published online 25.06.2024.

Translated by Valentina Mittova



## Original articles

Research article

<https://doi.org/10.17308/kcmf.2024.26/11946>

## Synthesis and sensory properties of tungsten (VI) oxide-based nanomaterials

A. V. Shaposhnik<sup>1</sup>✉, A. A. Zvyagin<sup>1</sup>, S. V. Ryabtsev<sup>2</sup>, O. V. Dyakonova<sup>1</sup>, E. A. Vysotskaya<sup>1</sup>

<sup>1</sup>Voronezh State Agrarian University  
1 Michurin str., Voronezh 394087 Russian Federation

<sup>2</sup>Voronezh State University,  
1 Universitetskaya pl., Voronezh 394018, Russian Federation

### Abstract

The purpose of this work was to develop a methodology for the synthesis of WO<sub>3</sub>-based nano-scale materials, to provide their characterization, and to study their sensory properties.

The nanopowder was made by slowly adding nitric acid to an aqueous solution of ammonium paratungstate, (NH<sub>4</sub>)<sub>10</sub>W<sub>21</sub>O<sub>41</sub>·xH<sub>2</sub>O, followed by centrifugation, drying, and calcination. The size of tungsten trioxide grains, which was 10–20 nm, was determined by transmission electron microscopy. According to X-ray phase analysis, the powder, which was calcined at a temperature of 500 °C, mainly consisted of a triclinic phase. Subsequently, diammine palladium (II) nitrate and terpenol were added to the WO<sub>3</sub> nanopowder to form a paste. The resulting paste was applied to a special dielectric substrate and calcined to a temperature of 750 °C. As a result, a fragile tungsten trioxide-based gel formed. The mass fraction of palladium in the fragile gel was 3%. The sensory properties of the obtained gas-sensitive material were studied under stationary (300 °C) and non-stationary temperature conditions (quick heating to 450 °C and slow cooling to 100 °C).

A sharp increase in the sensitivity of a tungsten trioxide-based sensor was observed under non-stationary temperature conditions which depended on the composition of the gas-sensitive layer.

**Keywords:** MOX sensor; Sensitivity; Temperature modulation

**Acknowledgements:** The study was supported by the Russian Science Foundation grant (project No. 23-23-00329).

**For citation:** Shaposhnik A. V., Zviagin A. A., Ryabtsev S. V., Dyakonova O. V., Vysotskaya E. A. Synthesis and sensory properties of tungsten (VI) oxide-based nanomaterials. *Condensed Matter and Interphases*. 2023;24(2): 349–355. <https://doi.org/10.17308/kcmf.2024.26/11946>

**Для цитирования:** Шапошник А. В., Звягин А. А., Рябцев С. В., Дьяконова О. В., Высоцкая Е. А. Синтез и сенсорные свойства наноматериалов на основе оксида вольфрама (VI). *Конденсированные среды и межфазные границы*. 2023;24(2): 349–355. <https://doi.org/10.17308/kcmf.2024.26/11946>

✉ Alexey V. Shaposhnik, e-mail: [a.v.shaposhnik@gmail.com](mailto:a.v.shaposhnik@gmail.com)

© Shaposhnik A. V., Zviagin A. A., Ryabtsev S. V., Dyakonova O. V., Vysotskaya E. A., 2024



## 1. Introduction

Tungsten trioxide is a semiconductor with a band gap of 2.4–2.8 eV [1]. The application of  $\text{WO}_3$  is quite wide: for example, it is used to manufacture scintillators, luminophores, and electrochromic glass that can change light transmission with the changes in electrical voltage. Tungsten trioxide-based materials are used as hydrogenation catalysts during hydrocarbon cracking. Recently, nanodispersed tungsten (VI) oxide has become widely used as a gas-sensitive material for chemical sensors [2].

In most cases,  $\text{WO}_3$  is the basis of the gas-sensitive material, while additives increase sensitivity and selectivity. For example, a highly sensitive acetone sensor was obtained from the  $\text{WO}_3/\text{Au}$  nanocomposite [3]. The mesoporous sensor based on the  $\text{WO}_3\text{-TiO}_2$  heterojunction is highly sensitive to hydrogen [4]. A sensor with a p-n heterojunction at the boundary of NiO nanosheets and  $\text{WO}_3$  nanorods has a high sensitivity to acetaldehyde [5].

Sensors with very low power consumption can be created using individual metal oxide nanofilaments [6]. A very fast nanosecond response and extremely low power consumption at the level of several microwatts was achieved using an individual  $\text{WO}_3$  nanofilament coated with platinum [7]. The mechanism of chemical processes involved in detection of hydrogen in air was investigated using a gas-sensitive material consisting of  $\text{WO}_3$  nanorods [8]. The  $p\text{-NiCo}_2\text{O}_4/n\text{-WO}_3$  heterojunction was used to obtain a sensor with high sensitivity to nitrogen dioxide [9]. In addition, a NO<sub>x</sub> sensor was created based on palladium doped  $\text{WO}_3$  [10]. Doping of a n-type semiconductor,  $\text{WO}_3$  nanospheres, with a p-type semiconductor (antimony) made it possible to obtain an ammonia sensor operating at a temperature close to room temperature [11].

Flower-like  $\text{WO}_3\text{-In}_2\text{O}_3$  hollow microspheres were used as a gas-sensitive material used to detect acetone [12]. Iron doped reduced graphene oxide (rGO) was added to  $\text{WO}_3$  to create a low temperature acetone sensor [13]. A sensor capable of detecting amines at the level of ppb concentrations was created using  $\text{WO}_3\text{-W}_{18}\text{O}_{49}$  heterostructures with the addition of graphene layers and PdO nanoparticles [14].

A  $\text{WO}_3/\text{CuWO}_4$  heterostructure with 3D hierarchical pores was used to create a highly sensitive sensor operating at room temperature under the influence of visible radiation [15]. A Pd- $\text{WO}_3$  sensor with reinforced “self-assembly” made it possible to detect hydrogen even at room temperature [16].

A chemoresistive  $\text{NO}_2$  sensor using lanthanum doped  $\text{WO}_3$  was synthesized by flame spray pyrolysis [17]. A highly sensitive and highly selective  $\text{H}_2\text{S}$  sensor based on a flower-like  $\text{WO}_3/\text{CuO}$  nanocomposite can operate at low temperatures close to room temperature [18].

An ultra-low detection limit for ammonia detection at room temperature was achieved for a nanocomposite consisting of  $\text{WO}_3$  and multi-walled carbon nanotubes (MWCNT) [20]. A low-temperature  $\text{WO}_3\text{-Bi}_2\text{WO}_6$  sensor with a hierarchical flower-like structure made it possible to detect  $\text{H}_2\text{S}$  at the level of ppb concentrations [21]. A fast responding and highly reversible hydrogen sensor was obtained by doping amorphous  $\text{WO}_3$  thin films with palladium [22].  $\text{WO}_3$ -decorated  $\text{TiO}_2$ -based nanofiber allowed obtaining a heterostructure with high sensitivity to hydrogen [23]. Surface modification of the  $\text{WO}_3$  nanomaterial with Pt and Ru particles was used to obtain sensors sensitive to vapors of low-boiling liquids [24]. A  $\text{WO}_3\text{-PdO}$  core-shell architecture was used to obtain a highly sensitive acetone sensor [25].

The sensory properties of  $\text{WO}_3$ -based nanofilms obtained by magnetron sputtering have been studied in detail [26].  $\text{WO}_3$  nanofilms can also be prepared by thermal oxidation of metallic tungsten, however, its responses to nitrogen oxides and ammonia were not very high [27]. A micro-machined  $\text{WO}_3$ -based sensor was created to detect oxidizing gases. Importantly, the authors managed to achieve not only high responses, but also high selectivity by processing the results by the “electronic nose” methodology [28]. A highly sensitive hydrogen sensor was created by co-spraying tungsten and platinum [29].

One of the greatest challenges related to gas analysis with the help of sensors is their insufficient selectivity [30], which can be increased using a non-stationary temperature conditions of the sensor [31–33].

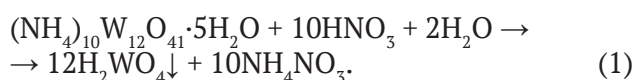


The purpose of this work was to synthesize  $WO_3$ -based nanomaterials, to provide their characterization, and to study their sensory properties in relation to hydrogen sulfide and carbon monoxide. In addition, the purpose of this study was to compare two temperature conditions: stationary and non-stationary.

## 2. Experimental

### 2.1. Synthesis and characterization of the gas-sensitive material

6.25 g of ammonium paratungstate (Sigma-Aldrich, Product Number 510114, Batch number MKCL8549) was dissolved in 250 ml of deionized water at 80 °C. Further, 3M nitric acid solution was added dropwise to the constantly stirred solution until pH = 0. The temperature was maintained at 80 °C. The resulting mixture was kept at 80 °C for 30 minutes and then cooled to room temperature and kept for one hour.



The tungstic acid precipitate was separated by centrifugation, washed with deionized water, and dried at 80 °C for 12 hours. As a result of further heat treatment of the dried tungstic acid precipitate for 24 hours at a temperature of 500 °C, tungsten trioxide formed:



The tungsten trioxide nanopowder was characterized by transmission electron microscopy (Fig. 1) and by X-ray phase analysis (XRD) using a DRON-4 device with a cobalt anode (Fig. 2). According to the electron microscopy data, the size of  $WO_3$  grains was 10–20 nm. The diffraction pattern was interpreted using the Powder Diffraction File (PDF-2) database. The PDF data for hexagonal and triclinic modifications of  $WO_3$  were plotted to the left side of Y-axis. The experimental XRD data were plotted to the right side of Y-axis. It was found that the sample

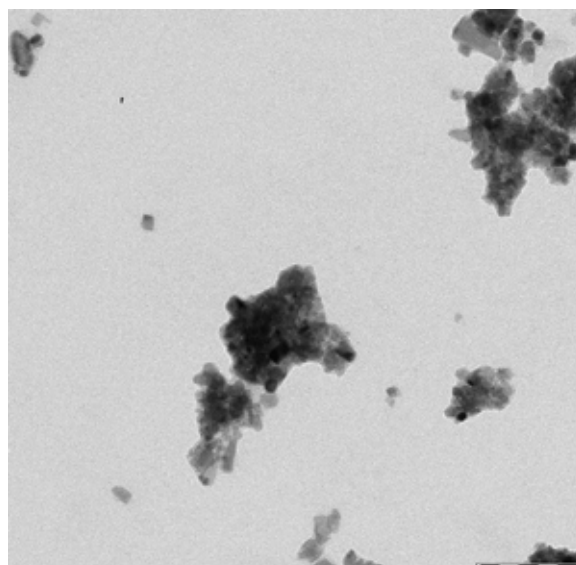


Fig. 1. Transmission electron microscopy image of tungsten (VI) oxide nanopowder

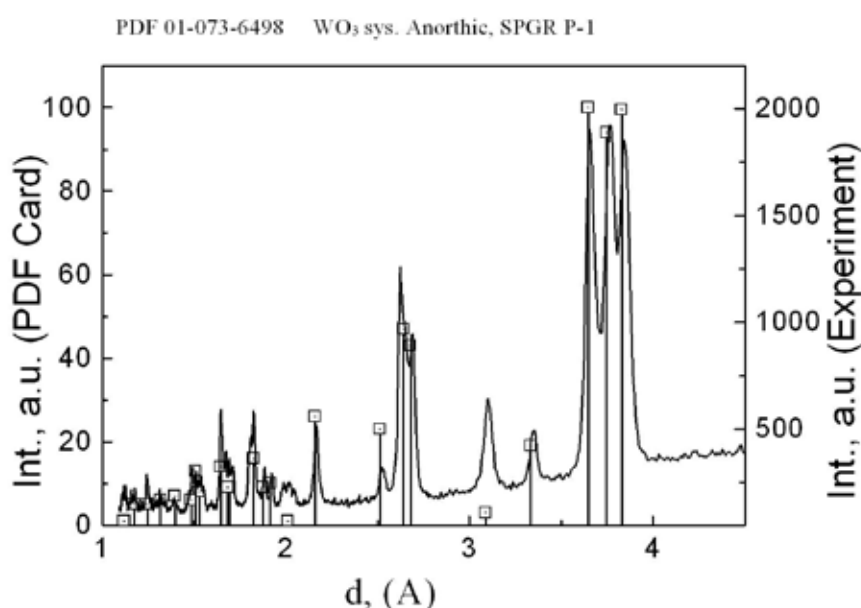


Fig. 2. X-ray diffraction pattern of tungsten (VI) oxide nanopowder calcinated at 500 °C

corresponded to the triclinic phase of  $\text{WO}_3$  (PDF card 01-073-6498).

A gas-sensitive layer based on  $\text{WO}_3$  with the addition of palladium oxide was obtained by treating tungsten trioxide powder with a solution of tetraammine palladium (II) nitrate with the addition of terpeniol as a binder component. The resulting paste was applied on a dielectric substrate made of aluminum oxide with platinum electrodes and a heater, then it was calcined to a temperature of 750 °C. As a result, terpeniol burned out and a layer of tungsten trioxide with the addition of palladium oxide in the form of a gel formed on the substrate.

## 2.2. Measuring sensory characteristics

Control gas mixtures “hydrogen sulfide in synthetic air” and “carbon monoxide in synthetic air” with concentrations of 10 ppm and 200 ppm diluted with synthetic air at a flow rate of 250 ml/min were used to study the sensory properties of the obtained materials. A metal-enclosed TO-8 sensor was placed in a stainless steel chamber. The temperature of the sensor was set by a special electronic device according to the temperature coefficient of resistance of the heater.

The electrical resistivity of the gas-sensitive layer of the sensor was measured with a special electronic device with a sampling rate of 40 Hz and recorded as a computer file. Each measurement

cycle lasted 15 seconds: 2 seconds of heating from 100 to 450 °C and then 13 seconds of cooling from 450 to 100 °C. These cycles were continuous (Fig. 3). The results of the first five cycles of measurements were not taken into account. Only one of the 575 cycle points was used for quantitative determination, which corresponded to a time of 14.95 seconds after the start of the measurements.

The response  $S$  was calculated by the ratio of the active electrical resistance  $R_0$  in clean air to the active electrical resistance  $R_g$  in the studied gas medium according to the formula:

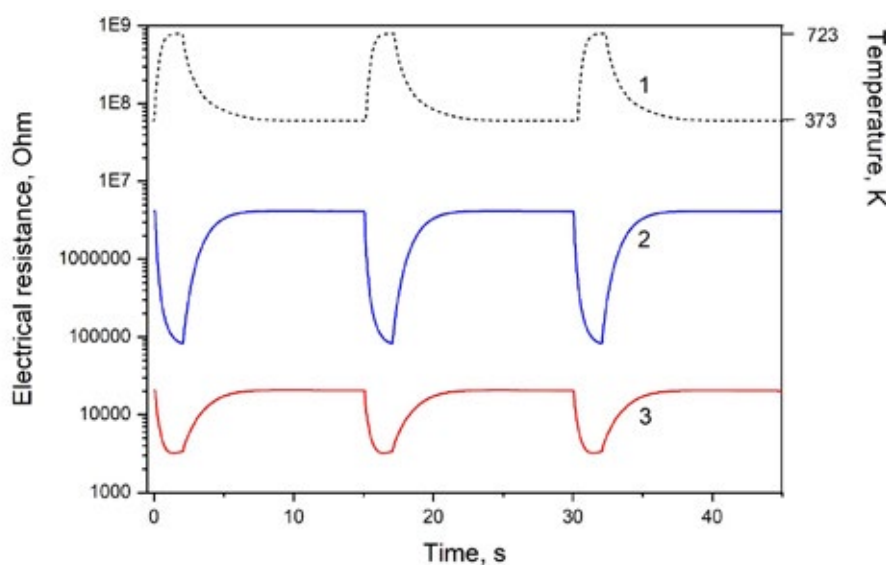
$$S = R_0/R_g. \quad (3)$$

## 3. Results and discussion

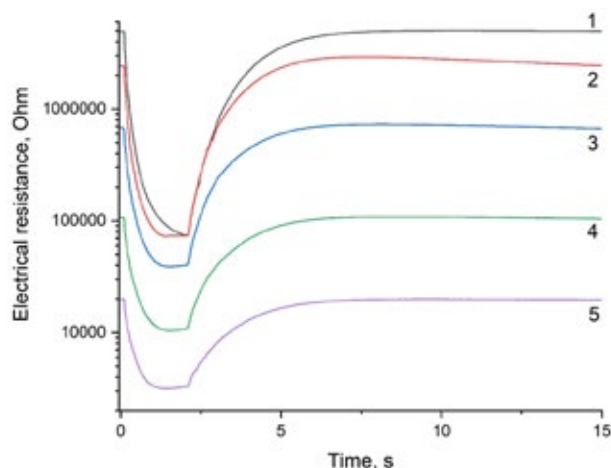
The sensor temperature (curve 1) and the electrical resistivity of the  $\text{WO}_3$ -Pd sensor when detecting carbon monoxide (curve 2) and hydrogen sulfide (curve 3) over three measurement cycles are shown in Fig. 3.

Fig. 4 shows the concentration dependences of the electrical resistance of the  $\text{WO}_3$ -Pd sensor on time during one measurement cycle for hydrogen sulfide.

Fig. 5 shows the dependence of the  $\text{WO}_3$ -Pd sensor response on the concentration of hydrogen sulfide in stationary (curve 1) and non-stationary temperature conditions (curve 2). According to the figure, the non-stationary conditions



**Fig. 3.** Temperature (curve 1) and the electrical resistance of the  $\text{WO}_3$ -Pd sensor at 50 ppm carbon monoxide (curve 2) and at 50 ppm hydrogen sulfide (curve 3) in a non-stationary temperature regime over three measurement cycles



**Fig. 4.** Electrical resistance of  $\text{WO}_3$ -Pd sensor in hydrogen sulfide of various concentrations at a non-stationary temperature condition during one measurement cycle. 1 – synthetic air, 2 – 5 ppm  $\text{H}_2\text{S}$ , 3 – 10 ppm  $\text{H}_2\text{S}$ , 4 – 20 ppm  $\text{H}_2\text{S}$ , 5 – 50 ppm  $\text{H}_2\text{S}$

contribute to an increase in the sensor response to hydrogen sulfide by about an order of magnitude. The difference in the form of sensor resistance versus time dependences when detecting carbon monoxide and hydrogen sulfide can be used to increase the analysis selectivity [33].

An increase in the sensitivity of the  $\text{WO}_3$ -Pd sensor to hydrogen sulfide may be explained by the temporary separation of the catalytic activity of the gas-sensitive layer of the sensor and the sorption of the analyte gas [31]. The non-stationary temperature conditions seem to activate the gas-sensitive layer of the sensor before the analyte gas desorption begins. In addition, the sensor response also depends on the total concentration of the charge carriers. The higher the sensor response, the fewer charge carriers are present in the metal oxide sensor before the analyte gas is released. As a result, the impulsed temperature changes increase the resistance of the  $\text{WO}_3$ -Pd sensor in air due to high oxygen sorption.

#### 4. Conclusions

As a result of the study, the traditional sol-gel technology was used to produce a  $\text{WO}_3$ -Pd sensor by adding palladium oxide (3% by weight) to a tungsten trioxide nanopowder. The sensory characteristics of the resulting material in relation to hydrogen sulfide and carbon monoxide were

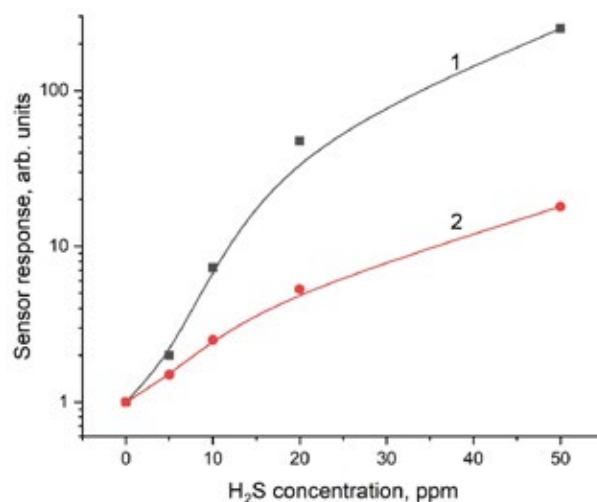


**Fig. 5.** Dependence of the response of the  $\text{WO}_3$ -Pd sensor on the concentration of hydrogen sulfide in non-stationary mode (1) and at a stationary temperature of 300 °C (2)

investigated. The conducted studies of sensory characteristics in two types of temperature conditions showed that the impulsed temperature changes result in a significant increase in the sensitivity of the sensor to hydrogen sulfide. Therefore, when operating in non-stationary temperature conditions, the  $\text{WO}_3$ -Pd sensor can be used to detect hydrogen sulfide and other reducing gases.

#### Contribution of the authors

The authors contributed equally to this article.

#### Conflict of interests

The authors declare that they have no known competing financial interests or personal relationships that could have influenced the work reported in this paper.

#### References

1. Tesfamichael T., Ponzoni A., Ahsan M., Faglia G. Gas sensing characteristics of Fe-doped tungsten oxide thin films. *Sensors and Actuators B: Chemical*. 2012;168(2): 345–353. <https://doi.org/10.1016/j.snb.2012.04.032>
2. Tesfamichael T., Ahsan M., Notarianni M., ... Bell J. Gas sensing of ruthenium implanted tungsten oxide thin films. *Thin Solid Films*. 2014;558: 416–422. <https://doi.org/10.1016/j.tsf.2014.02.084>
3. Zhang X., Dong B., Liu W., ... Song H. Highly sensitive and selective acetone sensor based on three-dimensional ordered  $\text{WO}_3/\text{Au}$  nanocomposite with

- enhanced performance. *Sensors Actuators, B Chemical*. 2020;320(4): 128405. <https://doi.org/10.1016/j.snb.2020.128405>
4. Li H., Wu C.-H., Liu Y.-C., ... Wu R.-J. Mesoporous  $\text{WO}_3$ - $\text{TiO}_2$  heterojunction for a hydrogen gas sensor. *Sensors Actuators, B Chemical*. 2021;341(2): 130035. <https://doi.org/10.1016/j.snb.2021.130035>
5. Nakate U. T., Yu Y. T., Park S. High performance acetaldehyde gas sensor based on  $p$ - $n$  heterojunction interface of NiO nanosheets and  $\text{WO}_3$  nanorods. *Sensors Actuators, B Chemical*. 2021;344(5): 130264. <https://doi.org/10.1016/j.snb.2021.130264>
6. Shaposhnik A. V., Shaposhnik D. A., Turishchev S. Y., ... Morante J. R. Gas sensing properties of individual  $\text{SnO}_2$  nanowires and  $\text{SnO}_2$  sol-gel nanocomposites. *Beilstein Journal of Nanotechnology*. 2019;10: 1380–1390. <https://doi.org/10.3762/bjnano.10.136>
7. Fan L., Xu N., Chen H., Zhou J., Deng S. A millisecond response and microwatt power-consumption gas sensor: Realization based on cross-stacked individual Pt-coated  $\text{WO}_3$  nanorods. *Sensors Actuators B Chemical*. 2021;346(2): 130545. <https://doi.org/10.1016/j.snb.2021.130545>
8. Mineo G., Moulaei K., Neri G., Mirabella S., Bruno E.  $\text{H}_2$  detection mechanism in chemoresistive sensor based on low-cost synthesized  $\text{WO}_3$  nanorods. *Sensors Actuators B Chemical*. 2021;348: 130704. <https://doi.org/10.1016/j.snb.2021.130704>
9. Hu Y., Li T., Zhang J., Guo J., Wang W., Zhang D. High-sensitive  $\text{NO}_2$  sensor based on  $p$ - $\text{NiCo}_2\text{O}_4/n$ - $\text{WO}_3$  heterojunctions. *Sensors Actuators B Chemical*. 2022;352(P2): 130912. <https://doi.org/10.1016/j.snb.2021.130912>
10. Karpe S. B., Bang A. D., Adhyapak D. P., Adhyapak P. V. Fabrication of high sensitive proto-type  $\text{NO}_x$  sensor based on Pd nanoparticles loaded on  $\text{WO}_3$ . *Sensors Actuators B Chemical*. 2022;354: 131203. <https://doi.org/10.1016/j.snb.2021.131203>
11. Yao G., Yu J., Wu H., ... Tang Z.  $P$ -type Sb doping hierarchical  $\text{WO}_3$  microspheres for superior close to room temperature ammonia sensor. *Sensors Actuators B Chemical*. 2022;359: 131365. <https://doi.org/10.1016/j.snb.2022.131365>
12. Hu J., Xiong X., Guan W., Long H., Zhang L., Wang H. Self-templated flower-like  $\text{WO}_3$ - $\text{In}_2\text{O}_3$  hollow microspheres for conductometric acetone sensors. *Sensors Actuators B Chemical*. 2022;361(10): 131705. <https://doi.org/10.1016/j.snb.2022.131705>
13. Sen S., Maity S., Kundu S. Fabrication of Fe doped reduced graphene oxide (rGO) decorated  $\text{WO}_3$  based low temperature ppm level acetone sensor: Unveiling sensing mechanism by impedance spectroscopy. *Sensors Actuators B Chemical*. 2022;361(3): 131706. <https://doi.org/10.1016/j.snb.2022.131706>
14. Wang X., Han W., Yang J., ... Lu G. Conductometric ppb-level triethylamine sensor based on macroporous  $\text{WO}_3$ - $\text{W}_{18}\text{O}_{49}$  heterostructures functionalized with carbon layers and PdO nanoparticles. *Sensors Actuators B Chem*. 2022;361(1): 131707. <https://doi.org/10.1016/j.snb.2022.131707>
15. Liu Y., Li X., Li X., ... Liu Y. Highly permeable  $\text{WO}_3/\text{CuWO}_4$  heterostructure with 3D hierarchical porous structure for high-sensitive room-temperature visible-light driven gas sensor. *Sensors Actuators B Chemical*. 2022;365(4): 131926. <https://doi.org/10.1016/j.snb.2022.131926>
16. Lee J., Kim S. Y., Yoo H. S., Lee W. Pd- $\text{WO}_3$  chemiresistive sensor with reinforced self-assembly for hydrogen detection at room temperature. *Sensors Actuators B Chemical*. 2022;368(6): 132236. <https://doi.org/10.1016/j.snb.2022.132236>
17. Zhang Y., Wu C., Xiao B., ... Lin H. Chemo-resistive  $\text{NO}_2$  sensor using La-doped  $\text{WO}_3$  nanoparticles synthesized by flame spray pyrolysis. *Sensors Actuators B Chemical*. 2022;369(2): 132247. <https://doi.org/10.1016/j.snb.2022.132247>
18. He M., Xie L., Zhao X., Hu X., Li S., Zhu Z.-G. Highly sensitive and selective  $\text{H}_2\text{S}$  gas sensors based on flower-like  $\text{WO}_3/\text{CuO}$  composites operating at low/room temperature. *Journal of Alloys and Compounds*. 2019;788: 36–43. <https://doi.org/10.1016/j.jallcom.2019.01.349>
19. Marikutsa A., Yang L., Kuznetsov A. N., Romyantseva M., Gaskov A. Effect of W–O bonding on gas sensitivity of nanocrystalline  $\text{Bi}_2\text{WO}_6$  and  $\text{WO}_3$ . *Journal of Alloys and Compounds*. 2021;856: 158159. <https://doi.org/10.1016/j.jallcom.2020.158159>
20. Duong V. T., Nguyen C. T., Luong H. B., Nguyen D. C., Nguyen H. L. Ultralow-detection limit ammonia gas sensors at room temperature based on MWCNT/ $\text{WO}_3$  nanocomposite and effect of humidity. *Solid State Sciences*. 2021;113(11): 106534. <https://doi.org/10.1016/j.solidstatesciences.2021.106534>
21. Zhang C., Wu K., Liao H., Debliquy M. Room temperature  $\text{WO}_3$ - $\text{Bi}_2\text{WO}_6$  sensors based on hierarchical microflowers for ppb-level  $\text{H}_2\text{S}$  detection. *Chemical Engineering Journal*. 2022;430(P2): 132813. <https://doi.org/10.1016/j.cej.2021.132813>
22. Hwan Cho S., Min Suh J., Jeong B., ... Won Jang H. Fast responding and highly reversible gasochromic  $\text{H}_2$  sensor using Pd-decorated amorphous  $\text{WO}_3$  thin films. *Chemical Engineering Journal*. 2022;446(P1): 136862. <https://doi.org/10.1016/j.cej.2022.136862>
23. Kumaresan M., Venkatachalam M., Saroja M., Gowthaman P.  $\text{TiO}_2$  nanofibers decorated with monodispersed  $\text{WO}_3$  heterostructure sensors for high gas sensing performance towards  $\text{H}_2$  gas. *Inorganic Chemistry Communications*. 2021;129(2): 108663. <https://doi.org/10.1016/j.inoche.2021.108663>



24. Chen L., Zhang Y., Sun B., ... Tian C. Surface modification of  $WO_3$  nanoparticles with Pt and Ru for VOCs sensors. *Chinese Journal of Analytical Chemistry*. 2022; 100143. <https://doi.org/10.1016/j.cjac.2022.100143>

25. Hu J., Xiong X., Guan W., Long H. Designed construction of  $PdO@WO_3$  core-shell architecture as a high-performance acetone sensor. *Journal of Environmental Chemical Engineering*. 2021;9(6): 106852. <https://doi.org/10.1016/j.jece.2021.106852>

26. *Sensor electronics, sensors: solid state sensors on silicon: a study guide for students of higher education institutions* / E. P. Domashevskaya [et al.]; edited by A. M. Hoviv. Moscow: Yurayt Publishing House, 2020. 203 p. (in Russ). Available at: <https://urait.ru/bcode/518779>

27. Siciliano T., Tepore A., Micocci G., Serra A., Manno D., Filippo E.  $WO_3$  gas sensors prepared by thermal oxidization of tungsten. *Sensors and Actuators B: Chemical*. 2008;133(1): 321–326. <https://doi.org/10.1016/j.snb.2008.02.028>

28. Vallejos S., Khatko V., Calderer J., ... Correig X. Micro-machined  $WO_3$ -based sensors selective to oxidizing gases. *Sensors and Actuators B: Chemical*. 2008;132(1): 209–215. <https://doi.org/10.1016/j.snb.2008.01.044>

29. Zhang C., Boudiba A., Navio C., ... Debliquy M. Highly sensitive hydrogen sensors based on co-sputtered platinum-activated tungsten oxide films. *International Journal of Hydrogen Energy*. 2010;36(1): 1107–1114. <https://doi.org/10.1016/j.ijhydene.2010.10.011>

30. Yakovlev P. V., Shaposhnik A. V., Voishchev V. S., Kotov V. V., Ryabtsev S. V. Determination of gases using polymer-coated semiconductor sensors. *Journal of Analytical Chemistry*. 2002;57(3): 276–279. <https://doi.org/10.1023/A:1014412919822>

31. Shaposhnik A. V., Moskalev P. V., Zviagin A. A., ... Vasiliev A. A. Selective determination of hydrogen sulfide using  $SnO_2$ -Ag sensor working in non-stationary temperature regime. *Chemosensors*. 2021;9(8): 203. <https://doi.org/10.3390/chemosensors9080203>

32. Shaposhnik A., Zvyagin A., Vasiliev A., Ryabtsev S., Shaposhnik D., Nazarenko I., Buslov V. Optimal temperature regimes of semiconductor sensors determination. *Sorbtsionnye i Khromatograficheskie Protsessy*. 2008;8(3): 501–506. (In Russ., abstract in Eng.). Available at: <https://www.elibrary.ru/item.asp?id=11928774>

33. Shaposhnik A., Moskalev P., Sizask E., Ryabtsev S., Vasiliev A. Selective detection of hydrogen sulfide and methane by a single MOX-sensor. *Sensors (Switzerland)*. 2019;19(5): 1135. <https://doi.org/10.3390/s19051135>

### Information about the authors

*Alexey V. Shaposhnik*, Dr. Sci. (Chem.), Professor at the Department of Chemistry, Voronezh State Agrarian University (Voronezh, Russian Federation).

<https://orcid.org/0000-0002-1214-2730>

[a.v.shaposhnik@gmail.com](mailto:a.v.shaposhnik@gmail.com)

*Alexey A. Zviagin*, Cand. Sci. (Chem.), Associate Professor at the Department of Chemistry, Voronezh State Agrarian University (Voronezh, Russian Federation).

<https://orcid.org/0000-0002-9299-6639>

[a.a.zviagin@rambler.ru](mailto:a.a.zviagin@rambler.ru)

*Stanislav V. Ryabtsev*, Dr. Sci. (Phys.–Math.), Head of the Laboratory, Voronezh State University, (Voronezh Russian Federation).

<https://orcid.org/0000-0001-7635-8162>

[raybtsev@niif.vsu.ru](mailto:raybtsev@niif.vsu.ru)

*Olga V. Dyakonova*, Cand. Sci. (Chem.), Associate Professor at the Department of Chemistry, Voronezh State Agrarian University (Voronezh, Russian Federation).

[dyakol@yandex.ru](mailto:dyakol@yandex.ru)

*Elena A. Vysotskaya*, Dr. Sci. (Biol.), Dean of the Faculty of Technology and Commodity Science, Voronezh State Agrarian University (Voronezh, Russian Federation).

[murka1979@mail.ru](mailto:murka1979@mail.ru)

Received 03.06.2023; approved after reviewing 03.09.2023; accepted for publication 15.09.2023; published online 25.06.2024.

Translated by Irina Charychanskaya



## Short communication

Short communication

<https://doi.org/10.17308/kcmf.2024.26/12044>

## Influence of the particle size of sulfonated cation exchange resin on the physicochemical properties and surface morphology of MK-40 heterogeneous membranes

S. V. Dobryden, E. M. Akberova, D. R. Mamonov, Ya. R. Bespalova, V. I. Vasil'eva✉

Voronezh State University,  
1 Universitetskaya pl., Voronezh 394018, Russian Federation

### Abstract

The article presents the results of the study of the physicochemical properties and surface morphology of MK-40 heterogeneous membranes with a given particle size of sulfonated cation exchange resin within the ranges of  $< 20 \mu\text{m}$ ,  $32\text{--}40 \mu\text{m}$  and  $56\text{--}71 \mu\text{m}$  with the resin-polyethylene ratio of 65:35. The experimental membranes were manufactured at LLC Innovative Enterprise *Shchekinoazot* (Russia). A comparative analysis of the characteristics of the membranes showed that their main physicochemical properties change in accordance with the changes in surface parameters. With an increase in the particle size of the ion exchange resin, the moisture content and the thickness of the membranes decreased together with the surface macroporosity. What is more, the exchange capacity of the membranes did not depend on the particle size of the ion exchange resin.

Quantitative analysis of SEM images of swollen membranes revealed a number of peculiarities of their surface morphology. First, it was established that membranes with a size of resin particles within the range of  $56\text{--}71 \mu\text{m}$  had small ion-exchangers with a radius of  $R < 10 \mu\text{m}$  and no large ( $R > 20 \mu\text{m}$ ) ion-exchangers. Secondly, it was found that the fraction of the ion exchanger and the weighted average radius of the ion exchange resin particles decreased by 14% and 15% respectively with an increase in the preset dimensions of the ion exchanger. Thirdly, with an increase in the size of the resin particles, the surface macroporosity decreased by 7%, while the size of the macropores increased by more than 20%. To explain the revealed peculiarities of the surface morphology of MK-40 heterogeneous membranes with different particle sizes of sulfonated cation exchange resin, it is necessary to study the structure of their internal phase.

**Keywords:** Heterogeneous cation exchange membrane, Particle size of ion exchange resin, Surface morphology, Physicochemical properties

**Acknowledgements:** The study was supported by a grant from the Russian Science Foundation No. 21-19-00397, <https://rscf.ru/en/project/21-19-00397/>

Microphotographs of membrane surfaces were obtained using the equipment of the Centre for Collective Use of Scientific Equipment of Voronezh State University. URL: <https://ckp.vsu.ru>

**For citation:** Dobryden S. V., Akberova E. M., Mamonov D. R., Bespalova Ya. R., Vasil'eva V. I. Influence of the particle size of sulfonated cation exchange resin on the physicochemical properties and surface morphology of MK-40 heterogeneous membranes. *Condensed Matter and Interphases*. 2024;26(2): 356–361. <https://doi.org/10.17308/kcmf.2024.26/12044>

**Для цитирования:** Добрыдень С. В., Акберова Э. М., Мамонов Д. Р., Беспалова Я. Р., Васильева В. И. Влияние размера частиц сульфокатионообменной смолы на физико-химические свойства и морфологию поверхности гетерогенной мембраны МК-40 Конденсированные среды и межфазные границы. 2024;26(2): 356–361. <https://doi.org/10.17308/kcmf.2024.26/12044>

✉ Vera I. Vasil'eva, e-mail: [viv155@mail.ru](mailto:viv155@mail.ru)

© Dobryden S. V., Akberova E. M., Mamonov D. R., Bespalova Ya. R., Vasil'eva V. I., 2024



The content is available under Creative Commons Attribution 4.0 License.

## 1. Introduction

Currently, researchers and practitioners are focused on developing specialized membrane products that meet specific technological requirements, such as low membrane electrical resistance [1], specific selectivity [2], chemical and thermal stability [3], and/or scaling resistance [4]. The manufacture of new or the modification of existing commercial membranes for specific purposes is a complex interdisciplinary task since the parameters that determine their properties often act in opposite directions. For example, a high concentration of fixed ions in the membrane matrix results in a low electrical resistance, however, it also causes a high degree of swelling in combination with poor mechanical stability [1, 5]. In addition, one of the biggest challenges for the manufacture of heterogeneous membranes with an optimal combination of mechanical strength and electrochemical properties is the need for two continuous phases: ion exchange and inert phases. Continuous paths for ion transport are necessary for effective contact between ion exchange particles, while mechanical strength can be ensured by a continuous layer of binder material [6]. What is more, the deformation of the inert binder and ion exchange resin particles during swelling results in the formation of channels filled with the solution, which connect the ion-exchangers. To achieve high mechanical strength, ion exchange membranes can be reinforced with fabrics made of polymers such as nylon and polyester (Lavsan). This structure causes significant changes in the physicochemical properties of the membrane surface and volume on a micrometer scale. The presence of conductive (the ion-exchanger phase) and non-conductive (inert binder) sections and reinforcing fabric contributes to the development of electrical and geometric heterogeneity on the surface, which contributes to the development of electroconvection in electromembrane systems, the main mechanism for the overlimiting conductivity of membranes [7, 8].

The aim of the work is to study the influence of the particle size of the sulfonated cation exchange resin on the physicochemical properties and structural characteristics of the surface of the MK-40 heterogeneous membrane.

## 2. Experimental

In our study, we used experimental samples of the MK-40 heterogeneous cation exchange membrane with a preset size of particles of the ion exchange resin within the range of: < 20, 32–40, and 56–71  $\mu\text{m}$ . The samples were manufactured at the well-known Russian enterprise, LLC IE *Shchekinoazot*. The MK-40 membrane is a polymer composition of a strongly acidic cation exchanger KU-2-8, low-pressure L461N19 polyethylene, and a reinforcing fabric, Excelsior capron mesh, art. 56314. Fixed groups of MK-40 membranes are sulfonic acid groups,  $\text{SO}_3^-$ . The ratio of ion exchange resin and polyethylene in the composition of the experimental MK-40 membranes was traditional and was 65 wt. % to 35 wt. %. Particles of ion exchange resin of a certain size were selected using a complex of five sieves with a mesh diameter of 71, 32, and 20  $\mu\text{m}$ .

Physicochemical properties of the studied samples were determined using standard testing methods for ion exchange membranes [9]. The total exchange capacity was determined under static conditions using acid-base titration. The total exchange capacity  $Q$  ( $\text{mmol/g}_{\text{dry}}$ ) was calculated taking into account the moisture content  $W$ . The moisture content  $W$  (%) in the membranes was determined by air-heat drying, the thickness  $l$  ( $\mu\text{m}$ ) was measured using a micrometer, and the density  $\rho$  ( $\text{g/cm}^3$ ) was measured using a pycnometer.

The surface morphology of the membranes was studied by scanning electron microscopy (SEM) using a JSM-6510 LV microscope (Japan). Since ion exchange membranes are swollen when activated, the study was carried out in a low vacuum mode using reflected electrons at an accelerating voltage of 20 kV. This SEM mode does not require preliminary drying of the sample and spraying a conductive layer on its surface [10]. The quantitative assessment of the fraction of ion exchange material ( $S$ , %) and porosity ( $P$ , %) on the surface of the membranes was carried out using an original software package [11]. The concept of a “pore” was understood as the space between the ion-exchanger and an inert binder (polyethylene). Taking into account the “size effect” of the inhomogeneous surface of heterogeneous membranes, to determine simultaneously the fraction and the radius of the

particles of the ion exchange resin ( $R$ ,  $\mu\text{m}$ ) and macropores ( $r$ ,  $\mu\text{m}$ ), the value of 500 was chosen as the optimal magnification ratio of the surface image [5].

### 3. Results and discussion

A comparison of the properties of the experimental MK-40 membranes with different particle sizes of ion exchange resin revealed the influence of the sizes of ion-exchanger particles on their physicochemical and structural properties (Table 1).

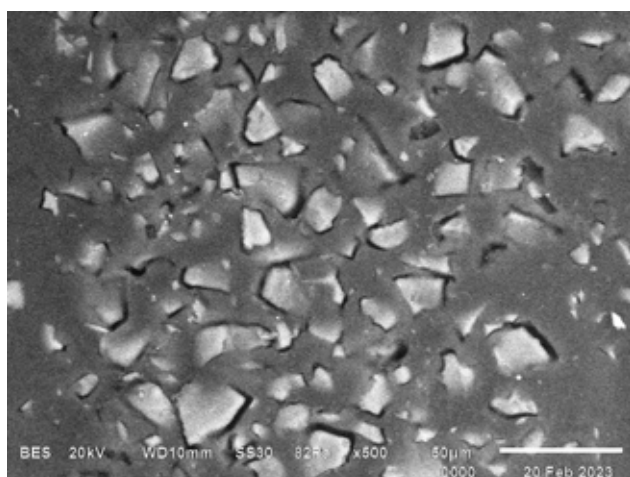
The surface structure of the studied heterogeneous cation exchange membranes was heterogeneous (Fig. 1). There were visible light areas of the conductive surface (ion-exchanger particles) and dark areas of inert polyethylene (non-conductive surface). A comparison of electron micrographs of the membrane surfaces with the minimum and maximum particle sizes of the ion exchange resin showed that with an increase in particle sizes, the fraction of the ion-exchanger  $S$  on the surface of the membranes in the swollen state decreased by 14% (Table 1). Quantitative analysis of the size of the ion

exchange resin particles on the surface revealed a difference in the values of the weighted average radius of slightly more than 15%.

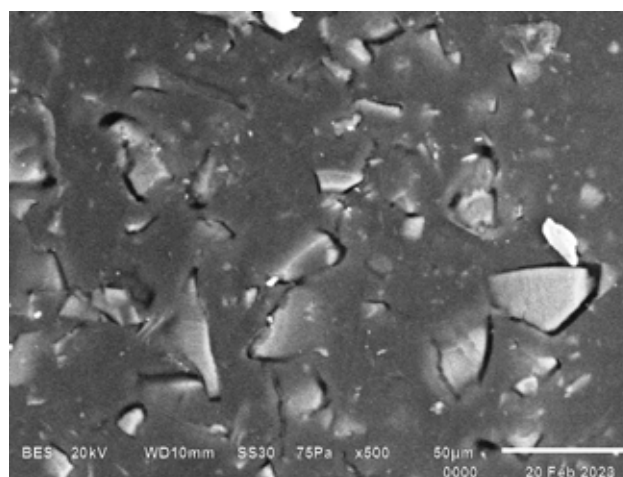
Histograms of the distribution of the fraction of resin particles of different radii  $S_R$  of the total phase area of the ion exchanger  $S_0$  on the surface of the experimental MK-40 membranes are shown in Fig. 2. For the MK-40 membrane with a minimum preset particle size of the ion-exchange resin, the maximum proportion (85%) were particles with a radius within the range from 1 to 10  $\mu\text{m}$ , 14% constituted particles with a radius of 11–13  $\mu\text{m}$ , the rest was resin particles with  $R < 1 \mu\text{m}$ . In the case of the membrane with the maximum preset particle size of the ion-exchange resin (from 56 to 71  $\mu\text{m}$ ) it was found that large particles were absent on their surface. Particles with a radius within the ranges from 1 to 10  $\mu\text{m}$  and from 11 to 16  $\mu\text{m}$  made up 70% and 28% of the total area of the ion exchange phase, respectively. It was revealed that with an increase in the particle size of the ion exchange resin, the surface macroporosity  $P$  (Table 1) tended to decrease by 7%. However, the value of the weighted average radius of macropores

**Table 1.** Physicochemical properties and structural characteristics of the surface of MK-40 membranes with different particle sizes of ion exchange resin

Resin particle sizes, $\mu\text{m}$	IEC, $\text{mmol/g}_{\text{dry}}$	$W$ , %	$\rho$ , $\text{g/cm}^3$	$l$ , $\mu\text{m}$	$S$ , %	$P$ , %	$R$ , $\mu\text{m}$	$r$ , $\mu\text{m}$
<20	$2.54 \pm 0.02$	$40.4 \pm 0.6$	$1.10 \pm 0.06$	$566 \pm 7$	$21 \pm 1$	$4.7 \pm 0.8$	$2.6 \pm 0.3$	$1.8 \pm 0.3$
32-40	$2.49 \pm 0.02$	$37.7 \pm 0.9$	$1.06 \pm 0.07$	$554 \pm 7$	$18 \pm 4$	$3.8 \pm 0.9$	$2.7 \pm 0.2$	$1.8 \pm 0.1$
56-71	$2.54 \pm 0.03$	$35.7 \pm 0.6$	$1.03 \pm 0.07$	$492 \pm 6$	$18 \pm 2$	$4.4 \pm 1.7$	$2.2 \pm 0.3$	$2.2 \pm 0.2$



a



b

**Fig. 1.** SEM images of the surface of MK-40 sulfonated cation exchange membranes at a magnification of 500. The particle size of ion exchange resin is < 20  $\mu\text{m}$  (a), 56-71  $\mu\text{m}$  (b)



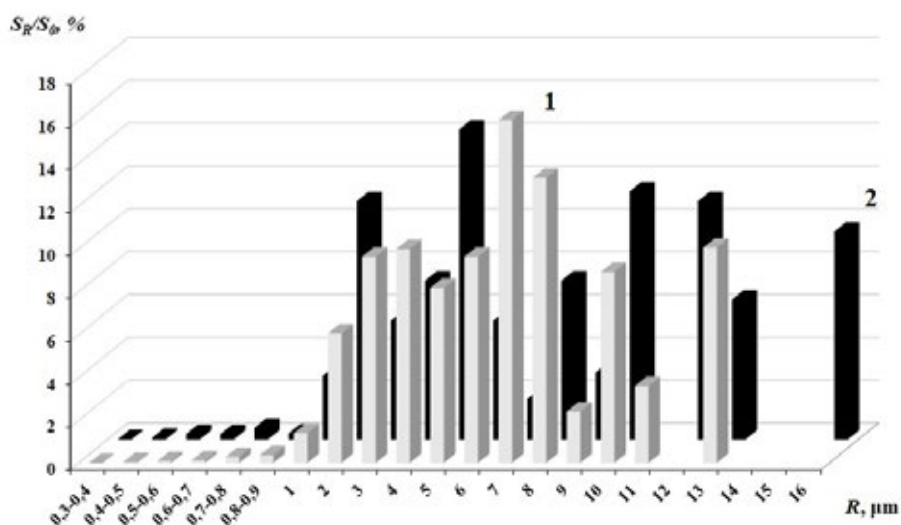


**Fig. 2.** Fractions of resin particles  $S_R$  of different radii  $R$  of the total area of the ion exchange phase  $S_0$  on the surface of the MK-40 membrane with the particle size of the ion exchange resin of  $< 20 \mu\text{m}$  (1) and  $56\text{--}71 \mu\text{m}$  (2)

increased by more than 20%. Histograms of the distribution of the macropore fractions along the radii on the surface of the experimental samples of the MK-40 membrane in the swollen state are shown in Fig. 3. For a membrane with a preset resin particle size of  $56\text{--}71 \mu\text{m}$ , a wider pore size variation interval was established, which was  $0.5\text{--}8 \mu\text{m}$  for swollen samples. What is more, the fraction of macropores in the range of  $1 < r < 5 \mu\text{m}$  and more than  $7 \mu\text{m}$  was 80 and 19%, respectively. For the MK-40 membrane with a minimum resin particle size, the maximum

fraction of macropores (97%) corresponded to sizes within the range of  $1 < r < 5 \mu\text{m}$ , while there were no macropores with  $r > 5 \mu\text{m}$ .

The obtained physicochemical characteristics of the studied membranes are given in Table 1. With an increase in the particle size of the ion exchange resin, the total exchange capacity did not change, and the moisture content, density, and thickness decreased by 12, 6, and 15%, respectively. The change in the basic physicochemical properties of the studied membranes with an increase in the particle size of

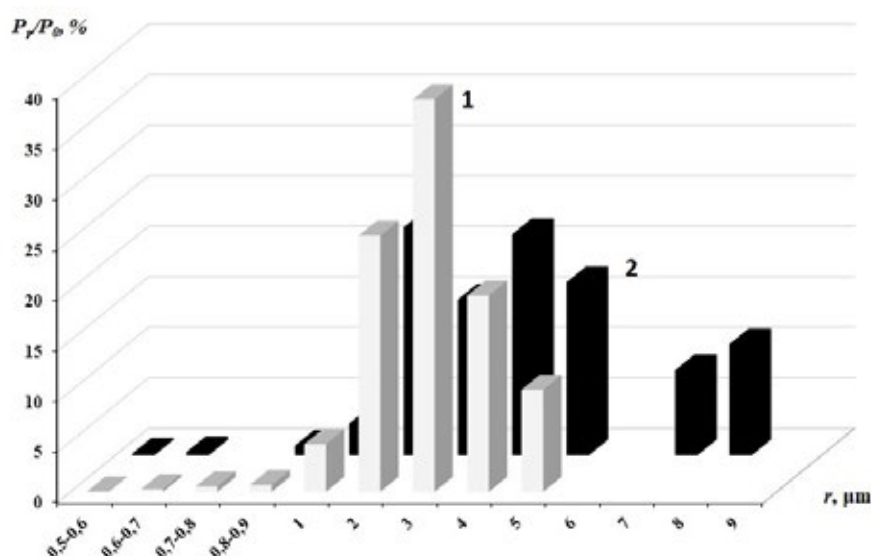


**Fig. 3.** Macropore fractions  $P_r$  of different radii  $r$  of their total area  $P_0$  on the surface of the MK-40 membrane with the particle size of the ion exchange resin of  $< 20 \mu\text{m}$  (1) and  $56\text{--}71 \mu\text{m}$  (2)

the ion exchange resin corresponded to a change in the structural characteristics of their surface. The moisture content ( $W$ ) and the thickness ( $l$ ) of the membranes fell with a decrease in their surface macroporosity and an increase in the particle size of the ion-exchanger. However, an inconsistent decrease in the density of membranes by 6% was also established. Typically, the change in the density and porosity of materials is of an antibatic nature. The exchange capacity ( $Q$ ) of the membranes did not depend significantly on the particle size of the ion exchange resin due to its equal content by weight per dry sample.

In previous studies [5] of Ralex sulfonated ion exchange membranes (MEGA a.s., Czech Republic), we established that the fraction and size of pores on their surface grew with an increase in the particle size of the ion exchange resin in the grinding. In the case of the studied experimental MK-40 membranes, an increase in the specified resin particle size resulted in a decrease in the macroporosity and an increase in the size of macropores.

#### 4. Conclusions

We studied the influence of the particle size of the sulfonated ion exchange resin on the physicochemical properties and structural characteristics of the surface of the MK-40 heterogeneous membrane. The change in the basic physicochemical properties of the studied membranes with an increase in the particle size of the ion exchange resin corresponded to a change in the structural characteristics of their surface.

However, a comparative analysis of the experimental results requires an explanation of the following facts established during the study: 1. a decrease in the weighted average radius of the ion exchanger sections on the surface of the membranes with an increase in the preset particle size of the ion exchange resin; 2. the presence of small ion-exchangers with a radius of  $R < 10 \mu\text{m}$  and the absence of large ion-exchangers with a radius of  $R < 20 \mu\text{m}$  in the samples of membranes with a particle size of 56–71  $\mu\text{m}$ ; 3. the symbatic nature of the change in the surface macroporosity and density of the membranes with an increase in the particle size of the ion-exchanger. To better understand and explain the identified changes in surface morphology and the physicochemical

properties of the membranes, it is necessary to further study their internal phase.

#### Contribution of the authors

The authors contributed equally to this article.

#### Conflict of interests

The authors declare that they have no known competing financial interests or personal relationships that could have influenced the work reported in this paper.

#### References

1. Strathmann H., Grabowski A., Eigenberger G. Ion-exchange membranes in the chemical process industry. *Industrial & Engineering Chemistry Research*. 2013;52: 10364–10379. <https://doi.org/10.1021/ie4002102>
2. Stenina I., Golubenko D., Nikonenko V., Yaroslavtsev A. Selectivity of transport processes in ion-exchange membranes: Relationship with the structure and methods for its improvement. *International Journal of Molecular Sciences*. 2020;21: 5517. <https://doi.org/10.3390/ijms21155517>
3. Solonchenko K., Kirichenko A., Kirichenko K. Stability of ion exchange membranes in electro dialysis. *Membranes*. 2023;13: 52. <https://doi.org/10.3390/membranes13010052>
4. Butylskii D. Y., Troitskiy V. A., Ponomar M. A., Moroz I. A., Sabbatovskiy K. G., Sharafan M. V. Efficient anion-exchange membranes with anti-scaling properties obtained by surface modification of commercial membranes using a polyquaternium-22. *Membranes*. 2022;12: 1065. <https://doi.org/10.3390/membranes12111065>
5. Akberova E. M., Vasil'eva V. I., Zabolotsky V. I., Novak L. A study of ralex membrane morphology by SEM. *Membranes*. 2019;9: 169. <https://doi.org/10.3390/membranes9120169>
6. Rubinstein I., Staude E., Kedem O. Role of the membrane surface in concentration polarization at ion-exchange membrane. *Desalination*. 1988;69: 101–114. [https://doi.org/10.1016/0011-9164\(88\)80013-4](https://doi.org/10.1016/0011-9164(88)80013-4)
7. Nikonenko V. V., Mareev S. A., Pis'menskaya N. D., Kovalenko A. V., Urtenov M. K., Uzdenova A. M., Pourcelly G. Effect of electroconvection and its use in intensifying the mass transfer in electro dialysis (review). *Russian Journal of Electrochemistry*. 2017;53(10): 1122–1144. <https://doi.org/10.1134/S1023193517090099>
8. Akberova E. M., Vasil'eva V. I. Effect of the resin content in cation-exchange membranes on development of electroconvection. *Electrochemistry Communications*. 2020;111: 106659. <https://doi.org/10.1016/j.elecom.2020.106659>

9. Berezina N. P., Kononenko N. A., Dvorkina G. A., Sheldeshov N. V. *Physico-chemical properties of ion-exchange materials\**. Krasnodar: Kuban State University Publ; 1999. 82 p. (In Russ.)

10. Reed S. J. B. *Electron probe microanalysis and scanning electron microscopy in geology*. Cambridge: Cambridge University Press; 2005. 231 p.

11. Sirota E. A., Kranina N. A., Vasil'eva V. I., Malykhyn M. D., Selemenev V. F. Development and experimental approbation of program complex for definition of a share ion-spending surfaces of heterogeneous membranes according to raster electronic microscopy. *Proceedings of Voronezh State University. Series: Chemistry. Biology. Pharmacy*. 2011;2: 53–59. (In Russ., abstract in Eng.). Available at: <https://www.elibrary.ru/item.asp?id=17111009>

\* Translated by authors of the article

### Information about the authors

*Svetlana V. Dobryden*, 2nd year master's student of the Department of Analytical Chemistry, Voronezh State University (Voronezh, Russian Federation).

<https://orcid.org/0009-0008-5393-2756>  
dobryden\_00@mail.ru

*Elmara M. Akberova*, Cand. Sci. (Chem.), a lead engineer at the Department of Analytical Chemistry, Voronezh State University (Voronezh, Russian Federation).

<https://orcid.org/0000-0003-3461-7335>  
elmara\_09@inbox.ru

*Danila R. Mamonov*, 4th year student of the Chemical Faculty, Voronezh State University (Voronezh, Russian Federation).

<https://orcid.org/0009-0008-9418-1653>  
mamonov\_danila02@mail.ru

*Yana R. Bespalova*, 3rd year student of the Chemical Faculty, Voronezh State University (Voronezh, Russian Federation).

<https://orcid.org/0009-0006-4002-0411>  
bespalova@chem.vsu.ru

*Vera I. Vasil'eva*, Dr. Sci. (Chem.), Professor at the Department of Analytical Chemistry, Voronezh State University (Voronezh, Russian Federation).

<https://orcid.org/0000-0003-2739-302X>  
viv155@mail.ru

Received 29.11.2023; approved after reviewing 11.12.2023; accepted for publication 15.12.2023; published online 25.06.2024.

Translated by Irina Charychanskaya



## Short communication

Short communication

<https://doi.org/10.17308/kcmf.2024.26/12071> **$1/f^2$  noise as a precursor of structural reconstructions near the melting point of crystalline materials with different types of chemical bonds**E. S. Mashkina Voronezh State University,  
1 Universitetskaya pl., Voronezh 394018, Russian Federation**Abstract**

Transition phenomena near the melting point (premelting effect) are fundamental processes occurring in materials with different types of chemical bonding. At  $T \geq 0.8T_m$ , there is a fluctuating heat release. The analysis of fluctuation processes allows obtaining information about dynamic reconstructions in various subsystems and interconnections between them within the system. The purpose of this work was to study the spectral characteristics of heat fluctuations in stationary modes of premelting materials with ionic, covalent, and metallic chemical bonds (KCl, Ge, Cu, and Sb) and to determine the type of the fluctuation process using the Hurst parameter.

The spectral characteristics of heat fluctuations in stationary modes of pre-melting KCl, Ge, Cu, and Sb at  $T \sim 0.9T_m$  were determined by wavelet analysis. This method allows analyzing the behavior of complex systems at critical points in order to identify certain correlations and development trends in them.


The study showed that in the premelting region, the frequency spectrum of heat fluctuations was characteristic of  $1/f^2$  noise or nonlinear Brownian noise, which is a precursor of structural reconstructions during phase transitions. The type of fluctuation processes in the premelting region of KCl, Ge, Cu, and Sb was determined using the Hurst parameter ( $H$ ). It was shown that in stationary modes of premelting  $H > 0.5$ . Consequently, the previous trend of the process dynamics was very likely to develop in the same direction. However, with a decrease in the energy of the chemical bond  $H \rightarrow 0.5$ , which indicated a decrease in the stability of the system and a likely change in the development trend for the structural reconstructions in the premelting transition region.

Thus, near the melting point, there are unstable dynamic states, which are precursors to structural changes in the system, which have certain developmental trends. This should be taken into account when calculating the stability and reliability of materials and systems.

**Keywords:** Premelting, Fluctuations, Wavelet analysis,  $1/f^2$  noise, Hurst parameter, Structural reconstructions

**For citation:** Mashkina E. S.  $1/f^2$  noise as a precursor of structural reconstructions near the melting point of crystalline materials with different types of chemical bonds. *Condensed Matter and Interphases*. 2024;26(2): 362–366. <https://doi.org/https://doi.org/10.17308/kcmf.2024.26/12071>

**Для цитирования:** Машкина Е. С.  $1/f^2$  шум как предвестник структурных перестроек вблизи точки плавления кристаллических веществ с различным типом химической связи. *Конденсированные среды и межфазные границы*. 2024;26(2): 362–366. <https://doi.org/https://doi.org/10.17308/kcmf.2024.26/12071>

 Ekaterina S. Mashkina, e-mail: [me22-1@phys.vsu.ru](mailto:me22-1@phys.vsu.ru)

© Mashkina E. S., 2024



The content is available under Creative Commons Attribution 4.0 License.



## 1. Introduction

There is a large amount of data on  $1/f^\beta$  noise in various complex systems [1–3]. Fluctuations occurring in the transition region during the first order phase transitions are especially interesting since such noise, in contrast to uniform distribution, predetermines certain correlations associated with the occurrence of a spatial or temporal ordering similar to a phase transition. Fluctuating precursors manifest themselves in the form of anomalous behavior of various macroscopic parameters: physical, electrophysical, and structural [4, 5]. This indicates that at certain critical points (bifurcation points) there is a loss of stability of the previous state accompanied by the emergence of dynamic dissipative structures. In this case, the system becomes sensitive to small changes in the initial conditions and fluctuations begin to play an important role. This phenomenon is known as “ordering through fluctuations” [6]. Thus, fluctuating precursors during phase transitions require specifying the degree of spatio-temporal localizations in the system and identifying new information about the behavior of the system in these nonequilibrium conditions.

The purpose of this paper is to study the spectral characteristics of heat fluctuations in stationary modes of pre-melting materials with different types of chemical bonding and to determine the type of the fluctuation process using the Hurst parameter.

## 2. Experimental

Our earlier studies of melting of materials with ionic, covalent, and metallic chemical bonds conducted by the DTA method at  $T \geq 0.8T_m$  revealed temperature-temporal regions of premelting fluctuation phases [7].

The experiments were carried out using materials with different types of chemical bonds without phase transformations before and after the melting point: KCl, Ge, Cu, and Sb. Isothermal endurance (stationary mode) was carried out at  $T^* \sim 0.9T_m$ . The time of isothermal endurance was 35 minutes. What is more, the fluctuation state remained for a long time with slow relaxation to equilibrium, which is characteristic of dissipative processes.

For the spectral analysis of fluctuation processes and parameterization of the premelting phases of materials with different types of chemical bonding in stationary modes, we used the method of continuous wavelet transform [8]. Spectral analysis of fluctuation signals was carried out using the MatLab software environment with the Symlet8 basic function.

## 3. Results and discussion

The study considered the impact of the chemical bonding on the spectral characteristics of heat fluctuations in the premelting region of KCl, Ge, Cu, and Sb. Heat fluctuations in stationary modes are most interesting in terms of obtaining information on the regularities of the evolution of dynamic transition states during melting since in these premelting modes there is a long-term sequence of correlated fluctuation bursts producing nonlinear Brownian noise. What is more, such spectral parameters as the self-similarity coefficient ( $\beta$ ) and the intensity of heat fluctuations provide information on the dynamics of the formation of transient phases.

As an example, we considered the wavelet transform pattern  $W(a,b)$  of the premelting effect of Cu in the stationary mode at  $T^* = 1,221.8$  K (Fig. 1). In this pattern, a hierarchical self-similar structure of local extrema was visible at different scales. The branching of the local extrema pattern corresponded to the rescaling of fluctuations and the transition to another level of the process. In general, this pattern of wavelet transform of heat fluctuations in KCl, Ge, and Sb, as well as Cu, is characteristic of signals of nonlinear Brownian noise or  $1/f$  noise $^\beta$ , which indicates correlations in the premelting transition regions. [9]. This was also confirmed by the statistical, correlation, and Fourier analysis which were carried out in [10]. They showed that fluctuation processes in the premelting region are random processes with normally distributed correlated increments.

The values of the spectrum coefficient  $\beta$  of heat fluctuations of transient processes during KCl, Ge, Cu, and Sb melting at isothermal endurance are given in Table 1. The self-similarity coefficient  $\beta \sim 2$  indicated that dissipative processes in the transition region during melting were of the same physical nature. It also indicated the generic

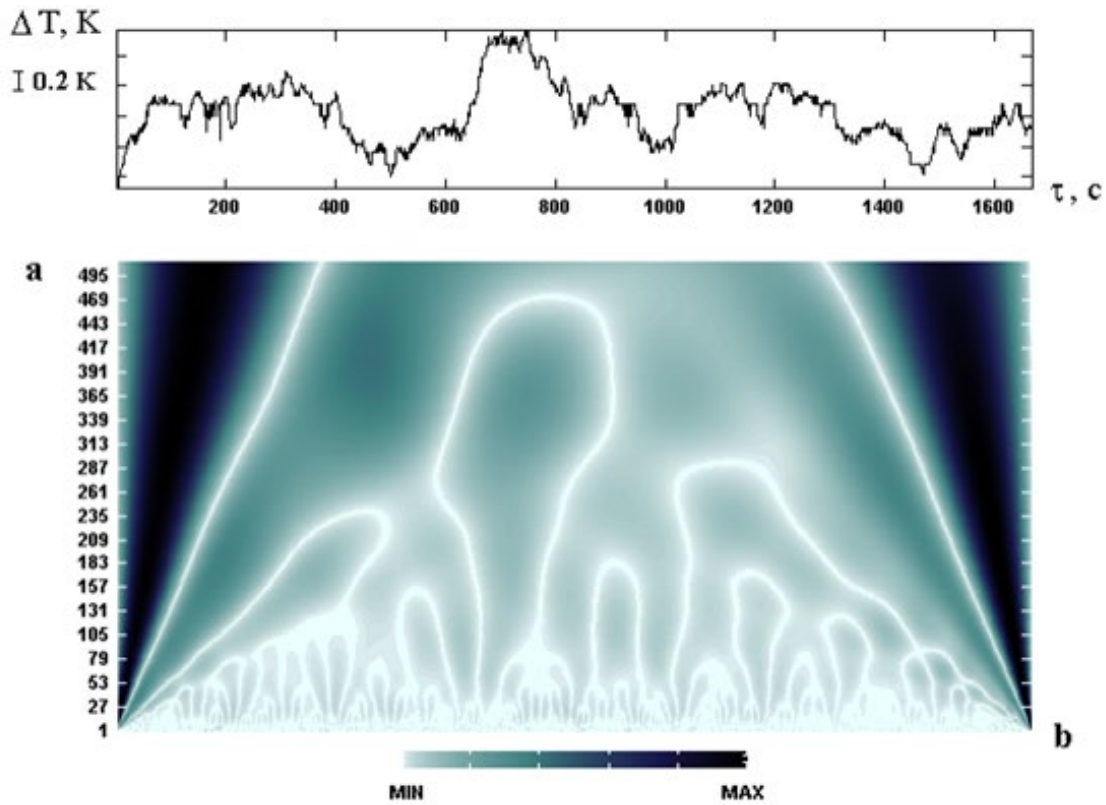


Fig. 1. DTA curve and wavelet transform of the fluctuation process of premelting of Cu ( $T^* = 1,221.8$  K)

**Table 1.** Parameters of transient processes of premelting of KCl, Ge, Cu, and Sb in a stationary mode and the energy of the chemical bond

	$T^*, K$	$\beta$	$H$	$\Delta E, kJ/mol$
KCl	940	2.1	0.58	423.2
Ge	1180	2.2	0.56	327.6
Cu	1220	2	0.55	306.7
Sb	814	2.1	0.52	165.8

nature of transient processes of premelting of crystalline materials with different types of chemical bonding. This indirectly reflected the occurrence of structural reconstructions in the materials in the premelting phase.

The energy spectrum  $E_w(a)$  of heat fluctuations of transient processes of premelting KCl, Ge, Cu, and Sb in stationary modes is shown in Fig. 2. The analysis of the energy spectrum showed that with a decrease in the energy of the chemical bond from KCl to Sb, there was a decrease in the intensity of the fluctuation process in the pretransition region. The change in the intensity of heat fluctuations reflected the varying degree

of correlation in the system. For example, a low value of the energy of chemical bond ( $\Delta E$ ) of Sb apparently resulted in emergence of long-time correlation bonds in the dynamic system. However, KCl, which had the largest energy of chemical bond among the studied group of materials, was characterized by the occurrence of short-lived correlation states.

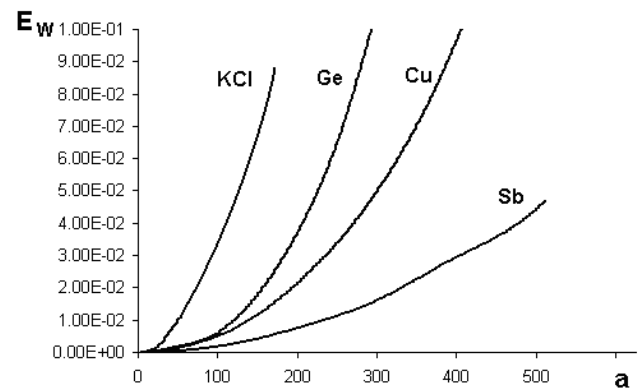


Fig. 2. Energy spectra of heat fluctuations in the pre-melting phase of KCl, Ge, Cu, and Sb in a stationary mode

Evaluation of the Hurst parameter allowed identifying certain hidden patterns or so-called trends in the fluctuation process in the premelting region. At a value of  $H > 0.5$ , the previous trend for the system transformation was highly likely to continue in the same direction. If  $H < 0.5$ , the direction of the trend was to change, while at  $H = 0.5$  it was difficult to determine the direction of the trend [11, 12]. The Hurst parameter was calculated using RS-analysis.

For all types of the studied materials, the Hurst parameter was  $H > 0.5$  (Table 1). In our case, the value of  $H > 0.5$  indicated a persistent behavior of correlations in the system, i.e. the trend for the character of changes of the process persisted. However, a decrease in the energy of the chemical bond led to a decrease in the stability of the system and an approximation to uncertainty. This correlated with the change in the intensity of the fluctuation process within the premelting region in the series KCl, Ge, Cu, and Sb.

#### 4. Conclusions

Regardless of the type and energy of the chemical bond, the pattern of the wavelet transform of the premelting heat fluctuations of Ge, Sb, and Cu in stationary modes is that characteristic of  $1/f^2$  noise signals (non-linear Brownian noise). Thus, it can be stated that the processes that occur during nonequilibrium phase transitions in materials with ionic, covalent, and metallic chemical bonds have identical energy patterns.

With a decrease in the energy of the chemical bond in the series from KCl to Sb, the intensity of the fluctuation process in the pre-melting phase decreases, which indicates the determining influence of the energy of the chemical bond on the nature of formation and the fluctuation parameters of the premelting transient processes of various crystalline materials.

Evaluation of the chaotic state of fluctuation processes using a stochastic parameter, the Hurst ( $H$ ) parameter, showed that a previous trend for structural reconstructions is not likely to change. Therefore, the analysis of the spectral characteristics of fluctuation processes near the melting point can provide information not only about the state of the system, but also can be used in methods aimed at predicting its evolution.

#### Conflict of interests

The author declares that they has no known competing financial interests or personal relationships that could have influenced the work reported in this paper.

#### References

1. Zhigalskii G. P. *Fluctuations and noises in electronic solid-state devices*. Moscow: Fizmatlit Publ.; 2012. 512 p. (In Russ.)
2. Gerashchenko O. V., Matveev V. A., Pleshonov N. K., Bairamukov V. Yu. Electrical resistance and  $1/f$ -fluctuations in thin titanium films. *FTT (Physiscs of the Solis State)*. 2014;56(7):1443-1448. (In Russ.). Available at: <https://journals.ioffe.ru/articles/viewPDF/26940>
3. Pavlov A. N., Pavlova O. N., Koronovskii A. A. Jr. A modified fluctuation analysis of nonstationary processes. *Technical Physics Letters*. 2020;46: 299–302. <https://doi.org/10.1134/S1063785020030281>
4. Shibkov A. A. Gasanov M. F., Zolotov A. E., ... Kochegarov S. S. Electrochemical emission during the straining and destruction of an aluminum–magnesium alloy in an aqueous medium. *Technical Physics*. 2020;65(1): 78–86. <https://doi.org/10.1134/s1063784220010247>
5. Koposov G. D., Bardug D. Yu. Analysis of premelting of ice in moisture-containing disperse media. *Pisma v ZhTF (Technical Physics Letters)*. 2007;33(14): 80–86. (In Russ). Available at: <https://journals.ioffe.ru/articles/viewPDF/13605>
6. Malinetsky G. G., Potapov A. B. *Nonlinear dynamics and chaos: Basic concepts*. Moscow: URSS Publ.; 2018. 240 p. (In Russ.)
7. Bityutskaya L. A., Mashkina E. S. System of thermodynamic parameters of the transient processes under melting of crystalline substances. *Phase Transition*. 2000;71: 317–330. <https://doi.org/10.1080/01411590008209312>
8. Smolentsev N. K. *Fundamentals of wavelet theory. Wavelets in MATLAB*. Moscow: DMK Press; 2014. 628 p. (In Russ).
9. Mashkina E. S. Spectral analysis of heat fl uctuations in KI transient premelting states. *Condensed Matter and Interphases*. 2020;22(2): 238–244. <https://doi.org/10.17308/kcmf.2020.22/2837>
10. Bityutskaya L. A., Selezvev G. D. Thermal flicker noise in dissipative pre-melting processes\*. *Physiscs of the Solis State*. 1999;41(9): 1679–1682. (In Russ.). Available at: <https://journals.ioffe.ru/articles/viewPDF/35546>
11. Alfyorova E. A., Lychagin D. V. Relation between the Hurst exponent and the efficiency of self-organization of a deformable system. *Technical Physics*.

2018;(63): 540–545. <https://doi.org/10.1134/S1063784218040035>

12. Chen B. B., Imashev S. A. Evaluation of Hurst parameter on energetic spectrum based on wavelet transform. *Vestnik KRSU*. 2007;7(8): 65–75. (In Russ., abstract in Eng.). Available at: <https://www.elibrary.ru/item.asp?id=13519890>

*\* Translated by author of the article*

### Information about the authors

*Ekaterina S. Mashkina*, Cand. Sci. (Phys.-Math.), Assistant Professor at Semiconductor Physics Department, Voronezh State University (Voronezh, Russian Federation).

<https://orcid.org/0000-0002-9911-5208>  
me22-1@phys.vsu.ru

*Received 26.03.2024; approved after reviewing 18.04.2024; accepted for publication 15.05.2024; published online 25.06.2024.*

*Translated by Irina Charychanskaya*